Activating molecules and complexes for diagnosis and therapy

Ceri A. Foster

Brasenose College

University of Oxford

A thesis submitted for the degree of

Doctor of Philosophy

in Inorganic Chemistry

October 2025

Under the supervision of: Prof. Stephen Faulkner, Prof. Stuart J. Conway, Prof. Geoffrey Higgins

Abstract

Development of new molecules for cancer imaging, for diagnosis and prognosis evaluation, is crucial to expand the information available to clinicians. The formation of activatable profluorophores is desirable to enable imaging of disease and upregulation of enzymes or biological molecules in certain regions, such as in the presence of hypoxia (low oxygen concentration) in cancerous tissues.

In hypoxic tissue, found in solid tumours, the effects of both chemotherapy and radiotherapy are reduced, therefore selective delivery of a compound which is activated in the presence of both hypoxia and X-ray irradiation is a route to overcome this. Chapter II highlights the design of a series of profluorophores, based on known fluorophores and the tetrafluoroaryl azide group, as proof-of-concept work to determine whether activation of a profluorophore under hypoxia and X-ray irradiation is orthogonal or can be used advantageously in combination. The chapter explores profluorophore design and the poor activation of the novel profluorophores under reductive chemical and enzymatic conditions and X-ray irradiation, highlighting the need for development of new moieties which can be activated at lower, clinically relevant doses of X-ray irradiation to further investigate the orthogonality of activation.

Investigation of lanthanide complexes as imaging agents, due to their advantages over organic fluorophores, is an expanding field and these complexes have utility for both optical imaging and MRI, based on the lanthanide metal employed (Eu, Tb or Gd). Chapter III discusses the synthesis, spectroscopy and activation of complexes which contain ester linkages to common hypoxia-activated groups and highlights the change in luminescence and relaxivity between the profluorophores and known LnDOTA complexes. It is proposed that these complexes release LnDOTA in the presence of chemical and enzymatic reductants *via* a hydrolysis mechanism, therefore they do not exhibit the desired selectivity profile for biological applications and emphasise the need to balance activity and selectivity.

However, these novel probes act as a proof-of-concept for activatable optical imaging and MRI complexes and give insight into the design considerations needed for their future development.

Chapter IV builds on the drawbacks from chapter III, involving the design of leucine and alkyl appended azobenzene bimetallic lanthanide complexes, aiming for improved cell permeability and emission intensity for biological application of reductively activated lanthanide complexes *in vivo*. However, derivatised azobenzene bimetallic complexes were synthetically challenging to make and further work is needed to expand on approaches to overcome the problem of cell permeability.

Chapter V summarises the work carried out in this thesis and chapter VI describes the experimental synthetic and assay procedures utilised to obtain the results in chapters II-IV.

Acknowledgements

My PhD has been highly collaborative and therefore this work wouldn't have been possible without the input and support of many people.

Firstly, thank you to my supervisors Professor Stuart Conway, Professor Steve Faulkner and Professor Geoffrey Higgins. Stuart and Steve, thank you for both accepting me into your groups when my project had to change in the first few months of my degree and for making me constantly question whether to classify myself as an organic or inorganic chemist – I've decided now that I'm both rather than neither! Stuart, thank you for assisting me in becoming the meticulous, organised and hard-working chemist that I am today, I learned a lot during my time in your lab. Steve, thank you for giving me your knowledge about lanthanides and spectroscopy, always making time for a discussion and for your endless support, without which I would not have gained some confidence in my scientific abilities (I'm still working on it!). Geoff, thank you for your support in all things X-ray related and your willingness to help, despite not making the X-ray activatable probes that we had aimed for at the start.

As one of the final members of the Conway group in Oxford, there are a lot of previous members to thank! Darius, Patrick and Katrina, thank you for your advice and assistance in the lab. Glen, I'm grateful for our discussions about Scottish music and board games. Bernie, thank you for the great cake. Jenny, I always appreciated our discussions about athletics as well as your initial chemistry advice when I joined the lab. As fellow members of the redox subgroup, particular thanks to Marta, Max and Sophie for your advice, inspiration to run many reactions and columns at once and for your understanding of hypoxia and cancer biology. To the final members of G12, Alistair, Oli, Michael, Harriet and Antoine, thank you for your assistance in sorting out the labs but also the moral support over the years. Alistair, you never fail to amaze me with your knowledge of relevant literature and willingness to learn about my lanthanide project. Oli, thank you for all of your

HPLC help and general lab advice. Michael, I will always remember our many trips to Pieminister and the accompanying discussions. Harriet, thank you for being my initial desk buddy and putting up with endless questions and for generally being a great sounding board for ideas and providing advice, both in chemistry and in life in general. Keefe and Ada, as the fellow final PhD students from the Conway group in Oxford (despite one of you being in LA and one at the Kennedy), thank you for being on this journey together and your positivity. Finally, Antoine I am forever grateful for your continued lab advice and for boosting my confidence when needed, I have gained so much working alongside you over the years. I was very happy that you joined me with the move to G10 for a few months, after being the final members of G12 together, following our joint move from G11. I will cherish our conversations in French and our many discussions over the years, from chemistry to tennis and wine.

Thank you to all of the members of the Faulkner group for welcoming me, particularly those mentioned here and especially during the big Conway lab move/closure in the summer of 2024. Dani and Debs, thank you for your introduction to lanthanides and training using the spectrometers and your assistance in the activatable lanthanide probes project. Debs, your continued support and optimism was crucial for publishing my first author paper! Clara, Marie, Jevon and Shitong, thanks for your advice from the start of my PhD and the positive vibes you brought to S9 and upon your visits to the ground floor. Euan, thank you for your assistance with the paper and for all of our chemistry discussions. Charlie, thank you for your advice as part of the redox team, introducing me to good beer and the late-night chats in Stuttgart. Charlotte and Jonny, thank you for being in G10 with me, your company and discussion helped me get through the final months of the PhD. Andy, thanks for your assistance with the lyophiliser on my many trips up to S9 and listening to my rants about frustrating chemistry. To the G10 part II students, particularly Jazz and Asees, thank you for increasing my own confidence in chemistry (as I hope I have yours), distracting me from my own chemistry problems and trusting me to help supervise you in the lab. Finally, Matt

thank you for your general support and belief in me over the past two years, your photophysics help is truly appreciated and I'm sorry that you've had to assist with so many lab moves but you've made G10 and S9 wonderful labs to work in. I'm eternally grateful to you for giving up your time to help me with measurements and with feedback, and for assisting me in organising group pub trips.

From other lab groups, thank you to the remaining members of the redox team who have helped me throughout my PhD (whether that be inside the lab or outside), Ester, Lina, Louise and Jie. Thank you to Gonzalo, Rathi, Kylie, Daria and Max for helping to test my compounds and for useful discussions. Kel, your advice and support has been appreciated since the first day of the OxICFM taught course.

Thank you to Steve at Vertex Pharmaceuticals for hosting me for three months and allowing me insight into the industry, and the rest of the high-throughput team and the other chemists for making my placement so enjoyable.

Outside of the lab, thanks to all members of the Oxford Scout and Guide Group and 1st Botley Brownies and Rainbows for providing opportunities to escape thinking about my PhD for a few hours each week. Jean, Harriet, Charlotte and Amy, thank you for being there through the highs and lows of the PhD (and life), for making me believe in myself as a Brownie leader and for also allowing me to have Brownie meetings where I could switch-off and do some arts and crafts for an hour and a half with the girls.

Paul and Gabe, thank you for being there for me in my first year and allowing me to live with you and have the stability of some familiar faces to come home to. Ellie, it was wonderful having another familiar face in Oxford for a couple of years and I appreciated our sporadic coffee/lunch/dinner catch-ups. Ariel, between us we've changed a lot over the past four years but I wouldn't be where I am now without your constant support, without you taking on the majority of cooking and cleaning when I was stressed, the endless supply of baked goods and without you reminding me to take needed time off. Georgia and Hobie,

thank you for helping me to worry less and for distracting me when needed throughout thesis writing, viva preparation and corrections.

Finally, to my parents for the trips away to reduce my stress and for unconditionally supporting me in everything that I do, thank you. I appreciate everything you've done for me over the years.

Declaration

The work in this thesis was carried out during my time as a DPhil student as part of the OxICFM CDT, within the Department of Chemistry, University of Oxford, under the supervision of Prof. Stuart J. Conway and Prof. Stephen Faulkner, and the Department of Oncology, under the supervision of Prof. Geoffrey Higgins. Contributions by others to this work are clearly noted where appropriate. This work was funded by the EPSRC Centre for Doctoral Training in Inorganic Chemistry for Future Manufacturing (OxICFM), EP/S023828/1.

Previously Published Work

LnDOTA Releasing Probes for Luminescence and Magnetic Resonance Imaging

C. A. Foster, D. Sneddon, L. Hacker, E. T. Sarson, M. Robertson, D. Sokolova, L. A. W. Martin, M. F. Allen, A. Khrapichev, K. A. Vincent, E. M. Hammond, S. J. Conway and S. Faulkner, *Inorg. Chem.*, 2025, **64**, 13, 6640-6647

Oral Presentations

"Activating molecules and complexes for diagnosis and therapy"

1. OxICFM CDT Science Day, University of Oxford, June 2025

Poster Presentations

"Activatable lanthanide complexes for luminescence and MRI"

1. ECR MASC, University of Oxford, July 2025
2. ISMSC, Kyoto, Japan, May 2025
3. Terrae Rarae, University of Stuttgart, Japan, September 2024

"Hypoxia-activated lanthanide complexes for luminescence and MRI"

1. European Molecular Imaging Meeting, Porto, Portugal, March 2024

"Reductive activation of azido compounds for imaging and therapy"

1. OxICFM CDT Science Day, University of Oxford, July 2023
2. OxICFM CDT Science Day, University of Oxford, July 2022

Abbreviations

Abs	absorbance
Ac	acetyl
Ac_2O	acetic anhydride
AcOH	acetic acid
ADME	absorption, distribution, metabolism and elimination
APN	aminopeptidase N
ar	aryl
Arg	arginine
Asp	aspartyl
Azo	azobenzene
BET	back energy transfer
Bn	benzyl
Boc	*tert*-butyloxycarbonyl
br	broad
CBS	cystathionine-ß-synthase
Cbz	benzyloxycarbonyl
CDI	1'-carbonyldiimidazole
CEST	chemical exchange saturation transfer
CNS	central nervous system
COSY	correlation spectroscopy
CPP	cell penetrating peptide
cRGD	cyclic Arg-Gly-Asp
CT	computed tomography
CV	cyclic voltammetry
cyclen	1,4,7,10-tetraazacyclododecane
CYP	cytochrome P450
d	doublet
DCC	*N,N'*-dicyclohexylcarbodiimide
DCM	dicyanomethylene (dye)
DCM-OH	(*E*)-2-(3-(4-hydroxystyryl)-4-oxonaphthalen-1(4*H*)-ylidene)malononitrile
DE	direct excitation
dec.	decomposes
DIPEA	*N,N*-diisopropylethylamine
DMAP	4-dimethylaminopyridine
DMEM	Dulbecco's Modified Eagle Medium
DMSO	dimethyl sulfoxide
DMF	*N,N*-dimethylformamide
DNA	deoxyribonucleic acid
DO2A	1,4,7,10-tetraazacyclododecane-1,7-diacetic acid
DO3A	1,4,7,10-tetraazacyclododecane-1,4,7-triacetic acid
DOTA	1,4,7,10-tetraazacyclododecane-1,4,7,10-tetraacetic acid
DOTAM	1,4,7,10-tetrakis(carbamoylmethyl)-1,4,7,10-tetraazacyclododecane
DTPA	diethylenetriaminepentaacetic acid
EDC	1-ethyl-3-(3-dimethylaminopropyl)carbodiimide
EF5	2-(2-nitro-1H-imidazol-1-yl)-N-(2,2,3,3,3-pentafluoropropyl)acetamide
EI	electron ionisation
eq.	equivalents

ER	endoplasmic reticulum
ESI	electrospray ionisation
ET	energy transfer
Et	ethyl
Et_2O	diethyl ether
EtOAc	ethyl acetate
EtOH	ethanol
F	fluorescence
FA	formic acid
FBS	fetal bovine serum
FcMeOH	ferrocenemethanol
FDA	United States food and drug administration
FLIM	fluorescence lifetime imaging microscopy
FMISO	1H-1-(3-fluoro-2-hydroxypropyl)-2-nitroimidazole
FMN	flavin mononucleotide
Fmoc	9-fluorenylmethyloxycarbonyl
fMRI	functional MRI
FRET	Förster resonance energy transfer
GBCA	gadolinium-based contrast agent
Gly	glycine
GSH	glutathione
h	hours
HBTU	*N,N,N′,N′*-Tetramethyl-O-(1H-benzotriazol-1-yl)uronium hexafluorophosphate
HMBC	heteronuclear multiple bond correlation spectroscopy
HMTA	hexamethylenetetramine
HOBt	1-hydroxybenzotriazole
HPLC	high-performance liquid chromatography
HRMS	high resolution mass spectrometry
HSA	human serum albumin
HSQC	heteronuclear single quantum coherence spectroscopy
Hyd-1	hydrogenase 1
IC_{50}	half-maximal (50%) inhibitory concentration
ICP-MS	inductively coupled plasma mass spectrometry
ICT	intramolecular charge transfer
IPA	isopropanol
IQ	indolequinone
IR	infrared (spectroscopy)
ISC	inter-system crossing
J	total angular momentum quantum number
J	coupling constant
KDAC	lysine deacetylase
LAP	leucine aminopeptidase
LAT	L-type amino acid transporter
LAP	leucine aminopeptidase
LCMS	liquid chromatography mass spectrometry
Leu	leucine
lit.	literature value
Ln	lanthanide
log*K*	stability constant
LRMS	low resolution mass spectrometry
Lys	lysine
m	multiplet

Me	methyl
MeCN	acetonitrile
MES	2-(N-morpholino)ethanesulfonic acid
MeOH	methanol
min	minutes
m.p.	melting point
MR	magnetic resonance
MRI	magnetic resonance imaging
MRS	magnetic resonance spectroscopy
MS	mass spectrometry
MTT (assay)	3-(4,5-dimethylthiazol-2-yl)-2,5-diphenyltetrazolium bromide
NADH	nicotinamide adenine dinucleotide
NADPH	nicotinamide adenine dinucleotide phosphate
NB	nitrobenzyl (4-nitrobenzyl)
NBS	*N*-bromosuccinimide
NHE	normal hydrogen electrode
NI	nitroimidazole (1-methyl-2-nitroimidazole)
NIR	near-infrared
NMR	nuclear magnetic resonance
NOTA	1,4,7-triazacyclononane-1,4,7-triacetic acid
NTR	nitroreductase
NR	non-radiative
P	phosphorescence
PARACEST	paramagnetic chemical exchange saturation transfer
PBS	phosphate buffered saline
PDT	photodynamic therapy
PE	petroleum ether
PEG	polyethylene glycol
PeT	photoinduced electron transfer
PET	positron emission tomography
PFI	property forecast index
pH	potential of hydrogen
pHLIP	pH low insertion peptide
PLIM	phosphorescence lifetime imaging microscopy
PLQY	photoluminescence quantum yield
ppm	parts per million
PSS	photostationary state
q	number of water molecules in the inner-coordination sphere
QY	quantum yield
ROS	reactive oxygen species
R_f	retention factor
R_t	retention time
rt	room temperature
s	singlet
SABR	stereotactic ablative radiotherapy
SAP	square antiprismatic
S-DCM-OH	(*E*)-2-(3-(4-hydroxystyryl)-4-thioxonaphthalen-1(4*H*)-ylidene)malononitrile
SHE	standard hydrogen electrode
SM	starting material
S_NAr	nucleophilic aromatic substitution
SPECT	single-photon emission computed tomography
t	triplet

T_1	longitudinal relaxation time
T_2	transverse relaxation time
TASF	tris(dimethylamino)sulfonium difluorotrimethylsilicate
TBAI	tetra-n-butylammonium iodide
TBAF	tetra-n-butylammonium fluoride
TBDMS	*tert*-butyldimethylsilyl
TBDMSCl	*tert*-butylchlorodimethylsilane
TBDPS	*tert*-butyldiphenylsilyl
^{t}Bu	*tert*-butyl
TEA	triethylamine
TFA	trifluoroacetic acid
THF	tetrahydrofuran
TLC	thin layer chromatography
TOF	time of flight
Tris	tris(hydroxymethyl)aminomethane
trityl	triphenylmethyl
TSAP	twisted square antiprismatic
UV	ultraviolet
UV-Vis	ultraviolet-visible spectroscopy
ν_{max}	maximum frequency
Z	nuclear charge

Table of contents

1. Chapter I - Introduction

This thesis explores the behaviour of molecular probes that can be used to investigate biological reductive stress, for cancer imaging and diagnosis purposes. It is focused on the preparation, characterisation and activation of luminescent or MRI active organic and lanthanide-containing compounds that can undergo chemical change in reductive environments, such as those associated with hypoxia.

1.1 Cancer and hypoxia

Statistics shows that 1 in 2 people will be diagnosed with cancer in their lifetime, therefore accurate cancer imaging and diagnosis and effective treatment is crucial. However, developing new tools and translating them to the clinic is a complex process, therefore this has been a large field of research for the last 80 years.[1] One issue with current cancer treatments, such as chemotherapy and radiotherapy, is the poor selectivity, causing side effects for patients. Therefore, many research efforts are focused on developing more selective tools for more accurate and effective diagnosis and therapy.

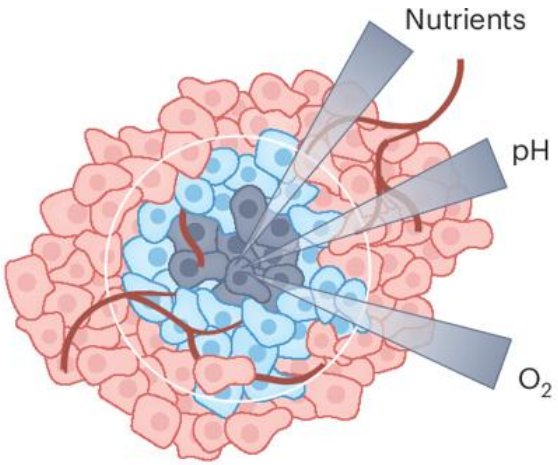

Figure 1.1: A depiction of hypoxia within tumour tissues. Pink represents a normoxic region, blue represents a hypoxic region and black represents a necrotic region (containing dead cells). The triangles show that the nutrient concentration, pH and oxygen concentration decrease towards the centre of the tumour. Figure reproduced with permission.[2]

Hypoxia is defined as low oxygen concentration (typically less than 2% oxygen) in comparison to that present in normal tissues, physoxia (typically 3-7% oxygen), and

atmospheric oxygen pressure, normoxia (21% oxygen).[3, 4] Solid tumours are characteristically hypoxic due to their abnormal vasculature and high rate of tumour growth, with varying severity of hypoxia observed (Figure 1.1). Hypoxic tumours commonly lead to poor patient prognosis as there is increased resistance to chemotherapy and radiotherapy.[3-6] Despite this, current research focuses on the use of hypoxia as a tool for selective activation of prodrugs and profluorophores for cancer diagnosis, imaging and therapy, due to the highly reducing environment not generally present elsewhere in the body and the upregulation of certain enzymes and cofactors.[7]

1.2 Prodrugs and profluorophores

Current research in the field of cancer therapy and imaging focuses on using prodrugs and profluorophores to help overcome selectivity issues. Prodrugs and profluorophores are defined as compounds which contain a known drug or fluorescent moiety and have an activatable functional group attached, to give a compound with overall low cytotoxicity or luminescence. Activation of the activatable group occurs only under certain conditions to release the active cargo (drug or fluorophore). Therefore, prodrugs and profluorophores are more selective than their drug or fluorophore counterparts and are being investigated to overcome issues with side effects of cancer treatment and to improve the diagnostic tools available to clinicians. Common prodrug strategies have included attachment of esters, phosphates, cell-targeting groups or photo-, reduction- and radiation-activated groups to alter the properties (solubility, toxicity and pharmacokinetics) of a drug. The development of prodrugs in early-stage candidate design is becoming more widespread, to overcome predicted problems and reduce overall cost (in comparison to development of a prodrug following a drug failing clinical trials).[8] The same strategies can be employed for the development of profluorophores to increase the information available clinically for diagnosis and prognosis evaluation.[9]

Prodrugs and profluorophores often have the generic structure shown in Figure 1.2a and contain an activatable group, which may be changed or cleaved in the presence of the

stimuli, attached to a known drug or fluorophore. The activatable group may either be directly attached to the known drug or fluorophore, commonly *via* an ether, carbonate or carbamate bond, or be attached using a linker group, which may also be removed following activation. Various exogenous and endogenous stimuli (Figure 1.2b) may be used to cause selective activation of these molecules: changes in pH;[10, 11] the presence of reactive oxygen species (ROS), such as hydrogen peroxide;[12] the presence of enzymes, including the upregulation of reducing enzymes under hypoxia and the presence of hydrolases, phosphatases, transferases and lyases;[13-17] biological reductants, such as thiols including glutathione and NaHS, and cofactors such as NAD(P)H;[18-21] light, including in the visible and ultraviolet range;[22] X-rays;[23] and other stimuli, including heat,[24] magnetic field and ultrasound.[25] The activatable moiety used is designed and chosen based on the stimuli desired, with different stimuli used for different applications and modes of imaging.

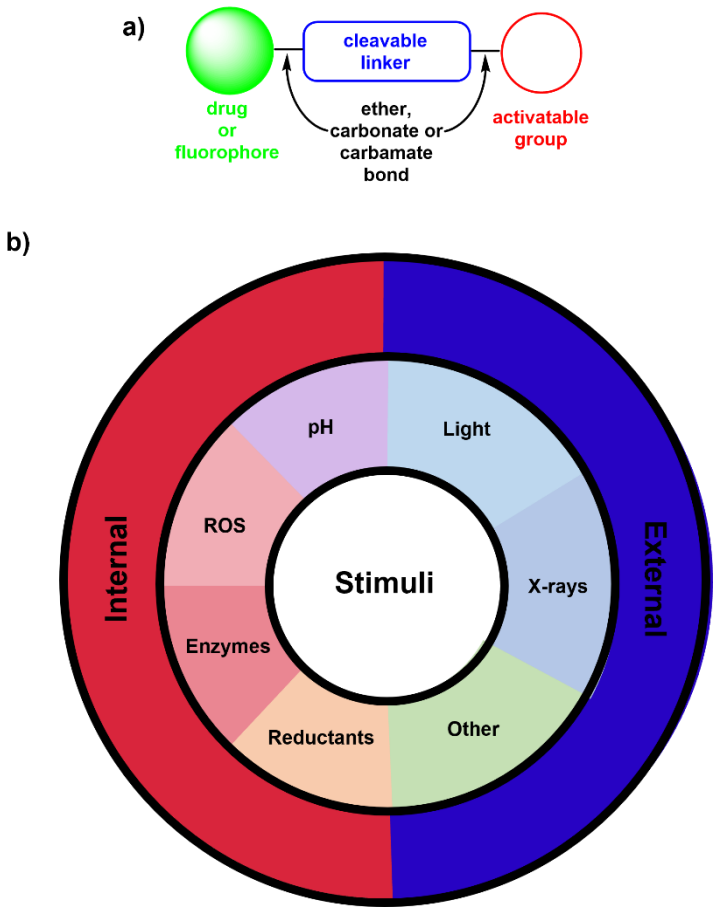

Figure 1.2: a) The generic design of prodrugs and profluorophores. b) The stimuli that may be used to activate prodrugs and profluorophores, sorted into internal and external.

Organic redox activatable groups have been investigated to varying degrees in the literature and include N-oxides,[26] nitroaromatics,[14, 27-31] azides,[13] azobenzenes[32-34] and indolequinones[15, 35, 36] (Figure 1.3a). Nitroaromatics and azobenzenes are the most studied cleavable moieties of those discussed, with the 2-nitroimidazole moiety favoured over the more commonly used 4-nitrobenzyl moiety due to its higher reduction potential[27] and evidence of easier activation.[28] Derivatives of these moieties have biologically relevant reduction potentials, as shown in Figure 1.3b, therefore they can be activated by biological reductants and enzymes.[27, 37-40] Other redox activatable compounds take advantage of redox active metals such as Pt(IV)/Pt(II), Cu(II)/Cu(I), Fe(III)/Fe(II) and Mn(III)/Mn(II).[41-44]

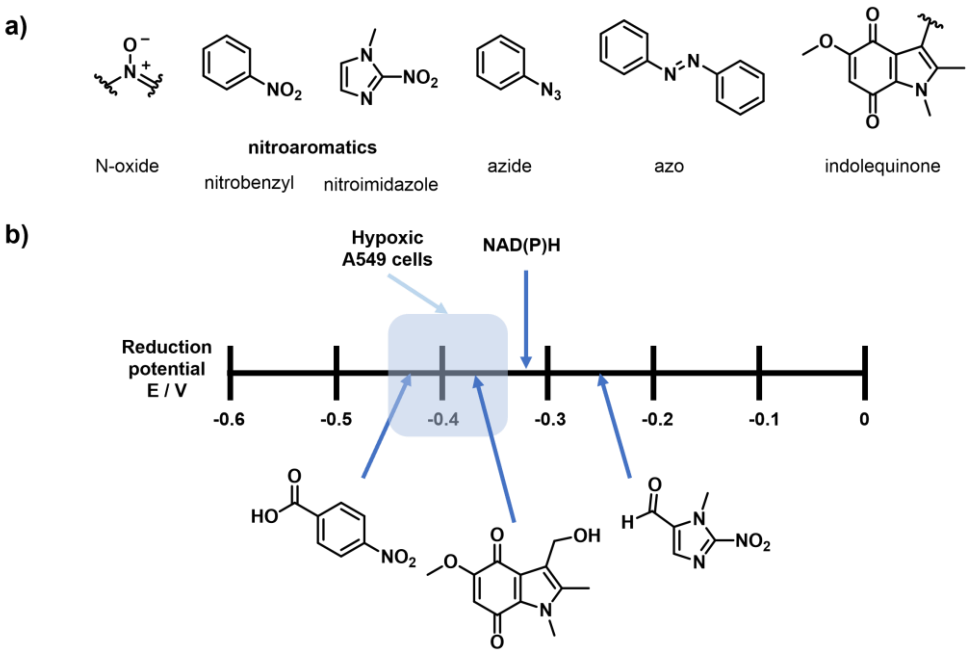

Figure 1.3: a) The activatable moieties commonly employed. b) The reported reduction potentials of some redox activatable moieties and biological reductants/conditions.[27, 37-39]

Figure 1.4 shows the proposed mechanism of activation of a generic nitrobenzyl prodrug, which occurs selectively under hypoxia in the presence of nitroreductases and NAD(P)H, *via* a sequential 6 electron reduction pathway.[27, 29] This occurs by oxidation of the external cofactor NAD(P)H to $NAD(P)^+$, transfer of electrons to the cofactor within the enzyme flavin mononucleotide (FMN) to give the reduced form, which transfers electrons and protons to the nitro substrate. In contrast, N-oxide activation to produce a hydroxy radical occurs *via* one electron reduction;[45] indolequinone activation is proposed to occur by one electron

reduction to the semiquinone intermediate, or two electron reduction to the hydroquinone, and subsequent cleavage;[35] azide activation can occur by photolysis to give the radical anion and subsequent loss of dinitrogen to give the corresponding aniline,[46] or proposed coordination to an enzyme metal centre and loss of dinitrogen;[13] and, azobenzene activation is proposed to occur by 2 sequential 2 electron reductions, *via* the hydrazine intermediate, in the presence of azoreductases.[34] Activatable azide prodrugs and profluorophores are discussed further in section 2.1 and azobenzenes are discussed further in section 4.1.3.

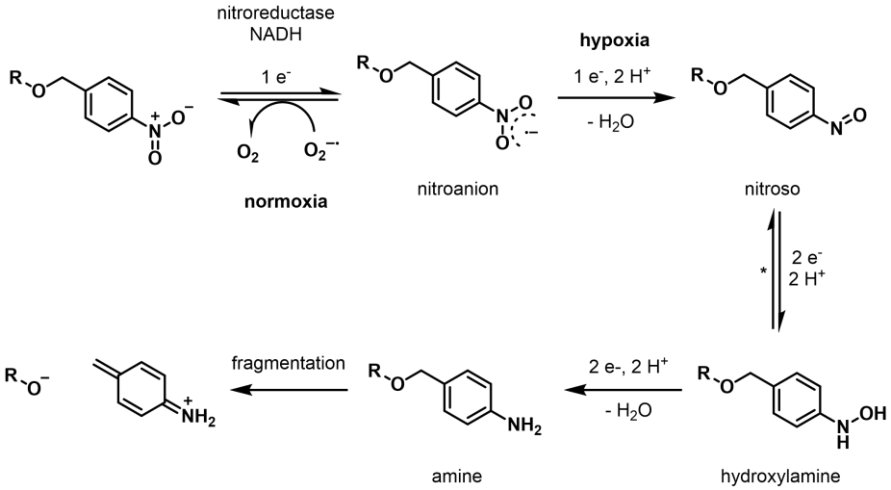

Figure 1.4: The mechanism of activation of nitrobenzyl containing prodrugs and profluorophores, selectively under hypoxia in the presence of nitroreductases, adapted from Calder *et al.*[29] and Denny.[27] * indicates that the nitroso/hydroxylamine couple can be reversible or irreversible.[47] Reduction is mediated by the reduction and oxidation of NAD(P)H/NAD(P)$^+$ and the cofactor within the enzyme, commonally flavin mononucleotide (FMN) (not shown).

Despite some promising phase I and II clinical trials, hypoxia activated prodrugs have failed phase III clinical trials. This is due to difficulty in selecting suitable patients due to the limitations of current methods to detect and accurately characterise the level of hypoxia.[48, 49] Therefore, new tools are needed to accurately assess the level of hypoxia (percentage of oxygen present) using non-invasive methods, over the current gold standard technique of direct oxygen pressure measurement using oxygen electrodes.[49] Recent progress in the field involves the report of indolequinone-based hypoxia activated prodrugs, by Wallabregue *et al.*,[15] which can detect differing levels of hypoxia and can be used in

combination with each other to assess the percentage of oxygen present in spheroids, giving more information than standard staining with pimonidazole.

1.3 Biological imaging modalities

Various imaging modalities are used for disease diagnosis, including optical imaging and magnetic resonance imaging (MRI). Each technique has its advantages and disadvantages and these techniques can be used in combination to gain more information. Common imaging modalities are summarised briefly in Table 1.1.

Table 1.1: A table summarising different imaging modalities used for disease diagnosis and monitoring, adapted from several references.[50-53]

Imaging modality	Main use / other information	Electromagnetic spectrum, molecules and/or isotopes used	Advantages	Disadvantages
Optical imaging	Includes endoscopy, photoacoustic imaging and optical coherence tomography for ophthalmology or imagining heart diseases	Visible/UV light Organic/inorganic fluorophores and profluorophores	Real time imaging Quick Relatively affordable High spatial resolution	Poor penetration depth Cannot do whole body imaging
Magnetic resonance imaging (MRI)	Used to detect bone and CNS tumours, muscle degradation, stroke Detailed imaging of organs, bones, muscles, blood vessels	Radio waves Gd(III) Manganese Iron oxide nanoparticles ^{19}F	Good soft tissue contrast Can do whole body imaging Good penetration depth High spatial resolution	Slower technique Expensive Low sensitivity
MR spectroscopy (MRS) and functional MRI (fMRI)	Used to detect abnormalities and tumours in the brain Can detect a response to therapy and differentiate malignant and benign tissues	Radio waves choline lactate	Can do whole body imaging	Expensive Slower technique
X-ray	Chest X-rays Diagnosing fractures	X-rays	Lower dosage than CT Quick Relatively affordable	Radiation exposure Limited soft tissue contrast
Computed tomography (CT)	3D anatomical imaging Crucial for planning radiotherapy treatment	X-rays Iodine Xenon	Quick High spatial resolution Good penetration depth	Radiation exposure Limited soft tissue contrast
Positron emission spectroscopy (PET)	^{18}F-FDG used for tumour diagnosis and staging	^{11}C ^{18}F ^{64}Cu	Can do whole body imaging Sensitive technique Good penetration depth	Radiation exposure Slower technique Expensive Low spatial resolution
Single-photon emission computed tomography (SPECT)	Used for brain imaging Identifying bone trauma Often combined with CT	^{99m}Tc ^{111}In	Can do whole body imaging Good penetration depth	Radiation exposure Expensive Slower technique
Ultrasound	Pregnancy monitoring Diagnosis Guidance for certain procedures	High frequency sound waves Microbubbles	Real time imaging Quick High spatial resolution Relatively affordable	Cannot do whole body imaging Limited contrast agents

1.4 Lanthanides for biological imaging

The lanthanide elements are the first row of the f-block of the periodic table (lanthanum to lutetium). For lanthanum the atomic electronic configuration is $[Xe]5d^16s^2$, as the 5d orbitals are lower in energy than the 4f orbitals, however as the effective nuclear charge increases (due to poor shielding) across the series the 4f orbitals contract and are stabilised, therefore cerium has the electronic configuration $[Xe]4f^15d^16s^2$ and praseodymium has the configuration $[Xe]4f^36s^2$. From praseodymium the 4f orbital is filled sequentially, except for gadolinium which has the electronic configuration $[Xe]4f^75d^16s^2$ due to the stability of the half-filled 4f subshell, avoiding unfavourable pairing of spins, however the sequential filling continues from terbium ($[Xe]4f^96s^2$).[54] The most common oxidation state for the lanthanides is +3, with the 6s (and 5d, where relevant) electrons removed first as the valence 4f orbitals are 'core-like' due to shielding from the nucleus by the more spatially extended 5s and 5p orbitals.[55] Therefore, Ln(III) ions have the general electronic configuration $[Xe]4f^{n-1}$, where n=1 for lanthanum.[56] The shielding of the 4f orbitals by penetration of the xenon core is key to the chemistry and spectroscopy of the lanthanides, causing the lanthanide contraction (where the radius of the lanthanide ion decreases across the series) and similar properties of the lanthanides.[57]

1.4.1 Coordination chemistry of lanthanides

Free lanthanide ions are toxic to the body. Free Gd^{3+} ions have been shown to cause nephrogenic systemic fibrosis, mediated through formation of insoluble phosphate colloids, in patients with pre-existing kidney problems[58] and free Ln^{3+} ions (such as Eu^{3+} and La^{3+}) are a similar size to Ca^{2+} ions therefore free europium can block calcium channels.[59-61] Due to the issues of free lanthanide ions in the body, the chelate and macrocyclic effects are used advantageously to bind lanthanide ions with high affinity to give kinetically stable lanthanide complexes. The 'core-like' nature of the 4f orbitals leads to poor overlap with ligand orbitals, meaning that crystal-field effects are small, bonding is mostly ionic and non-directional and that the electronic and magnetic properties of the lanthanides are not largely

influenced by the ligand environment.[54] The coordination number of a lanthanide ion (typically 8-12) is largely dominated by steric effects. Commonly used chelating ligands for lanthanide ions (Figure 1.5) include the acyclic DTPA and macrocyclic DOTA, DO3A, DO2A, DOTAM and NOTA. High kinetic stability of these complexes is afforded by the high coordination number and the hard O and N donors.

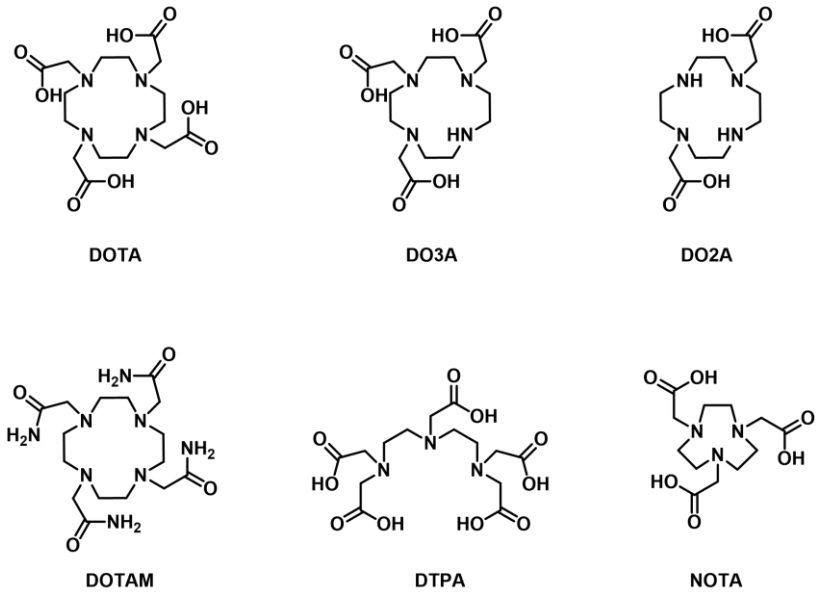

Figure 1.5: The structures of various ligands which have been used for chelating lanthanide ions.

The ligand DOTA is well studied due to the common use of $[GdDOTA]^-$ as an MRI contrast agent (discussed further in section 1.4.3). DOTA is octadentate (8 coordinate), resulting in complexes with high thermodynamic stability and conformational rigidity. X-ray crystal structures of $[LnDOTA]^-$ complexes (Ln = Eu, Gd, Lu, Y) confirm that DOTA is octadentate, with a square-antiprismatic geometry and a ninth axial coordination site above the plane of the four oxygen atoms, commonly filled by a water molecule.[62-64]

DOTA is the parent ligand of the cyclen-based ligands, as DO3A derivatives can be made by replacing or removing one acetate arm. DO3A itself is heptadentate and has a lower thermodynamic stability than DOTA (log*K* 21.0 for demetallation of [GdDO3A] compared to log*K* 25.3 for $[GdDOTA]^-$, measured at 25 °C).[65, 66] This trend extends to the hexadentate DO2A (log*K* 11.3 for $[GdDO2A]^+$ vs log*K* 23.4 for $[GdDOTA]^-$, measured at 25 °C, 0.1 M KCl).[67] DOTA and DO3A derivatives are commonly used as imaging agents, *via*

functionalisation of the cyclen ring or pendant arms, with addition of arms containing carboxylate, phosphonate, amide or alcohol functional groups increasing the stability of DO3A ligands.[68] The stability trend DOTA>DO3A>DO2A shows that stability of lanthanide complexes increases with the number of coordinating atoms and chelating rings.

The amide derivative of DOTA, DOTAM, has a stability constant 10-11 magnitudes lower than that of the corresponding DOTA complexes (log*K* 13.12 for [GdDOTAM] vs 24.7 for $[GdDOTA]^-$, 1.0 M KCl, at 25 °C).[69] As expected, due to the macrocyclic effect, DOTA is more kinetically stable than its acyclic analogue DTPA (k_{obs} 10^{-3} s^{-1} for $[GdDTPA]^{2-}$ at pH 1, compared to k_{obs} 3 x 10^{-7} s^{-1} for $[GdDOTA]^-$),[70, 71] despite both being used commercially as MRI contrast agents. Due to the smaller cavity size of the macrocyclic ligand, the hexadentate analogue of DOTA, NOTA, is a more suitable ligand for smaller lanthanide ions, such as holmium and ytterbium (log*K* 1.9 for [YbNOTA] at 5 °C in ammonium acetate at pH 6.5, compared to log*K* 0.66 for [GdNOTA]).[72]

Lanthanide DOTA and DO3A complexes exhibit conformation isomerism, existing as four stereoisomers as two enantiomeric pairs (square antiprism, SAP, and twisted square antiprism, TSAP, Figure 1.6) which may be interconverted by arm rotation and ring inversion. These isomers are distinguishable by NMR spectroscopy due to slow exchange on the NMR timescale at room temperature. The relative proportion of SAP and TSAP isomers in solution is important to consider when designing lanthanide complexes for biological applications, especially for MRI due to their different water exchange rates. Moving across the lanthanide series the proportion of SAP isomer increases – larger earlier lanthanide ions prefer the TSAP isomer due to the torsion angles. Additionally, the proportion of TSAP isomer is increased by increasing the steric bulk of pendant arms. For MRI applications higher proportions of TSAP isomer may be advantageous, as the water exchange rate of the TSAP isomer of GdDOTAM was found to be 50 times faster than the SAP isomer,[73] which may be explained by the reduced angle between the N and O planes and reduced angle for water coordination causing longer Gd-H_2O distances.[74]

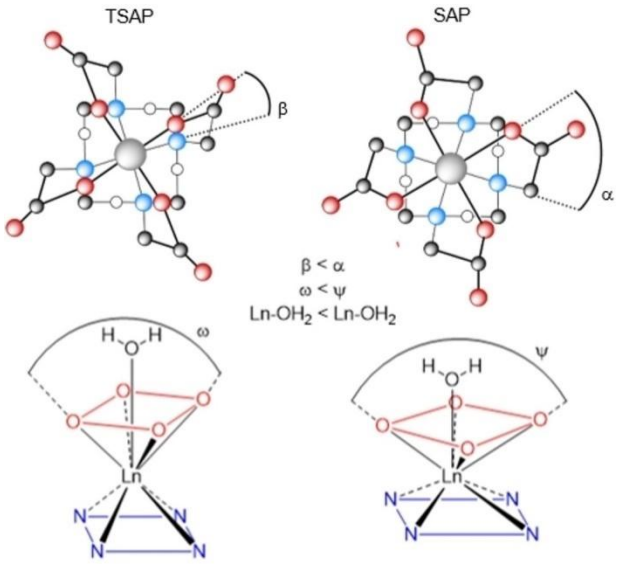

Figure 1.6: Depictions of the TSAP and SAP isomers of LnDOTA complexes, showing the torsion angles (α and ß) and opening angles (ω and ψ). Figure reused with permission.[74]

1.4.2 Lanthanide photophysics

Lanthanide complexes exhibit emission spectra with sharp, narrow emission bands and have long luminescence lifetimes. These desirable imaging properties arise from f-f transitions which are characteristic for each lanthanide ion but have weak intensity, as they are formally forbidden by Laporte's rules (due to no parity change between the ground and excited states). The transitions are observed due to relaxing of the rules via spin orbit coupling, which scales with nuclear charge (proportional to Z^4), and vibronic coupling, which is mixing of excited states with opposite parity. Vibronic coupling for lanthanide complexes is weaker than that observed for transition metals due to the shielding of the 4f electrons, therefore the absorption coefficients for lanthanide complexes are typically weaker than that of transition metal complexes (Table 1.2), giving rise to weaker emission spectra.

Table 1.2: A comparison of the photophysical properties of organic, transition metal and lanthanide compounds as fluorophores based on the different transitions they may contain.[75-77]

Transition	Molar absorptivity ε / dm^3 mol^{-1} cm^{-1}	Excited state lifetime
Charge transfer	> 10,000	ps-ns
Organic	10-10,000	ns
d-d	0.5-1,000	ns-µs
f-f	< 10	µs-ms

The formally forbidden nature of the f-f transitions leads to the desirable long-lived emission lifetimes (µs to ms), due to the low probabilities of transitions and the presence of long-lived excited states. The desirable sharp peaks in the emission spectra occur due to shielding of the f-electrons, as there is only a small influence from the surrounding ligand environment and excitation or emission of an electron only weakly changes the interaction with the crystal field therefore there is little change in geometry between the ground state and excited state, leading to narrow emission peaks. Due to this, the transitions which make up the emission spectra of lanthanide complexes are characteristic of each lanthanide (Figure 1.7) and are not heavily influenced by the ligand environment. However, the fine structure of the emission spectra (such as relative heights and splitting of the characteristic lanthanide peaks) give information about geometry and symmetry of lanthanide complexes. For example, for europium the $^5D_0 \rightarrow {}^7F_1$ transition (J=1 peak) is the magnetic dipole transition which gives information on the crystal field splitting of the complex, from the number of bands present within the transition, and the $^5D_0 \rightarrow {}^7F_2$ transition is the hypersensitive transition, which is sensitive to local symmetry of the europium ion and the intensity of the peak is related to the asymmetry around the europium centre.[78, 79]

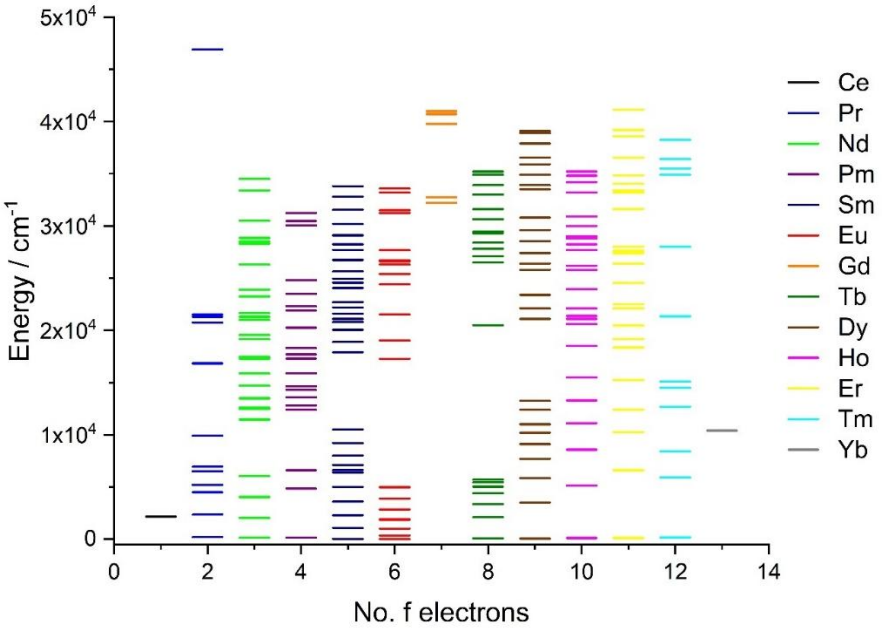

Figure 1.7: Energy level diagram for the Ln^{3+} aqua ions, determined by Carnall.[80-83]

Eu^{3+} and Tb^{3+} are most commonly used for biological optical imaging due to their large Stokes shift and intense emission in the visible region, with quantum yields typically over 10%.[84, 85]

1.4.2.1 Sensitisation of emission

As direct excitation of lanthanide ions results in weak emission due to the low molar absorptivities, optical imaging of lanthanide complexes often relies on the presence of organic chromophores appended to the chelating macrocycle and the antenna effect. The antenna effect (Figure 1.8a) is the process of excitation of an organic chromophore (possessing a high molar absorptivity, 5,000-50,000 $dm^3\ mol^{-1}\ cm^{-1}$), transfer of energy to the lanthanide and emission of characteristic lanthanide-based sharp peaks.[86]

There are many competing pathways for energy transfer upon excitation of part of a lanthanide complex, which may be described by the different rates of energy transfer in a Jablonski diagram (Figure 1.8b). Photons are absorbed by an organic chromophore (part of the ligand) into a singlet excited state which may fluoresce, undergo non-radiative decay to the ground state or intersystem crossing to a longer-lived triplet excited state, which allows subsequent energy transfer into lanthanide excited states (in competition with rates of non-radiative decay and ligand luminescence). For efficient sensitisation of the lanthanide to occur, causing an increase in lanthanide emission compared to direct excitation, the energy level of the triplet state of the chromophore must be well matched to those of the lanthanide excited state.[87] If the energy gap between the chromophore and lanthanide excited states are too large then sensitisation is inefficient, whereas a small difference in energy levels (< 1850 cm^{-1}) increases the rate of back energy transfer (BET).[84, 88]

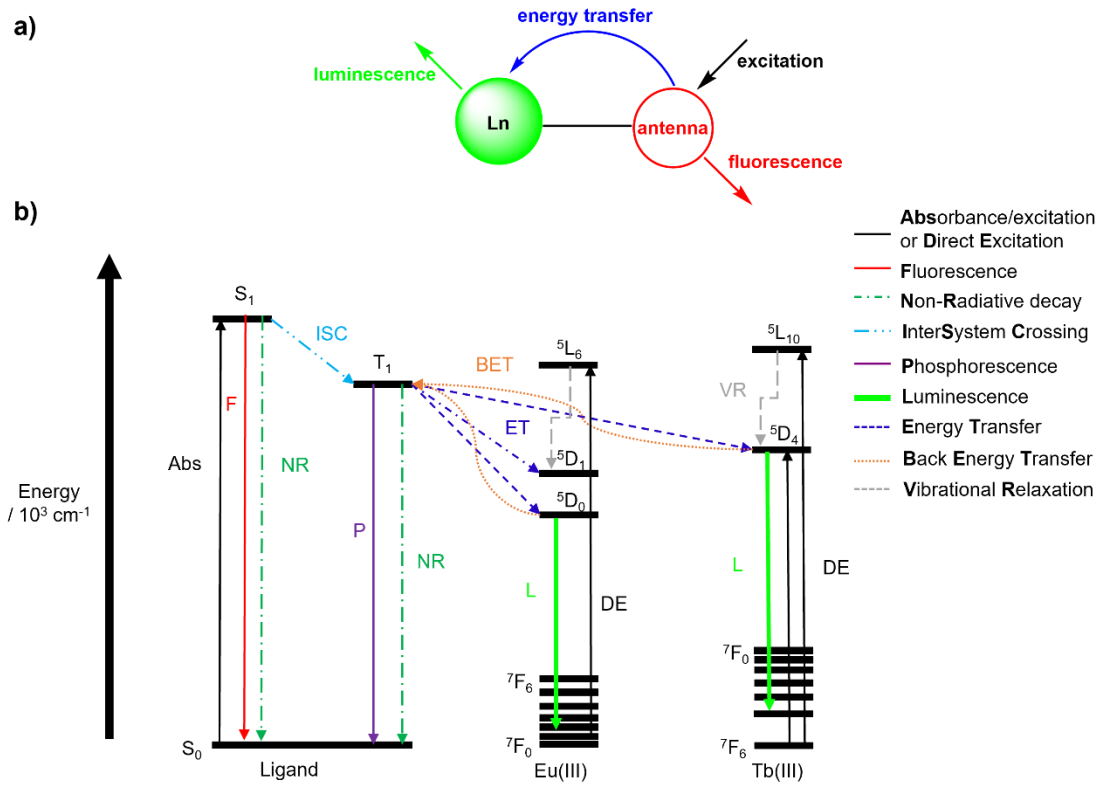

Figure 1.8: a) Diagram showing the antenna effect and sensitisation of a lanthanide metal. b) Jablonski diagram highlighting the different rates of processes which may occur, as labelled, to cause transfer and emission of energy, with the europium and terbium energy levels labelled.[78, 82]

Energy transfer from the organic chromophore (donor*) and lanthanide ion (acceptor) may occur via two main mechanisms, Förster resonance energy transfer (FRET) and Dexter energy transfer (Figure 1.9). FRET is a through-space interaction due to Coulombic interaction between multipole changes associated with the changes between the ground state and excited state in the donor and acceptor. Dipole-dipole interactions are the major component of FRET and these have a distance dependence of d^{-6}, therefore FRET can operate over long distances up to 100 Å. Dexter is the commonly assumed mechanism for lanthanide sensitisation where the chromophore coordinates directly to the lanthanide. Dexter energy transfer is a double electron exchange mechanism which requires orbital overlap between the donor and acceptor and therefore typically acts over shorter distances, with a distance dependence of e^{-d}. This short-range interaction may be extended by the presence of conjugated bridging ligands which mediate electron transfer (superexchange) for distances up to 20 Å.[89-92]

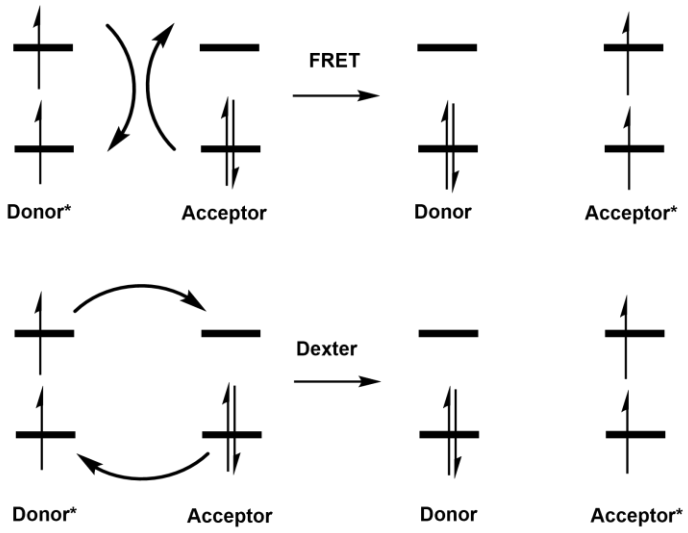

Figure 1.9: A simplified diagram showing the mechanism of Förster Resonance Energy Transfer (FRET) and Dexter exchange.[89-91]

1.4.2.2 Quenching of emission

A lanthanide complex's quantum yield (Φ) is a measure of the efficiency of its luminescence. The quantum yield upon ligand excitation (Φ_{Ln}^{L}, equation 1.1) can be calculated by taking into account the efficiency of sensitisation from the chromophore (η_{sens}) and the intrinsic quantum yield of the lanthanide (Φ_{Ln}^{Ln}). The 'brightness' of different complexes can be compared by considering both their quantum yield and their molar absorption coefficient (ε).

$$\Phi_{Ln}^{L} = \eta_{sens}\Phi_{Ln}^{Ln} \qquad \text{(eqn. 1.1)}$$

As the quantum yield is defined as the ratio between photons absorbed and photons emitted (equation 1.2), it can also be evaluated by considering the rates of radiative decay (k_R) which leads to the desired luminescence against the total of all emissive rates (the observed rate, k_{obs}), which include the radiative pathways and non-radiative, or quenching, pathways (k_{NR}, equation 1.3). For europium complexes, the intrinsic quantum yield may be estimated by evaluation of the magnetic dipole transition peak (J=1 band) area compared to the area of the total emission spectrum (see chapter III). The observed lifetime for the luminescence decay of a complex (τ_{obs}) can be measured experimentally and used in combination with the intrinsic quantum yield to estimate rates of radiative pathways.[93, 94]

$$\Phi_{\mathrm{Ln}}^{\mathrm{Ln}} = \frac{\text{emitted photons}}{\text{absorbed photons}} \qquad \text{(eqn. 1.2)}$$

$$\Phi_{\mathrm{Ln}}^{\mathrm{Ln}} = = \frac{k_R}{k_R + k_{NR}} = \frac{k_R}{k_{obs}} = k_R \tau_{\mathrm{obs}} \qquad \text{(eqn. 1.3)}$$

There are multiple processes which quench the luminescence of lanthanide complexes (by contributing to k_{NR}); these can include back energy transfer (BET), photoinduced electron transfer (PeT), cross-relaxation, other intermolecular energy transfer processes and vibrational relaxation.[95] Back energy transfer (denoted by orange arrows in Figure 1.9b), as briefly discussed above, occurs by transfer of energy from a lanthanide triplet excited state to the organic chromophore and occurs when the energy levels of the lanthanide and chromophore triplet states are close in energy.[88] Measurement of the emission spectra of analogous gadolinium complexes at 77 K can be used to estimate the triplet state of the chromophore in order to evaluate contributions to non-radiative pathways arising from back energy transfer processes.[96, 97] Photoinduced electron transfer (PeT) between a donor and an acceptor (in this case between the chromophore and the lanthanide ion) gives a charge separated radical cation and radical anion. In most cases the charge separated state is lower in energy than the lanthanide emissive excited states, therefore PeT quenches lanthanide emission, however for Yb the charge separated state is higher in energy so PeT contributes to sensitisation and leads to emission in the NIR region. The rate of PeT can be reduced by use of a less reducing chromophore; however, this also affects the triplet energy level and therefore sensitisation.[95, 98-100] Cross-relaxation is a quenching process which can occur in a system containing two lanthanide ions where the energy gap between two excited states of a donor lanthanide ion is similar to that of the energy gap between the ground state and an excited state of the acceptor lanthanide ion, leading to non-radiative emission for a lower excited state.[101] Other intermolecular energy transfer processes that contribute to the quenching of lanthanide emission include the presence of triplet oxygen[102] and the presence of other metal ions, such as biologically relevant Mn(II) and Cu(II).[103]

Quenching of luminescence is also observed through interactions with vibrations of X-H bonds (where X is O, C or N).[104-106] The impact of this quenching on luminescence varies between lanthanide ions as it occurs when the difference between the lanthanide ground state and excited states is similar to the overtone of X-H frequencies – for example, the energy gap of the europium transition $^5D_0 \rightarrow {}^7F_6$ matches decently with the *v*=5 vibrational overtone of C-H bonds and the energy gap of the terbium transition $^5D_4 \rightarrow {}^7F_0$ matches with the *v*=6 vibrational overtone of C-H and *v*=4 of O-H.[107, 108] As this quenching can occur intramolecularly or intermolecularly it is a consideration for both design of a lanthanide chromophore and measurements of luminescence in biologically relevant aqueous media. For the design of lanthanide probes for optical imaging, aiming to minimise the number of N-H and O-H quenchers close to the lanthanide is crucial to increase luminescence and saturation of the lanthanide coordinate site is important to prevent bound water molecules from quenching luminescence. However, bound water molecules are essential for MRI applications therefore some intermediate approach should be taken for the design of lanthanide complexes for multimodal purposes. Substitution of X-H bonds to X-D or X-F bonds may be employed to reduce quenching – due to their higher reduced mass the vibrational frequencies are smaller leading to a poorer energy match between lanthanide excited states and X-D or X-F oscillators.[109] Measurements of lanthanide luminescence should ideally be carried out in water or buffer solutions to mimic the brightness expected *in vivo*, as the amount of quenching observed varies between solvents.[94]

For MRI applications, the number of coordinated water molecules, *q*, for the Gd(III) lanthanide complexes can be estimated from the rate of luminescent decay of analogous Eu(III) and Tb(III) complexes in water and D_2O. This *q* value can be determined using a modified version of Horrock's equation, equation 1.4, where A is the inner-sphere contribution, B is the outer-sphere contribution (Table 1.3) and τ is the rate of decay.[107, 110] This equation for prediction of number of coordinated water molecules is widely used and good for mononuclear lanthanide complexes, however it becomes less reliable for

multinuclear lanthanide complexes due to self-quenching occurring between the lanthanide centres.

$$q = A\left(\frac{1}{\tau_{H_2O}} - \frac{1}{\tau_{D_2O}} - B\right) \qquad \text{(eqn. 1.4)}$$

Table 1.3: The value of parameters A (inner-sphere contribution) and B (outer-sphere contribution) for Eu(III) and Tb(III) in water. n_{OH} is the number of O-H oscillators in the complex and n_{CONH} is the number of amide N-H oscillators in the complex.

Ln(III) ion	A / ms	B / ms
Eu	1.2	$0.25 + 0.44n_{OH} + 0.075n_{CONH}$
Tb	5.0	0.06

1.4.3 MR of lanthanide complexes

1.4.3.1 NMR spectroscopy

The lanthanide(III) ions are all paramagnetic, based on their ground state electronic configurations, except for La ($5d^16s^2$), Lu ($4f^{14}$) and Eu ($4f^6$), however Eu(III) acts as paramagnetic due to its thermally partially populated low-lying paramagnetic excited states. This paramagnetism gives rise to the broad signals (due to fast relaxation times) and large chemical shift ranges observed in ^{1}H NMR spectra. The chemical shifts observed arise due to contributions from the diamagnetic shift (δ_d), Fermi contact shift (δ_C) and pseudocontact shift (δ_{PCS}, equation 1.5).[111]

$$\delta_p = \delta_d + \delta_C + \delta_{PCS} \qquad \text{(eqn. 1.5)}$$

The diamagnetic shift contributions (δ_d) are usually small and are due to the conformation of the molecule and inductive and field effects, similar to those of organic compounds, which can be determined from the NMR spectra of lutetium or lanthanum analogues of lanthanide complexes.[112] The Fermi contact shift contributions (δ_C) arise from through-bond interactions (similar to J-coupling in diamagnetic NMR spectra) between lanthanide unpaired electrons with the nucleus of interest[113] and is proportional to the magnetic moment of the lanthanide ion and the hyperfine coupling constant.[111] As expected, the Fermi contact decreases as the distance between the lanthanide and the nucleus of interest

increases (with some deviations noted in the case of conjugation).[114] The pseudocontact shift (δ_{PCS}) is a through-space interaction and is often considered dominant for lanthanide complexes. Its dependence on the angles between and orientation of the nucleus of interest and the lanthanide ion allows for information on structure to be obtained. The pseudocontact shift may be described by equation 1.6, assuming the lanthanide is treated as a point charge with infinitely fast relaxation, where θ, ω and r are the 3D polar coordinates (with respect to the lanthanide ion and the magnetic axis) and χ_{ax} and χ_{rh} are the axial and rhombic components of the magnetic susceptibility tensor, respectively.[111]

$$\delta_{PCS} = \frac{1}{12\pi r^3}[\chi_{ax}(3\cos^2\theta\text{-}1)+3\chi_{rh}\sin^2\theta\cos 2\omega] \quad \text{(eqn. 1.6)}$$

Bleaney's theory (for the chemical shift of nuclei over 3 bonds away from the lanthanide centre) states that the contact contribution is small and therefore the pseudocontact contribution dominates and the chemical shift observed is only related to the crystal field, geometry of the complex, temperature and a constant which is related to the specific lanthanide ion.[115-117] Under Bleaney's theory, the anisotropy of the susceptibility tensor (equations 1.7 and 1.8) depends on the ligand field parameters, B_0^2 and B_2^2, and the Bleaney constant, C_J, which is dependent on the lanthanide ion (equation 1.9) as it varies with g_J, the Landé factor, and J, the total angular momentum quantum number.[111, 114, 118]

$$\chi_{ax} = -\frac{\mu_0\mu_B{}^2 C_J B_2^0}{10(kT)^2} \quad \text{(eqn. 1.7)}$$

$$\chi_{rh} = -\frac{\mu_0\mu_B{}^2 C_J B_2^2}{30(kT)^2} \quad \text{(eqn. 1.8)}$$

$$c_J = g_J{}^2 J(J+1)(2J-1)(2J+3)\langle J|a|J\rangle \quad \text{(eqn. 1.9)}$$

The shape of the lanthanide ion's ground state f-electron distribution (Figure 1.10a) is related to the magnetic anisotropy and lanthanide-induced shift (the difference in chemical shift between paramagnetic and diamagnetic analogues of analogous complexes) and therefore influences the range of the NMR spectral window. A lanthanide complex is oblate

if the ground state is perpendicular to the magnetic axis (Figure 1.10b), such as for cerium and terbium, or prolate if the ground state is parallel to the magnetic axis, as for europium.[119]

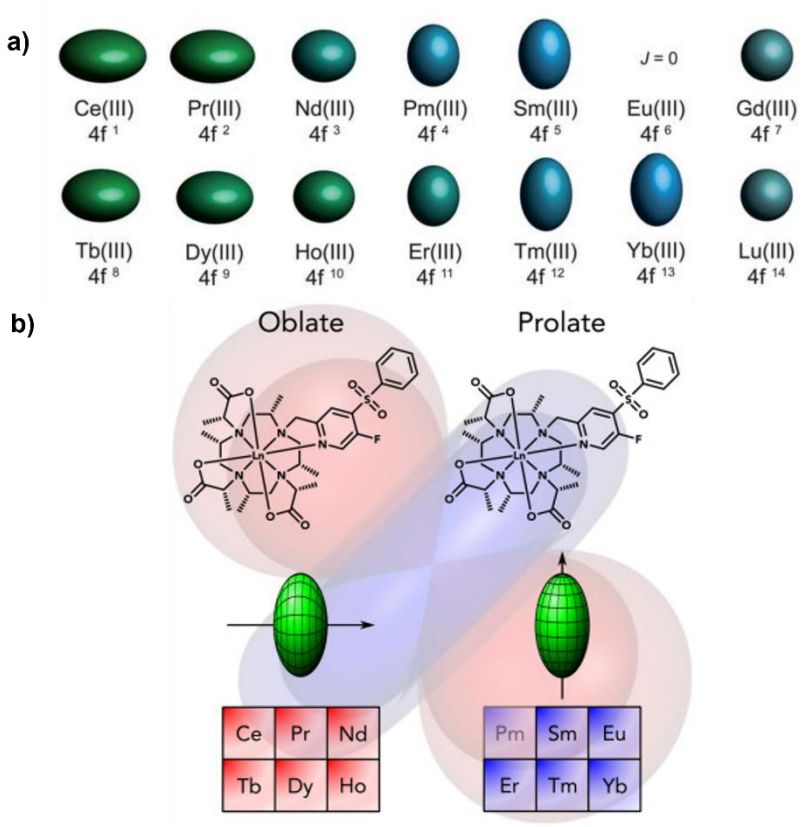

Figure 1.10: a) The shape of the ground state lanthanide(III) ions' f-electron distribution, reproduced with permission from Rinehart *et al.*[120] b) A figure showing the relationship between lanthanide ion, f-electron ground state distribution and orientation of the magnetic axis, reproduced with permission from Vogel *et al.*[119]

In general, Bleaney's theory may be used to understand the solution structure and dynamics of paramagnetic lanthanide complexes, particularly by independent analysis of the pseudocontact contributions. However, it suffers from some limitations through the assumptions that it makes which may not always be applicable, such as that the lanthanide ion acts as a point magnetic source, the analogous complexes being isostructural across the lanthanide series, the ligand field splittings are small compared to kT (otherwise the shift is temperature dependent) and that the hyperfine coupling is constant across the lanthanide series. Therefore, whilst Bleaney's theory has been used for analysis of NMR spectra of lanthanide complexes for many years, it should not be relied upon for the design of paramagnetic shift reagents, including those for CEST imaging.[111, 113, 117]

1.4.3.2 Magnetic resonance imaging (MRI)

Magnetic resonance imaging (MRI) is a crucial non-invasive tool used for clinical imaging, with 45 million MRI scans taken each year.[121] The technique involves application of an external magnetic field, B_0, to align protons in water and then application of a radiofrequency pulse at the same frequency as the processional frequency of the protons, perpendicular to B_0. The signal observed in an MRI is created by monitoring the relaxation of the protons following application of the radiofrequency pulse, allowing for differentiation between types of soft tissue and abnormal tissue due to their differing rates of relaxation. To obtain spatial resolution, a gradient magnetic field B_0 is applied and either the gradient magnetic field applied or the radiofrequency pulse applied (perpendicular to B_0) is altered to obtain slices of signal, as only protons processing at certain frequencies will be measured.

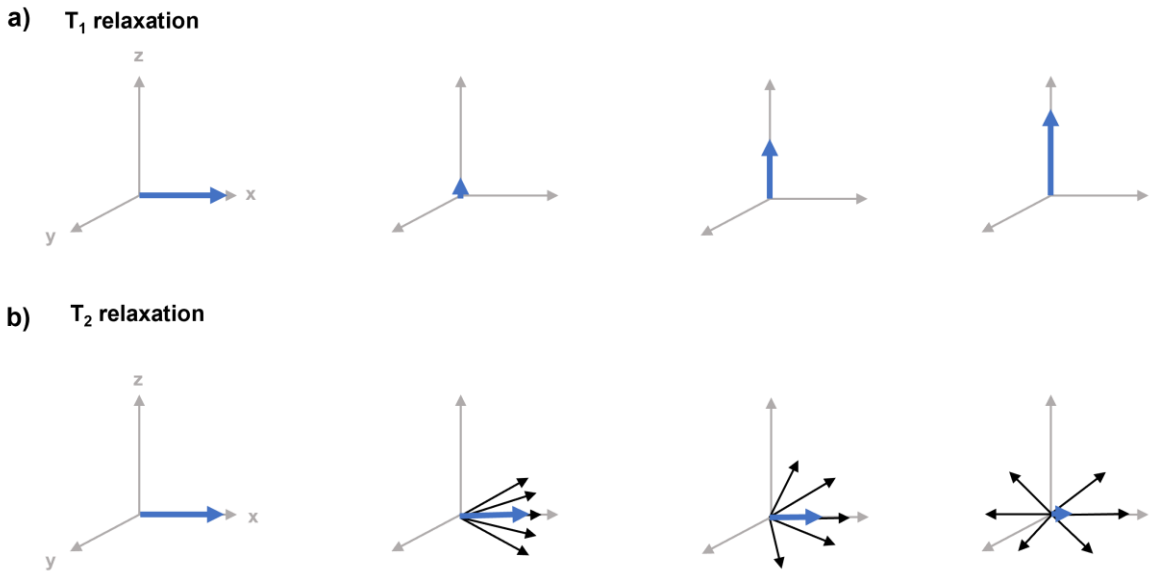

Figure 1.11: An explanation of the relaxation process that give rise to MRI signal, after application of a magnetic field in the z-direction, with relaxation occurring from left to right. a) T_1 relaxation in the z direction, b) T_2 relaxation in the xy direction. Blue arrows show the overall vector, black arrows are individual components that average out to give the overall vector.

The relaxation time can be characterised as either T_1 or T_2: T_1, the longitudinal relaxation time, is the time for the protons to realign with the applied external magnetic field (loss of the z-component of magnetisation, Figure 1.11a) and T_2, the transverse relaxation time, is the time for the loss of phase coherence by interaction with surroundings (loss of the xy-

component of magnetisation, Figure 1.11b). T_1-weighted and T_2-weighted MRI are used for imaging of different things – T_1 gives a bright signal for fatty tissue whereas T_2 enhances water.

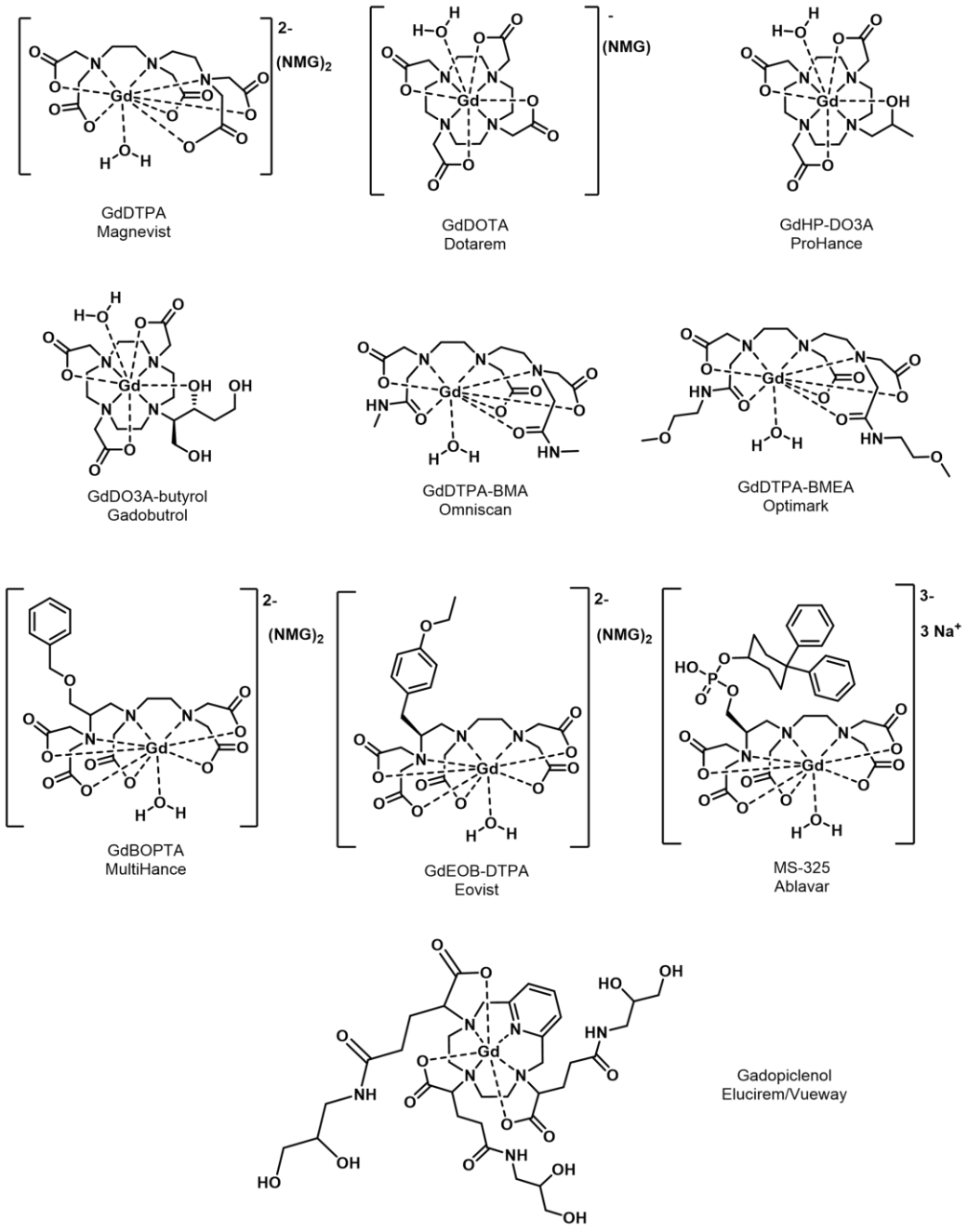

Figure 1.12: Gadolinium-based contrast agents (GBCAs) which have previously been approved by the FDA, with their commercial names listed below their abbreviations used in the text. [122, 123]

Contrast agents are often injected into patients prior to their MRI (in 40% of cases) to enhance the sensitivity and accuracy of diagnosis. These often work by shortening the relaxation times of water protons, causing a greater contrast within the image, by interaction

of the water protons with the MRI contrast agent. Most of the MRI contrast agents which are FDA-approved and used in clinics are gadolinium-based contrast agents (GBCAs, Figure 1.12), such as the widely used GdDOTA, with others being manganese-based (Figure 1.13a) or iron oxide nanoparticles (Figure 1.13b, primarily used for T_2 imaging), although the marketing for the latter two classes has been discontinued.[124] The first GBCA, GdDTPA, was FDA approved in 1988, with the most recent advancement being the FDA approval of gadopiclenol in 2022 (approved in the EU in 2023), which requires lower doses compared to previous contrast agents due to its higher relaxivity.[125]

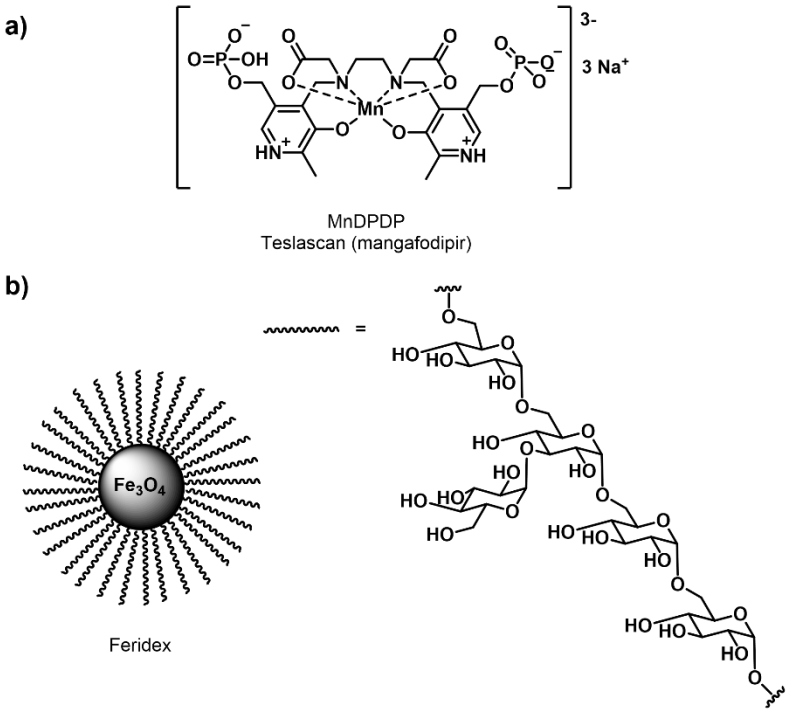

Figure 1.13: Contrast agents which have previously been approved by the FDA, with their commercial names listed below their abbreviations used in the text - a) manganese-based and b) nanoparticle.[122, 123]

The relaxivity of GBCAs has inner-sphere contributions (from water bound directly to the metal) and outer-sphere contributions (from water molecules nearby the contrast agent). GBCAs are typically used as T_1 contrast agents as they have a larger effect on tissue T_1 than T_2.[126] For monomeric GBCAs, the inner-sphere contribution is a major component whereas the change in outer-sphere contribution is often small.

The signal intensity of the MRI contrast agent can be varied by changing the number of inner sphere water molecules (q), the rate of molecular tumbling (τ_r) and the rate of water

exchange (τ_m). The inner-sphere relaxivity (r^{IS}, equation 1.10) also depends on applied magnetic field strength and temperature, in addition to the electron spin of the complex (S) and electronic relaxation times (T_{1e} or T_{2e}).[122, 127, 128] Inner-sphere relaxivity can be described in the Bloch equations, where it is assumed that there is fast exchange between two sites and one bulk water is present at much higher concentration than one metal bound water. For simple metal complexes, these equations can be simplified to equation 1.11, where C is a constant.[122]

$$r_1^{IS} = \frac{q/[H_2O]}{T_{1m}+\tau_m} \quad \text{(eqn. 1.10)}$$

$$r_1^{IS} = Cq\tau_R \quad \text{(eqn. 1.11)}$$

Relaxivity of GBCAs can be modulated by impacting many factors, namely: q, by changing the coordination environment of ligand donors, whilst noting that higher q likely means a less stable lanthanide complex; metal-water proton distance and residency time of water, which are influenced by the relative amounts of TSAP and SAP isomers in solution; and rotational correlation time, which depend on the size of the complex or immobilisation on a surface and can be estimated using the Debye-Stokes equation (equation 1.12). Many of these factors are interlinked and therefore the effect of modifying a molecule on its relaxivity can be difficult to predict.

$$\tau_R = \frac{4\pi\eta r_{eff}^3}{3k_BT} \quad \text{(eqn. 1.12)}$$

1.4.4 Lanthanide probes for biological imaging

As discussed previously, lanthanide complexes are generally thought to be advantageous over organic-based fluorophores for optical imaging, when using europium or terbium, due to their sharp emission spectra (causing less overlap with biologically relevant species) and long-lived lifetimes (enabling time-gated emission techniques to be used), despite their lower molar extinction coefficients. However, lanthanide complexes are most commonly

used in biological imaging for MRI, due to the high paramagnetism of the gadolinium (III) ion (see section 1.4.3.2).

Ideal lanthanide complexes for imaging of disease require high quantum yields in physiologically relevant media (>10%), *via* use of a chromophore-containing ligand which may be synthesised cheaply and easily, to give a kinetically and thermodynamically stable complex, which is cell permeable and non-toxic. Excitation wavelengths above 337 nm and at wavelengths close to those of commonly used lasers or LEDs is crucial for easy transition for medical use.[129]

Activatable lanthanide complexes for imaging are discussed briefly in section 1.5.2 and expanded upon in sections 3.1, 4.1.2 and 4.1.3, with section 4.1.1 highlighting the challenges of developing cell permeable lanthanide complexes for imaging.

1.5 Redox activatable probes for biological imaging

Preclinical progress in activatable compounds has mainly focused on development of prodrugs (such as the development of tirapazamine and evofosfamide which have reached phase I-II clinical trials) to overcome issues with side effects for patients and to improve properties of the parent drug, such as greater absorption or slower metabolism. As mentioned previously, activatable profluorophores may be useful for detection of certain species in the body and gaining information, including their use in image-guided surgery,[130, 131] diagnosis and prognosis evaluations. A selection of relevant developments in redox activatable probes are reviewed in this section to highlight the breadth of the field that is currently being developed, spanning organic and inorganic molecules and nanoparticles, which may be activated in the presence of differing redox molecules, environments or enzymes to cause changes for readout by optical imaging, PET and MRI. Examples of other responsive compounds, including those with dual functionality and those used for other modes of imaging, are discussed and summarised elsewhere.[9, 132-136]

1.5.1 Organic profluorophores

EF5 and pimonidazole (Figure 1.14a) are simple organic molecules which are routinely used in oncology research and preclinical settings as detectors of hypoxia. These small molecules function by reduction of the nitroimidazole moiety, reaction with thiol-containing proteins and subsequent interaction with fluorescent labelled antibodies allowing detection. Recently Tosun et al.[14] reported a profluorophore of the anticancer drug panobinostat which contained the epitope of EF5 (Figure 1.14b), allowing for simultaneous antibody-based imaging and cell death. [^{18}F]EF5 has also been developed as a non-invasive tool for PET imaging of hypoxia, with evidence that it can be prepared in clinically-relevant quantities and that its metabolism in rats does not lead to other ^{18}F-labelled products.[137] This affords it an advantage over [^{18}F]FMISO (Figure 1.14c), which has previously been used to predict the change in prognosis for patients prior to radiotherapy for lung or head and neck cancer, but suffers from slow blood clearance (causing a small change in PET signal contrast between hypoxia and normoxia) and production of several radioactive products upon excretion.[137, 138]

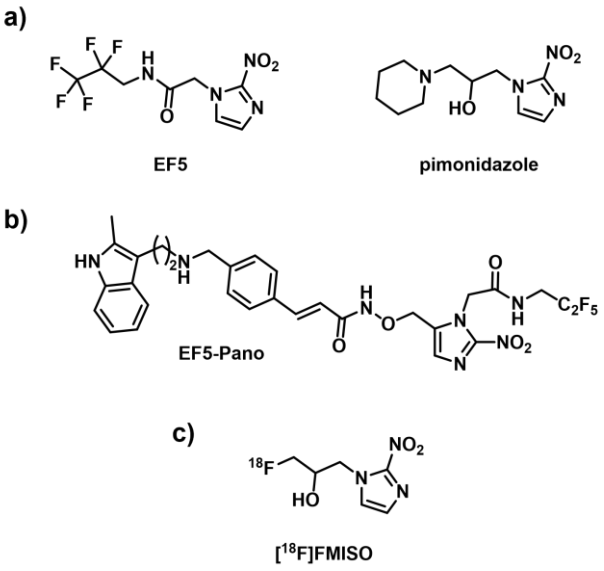

Figure 1.14: The structure of nitroimidazole-based small molecules for hypoxia detection. a) EF5 and pimonidazole, used in preclinical settings for validating hypoxia. b) EF5-pano, a molecule that combines an anticancer drug and a group that affords antibody imaging.[14] c) [^{18}F]FMISO which may be used for hypoxia detection by PET imaging.[138]

Activatable near-infrared (NIR) probes are advantageous for biological imaging over UV or visible light emitting probes due to their deeper tissue penetration depth and the minimised autofluorescence observed.[139] One example of an activatable NIR probe is that reported by Liu *et al.*[140] which has been used to selectively detect mitochrondia in hypoxic cells (at 2% O_2) and solid tumours of mice. An increase in fluorescence intensity at 670 nm was observed upon reduction of the nitrobenzyl group (which inhibits intramolecular charge transfer, Figure 1.15) to the aniline and cleavage to give the rhodamine-based dye.

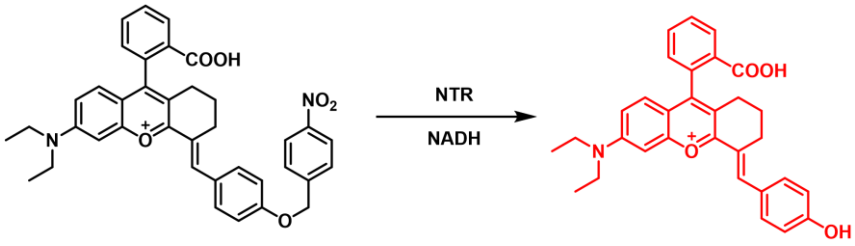

Figure 1.15: The structure and activation of an activatable NIR probe reported by Liu *et al.*[140]

Two-photon excitation imaging may similarly be used for deep tissue penetration depth, high sensitivity and good temporal resolution.[141] Wang *et al.*[142] reported a nitrobenzyl-based probe (Figure 1.16a) which was activated in the presence of nitroreductase enzyme, causing an increase in fluorescence emission at 580 nm (upon excitation at 450 nm, Figure 1.16b). The probe also showed an increase in fluorescence in hypoxic A549 cells, detected by two-photon confocal microscopy (Figure 1.16c, excitation at 840 nm), which was inhibited by the presence of dicoumarin (a known nitroreductase inhibitor).

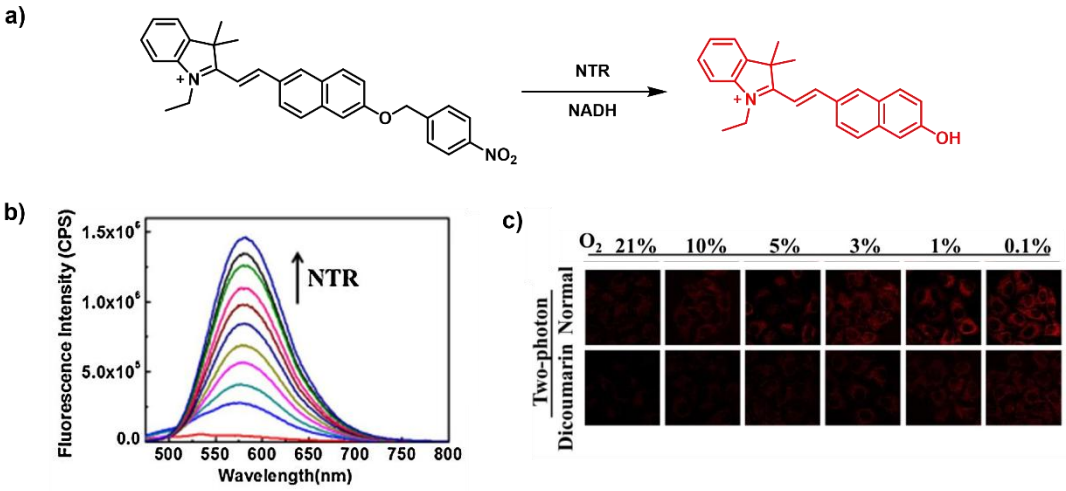

Figure 1.16: a) The structure and activation of the nitrobenzyl-based activatable probe reported by Wang *et al*. b) The change in fluorescence emission observed upon activation of the probe (10 µM) in the presence of nitroreductase (0-20 µg/mL) upon excitation at 450 nm. c) Two-photon microscopy of A549 cells in the presence of the probe under normoxia and hypoxia, upon excitation at 840 nm, including in the presence of dicoumarin (100 µM) as a nitroreductase inhibitor. Panels b and c reproduced with permission.[142]

1.5.2 Lanthanide complexes

Gadolinium complexes are widely used as MRI contrasts, as discussed in section 1.4.3.2, and activatable MRI contrasts are being developed to aid patient diagnosis. Iwaki *et al*.[143] reported a series of hypoxia-sensitive MRI contrast agents containing aryl sulfonamide groups which change relaxivity based on the pH and upon reduction of the nitro moiety to the corresponding aniline. Testing of the derivative containing a methoxy group meta to the nitro moiety (Figure 1.17) in rat liver microsomes showed a significant change in relaxivity under hypoxia (3.6 mM^{-1} s^{-1}) in comparison to normoxia (2.1 mM^{-1} s^{-1}) at pH 7.4.

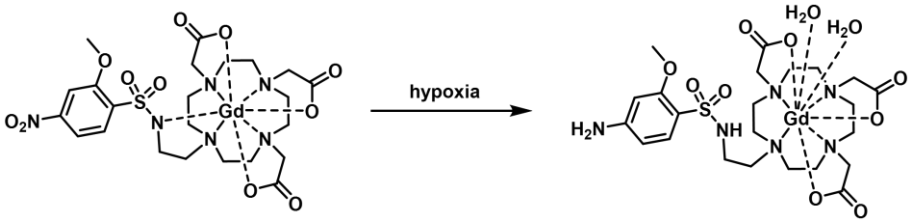

Figure 1.17: A hypoxia-activated MRI contrast agent, bearing a sulfonamide moiety, previously reported by Iwaki *et al*.[143]

Activatable lanthanide complexes, in particular those containing nitroaryl and azobenzene functional groups for optical imaging or MRI, and the challenges associated with making

these applicable for use *in vivo* is discussed further in sections 3.1, 4.1.1 and 4.1.3, as relevant.

1.5.3 Transition metal complexes and nanoparticles

Platinum(IV) complexes are emerging as a common prodrug strategy for release of platinum(II) species, such as the anticancer drugs cisplatin and oxaliplatin, to overcome their resistance, side effects and bioavailability issues by saturating the coordination sites. Whilst many research efforts have focused on light-activated platinum(IV) complexes,[144, 145] these complexes may be used as theranostic tools by the incorporation of a fluorophore into one of the axial positions which is released upon reduction to give the platinum(II) species.[8] Recent work by Sedgwick and co-workers have described a series of activatable platinum(IV) complexes (Figure 1.18a) which may be reduced in the presence of sodium ascorbate, light or under hypoxic conditions (0.1% O_2) in HCT116 or A549 cells, causing an increase in both fluorescence and cell death.[146-148]

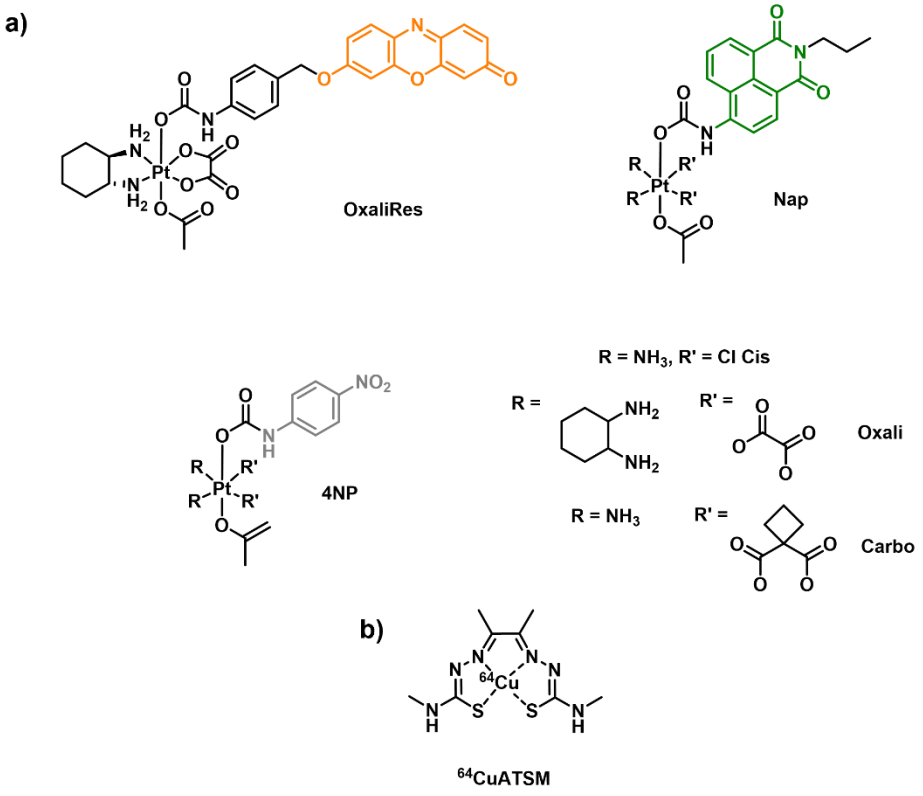

Figure 1.18: a) The structures of reductively activated platinum(IV) profluorophores/prodrugs reported by Sedgwick and co-workers.[146-148] b) The structure of [^{64}Cu]CuATSM for PET imaging of hypoxia.[149]

CuATSM (Figure 1.18b) is another metal-based probe which may be used for biological imaging.[43] The probe is trapped upon reduction of the Cu(II) centre to Cu(I) selectively in hypoxic tissue. In the case of [^{64}Cu]CuATSM the Cu(I) complex dissociates to release ^{64}Cu for PET imaging of hypoxia.[3] It has been demonstrated that this hypoxic contrast is not due to protonation and is independent of intracellular pH, which is crucial as acidosis is another marker of ischemic tissue.[149]

Nanoparticles for biological imaging are also being investigated due to their advantages over organic fluorophores, such as their enhanced sensitivity and greater signal density, ease of synthesis and functionalisation, and their abilities to have multi-functional properties, by attachment of differing groups for targeting and luminescence, afforded by their large surface area, and tuneable properties, based on size.[130] Photosensitiser functionalised nanoparticles may also be used for image-guided photodynamic therapy (PDT). An *et al.*[150] reported a multifunctional nanoparticle (Figure 1.19) for NIR fluorescence and MRI. The nanoparticles were formed by self-assembly of a small molecule probe which contains a NIR photosensitiser (enabling fluorescence imaging and PDT), a disulfide linker, a quenched luciferin-based fluorophore to aid self-assembly, a gadolinium chelate for MRI and a cyclic peptide for tumour targeting. Upon disulfide reduction in the presence of glutathione, the nanoparticle undergoes fragmentation to release an oxyluciferin fluorophore (with emission at 547 nm) and the photosensitiser, which upon binding to albumin leads to increased fluorescence at 677 nm and retention in cells for PDT – singlet oxygen production was observed upon irradiation at 690 nm only after reduction with glutathione. The high relaxivity of the parent nanoparticle (r_1 21 mM^{-1} s^{-1} in PBS) lead to good signal enhancement in T_1-weighted MRI of U87MG cell pellets (glioblastoma), showing that MR and fluorescence could be used complimentarily for tumour detection.[150]

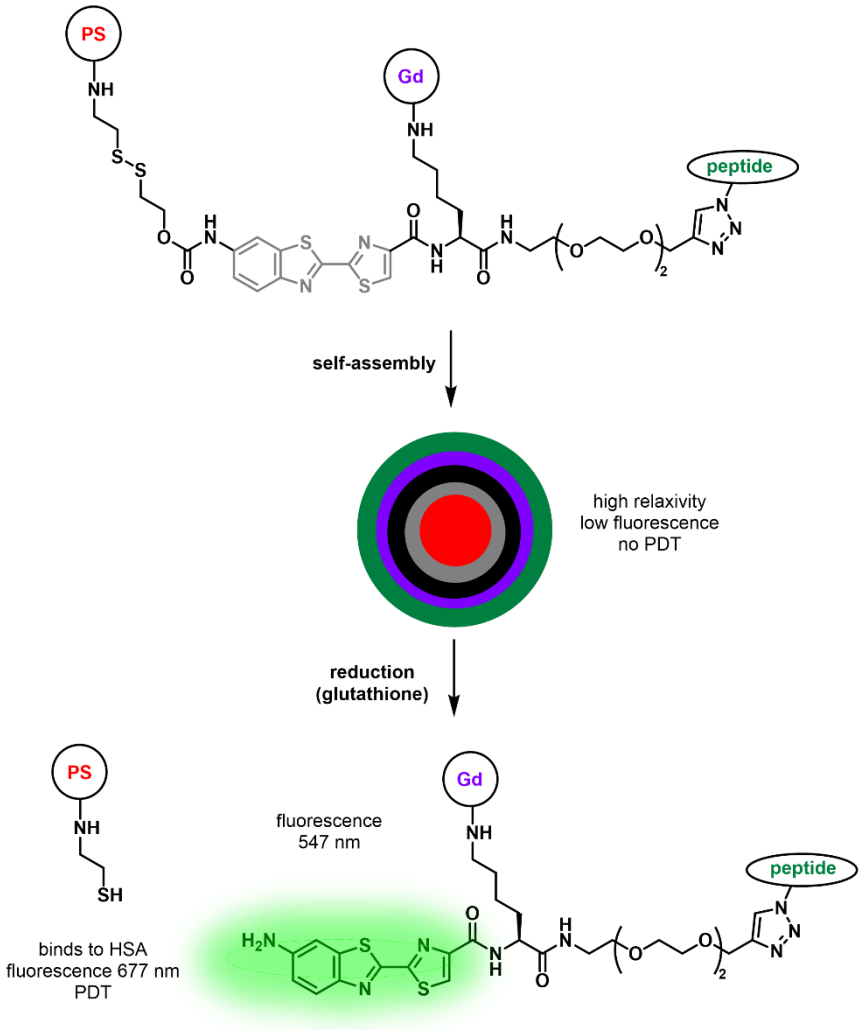

Figure 1.19: The structure and activation of a nanoparticle assembly reported by An *et al.* for optical imaging, MRI and PDT.[150] PS = NIR photosensitiser, Gd = Gd-containing macrocycle, peptide = cyclic peptide for targeting.

1.5.4 Outlook for activatable probes for biological imaging

As outlined above, desirable properties for optical imaging *in vivo* include NIR emission or long-lived luminescence for time-gated detection to reduce interference from cellular autofluorescence and other strategies include visualisation using two photon excitation, MRI or PET imaging. For lanthanide complexes and organic molecules in particular for optical imaging, fluorophores should be designed to have high molar absorption coefficients and activation with excitation wavelengths above 350 nm is desirable to avoid background signal from fluorescence of biological molecules such as NADH.[84]

Current limitations of profluorophores and biological imaging agents are related to localisation (encompassing the lack of selectivity for cancerous tissues and lack of cell permeability of probes), accurate quantification (requiring large changes upon activation of profluorophores), sensitivity and detection limits (in terms of analyte concentration to cause activation of a profluorophore and balancing concentrations for image brightness against cytotoxicity) and the time scale of activation (balancing quick detection and degradation or clearance times).[121] For the design of new imaging agents for use in clinical settings, significant advancements will be made through the development of dual imaging probes or theranostics to gain more information (despite some current practical limitations) for diagnosis and prognosis evaluation. Other advances will involve research focused on imaging agents for informing the pre-clinical development of drugs (for example, to aid mechanistic understanding in clinical trials) and for image-guided surgery.[151] These developments in novel imaging agents for clinical use requires input from multiple disciplines (chemistry, biology, oncology, clinicians) to enable a complete understanding of the relevant requirements, practicalities and feasibility of chemical design.

1.6 Aims

The aim of this project was to develop redox activatable compounds (lanthanide complexes or organic profluorophores) for selective cancer imaging applications, with the desired properties described in Figure 1.20.

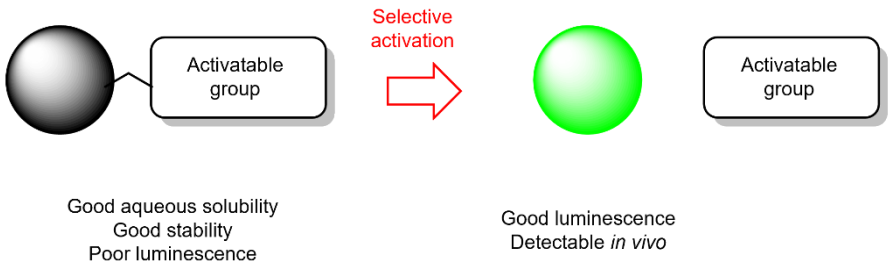

Figure 1.20: The desirable properties of the compounds (profluorophores) described in this thesis.

Chapter 2 outlines the investigation of two methods of activation, the presence of hypoxia and X-ray irradiation, to determine if an azide-based organic prodrug or profluorophore may

be activated in the same way under differing conditions. Activation of the same profluorophore or prodrug under differing conditions (including the use of an external source of activation) would enable further selectivity of cancer imaging and/or treatment and could lead to treatment of hypoxic solid tumours, which are largely radioresistant, through combined radiotherapy and chemotherapy. This work highlights the challenges of designing a small molecule profluorophore for activation under biologically relevant conditions and the need for moving towards activation by more clinically relevant doses of X-rays.

Chapters 3 and 4 describe the synthesis of lanthanide complexes for optical imaging and MRI, exploiting their advantages over organic profluorophores with their long-lived luminescence. Chapter 3 explores the synthesis, characterisation and testing of a series of simple DO3A-based lanthanide complexes which employ hypoxia-activatable moieties as a proof-of-concept for simple lanthanide complexes which can be activated to cause changes in luminescence emission and relaxivity for optical imaging and MRI applications.[152] Activation of these complexes was evaluated under various chemical and biologically-relevant systems to understand their selectivity and stability. Chapter 4 addresses the challenges of designing and synthesising cell permeable activatable lanthanide complexes. It expands on the previous chapter by applying similar concepts, through attachment of a redox activatable azobenzene moiety to a DO3A ligand scaffold for bimetallic complexes, for enhancement of luminescence properties. Variation of the substituent on the azobenzene is discussed, including the synthetic challenges posed. This work contributes to the knowledge of the design, synthesis, stability and selectivity of monometallic and bimetallic lanthanide complexes for use in biological imaging applications.

Chapter 5 provides a summary of the work carried out, the conclusions that can be taken from it and the future work proposed, particularly focusing on the development of cell permeable lanthanide complexes for imaging *in vivo* for cancer diagnosis and prognosis

evaluation. Chapter 6 outlines the experimental procedures utilised during this work, including the synthesis and activation assays.

1.7 References

1. B. A. Chabner and T. G. Roberts, *Nature Reviews Cancer*, 2005, **5**, 65–72.
2. I. Regeni and S. Bonnet, *Nature Reviews Chemistry*, 2025, **9**, 365–377.
3. E. M. Hammond, M. C. Asselin, D. Forster, J. P. B. O'Connor, J. M. Senra and K. J. Williams, *Clinical Oncology*, 2014, **26**, 277–288.
4. S. R. McKeown, *The British Journal of Radiology*, 2014, **87**, 20130676.
5. S. Ramachandran, J. Ient, E.-L. Göttgens, A. J. Krieg and E. M. Hammond, *Genes*, 2015, **6**, 935–956.
6. H. Tharmalingham and P. Hoskin, *Br J Radiol*, 2019, **92**, 20170966.
7. W. R. Wilson and M. P. Hay, *Nature Reviews Cancer*, 2011, **11**, 393–410.
8. D. G. Brown and H. Park, *Journal of Medicinal Chemistry*, 2025, DOI: 10.1021/acs.jmedchem.5c00826.
9. X. Wang, Q. Ding, R. R. Groleau, L. Wu, Y. Mao, F. Che, O. Kotova, E. M. Scanlan, S. E. Lewis, P. Li, B. Tang, T. D. James and T. Gunnlaugsson, *Chemical Reviews*, 2024, **124**, 7106–7164.
10. B. K. McMahon, R. Pal and D. Parker, *Chemical Communications*, 2013, **49**, 5363–5365.
11. M. Giardiello, M. Botta and M. P. Lowe, *Inorganic Chemistry*, 2013, **52**, 14264–14269.
12. E. Pershagen and K. E. Borbas, *Angewandte Chemie International Edition*, 2015, **54**, 1787–1790.
13. L. J. O'Connor, I. N. Mistry, S. L. Collins, L. K. Folkes, G. Brown, S. J. Conway and E. M. Hammond, *ACS Central Science*, 2017, **3**, 20–30.
14. Ç. Tosun, A. L. D. Wallabregue, M. Mallerman, S. E. Phillips, C. M. Edwards, S. J. Conway and E. M. Hammond, *JACS Au*, 2023, **3**, 3237–3246.
15. A. L. D. Wallabregue, H. Bolland, S. Faulkner, E. M. Hammond and S. J. Conway, *Journal of the American Chemical Society*, 2023, DOI: 10.1021/jacs.2c12493.
16. J.-H. Tang, H. Li, C. Yuan, G. Parigi, C. Luchinat and T. J. Meade, *Journal of the American Chemical Society*, 2023, **145**, 10045–10050.
17. H. Martin, L. R. Lázaro, T. Gunnlaugsson and E. M. Scanlan, *Chemical Society Reviews*, 2022, **51**, 9694–9716.
18. M. Tropiano and S. Faulkner, *Chemical Communications*, 2014, **50**, 4696–4698.
19. Y. Zheng, M. Zhao, Q. Qiao, H. Liu, H. Lang and Z. Xu, *Dyes and Pigments*, 2013, **98**, 367–371.
20. W. Sun, J. Fan, C. Hu, J. Cao, H. Zhang, X. Xiong, J. Wang, S. Cui, S. Sun and X. Peng, *Chemical Communications*, 2013, **49**, 3890–3892.
21. B. Chen, P. Wang, Q. Jin and X. Tang, *Organic & Biomolecular Chemistry*, 2014, **12**, 5629–5633.
22. K. S. Troelsen, E. D. D. Calder, A. Skwarska, D. Sneddon, E. M. Hammond and S. J. Conway, *ChemMedChem*, 2021, **16**, 3691–3700.
23. J. Geng, Y. Zhang, Q. Gao, K. Neumann, H. Dong, H. Porter, M. Potter, H. Ren, D. Argyle and M. Bradley, *Nature Chemistry*, 2021, **13**, 805–810.
24. T. Gorai, J. I. Lovitt, B. Twamley, E. T. Luis and T. Gunnlaugsson, *Dalton Transactions*, 2025, **54**, 10022–10029.
25. A. Xie, S. Hanif, J. Ouyang, Z. Tang, N. Kong, N. Y. Kim, B. Qi, D. Patel, B. Shi and W. Tao, *EBioMedicine*, 2020, **56**, 102821.
26. M. Kobus, T. Friedrich, E. Zorn, N. Burmeister and W. Maison, *Journal of Medicinal Chemistry*, 2024, **67**, 5168–5184.
27. W. A. Denny, *Pharmaceuticals (Basel)*, 2022, **15**.
28. A. Skwarska, E. D. D. Calder, D. Sneddon, H. Bolland, M. L. Odyniec, I. N. Mistry, J. Martin, L. K. Folkes, S. J. Conway and E. M. Hammond, *Cell Chemical Biology*, 2021, **28**, 1258–1270.e1213.
29. E. D. D. Calder, A. Skwarska, D. Sneddon, L. K. Folkes, I. N. Mistry, S. J. Conway and E. M. Hammond, *Tetrahedron*, 2020, **76**, 131170.
30. B. Brennecke, Q. Wang, Q. Zhang, H.-Y. Hu and M. Nazaré, *Angewandte Chemie International Edition*, 2020, **59**, 8512–8516.
31. Y.-T. Bao, H.-B. Mao, K.-W. Lei, J.-B. Hu and J. Huang, *Talanta*, 2025, **285**, 127392.
32. A. Khan, *Chemical Communications*, 2024, **60**, 6591–6602.
33. S. Guisán-Ceinos, A. R. Rivero, F. Romeo-Gella, S. Simón-Fuente, S. Gómez-Pastor, N. Calvo, A. H. Orrego, J. M. Guisán, I. Corral, F. Sanz-Rodriguez and M. Ribagorda, *Journal of the American Chemical Society*, 2022, **144**, 8185–8193.
34. Y. Zhao, Q. Huang and Y. Liu, *ChemBioChem*, 2024, **25**, e202400635.
35. S. A. Everett, E. Swann, M. A. Naylor, M. R. L. Stratford, K. B. Patel, N. Tian, R. G. Newman, B. Vojnovic, C. J. Moody and P. Wardman, *Biochemical Pharmacology*, 2002, **63**, 1629–1639.
36. Y. Zeng, J. Ma, Y. Zhan, X. Xu, Q. Zeng, J. Liang and X. Chen, *Int J Nanomedicine*, 2018, **13**, 6551–6574.
37. P. Wardman, *Environ Health Perspect*, 1985, **64**, 309–320.
38. J. Jiang, C. Auchinvole, K. Fisher and C. J. Campbell, *Nanoscale*, 2014, **6**, 12104–12110.

39. S. A. Everett, M. A. Naylor, P. Barraja, E. Swann, K. B. Patel, M. R. L. Stratford, A. R. Hudnott, B. Vojnovic, R. J. Locke, P. Wardman and C. J. Moody, *Journal of the Chemical Society, Perkin Transactions 2*, 2001, DOI: 10.1039/B009652K, 843–860.
40. E. Tran, Z. Luo, A. X.-Y. Tang, C. Huang, Y. S. Gee, J. Baell, A. Kaur and M. Jörg, *ACS Sensors*, 2025, DOI: 10.1021/acssensors.5c01474.
41. H. Wang, V. C. Jordan, I. A. Ramsay, M. Sojoodi, B. C. Fuchs, K. K. Tanabe, P. Caravan and E. M. Gale, *Journal of the American Chemical Society*, 2019, **141**, 5916–5925.
42. G. S. Loving, S. Mukherjee and P. Caravan, *Journal of the American Chemical Society*, 2013, **135**, 4620–4623.
43. J. P. Holland, P. J. Barnard, D. Collison, J. R. Dilworth, R. Edge, J. C. Green and E. J. L. McInnes, *Chemistry – A European Journal*, 2008, **14**, 5890–5907.
44. N. Graf and S. J. Lippard, *Advanced Drug Delivery Reviews*, 2012, **64**, 993–1004.
45. R. M. Phillips, *Cancer Chemotherapy and Pharmacology*, 2016, **77**, 441–457.
46. Y. Zhang, J. Tan and Y. Chen, *Chemical Communications*, 2023, **59**, 2413–2420.
47. D. Sokolova, T. C. Lurshay, J. S. Rowbotham, G. Stonadge, H. A. Reeve, S. E. Cleary, T. Sudmeier and K. A. Vincent, *Nature Communications*, 2024, **15**, 7297.
48. L. Spiegelberg, R. Houben, R. Niemans, D. de Ruysscher, A. Yaromina, J. Theys, C. P. Guise, J. B. Smaill, A. V. Patterson, P. Lambin and L. J. Dubois, *Clinical and Translational Radiation Oncology*, 2019, **15**, 62–69.
49. J. C. Walsh, A. Lebedev, E. Aten, K. Madsen, L. Marciano and H. C. Kolb, *Antioxid Redox Signal*, 2014, **21**, 1516–1554.
50. S. Hussain, I. Mubeen, N. Ullah, S. Shah, B. A. Khan, M. Zahoor, R. Ullah, F. A. Khan and M. A. Sultan, *Biomed Res Int*, 2022, **2022**, 5164970.
51. A. Rembielak, M. Green, A. Saleem and P. Price, *Medicine*, 2016, **44**, 6–9.
52. M. A. Pysz, S. S. Gambhir and J. K. Willmann, *Clinical Radiology*, 2010, **65**, 500–516.
53. Optical Imaging, https://www.nibib.nih.gov/science-education/science-topics/optical-imaging, (accessed 2nd January 2025).
54. in *Lanthanide and Actinide Chemistry*, 2006, DOI: https://doi.org/10.1002/0470010088.ch2, pp. 9–22.
55. J.-C. G. Bünzli and S. V. Eliseeva, in *Lanthanide Luminescence: Photophysical, Analytical and Biological Aspects*, eds. P. Hänninen and H. Härmä, Springer Berlin Heidelberg, Berlin, Heidelberg, 2011, DOI: 10.1007/4243_2010_3, pp. 1–45.
56. A. de Bettencourt-Dias, *Luminescence of Lanthanide Ions in Coordination Compounds and Nanomaterials*, John Wiley & Sons, Incorporated, Newark, UNITED KINGDOM, 2014.
57. in *Lanthanide and Actinide Chemistry*, 2006, DOI: https://doi.org/10.1002/0470010088.ch1, pp. 1–7.
58. A. Weller, J. L. Barber and Ø. E. Olsen, *Pediatric Nephrology*, 2014, **29**, 1927–1937.
59. B. Mlinar and J. J. Enyeart, *The Journal of Physiology*, 1993, **469**, 639–652.
60. B. D. Lewis and E. P. Spalding, *J Membr Biol*, 1998, **162**, 81–90.
61. G. W. Bourne and J. M. Trifaró, *Neuroscience*, 1982, **7**, 1615–1622.
62. C. A. Chang, L. C. Francesconi, M. F. Malley, K. Kumar, J. Z. Gougoutas, M. F. Tweedle, D. W. Lee and L. J. Wilson, *Inorganic Chemistry*, 1993, **32**, 3501–3508.
63. S. Aime, A. Barge, M. Botta, M. Fasano, J. Danilo Ayala and G. Bombieri, *Inorganica Chimica Acta*, 1996, **246**, 423–429.
64. M. R. Spirlet, J. Rebizant, J. F. Desreux and M. F. Loncin, *Inorganic Chemistry*, 1984, **23**, 359–363.
65. K. Kumar, C. A. Chang and M. F. Tweedle, *Inorganic Chemistry*, 1993, **32**, 587–593.
66. K. Kumar, C. A. Chang, L. C. Francesconi, D. D. Dischino, M. F. Malley, J. Z. Gougoutas and M. F. Tweedle, *Inorganic Chemistry*, 1994, **33**, 3567–3575.
67. E. Szilágyi, É. Tóth, Z. Kovács, J. Platzek, B. Radüchel and E. Brücher, *Inorganica Chimica Acta*, 2000, **298**, 226–234.
68. G. J. Stasiuk and N. J. Long, *Chemical Communications*, 2013, **49**, 2732–2746.
69. A. Pasha, G. Tircsó, E. T. Benyó, E. Brücher and A. D. Sherry, *European Journal of Inorganic Chemistry*, 2007, **2007**, 4340–4349.
70. T. J. Sørensen and S. Faulkner, *Accounts of Chemical Research*, 2018, **51**, 2493–2501.
71. S. Faulkner and O. A. Blackburn, in *The Chemistry of Molecular Imaging*, 2014, DOI: https://doi.org/10.1002/9781118854754.ch8, pp. 179–197.
72. D. Kretschy, G. Koellensperger and S. Hann, *Metallomics*, 2011, **3**, 1304–1309.
73. J. Blahut, P. Hermann, Z. Tošner and C. Platas-Iglesias, *Physical Chemistry Chemical Physics*, 2017, **19**, 26662–26671.
74. M. Holzapfel, T. Baldau, S. Kerpa, G. Guadalupi, B. Qi, Y. Liu, W. J. Parak and W. Maison, *European Journal of Inorganic Chemistry*, 2022, **2022**, e202200432.
75. J. R. Lakowicz, in *Principles of Fluorescence Spectroscopy*, Springer, Third Edition edn., 2006.
76. Y. Hasegawa, Y. Kitagawa and T. Nakanishi, *NPG Asia Materials*, 2018, **10**, 52–70.
77. M. Y. Berezin and S. Achilefu, *Chemical Reviews*, 2010, **110**, 2641–2684.
78. K. Binnemans, *Coordination Chemistry Reviews*, 2015, **295**, 1–45.
79. M. S. Thomsen, P. R. Nawrocki, N. Kofod and T. J. Sørensen, *European Journal of Inorganic Chemistry*, 2022, **2022**, e202200334.

80. W. T. Carnall, P. R. Fields and K. Rajnak, *The Journal of Chemical Physics*, 1968, **49**, 4424–4442.
81. W. T. Carnall, P. R. Fields and K. Rajnak, *The Journal of Chemical Physics*, 1968, **49**, 4443–4446.
82. W. T. Carnall, P. R. Fields and K. Rajnak, *The Journal of Chemical Physics*, 1968, **49**, 4447–4449.
83. W. T. Carnall, P. R. Fields and K. Rajnak, *The Journal of Chemical Physics*, 1968, **49**, 4450–4455.
84. E. G. Moore, A. P. S. Samuel and K. N. Raymond, *Accounts of Chemical Research*, 2009, **42**, 542–552.
85. M. Murru, D. Parker, G. Williams and A. Beeby, *Journal of the Chemical Society, Chemical Communications*, 1993, DOI: 10.1039/C39930001116, 1116–1118.
86. A. K. R. Junker, L. R. Hill, A. L. Thompson, S. Faulkner and T. J. Sørensen, *Dalton Transactions*, 2018, **47**, 4794–4803.
87. M. Shi, F. Li, T. Yi, D. Zhang, H. Hu and C. Huang, *Inorganic Chemistry*, 2005, **44**, 8929–8936.
88. M. Latva, H. Takalo, V.-M. Mukkala, C. Matachescu, J. C. Rodríguez-Ubis and J. Kankare, *Journal of Luminescence*, 1997, **75**, 149–169.
89. M. D. Ward, *Coordination Chemistry Reviews*, 2010, **254**, 2634–2642.
90. D. L. Dexter, *The Journal of Chemical Physics*, 1953, **21**, 836–850.
91. T. Főrster, *Discussions of the Faraday Society*, 1959, **27**, 7–17.
92. T. Lazarides, D. Sykes, S. Faulkner, A. Barbieri and M. D. Ward, *Chemistry – A European Journal*, 2008, **14**, 9389–9399.
93. M. H. V. Werts, R. T. F. Jukes and J. W. Verhoeven, *Physical Chemistry Chemical Physics*, 2002, **4**, 1542–1548.
94. M. Hasegawa, H. Ohmagari, H. Tanaka and K. Machida, *Journal of Photochemistry and Photobiology C: Photochemistry Reviews*, 2022, **50**, 100484.
95. A. K. R. Junker and T. J. Sørensen, *European Journal of Inorganic Chemistry*, 2019, **2019**, 1201–1206.
96. F. A. Kolokolov, M. A. Magomadova, K. K. Shapieva and V. T. Panyushkin, *Journal of Applied Spectroscopy*, 2019, **86**, 321–324.
97. V. M. Korshunov, M. A. Kiskin and I. V. Taydakov, *Journal of Luminescence*, 2022, **251**, 119235.
98. D. Kovacs, E. Mathieu, S. R. Kiraev, J. A. L. Wells, E. Demeyere, A. Sipos and K. E. Borbas, *Journal of the American Chemical Society*, 2020, **142**, 13190–13200.
99. D. Escudero, *Accounts of Chemical Research*, 2016, **49**, 1816–1824.
100. D. Kovacs and K. E. Borbas, *Coordination Chemistry Reviews*, 2018, **364**, 1–9.
101. T. A. Shakhverdov, *Optics and Spectroscopy*, 2003, **95**, 571–580.
102. A. Watkis, R. Hueting, T. J. Sørensen, M. Tropiano and S. Faulkner, *Chemical Communications*, 2015, **51**, 15633–15636.
103. D. Parker, J. D. Fradgley, M. Delbianco, M. Starck, James W. Walton and J. M. Zwier, *Faraday Discussions*, 2022, **234**, 159–174.
104. R. S. Dickins, D. Parker, A. S. de Sousa and J. A. G. Williams, *Chemical Communications*, 1996, DOI: 10.1039/CC9960000697, 697–698.
105. P. B. Glover, A. P. Bassett, P. Nockemann, B. M. Kariuki, R. Van Deun and Z. Pikramenou, *Chemistry – A European Journal*, 2007, **13**, 6308–6320.
106. J.-Y. Hu, Y. Ning, Y.-S. Meng, J. Zhang, Z.-Y. Wu, S. Gao and J.-L. Zhang, *Chemical Science*, 2017, **8**, 2702–2709.
107. A. Beeby, I. M. Clarkson, R. S. Dickins, S. Faulkner, D. Parker, L. Royle, A. S. de Sousa, J. A. Gareth Williams and M. Woods, *Journal of the Chemical Society, Perkin Transactions 2*, 1999, 493–504.
108. Y. Hasegawa and Y. Kitagawa, *Journal of Photochemistry and Photobiology C: Photochemistry Reviews*, 2022, **51**, 100485.
109. C. Doffek, N. Alzakhem, M. Molon and M. Seitz, *Inorganic Chemistry*, 2012, **51**, 4539–4545.
110. W. D. Horrocks, Jr. and D. R. Sudnick, *Journal of the American Chemical Society*, 1979, **101**, 334–340.
111. D. Parker, E. A. Suturina, I. Kuprov and N. F. Chilton, *Accounts of Chemical Research*, 2020, **53**, 1520–1534.
112. J. A. Peters, J. Huskens and D. J. Raber, *Progress in Nuclear Magnetic Resonance Spectroscopy*, 1996, **28**, 283–350.
113. A. Rodríguez-Rodríguez, D. Esteban-Gómez, A. de Blas, T. Rodríguez-Blas, M. Botta, R. Tripier and C. Platas-Iglesias, *Inorganic Chemistry*, 2012, **51**, 13419–13429.
114. S. Di Pietro, S. L. Piano and L. Di Bari, *Coordination Chemistry Reviews*, 2011, **255**, 2810–2820.
115. B. Bleaney, *Journal of Magnetic Resonance (1969)*, 1972, **8**, 91–100.
116. B. Bleaney, C. M. Dobson, B. A. Levine, R. B. Martin, R. J. P. Williams and A. V. Xavier, *Journal of the Chemical Society, Chemical Communications*, 1972, 791b–793.
117. A. M. Funk, K.-L. N. A. Finney, P. Harvey, A. M. Kenwright, E. R. Neil, N. J. Rogers, P. Kanthi Senanayake and D. Parker, *Chemical Science*, 2015, **6**, 1655–1662.
118. M. Vonci, K. Mason, E. A. Suturina, A. T. Frawley, S. G. Worswick, I. Kuprov, D. Parker, E. J. L. McInnes and N. F. Chilton, *Journal of the American Chemical Society*, 2017, **139**, 14166–14172.
119. R. Vogel, T. Müntener and D. Häussinger, *Chem*, 2021, **7**, 3144–3156.
120. J. D. Rinehart and J. R. Long, *Chemical Science*, 2011, **2**, 2078–2085.
121. D. Parker, N. J. Long and S. Faulkner, *Philosophical Transactions of the Royal Society A: Mathematical, Physical and Engineering Sciences*, 2017, **375**, 20170024.
122. J. Wahsner, E. M. Gale, A. Rodríguez-Rodríguez and P. Caravan, *Chemical Reviews*, 2019, **119**, 957–1057.
123. V. C. Pierre, M. J. Allen and P. Caravan, *JBIC Journal of Biological Inorganic Chemistry*, 2014, **19**, 127–131.

124. Drugs@FDA: FDA-Approved Drugs, https://www.accessdata.fda.gov/scripts/cder/daf/index.cfm, (accessed 30th June 2025).
125. Guerbet, Guerbet announces marketing authorisation approval of Elucirem™ (Gadopiclenol) in the European Union, https://www.guerbet.com/news/guerbet-announces-marketing-authorisation-approval-of-elucirem-gadopiclenol-in-the-european-union, (accessed 30th June 2025).
126. V. Jacques, S. Dumas, W. C. Sun, J. S. Troughton, M. T. Greenfield and P. Caravan, *Invest Radiol*, 2010, **45**, 613–624.
127. P. Caravan, D. Esteban-Gómez, A. Rodríguez-Rodríguez and C. Platas-Iglesias, *Dalton Transactions*, 2019, **48**, 11161–11180.
128. C. F. G. C. Geraldes and J. A. Peters, *Molecules*, 2022, **27**.
129. S. Pandya, J. Yu and D. Parker, *Dalton Transactions*, 2006, DOI: 10.1039/B514637B, 2757–2766.
130. Q.-J. Duan, Z.-Y. Zhao, Y.-J. Zhang, L. Fu, Y.-Y. Yuan, J.-Z. Du and J. Wang, *Advanced Drug Delivery Reviews*, 2023, **196**, 114793.
131. R. Ito, M. Kamiya and Y. Urano, *Current Opinion in Chemical Biology*, 2022, **67**, 102112.
132. P. Zhang, Y. Zhu, C. Xiao and X. Chen, *Advanced Drug Delivery Reviews*, 2023, **195**, 114725.
133. Y. Yao, C. Kong, L. Yin, A. D. Jain, K. Ratia, G. R. J. Thatcher, T. W. Moore, T. G. Driver and L. W. Miller, *Chemistry – A European Journal*, 2017, **23**, 752–756.
134. A. Li, X. Luo, L. Li, D. Chen, X. Liu, Z. Yang, L. Yang, J. Gao and H. Lin, *Analytical Chemistry*, 2021, **93**, 16552–16561.
135. S. Karan, J.-H. Cho, C. Thi Ngoc Tran, M. Y. Cho, H. Lee, R. Naskar, I. Hwang, S. Pradhan, H. S. Park, E. H. Han, J. L. Sessler and K. S. Hong, *Sensors and Actuators B: Chemical*, 2024, **413**, 135839.
136. H. Niu, J. Liu, H. M. O'Connor, T. Gunnlaugsson, T. D. James and H. Zhang, *Chemical Society Reviews*, 2023, **52**, 2322–2357.
137. W. R. Dolbier, A.-R. Li, C. J. Koch, C.-Y. Shiue and A. V. Kachur, *Applied Radiation and Isotopes*, 2001, **54**, 73–80.
138. L. Jiang, Y. Tu, H. Shi and Z. Cheng, *J Biomed Res*, 2014, **28**, 435–446.
139. H. Jeong, X. Wu, J.-S. Lee and J. Yoon, *TrAC Trends in Analytical Chemistry*, 2023, **168**, 117335.
140. X. Liu, S. Zeng, M. Zhang, M. Jiang, Y. S. Kafuti, P. Shangguan, Y. Yu, Q. Chen, J. Wang, X. Peng, J. Yoon and H. Li, *Chemical Communications*, 2022, **58**, 11438–11441.
141. J. Gao, M. Liu, L. Wu, Z. Tian, J.-H. Tang and Y. Sun, *ACS Applied Engineering Materials*, 2024, **2**, 2504–2520.
142. Y. Wang, L. Zhang, Y. Huang, X. Wang, L. Zhang and L. Chen, *Sensors and Actuators B: Chemical*, 2020, **310**, 127755.
143. S. Iwaki, K. Hanaoka, W. Piao, T. Komatsu, T. Ueno, T. Terai and T. Nagano, *Bioorg Med Chem Lett*, 2012, **22**, 2798–2802.
144. N. J. Farrer, J. A. Woods, L. Salassa, Y. Zhao, K. S. Robinson, G. Clarkson, F. S. Mackay and P. J. Sadler, *Angewandte Chemie International Edition*, 2010, **49**, 8905–8908.
145. K. Yao, A. Bertran, A. Howarth, J. M. Goicoechea, S. M. Hare, N. H. Rees, M. Foroozandeh, A. M. Bowen and N. J. Farrer, *Chemical Communications*, 2019, **55**, 11287–11290.
146. M. H. C. Boulet, H. R. Bolland, E. M. Hammond and A. C. Sedgwick, *Journal of the American Chemical Society*, 2023, **145**, 12998–13002.
147. S. Huang, J. W. Marsh, J. R. G. White, T. Q. Ha, S. A. Twigger, I. Diez-Perez and A. C. Sedgwick, *New Journal of Chemistry*, 2024, **48**, 7548–7551.
148. J. W. Marsh, L. Hacker, S. Huang, M. H. C. Boulet, J. R. G. White, L. A. W. Martin, M. A. Yeomans, H.-H. Han, I. Diez-Perez, R. A. Musgrave, E. M. Hammond and A. C. Sedgwick, *Dalton Transactions*, 2024, **53**, 14811–14816.
149. F. Baark, F. Shaughnessy, V. R. Pell, J. E. Clark, T. R. Eykyn, P. Blower and R. Southworth, *Sci Rep*, 2019, **9**, 499.
150. R. An, X. Cheng, S. Wei, Y. Hu, Y. Sun, Z. Huang, H.-Y. Chen and D. Ye, *Angewandte Chemie International Edition*, 2020, **59**, 20636–20644.
151. P. S. Murphy, N. Patel and T. J. McCarthy, *Philosophical Transactions of the Royal Society A: Mathematical, Physical and Engineering Sciences*, 2017, **375**, 20170112.
152. C. A. Foster, D. Sneddon, L. Hacker, E. T. Sarson, M. Robertson, D. Sokolova, L. A. W. Martin, M. F. Allen, A. Khrapichev, K. A. Vincent, E. M. Hammond, S. J. Conway and S. Faulkner, *Inorganic Chemistry*, 2025, **64**, 6640–6647.

2. Chapter II - Development of hypoxia- and X-ray activated tetrafluoroaryl azide profluorophores

2.1 Azides as activatable moieties

Azides can be used as bioreductive moieties for cancer imaging due to their resistance to biological hydrolysis and high kinetic stability.[1] Prior to the start of this research, there were few examples in the literature for the use of azides as either hypoxia-activatable[1] or X-ray activatable moieties,[2] or for imaging the presence of NaHS/H_2S.[3-6]

As azides can be activated under a variety of conditions, including under hypoxia, X-ray irradiation, or in the presence of sulfides, a key question in the field is whether these mechanisms of activation cause activation to different intermediates or products, or whether different modes of activation can be used in combination. For example, X-ray activation of a prodrug which is partially activated in a hypoxic tumour could be used to achieve higher levels of drug release. O'Connor *et al*.[1] reported an organic azide compound (reported as CH-02, hereafter referred to as DCM-N_3, **1**, Figure 2.1a) which is reduced selectively under hypoxic conditions to the more fluorescent amine compound (DCM-NH_2, **2**), both *in vitro* (using CYP enzymes) and in HepG2 and OE21 cells. Despite previous reports of activation of DCM-N_3 in the presence of hydrogen sulfide both *in vitro* and *in cellulo*,[4, 5] DCM-N_3 was reported to be stable in the presence of GSH and L-cysteine, in both normoxia and hypoxia, and cystathionine-β-synthase (CBS), an enzyme which accumulates in hypoxic tissue. This suggests that reaction with thiols is not a dominant mechanism of activation for this compound. The mechanism of reduction of the azide moiety was further investigated using steady-state γ-radiolysis (total 84 Gy, ~60% conversion), demonstrating its ability to be activated by sequential single-electron transfer reduction.[1]

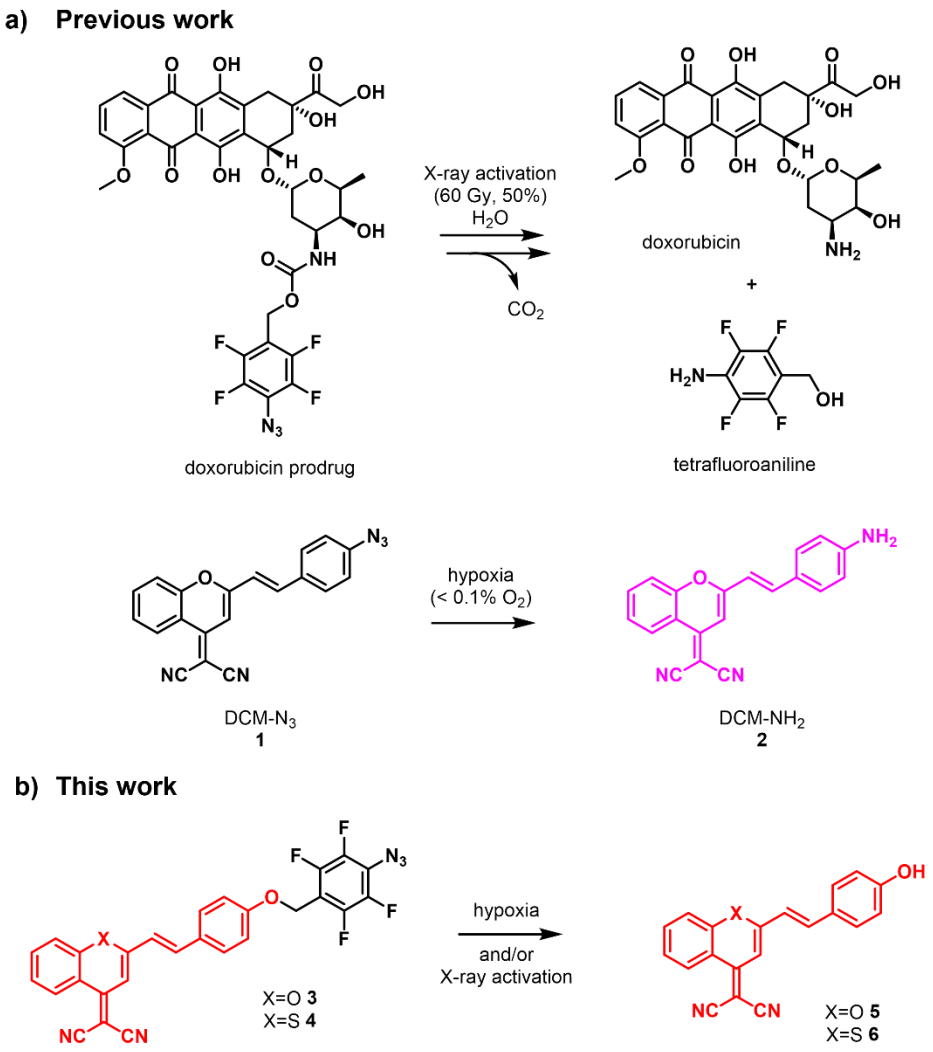

Figure 2.1: a) Previously reported activatable azide profluorophores developed by Geng *et al*. (the tetrafluoroaryl azide prodrug which releases doxorubicin and tetrafluoroaniline upon 60 Gy X-ray irradiation) and O'Connor *et al.* (used as positive controls in this chapter, DCM-N_3 **1** and DCM-NH_2 **2**).[1, 2] b) The structures of the initial targets of chapter 2 (**3** and **4**) and the corresponding fluorophores (DCM-OH, **5** and **6**).

Recent work by Geng *et al.*[2] demonstrated that azide moieties may be activated using high doses of X-ray irradiation *in vitro*. Their initial study of X-ray irradiation of different functional groups was carried out using 60 Gy doses. This is much higher than doses used clinically for radiotherapy, which are typically 1.8-2.0 Gy[7] for large tumours, or up to 18 Gy for stereotactic ablative radiotherapy (SABR),[8-10] which uses hypofractioned radiotherapy doses (≥ 5 Gy) for treatment of small tumours.[11] The study highlighted that sulfonyl and aromatic azides are promising moieties for irradiation as they only produce one or two compounds which may be fully characterised, reducing the likelihood of off-target activity from the production of multiple fragments. Testing of their tetrafluoroaryl azide doxorubicin

prodrug (Figure 2.1a) demonstrated that *in vitro* 50% activation was observed with 60 Gy X-ray irradiation and that tumour growths in xenograft mice models were inhibited using 6 Gy X-ray irradiation. This prior work demonstrates promise for the development of X-ray activated prodrugs for combined chemotherapy and radiotherapy uses, however for clinical utility prodrugs should be activatable at doses closer to 2 Gy to assist outcomes for patients with large tumours, as SABR works well for patients with small tumours.

2.2 Design rationale of initial profluorophores

The work in this chapter aimed to expand on and combine the motifs previously reported by O'Connor *et al.*[1] and Geng *et al.*[2] to develop a profluorophore that could be activated under hypoxia and/or X-ray irradiation*, via* the mechanisms proposed in Figure 2.2. These profluorophores were chosen to investigate whether activation under hypoxia gives the same products as activation following X-ray irradiation and therefore whether these methods could be used complementarily to increase drug or fluorophore release *in vivo.* Under hypoxia the effect of radiotherapy is impaired, therefore simultaneous delivery of prodrugs or profluorophores, activated by radiation and hypoxia, is a potential route to overcome this. This chapter reports the synthesis of four novel azide profluorophores, in addition to their controls, photophysical characterisation (by UV-Vis and fluorescence spectroscopy), solubility measurements, and preliminary activation analysis (in the presence of zinc, enzymes, and X-rays).

The initial target profluorophore, compound **3** (Figure 2.1b), was the tetrafluoroaryl azide-protected profluorophore of the well-characterised dye (*E*)-2-(2-(4-hydroxystyryl)-4*H*-chromen-4-ylidene)malononitrile, (DCM-OH, **5**). The sulfur-containing analogues (profluorophore **4** and S-DCM-OH dye **6**) were proposed due to the advantageous photophysical properties (larger Stokes shift) of similar sulfur- or selenium-based dyes previously reported.[12] The compounds DCM-N_3 (**1**) and DCM-NH_2 (**2**) which have previously been reported in the literature are used throughout this chapter as positive controls.[1]

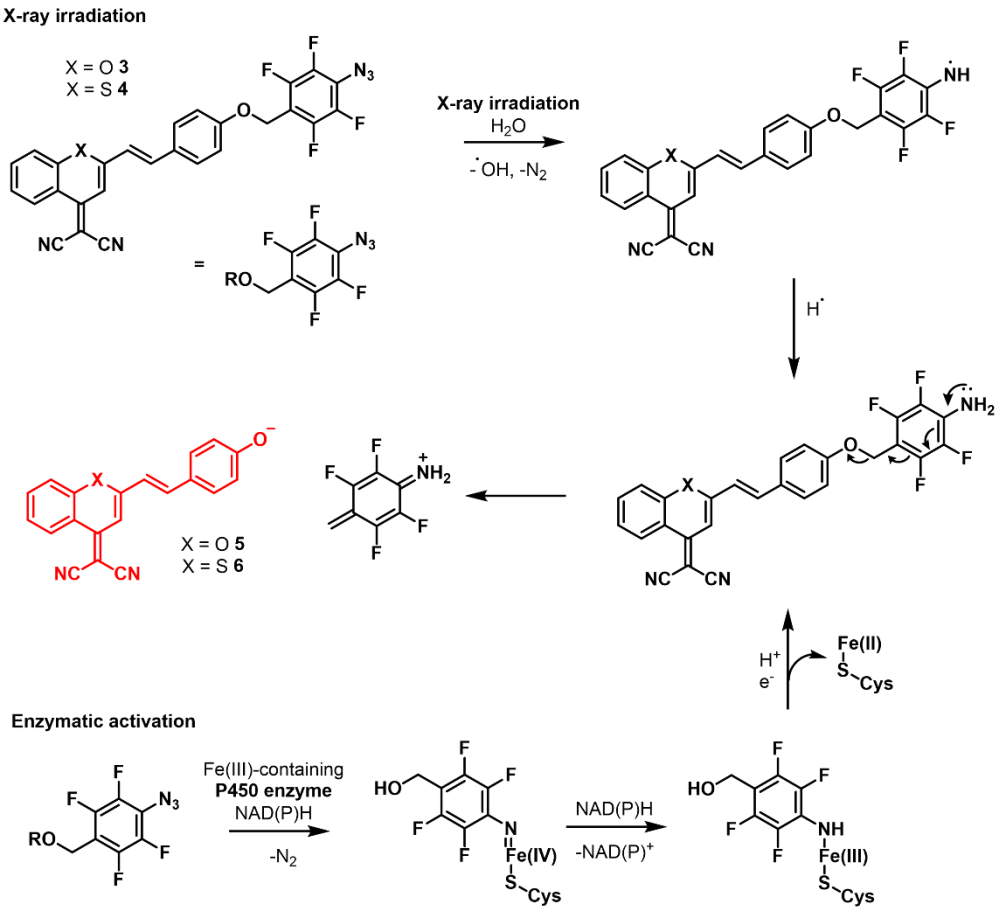

Figure 2.2: The proposed mechanisms of X-ray activation (top) and simplified mechanism of enzymatic activation (bottom) of compounds **3** and **4** to give the aniline intermediate and subsequent fragmentation, based on the mechanisms proposed by Geng *et al*.[2] and O'Connor *et al*.[1] X = O/S. Cys = cysteine.

2.3 Evaluation of dichromenone-based profluorophores

2.3.1 Synthesis of dichromenone-based profluorophores

Scheme 2.1 outlines the synthesis of the initial target DCM-derived profluorophores, **3** and **4**.

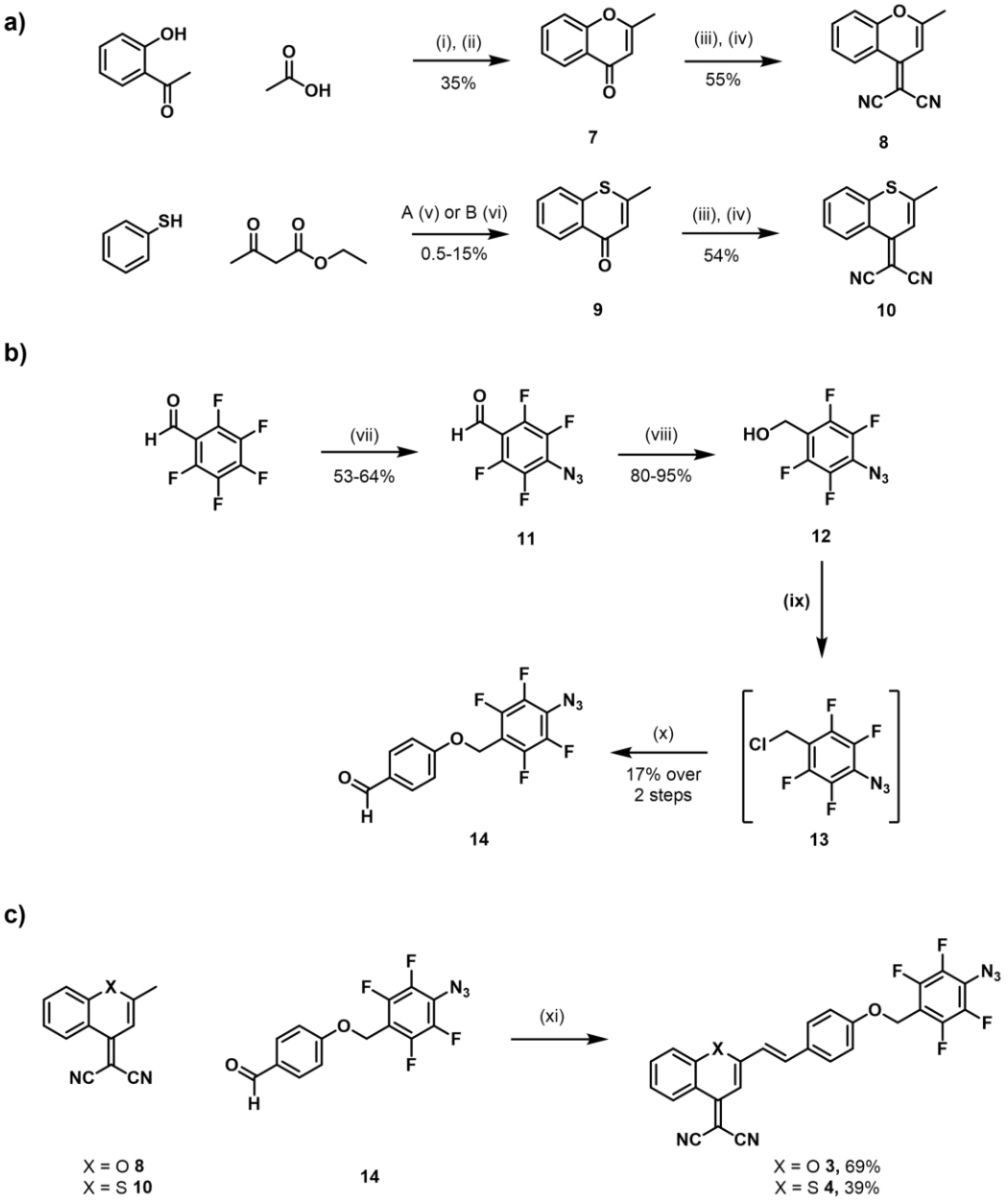

Scheme 2.1: The synthetic route for profluorophores 3 and 4: a) the synthesis of the dichromenone core, b) the synthesis of the azide-based activatable group and c) the combination of the fluorophore and activatable group. Reagents and conditions: (i) Sodium metal, ethanol, rt, 17 h; (ii) Acetic acid, water, concentrated sulfuric acid, 100 °C, 1 h; (iii) Malononitrile, acetic anhydride, 140 °C, 5 h; (iv) MeOH, 50 °C, 30 min; (v) Phosphoric acid (85% in water), phosphorus pentoxide, 70 °C, 5 h; (vi) Polyphosphoric acid, 90 °C, 30 min – 5 h; (vii) Sodium azide, acetone, water, 100 °C; (viii) Dimethylamine borane, acetic acid, rt, 1 h; (ix) Thionyl chloride, CH_2Cl_2, rt, 1 h; (x) 4-Hydroxybenzaldehyde, caesium carbonate, tetrabutylammonium iodide, dry DMF, 0 °C to rt, 2 h; (xi) Piperidine, EtOH, 80 °C, 5-7 h.

Synthesis of the chromenone dye **8** was carried out according to the reported literature procedures.[1] The thiochromenone dye **10** (Scheme 2.1a) was synthesised by a Simonis chromone cyclisation reaction,[13, 14] where ethyl acetoacetate is activated by phosphorus pentoxide, using two different reported routes. The initial route used (route A,[15-17] Table 2.1) resulted in extremely poor yields over two steps (< 2%) due to the poor yield of the

cyclisation step. Many by-products were observed by TLC and degradation of these by-products was observed during column chromatography (6 spots observed after work-up, over 10 spots observed during purification). Use of route B, using polyphosphoric acid,[12, 13] gave **10** in higher yields and purity, as fewer by-products were observed by TLC for the formation of **9** and the purification of both **9** and **10** were optimised.

Table 2.1: Analysis of the two methods used to form the thiochromenone core, **10**.[12, 13, 15-17]

		Method A	**Method B**
Reagents		Phosphoric acid (85% in H_2O), phosphorus pentoxide	Polyphosphoric acid
Purification	Step 1	Gradient column	Slow gradient or isocratic column
	Step 2	Recrystallisation	Isocratic column
Yield / %	Step 1	0.5–10	8–15
	Step 2	9–53	53

The tetrafluoroaryl azide alcohol intermediate **12** was synthesised using the previously reported literature procedure (Scheme 2.1b).[18] Column chromatography was used to purify the aldehyde intermediate **11** (formed by a selective S_NAr reaction), in favour of the sublimation method used in the literature,[19-21] for safety reasons and to obtain higher yields (64% compared to 53%) and purity (96% compared to 91% previously). Compound **11** was reduced using dimethylamine borane to form the alcohol **12**, according to the literature procedure.[18] The chloride intermediate **13**, formed by treatment of **12** with thionyl chloride, was used directly in subsequent reactions, and was not stored or purified due to stability concerns, evidenced by the formation of an unidentified fluorinated by-product over time, according to ^{1}H and ^{19}F NMR analysis. The final profluorophores, **3** and **4**, were obtained (Scheme 2.1c), *via* Knoevenagel condensation, in moderate yields of 39-69%.

For use as control compounds, DCM-OH (**5**) was synthesised according to the literature procedure,[22, 23] and the sulfur derivative S-DCM-OH (**6**) was synthesised analogously (Scheme 2.2a). For comparison to the literature, DCM-N_3 (**3**) and DCM-NH_2 (**4**) were synthesised according to the previously reported procedure and obtained in moderate yields of 38-47% (Scheme 2.2b).[1]

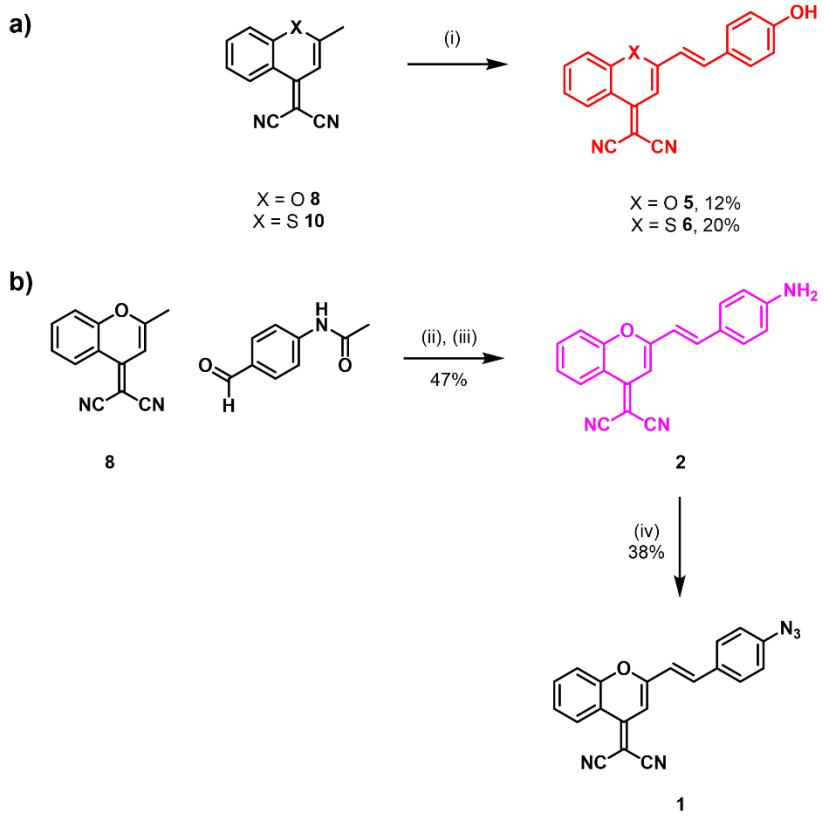

Scheme 2.2: a) The synthesis route of the positive control fluorophores, DCM-OH (**5**) and S-DCM-OH (**6**), b) the synthesis route for the control compounds DCM-N_3 (**1**) and DCM-NH_2 (**2**), according to the literature procedures.[1, 22, 23] *Reagents and conditions*: (i) 4-Hydroxybenzaldehyde, acetic acid: piperidine 1:1 (v/v), toluene, 115 °C, 16 h; (ii) Acetic acid : piperidine 1:1 (v/v), toluene, 115 °C, 3 h; (iii) Hydrochloric acid (37%) : ethanol 2:3 (v/v), 80 °C, 3 h; (iv) Sodium nitrite, sodium azide, aqueous hydrochloric acid (5M), 0 °C, 1 h.

2.3.2 Photophysical characterisation of dichromenone-based profluorophores

The profluorophores and corresponding fluorophores were characterised using ^{1}H and ^{13}C NMR spectroscopy and HRMS and their purity was determined by analytical HPLC. Their photophysics were characterised by UV-Vis and fluorescence spectroscopy in a variety of solvents (Figure A2.1, Table A1.1, Figure 2.3) relevant to the chemical activation assays, to asses any differences and solvatochromism observed. Figure 2.3 shows that, in DMSO:PBS 1:1, the fluorophores display stronger absorbance in the 500–600 nm range than the profluorophores and there are differences in the shapes of the bands, consistent with those previously observed for alkylation of a fluorophore phenol.[24] Their fluorescence emission spectra show that the profluorophores do not emit whereas the fluorophores are highly emissive. This emission occurs due to intramolecular charge transfer (ICT), as the fluorescent phenolates (e.g. DCM-O^-) are highly conjugated and contain a donor-π-

acceptor system. As predicted, S-DCM-OH **6** has a larger Stokes' shift (179 nm, measured at 10 µM in DMSO:PBS 1:1) than DCM-OH **5** (142 nm). It is noted that for the profluorophores the largest UV-Vis absorbance (Table A1.1) is observed in DMSO only and there is only a small change in absorbance for profluorophore **13** observed upon doubling the concentration in DMSO:PBS from 10 µM to 20 µM, which suggests there may be solubility issues and aggregation in partially aqueous solutions. In addition, the UV-Vis spectra of **13** in DMSO:PBS, MeCN:PBS and PBS (Figure A2.1b-d and f) do not go to zero, further suggesting insolubility.

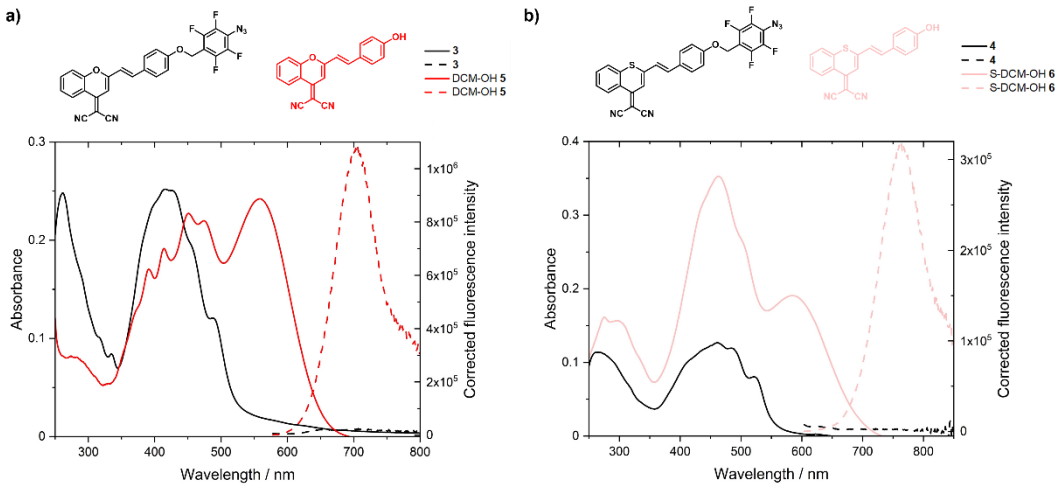

Figure 2.3: The UV-Vis spectra (solid lines) and fluorescence emission spectra (dashed lines) of a) profluorophore **3** (black) vs DCM-OH (**5**, red) and b) profluorophore **4** (black) vs S-DCM-OH (**6**, pink), measured at 10 µM in DMSO:PBS (1:1 *v/v*, buffer pH 7.4). For panel a fluorescence emission, λ_{ex} 558 nm, λ_{em} 580–800 nm, slits 5 nm / 2 nm; for panel b fluorescence emission, λ_{ex} 584 nm, λ_{em} 605–800 nm, slits 10 nm / 2 nm. S1c/R1c channel.

The excitation spectra (Figure 2.4) of compounds **3-6** were measured at 10 µM in DMSO:PBS 1:1 and generally overlayed well with their corresponding UV-Vis spectra, confirming that any fluorescence (or lack thereof) is due to the desired compound. The excitation spectrum of compound **4** (Figure 2.4c) was too noisy to meaningfully compare to the UV-Vis spectrum, likely due to lack of emission at the excitation wavelength.

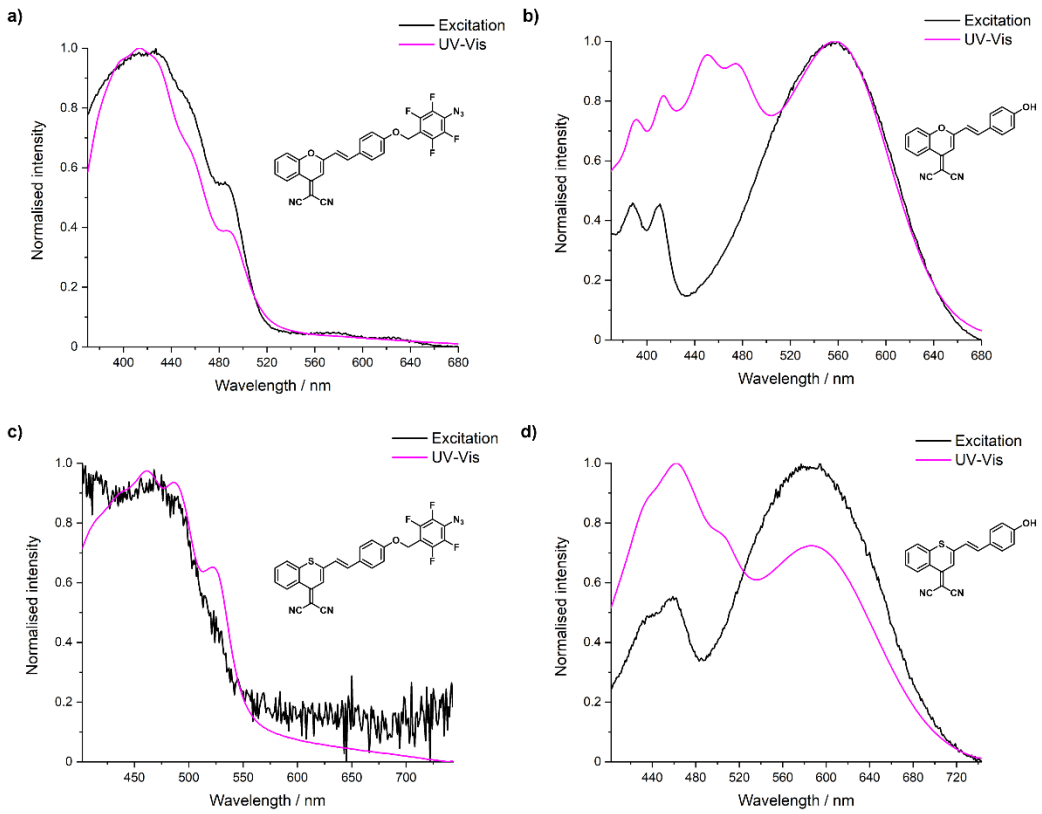

Figure 2.4: The excitation spectra, normalised and compared to the corresponding UV-Vis spectra, for a) compound **3**, b) DCM-OH **5**, c) compound **4,** and d) S-DCM-OH **6**. For **3** and **5**, λ_{em} 700 nm, λ_{ex} 360–680 nm, slits 5 nm / 2 nm. For **4** and **6**, λ_{em} 763 nm, λ_{em} 400–740 nm, slits 10 nm / 2 nm. All compounds measured at 10 µM in DMSO:PBS (1:1 *v/v*, buffer pH 7.4). S1c/R1c channel used for excitation spectra.

2.3.3 Chemical activation of the dichromenone-based profluorophores

To study the bioreduction of prodrugs and profluorophores *in vitro*, a chemical reduction assay is commonly carried out prior to an enzymatic assay. The reduction of hypoxia-activated species is commonly assessed in the literature using zinc powder and ammonium chloride[1, 25] and NaHS (as a sulfide source) is employed to assess the reduction of azide compounds, as a surrogate for endogenous sulfide species.[3, 4, 26]

2.3.3.1 Zinc reduction assays

DCM-N_3 (**1**) was evaluated as a positive control in the presence of zinc powder/ammonium chloride (Figure 2.5) and similar results to those reported in the literature were observed.[1] A 5-fold increase in fluorescence emission intensity was observed after 25 minutes of reaction of DCM-N_3 with zinc powder and ammonium chloride in IPA (zinc reduction assay

method 1, Figure 2.5b), in comparison to the 24-fold increase observed between DCM-N_3 and the positive control DCM-NH_2.This corresponds to partial conversion of DCM-N_3 to DCM-NH_2 (**2**) and was corroborated by HPLC analysis (Figure 2.5c, HPLC method 1B). Analysis of the area under the curve of the emission spectra over time (Figure 2.5d) suggests that the reduction is not complete, as a plateau is not reached, and further timepoints could be taken to further probe this reduction, however this was not carried out as the assay was only used for comparison to prior literature.

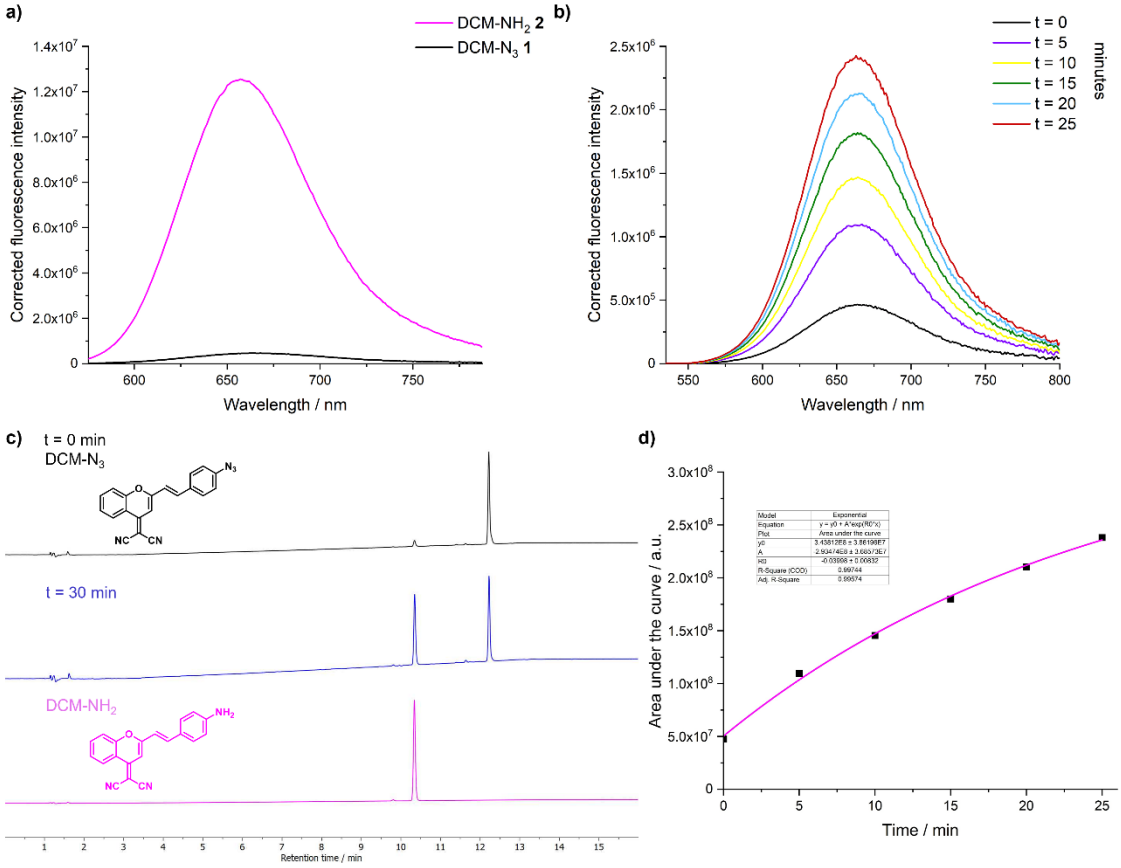

Figure 2.5: a) Fluorescence baselines for DCM-N_3 (**1,** black) and DCM-NH_2 (**2**, pink) at 50 µM in IPA. λ_{ex} 515 nm, λ_{em} 530–800 nm, slits 3 nm / 1 nm, integration time 0.5 s. b and c) Results of the zinc reduction assay (method 1) of DCM-N_3 (**1**) over 25 minutes, measured at 50 µM in IPA, by fluorescence emission spectroscopy (panel b) and by analytical HPLC (method 1B) at 480 nm (panel c). d) Analysis of the area under the curve from the fluorescence emission spectra (panel b) from the zinc assay of **1** over time, between 550 nm and 800 nm, fit to an exponential curve.

Following the analysis of the positive control DCM-N_3, the zinc-mediated activation of profluorophores **3** and **4** was evaluated using two methods: zinc/ammonium chloride reduction carried out in DMF, with aliquots diluted in DMSO and PBS buffer for analysis by HPLC, UV-Vis and fluorescence spectroscopy (zinc reduction assay method 2, adapted

from a literature procedure,[27] 20 µM final concentration); or direct fluorescence monitoring over time in IPA (zinc reduction assay method 1, adapted from the literature procedure for DCM-N_3,[1] 50 µM final concentration). Upon evaluation of compound **3** under zinc reduction conditions in DMF (using method 2), only a small change in fluorescence was observed over time (Figure 2.6a and b). Despite diluting the assay aliquots from 1 mM to 20 µM with DMSO:PBS (1:1 *v/v*) prior to fluorescence analysis, the pH of the aliquots was not adjusted or measured and is affected by the presence of organic solvents – the pH of the PBS buffer was 7.4 however this was not remeasured upon dilution in DMSO and dilution with a significant amount of DMSO is known to affect pH. pH is known to greatly affect the fluorescence emission of phenolic fluorophores, therefore inconsistencies in the pH throughout assays (or low pH) may affect the changes in fluorescence emission observed, as protonation of the phenol reduces fluorescence emission, however the presence of 10% NH_4Cl is unlikely to cause a large change in pH during the assay. Therefore, fluorescence emission assays were corroborated using analytical HPLC, with the corresponding fluorophore analysed as a positive control in the same solvent used for the assay (see chapter VI for more details). HPLC analysis of the zinc assay of **3** in DMF suggested that no fragmentation to the fluorescent DCM-OH occurred (Figure 2.6c). A yellow precipitate was formed throughout the zinc assay which was subsequently isolated and HPLC analysis (dissolved in MeCN, HPLC method 1B, Figure 2.6c) determined it to be formed of predominantly the azide starting material (R_t 13.0 min) and a small amount of a postulated aniline intermediate (R_t 12.2 min, Figure 2.6d). Compound **4** was subjected to the zinc reduction assay, according to method 2, and similar results were observed – a small change in fluorescence occurred over time (Figure 2.7a and b), there was little change in the HPLC trace over time (Figure 2.7c) and an orange precipitate formed during the assay which was determined by HPLC analysis to be the azide starting material (Figure 2.7c). Overnight incubation (16 h at 37 °C) of the assay aliquots for HPLC (0-8 h timepoints) in PBS buffer (buffer at pH 7.4) caused no change to the HPLC traces and no fluorophore release, in contrast to that observed by Calder *et al*.[27] for the nitrobenzyl prodrug of the hydroxamic

acid SAHA. The zinc reduction assay was also carried out in IPA (method 1), under similar conditions to the DCM-N_3 control (Figure 2.5), however, no significant changes in the fluorescence (Figure A2.2a and c) or UV-Vis spectra (Figure A2.2b and d) were observed and no fluorophore release was determined by HPLC analysis (Figure A2.2e and f).

In conclusion, whilst similar activation under the zinc assay conditions were observed for DCM-N_3 **1** to those previously reported in the literature,[1] the novel profluorophores **3** and **4** were not activated under similar conditions, therefore they do not appear to be promising candidates for selective activation under reducing conditions.

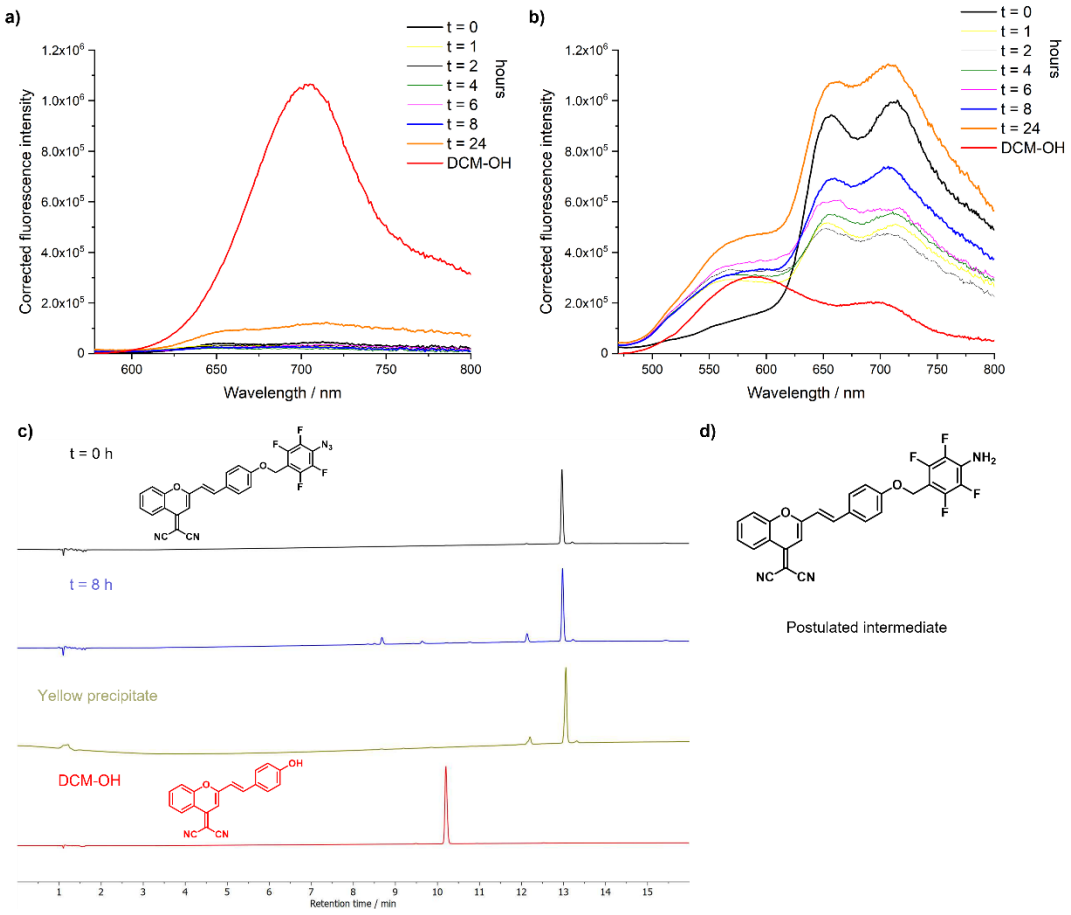

Figure 2.6: The results of the zinc reduction assay of compound **3** (method 2) over time. a) Fluorescence spectra, λ_{ex} 558 nm, λ_{em} 578–800 nm, slits 5 nm / 2 nm. b) Fluorescence spectra, λ_{ex} 450 nm, λ_{em} 470–800 nm, slits 5 nm / 2 nm. c) HPLC analysis (method 1B) showing the change in the HPLC trace over time, in comparison to the DCM-OH control, analysed at 480 nm, including the HPLC trace of the yellow precipitate, formed throughout the assay, dissolved in MeCN. Note: 24 h timepoint looked the same as 8 h. d) The structure of the postulated aniline intermediate formed during the zinc assay.

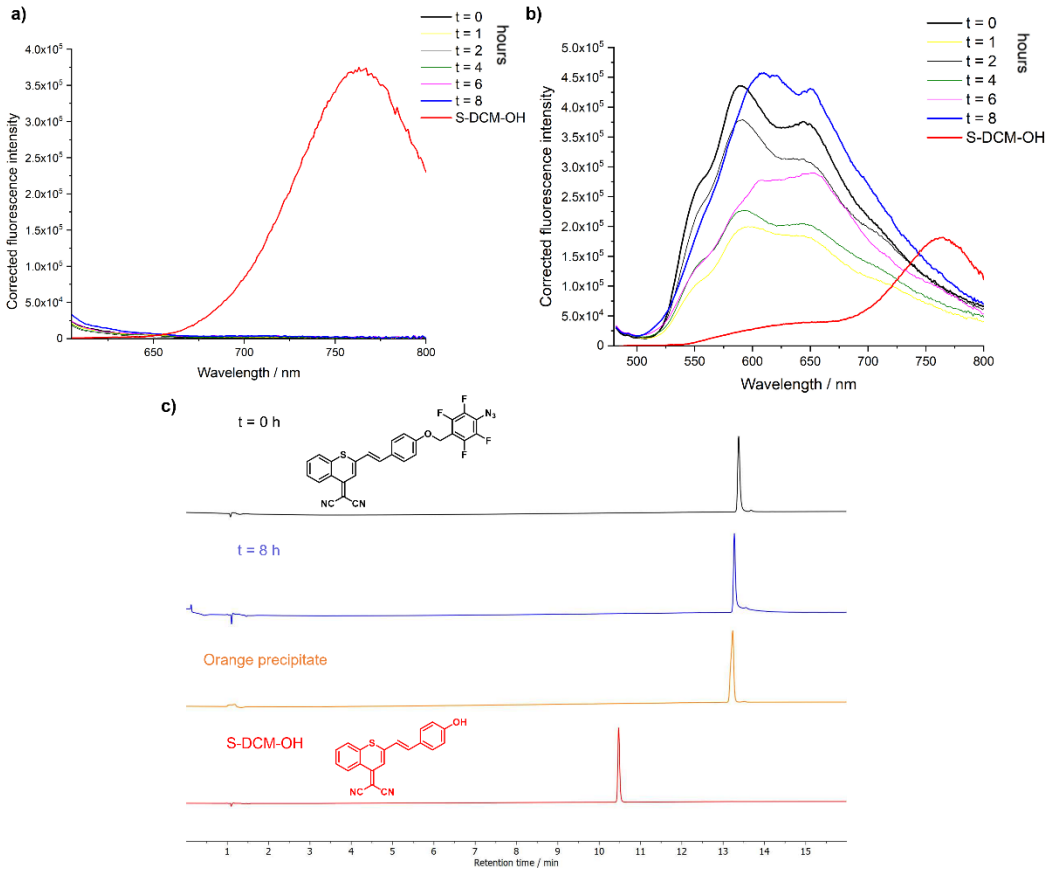

Figure 2.7: The results of the zinc reduction assay of compound **4** (method 2) over time. a) Fluorescence spectra, λ_{ex} 584 nm, λ_{em} 604–800 nm, slits 10 nm / 2 nm. b) Fluorescence spectra, λ_{ex} 462 nm, λ_{em} 482–800 nm, slits 10 nm / 2 nm. c) HPLC analysis (method 1B) showing the change in the HPLC trace over time, in comparison to the S-DCM-OH control, analysed at 480 nm, including the HPLC trace of the orange precipitate, formed throughout the assay, dissolved in MeCN.

2.3.3.2 NaHS assays

Activation of DCM-N_3 (**1**) was also evaluated in the present of NaHS (NaHS methods 1-3) according to literature procedures and was found to be activated less than observed previously in the literature.[4] Compound **1** was initially tested at 10 µM in MeCN:PBS 1:1 (PBS at pH 7.4) with at least 7 equivalents of NaHS hydrate (NaHS.xH_2O, where x is assumed to be 3 as NaHS exists commonly as both the dihydrate and trihydrate) and was monitored by fluorescence and HPLC (NaHS method 1). A small increase in fluorescence was observed (Figure 2.8a), however, this was negligible compared to the fluorescence of DCM-NH_2 **2** measured in the same solvent (Figure 2.8b). HPLC analysis showed only a small increase in the peak corresponding to the aniline (at 10.4 minutes) after 1 hour (Figure 2.8c). This was repeated with between 7 and 56 equivalents of NaHS hydrate (NaHS

method 2) and analysed using fluorescence spectroscopy (Figure 2.8d) and HPLC (Figure A2.3) after 1 hour, as the lifetime of NaHS is short. It is noted that these titrations were not carried out as non-diluting titrations, however the volume of NaHS solution added was small and the resulting final concentration of **1** at the end of the assay was 9.8 μM, therefore dilution is determined to have had a negligible effect on fluorescence emission intensity. A 5-fold increase in fluorescence was observed with at least 56 equivalents of NaHS hydrate (Figure 2.8e), compared to the 96-fold increase in fluorescence reported in the literature in the presence of 10 equivalents of NaHS.[4] However, it is noted that under these conditions we observe only a 48-fold increase in fluorescence emission between the baselines of DCM-N_3 **1** and DCM-NH_2 **2** (Figure 2.8b). Zheng *et al.*[4] reported that reduction occurred quicker in MeCN compared to MeCN:PBS 1:1 (postulated to be due to the poorer solubility of **1** in aqueous solution than in MeCN), therefore the assay was repeated in MeCN only with at least 7-56 equivalents NaHS (NaHS method 3), however a smaller increase in fluorescence (Figure 2.8f) was observed compared to the MeCN:PBS system. The smaller increase in fluorescence observed with NaHS in MeCN compared to in MeCN:PBS may be due to only monitoring the fluorescence in MeCN after 30 minutes, whereas Zheng *et al.*[4] reported that the reaction may be finished in 3 minutes in the presence of 10 equivalents of NaHS (or 30 minutes in the presence of 2 equivalents NaHS). Therefore, compounds **3** and **4** were tested in MeCN:PBS due to the slower reaction time. Discrepancies between the results observed here and those observed in the literature may arise due to differences in pH (here only the PBS is pH-adjusted and then diluted in MeCN and pH was not monitored over the course of the assay), local solvation and buffer concentrations and due to the short lifetime of NaHS in solution (despite the stock solution being made fresh for each assay and as close to the assay commencing as possible).

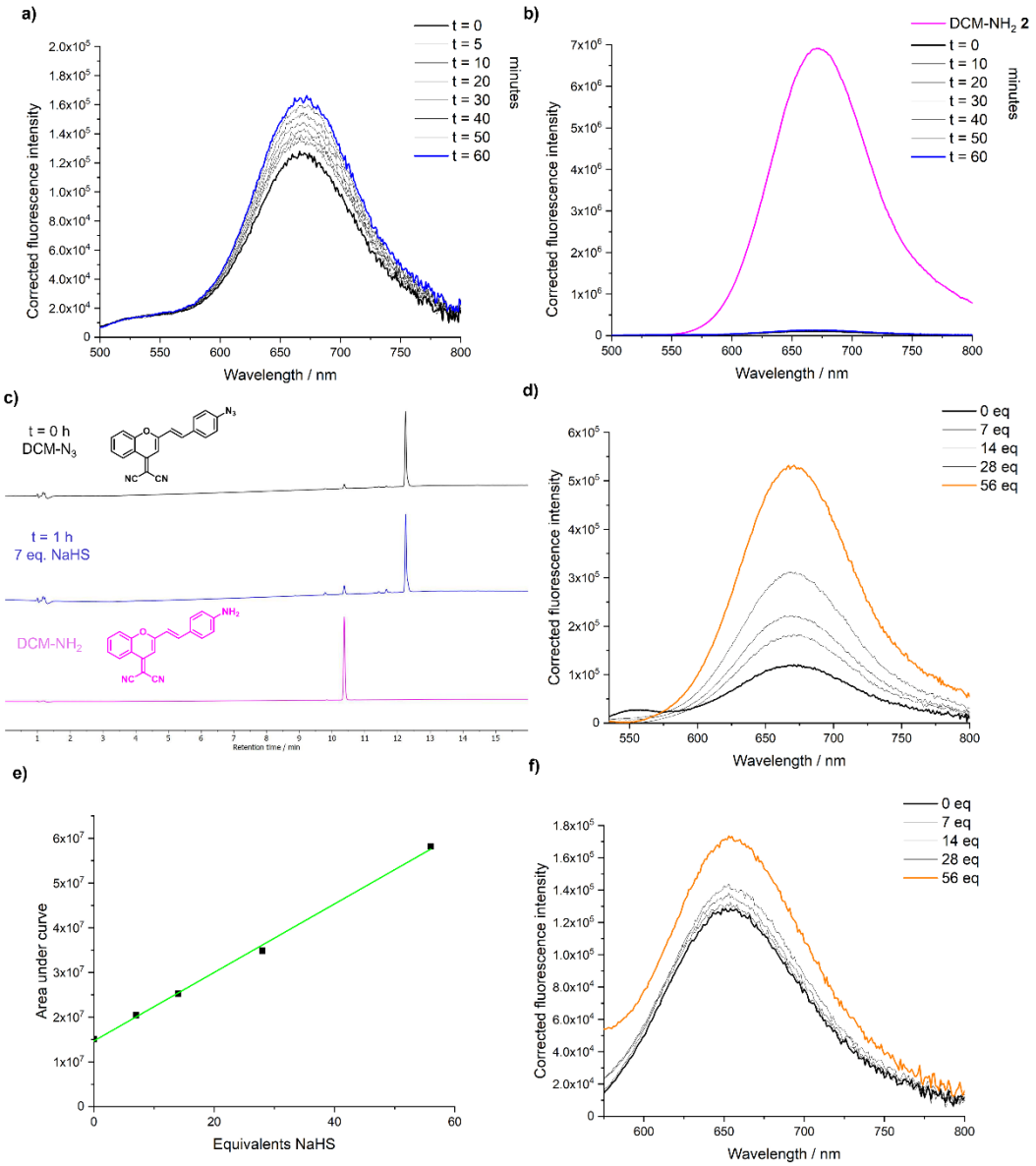

Figure 2.8: a) The results of the NaHS assay (NaHS method 1) of DCM-N_3 (**1**), measured in MeCN:PBS buffer (1:1 *v/v*, buffer pH 7.4), using 7 equivalents of NaHS hydrate (assuming for NaHS.xH_2O that x=3, 70 µM in H_2O), to show the increase in fluorescence over time. b) Expansion of panel a to show change in fluorescence in comparison to DCM-NH_2 (**2**, pink) measured under the same conditions. c) Analytical HPLC analysis of the NaHS assay of DCM-N_3 with 7 equivalents NaHS, analysed at 480 nm. d) The results of the NaHS assay, as in panel a, using increasing equivalents of NaHS (NaHS method 2), where the line shown is the fluorescence after 1 hour. e) Area under the curve analysis of panel c. f) The results of the NaHS assay, using 7–56 equivalents, measured in MeCN only (NaHS method 3), where the line shown is the fluorescence after 30 minutes. All compounds measured at 10 µM, λ_{ex} 491 nm, λ_{em} 500–800 nm, slits 5 nm / 2 nm.

The NaHS assay was carried out on compounds **3** and **4** with at least 56 equivalents NaHS hydrate (NaHS method 4, assuming the salt was the trihydrate), analogously to the DCM-N_3 positive control testing, however no increase in fluorescence was observed (Figure 2.9a and c). Moreover, a decrease in the absorbance in the UV-Vis spectra was observed

(Figure 2.9b and d) and no change, or release of DCM-OH or S-DCM-OH, was observed by HPLC analysis (Figure 2.9e and f).

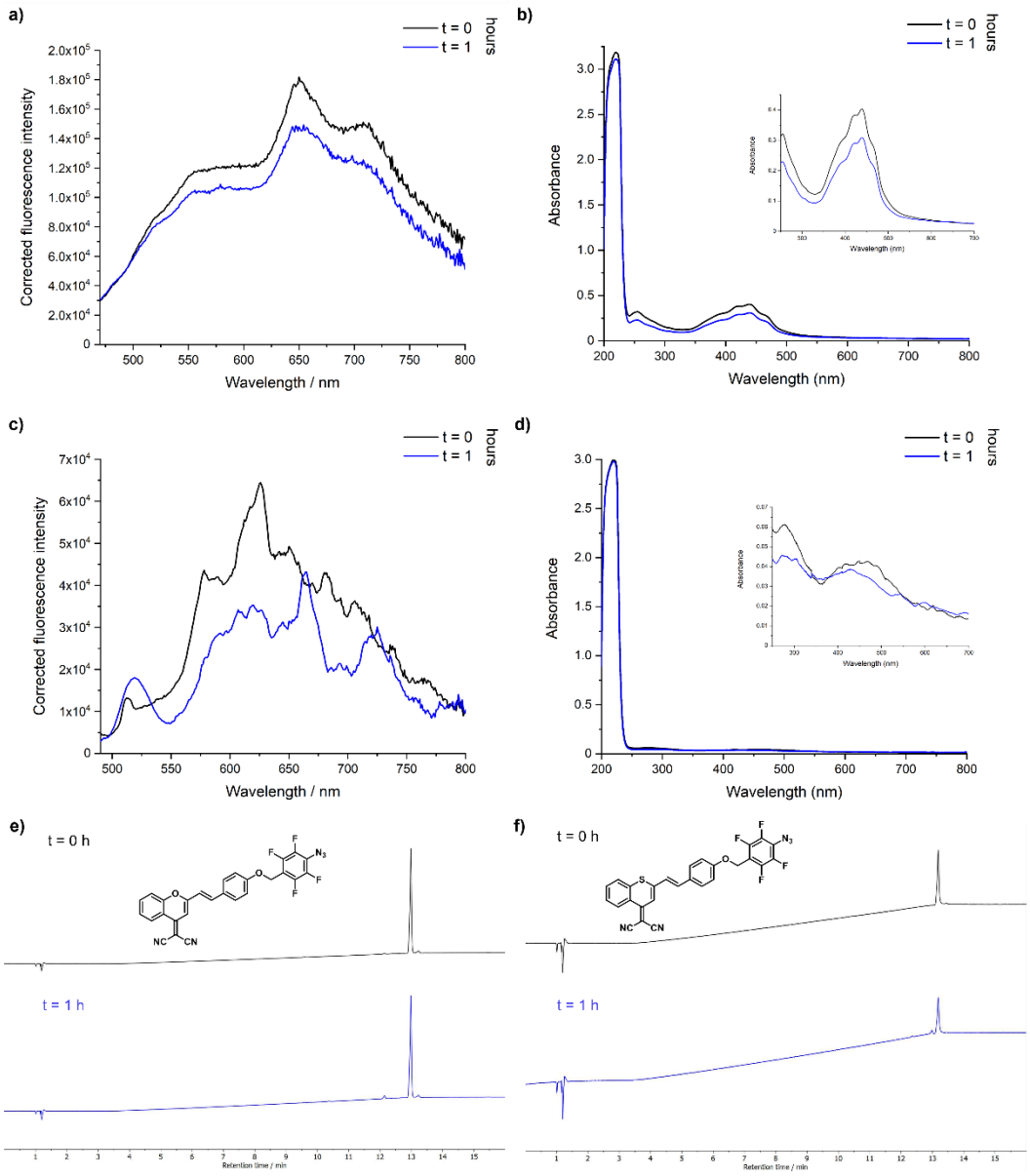

Figure 2.9: Results of the NaHS assay of compounds **3** (panels a, b and e) and **4** (panels c, d and f) according to NaHS method 4. a) Fluorescence spectra, λ_{ex} 443 nm, λ_{em} 470–800 nm, slits 5 nm / 2 nm. b and d) UV-Vis spectra over time. c) fluorescence spectra, λ_{ex} 467 nm, λ_{em} 490–800 nm, slits 10 nm / 2 nm. e and f) HPLC analysis (method 1B) showing the change in the HPLC trace over time, analysed at 480 nm.

2.3.3.3 Chemical activation assay conclusions

From the results of the zinc and NaHS reduction assays of **3** and **4**, in comparison to the control assays of DCM-N_3 **1**, we can conclude that compounds **3** and **4** are not activated to release DCM-OH or S-DCM-OH under these conditions. The lack of activation observed

may be partially due to the solubility issues observed throughout the assays, in both aqueous and organic solvents, and due to lack of fragmentation of any aniline intermediate formed, such as that postulated to have formed in the zinc assay of profluorophore **3** (R_t 12.2 min), however further work is needed to confirm this. The solubility of compound **4** is especially poor, as it precipitated out of the DMSO stock solution (5 mM) over time. Therefore, further work on this project should aim to increase the solubility of the profluorophores in aqueous solution (analysed by chromlogD assay in section 2.4) so that the compounds may be accurately evaluated in enzymatic assays and cellular environments. Based on the preliminary results discussed in section 2.3, profluorophores **3** and **4** are not promising probes for selective imaging of reducing environments.

2.4 Optimisation of profluorophore properties

Following the lack of activation observed for compounds **3** and **4** under chemical reduction conditions and issues with their solubility, new target molecules **15** and **16** were designed. Profluorophores **15** and **16** were designed to release the known fluorophores resorufin and Me-Tokyo Green,[28, 29] respectively, which are known to be more emissive than the DCM-OH dye, therefore lower concentrations of profluorophore could be used for detection, aiding solubility issues. In addition, these fluorescent dyes have lower pK_as compared to the DCM-based targets (5.8 for resorufin[30] and 6.2 for Me-Tokyo Green,[31] compared to 7.2 for DCM-OH)[32] and lower pK_as have previously been shown to increase the rate of activation of organic profluorophores.[24]

Profluorophores **15** and **16** were synthesised (Scheme 2.3) by reaction of the chloro-tetrafluoroaryl azide intermediate **13** with the corresponding fluorophore containing a phenol group. The Me-Tokyo Green fluorophore intermediate (and positive control) was synthesised by Dr. Antoine Wallabregue according to the reported literature procedure,[24] and commercially available resorufin was used.

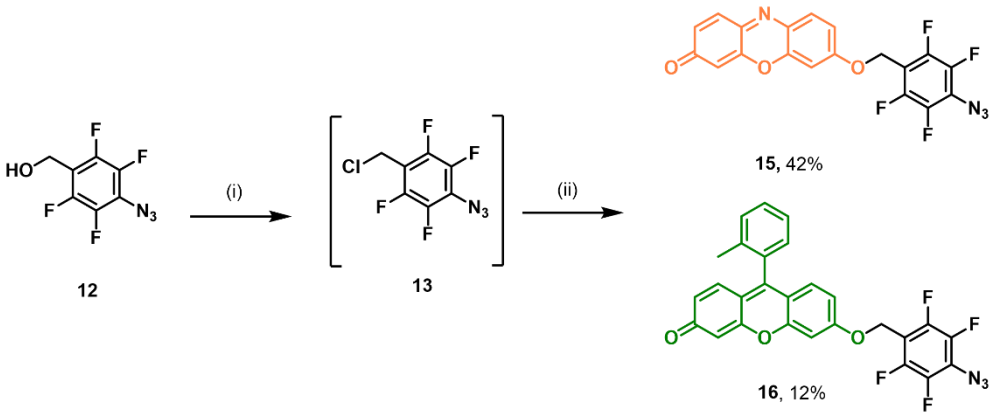

Scheme 2.3: Synthesis of the optimised profluorophores, **15** and **16**. *Reagents and conditions*: (i) Thionyl chloride, CH_2Cl_2, rt, 1 h; (ii) Fluorophore, caesium carbonate, tetrabutylammonium iodide, dry DMF, rt, 20-22 h.

The solubility of compounds **1-6, 15** and **16** was evaluated by running a chromlogD assay[33] using HPLC. This assay produces a logD value (equation 2.1) which can be converted into Property Forecast Index (PFI, equation 2.2), an indicator of compound aqueous solubility. logD (distribution coefficient) is a pH-dependent measurement of lipophilicity, taking into account both ionised and non-ionised forms of a molecule, as opposed to logP (partition coefficient) which is pH-independent – logD is a better predictor for analysis of compounds in the body, such as under physiological conditions at pH 7.4. A PFI value less than 7 has been found to be advantageous in many biological applications,[33, 34] with a PFI between 3 and 6 desirable in drug discovery due to the typically good absorption, distribution, metabolism and elimination (ADME) properties for compounds in this range.[35] Compound **15** has a similar PFI value to DCM-N_3 (10.89 compared to 11.10, Table 2.2), which has been previously shown to have good solubility for application *in cellulo*,[1] whereas **16** has similar PFI value to the less soluble compounds **3** and **4** (13.04 compared to 12.69 and 12.89), therefore resorufin-based compound **15** was primarily taken forward for testing in assays.

$$\log \mathrm{D} = \log\left(\frac{[\mathrm{solute}]_{\mathrm{octanol}}}{[\mathrm{solute}]_{\mathrm{ionised\ water}} + [\mathrm{solute}]_{\mathrm{neutral\ water}}}\right) \qquad \text{(eqn. 2.1)}$$

$$\mathrm{PFI} = \mathrm{Chrom}\ \log \mathrm{D}_{\mathrm{pH7.4}} + \mathrm{no.\,aromatic\ rings} \qquad \text{(eqn. 2.2)}$$

Table 2.2: A summary of the results of the chromlogD determination (n=1) for compounds **1-8**, indicating their water solubility. Colouring (red-yellow-green) suggests undesirable or desirable properties, with red highly unfavourable for biological application and green favourable.

Compound	Fluorophores					Profluorophores				
	2 DCM-NH_2	**5** DCM-OH	**6** *S*-DCM-OH	Resorufin	Me-Tokyo Green	**1** DCM-N_3	**3**	**4**	**15**	**16**
chromlogD$_{7.4}$	6.34	6.10	6.36	0.72	3.82	8.10	8.69	8.89	6.89	8.04
PFI	9.34	9.10	9.36	3.72	7.82	11.10	12.69	12.89	10.89	13.04

2.5 Testing of optimised profluorophore

2.5.1 Photophysical analysis of optimised profluorophores

Prior to carrying out chemical or enzymatic assays, the baseline UV-Vis and fluorescence spectra of compounds **15** and **16** were determined, in comparison to their corresponding fluorophore resorufin and Me-Tokyo Green. The compounds were measured at 1 µM, ten times lower concentration than the previous profluorophores (due to the higher intensity emission of the fluorophores), in MeCN:PBS 1:1 (Figure A2.4) and PBS only (Figure 2.10). The profluorophores showed reduced absorbances and fluorescence emission compared to that of the fluorophores resorufin and Me-Tokyo Green when measured in PBS only (Figure 2.10). The shapes of the UV-Vis and fluorescence emission spectra are similar to those reported previously for the fluorophores and alkylated versions of the fluorophores.[24]

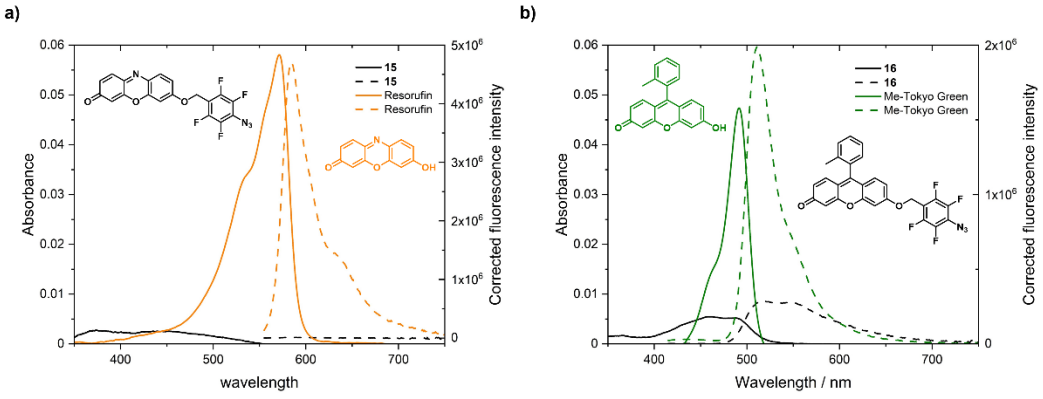

Figure 2.10: The UV-Vis spectra (solid lines) and fluorescence emission spectra (dashed lines) of a) profluorophore **15** (black) vs resorufin (orange) and b) profluorophore **16** (black) vs Me-Tokyo Green (green), measured at 1 µM in PBS (pH 7.4). For panel a fluorescence emission, λ_{ex} 540 nm, λ_{em} 555–800 nm, slits 2 nm / 1 nm; for panel b fluorescence emission, λ_{ex} 400 nm, λ_{em} 415–800 nm, slits 2 nm / 2 nm. S1c/R1c channel.

2.5.2 Chemical activation of optimised profluorophores

The chemical activation of profluorophores **15** and **16** were tested using zinc powder and ammonium chloride (zinc reduction assay methods 3 and 4, 100 µM compound, in DMF with aliquots diluted in MeCN and PBS buffer). Analysis was performed by HPLC (zinc reduction assay method 3) and fluorescence (zinc reduction assay method 4). Prior analysis of the positive control fluorophores, resorufin and Me-Tokyo Green, under the zinc reduction assay conditions (Figure 2.11) suggests that there is a stability or solubility issue over time for both fluorophores, which is more pronounced when monitored by fluorescence spectroscopy (Figure 2.11b and d). Previous literature shows that resorufin's emission is highly dependent on pH (with the phenolate more emissive than the phenol, as expected) and that fluorescence emission decreases considerably at pH 5.[36] The zinc assay aliquots were diluted in MeCN:PBS (1:1 *v/v*) with the PBS buffered to pH 7.4 and addition of 10% ammonium chloride is expected to cause only a small decrease in overall pH, however pH was not checked upon dilution of the PBS in MeCN or throughout the course of the assay to evaluate whether the loss of fluorescence intensity over time was due to protonation of the fluorophore or other effects. Due to the changes observed, the percentage of fluorophore release during the zinc assay of the profluorophores was calculated by comparison to the fluorophore peak area at the given time interval (detected by analytical HPLC).

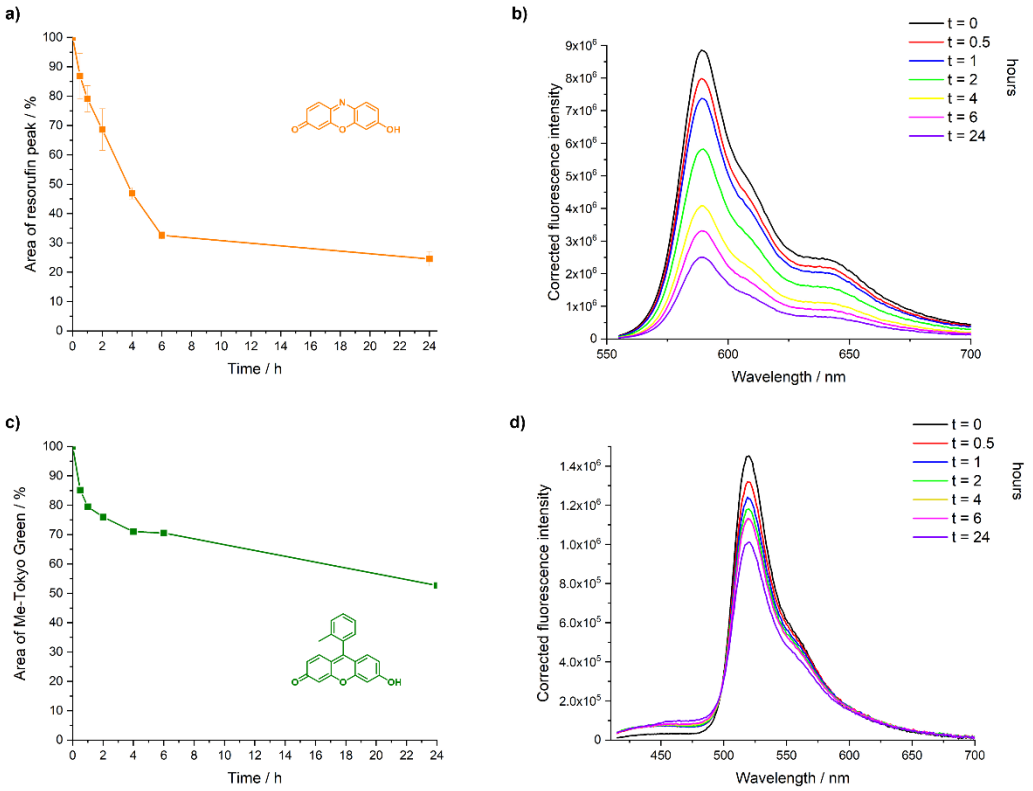

Figure 2.11: Results from the zinc reduction assay (methods 3 and 4) of resorufin (a and b, n=3) and Me-Tokyo Green (c and d, n=1), with aliquots taken from the reaction conducted at 100 µM in DMF. a and c) HPLC analysis (at 480 nm, 75 µL injection, method 1B) of aliquots diluted to 10 µM in MeCN:PBS 1:1, showing the percentage peak area over time in comparison to the t=0 area. b and d) Fluorescence spectra over time of aliquots diluted to 1 µM in MeCN:PBS 1:1. b) λ_{ex} 540 nm, λ_{em} 555–700 nm, slits 2 nm / 1 nm; d) λ_{ex} 400 nm, λ_{em} 415–700 nm, slits 2 nm / 2 nm. Representative graphs are shown.

The zinc reduction assay was carried out on profluorophores **15** (Figure 2.12) and **16** (Figure 2.13) and analysed by HPLC for loss of the azide peak and release of the fluorophore (Figure 2.12a-c and Figure 2.13a-c), and by fluorescence (Figure 2.12d and Figure 2.13d). A substantial loss of the azide peak, compared to the t=0 area, was observed by HPLC analysis (Figure 2.12a and Figure 2.13a, 20-55%) and a small percentage of fluorophore was observed to be released (2-5% after 24 hours, Figure 2.12b and c, Figure 2.13b and c). It is noted that analysis by HPLC is more informative than analysis by fluorescence spectroscopy (Figure 2.12d and Figure 2.13d), due to the decrease in fluorescence intensity for the positive control fluorophores (Figure 2.11) and the decrease in fluorescence observed for the profluorophores under the zinc reduction assay conditions. For **15** the fluorescence intensity initially increases then decreases and for **16** the fluorescence intensity decreases over time, despite release of fluorophore suggested by

HPLC analysis. In addition to the fluorophore release observed by HPLC, increase in intensity in peaks with a retention time of 9.4 minutes (compound **15**) or 10.5 minutes (compound **16**), proposed to be the corresponding aniline intermediates, were observed by HPLC, and other unidentified impurities were formed during the zinc assay reduction of **15**.

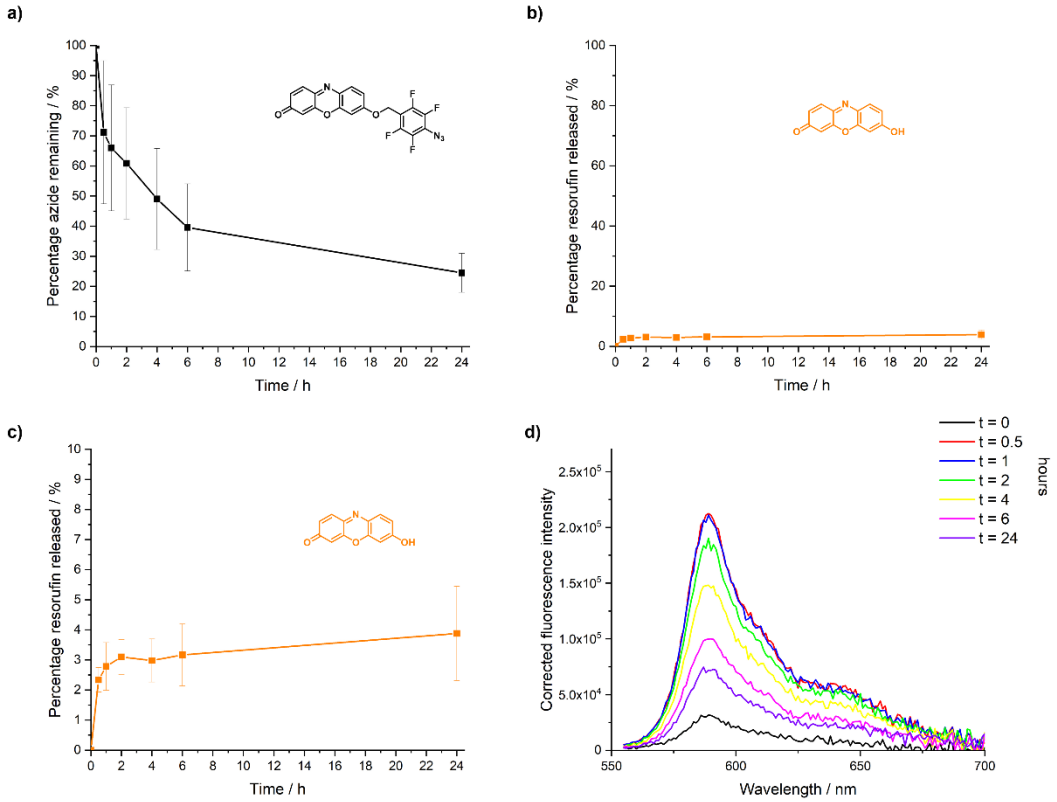

Figure 2.12: Results from the zinc reduction assay (methods 3 and 4) of profluorophore **15**. a) HPLC analysis (480 nm, 75 µL injection, method 1B) of the percentage of azide remaining over time, in comparison to the t=0 control, b) the percentage of resorufin released over time, in comparison to the area of the resorufin peak in the resorufin zinc assay experiment at the given time interval, and c) a zoom-in on panel b. d) Fluorescence spectra over time of aliquots diluted to 1 µM in MeCN:PBS 1:1, λ_{ex} 540 nm, λ_{em} 560–700 nm, slits 2 nm / 1 nm. Representative fluorescence spectra graph shown, the error bars represent the standard deviation of repeats, n=3.

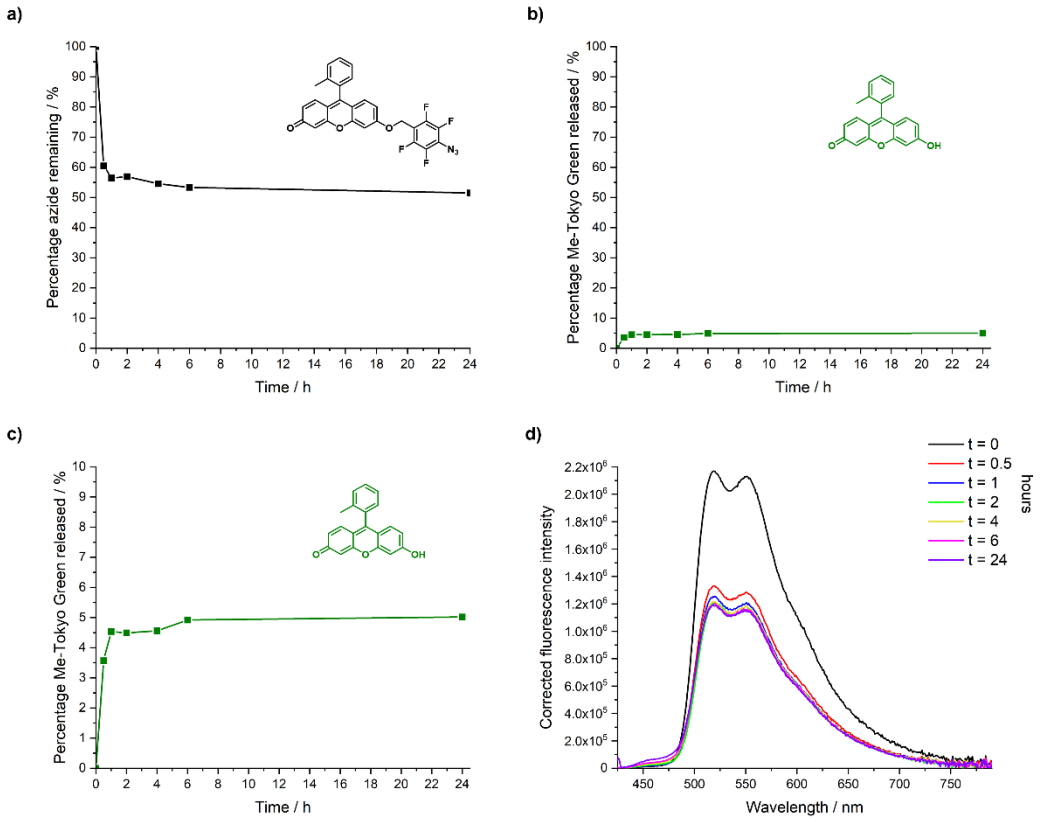

Figure 2.13: Results from the zinc reduction assay (methods 3 and 4) of profluorophore **16**. a) HPLC analysis (480 nm, 75 µL injection, method 1B) of the percentage of azide remaining over time, in comparison to the t=0 control, b) the percentage of Me-Tokyo Green released over time, in comparison to the area of the Me-Tokyo Green peak in the resorufin zinc assay experiment at the given time interval, and c) a zoom-in on panel b. d) Fluorescence spectra over time of aliquots diluted to 1 µM in MeCN:PBS 1:1, λ_{ex} 400 nm, λ_{em} 415–700 nm, slits 2 nm / 2 nm.

Overall, the chemical reduction assays of **15** and **16** demonstrate that these profluorophores can be reduced to give the corresponding fluorophore, but only in small amounts (< 5%). Due to the loss of fluorescence observed for the positive control fluorophores resorufin and Me-Tokyo Green in the presence of zinc and ammonium chloride (Figure 2.11) and the effect of pH on fluorophore emission, analysis of fluorophore release by HPLC is confirmed to be a more accurate technique to assess compound reduction. HPLC analysis of the zinc assays suggests that one main intermediate compound is produced, postulated to be the corresponding aniline compounds, although further work would be needed to validate this (for example by scale-up of the assay, isolation of the peak at R_t 9.4 min or R_t 10.5 min and analysis by LRMS and ^{1}H NMR). This result suggests that some reduction is occurring however fragmentation is not readily

occurring under the assay conditions, due to the ether linkage employed between the fluorophore and the activatable group and the stability of the aniline intermediate due to the electron withdrawing fluorine atoms nearby.

2.5.3 Enzymatic reduction

NADPH reductases (such as CYP004[27, 37] or PH51[24]) and other biological enzymes (such as CYP oxidases[1] and azoreductases) are associated with the activation of hypoxia-activated drugs and profluorophores in the literature. O'Connor *et al.*[1] reported that DCM-N_3 **1** can be activated by five CYP oxidases selectively under hypoxia (CYP1A2, CYP2D6, CYP2C19, CYP2C9 and CYP3A4) in the presence of regenerative solutions, containing $MgCl_2$, $NADP^+$ and glucose-6-phosphate and glucose-6-phosphate dehydrogenase. The propensity of profluorophore **15** to be activated selectively in hypoxia was investigated using enzymes CYP2D6 and CYP2C9, as these showed the greatest activation of DCM-N_3 to DCM-NH_2 **2**, in severe hypoxia (0.1% compared to 21% O_2).

Prior to analysis of the profluorophores of interest, the activity of the enzymes was confirmed by evaluating the positive control DCM-N_3 in hypoxia in the presence of CYP2D6 and CYP2C9, following the literature procedure (see enzymatic assay conditions 1-2). Evaluation of the concentration of DCM-NH_2 formed was carried out by comparison to a calibration curve conducted in H_2O/$KHPO_4$ buffer, to more accurately reflect the assay conditions, compared to the literature calibration curve in MeCN. The results showed a similar level of activation to that reported in the literature - 0.15 µM DCM-NH_2 compared to 0.15-0.25 µM in the literature with CYP2D6 and 0.09 µM compared to 0.10-0.25 µM in the literature with CYP2C9 (Figure A2.5).

Profluorophore **15** was chosen to be evaluated in the enzymatic assay (Figure 2.14**,** enzymatic assay conditions 3-4) due to the higher solubility indicated by the chromlogD assay carried out and the poor stability observed for Me-Tokyo Green and its profluorophore **16** in the presence of a different CYP enzyme (CYP004). The enzymatic assay was

optimised to be carried out with 100 µM profluorophore (as initial analysis at 1 µM was determined to be too low for accurate analysis by HPLC due to the limit of the UV detector) and 9.2 pmol/mL enzyme. Under the stability (black, in phosphate buffer and regenerative solutions, n=3) and normoxia conditions (red, with the enzyme, at 21% O_2) the resorufin profluorophore **15** appeared to be stable and no resorufin release was observed. Under hypoxia (0.1% O_2, n=1) a small percentage of resorufin release (< 2%) was observed (by comparison to a calibration curve for resorufin). Only n=1 was obtained for this assay as at 100 µM some precipitation was observed, therefore an intermediate concentration (10–50 µM) should be used for more accurate subsequent evaluation, alongside stability testing of the resorufin fluorophore under the same conditions. However, these preliminary data suggests that profluorophore **15** can be activated selectively in hypoxia, as desired, albeit in small amounts (< 2%).

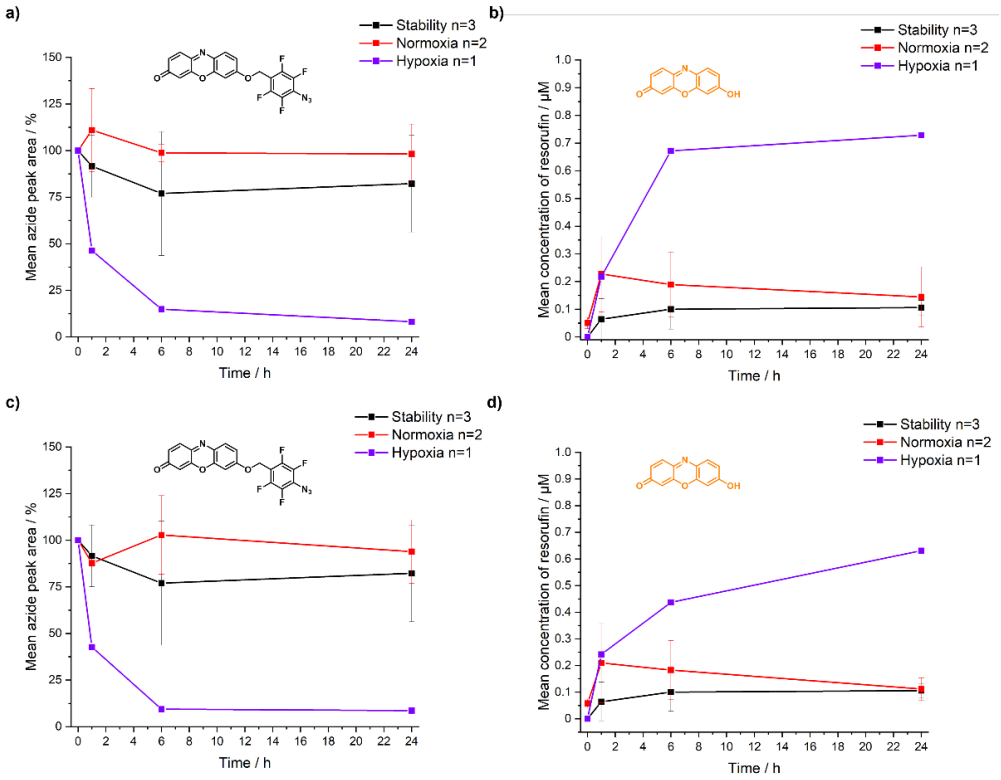

Figure 2.14: The results of the enzyme assay of compound **3** under hypoxia (n=1), normoxia (n=2) and stability (absence of enzyme, n=3) assays (enzyme assay conditions 3-4). a and b) Using enzyme CYP2D6, c and d) using enzyme CYP2C9. a and c) Percentage of azide remaining over time, by comparison of the peak area by HPLC (analysed at 480 nm) in comparison to the t=0 peak area. b and d) Concentration of resorufin released, analysed by comparison of the peak area to the calibration curve of peak area for resorufin. Final assay concentration 50 µM of substrate.

2.5.4 X-ray activation

Following evidence of some activation of profluorophore **15** under enzymatic conditions in hypoxia, activation under X-ray irradiation was evaluated at 0 Gy, 30 Gy and 60 Gy, in collaboration with the Higgins group (X-ray assay and irradiation carried out by Rathi Puliyadi). X-ray irradiation (using a Cs irradiator with a dose rate of 1.1 Gy/min) was carried out following overnight incubation at 37 °C in hypoxia (< 0.1% O_2) to reduce the formation of ROS upon irradiation (see X-ray irradiation assay method). The profluorophore **15** was evaluated, alongside the resorufin fluorophore positive control, at both 20 µM and 100 µM. Precipitation was observed in the 100 µM samples over the course of the assay and some loss of total assay volume was observed due to condensation. Following X-ray irradiation, the samples were diluted in MeCN and analysed by HPLC (Figure 2.15, 20 µM samples diluted to 10 µM, HPLC method 1B). No activation was observed under these conditions for profluorophore **15** (Figure 2.15a) and some degradation was observed for resorufin (Figure 2.15b). The X-ray irradiation protocol used could be further optimised by using the commercially available 7-azido-4-methylcoumarin as a positive control (previously reported by Geng *et al.*[2] to be activated under 60 Gy irradiation).

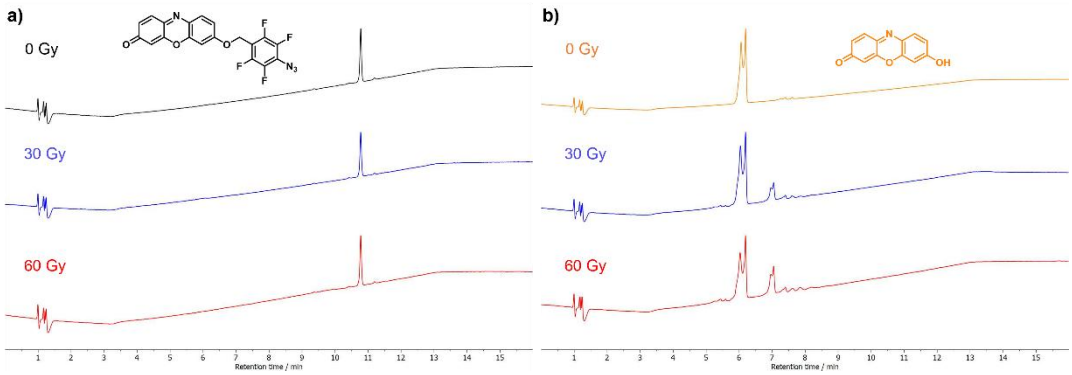

Figure 2.15: Results of the X-ray irradiation assay (see X-ray irradiation assay method) of profluorophore **15** (a) and the corresponding fluorophore resorufin (b), with samples diluted to 10 µM and analysed by HPLC (method 1B) at 480 nm. Note that the control (0 Gy) samples were prepared and incubated under the same conditions at the same time as the irradiated samples.

2.6 Conclusion and Future Work

In conclusion, the initially synthesised profluorophores **3** and **4** were not activated in the presence of zinc or NaHS and their poor solubility in both aqueous and organic solvents led to the development of more soluble profluorophores **15** and **16**, based on the more emissive dyes resorufin and Me-Tokyo Green. A small percentage of activation (2-5%) was observed for profluorophores **15** and **16** in the presence of zinc and profluorophore **15** was activated selectively (n=1, < 2% activation observed) under hypoxia (0.1% O_2) in the presence of CYP2D6 and CYP2C9 enzymes, at 100 µM (final assay concentration 50 µM). No activation of profluorophore **15** was observed following a preliminary X-ray irradiation assay at 30 Gy or 60 Gy (n=1), after overnight hypoxia incubation. Despite the better predicted aqueous solubility of profluorophore **15** compared to **3**, **4** and **16** according to the chromlogD assay, for more accurate results the enzymatic and X-ray irradiation assays of **15** should be repeated at concentrations lower than 100 µM as some evidence of insolubility was observed at this concentration in water over time.

Profluorophores **3**, **4**, **15** and **16** were overall determined to not be promising compounds for either enzymatic or X-ray irradiation therefore further validation of these compounds was not performed. These findings suggest that attachment of the tetrafluoroaryl azide group *via* a simple ethyl linker is not a good strategy for designing a profluorophore for activation in the presence of both hypoxia and X-ray irradiation – alternative linker strategies and activatable moieties should be investigated.

The lack of activation may occur due to the presence of the four fluorine atoms acting as electron-withdrawing groups and reducing the rate of cleavage of any reduction intermediate formed. This rate of cleavage could be enhanced by introduction of methyl groups adjacent to the ethyl linker, as this strategy has previously been shown to both increase the rate of activation of nitro-containing prodrugs and profluorophores and decrease their rate of oxidation to undesired benzylic esters.[24, 38] Recent developments in

the literature on the development of radiation activated prodrugs[39-43] has suggested that employment of a carbamate or carbonate linkage may be crucial for activation, due to the entropic driving force of CO_2 production. Synthesis of the carbonate analogue of profluorophore **15** was attempted following Scheme 2.4 but was unsuccessful, likely due to the inherent instability of the carbamate intermediate **17** (which was isolated and purified). This synthesis could be attempted by immediate use of the carbamate intermediate **17** in the next step and optimisation of the synthesis conditions, or alternatively the use of triphosgene for the carbamate formation. Whilst introduction of a carbonate group will likely increase the rate of activation of the profluorophore, it may also decrease its selectivity.

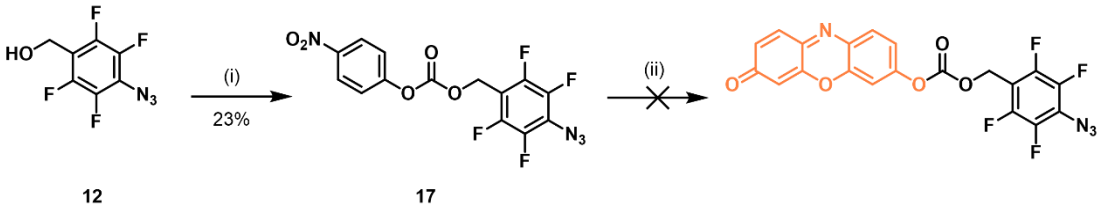

12 17

Scheme 2.4: Proposed synthesis route of the carbonate analogue of profluorophore **15**. (i) 4-Nitrophenyl chloroformate, pyridine, dry THF, rt, 72 h; (ii) Resorufin, dry pyridine and DMAP, dry DMF, rt, 24 h.

In addition to modification of the linker attachment, design of a new X-ray activated functional group is crucial for clinically relevant future work in this field. The clinical need is for probes which may be suitably activated under the 1.8-2.0 Gy doses for curative treatment of patients with large tumours, rather than those currently available in the literature which are activated using hypofractionated treatment doses (6-60 Gy).

Due to development in the literature over the duration of the project and the poor solubility and activation observed of the synthesised profluorophores, further work on the development of activatable compounds in this thesis is focused on the development of more clinically relevant activatable lanthanide complexes for MRI, rather than small molecule fluorophores.

2.7 References

1. L. J. O'Connor, I. N. Mistry, S. L. Collins, L. K. Folkes, G. Brown, S. J. Conway and E. M. Hammond, *ACS Central Science*, 2017, **3**, 20–30.
2. J. Geng, Y. Zhang, Q. Gao, K. Neumann, H. Dong, H. Porter, M. Potter, H. Ren, D. Argyle and M. Bradley, *Nature Chemistry*, 2021, **13**, 805–810.
3. M. Tropiano and S. Faulkner, *Chemical Communications*, 2014, **50**, 4696–4698.
4. Y. Zheng, M. Zhao, Q. Qiao, H. Liu, H. Lang and Z. Xu, *Dyes and Pigments*, 2013, **98**, 367–371.
5. W. Sun, J. Fan, C. Hu, J. Cao, H. Zhang, X. Xiong, J. Wang, S. Cui, S. Sun and X. Peng, *Chemical Communications*, 2013, **49**, 3890–3892.
6. B. Chen, P. Wang, Q. Jin and X. Tang, *Organic & Biomolecular Chemistry*, 2014, **12**, 5629–5633.
7. in *Radiotherapy dose fractionation*, The Royal College of Radiologists, Fourth Edition edn., 2024, ch. Paedriatic cancer.
8. G. G. Hanna, L. Murray, R. Patel, S. Jain, K. L. Aitken, K. N. Franks, N. van As, A. Tree, P. Hatfield, S. Harrow, F. McDonald, M. Ahmed, F. H. Saran, G. J. Webster, V. Khoo, D. Landau, D. J. Eaton and M. A. Hawkins, *Clinical Oncology*, 2018, **30**, 5–14.
9. in *Radiotherapy dose fractionation*, The Royal College of Radiologists, Fourth Edition edn., 2024, ch. Skin cancer.
10. *Stereotactic Ablative Body Radiation Therapy (SABR): A Resource*, SABR UK Consortium, 6.1 edn., 2019.
11. K. Aitken and S. Mukherjee, *Clin Oncol (R Coll Radiol)*, 2022, **34**, 277–279.
12. X. Zeng, Z. Chen, L. Tang, H. Yang, N. Liu, H. Zhou, Y. Li, J. Wu, Z. Deng, Y. Yu, H. Deng, X. Hong and Y. Xiao, *Chemical Communications*, 2019, **55**, 2541–2544.
13. F. Bossert, *Justus Liebigs Annalen der Chemie*, 1964, **680**, 40–51.
14. E. Petschek and H. Simonis, *Chemistry – A European Journal*, 1913, 2014–2020.
15. M. H. Holshouser, L. J. Loeffler and I. H. Hall, *Journal of Medicinal Chemistry*, 1981, **24**, 853–858.
16. Y. Zhang, H. Tanimoto, Y. Nishiyama, T. Morimoto and K. Kakiuchi, *Synlett*, 2012, **2012**, 367–370.
17. H. Nakazumi, T. Ueyama, Kitao and Teijiro, *Journal of Heterocyclic Chemistry*, 1984, **21**, 193–196.
18. K. Strømgaard, D. R. Saito, H. Shindou, S. Ishii, T. Shimizu and K. Nakanishi, *Journal of Medicinal Chemistry*, 2002, **45**, 4038–4046.
19. J. F. W. Keana and S. X. Cai, *The Journal of Organic Chemistry*, 1990, **55**, 3640–3647.
20. M. Sechi, F. Carta, L. Sannia, R. Dallocchio, A. Dessì, R. I. Al-Safi and N. Neamati, *Antiviral Research*, 2009, **81**, 267–276.
21. C. Yang, Y. Yang, Y. Li, Q. Ni and J. Li, *Journal of the American Chemical Society*, 2022, DOI: 10.1021/jacs.2c10177.
22. M. Wang, N. Yang, Z. Guo, K. Gu, A. Shao, W. Zhu, Y. Xu, J. Wang, R. K. Prud'homme and X. Guo, *Industrial & Engineering Chemistry Research*, 2015, **54**, 4683–4688.
23. L. O'Connor, Doctor of Philosophy, University of Oxford, 2016.
24. A. L. D. Wallabregue, H. Bolland, S. Faulkner, E. M. Hammond and S. J. Conway, *Journal of the American Chemical Society*, 2023, DOI: 10.1021/jacs.2c12493.
25. S. Guisán-Ceinos, A. R. Rivero, F. Romeo-Gella, S. Simón-Fuente, S. Gómez-Pastor, N. Calvo, A. H. Orrego, J. M. Guisán, I. Corral, F. Sanz-Rodriguez and M. Ribagorda, *Journal of the American Chemical Society*, 2022, **144**, 8185–8193.
26. C. Brito da Silva, E. S. Gil, F. da Silveira Santos, A. M. Morás, L. Steffens, P. F. Bruno Gonçalves, D. J. Moura, D. S. Lüdtke and F. S. Rodembusch, *The Journal of Organic Chemistry*, 2018, **83**, 15210–15224.
27. E. D. D. Calder, A. Skwarska, D. Sneddon, L. K. Folkes, I. N. Mistry, S. J. Conway and E. M. Hammond, *Tetrahedron*, 2020, **76**, 131170.
28. L. D. Lavis and R. T. Raines, *ACS Chemical Biology*, 2014, **9**, 855–866.
29. Y. Urano, M. Kamiya, K. Kanda, T. Ueno, K. Hirose and T. Nagano, *Journal of the American Chemical Society*, 2005, **127**, 4888–4894.
30. C. Bueno, M. L. Villegas, S. G. Bertolotti, C. M. Previtali, M. G. Neumann and M. V. Encinas, *Photochemistry and Photobiology*, 2002, **76**, 385–390.
31. L. F. Mottram, S. Boonyarattanakalin, R. E. Kovel and B. R. Peterson, *Organic Letters*, 2006, **8**, 581–584.
32. J. Yang, M. Li and W.-H. Zhu, *Research on Chemical Intermediates*, 2018, **44**, 3959–3969.
33. A. P. Hill and R. J. Young, *Drug Discovery Today*, 2010, **15**, 648–655.
34. R. J. Young, D. V. S. Green, C. N. Luscombe and A. P. Hill, *Drug Discovery Today*, 2011, **16**, 822–830.
35. K. L. Valko, *Future Drug Discovery*, 2019, **1**, FDD11.
36. M. Perri, M. S. Khan, A. L. D. Wallabregue, V. Voloboeva, A. M. Ridgway, E. N. Smith, H. Bolland, E. M. Hammond, S. J. Conway, D. A. Weits and E. Flashman, *New Phytologist*, 2025, **247** (6), 2998-3009.
37. A. Skwarska, E. D. D. Calder, D. Sneddon, H. Bolland, M. L. Odyniec, I. N. Mistry, J. Martin, L. K. Folkes, S. J. Conway and E. M. Hammond, *Cell Chemical Biology*, 2021, **28**, 1258–1270.e1213.
38. P. Thomson, M. A. Naylor, S. A. Everett, M. R. L. Stratford, G. Lewis, S. Hill, K. B. Patel, P. Wardman and P. D. Davis, *Molecular Cancer Therapeutics*, 2006, **5**, 2886–2894.
39. Z. Ding, Z. Guo, Y. Zheng, Z. Wang, Q. Fu and Z. Liu, *Journal of the American Chemical Society*, 2022, **144**, 9458–9464.

40. Q. Fu, H. Li, D. Duan, C. Wang, S. Shen, H. Ma and Z. Liu, *Angewandte Chemie International Edition*, 2020, **59**, 21546–21552.
41. Q. Fu, Z. Gu, S. Shen, Y. Bai, X. Wang, M. Xu, P. Sun, J. Chen, D. Li and Z. Liu, *Nature Chemistry*, 2024, DOI: 10.1038/s41557-024-01501-4.
42. J. M. Quintana, M. Kang, H. Hu, T. S. C. Ng, G. R. Wojtkiewicz, E. Scott, S. Parangi, J. Schuemann, R. Weissleder and M. A. Miller, *ACS Central Science*, 2024, **10**, 1371–1382.
43. L. Wang, M. Zhang, X. Gao, J. Li, M. Wu, X. Zhang and Z. Ye, *RSC Advances*, 2022, **12**, 32297–32306.

3. Chapter III[§] – Development of activatable lanthanide complexes for luminescence and MRI

3.1 Introduction to activatable lanthanide complexes

As previously discussed, current imaging and therapy research is mainly focused on the development of organic-based (and nanoparticle-based) prodrugs and profluorophores which may be activated in reducing environments or in the presence of biological molecules. Expanding on this approach, various activatable lanthanide complexes have been previously reported, as briefly discussed in section 1.5.2. Stimuli for activation are similar to those for organic compounds and include anion or cation binding,[1, 2] the binding of biologically relevant molecules,[3] the presence of biological reductants or enzymes,[4-8] irradiation with visible light or X-rays, a change in pH[9, 10] or a change in solvent or viscosity. These stimuli can influence the properties (such as luminescence and relaxivity) of the lanthanide complexes in several ways, including changing the conformation (preventing or causing energy transfer pathways), protonation, number of coordinated water molecules, and changing the chromophore by reduction or cleavage of the complex. The field of responsive lanthanide complexes is summarised well in reviews by Parker *et al.*[11] and Heffern *et al*.[12]

Notable examples of activatable lanthanide complexes include the europium complex of azidophenacylDO3A (Figure 3.1a) reported by Tropiano *et al.*[4] which is reduced to the more luminescent aniline by nanomolar concentrations of NaHS within 30 minutes. This large

[§] Aspects of the work in this chapter have now been published: C. A. Foster et al. *Inorg. Chem*. 2025, **64**, 6640–6647

increase in luminescence is observed selectively for NaHS in comparison to other reducing agents and anions such as GSH, cysteine, chloride and bicarbonate.

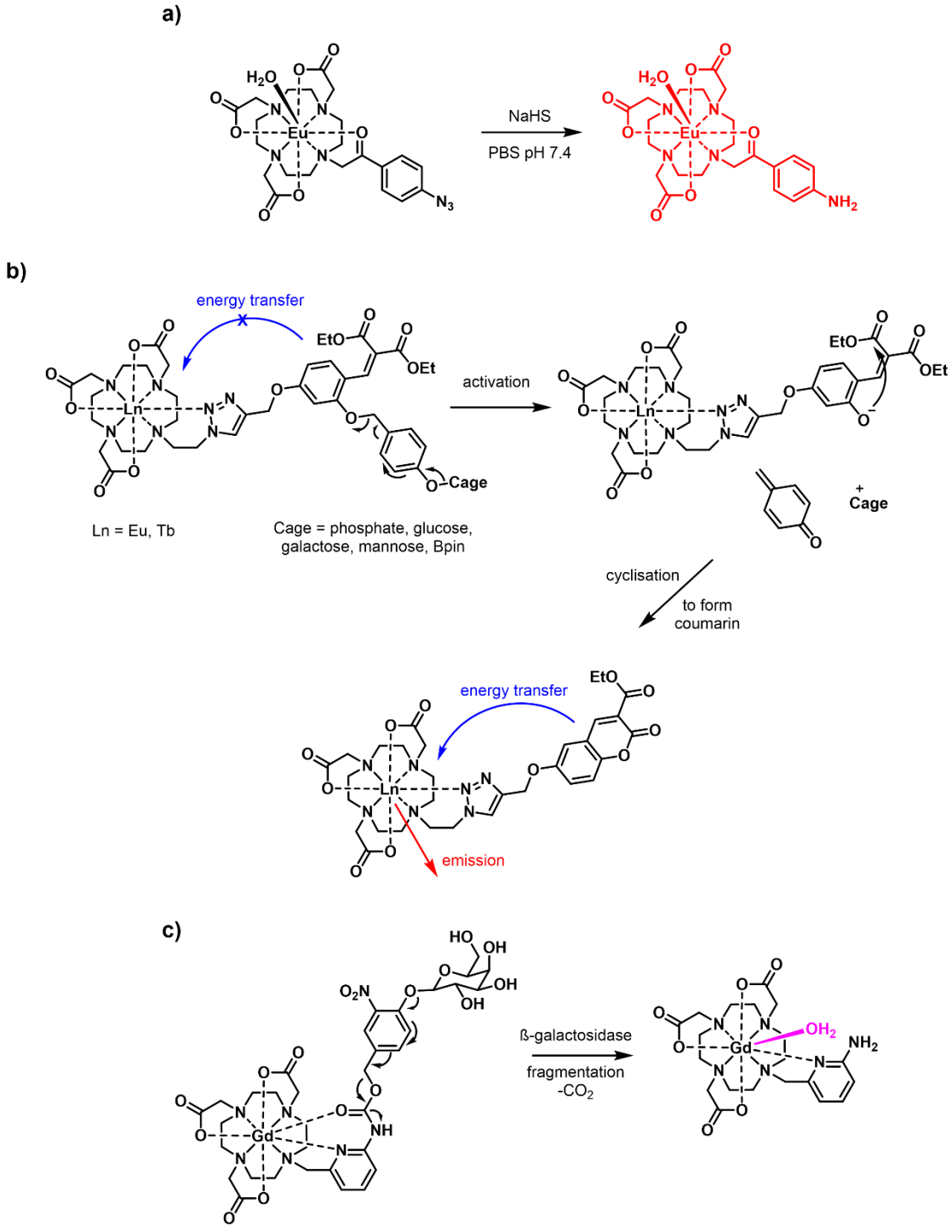

Figure 3.1: Selected examples of activatable lanthanides complexes. a) Activation of an azide complex to an aniline, causing an increase in luminescence.4 b) Decaging, due to activation, and cyclisation of complex to give a coumarin-base complex which can sensitise and cause an increase in lanthanide luminescence.[7] c) Enzymatic activation and subsequent fragmentation of a nitrobenzyl group to give a free amine from a carbamate, causing a change in *q* value, hence change in MRI signal.[8]

Pershagen *et al.*[7] reported a series of terbium and europium complexes (Figure 3.1b) which may be 'decaged' in the presence of an analyte (such as ROS, phosphatases or other cleaving enzymes, depending on the 'cage' used) and subsequently undergoes rearrangement to form a coumarin complex which may be used as a good antenna for lanthanide luminescence, hence the increase in luminescence observed upon activation. This work resulted in simultaneous detection of phosphatase and ß-galactosidase by using a plate reader to monitor emission at 545 nm for the terbium complex detecting ß-galactosidase and 655 nm for the europium complex detecting phosphatase (both upon excitation at 365 nm). This was subsequently expanded to three colour imaging to monitor hydrogen peroxide, phosphatase and ß-galactosidase with minimal interference, by combination of an organic coumarin fluorophore (by monitoring emission at 450 nm upon excitation at 410 nm) with the europium and terbium complexes.

Tang *et al.*[8] reported a self-immolative lanthanide complex which is activated in the presence of the ß-galactosidase enzyme (Figure 3.1c), causing a large increase in relaxivity (106%), therefore acting as a responsive MRI contrast agent. The probe works by hydrolysis of the galactose moiety and subsequent cleavage of the nitroaromatic group and carbamate bond to give a free aniline. This changes the direct coordination environment of gadolinium by replacing the coordination of the carbamate carbonyl group and increasing the *q* value from 0 to 1.

Nitroimidazole moieties have been investigated as hypoxia-activatable groups, as alternatives to the prevalent nitrobenzyl moiety. This is due to the favourable reduction properties of the nitroimidazole moiety, as discussed in section 1.2. Calder *et al.* previously reported 1-methyl-2-nitroimidazole (NI) prodrugs of the organic KDAC inhibitors vorinostat (Figure 3.2a)[13] and panobinostat (Figure 3.2b)[14] which selectively release the drugs under severe hypoxia (< 0.1% oxygen). Work on prodrugs of vorinostat highlighted that release of vorinostat occurs more readily from the nitroimidazole prodrug in comparison to its 4-nitrobenzyl (NB) analogue. The follow-up paper[14] on the more metabolically stable KDAC

inhibitor panobinostat showed that a nitroimidazole prodrug may be selectively activated in hypoxic cancer cell lines, spheroids and mouse xenografts.

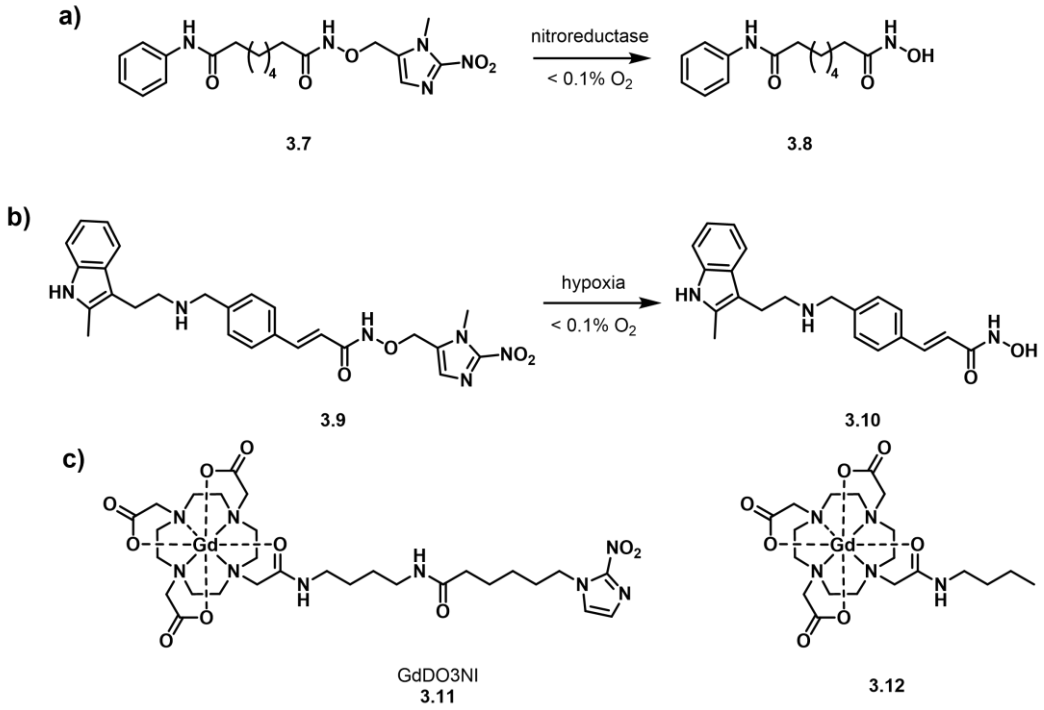

Figure 3.2: Examples of nitroimidazole-based prodrugs and profluorophores. a) 1-methyl-2-nitroimidazole prodrug of the KDAC inhibitor vorinostat. b) Nitroimidazole prodrug of the KDAC inhibitor panobinostat. c) Gadolinium complex GdDO3NI which has been used to detect hypoxia by MRI, in comparison to its control.

In addition to the organic prodrugs and profluorophores reported, there have been several reports of activatable lanthanide imaging agents containing nitroimidazole groups,[5, 15-17] in addition to those containing nitrobenzyl groups.[18] Rojas-Quijano *et al.*[5] reported a DO3A monoamide containing a 2-nitroimidazole moiety attached to an amide linker (GdDO3NI, Figure 3.2c), which may be activated under hypoxia causing a decrease in T_1. *In vitro* MRI of the activatable complex in hypoxic 9L rat glioma cells suggests that it is selectively trapped in hypoxic cells and activated, causing an increase in MRI signal, in comparison to the control complex which is not retained in hypoxic cells. Further *in vivo* measurements in rats with prostate tumours[15] confirmed the difference in MRI enhancement between the control and nitroimidazole-containing complex in the central region of the tumours, and GdDO3NI has been used to visualise hypoxia in traumatic brain injury-induced mice.[16]

3.2 Design of activatable lanthanide complexes

This chapter describes the synthesis, photophysics, relaxivity and activation testing of two different activatable lanthanide complexes, in comparison to their controls. The majority of this work is discussed in the publication 'LnDOTA releasing probes for luminescence and magnetic resonance imaging'.[19] The target complexes (Figure 3.3) were designed as proof-of-concept molecules for activatable lanthanide complexes, where a measurable change in luminescence or relaxivity can be observed upon reduction and cleavage. The design of the complexes is such that well studied hypoxia activatable groups are attached to the DO3A macrocycle by an ester linkage to give the nitrobenzyl (NB, **18**), nitroimidazole (NI, **19**) and indolequinone (IQ, **20**) complexes (Figure 3.3a), which may be activated to give the known DOTA complexes (**21**, Figure 3.3b). This work directly expands on the work on the gadolinium nitrobenzyl complex (GdNB, **18c**) previously reported by Liu *et al.*,[20] which showed that this complex may be activated to GdDOTA (by a proposed nitro reduction and fragmentation mechanism, Scheme 3.1), causing a change in relaxivity, which may be observed both in the presence of nitroreductase enzymes and in bacteria lysate.

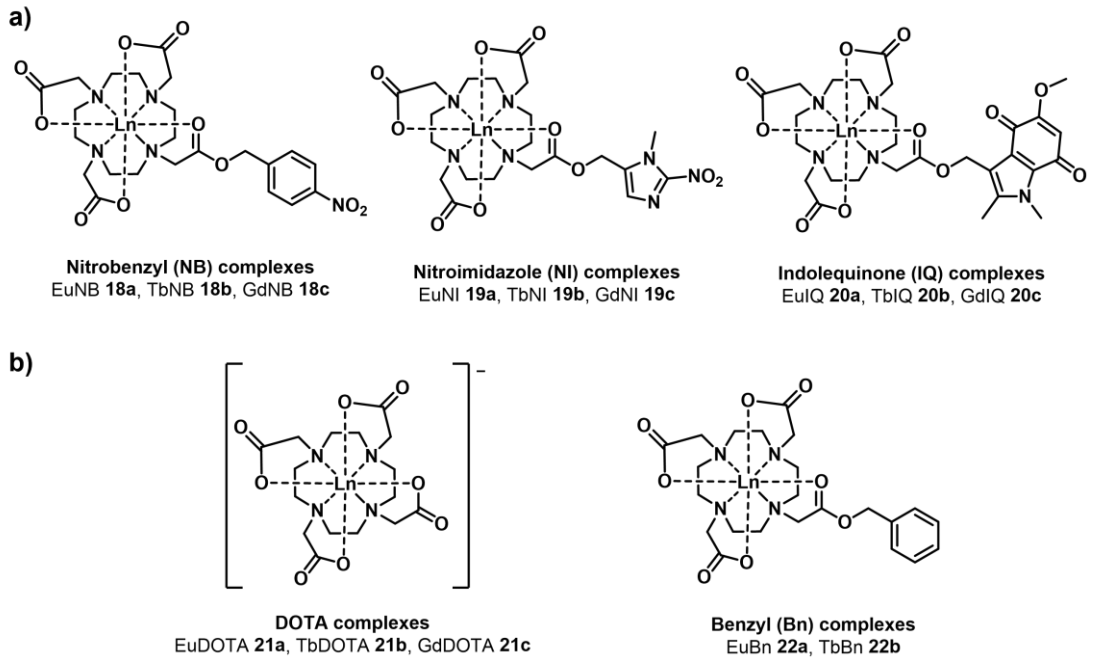

Figure 3.3: A summary of the target molecules for chapter III: a) hypoxia-activated targets, **18-20**, and b) the positive control DOTA complexes, **21**, and the reduction control benzyl (Bn) complexes **22**.

Activation of nitro-containing prodrugs and profluorophores, in the presence of nitroreductase enzymes and NAD(P)H, is proposed to occur *via* nitro reduction to the corresponding aniline and fragmentation (Scheme 3.1, activation mechanism 1), according to various literature sources.[13, 21] To investigate the mechanism of action of these activatable lanthanide complexes, the nitrobenzyl (NB) and nitroimidazole (NI) complexes were evaluated in comparison to the DOTA positive controls. In addition, the benzyl complexes (**22**, Bn, Figure 3.3b) were synthesised as reduction negative controls, as these cannot be activated *via* activation mechanism 1.

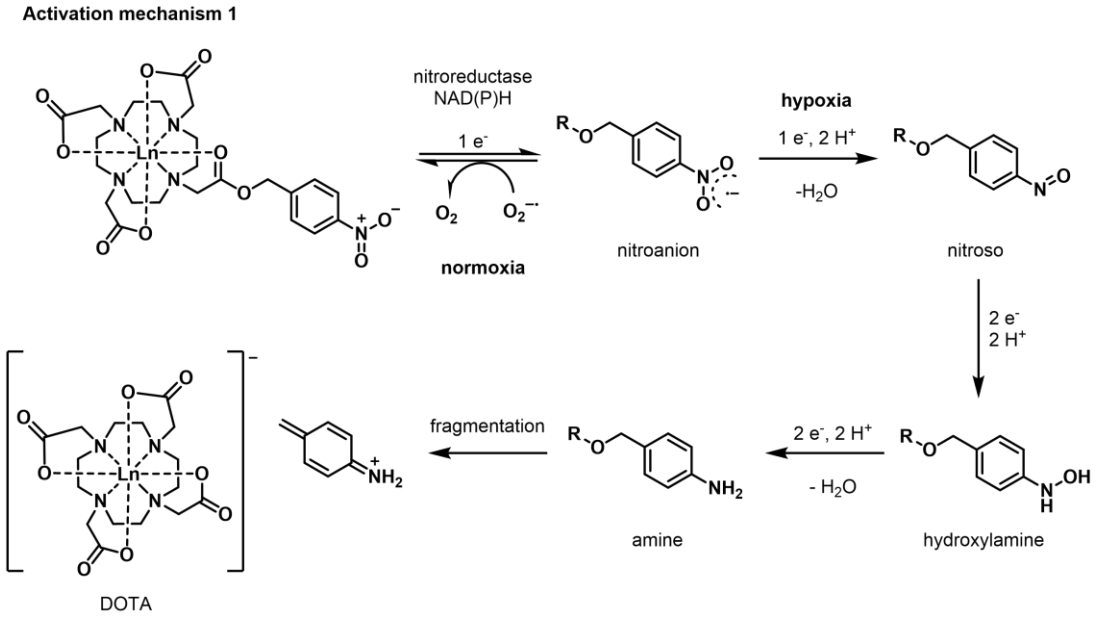

Scheme 3.1: Activation mechanism 1: the proposed mechanism of activation of the activatable complexes to DOTA (demonstrated with the nitrobenzyl complexes), selectively under reductive conditions in the presence of nitroreductase enzymes and NAD(P)H, by 6 electron reduction of the nitro group followed by fragmentation. Adapted from Calder et al.[13]

3.3 Synthesis

3.3.1 Nitrobenzyl complexes

The synthesis of the desired nitrobenzyl complexes, **18a-c**, was carried out according to Scheme 3.2. This synthetic route and the analysis of the nitrobenzyl complexes was initially carried out by Dr Deborah Sneddon, however the synthesis, spectroscopy, testing and analysis was repeated and expanded upon and only this work is reported here. The *tert*-

butyl protected DO3A core **23** was synthesised by alkylating cyclen with *tert*-butylbromoacetate and selectively isolating the tri-protected salt by precipitation.[2] Commercially available 4-nitrobenzyl alcohol was reacted with bromoacetyl bromide to form the activatable arm **24**, which was reacted with the *tert*-butyl protected DO3A core to give product **25**. The *tert*-butyl protecting groups were removed using standard reactions conditions for *tert*-butyl deprotection - TFA in CH_2Cl_2.[22]

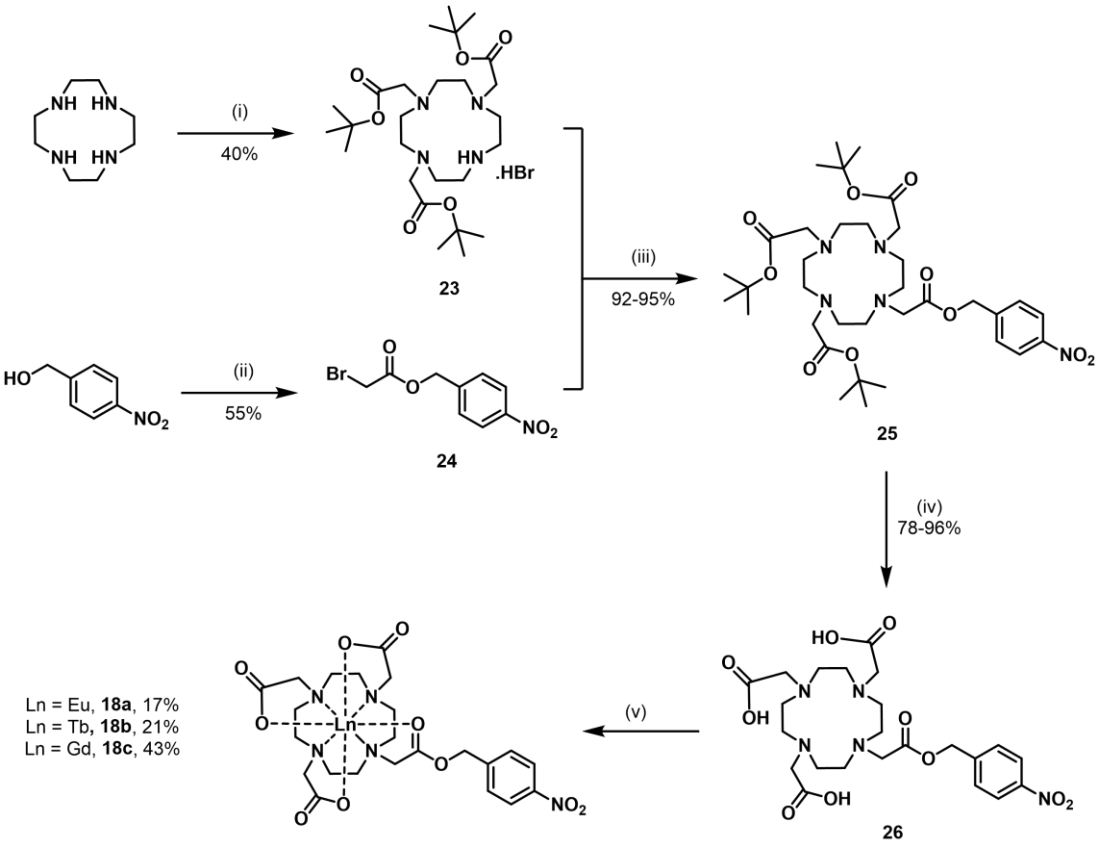

Scheme 3.2: The synthesis route of the nitrobenzyl lanthanide complexes **18a-c**. Reagents and conditions: (i) $NaHCO_3$, tert-butylbromoacetate, MeCN, 0 °C to rt, 44 h; (ii) Bromoacetyl bromide, $NaHCO_3$, MeCN, 45 °C, 18 h; (iii) $NaHCO_3$, dry MeCN, 80 °C, 39 h; (iv) TFA, CH_2Cl_2, rt, 42 h; (v) $Ln(OTf)_3$, MES buffer, pH 6.0, rt, 1-1.5 h.

The resulting triacid **26** was reacted with the corresponding lanthanide triflate under buffered conditions (MES buffer, pH 6.0) and purified by semi-preparative HPLC (method 1) to give the desired nitrobenzyl (NB) complexes (**18a-c**), which were isolated by lyophilisation. Buffered conditions were used to decrease the reaction time, from overnight (standard for complexation reactions in water) to under 1.5 hours, due to stability concerns. It is also noted that the purity of compound produced varied between batches and between

metals, due to the Lewis acidity of the lanthanides increasing degradation of the complexes by ester hydrolysis and based on the time the complex spent exposed to water and/or light at room temperature following purification.

3.3.2 Nitroimidazole complexes

Nitroimidazole alcohol **29** was synthesised over 5 steps (Scheme 3.3a), by adapting the optimised route described by O'Connor *et al.*[23] to obtain the product in good yields (20% yield over 5 steps). The reaction with bromoacetyl bromide to form **30** was carried out using 2,6-di-*tert*-butylpyridine as the base in DMF:CH_2Cl_2 1:1, instead of the previous method using $NaHCO_3$ in MeCN. The reaction of **29** with the tri-protected DO3A compound **23** (Scheme 3.3b) was initially carried out using K_2CO_3 as the base, however after column chromatography some impurities were still observed in the ^1H and ^{13}C NMR spectra. Repeating the reaction using $NaHCO_3$ yielded a slightly purer compound according to ^1H NMR spectroscopy, despite the longer reaction time needed (40 hours compared to 18 hours previously). The triacid (**32**) isolated and purified following the TFA deprotection of **30** formed by either method appeared pure according to LCMS, ^1H and ^{13}C NMR analysis. The ^1H NMR spectra of **31** and **32** contain split peaks for some proton environments which would be expected to show no coupling to other protons (the proton environments belonging to the nitroimidazole moiety), which is ascribed to slow exchange of fluxional diastereomers on the NMR timescale, as observed previously in the group.[24] Triacid **32** was reacted with the corresponding lanthanide triflate, under the same buffered conditions as for the nitrobenzyl complexes. This gave the nitroimidazole (NI) complexes **19a-c**, in moderate yields, 21-46%, following purification by semi-preparative HPLC (method 2) and isolation by lyophilisation.

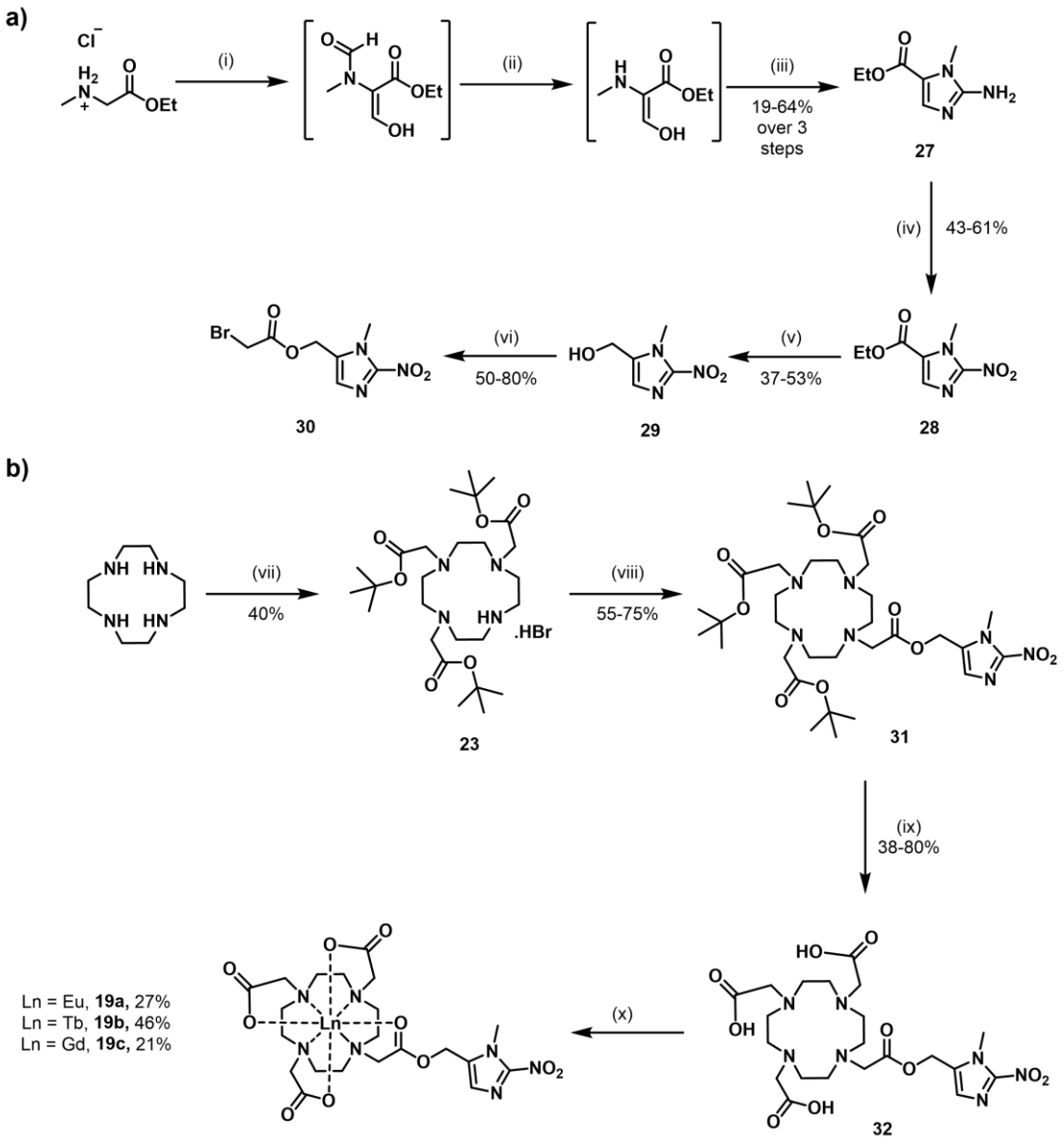

Scheme 3.3: The synthesis route of the nitroimidazole lanthanide complexes **19a-c**, highlighting a) the nitroimidazole arm synthesis and b) the ligand and complex synthesis. Reagents and conditions: (i) NaH, ethyl formate, dry THF, EtOH, 0 °C to rt, 3 h; (ii) EtOH, conc. HCl, reflux, 2 h; (iii) Cyanamide, EtOH, water, reflux, 1.5 h; (iv) $NaNO_2$, water, acetic acid, 0 °C to rt, 1.5 h; (v) $NaBH_4$, dry THF, MeOH, 0 °C, 2 h; (vi) Bromoacetyl bromide, 2,6-di-tertbutylpyridine, DMF:CH_2Cl_2 1:1, rt, 15 h; (vii) $NaHCO_3$, tert-butylbromoacetate, MeCN, 0 °C to rt, 20 h; (viii) **23**, K_2CO_3 or $NaHCO_3$, MeCN, 80 °C, 18-40 h; (ix) TFA, CH_2Cl_2, rt, 20 h; (x) $Ln(OTf)_3$, MES buffer, pH 6.0, rt, 1 h.

3.3.3 Attempts to synthesise the indolequinone complexes

The indolequinone alcohol, **38**, was synthesised (Scheme 3.4a), following the optimised procedure previously reported by Wallabregue *et al.,*[25] in 6 steps (25% yield over 6 steps). The quinone formation step (**36** to **37**) was carried out immediately following the nitro reduction (**35** to **36**) due to concerns of the stability of the formed aniline. Formation of the chlorinated indolequinone arm **39** and indolequinone triester **40** (Scheme 3.4b), using

similar routes to those used for the nitrobenzyl and nitroimidazole analogues, were carried out by Dr. Daniel Kovacs.

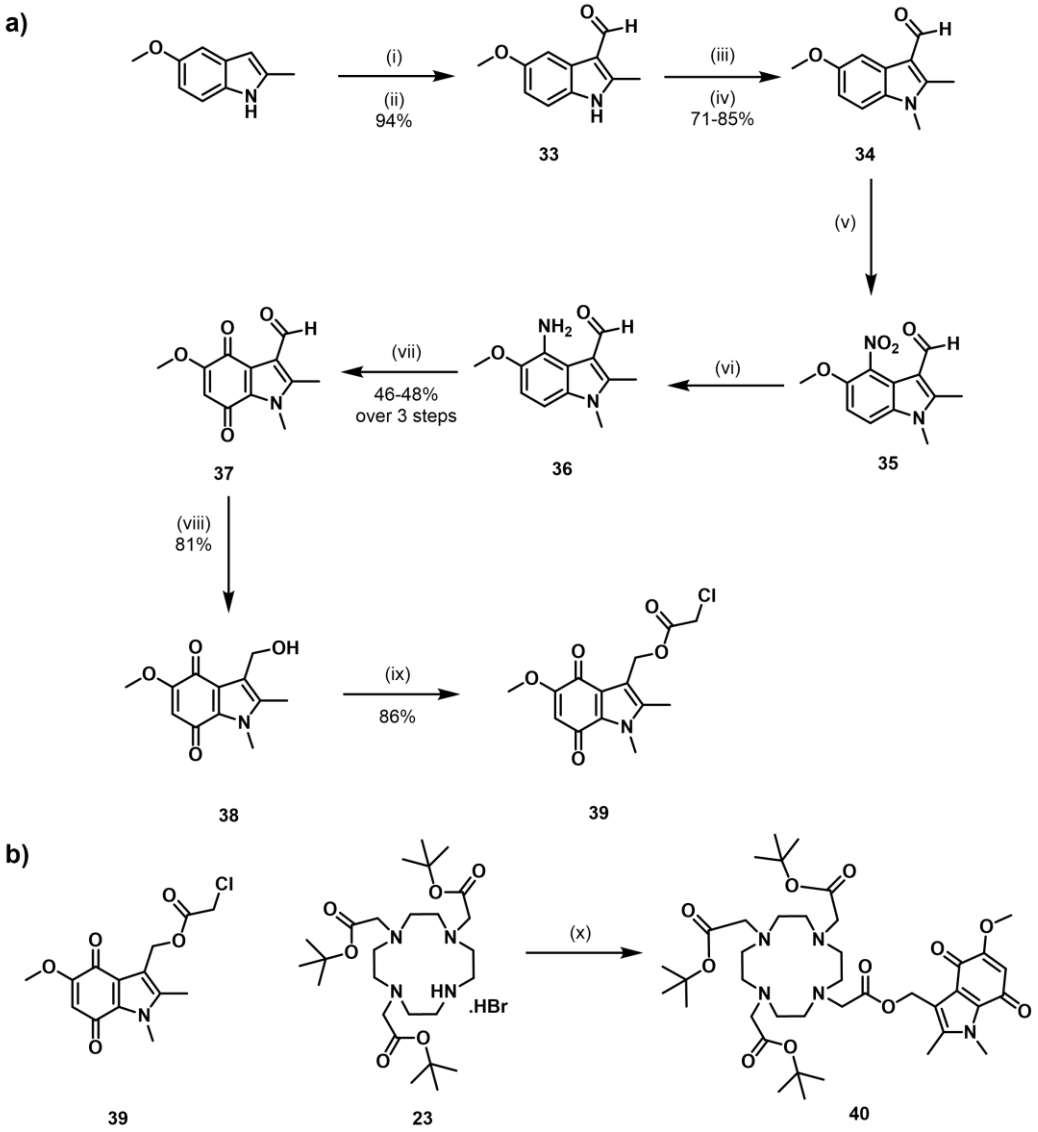

Scheme 3.4: The proposed synthesis of a) the indolequinone-based arm to attach to a lanthanide-based complex, based on literature procedures,[25] and b) the synthesis of the tert-butyl protected indolequinone compound. Reagents and conditions: (i) $POCl_3$, dry DMF, 0 °C, 10 min; (ii) Indole, dry DMF, −10 °C, 1.25 h; (iii) NaH, dry DMF, rt, 2 h; (iv) MeI, rt, 2 h; (v) Nitric acid, acetic acid, 0 °C, 3 h; (vi) Sn, EtOH, aq. HCl, 80 °C, 1 h; (vii) Fremy's salt, NaH_2PO_4/Na_2HPO_4 buffer, rt, 1 h; (viii) $NaBH_4$, dry MeOH, dry THF, 0 °C, 45 min; (ix) Chloroacetyl chloride, 2,6-di-tertbutylpyridine, DMF:CH_2Cl_2 1:1, rt, 2 h; (x) Na_2CO_3, MeCN, 50 °C, 18 h.

Subjecting the indolequinone triester **40** to the standard TFA deprotection conditions used for the nitrobenzyl and nitroimidazole analogues caused degradation of the chromophore (observed by TLC and ^{1}H NMR spectroscopy, carried out by Dr Daniel Kovacs) – previous work in the Conway group has suggested that the indolequinone moiety is acid sensitive. Subsequent attempts to deprotect **40** using $ZnBr_2$ or oxalyl chloride (giving slow release of

HCl over time, which was previously used for removal of a Boc protecting group under mild conditions)[26] were also unsuccessful. Table 3.1 summarises the reported conditions for deprotection of a *tert*-butyl ester group and why these conditions were determined to be incompatible with the desired compound.[27]

Table 3.1: Comments on the conditions attempted and reported[27] for the deprotection of tertbutyl ester groups.

Conditions	Comments
TFA, CH_2Cl_2, rt, 2 h	Degradation to indolequinone observed
$ZnBr_2$, CH_2Cl_2, rt, 1 h	Product not observed by ^{1}H NMR, likely Zn bound to ligand
Oxalyl chloride, MeOH, rt, 24 h	Product not detected by MS or LCMS, change in ^{1}H NMR spectra but not product
The use of $CeCl_3$, $Yb(OTf)_3$, MgI_2 or $TiCl_4$ as Lewis acids	Metal may bind to ligand, would be difficult to remove
Reported enzymatic conditions (e.g. thermitase or pig liver enzymes)	Only used previously on one substrate or for peptides
Heat to 190-200 °C	Harsh conditions undesirable due to observed instability of nitrobenzyl and nitroimidazole complexes in water over time when heated

An alternative protecting group strategy was devised, employing the TBDMS protecting group of a phenol hydroxyl group attached to the carboxyl group, with the hypothesis that the TBDMS protecting group could be removed using a fluoride source (e.g. TASF or TBAF) and the resulting phenol would fragment to give the corresponding carboxylic acid (Scheme 3.5). The proposed synthetic route using this protecting group strategy is outlined in Scheme 3.6 and Scheme 3.7.

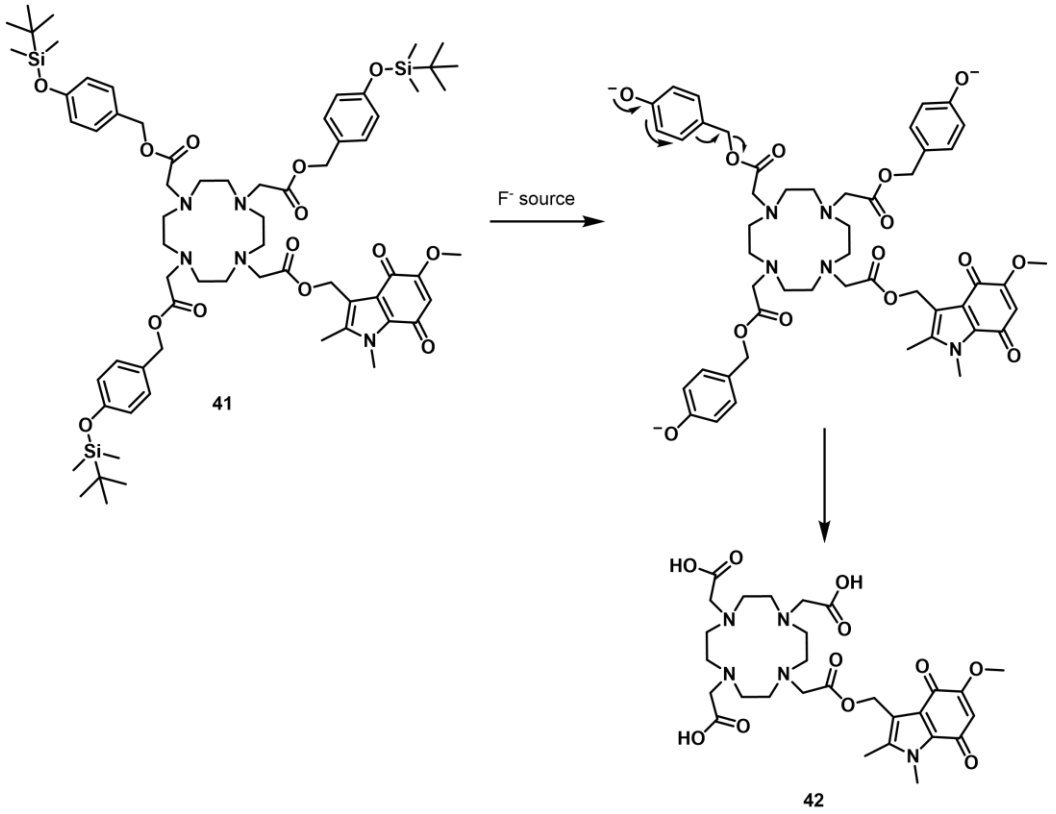

Scheme 3.5: The proposed mechanism for the deprotection of **41**.

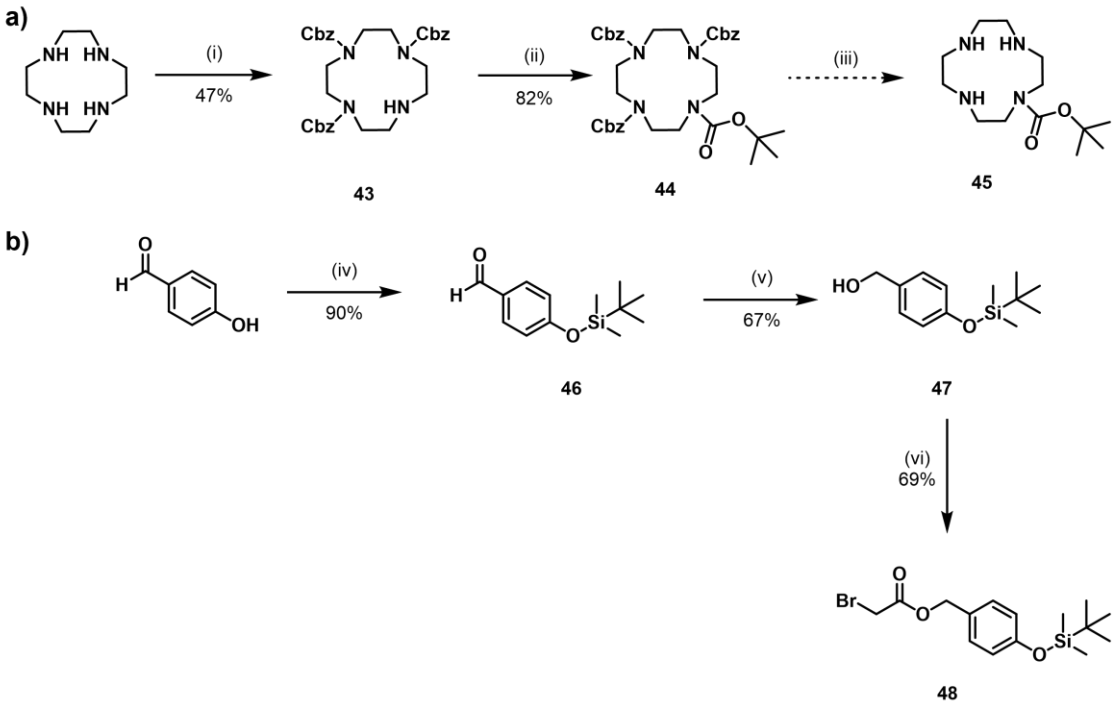

Scheme 3.6: The proposed synthesis of the indolequinone lanthanide complexes **20a-c**, highlighting the synthesis of a) the mono-protected cyclen (to aid attachment of three protecting groups) and b) the TBDMS protected arm. *Reagents and conditions:* (i) Benzyl chloroformate, TEA, CH_2Cl_2, rt, 17 h; (ii) Di-tert-butyl dicarbonate, dry TEA, dry CH_2Cl_2, rt, 16 h; (iii) H_2, $Pd(OH)_2$/C, MeOH, rt; (iv) Tert-butylchlorodimethylsilane, imidazole, DMF, rt, 17 h; (v) $NaBH_4$, MeOH, THF, 0 °C to rt; (vi) Bromoacetyl bromide, 2,6-di-tertbutylpyridine, DMF:CH_2Cl_2 1:1, rt, 2 h.

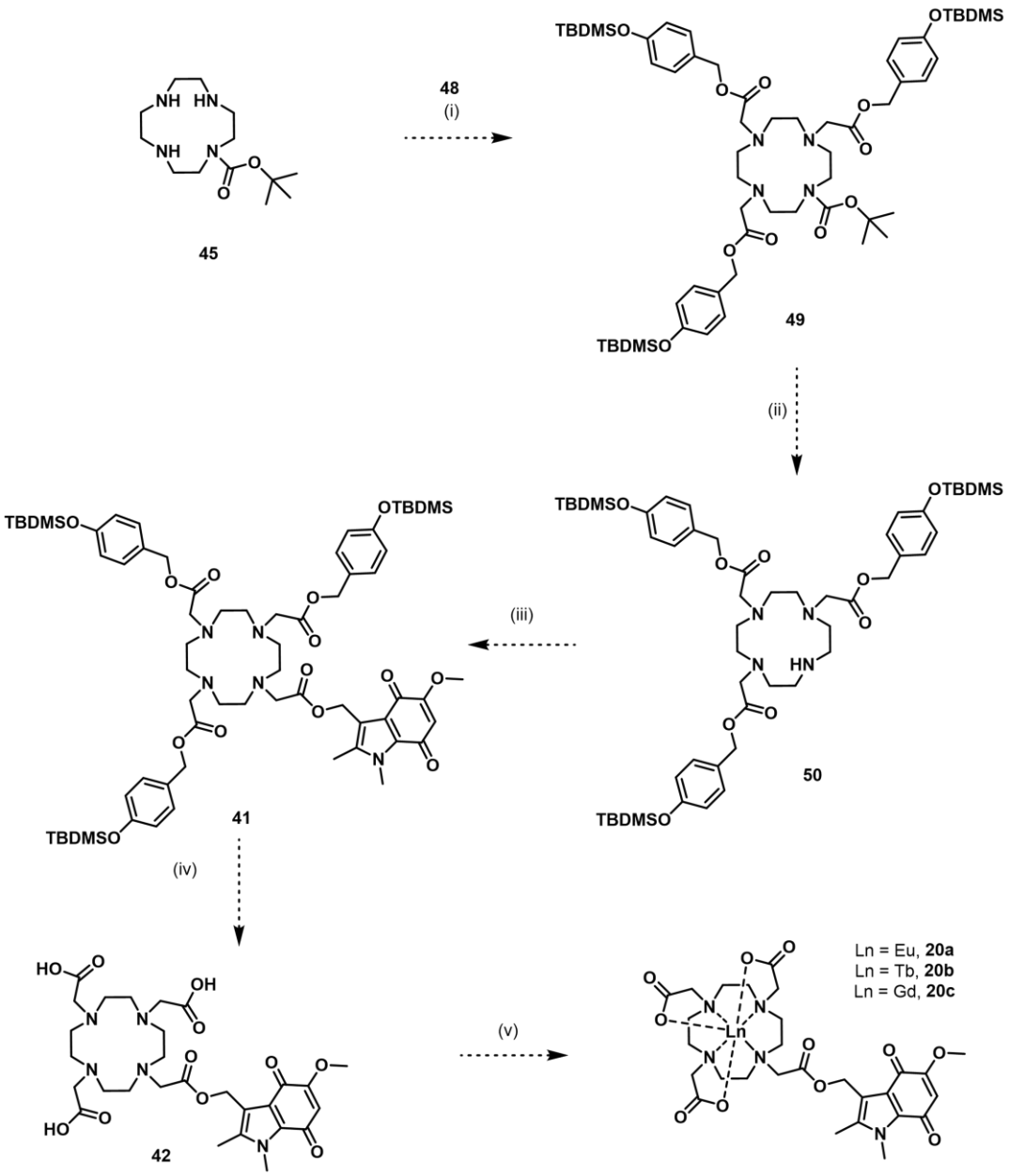

Scheme 3.7: The overall proposed synthesis route for formation of the indolequinone lanthanide complexes, **20a-c**. Reagents and conditions: (i) Na_2CO_3, MeCN, rt to 50 °C; (ii) TFA/CH_2Cl_2 or oxalyl chloride/MeOH; (iii) **39**, Na_2CO_3, MeCN, rt to 50 °C; (iv) HF or TASF or TBAF; (v) $Ln(OTf)_3$, MES buffer, rt.

Compounds **43-44** and **46-48** were synthesised according to literature protocols (Scheme 3.6).[28-34] To investigate the stability of the indolequinone moiety in the presence of fluoride sources, a test reaction was carried out with indolequinone alcohol **38** in the presence of the TBDMS-protected phenyl alcohol **47** and TBAF (Figure 3.4a) and was monitored by TLC and LCMS. Qualitative LCMS analysis (Figure 3.4b) shows that the deprotection occurs readily and that indolequinone alcohol is stable over four hours. Despite this, the synthesis of the indolequinone complexes was discontinued due to general concerns about

acid instability (as the lanthanide will act as a Lewis acid which destabilises the indolequinone ester bond). Further work to synthesise complexes **20a-c** was carried out by Harry McWilliam and Dr Antoine Wallabregue, attempting the use of ethyl, methyl and allyl groups as alternative ester protecting groups, as well as the synthesis of a directly attached complex, with the DO3A core N-alkylated with the indolequinone moiety.

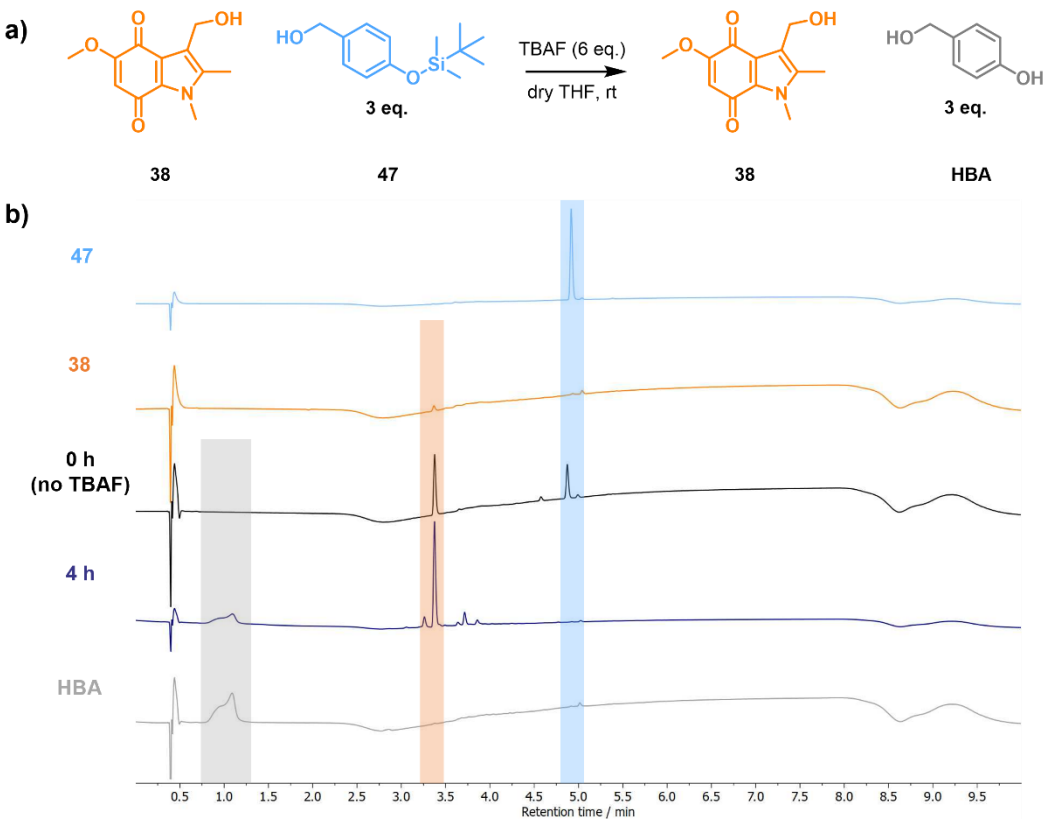

Figure 3.4: a) The scheme for the test reaction of the indolequinone moiety in the presence of TBAF. b) The LCMS traces from the test reaction, showing the deprotection of **47** and the stability of the indolequinone alcohol **38**. Evaluated at 254 nm – the small peak present at ~5 min in all traces is an impurity on the column.

3.3.4 Synthesis of control complexes

The positive control compounds, EuDOTA (**21a**) and TbDOTA (**21b**), were synthesised (Scheme 3.8) following standard complexation conditions by reacting the appropriate lanthanide triflate salt with DOTA in water or EtOH:water 1:1 at 40 °C overnight then adjusting the pH using 2 M NaOH. The compounds were purified by dialysis (500 Da cut-off) to remove any low molecular weight impurities.

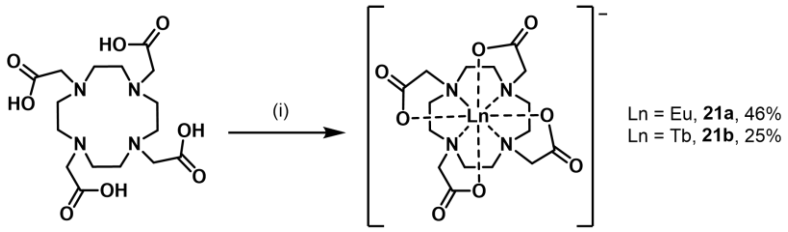

Scheme 3.8: The proposed synthesis of the positive control compounds EuDOTA **21a** and TbDOTA **21b**. Reagents and conditions: (i) $Ln(OTf)_3$, EtOH: H_2O (1:1) or H_2O, 40 °C, 17 h.

The negative reduction control benzyl complexes were synthesised (Scheme 3.9) in a similar manner to the nitrobenzyl and nitroimidazole complexes. The commercially available bromoester was used to alkylate the DO3A triester **23** to form **51** and TFA in CH_2Cl_2 was used for deprotection to yield the triacid **52**. The benzyl (Bn) lanthanide complexes, **22a**-**c**, were isolated by lyophilisation following reaction with the corresponding lanthanide triflate salt and purification by semi-preparative HPLC (method 3).

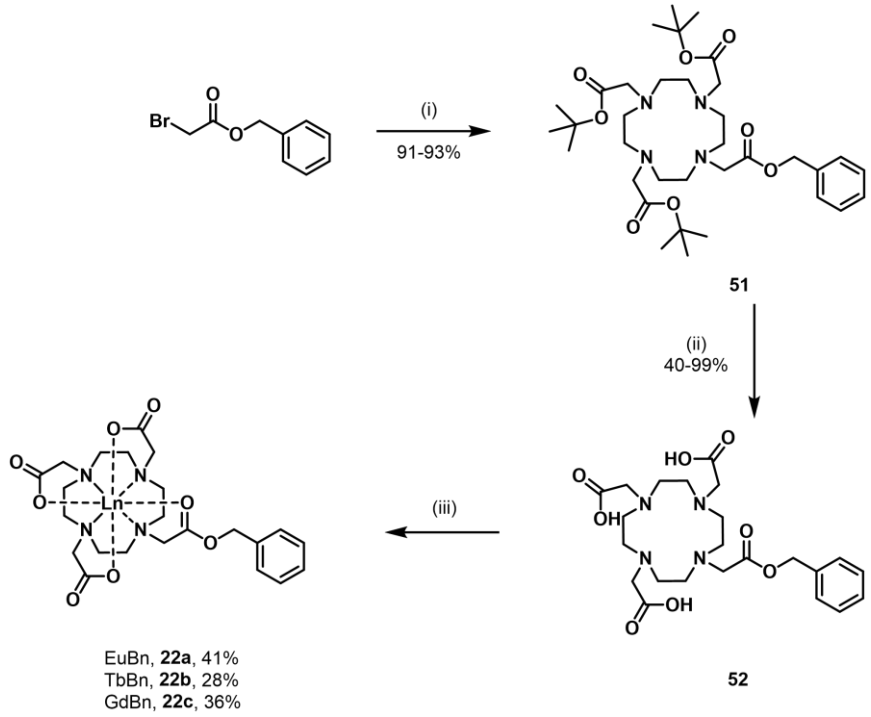

Scheme 3.9: The synthetic scheme for the synthesis of the Bn complexes, **22a-b**, to be used as controls for the reduction assays. Reagents and conditions: i) **23**, K_2CO_3, MeCN, rt, 3 h; ii) TFA, CH_2Cl_2, rt, 18 h; iii) $Ln(OTf)_3$, MES buffer (1 M, pH 6), rt, 1 h.

3.3.5 Characterisation of target complexes

The target lanthanide complexes were fully characterised by ^{1}H NMR spectroscopy (except for the gadolinium analogues), LRMS, HRMS and analytical HPLC and/or LCMS (except

for the DOTA complexes due to the lack of chromophore). The HRMS spectra of the complexes (Gd Figure 3.5, for Eu and Tb see Figure A3.1 and A3.2) confirm their formation, when compared to the experimental spectra.

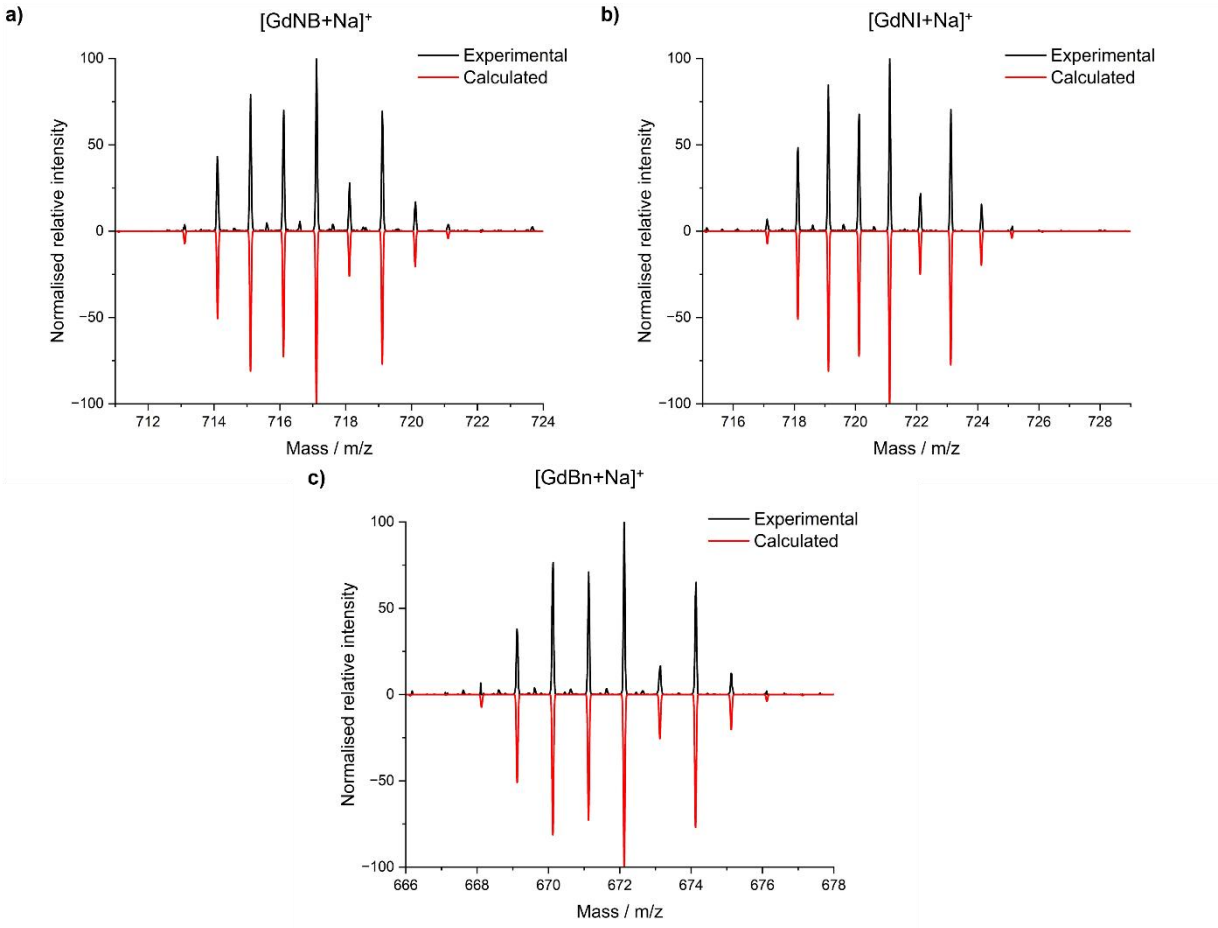

Figure 3.5: High resolution mass spectrometry (HRMS) analysis of the GdNB (a), GdNI (b) and GdBn (c) complexes (experimental, black) in comparison to the calculated spectra (red), highlighting the distinct isotopic pattern for gadolinium.

The ^{1}H NMR spectra of the europium (Figure 3.6a) and terbium analogues (Figure 3.6b) highlights the difference in symmetry between the parent DOTA complexes and the NB/NI/Bn complexes. As expected, the ^{1}H NMR spectrum of EuDOTA contains a total of 10 peaks, with 6 dominant peaks from the TSAP isomer and 4 minor peaks from the SAP isomer (with the remaining 2 expected peaks overlapping others)[35] due to the high symmetry resulting in 6 distinct chemical environments – 2 acetate protons, 2 axial protons from the cyclen ring and 2 equatorial protons from the cyclen ring. In comparison, the spectra of the europium NB/NI/Bn complexes contain 26-32 peaks, consistent with a

mixture of TSAP and SAP isomers of asymmetric DOTA monoester complexes, with inequivalent cyclen ring and arm protons giving up to 24 H in addition to the 6-7 H from the activatable moiety. This difference in symmetry suggests that we may expect a difference in relaxivity between the NB/NI and DOTA complexes, as symmetry impacts the rotational correlation time. All of the synthesised complexes contain some of the corresponding DOTA analogue due to stability issues resulting in cleavage of the ester arm (further discussed in section 3.6).

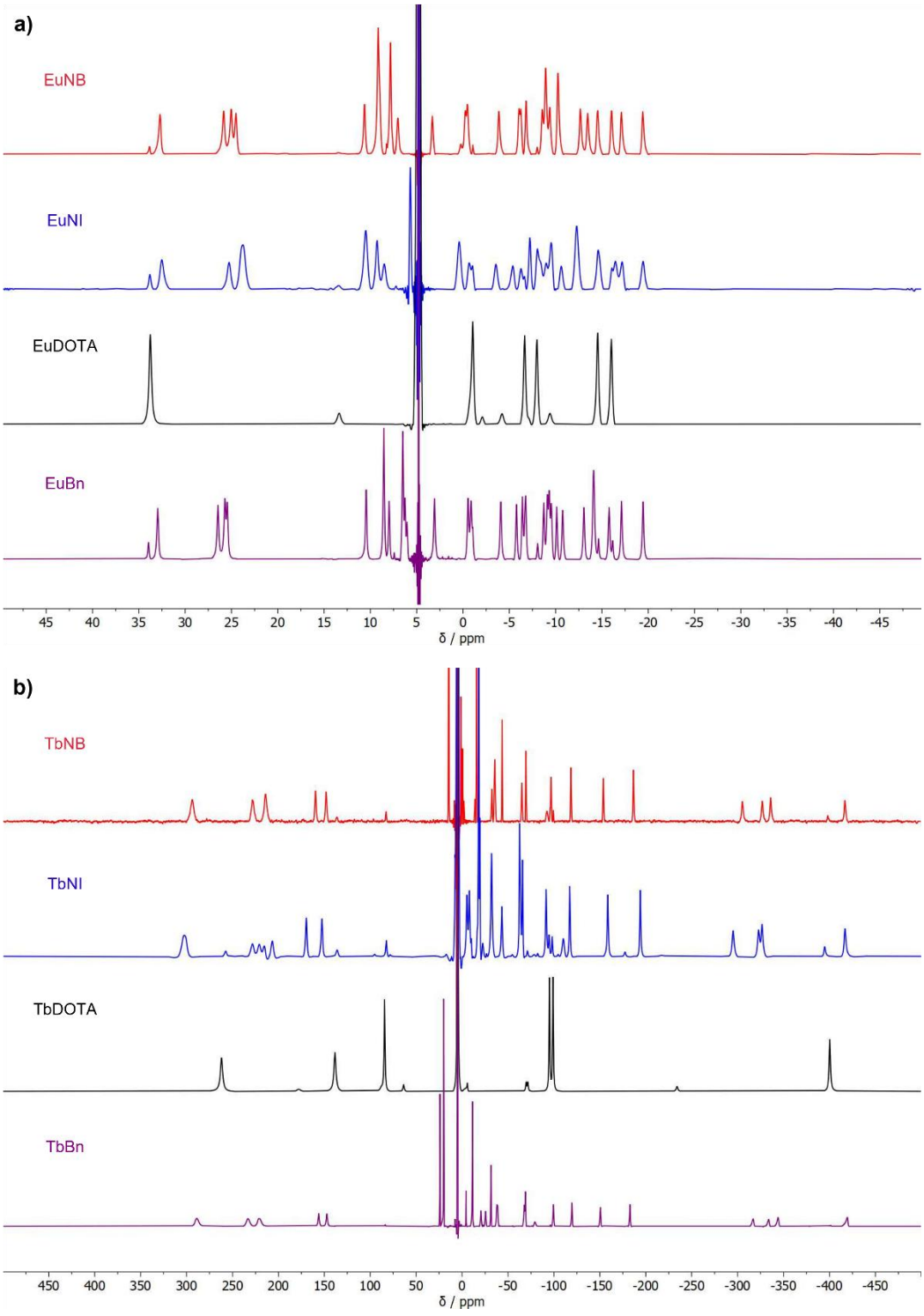

Figure 3.6: a) Stacked ^{1}H NMR spectra of compounds EuNB (**18a**, red), EuNI (**19a**, blue), EuDOTA (**21a**, black) and EuBn (**22a**, purple) to highlight the difference in symmetry between the DOTA complex (C_4 symmetric, 6 peaks, TSAP and SAP isomers clearly visible) vs the nitrobenzyl/nitroimidazole/benzyl complexes (C_1 symmetric). b) Stacked ^{1}H NMR spectra of complexes TbNB (**18b**, red), TbNI (**19b**, blue), TbDOTA (**21b**, black) and TbBn (**22b**, purple).

3.4 Photophysical characterisation

Luminescence measurements were carried out at 50 µM in water (unless otherwise specified). The UV-Vis spectra and steady state emission spectra (Figure 3.7) of the triacid ligands (**26** for NB, red, **32** for NI, blue, and **52** for Bn, purple) were measured to determine any shift observed upon complexation and any ligand emission.

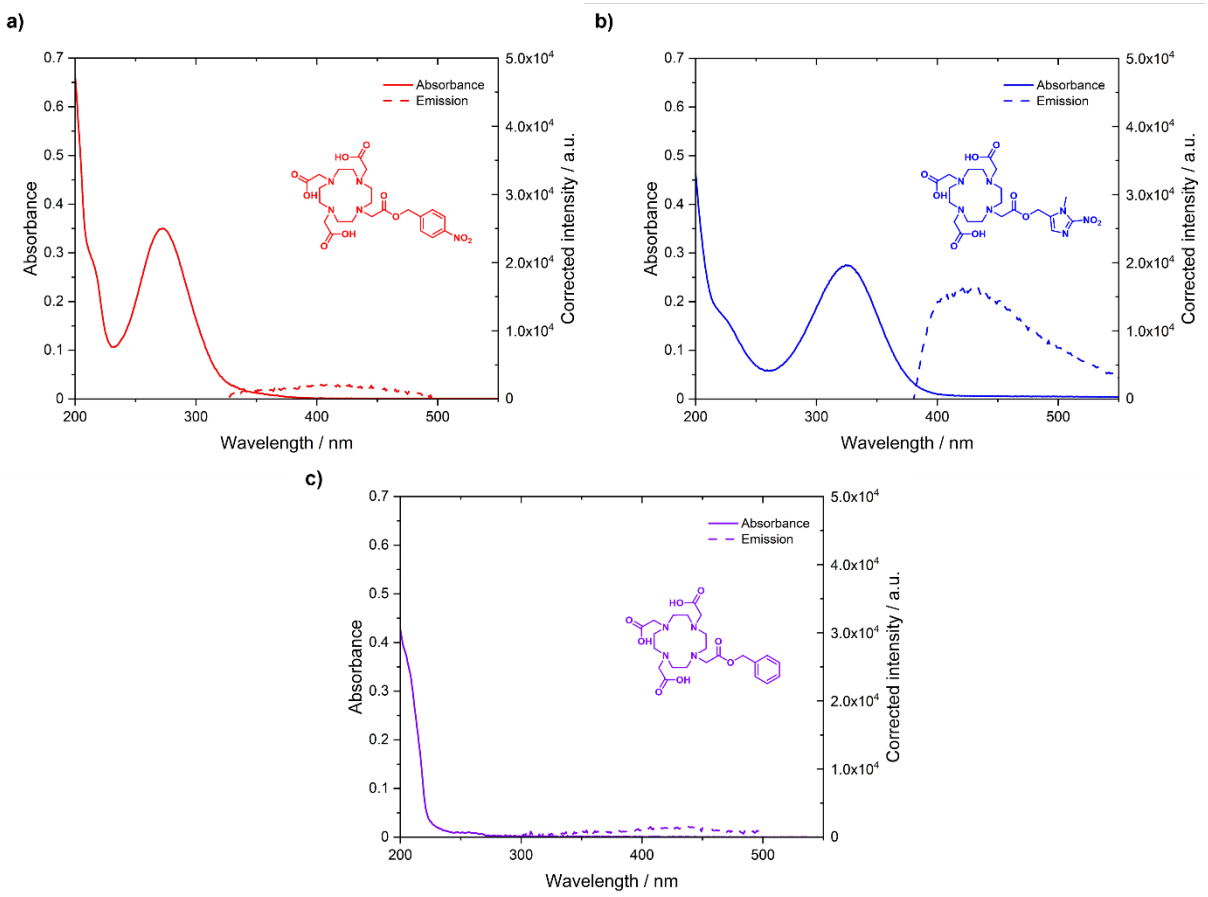

Figure 3.7: The UV-Visible absorption spectra (solid lines) and steady-state emission spectra (dotted lines) of a) NB ligand (**26**, red – λ_{ex} 269 nm), b) NI ligand (**32**, blue – λ_{ex} 320 nm) and c) Bn ligand (**52**, purple – λ_{ex} 262 nm). Slits 29 nm / 1 nm, integration time 0.5 s, S1 channel.

The ligands displayed maxima in the UV-Vis spectra at 272 nm for NB, 325 nm for NI and 262 nm for Bn, with the Bn complexes displaying much weaker absorbance than the nitro-containing ligands. The steady state emission spectra were recorded upon excitation at 269 nm, 320 nm and 262 nm, respectively, consistent with later emission spectra for the lanthanide complexes. Negligible fluorescence emission was observed for the ligands,

except for the NI ligand **32** which showed weak fluorescence emission, with a maximum around 415 nm (observed more clearly upon excitation at 300 nm, Figure A3.3).

The UV-Visible spectra of EuNB, EuNI and EuBn (Figure 3.8a) and TbNB, TbNI and TbBn (Figure 3.8b) were measured in comparison to their parent compound EuDOTA or TbDOTA which contain no chromophore. The europium and terbium complexes displayed maximum absorbance around 269 nm for NB (red), 320 nm for NI (blue) and 262 nm for Bn (purple), with small shifts observed from the ligand absorbance upon complexation.

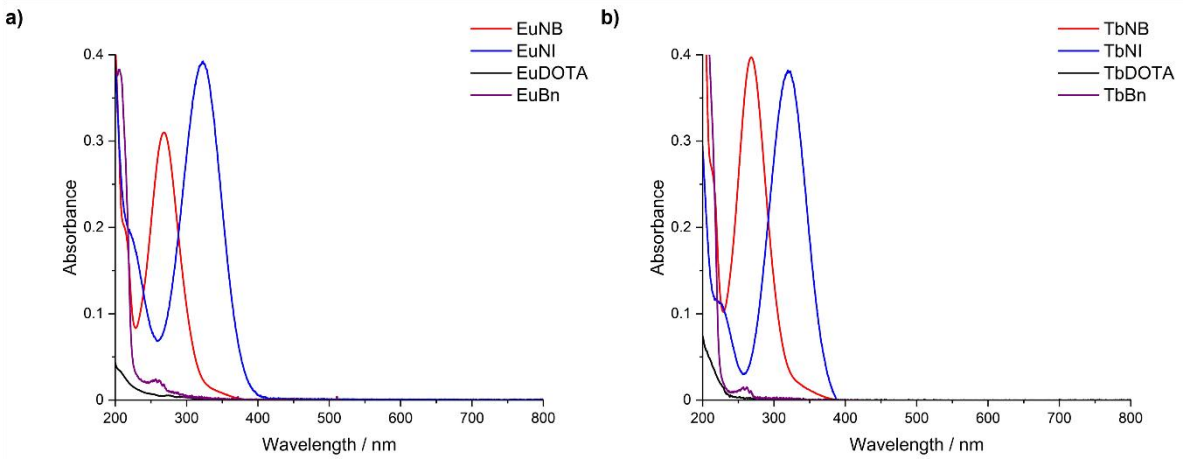

Figure 3.8: The UV-Vis absorption spectra of a) EuNB (**18a**, red), EuNI (**19a**, blue) and EuBn (**22a**, purple) in comparison to EuDOTA (**21a**, black) and b) TbNB (**18b**, red), TbNI (**19b**, blue) and TbBn (**22b**, purple) in comparison to TbDOTA (**21b**, black), at 50 µM in H_2O. UV bandwidth 1 nm, NIR bandwidth 20 nm, data interval 0.2 nm, scan rate 200 nm/min, source change at 340 nm.

3.4.1 Steady-state emission and excitation spectra

The activatable lanthanide complexes were evaluated under both steady-state and time-gated emission, in comparison to their DOTA analogues. Their steady-state emission was measured first to determine any interference of antenna fluorescence, to determine intrinsic quantum yield of the europium complexes (see section 3.4.4) and to investigate their structural properties and differences.

The activatable NB and NI lanthanide complexes were investigated under ligand excitation according to the λ_{max} for the UV-Vis spectra (Figure 3.8), with λ_{ex} 269 nm for NB complexes and λ_{ex} 320 nm for NI complexes. These were compared to the DOTA analogues (evaluated under the same conditions, λ_{ex} 269 nm or 320 nm) to evaluate any turn-on profluorophore

and antenna effect observed. For the europium NB (Figure 3.9a) and NI complexes (Figure 3.9b), the intensity of emission observed was similar to that of the EuDOTA. For the corresponding terbium complexes, an increase in intensity is observed for TbDOTA in comparison to TbNB (Figure 3.9c) and nitroimidazole ligand fluorescence increases the overall intensity observed for TbNI compared to TbDOTA (Figure 3.9d), obscuring the low intensity terbium emission.

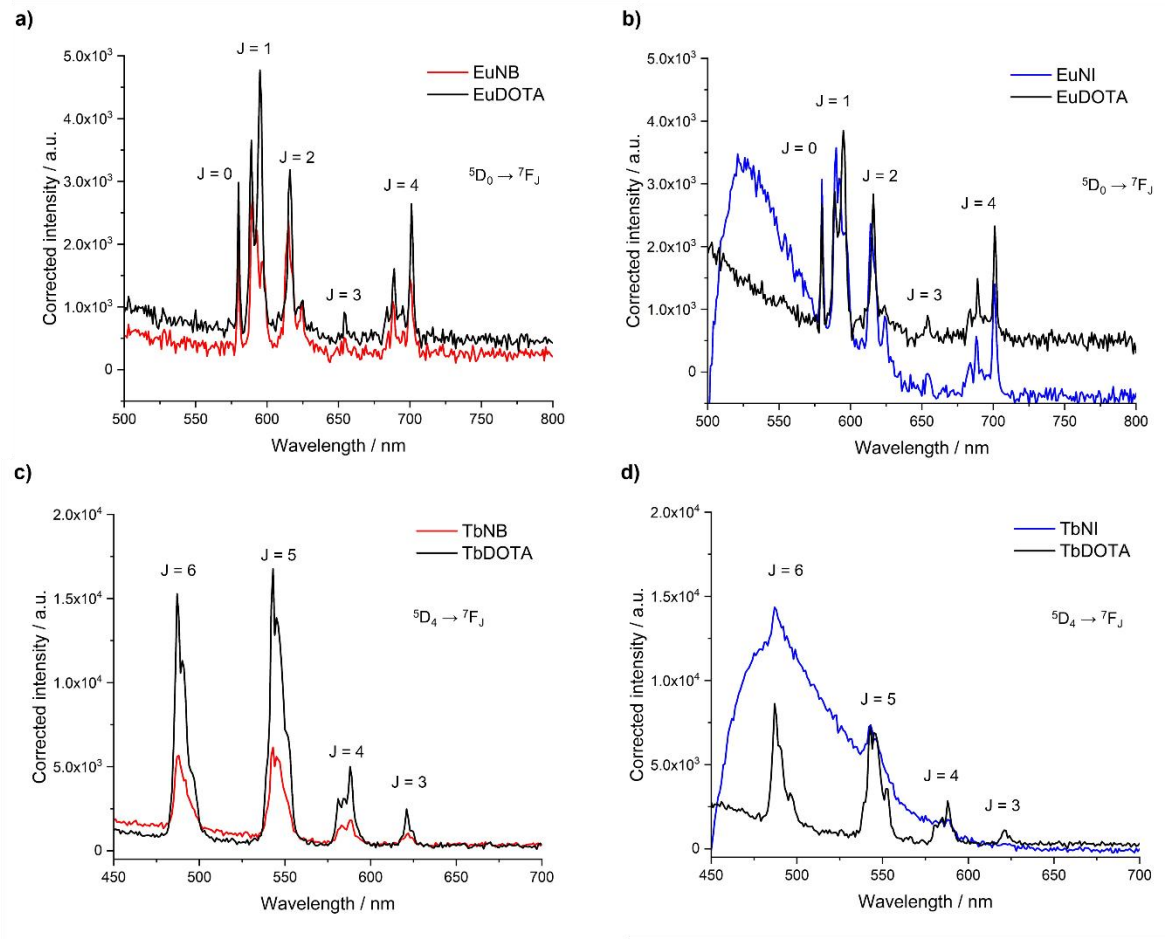

Figure 3.9: The steady-state emission spectra following ligand excitation (metal region) for a) EuNB (red), b) EuNI (blue), c) TbNB, d) TbNI. For NB, λ_{ex} 269 nm; for NI, λ_{ex} 320 nm. Slits 29 nm / 1 nm, integration time 0.5 s, S1 channel, 495 nm long pass filter for Eu, 400 nm long pass filter for Tb.

The weak sensitisation of the nitrobenzyl and nitroimidazole complexes is corroborated by the excitation spectra (Figure 3.10), with a poor intensity of emission occurring (lower magnitude than occurring through direct excitation of weakly absorbing lanthanide centred transitions, Figure 3.12), whereas sensitisation is observed for the benzyl complexes.

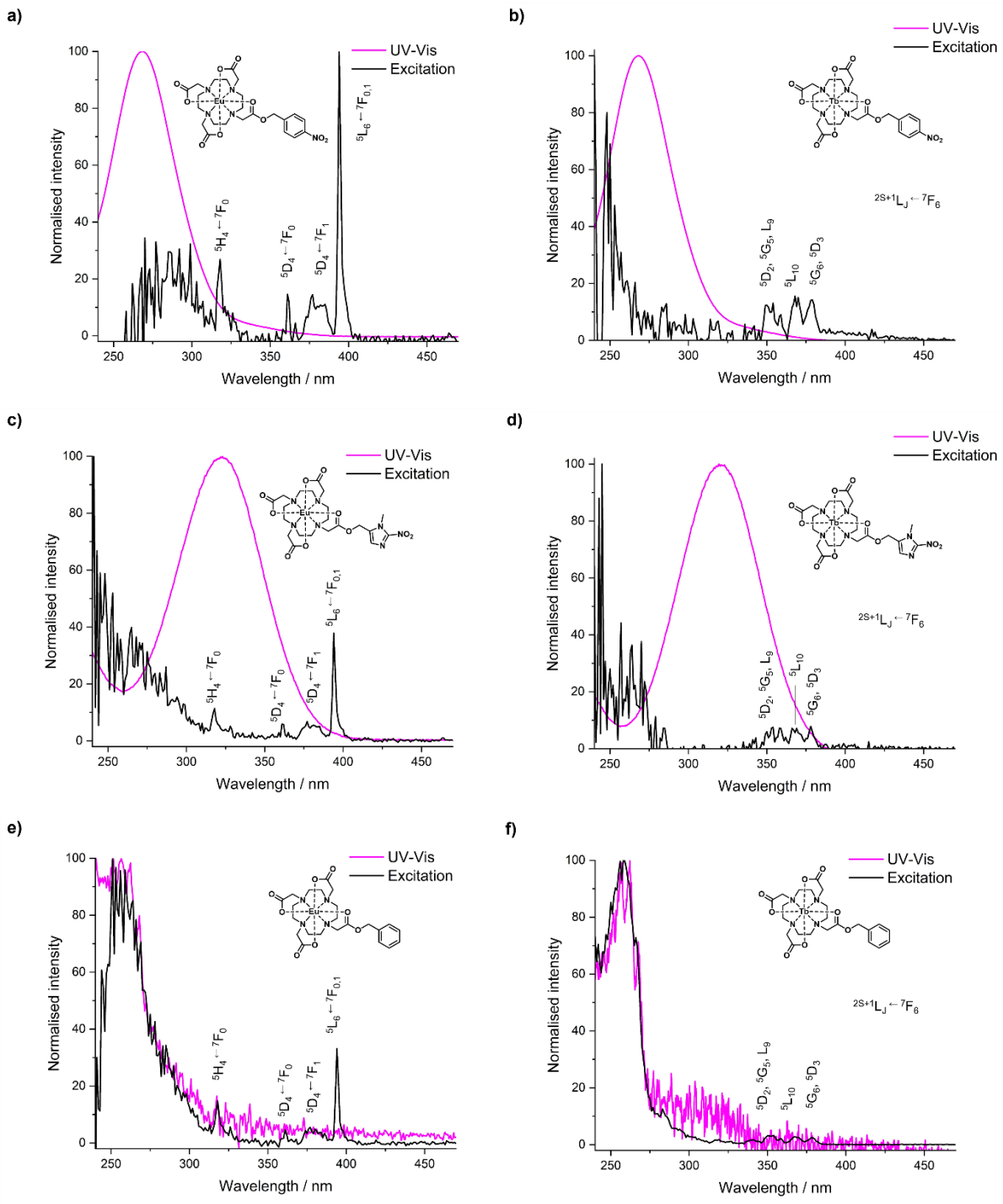

Figure 3.10: Normalised excitation spectra (black) compared to the normalised UV-Vis spectra (pink) of compounds measured at 50 µM in H_2O. a) EuNB, b) TbNB, c) EuNI, d) TbNI, e) EuBn, and f) TbBn. Eu excitation spectra: λ_{em} 616 nm, slits 1 / 10 nm, integration time 0.2 s, 495 nm long pass filter. Tb excitation spectra: λ_{em} 487 nm, slits 1 / 5 nm, integration time 0.2 s, 400 nm long pass filter. S1/R1 channel. The relevant transitions are labelled.[36]

The lanthanide sensitisation observed for the benzyl complexes observed in steady state emission spectra (Figure 3.11) is more evident for the terbium complexes (Figure 3.11b), where a tenfold change in intensity of the $^5D_4 \rightarrow {}^7F_5$ transition (J=5 band) is observed

between direct metal and ligand excitation (sevenfold change by area). Similar results are observed in the time-gated emission spectra (Figure A3.4), with a threefold increase in intensity of the $^5D_0 \rightarrow {}^7F_1$ transition (J=1 band) observed between direct metal and ligand excitation for EuBn (threefold based on area) and a fivefold increase in intensity of the J=5 band for TbBn, suggesting that the benzyl ligand is a more efficient sensitiser for terbium than europium. The poor sensitisation observed with the nitrobenzyl complexes compared to the benzyl complexes suggests that the presence of the nitro moiety may enable a quenching pathway by changing the triplet energy level of the ligand.

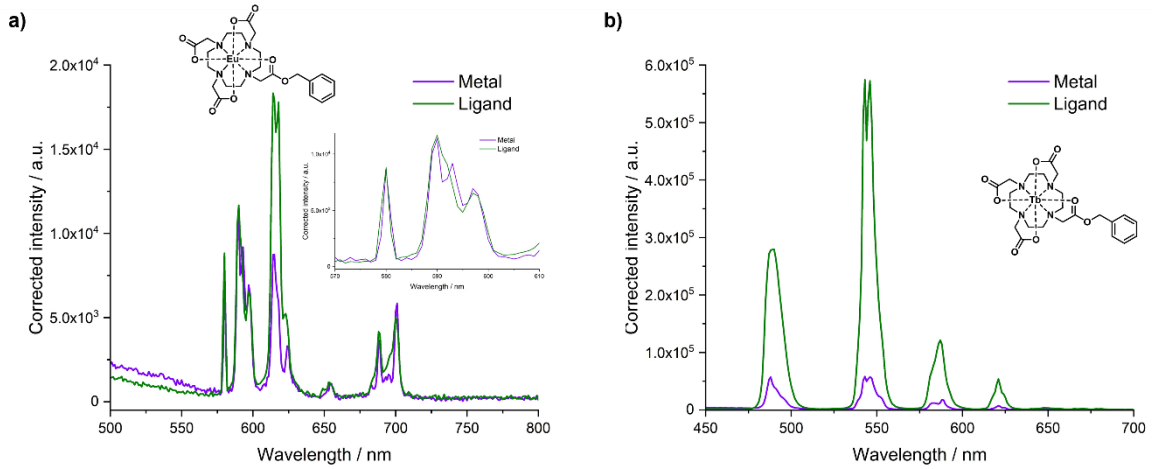

Figure 3.11: Steady-state emission spectra of a) EuBn and b) TbBn using metal (purple, λ_{ex} 397 nm for Eu, λ_{ex} 366 nm for Tb) or ligand (green, λ_{ex} 262 nm) excitation. Slits 29 nm / 1 nm, integration time 0.5 s, S1 channel, 495 nm long pass filter for Eu, 400 nm long pass filter for Tb.

Upon excitation of the metal (λ_{ex} 397 nm for europium, $^5L_6 \leftarrow {}^7F_0$, and λ_{ex} 366 nm for terbium, $^5L_{10} \leftarrow {}^7F_6$), little change in fluorescence intensity is observed between the nitrobenzyl or nitroimidazole complexes and the DOTA complexes. For the europium complexes, a change in the shape of the J=1 band is observed between EuDOTA (2 peaks) and EuNB or EuNI (3 peaks). This difference is ascribed to changes in crystal field splitting of the $^7F_1$ state, which arises due to differences in the overall symmetry of the complexes – EuDOTA is C_4 symmetric, therefore gives rise to 2 crystal field levels, a non-degenerate and twofold degenerate crystal-field level, whereas EuNB and EuNI are C_1 symmetric, giving three non-degenerate crystal field levels of the $^7F_1$ state.[37] A small change in fluorescence intensity is observed between TbNI and TbDOTA upon excitation at 366 nm ($^5L_{10} \leftarrow {}^7F_6$, Figure 3.12b),

potentially arising due to absorbance of the nitroimidazole ligand at this wavelength – similar emission intensities are observed for TbNB, TbNI and TbDOTA upon excitation at 488 nm (Figure 3.12c, $^5D_4 \leftarrow {}^7F_6$), with a slightly weaker intensity observed for TbNI compared to TbDOTA.

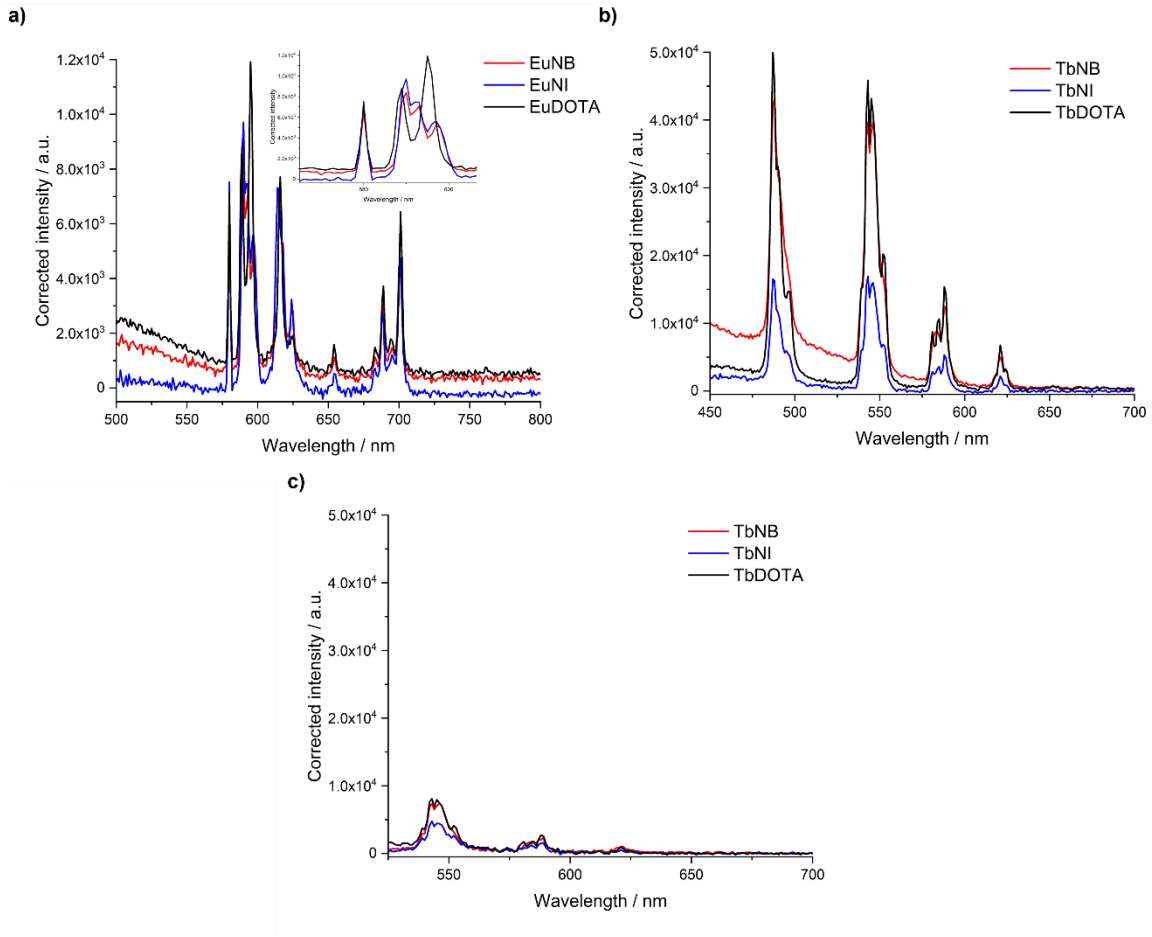

Figure 3.12: Steady-state emission spectra of a) EuNB (red) and EuNI (blue) vs EuDOTA (black), with the insert zoomed on the J=0 and J=1 bands, and b and c) TbNB and TbNI vs TbDOTA, upon direct metal excitation (λ_{ex} 397 nm for Eu, λ_{ex} 366 nm for Tb panel b, λ_{ex} 488 nm for panel c). Slits 29 nm / 1 nm, integration time 0.5 s, S1 channel, 495 nm long pass filter for Eu, 400 nm long pass filter for Tb.

Poor photostability of the nitroimidazole complexes was noted, due to the large excitation slit used for imaging and upon higher energy excitation. Figure 3.13a demonstrates that the largest decrease in UV-Vis absorbance is observed upon excitation at 320 nm (in comparison to 397 nm, $^5L_6 \leftarrow {}^7F_0$, for EuNI, Figure 3.13) and that the shape of the $^5D_0 \rightarrow {}^7F_1$ transition (J=1 band) changes depending on the order of spectra acquired, from 3 peaks in the J=1 band towards 2 peaks, Figure 3.13b, compared to the 2 peaks observed for

EuDOTA. These results suggest that upon exposure to large amounts of high energy light, the nitroimidazole complexes may partially degrade to EuDOTA, consistent with previous reports on the poor photostability of nitroimidazole-containing compounds. These results were measured upon excitation of EuNI 6 times over half an hour, however further tests could be carried out to further understand the photodegradation, including measurement of changes in the UV-Vis spectrum of EuNI as a function of time over an extended period of time upon light irradiation. Further stability issues of these complexes are discussed in section 3.6.

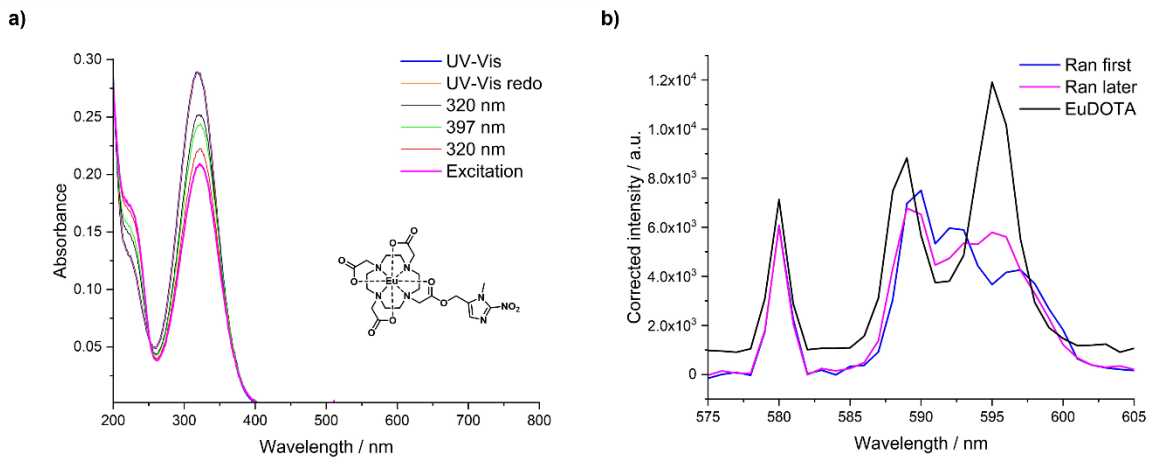

Figure 3.13: a) The UV-Vis spectra of EuNI at 50 µM following different UV-Vis and steady-state emission and excitation measurements (carried out after the measurement labelled, with measurements carried out in order from top to bottom). b) The steady-state emission spectra of EuNI at 50 µM, λ_{ex} 397 nm, zoom on the J=0 and J=1 bands, ran as the first spectra (blue) and ran after several other spectra (pink) in comparison to EuDOTA (black).

3.4.2 Time-gated spectra

Time-gated emission spectra were evaluated to accurately assess any changes in luminescence intensity between the activatable complexes and the DOTA complexes, as time-gated imaging techniques would be employed for imaging of lanthanide probes in biological settings to remove background signal from fluorescent biological molecules and improve the signal-to-noise ratio.

Similar to the steady-state emission spectra, little change in the intensity of the time-gated emission spectra was observed between the europium nitrobenzyl or nitroimidazole and

DOTA complexes, through either ligand excitation (Figure 3.14a-b & d-e) or direct metal excitation (Figure 3.14c & f-g). A twofold increase in emission intensity of the $^5D_4 \rightarrow {}^7F_6$ transition at 488 nm is observed in the time-gated emission spectra, upon excitation at 269 nm, between TbNB and TbDOTA (Figure 3.14d) and a 2.4-fold increase in intensity of the J=6 band (by area) is observed, upon excitation at 320 nm, between TbNI and TbDOTA. A 2.3-fold increase in intensity of the J=6 band is observed between TbNB and TbDOTA upon direct excitation at 366 nm ($^5L_{10} \leftarrow {}^7F_6$, Figure 3.14f) and a 4.9-fold increase in intensity is observed between TbNI and TbDOTA under the same conditions. The change in intensity of the $^5D_4 \rightarrow {}^7F_5$ transition (J=5 band) is reduced to 1.4-fold, for both TbNB and TbNI in comparison to TbDOTA, upon excitation at 488 nm ($^5D_4 \leftarrow {}^7F_6$, Figure 3.14g).

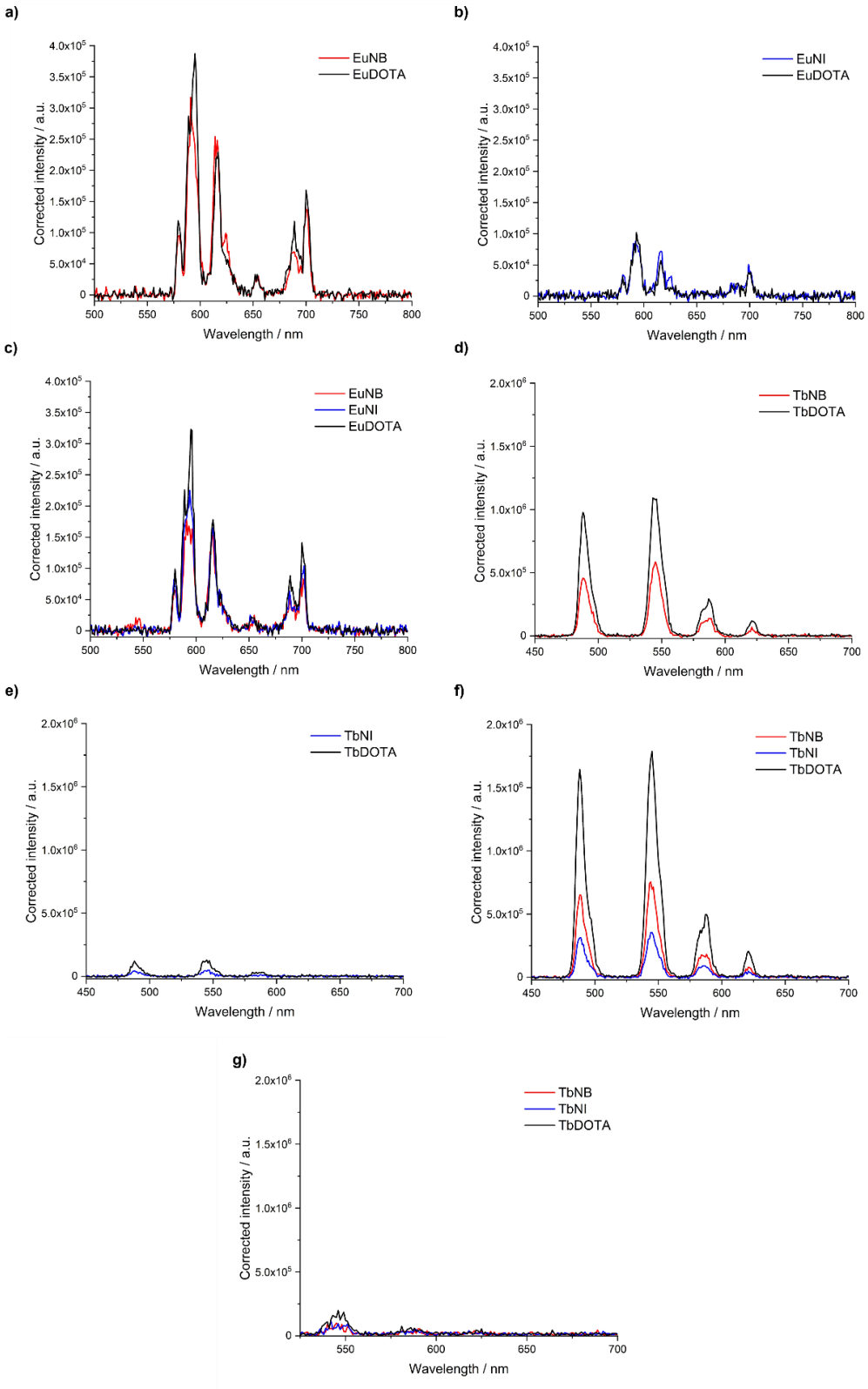

Figure 3.14: Time-gated emission spectra of a) EuNB (red) vs EuDOTA (black) upon ligand excitation (λ_{ex} 269 nm) and b) EuNI (blue) vs EuDOTA upon ligand excitation (λ_{ex} 320 nm), c) EuNB and EuNI vs EuDOTA upon direct metal excitation (λ_{ex} 397 nm), d) TbNB vs TbDOTA upon ligand excitation (λ_{ex} 269 nm) and e) TbNI vs TbDOTA upon ligand excitation (λ_{ex} 320 nm), f) TbNB and TbNI vs TbDOTA upon direct metal excitation (λ_{ex} 366 nm), g) TbNB and TbNI vs TbDOTA upon direct metal excitation (λ_{ex} 488 nm). Slits 29 nm / 4 nm for Eu, 29 nm / 3.5 nm for Tb (320 and 366 nm), 29 nm / 5 nm for Tb (488 nm), flash count 10, S1 channel, 495 nm long pass filter for Eu, 400 nm long pass filter for Tb.

3.4.3 Luminescence lifetime measurements

The luminescence lifetimes of the europium and terbium complexes were measured, upon both metal (Figure 3.15 and Table 3.2, measured at 200 μM for NB, NI and DOTA and at 50 μM for Bn) and ligand excitation (Table 3.3, measured at 50 μM). These were measured in water and deuterium oxide in order to evaluate *q*, the number of water molecules in the inner coordination sphere directly bound to the lanthanide centre, as this affects the relaxivity (of the gadolinium analogues). For all measured complexes, *q* is determined to be 1, suggesting that the ester carbonyl coordinates to the lanthanide metal, as expected. The measured lifetimes upon metal excitation and ligand excitation are generally in agreement with each other, considering experimental error of 10%. The data were fit to monoexponential or biexponential decays based on visual analysis of the fitting and the adjusted R^2 values reported for the fittings (included in figure captions were relevant).

Table 3.2: Direct excitation lifetime data (λ_{ex} 397 nm for Eu, 366 nm for Tb). For EuBn and TbBn, the lifetime given is from three averaged scans. Graphs of the luminescence lifetime measurements of TbNB, TbNI, TbDOTA and TbBn are shown in Figure 3.15. Full data (n=1 to n=3) for the NB, NI and DOTA complexes in the appendix (Table A3.1). All lifetimes are in ms. *Biexponential decay. † from analysis of the long component.

	EuNB		**EuNI**		**EuDOTA**		**EuBn**	
	τ_{H2O}	τ_{D2O}	τ_{H2O}	τ_{D2O}	τ_{H2O}	τ_{D2O}	τ_{H2O}	τ_{D2O}
Average	0.63	2.19	0.61	2.45	0.65	2.33	0.63	2.41
q value	**1.07**		**1.18**		**1.04**		**1.11**	

	TbNB		**TbNI**				**TbDOTA**		**TbBn**	
	τ_{H2O}	τ_{D2O}	τ_{H2O}*		τ_{D2O}*		τ_{H2O}	τ_{D2O}	τ_{H2O}	τ_{D2O}
Average	1.94	3.36	0.21	2.06	0.23	3.65	2.06	3.58	1.99	3.50
q value	**0.79**		**0.76†**				**0.73**		**0.78**	

Table 3.3: Ligand excitation lifetime data (λ_{ex} 269 nm for NB, 320 nm for NI). For EuBn and TbBn, the lifetime given is from three averaged scans. Full data (n=1 to n=3) for the NB and NI complexes in the appendix (Table A3.2). All lifetimes are in ms. *Biexponential decay.

	EuNB		**EuNI**		**EuBn**	
	τ_{H2O}	τ_{D2O}	τ_{H2O}	τ_{D2O}	τ_{H2O}	τ_{D2O}
Average	0.61	2.40	0.60	2.40	0.59	2.09
q value	**1.16**		**1.20**		**1.16**	

	TbNB		**TbNI**			**TbBn**	
	τ_{H2O}	τ_{D2O}	τ_{H2O}*		τ_{D2O}	τ_{H2O}	τ_{D2O}
Average	1.93	3.75	0.23	2.06	3.61	1.76	3.17
q value	**0.96**		**0.74**			**0.96**	

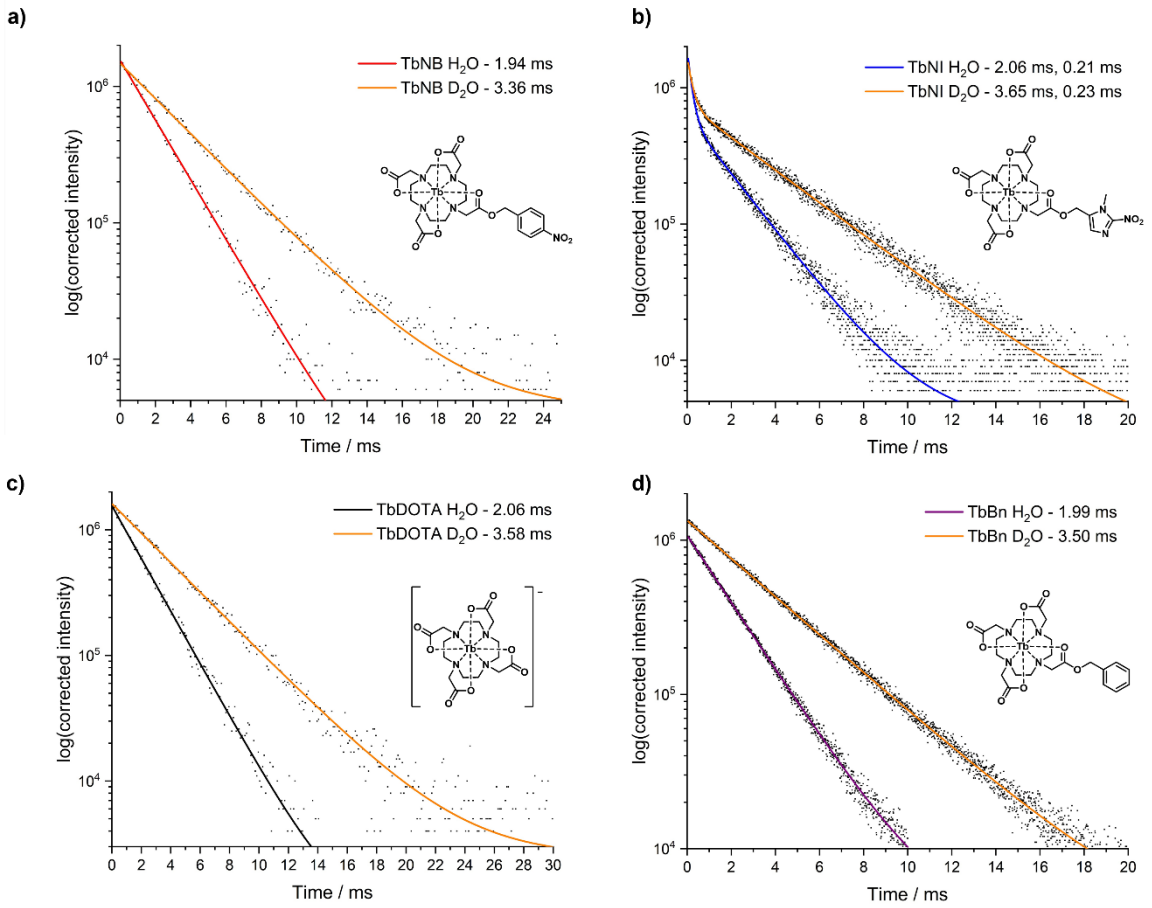

Figure 3.15: Representative graphs for the luminescence lifetime measurements (by direct metal excitation, dots) of a) TbNB, b) TbNI and c) TbDOTA at 200 µM and d) TbBn at 50 µM in H_2O and D_2O, λ_{ex} 366 nm, λ_{em} 545 nm, with the corresponding exponential decay curves (lines). Representative of n=3, sample window 1 ms, initial delay 0.05 ms, time per flash 61 ms, 400 nm long pass filter, delay increments 0.01 ms for NI and Bn, 0.1 ms for NB and DOTA. TbNB: H_2O slits 26-29.4 nm / 14 nm, flash count 12-16, R^2 0.998; TbNB D_2O slits 25-29 nm / 14 nm, flash count 10-14, R^2 0.999; TbNI H_2O slits 29 nm / 8-10 nm, flash count 7-10, R^2 0.997; TbNI D_2O slits 29 nm / 7-9 nm, flash count 5-10, R^2 0.997; TbDOTA H_2O slits 23-28 nm / 9 nm, flash count 4-8, R^2 0.999; TbDOTA D_2O slits 23-26 nm / 9 nm, flash count 4-9, R^2 0.998; TbBn H_2O slits 29 nm / 7 nm, flash count 10, average of 3 scans, R^2 0.999; TbBn D_2O slits 29 nm / 8 nm, flash count 10, average of 3 scans, R^2 0.999.

The lifetimes of TbNI measured in air were found to be biexponential (with adjusted R^2 values for the fitting around 0.997, compared to 0.956 for a monoexponential fit), more noticeably upon metal excitation at 366 nm ($^5L_{10} \leftarrow {}^7F_6$), with one short component ~0.2 ms and one longer component ~2.1 ms (in water). The relative weighting of the short and long components in their contribution to the overall biexponential decay was determined to be between 2:1 and 1:2 depending on the exact conditions used (concentration and excitation wavelength). The longer component was similar to that of the other terbium complexes and which was used to determine q, suggesting that there are multiple deactivation pathways involving non-radiative quenching. To further investigate the nature of the short component,

the lifetimes of $^5D_4 \rightarrow {}^7F_J$ (J=6-3) were investigated upon excitation at 366 nm ($^5L_{10} \leftarrow {}^7F_6$) as this also lies within the absorption band of the nitroimidazole ligand, particularly focusing on the transitions $^5D_4 \rightarrow {}^7F_4$ (586 nm) and $^5D_4 \rightarrow {}^7F_3$ (621 nm) as these are present outside of the region where the ligand is observed the emission in the steady-state (450-550 nm). The lifetimes of the $^5D_4 \rightarrow {}^7F_4$ and $^5D_4 \rightarrow {}^7F_3$ emission bands were found to be the same as for J=6 and J=5 (within error) and maintained the biexponential nature observed previously for the more intense J=6 and J=5 bands, suggesting that the short component of the lifetime is terbium centred rather than ligand centred. In addition, the length of the shorter component, 0.2 ms, is outside of the typical fluorescence lifetime of organic molecules, 0.1-20 ns.[38] Degassing of TbNI (Figure 3.16b-c) caused the luminescence decay spectra to be monoexponential, with lifetimes of ~2.0 ms, suggesting that oxygen impacts quenching of energy transfer. The fact that the longer-lived component is essentially identical in the presence and absence of molecular oxygen suggests that the two lifetimes relate to separate species.

a)

λ_{em} / nm	488	545	586	621
Short component	0.21	0.20	0.21	0.22
Long component	2.09	2.09	2.05	2.11

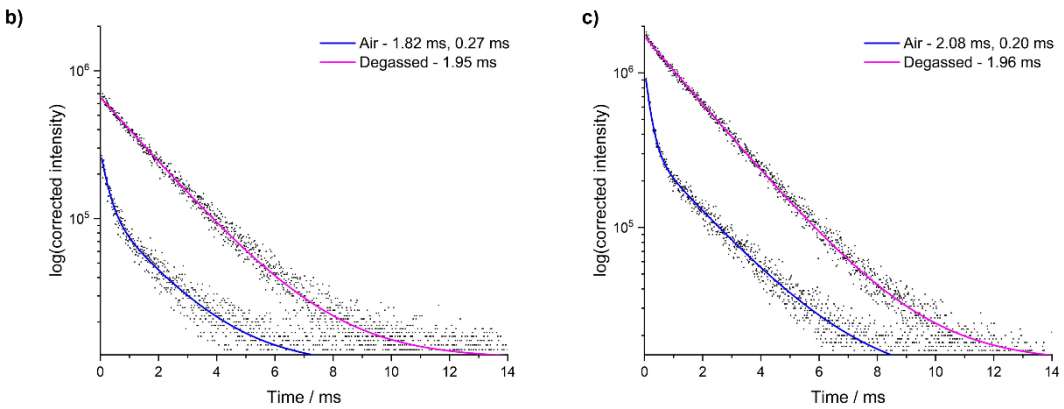

Figure 3.16: a) Lifetime analysis of TbNI at 50 μM, with λ_{ex} 366 nm and the emission wavelength (λ_{em}) as labelled. λ_{em} 488 nm and 586 nm, slits 29 nm / 8 nm; λ_{em} 545 nm, slits 29 nm / 6 nm; λ_{em} 621 nm, slits 29 nm / 12 nm. b and c) Degassed (pink) vs air (blue) lifetime measurements of TbNI upon ligand excitation at 320 nm (panel b, R^2 0.975 for air and 0.995 for degassed), measured at 50 μM, or excitation at 366 nm (panel c, R^2 0.994 for air and 0.997 for air), measured at 200 μM. λ_{em} 545 nm, 50 μM slits 29 nm / 12 nm, 200 μM slits 29 nm / 6 nm or 29 nm / 5 nm.

3.4.4 Quantum yield and energy level measurements

Intrinsic quantum yields (Φ_{Ln}^{Ln}, equation 3.1) of the europium complexes were calculated using the steady-state emission spectra upon excitation at 397 nm ($^5L_6 \leftarrow {}^7F_0$, uncorrected S1 data), comparing the area of the magnetic dipole transition (I_{MD}, J=1 band, $^5D_0 \rightarrow {}^7F_1$, defined here as 583-604 nm) to the total area (I_{total}, 500-800 nm, equation 3.2), and their lifetimes.[37, 39] A range of intrinsic quantum yields is reported (Table 3.4) due to multiple values of $A_{MD,0}$ reported for europium complexes (14.65, 18.45 and 20.46), with 20.46 reported for EuDOTA.[40] The intrinsic quantum yields of the europium complexes are within error of EuDOTA, as expected from the steady-state spectra. Therefore, the rates of non-radiative decay (obtained by rearrangement of equation 3.3) are within error of each other.

$$\Phi_{Ln}^{Ln} = \frac{\tau_{obs}}{\tau_{rad}} \qquad \text{(eqn. 3.1)}$$

$$k_{rad} = \frac{1}{\tau_{rad}} = A_{MD,0} n^3 \left(\frac{I_{total}}{I_{MD}}\right) \qquad \text{(eqn. 3.2)}$$

$$\Phi = \frac{k_{rad}}{k_{rad} + k_{nrad}} \qquad \text{(eqn. 3.3)}$$

Table 3.4: Calculations of the intrinsic quantum yields (Φ_{Ln}^{Ln}) and the rates of non-radiative decay (k_{nrad}) of the europium complexes, using equations 3.1 to 3.3, with n = 1.33 (as measurements were carried out in water). * Data taken from Table 3.2. ** Range reported due to varying reported values for $A_{MD,0}$ (14.65, 18.45 and 20.46).

Complex	I_{total}	I_{MD}	k_{rad} / s^{-1}	τ_{rad} / ms	τ_{obs}* / ms	Φ_{Ln}^{Ln}** / %	k_{nrad} / s^{-1}
EuNB	932209	214193	209	4.77	0.63	9-13	1410 ± 30
EuNI	1461723	264666	266	3.76	0.61	11-16	1410 ± 50
EuDOTA	845799	234773	173	5.77	0.65	8-11	1390 ± 30
EuBn	1450489	300589	232	4.31	0.63	10-15	1380 ± 40

Low temperature (77 K) emission spectra of the gadolinium complexes (Figure 3.17) were measured in order to estimate the energies of the triplet excited states of the complexes to rationalise the poor lanthanide sensitisation observed for NB and NI complexes and the antenna effect observed for the Bn complexes.[41] 50 μM solutions of the complexes in MeOH:EtOH 1:1 were frozen in liquid nitrogen to form a glass, measured upon ligand excitation (λ_{ex} 269 nm for NB, 320 nm for NI and 262 nm for Bn), with assistance from Dr. Matthew F. Allen. The data were fit to Gaussian distributions with multiple peaks, assuming

that the highest energy peak corresponds to the 0-0 transition.[42] The poor spectral resolution of GdNB measured at 77 K (Figure 3.17a) meant we were unable to fit the data reliably. The triplet energy of NI was not interpreted from the spectrum of GdNI (Figure 3.17b) due to the atypical shape and overlapping peaks, making it difficult to interpret.

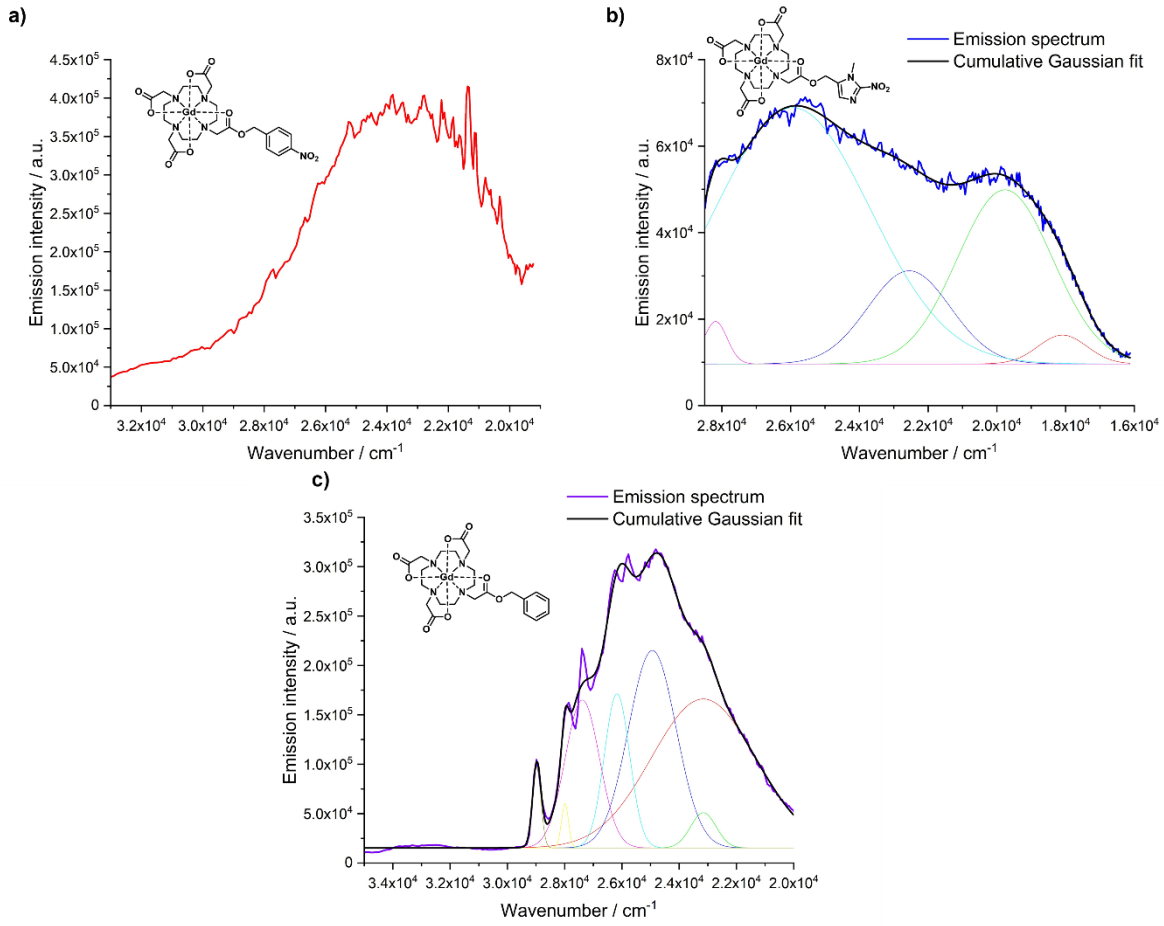

Figure 3.17: The emission spectra of the Gd complexes, a) GdNB (red), b) GdNI (blue) and c) GdNI measured at 77 K in MeOH:EtOH 1:1. The black line is the cumulative Gaussian fit, with other coloured lines the individual peaks that make up the total Gaussian fit. For panel a, λ_{ex} 269 nm, slits 5 nm / 1 nm, average of 3 scans, 0.1 s integration time; panel b, λ_{ex} 320 nm, slits 5 nm / 1 nm, 1 scan; panel c, λ_{ex} 262 nm, slits 5 nm / 1 nm, average of 3 scans, 0.1 s integration time.

From Figure 3.17c of GdBn, the 0-0 transition ($S_0 \rightarrow T_1$ transition) energy of Bn is estimated to be 28972 cm^{-1}. This triplet energy level of GdBn is significantly higher than those of the $^5D_0$ and $^5D_1$ states of europium (around 17300 and 19000 cm^{-1}, respectively)[43] and $^5D_4$ of terbium (20500 cm^{-1}),[44] therefore the energy gap is large enough to reduce the rates of back energy transfer from these lanthanide energy levels (> 1850 cm^{-1}).[42] The estimated triplet energy level of the Bn ligand is close to that of $^5L_9$ of terbium (28400 cm^{-1}),[44] with a

larger gap to $^5L_9$ or $^5L_{10}$ for europium (28244 cm^{-1} and 28813 cm^{-1}, respectively), therefore possible energy transfer processes are summarised in Figure 3.18.[43] However, it is noted that factors other than the ligand triplet energy affect ligand sensitisation and the intensity of lanthanide emission, such as the distance between the ligand triplet state (which could evaluated with computational modelling) and the lanthanide, overlap between the ligand emission spectrum and lanthanide absorption spectra and intramolecular quenching pathways.[42]

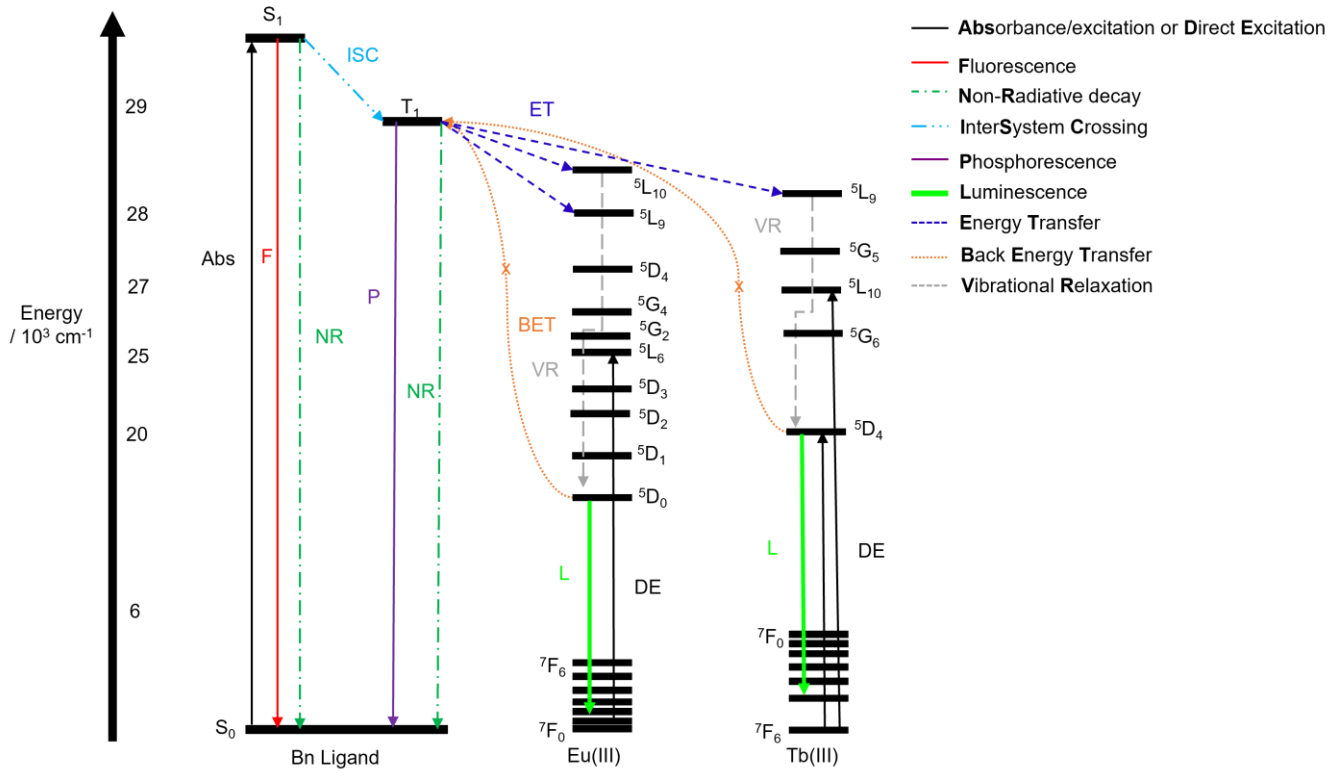

Figure 3.18: Jablonski diagram for the energy transfer pathways for the benzyl complexes. Diagram not to scale, not all europium or terbium energy levels are included. Relevant europium and terbium energy levels are labelled with term symbols, with energy levels taken from the literature.[43, 44]

3.5 Relaxivity measurements for MRI

To determine differences in MRI contrast between the nitrobenzyl and nitroimidazole complexes and the commercial Dotarem® (GdDOTA), T_1 relaxivity was measured in water and PBS (Figure 3.19a). T_1 relaxivity was initially measured in water using a 11.7 T (500 MHz) NMR spectrometer (Figure 3.19b), showing the general trend of relaxivity to be GdDOTA>GdNI>GdNB despite the lack of change in *q* value. This trend was corroborated

by measurements by Dr Lina Hacker on a more clinically relevant Agilent 7 T scanner, with higher relaxivities observed at lower magnetic field (Figure 3.19c). T_1 relaxivity measurements at 7 T in PBS (pH 7.4, Figure 3.19e) displayed the same trend as the water measurements but with a smaller difference between complexes, likely due to the impact of phosphate binding which has been previously observed for similar DO3A complexes.[45] These results show that both GdNB and GdNI could act as turn-on MRI contrast agents, with GdNB displaying a larger difference in relaxivity to the commercially available GdDOTA, especially in more biologically relevant buffered conditions. For further relevance for biological applications, relaxivity could be measured in the future at lower clinically relevant field strengths below 3.0 T, as most commonly 1.5 T or 3.0 T MRI machines are used.

a)

	r_1 / mM^{-1} s^{-1}		
Solvent	H_2O		PBS
Field	7 T	11.7 T	7 T
GdNB	2.55 ± 0.06	2.64 ± 0.03	3.22 ± 0.02
GdNI	3.3 ± 0.2	3.15 ± 0.03	3.75 ± 0.03
GdDOTA	4.0 ± 0.4	3.38 ± 0.02	4.33 ± 0.04

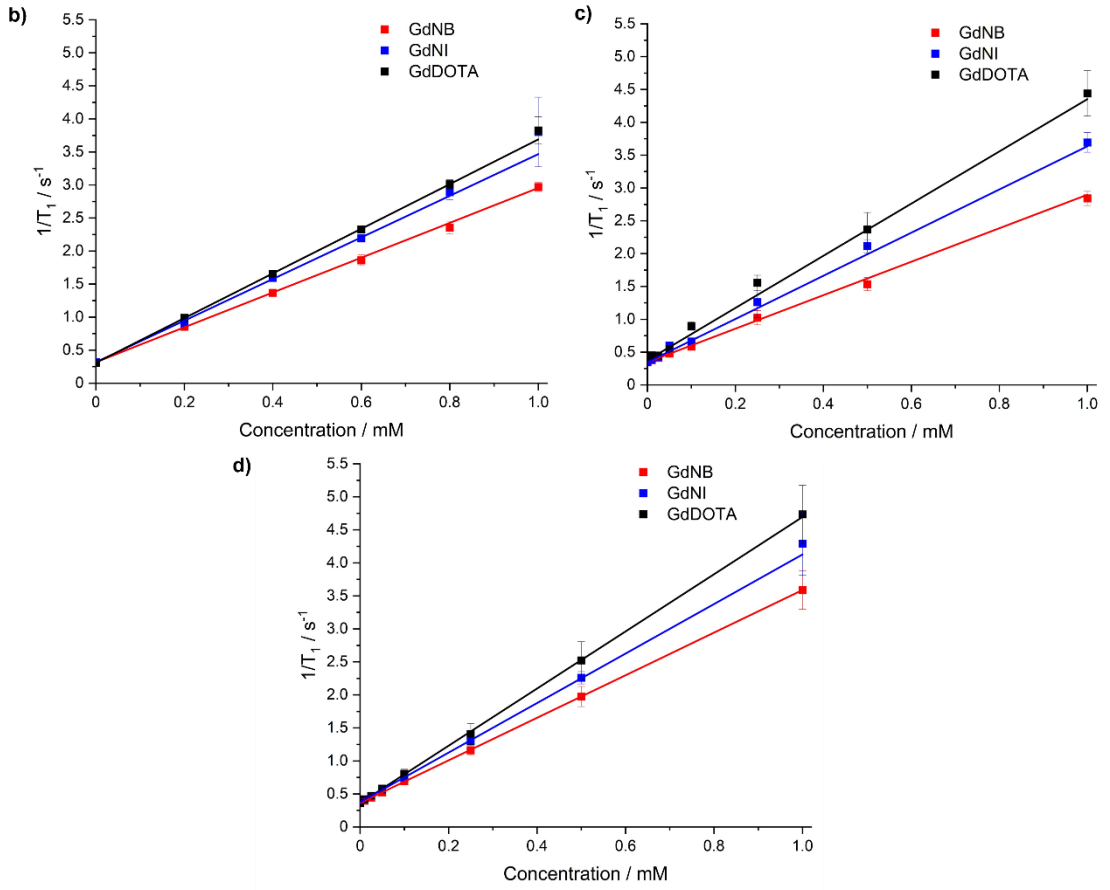

Figure 3.19: a) A table of the calculated relaxivities. b) T_1 relaxivity measured in H_2O at 11.7 T. c) T_1 relaxivity measured by Dr Lina Hacker in H_2O at 7 T. d) T_1 relaxivity measured by Dr Lina Hacker in PBS (pH 7) at 7 T. n=3, the error bars represent the standard deviation of repeats.

3.6 Stability testing of complexes in solution

An evaluation of the nitrobenzyl and nitroimidazole complexes' stability in water and buffered solutions was carried out prior to activation testing. Analysis of the terbium complexes in water by LCMS (Figure 3.20a and b) and of the analogous europium complexes in PBS (pH 7.4) by paramagnetic ^{1}H NMR spectroscopy (Figure 3.20c and d) demonstrated that these complexes are suitably stable at least up to 6 hours, therefore testing was carried out over this timeframe. However, it is noted that some degradation (to the corresponding DOTA complexes) is observed in all cases. The nitroimidazole

complexes are observed to be more susceptible to ester hydrolysis in water than the nitrobenzyl complexes and this rate, for both analogues, is accelerated in PBS.

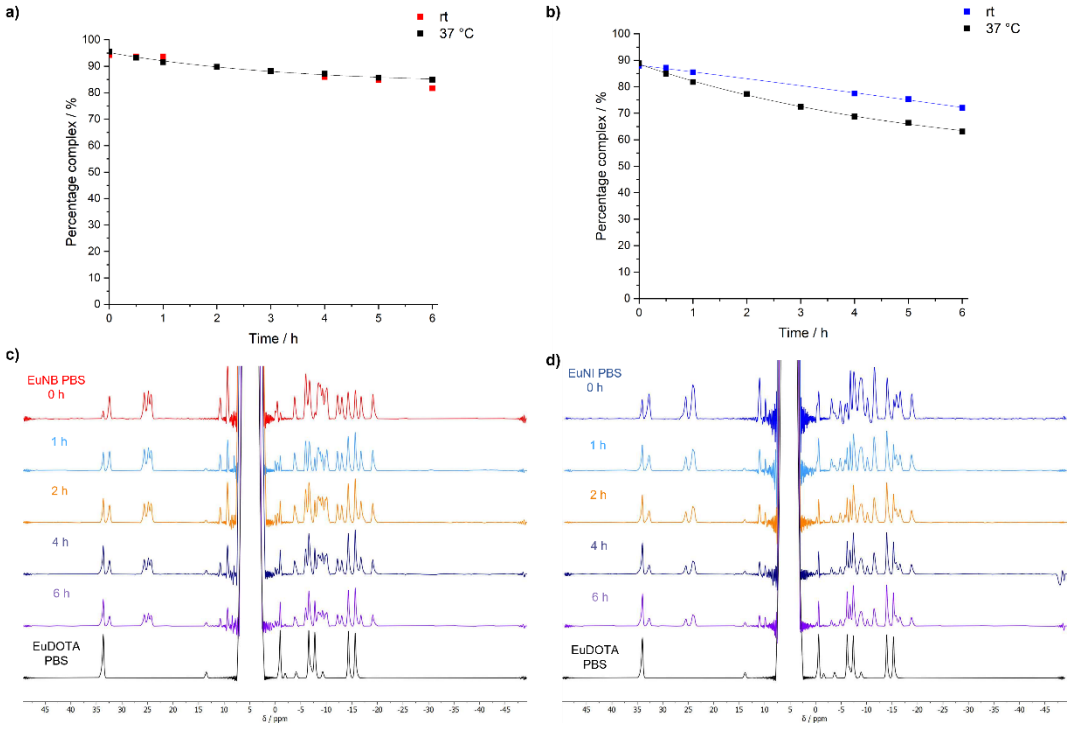

Figure 3.20: Evaluation of the stability of the nitrobenzyl and nitroimidazole complexes in aqueous media. a) TbNB and b) TbNI in water measured by LCMS, percentage purity over time. c) EuNB and d) EuNI in PBS buffer at pH 7.4 (~10 mM complex) measured by ^{1}H NMR spectroscopy over time, in comparison to EuDOTA.

3.7 Activation of lanthanide complexes

3.7.1 Chemical activation

Prior to carrying out chemical activation assays of the lanthanide complexes, cyclic voltammetry data was acquired, by Euan Sarson, to determine the relative thermodynamic favourability of activation. The terbium complexes were measured to avoid complications arising from the presence of the Eu(II)/Eu(III) redox couple. These measurements confirmed that nitroimidazole complexes are more favourably reduced than nitrobenzyl complexes (-236 mV vs SHE for TbNI compared to -356 mV for TbNB, at pH 7.4 – Table A3.3 and Figure A3.5-7), consistent with previous literature.[21] The onset reduction potentials of the terbium complexes can be attributed to the reduction/oxidation of the nitro group, as the benzyl control showed no electrochemical activity, as expected. These onset

potentials are close to that observed in biologically relevant reducing environments, as discussed previously in section 1.2.

The chemical activation of the lanthanide complexes was carried out using zinc powder and ammonium chloride (Figure 3.20a) in D_2O, using adapted literature conditions.[46] The assay was monitored by ^1H NMR spectroscopy to assess the conversion to EuDOTA and production of organic side products simultaneously. Full conversion of EuNB to EuDOTA was observed in under 2 hours under the assay conditions (Figure 3.21b), in comparison to under 1 hour for EuNI (Figure 3.21c). However, minimal conversion to EuDOTA was observed in the D_2O only and NH_4Cl controls for all europium complexes (Figure 3.21c), suggesting that the zinc is causing activation. Substantial conversion to EuDOTA was observed for the activation negative control, EuBn, under assay conditions (90 % after 6 hours, Figure 3.21d), suggesting that activation to give the DOTA complexes is predominantly not occurring by nitro reduction and fragmentation (activation mechanism 1, Scheme 3.1), contrary to the previously reported literature.[20] In addition, analysis of the 0-10 ppm range in the ^1H NMR spectra of the EuNB chemical reduction assay showed production of nitrobenzyl alcohol as the cleaved arm rather than the predicted aminobenzyl alcohol (Figure 3.21e). These results suggest that Lewis acid mediated ester cleavage (activation mechanism 2, Figure 3.21f) occurs in the presence of zinc. The rate of activation is observed to be EuNI>EuNB>EuBn and suggests that the rate of hydrolysis is influenced by the nature of the ester arm, with the experimental trend showing an increased rate of hydrolysis consistent with the increased electron-withdrawing nature of the ester.

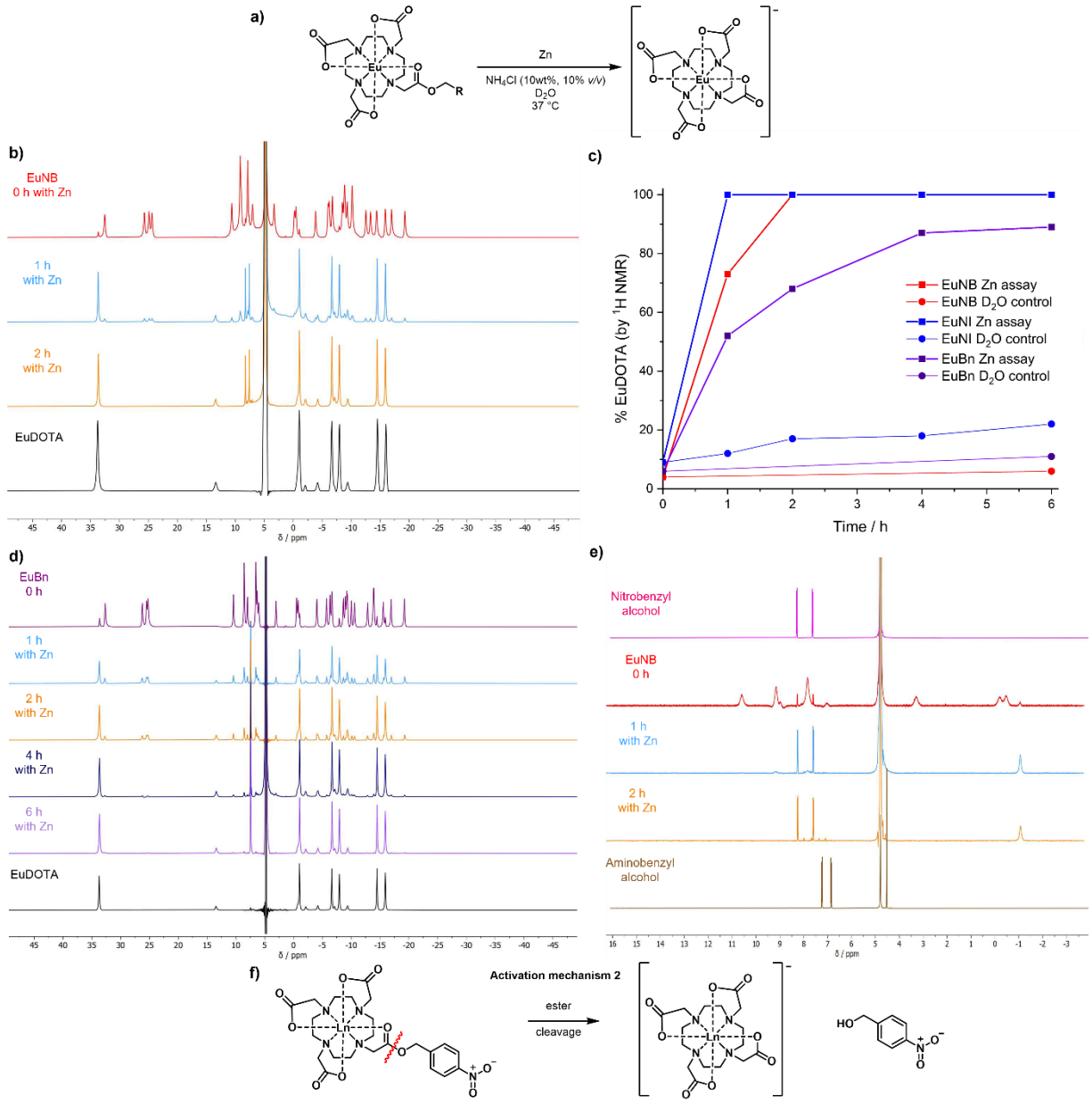

Figure 3.21: Analysis of the zinc assay of the europium complexes, carried out according to panel a. b) The ^{1}H NMR spectra showing the activation of EuNB to EuDOTA under assay conditions. c) The quantitative analysis of the chemical reduction assays, showing the percentage of EuDOTA released for each complex (EuNB red, EuNI blue, EuBn purple) in the full zinc assay (squares) and in the D_2O only control (circles), calculated by comparing the areas of the EuDOTA peak at 33.8 ppm (4H) compared to the corresponding peak of the starting Eu complex (1H). d) The ^{1}H NMR spectra from the chemical activation assay of EuBn. e) The ^{1}H NMR spectra from the chemical activation assay of EuNB, in comparison to nitrobenzyl alcohol and aminobenzyl alcohol. f) Schematic of the proposed ester cleavage/hydrolysis mechanism, activation mechanism 2.

3.7.2 Nitroreductase enzyme activation

Following the conversion to EuDOTA observed in the chemical reduction assay, the mechanism of activation of these complexes was further investigated using relevant enzymes. Nitroreductase from *E. coli* was previously reported to activate GdNB to GdDOTA by Liu *et al.*[20] and similar nitroreductase enzymes are commonly used to evaluate the

efficacy of activation of nitro-containing prodrugs and profluorophores prior to cellular testing. The nitroreductase assay (Figure 3.22a) was carried out using similar conditions to those previously reported, using 32 µg/mL nitroreductase enzyme, 500 µM NADH and 200 µM complex (final analysis concentration 100 µM) in NaCl solution and water. The assay was carried out under normoxic conditions as, despite oxygen-sensitive (type II) nitroreductases being found in *E. coli*,[47] the majority of bacterial nitroreductases are oxygen-insensitive (type I) and Liu *et al.*[20] conducted this assay under normoxia. Analytical HPLC analysis (at 269 nm) of the full assay (Figure 3.22b) showed full loss of the GdNB starting material peak (R_t 8.0 min) after 2 hours and production of nitrobenzyl alcohol (R_t 9.7 min). Quantitative analysis of the NADH only and nitroreductase only controls (Figure 3.22c and d) showed a ~40 % loss of starting material and corresponding ~40 µM release of nitrobenzyl alcohol after 6 hours, suggesting that NADH alone may be able to release DOTA complexes, reducing the selectivity of activation of these complexes. The nitroreductase assay was not carried out with GdNI due to the relative difficult of synthesis of the complex and it was not carried out with GdBn as a control due to limitations in the UV detection of the analytical HPLC instruments causing very low UV absorbance of the complex at 100 µM, which would cause large error in the area analysis of the assay.

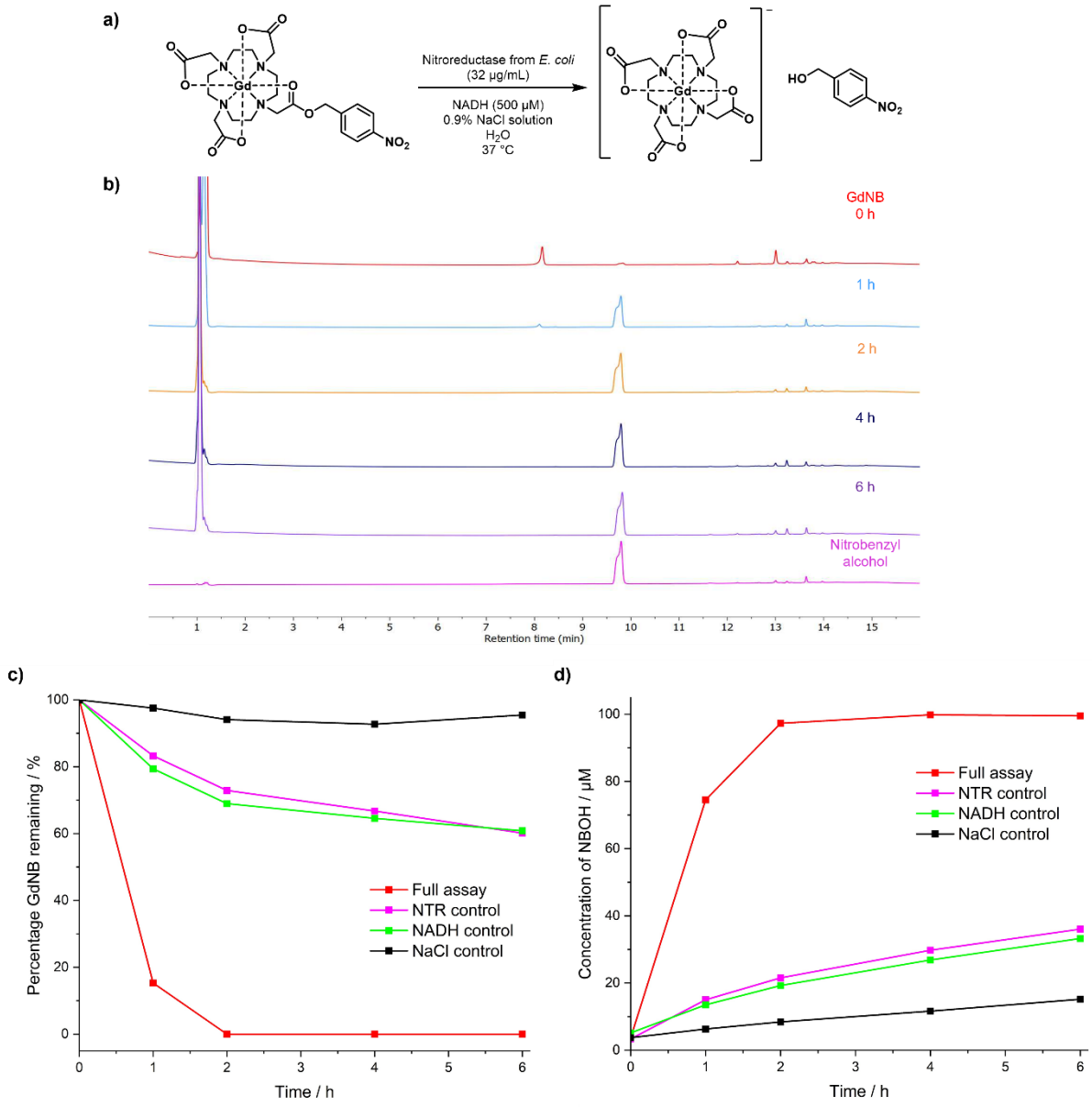

Figure 3.22: The results of the nitroreductase assay of GdNB (scheme in panel a), evaluated at 200 µM (final analysis concentration 100 µM) by analytical HPLC in the presence of nitroreductase enzyme (32 µg/mL), NADH (500 µM), 0.9 % NaCl solution and water, at 37 °C. b) The stacked HPLC traces from the full assay showing the timepoints taken in comparison to the nitrobenzyl alcohol control. c) Quantitative analysis of the percentage GdNB remaining (compared to the area of the t=0 timepoint) for the assay and controls. d) Quantitative analysis of the concentration of nitrobenzyl alcohol (NBOH) released (compared to the area of the nitrobenzyl alcohol control) for the assay and controls. All analysis was performed at 269 nm.

Activation of the nitrobenzyl complexes in the presence of NADH was further investigated by incubating EuNB (10 mM) with NADH (25 mM) in D_2O at 37 °C for analysis by ^1H NMR spectroscopy (Figure 3.23a), to confirm the cleavage of the ester arm to release DOTA complexes, as DOTA complexes cannot be detected by analytical HPLC (when monitoring by UV detection or by fluorescence detection below 10 mM concentration, upon direct metal excitation of terbium). The ^1H NMR spectra in the -50 to 50 ppm range (Figure 3.23b)

showed immediate partial conversion to EuDOTA upon addition of NADH (0 h timepoint) and showed significant conversion after 6 hours, with minimal change after 24 hours. From the ^{1}H NMR spectra in the -3 to 15 ppm range (Figure 3.23c) ran in D_2O only it was unclear which organic side products had formed, therefore the 24 hour sample was further diluted with MeOD to aid solubility. Formation of nitrobenzyl alcohol is tentatively confirmed by formation of a peak around 7.6 ppm (Figure 3.22d) and the lack of formation of aminobenzyl alcohol is evident by the absence of peaks around 6.8 ppm and 7.2 ppm. These enzymatic assays together suggest that both NADH and nitroreductase from *E. coli* may be used to activate the nitrobenzyl complexes to release nitrobenzyl alcohol and DOTA complexes, with differing levels of activation to the aqueous negative control.

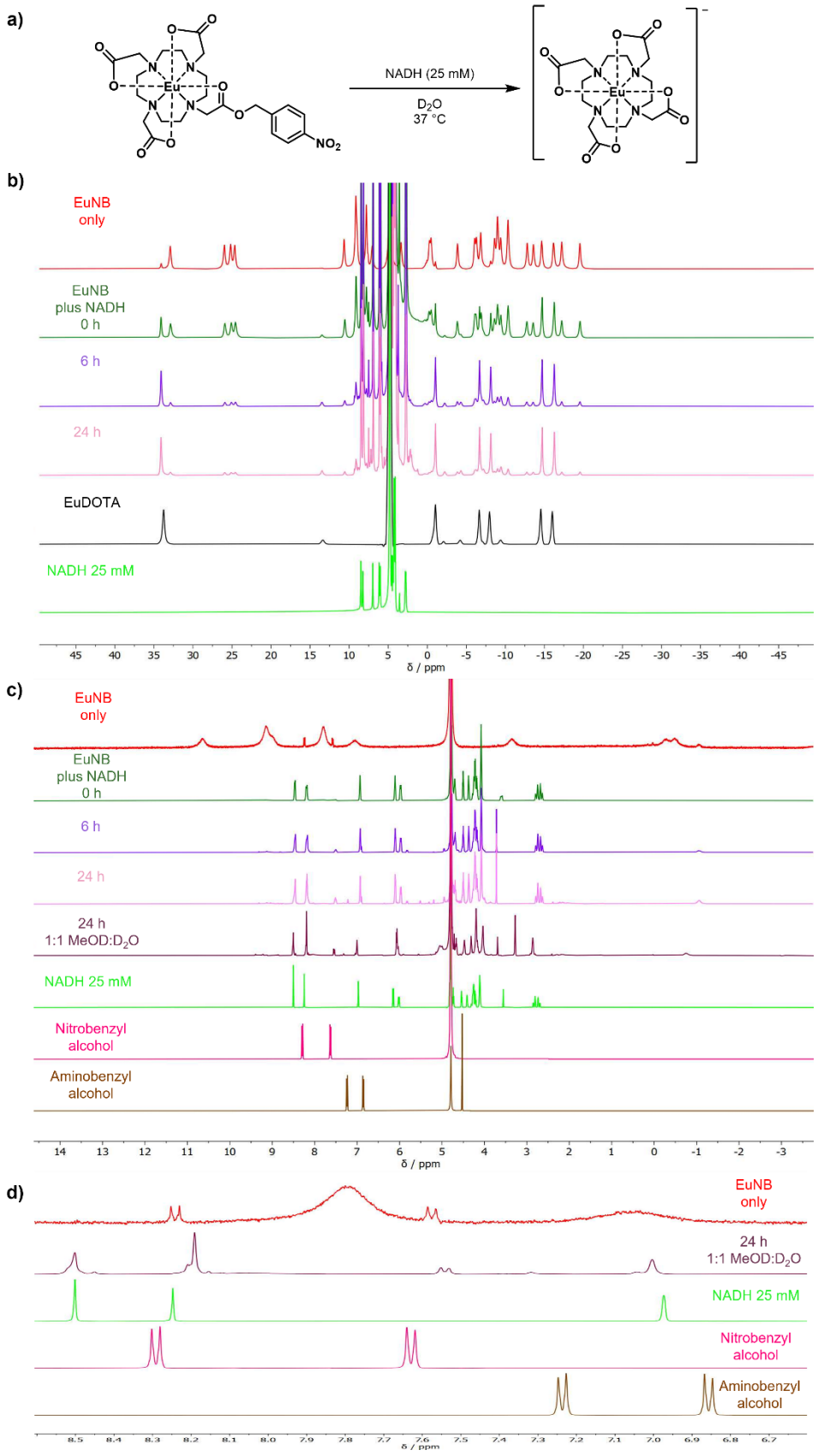

Figure 3.23: The results of the activation of EuNB (10 mM) in the presence of NADH (25 mM) at 37 °C in D_2O (scheme in panel a), analysed by ^1H NMR spectroscopy in the -50 to 50 ppm range (panel b) and ^1H NMR spectroscopy in the -3 to 15 ppm range (panel c, zoom in the range 6.6-8.6 ppm panel d), in comparison to the controls EuDOTA, nitrobenzyl alcohol and aminobenzyl alcohol.

3.7.3 Hydrogenase enzyme activation

To further probe potential mechanisms of activation of these lanthanide complexes, activation of the europium complexes in the presence of a hydrogenase enzyme, adsorbed onto carbon black, were monitored by ^{1}H NMR spectroscopy (Figure 3.24a). Hyd-1 is a nickel-iron hydrogenase from *E. coli* and has been previously reported to convert organic nitroaromatics to their corresponding anilines in the presence of hydrogen in phosphate buffer. The Hyd-1 on carbon system was investigated as an alternative to the nitroreductase enzyme due to its differing mode of activation of nitroaromatics. It is proposed that the hydrogenase enzyme converts hydrogen molecules to protons and electrons, in a buried active site which is inaccessible by large organic molecules, and the electrons are shuttled to the protein surface by iron-sulfur clusters, causing reduction to occur at the carbon surface where the nitro-containing compound is adsorbed.[48] The assay was carried out by Dr Daria Sokolova and Max Robertson, who provided the assay samples for ^{1}H NMR spectroscopy analysis. Under the assay conditions EuNB was fully converted to EuDOTA within 2 hours, with some selectivity over the control under hydrogen in the absence of the enzyme which showed 50 % conversion to DOTA (Figure 3.24b). No selectivity was observed for EuNI, with full conversion to EuDOTA observed in under an hour in the assay and corresponding enzyme-less control. Despite similarities to benzyl deprotection conditions (palladium on carbon under a hydrogen atmosphere), little activation to EuDOTA (6 % after 4 hours) was observed for EuBn in both the assay and control (Figure 3.24c). The ^{1}H NMR spectra from the Hyd-1 assay of EuNB (Figure 3.24d) in to 0 to 10 ppm range shows that after 2 hours, upon full conversion of the europium complex to EuDOTA, mostly nitrobenzyl alcohol is present, in addition to an intermediate species (postulated to be the hydroxylamine).[48] After 4 hours, the nitrobenzyl alcohol produced is converted by the enzyme to the intermediate and aminobenzyl alcohol. This suggests that activation of these europium complexes occurs predominantly *via* the ester cleavage mechanism (activation mechanism 2, Figure 3.21f), whose rate is increased in the presence of the enzyme and under hydrogen, that Hyd-1 selectively activates nitro-containing moieties and that the

production of aminobenzyl alcohol is due to subsequent activation by Hyd-1 following cleavage of the europium complex.

In summary, the nitrobenzyl and nitroimidazole complexes may be activated to give the corresponding DOTA complexes in the presence of zinc, nitroreductase from *E. coli* and Hyd-1 from *E. coli* adsorbed on carbon, with similar rates of activation observed across all assays (with the nitrobenzyl complexes full converted within 2 hours and nitroimidazole complexes converted within 1 hour). Activation of the benzyl control complex to the DOTA complex is observed in the presence of zinc, likely due to Lewis acid mediated ester cleavage, but is not observed in the presence of the Hyd-1 enzyme.

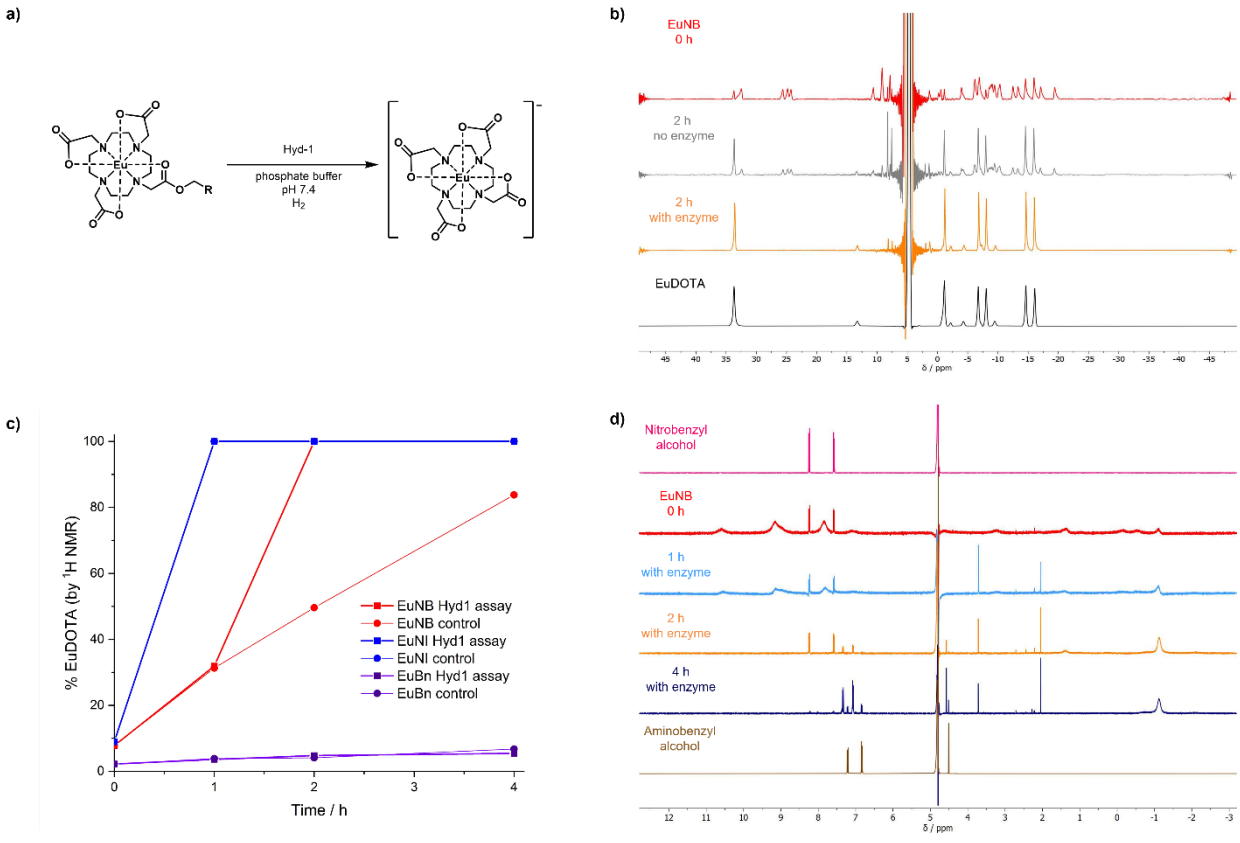

Figure 3.24: The results of activation of the europium complexes in the presence of the Hyd-1 enzyme in phosphate buffer at pH 7.4 under hydrogen (panel a) and the control (absence of enzyme), analysed by ^{1}H NMR spectroscopy (-50 to 50 ppm) and water suppression ^{1}H NMR spectroscopy (-3 to 13 ppm). b) The ^{1}H NMR spectra (-50 to 50 ppm) from the assay of EuNB, comparing the controls (t=0 and EuDOTA) to the 2 h timepoints (with and without the enzyme). c) Quantitative analysis of the assays, evaluating the percentage of EuDOTA released by dividing the area of the EuDOTA peak at 33.8 ppm (4H, therefore divided by 4) by the sum of the area of the EuDOTA peak (divided by 4 for 1H) and the corresponding peak of the starting Eu complex (1H – 32.5 ppm for EuNB, 32.3 ppm for EuNI, 32.7 ppm for EuBn). d) The water suppression ^{1}H NMR spectra (-3 to 13 ppm) for the assay of EuNB, in comparison to the nitrobenzyl alcohol and aminobenzyl alcohol controls.

3.8 Biological testing

Cellular testing was carried out by Dr Lina Hacker and Louise Martin (from the Department of Oncology, University of Oxford) to determine the cytotoxicity of the complexes, cellular permeability and ability to detect the complexes in cells by microscopy for optical imaging purposes. Cytotoxicity data (Figure 3.25a) upon incubation of the terbium complexes with HCT116 cells for 2 hours showed that high concentrations (250 μM) can be tolerated by cells. However, further investigation by LCMS analysis of cell lysate (following incubation of complexes for 2 hours under normoxia and hypoxia) suggested that the complexes are not cell permeable (within the limit of detection of the LCMS UV detector) as the complexes were not detected by LCMS analysis. Fluorescence microscopy of the terbium complexes (250 μM) incubated with HCT116 cells under normoxia (Figure 3.25b) and hypoxia (< 0.1 %, Figure 3.25c) displays only cellular autofluorescence, monitoring emission at 545 nm upon excitation at 488 nm (Tb direct excitation, $^5D_4 \leftarrow {}^7F_6$) and this result was corroborated by flow cytometry, giving further evidence that these complexes are not cell permeable. This lack of cell permeability reduces the efficacy of these complexes as profluorophores or activatable MRI contrast agents for biological imaging, as reductive enzymes are upregulated in cells within hypoxic regions and therefore the chemical probes must enter cells to be activated.

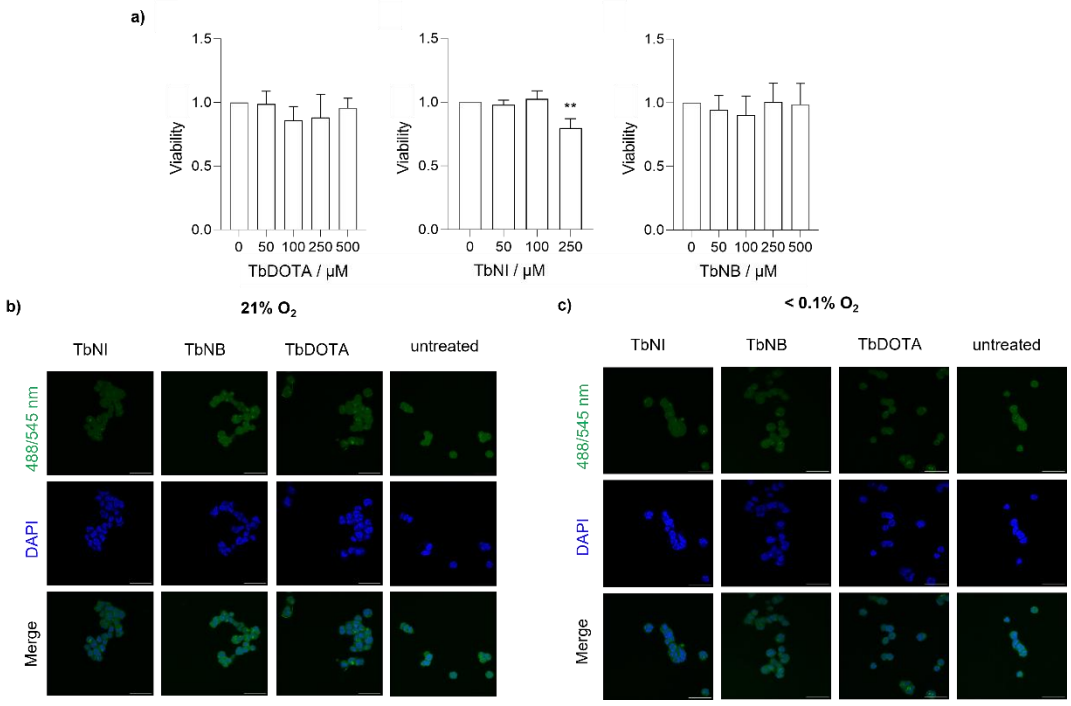

Figure 3.25: Biological testing carried out by Louise Martin and Dr Lina Hacker. a) Cytotoxicity evaluation of the compounds, in HCT116 cells, after exposure of the complex for 2 hours, in comparison to the untreated control. n=3, each repeat carried out in triplicate, ** $p < 0.01$. b and c) Fluorescence microscopy of 250 µM lanthanide complex in HCT116 cells, with panel c after hypoxia exposure for 2 hours, showing only cellular autofluorescence. Scale bar 12 µm.

3.9 Conclusions and future work

Novel europium, terbium and gadolinium complexes, bearing nitrobenzyl, nitroimidazole and benzyl ester arms appended to the known DOTA core, were synthesised and characterised by ^{1}H NMR, UV-Vis and luminescence spectroscopy. The nitrobenzyl and nitroimidazole complexes were investigated as activatable lanthanide complexes for optical imaging (Ln = Eu, Tb) and MRI (Ln = Gd) under a range of reductive conditions. Evaluation of the ^{1}H NMR spectra and steady-state and time-gated emission of the europium complexes highlighted changes in symmetry between the nitrobenzyl, nitroimidazole and benzyl complexes and the parent DOTA complexes. Both the nitrobenzyl and nitroimidazole ligands are poor sensitisers for europium and terbium, whereas the benzyl analogue is a more efficient sensitiser of europium and terbium emission. A turn-on profluorophore effect can be observed, relative to the DOTA positive controls, upon excitation of the terbium complexes at 366 nm ($^{5}L_{10} \leftarrow {}^{7}F_{6}$) and upon ligand excitation, by both steady-state and time-gated emission. Luminescence lifetime measurements suggest that one water

molecule is in the inner coordination sphere bound to the lanthanide centre (q=1) for all complexes and this is consistent with the small change in relaxivities observed between the complexes, with the greatest difference observed between GdNB and GdDOTA measured at 7 T in water (2.55 mM^{-1} s^{-1} vs 4.0 mM^{-1} s^{-1}), giving evidence that this complex could act as a turn-on MRI contrast agent.

Activation of the complexes to the desired EuDOTA is observed in the presence of zinc, nitroreductase enzymes, NADH and hydrogenase enzymes, however this activation was postulated to occur *via* an ester cleavage mechanism rather than the originally proposed nitro reduction and fragmentation mechanism. The activation of the nitrobenzyl complexes is complete within 2 hours in the presence of zinc, nitroreductase enzymes and hydrogenase enzymes and the activation of nitroimidazole complexes is complete within 1 hour in the presence of hydrogenase enzymes, whereas the benzyl control complex is activated more slowly, consistent with the relative electron withdrawing nature of the appended esters. Future work on activatable lanthanide complexes could employ amide or carbamate linkers, instead of esters, to investigate the impact of the linker on the relative rates of the reductive mechanism and the hydrolysis mechanism.

Despite the desirable activation to DOTA and changes in luminescence and relaxivity observed, these monometallic complexes are not sufficiently cell permeable for practical using in biological imaging, according to preliminary LCMS and fluorescence microscopy analysis following incubation in HCT116 cells. For application of reductively activated lanthanide complexes in the clinic, further work in the field is needed to develop highly emissive cell permeable lanthanide complexes, in particular those which respond to the upregulation of enzymes and biological reductants within the cell as markers of disease, for cancer diagnosis and prognosis evaluation.

3.10 References

1. M. Tropiano, O. A. Blackburn, J. A. Tilney, L. R. Hill, M. P. Placidi, R. J. Aarons, D. Sykes, M. W. Jones, A. M. Kenwright, J. S. Snaith, T. J. Sørensen and S. Faulkner, *Chemistry – A European Journal*, 2013, **19**, 16566–16571.
2. A. K. R. Junker, M. Tropiano, S. Faulkner and T. J. Sørensen, *Inorganic Chemistry*, 2016, **55**, 12299–12308.
3. S. E. Bodman, P. Stachelek, U. Rehman, F. Plasser, R. Pal and S. J. Butler, *Chemical Science*, 2025, **16**, 5602–5612.
4. M. Tropiano and S. Faulkner, *Chemical Communications*, 2014, **50**, 4696–4698.
5. F. A. Rojas-Quijano, G. Tircsó, E. Tircsóné Benyó, Z. Baranyai, H. Tran Hoang, F. K. Kálmán, P. K. Gulaka, V. D. Kodibagkar, S. Aime, Z. Kovács and A. D. Sherry, *Chemistry – A European Journal*, 2012, **18**, 9669–9676.
6. M. A. Kaster, M. A. Caldwell, C. M. Roach, M. D. Bailey and T. J. Meade, *Inorganic Chemistry*, 2025, **64**, 14785–14798.
7. E. Pershagen and K. E. Borbas, *Angewandte Chemie International Edition*, 2015, **54**, 1787–1790.
8. J.-H. Tang, H. Li, C. Yuan, G. Parigi, C. Luchinat and T. J. Meade, *Journal of the American Chemical Society*, 2023, **145**, 10045–10050.
9. B. K. McMahon, R. Pal and D. Parker, *Chemical Communications*, 2013, **49**, 5363–5365.
10. M. Giardiello, M. Botta and M. P. Lowe, *Inorganic Chemistry*, 2013, **52**, 14264–14269.
11. D. Parker, J. D. Fradgley and K.-L. Wong, *Chemical Society Reviews*, 2021, **50**, 8193–8213.
12. M. C. Heffern, L. M. Matosziuk and T. J. Meade, *Chemical Reviews*, 2014, **114**, 4496–4539.
13. E. D. D. Calder, A. Skwarska, D. Sneddon, L. K. Folkes, I. N. Mistry, S. J. Conway and E. M. Hammond, *Tetrahedron*, 2020, **76**, 131170.
14. A. Skwarska, E. D. D. Calder, D. Sneddon, H. Bolland, M. L. Odyniec, I. N. Mistry, J. Martin, L. K. Folkes, S. J. Conway and E. M. Hammond, *Cell Chemical Biology*, 2021, **28**, 1258–1270.e1213.
15. P. K. Gulaka, F. Rojas-Quijano, Z. Kovacs, R. P. Mason, A. D. Sherry and V. D. Kodibagkar, *JBIC Journal of Biological Inorganic Chemistry*, 2014, **19**, 271–279.
16. B. Moghadas, V. N. Bharadwaj, J. P. Tobey, Y. Tian, S. E. Stabenfeldt and V. D. Kodibagkar, *Journal of Magnetic Resonance Imaging*, 2022, **55**, 1161–1168.
17. Y. Luo, W. Jin, J. Zang, G. Wang, L. Zhu and H. F. Kung, *Journal of Medicinal Chemistry*, 2025, **68**, 348–360.
18. S. Iwaki, K. Hanaoka, W. Piao, T. Komatsu, T. Ueno, T. Terai and T. Nagano, *Bioorganic & Medicinal Chemistry Letters*, 2012, **22**, 2798–2802.
19. C. A. Foster, D. Sneddon, L. Hacker, E. T. Sarson, M. Robertson, D. Sokolova, L. A. W. Martin, M. F. Allen, A. Khrapichev, K. A. Vincent, E. M. Hammond, S. J. Conway and S. Faulkner, *Inorganic Chemistry*, 2025, DOI: 10.1021/acs.inorgchem.5c00199.
20. Y. Liu, L. Zhang, M. Nazare, Q. Yao and H.-Y. Hu, *Acta Pharmaceutica Sinica B*, 2018, **8**, 401–408.
21. W. A. Denny, *Pharmaceuticals (Basel)*, 2022, **15**.
22. P. G. M. Wuts and T. W. Greene, in *Greene's Protective Groups in Organic Synthesis*, 2006, DOI: https://doi.org/10.1002/9780470053485.ch5, pp. 533–646.
23. L. J. O'Connor, C. Cazares-Körner, J. Saha, C. N. G. Evans, M. R. L. Stratford, E. M. Hammond and S. J. Conway, *Organic Chemistry Frontiers*, 2015, **2**, 1026–1029.
24. M. Main, J. S. Snaith, M. M. Meloni, M. Jauregui, D. Sykes, S. Faulkner and A. M. Kenwright, *Chemical Communications*, 2008, DOI: 10.1039/B810083G, 5212–5214.
25. A. L. D. Wallabregue, H. Bolland, S. Faulkner, E. M. Hammond and S. J. Conway, *Journal of the American Chemical Society*, 2023, DOI: 10.1021/jacs.2c12493.
26. M. Serafini, S. A. Twigger, G. Delfas, M. Mallerman, E. Bailey, E. D. D. Calder, E. M. Hammond and S. J. Conway, unpublished work.
27. T. W. W. Greene, Peter G. M., John Wiley & Sons, Inc., United States of America, 3rd edn., 1999, ch. Protection for the carboxyl group, pp. 406–407.
28. S. C. Burdette and S. J. Lippard, *Inorganic Chemistry*, 2002, **41**, 6816–6823.
29. K.-L. N. A. Finney, A. C. Harnden, N. J. Rogers, P. K. Senanayake, A. M. Blamire, D. O'Hogain and D. Parker, *Chemistry – A European Journal*, 2017, **23**, 7976–7989.
30. H. Azuma, K. Miyasaka, T. Yokotani, T. Tachibana, A. Kojima-Yuasa, I. Matsui-Yuasa and K. Ogino, *Bioorganic & Medicinal Chemistry*, 2006, **14**, 1811–1818.
31. Y. Kaburagi, H. Osajima, K. Shimada, H. Tokuyama and T. Fukuyama, *Tetrahedron Letters*, 2004, **45**, 3817–3821.
32. A. B. Smith, J. B. Sperry and Q. Han, *The Journal of Organic Chemistry*, 2007, **72**, 6891–6900.
33. P. Tagliatesta, D. Giovannetti, A. Leoni, M. G. P. M. S. Neves and J. A. S. Cavaleiro, *Journal of Molecular Catalysis A: Chemical*, 2006, **252**, 96–102.
34. Abu T. Khan, S. Ghosh and Lokman H. Choudhury, *European Journal of Organic Chemistry*, 2004, **2004**, 2198–2204.
35. S. Aime, M. Botta and G. Ermondi, *Inorganic Chemistry*, 1992, **31**, 4291–4299.
36. D. Y. Medina-Velazquez, U. Caldiño, A. Morales-Ramirez, J. Reyes-Miranda, R. E. Lopez, R. Escudero, R. Ruiz-Guerrero and M. F. Morales Perez, *Optical Materials*, 2019, **87**, 3–10.
37. K. Binnemans, *Coordination Chemistry Reviews*, 2015, **295**, 1–45.
38. M. Y. Berezin and S. Achilefu, *Chemical Reviews*, 2010, **110**, 2641–2684.

39. M. W. Mara, D. S. Tatum, A.-M. March, G. Doumy, E. G. Moore and K. N. Raymond, *Journal of the American Chemical Society*, 2019, **141**, 11071–11081.
40. N. Kofod, L. G. Nielsen and T. J. Sørensen, *The Journal of Physical Chemistry A*, 2021, **125**, 8347–8357.
41. V. M. Korshunov, M. A. Kiskin and I. V. Taydakov, *Journal of Luminescence*, 2022, **251**, 119235.
42. M. Latva, H. Takalo, V.-M. Mukkala, C. Matachescu, J. C. Rodríguez-Ubis and J. Kankare, *Journal of Luminescence*, 1997, **75**, 149–169.
43. W. T. Carnall, P. R. Fields and K. Rajnak, *The Journal of Chemical Physics*, 1968, **49**, 4450–4455.
44. W. T. Carnall, P. R. Fields and K. Rajnak, *The Journal of Chemical Physics*, 1968, **49**, 4447–4449.
45. L. R. Tear, M. L. Maguire, M. Tropiano, K. Yao, N. J. Farrer, S. Faulkner and J. E. Schneider, *Dalton Transactions*, 2020, **49**, 2989–2993.
46. L. J. O'Connor, I. N. Mistry, S. L. Collins, L. K. Folkes, G. Brown, S. J. Conway and E. M. Hammond, *ACS Central Science*, 2017, **3**, 20–30.
47. M. D. Roldán, E. Pérez-Reinado, F. Castillo and C. Moreno-Vivián, *FEMS Microbiology Reviews*, 2008, **32**, 474–500.
48. D. Sokolova, T. C. Lurshay, J. S. Rowbotham, G. Stonadge, H. A. Reeve, S. E. Cleary, T. Sudmeier and K. A. Vincent, *Nature Communications*, 2024, **15**, 7297.

4. Chapter IV – Tuning the cellular uptake of redox activated lanthanide complexes

4.1 Introduction

Detection of dynamic processes in real time is crucial for the expansion of current understanding of disease, however this is a challenging field in imaging, particularly *in cellulo*. The detection of upregulation of enzymes or changes in redox state and pH requires cell permeable complexes with high quantum yields (upon excitation of a chromophore at biologically suitable wavelengths) and good stability in biological media. Development of novel lanthanide complexes for biological imaging therefore requires understanding of the factors that affect cell uptake, egress and subcellular localisation and the differing mechanisms of cell uptake.

4.1.1 Cell permeable lanthanide complexes

For the exploration of the factors which may affect cell uptake and localisation multiple studies have been carried out, using over 60 terbium and europium complexes with high quantum yields (Φ ~10% for europium and ~40% for terbium) containing heterocyclic sensitising moieties, most of which were found to be cell permeable. Many factors may affect uptake and localisation, including complex charge, lipophilicity, the nature of the sensitising group and its linker, the number and structure of the ligand donors which bind the lanthanide, the affinity of the complex to proteins, the sensitivity of the complex to quenching, the cytotoxicity of the complex and the stability of the complex in aqueous media.[1-3]

Prior to conducting permeability studies *in cellulo*, three other investigations should be carried out which may affect the results of any permeability studies: cytotoxicity, quenching and protein binding. Primarily, the cytotoxicity of the complex should be assessed over a variety of concentrations to establish the dosing concentration. This may be assessed using

a variety of tests (e.g. by perturbation of esterase activity, evaluation of mitochondrial redox by MTT assay or membrane permeability assessment by the staining of dead cells) and flow cytometry can be used to differentiate between necrotic or apoptotic cell death.[1] Trends in cytotoxicity may also be elucidated – for example, in one study neutral complexes were found to be less cytotoxic than their cationic analogues, and adding pyridine linkers or tert-butyl groups were found to increase cytotoxicity.[3] Luminescence quenching, particularly excited-state quenching in the presence of biological reductants such as ascorbate and urate, and protein binding should be evaluated prior to cellular microscopy. This is due to the fact that some cell permeable complexes were found to be difficult to observe by microscopy due to urate quenching emission and weak binding to serum albumin, as protein binding shields excited-state quenching.[1] Mathieu *et al.*[4] proposed that internalisation of lanthanide complexes may be driven by interaction with endogenous proteins, therefore the extent of protein binding to a lanthanide complex should be investigated to further probe this.

For accurate determination of the cell permeability and localisation of lanthanide complexes, microscopy should be utilised in tandem with other techniques such as ICP-MS (with results normalised to the protein content for comparison between samples). This allows for semi-quantitative measurement of cell permeability *via* detection of the lanthanide, as the emission observed by microscopy cannot be used to quantify the amount of lanthanide complex in cells due to aforementioned luminescence quenching. These quenching effects may arise due to the presence of electron rich endogenous molecules, interactions with proteins, DNA or promotors and inhibitors (often used to determine cell uptake mechanisms), or self-quenching caused by aggregation. Cell uptake and localisation studies are often carried out after incubation times between 5 minutes and 24 hours, with studies of uptake profiles over time suggesting that 4-hour incubation may be optimal for cell uptake and egress.[1, 3]

Understanding of the mechanism of cell uptake of lanthanide complexes is also important for molecular design, as it was previously proposed that the uptake pathway depends on the type of cell and the size, charge and lipophilicity of the compound. If a lanthanide complex is detected by a cell surface receptor then cell uptake may occur by receptor-mediated endocytosis (energy-dependent invagination of the cell membrane) to the endosome and the complex must be able to escape to a target organelle before the endosome progresses to a lysosome with low pH (increasing the rate of degradation).[5] Five main pathways have generally been considered for the uptake of lanthanide complexes, which are passive diffusion and four pathways of pinocytosis (Figure 4.1), which is a category of endocytosis – clathrin-mediated endocytosis, caveolin-mediated endocytosis, clathrin- or caveola-independent endocytosis and macropinocytosis.[4] The differing endocytosis pathways may be investigated by addition of molecules, which may act as either promotors or inhibitors of certain pathways (or general inhibitors or promotors such as low temperature or poly-L-lysine), during cell uptake and microscopy studies. Previously evaluated lanthanide complexes were found to generally enter the cell *via* macropinocytosis, except for at dosing concentrations above their IC_{50} where some passive diffusion may occur - the lack of change in diffusion rates with complexes of varying logP values suggests that passive diffusion does not readily occur for lanthanide complexes.[3] Macropinocytosis involves the formation of large vesicles of irregular shape (macropinosomes) which can leak complexes into the cell before being recycled and does not involve the engagement of receptors.[1, 4]

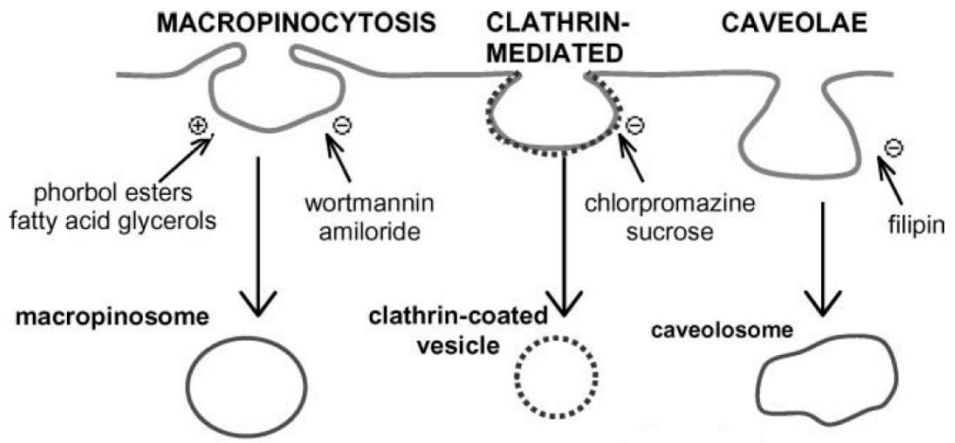

Figure 4.1: Three of the possible types of endocytosis as possible pathways for the cell uptake of lanthanide complexes, with inhibitors and activators of each pathway added. Reproduced with permission from New et al.[2]

The subcellular localisation of lanthanide complexes is also crucial to understand for imaging of certain processes. Studies of a variety of cell permeable complexes, analysed by co-staining with commercial stains for the lysosomes, mitochondria, nucleus and nucleolus, found that lanthanide complexes can be assigned to one of four groups in terms of their localisation (Figure 4.2): localisation to the lysosome only (the largest group and observed at all incubation times); localisation to the mitochondria only (up to 12 hours incubation, with lysosomal localisation and degradation observed after 24 hours); localisation in both the lysosome and mitochondria; and, localisation to protein-rich nucleoli (observed for some complexes at standard dosing concentrations and others only at high dosing concentrations, attributed to enhanced membrane permeability at higher concentrations). Variations in the overall charge, linker length and type and substitution positions between analogues of complexes were observed only to change the subcellular localisation of the probe not the cell uptake pathway. However, Figure 4.2 highlights that cationic or neutral complexes often exhibit good cell uptake.[3]

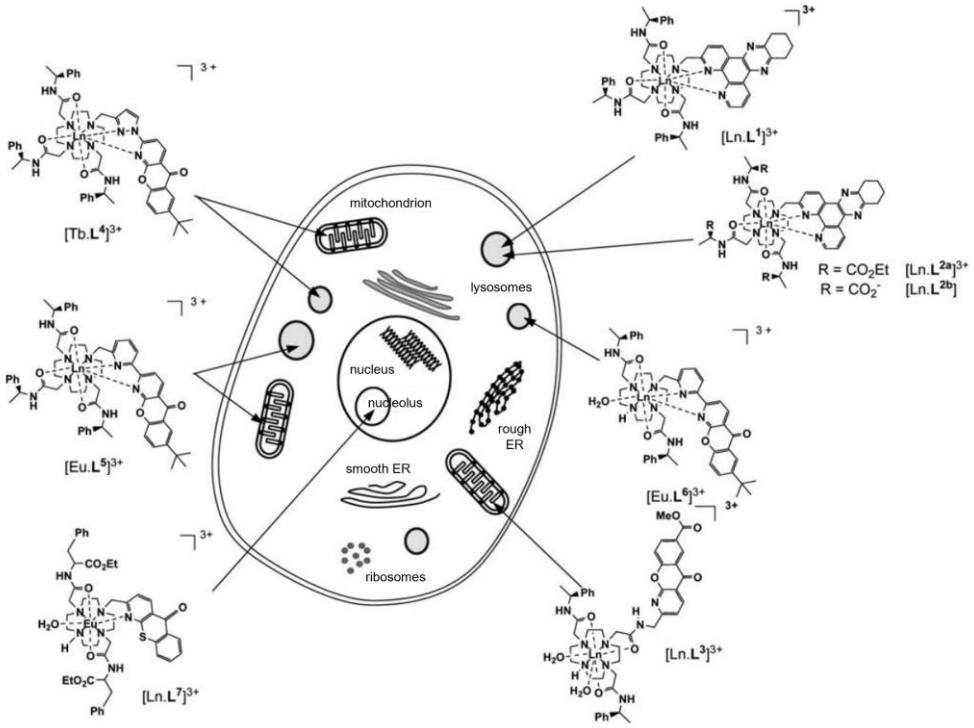

Figure 4.2: A labelled cell with examples of europium and terbium complexes and their localisation profiles – lysosomal only, mitochondrial only, lysosomal and mitochondrial or nucleolar. Adapted with permission from New et al.[3] and Montgomery et al.[1] ER = endoplasmic reticulum.

Studies into how the lanthanide ion, complex charge and counterion for cationic complexes and helicity of a complex affect subcellular localisation found that these factors have little to no effect.[3] To further probe the effect of sensitiser structure on cell uptake and localisation, a systematic study of substitution of the 7-position of a lanthanide complex's sensitising group was carried out (Figure 4.3). The complex attached to human serum albumin (HSA) showed no evidence of cell uptake whilst other analogues showed cell uptake and varying levels of cytotoxicity. The C_{12} amide analogue caused rapid necrotic cell death (IC_{50} 8 μM) and the oligo-guanidinium analogue caused apoptotic cell death (IC_{50} 12 μM) following localisation in the mitochondria. The *tert*-butyl analogue caused membrane destabilisation of HeLa cells after several hours (IC_{50} 58 μM), following localisation in the lysosomes and mitochondria. The methyl ester analogue (IC_{50} 78 μM) and peptide conjugates were generally nontoxic and were rapidly internalised into lysosomes, whereas the hydrophilic carboxylate derivative (IC_{50} 148 μM) was internalised slower. These findings are consistent with the hypothesis that protein binding to the

sensitising chromophore influences cell uptake and localisation.[1, 6, 7] Findings from the study of over 60 cell permeable complexes shows that the main factors affecting subcellular localisation are the nature of the sensitising moiety, the attachment point and length of linker between the sensitiser and the macrocycle and the denticity of the macrocycle used to bind the lanthanide ion (as complexes with a free NH in the macrocycle gave more well-defined localisation profiles than analogues with four identical pendant arms).[3, 8]

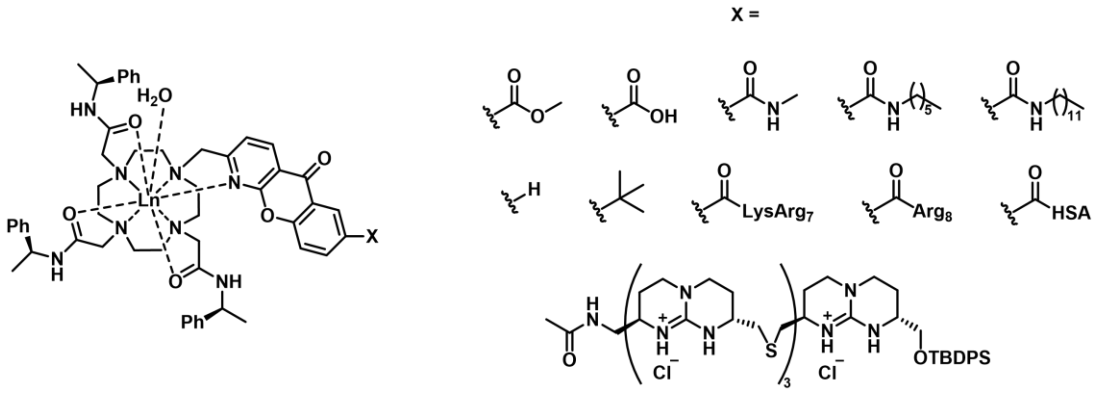

Figure 4.3: The structure of and substituted groups for a series of lanthanide complexes whose cell uptake and localisation were reported by Kielar et al.[6, 7] Lys = lysine, Arg = arginine, HSA = human serum albumin, TBDPS = tert-butyldiphenylsilyl.

Other studies into cell permeable lanthanide complexes have investigated the addition of delocalised lipophilic cations as mitochondrial targeting groups, alkyl groups for balancing uptake against toxicity, cell penetrating peptides (CPPs) and attachment to other targeting groups such as a folic acid targeting group, glucose or galactose to target membrane-bound glucose transporters and steroids to target progesterone receptors for MRI.[9] Alternative strategies to get lanthanide complexes into cells include the use of electroporation, microinjection into cells, incorporation into dendrimers or treatment with high percentages of ethanol or surfactants (such as Triton X) to enhance the permeability of the cell membrane.[2, 4]

4.1.1.1 Amino acid and peptide conjugation for cell targeting

One strategy to aid the cell uptake of lanthanide complexes involves the addition of a targeting group, such as the addition of amino acids or peptides which may be recognised by the cell.[10, 11]

Conjugation to cell penetrating peptides (CPPs) is an emerging strategy for drug delivery, among other uses, due to their high transduction efficiency and generally low cytotoxicity. CPPs consist of between 4 and 40 amino acid residues. They include examples such as polyarginine and oligoguanidinium vectors (as shown at the bottom of Figure 4.3) and are often amphipathic or cationic and interact electrostatically with membrane proteins. Their mechanism of uptake is dependent on the combination of the CPP and cargo used, its local concentration and its interaction with components of the cell membrane, such as lipids and polysaccharides.[4, 12-14] At lower concentrations (10 μM) they are often taken up by endocytosis whereas at higher concentrations uptake by a transduction mechanism is observed.[15] CPPs can be designed to target one localisation, such as mitochondria penetrating peptides, with their logP values suggestive of whether they will target mitochondria (high logP) or cytoplasm and nuclei (low logP).[11] Delivery of the cargo to the cell is improved upon cleavage of the peptide, for example disulfide cleavage by intracellular thiols, however this is balanced with retention time within cells as disulfide-containing compounds are retained longer in cells than those without.[4] Whilst natural CPPs often have low toxicity, peptides can be cytotoxic and their toxicity to organelles must be considered when designing cell permeable conjugates.[4, 14] Highly hydrophobic compounds are toxic to the mitochondria, causing membrane disruption and apoptosis, whereas high concentrations of more hydrophilic compounds can cause toxicity by modification of the membrane potential. These limitations mean that CPP conjugates should be dosed at low concentrations to avoid toxicity issues. Other issues with CPPs include their poor stability *in vivo* (evidenced by their short plasma half-life) caused by the action of proteases; this can be partially overcome by the use of D-amino acids and cyclisation of CPPs. Whilst

CPPs can target subcellular localisations they are not cell specific therefore often needed to be invasively administered directly to target cells or be selectively activated to release their cargo.[4, 12-14]

Amino acid residues or short peptides have previously been employed as a prodrug strategy to aid the cell uptake and water solubility of hydrophobic organic compounds.[16] Conjugation of amino acids to small bioactive molecules is a growing field, with their use applicable for prodrug applications, drug delivery, targeted imaging and the development of bifunctional molecules. This conjugation may allow for specific binding and transport of compounds with improved pharmacological properties such as greater cell permeability, metabolic stability and oral availability.[17] Transport of amino acids and their derivatives across the cell membrane requires the action of transporters and receptors whose action are often dependent on binding affinity, sodium concentration and pH. L-type amino acid transporter 1 (LAT1) is one transporter which transports large neutral amino acids, such as L-leucine, L-tryptophan and L-phenylalanine, from the extracellular matrix into cells, in exchange for the efflux of glutamine and other essential amino acids.[18-20] LAT1 carries out transport independent of sodium concentration and pH.[19] It is an emerging drug target for targeting the central nervous system, due to its expression at the blood-brain barrier, or selective cancer treatment, as it has been shown to be overexpressed in many cancers and is not detected in most non-cancerous tissues.[18, 20, 21] However, one limitation of targeting LAT1 for cancer treatment is that LAT expression does not increase linearly with increased tumour stages, therefore it cannot be used for prognosis evaluation.[20]

In addition to the targeting of LAT1, compounds which are activated in the presence of protease enzymes which cleave certain amino acids are being investigated, such as NIR fluorescent probes which are activated in the presence of aminopeptidase N (APN) and leucine aminopeptidase (LAP). Both APN and LAP are highly expressed in tumours, such as breast cancer and hepatocellular carcinoma. Increased levels of LAP present in serum is associated with liver disease or cancer and APN is a biomarker for cancer diagnosis and

treatment, due to its crucial role in tumour growth, therefore detection of proteases is useful for diagnosis and prognosis evaluation. APN cleaves alanine residues at the N-terminal site whereas LAP hydrolyses leucine residues, however leucine can react in the presence of both enzymes – these selectivity issues can be overcome by replacing leucine moieties with a *tert*-butyl alanine group.[22-24] Wang *et al.*[25] reported the synthesis and validation of a LAP-activated theranostic compound containing the fluorescent anticancer drug camptothecin attached to leucine (Figure 4.4a). The compound showed good stability between pH 5 and 9, good cell membrane permeability (visible by microscopy in HeLa cells after 30-minute incubation with 10 μM compound) and increased fluorescence emission and cytotoxicity in A549 cells compared to HEK 293 cells (normal cells). The anticancer drug was initially released in the cytoplasm, however after 1 hour localisation in the nucleoli were observed.

Similar strategies have also been employed previously by attaching leucine moieties or other amino acids to lanthanide complexes. Laine *et al*.[24] reported two gadolinium complexes containing peptides which are known to be activated by caspase and urokinase (two enzymes linked to cell death, cancer invasion and metastasis) for detection by MRI and PARACEST (Figure 4.4b). Despite the relatively high relaxivities reported (around 4-5 mM^{-1} s^{-1}), no change was observed upon incubation of the complexes with their corresponding enzymes. This is thought to be due to the coordination of the peptide side chains to the lanthanide metal centre, evidence by hydration numbers of zero.

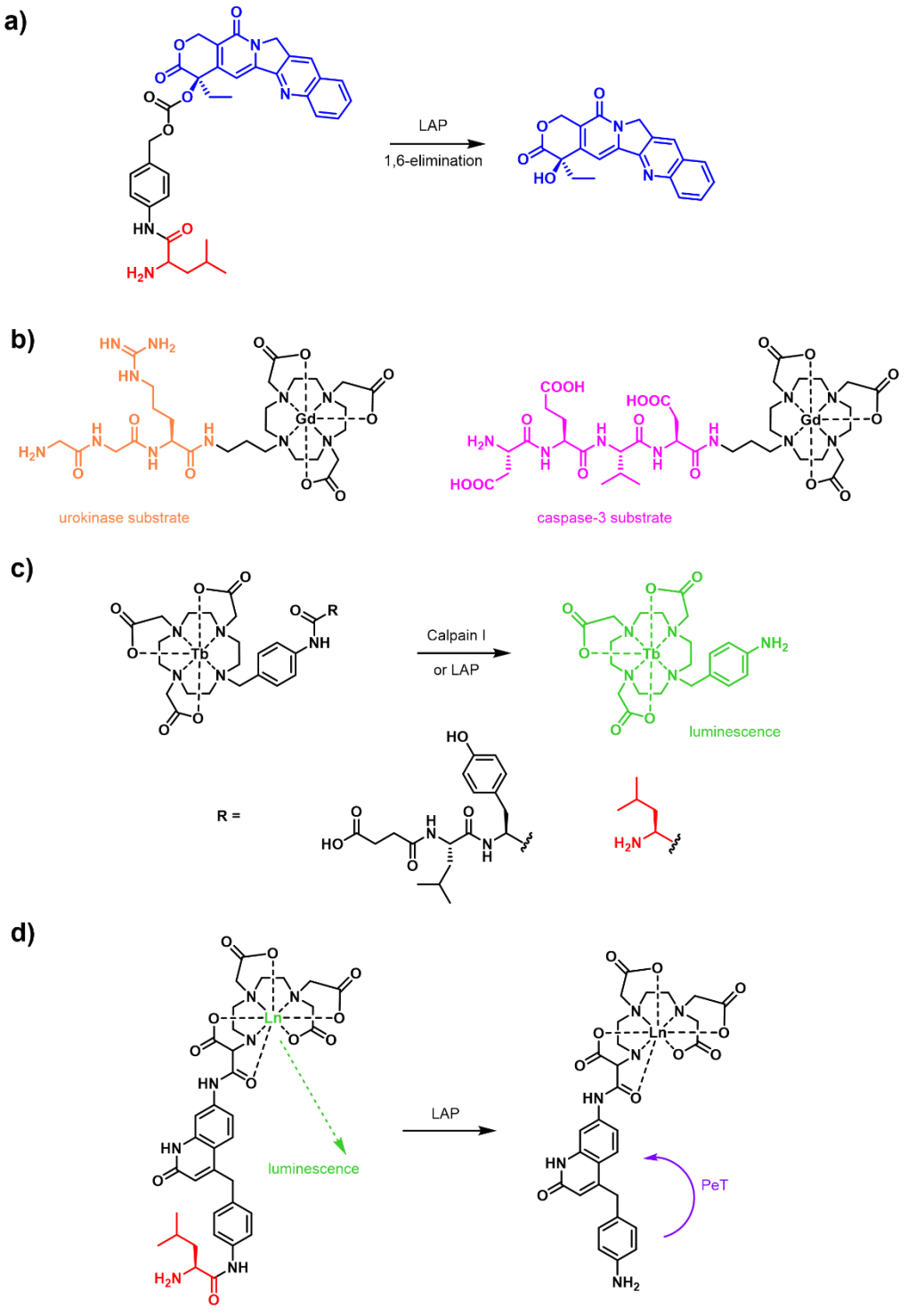

Figure 4.4: Literature examples of activatable compounds containing the amino acid leucine (red) or short peptide sequences. a) The leucine prodrug of anticancer drug and fluorophore camptothecin, activated in the presence of leucine aminopeptidase (LAP).[25] b) The gadolinium complexes with peptidic side chains described by Laine et al.[24] which have high relaxivities and are not activated in the presence of urokinase or caspase-3. c) The terbium complexes reported by Mizukami et al. [26] to be activated to the corresponding aniline in the presence of calpain I or LAP. d) Complexes reported by Terai et al.[22] whose luminescence are quenched in the presence of leucine aminopeptidase due to photoinduced electron transfer (PeT). Ln = Eu, Tb.

Mizukami *et al*.[26] reported two terbium complexes whose luminescence emission intensity increases in the presence of calpain I or LAP (Figure 4.4c), with time-gated imaging used to remove fluorescence from the antenna chromophore and the enzymes. Terai *et al.*[22] reported a complex whose luminescence is decreased in the presence of LAP by causing PeT to occur from the resulting aniline species (Figure 4.4d). This change in luminescence was detectable using nanomolar concentrations of the lanthanide probe and micromolar units of LAP in microplate assay format and was successfully employed to distinguish the amount of LAP in serums from healthy patients and cancer patients.

4.1.1.2 Modifying hydrophobicity

An alternative strategy for modifying cell permeability may be the modification of the overall hydrophobicity of the complex, as lanthanide complexes are typically polar and a balance between lipophilicity and solubility is needed. Small changes in hydrophobicity can change cell permeability and the mechanism of cell uptake of compounds. The conjugation of compounds to alkyl chains, PEG chains, triphenylphosphonium cationic groups or other lipophilic organic moieties has been extensively investigated, with only the former briefly reviewed here. Appending hydrophobic moieties to compounds decreases their water solubility leading to these complexes being initially dissolved in organic solvents prior to cell testing, such as ethanol or DMSO which are known to increase membrane permeability.[27]

Yao et al.[28] reported a series of fluorescent molecular rotor dyes with two alkyl chains C_2 to C_8, C_{10} or C_{12} carbons in length and discussed the effect of alkyl chain length on permeability, with the short alkyl chains (C_2) rapidly entering the cell, compared to no permeability observed for long alkyl chains (C_8 to C_{10}) or anchoring in the cell membrane observed for medium alkyl chains (C_3 to C_6). Increasing carbon chain length within the medium alkyl chain lengths correlated to longer staining of the cell membrane and poorer membrane permeability, with 33% of the fluorophore containing two C_4 chains observed inside the cell after 3 hours. Similar trends have been observed with the attachment of alkyl chains to transition metal complexes: Fernandez-Moreira et al.[29] reported good uptake of

rhenium complexes containing C_7 to C_{17} alkyl chains in MCF7 cells and an increase in toxicity observed with longer alkyl chains, with localisation observed in cell membranes as opposed to in the cytoplasm for shorter alkyl chains; Svensson et al.[30] reported iridium complexes containing two alkyl chains, where the complexes containing C_2 chains localised in the nucleus whereas those containing C_6 chains localised in the cell membrane; Caporale et al.[31] reported iridium complexes containing C_6-C_{16} complexes which exhibited low cytotoxicities and localised in the endoplasmic reticulum.

The effect of addition of alkyl chains or linkers has also been briefly studied for gadolinium complexes. Kielar *et al.*[32] reported the high relaxivity of gadolinium complexes (up to 40.0 mM^{-1} s^{-1}) appended with either one or two C_{12} chains due to their self-assembly or upon incorporation into liposomes. Hall *et al.*[33] demonstrated that gadolinium-phosphonium complexes with alkyl chain linkers (C_3-C_6) showed better cell uptake than their p-xylyl analogues and that the DOTA derivatives displaced reduced tumour cell selectivity compared to the DO3A analogues. Zheng *et al.*[34] reported gadolinium complexes based on the DTPA ligand with two alkyl chains (C_4, C_{10} or C_{12}) for MRI applications. T_1-weighted MR images showed that the C_4 analogue is not taken up by HeLa cells whereas the C_{10} and C_{12} showed increased image intensity. Quantification of uptake (in human T-lymphocyte Jurkat cells) using the terbium analogues, by measuring emission before addition of cells then complex incubation and an emission measurement following the removal of cells to analyse the amount of terbium remaining in the supernatant, showed that over 10% of the C_{10} or C_{12} derivatives were inside or attached to the cell. Subsequent investigation using diffusion enhanced FRET suggested that uptake occurs by interaction of the alkyl chain with the cell membrane and insertion into the outer leaflet with the terbium remaining in the extracellular medium. Overall, previous findings of compounds appended with alkyl chains suggests that addition of short to medium length chains ($C_{2\text{-}6}$) may enhance cell permeability whereas the attachment of longer chains ($C_{10\text{-}12}$) may cause compounds to get stuck in the cell membrane.

4.1.2 Multimetallic lanthanide complexes

Various multimetallic lanthanide complexes (containing either the same or different lanthanide ions), or mixed lanthanide and d-block complexes, have been previously reported for their luminescence[35-39] and their abilities to respond to stimuli (such as changes in pH or interaction with biologically relevant molecules).[40-43] Despite their often more difficult synthesis (particularly for heterometallic complexes),[44, 45] multimetallic lanthanide complexes often have the advantage of brighter luminescence in comparison to their monometallic analogues, either due to energy transfer pathways or simply the presence of two lanthanide metals.

Simms *et al.*[42] recently reported a series of activatable homobimetallic lanthanide complexes (Figure 4.5), employing europium and terbium for luminescence and gadolinium for relaxivity measurements. They show that nitro, azide and azobenzene moieties may be activated under reducing conditions to give the corresponding aniline, causing an increase in luminescence and change in relaxivity, highlighting the differing speed and modes of activation. EuEuN_3 was shown to be fully converted to EuEuNH_2 by NaHS within 2 hours and EuEuNO_2 is fully converted to EuEuNH_2 in the presence of zinc within 18 hours, whereas the conversion of EuEuAzo under similar conditions took 48 hours. Activation of TbTbAzo **53** to the corresponding aniline TbTbNH_2 **54** was also observed in the presence of the hydrogenase enzyme Hyd-1/C, within 24 hours.[42, 46] Despite their results suggesting that these complexes may act as effective profluorophores, with TbTbNH_2 **54** displaying an impressive quantum yield of 45% (upon excitation at 310 nm), cell uptake of these complexes was not observed in HCT116 cells and is proposed to be due to their polarity.

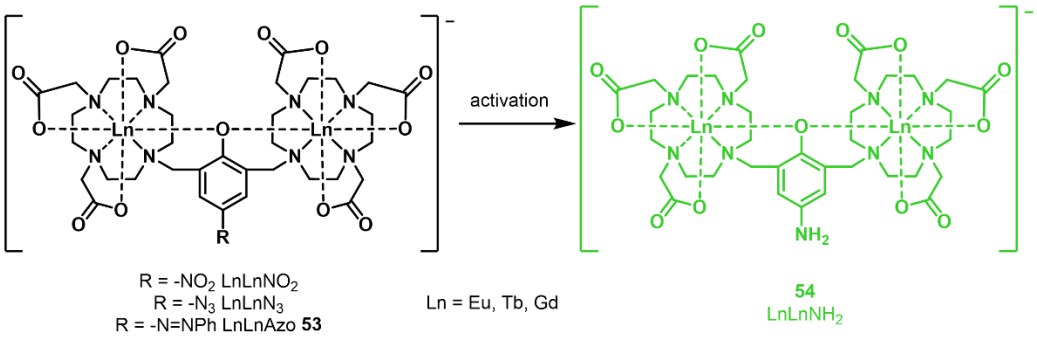

Figure 4.5: The activatable lanthanide complexes reported by Simms et al.,[42] (with the $EuEuNO_2$ complex previously reported by Blackburn et al.[40]) whose work is expanded on in this chapter.

4.1.3 Azobenzenes as activatable moieties

Azobenzene moieties have been widely studied in recent years for their use as photoswitches,[47-53] cleavable linkers[48, 54-56] and as redox activatable groups for use in biological imaging.[42, 48, 56-58] Their use in a variety of chemical fields, from nanomaterials to PROTACs, has been extensively reviewed elsewhere,[48, 49, 59] therefore only a few relevant examples are discussed here. Azobenzenes are sensitive to activation (switching and/or reduction) under thermal, chemical, photochemical or biological conditions.[54] Photoswitching of the N=N bond between *E* and *Z* isomers occurs typically in the presence of UV or visible light and upon heating (Figure 4.6a), causing a change in polarity and extension or contraction of the molecule, however the range of activation wavelengths can be extended based on structural modifications and gamma irradiation (2-20 Gy) may also be employed.[47, 48, 53] Azobenzene profluorophores are typically nonfluorescent as photoexcitation promotes fast conformational change around the N=N bond, therefore conjugation to a fluorophore quenches fluorophore emission, and often the spectral overlap between the photoswitch and fluorophore is high, so activation of the photoswitch and fluorophore does not occur orthogonally.[51, 58] Reduction of azobenzene moieties have previously been exemplified in the presence of sodium dithionite or zinc (as chemical reductants),[42, 56] rat liver microsomes containing several reductases,[57, 58] or azoreductases,[54, 56] which are produced in the colon, therefore azobenzene-containing prodrugs may be used to target colorectal cancer and inflammatory bowel disease.

Zhang *et al.*[57] reported a reversible azobenzene-containing fluorescent probe which was sensitive to cycles of hypoxia and normoxia. Fluorescence (upon excitation at 705 nm) from the mitochondria of MCF-7 cells was observed selectively under hypoxia, due to the unusual partial reduction of the azobenzene to the phenylhydrazine (Figure 4.6b) by stabilisation from the electron withdrawing trifluoromethyl groups. Zhao *et al.*[56] employed similar concepts to design a theranostic probe which incorporated a NIR fluorophore and an anticancer drug linked by an azobenzene group and demonstrated that the azobenzene may be fully reduced and cleaved to release the active fluorophore and drug (Figure 4.6c).

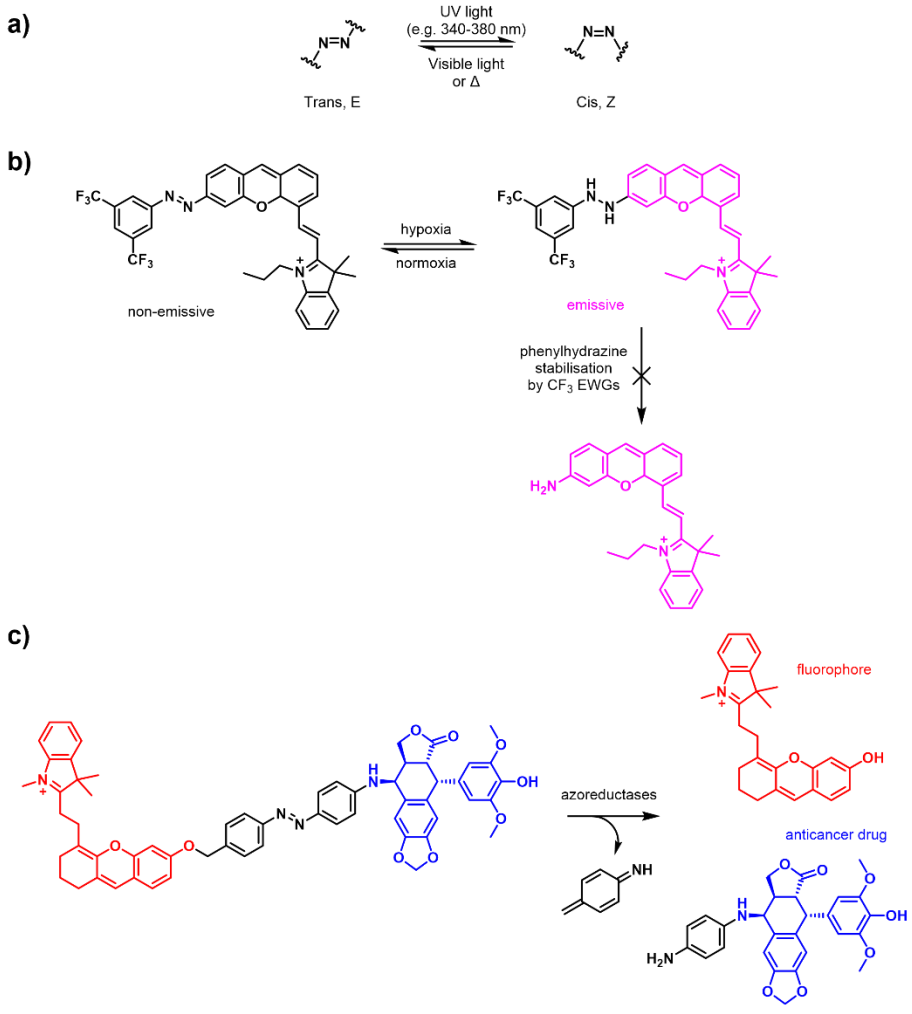

Figure 4.6: a) The properties of azobenzene moieties and possible photoswitching conditions.[47, 54] b) An example of the partial reduction of the azobenzene moiety to cause an increase in fluorescence and give a reversible hypoxia probe.[57] c) An example of a reductively cleavable azobenzene linker for delivery of a fluorophore and anticancer drug.[56]

There are few examples of azobenzene-containing lanthanide complexes in the literature, with most showing that azobenzenes act as effective quenchers of lanthanide luminescence. Simms *et al.*[51] demonstrated in their system which contained an azobenzene photoswitch and visible or NIR emitting lanthanides (Figure 4.7a) that photoswitching (excitation at 530 nm or 405 nm) does not cause lanthanide emission as no energy transfer occurs between the azobenzene and the lanthanide centre. Direct excitation of europium (393 nm, $^5L_6 \leftarrow {}^4F_0$) caused a change in the *E/Z* composition whereas excitation of neodymium at longer wavelengths (580 nm, $^4G_{5/2} \leftarrow {}^4I_{9/2}$) caused no change in the ratio of *E/Z* isomers.

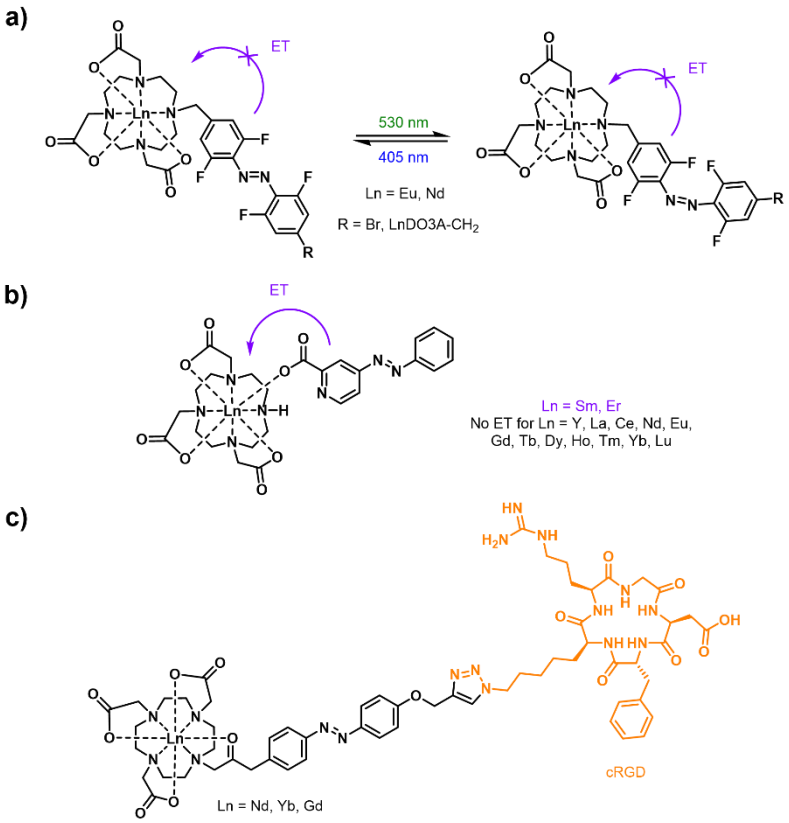

Figure 4.7: Literature examples of azobenzene-containing lanthanide complexes. a) Lanthanide complexes reported by Simms et al.[51] whose photoswitching does not cause lanthanide luminescence. b) Wilharm et al.[60] reported energy transfer between the picolinate azobenzene group and the lanthanide centre only for samarium and erbium analogues. c) Azobenzene lanthanide complexes containing a cyclic arginine-glycine-aspartyl (cRGD) group for tumour targeting.[52]

Wilharm *et al.*[60] recently reported that, in a system containing a picolinate azobenzene arm binding to DO3A complexes (Figure 4.7b), energy transfer between the azobenzene and lanthanide centre occurs only for samarium and erbium, due to the smaller changes in

absorbance observed at the photostationary state (PSS) upon irradiation at 355 nm. Cieslikiewicz-Bouet *et al.*[52] reported a series of lanthanide complexes (Nd/Yb/Gd, Figure 4.7c) containing an azobenzene sensitiser and linker attached to a Arg-Gly-Asp cyclopeptide (cRGD), which displayed characteristic neodymium and ytterbium emission upon antenna excitation at 450 nm, however no comment on their cell permeability was reported despite the attachment of a group for tumour targeting.

4.2 Aims

This chapter aims to explore the synthesis and photophysics of lanthanide complexes with added moieties to attempt to aid cellular uptake. This expands on the work of Dr Charlie Simms on the TbTbAzo complex (**53**, Figure 4.5),[42] as this complex was found to not be cell permeable based on fluorescence microscopy in HCT116 cells. Only the terbium homo-bimetallic complexes were synthesised in this chapter due to the compatibility of the wavelengths of excitation and emission (488 nm and 545 nm) with standard fluorescence microscopy setups to assess cell permeability and the high photoluminescence quantum yield of the reduction product TbTbNH$_2$ **54**.

The target complexes, shown in Figure 4.8a, are bimetallic complexes and contain either appended leucine or alkyl moieties. The simple TbTbLeu complex **55** is included as an initial control to test whether the leucine moiety aids cell permeability. Complexes **56-58** contain the activatable azobenzene group, based on the proposal that the added moieties will increase cell uptake but still be selectively activatable under reducing conditions to release the fluorescent TbTbNH$_2$ which will be trapped inside the cell (as it is not cell permeable). Attachment of leucine is proposed due to the previously evaluated literature (section 4.1.1.1) which suggests that the addition of a leucine moiety may increase cell uptake and cause recognition by receptors such as LAT1, and that enzymes such as LAP may cause cleavage of the leucine moiety to provide further levels of selectivity (Figure 4.8b). The addition of C_6 or C_{12} alkyl chains (**57** and **58**) are proposed as an alternative

strategy to increase the overall lipophilicity of the azobenzene lanthanide complexes and investigate the possibility of anchoring the bimetallic complex within cell membranes.

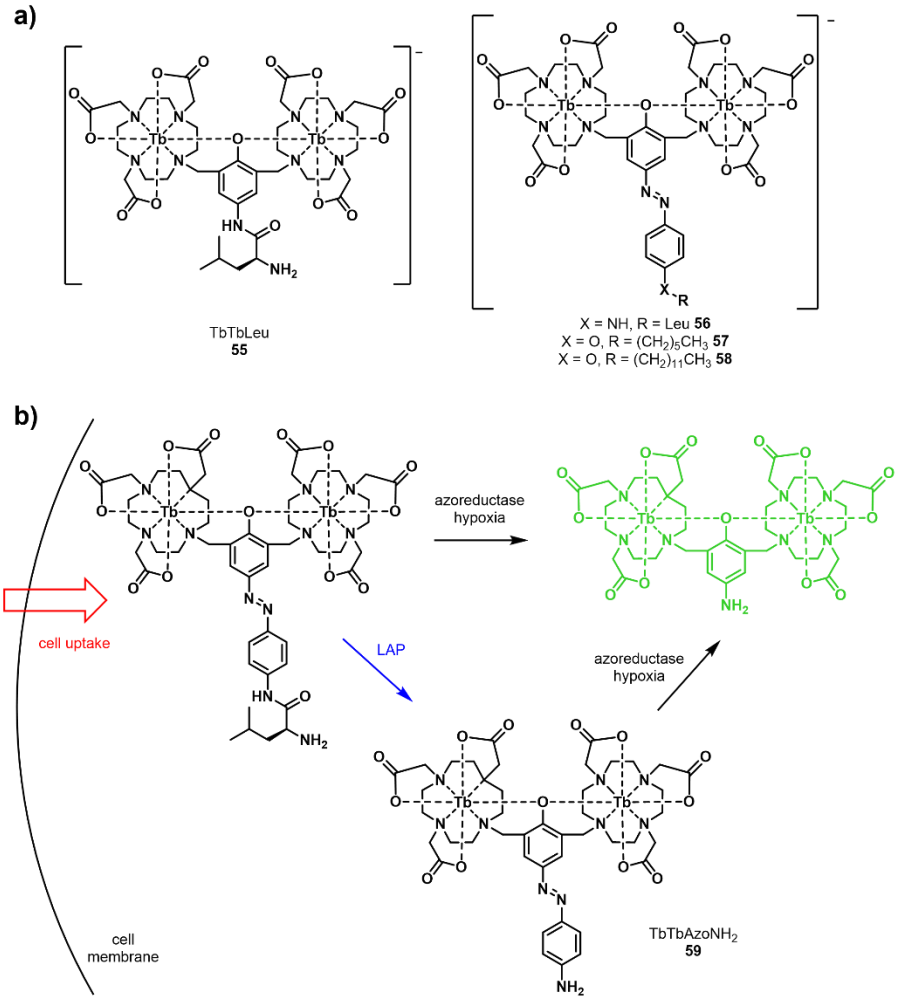

Figure 4.8: a) The target complexes for chapter IV, **55-58**. b) The proposed modes of activation of TbTbAzoLeu **57**. LAP = leucine amino peptidase. The negative charges are removed for simplicity.

4.3 Synthesis and characterisation of leucine-based complexes

4.3.1 Synthesis of leucine-based complex

Synthesis of the bimetallic leucine terbium complex, TbTbLeu **55**, was started by synthesis of the aniline triester **63** previously reported by Simms *et al*.,[42] according to Scheme 4.1.

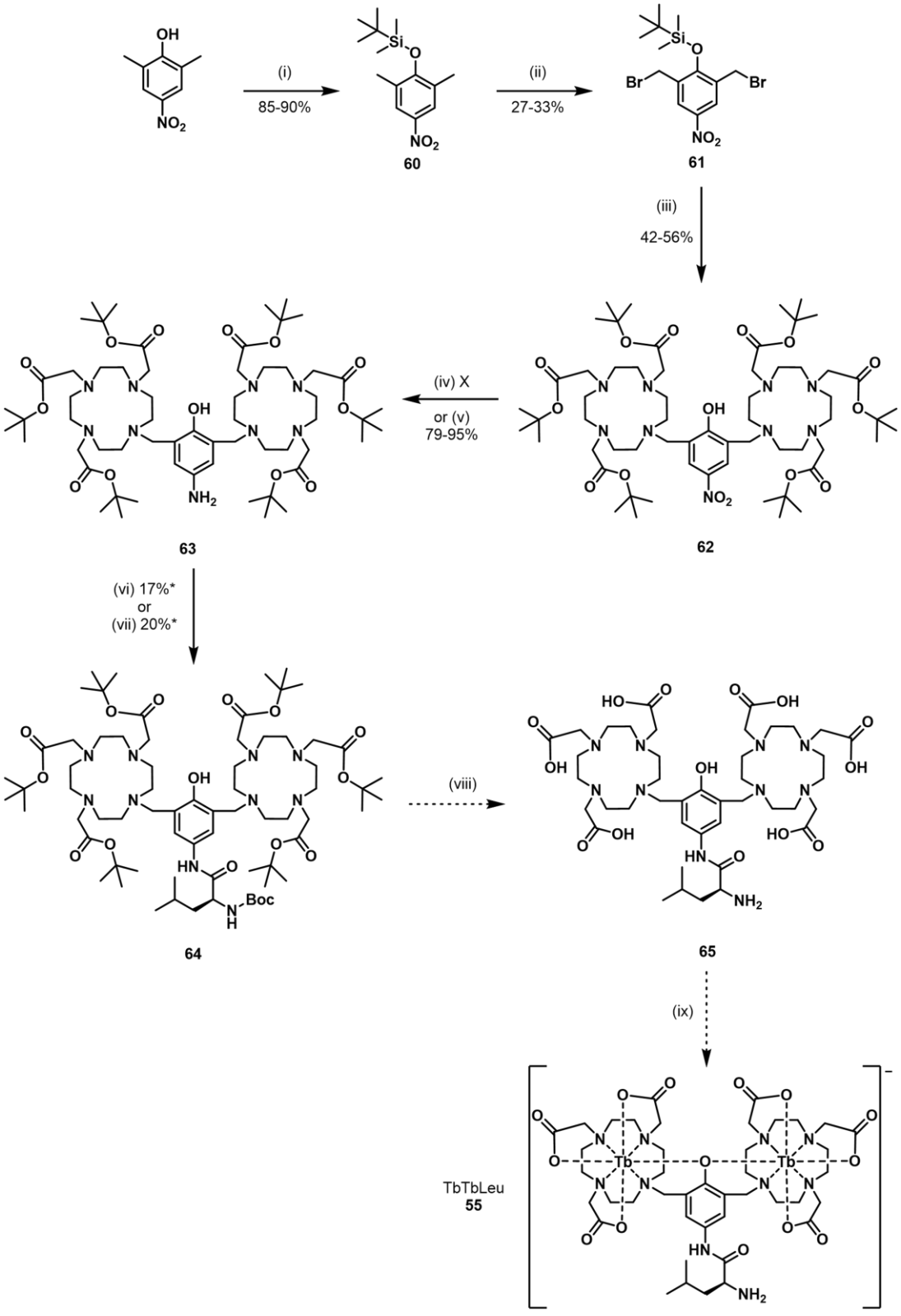

Scheme 4.1: The scheme for the synthesis of leucine complex TbTbLeu **55**, by amide coupling of the aniline triester. Reagents and conditions: i) TBDMSCl, imidazole, DMF, rt, 18 h; ii) NBS, benzoyl peroxide, CCl_4, 90-92 °C, 3 h; iii) **23**, Na_2CO_3, MeCN, 50 °C, 43 h; iv) H2, palladium on carbon, EtOH, rt, 5 days; v) Sn, HCl (2 M), EtOH, 80 °C, 2 h; vi) Boc-leucine, isobutyl chloroformate, TEA, dry CH_2Cl_2, rt, 48 h; vii) Boc-leucine, HBTU, HOBt, DIPEA, DMF, rt, 26 h; viii) TFA or HCl, CH_2Cl_2, rt, 18 h; ix) $Tb(OTf)_3$, NaOH (1 M), H_2O, rt, 4 days. *Product potentially impure.

This was carried out by TBDMS protection of 2,6-dimethyl-4-nitrophenol to give **60** in high yields (85-80%). Radical dibromination, using NBS and benzoyl peroxide in CCl_4, gave **61** in poor yields (27-33%, consistent with those previously reported),[42, 46] due to the multiple bromination products formed and difficulty of separation by column chromatography. Alkylation of the DO3A triester **23** with **61** gave the nitro hexaester **62** in moderate yields (42-56%). Reduction of the nitro group to amine to give **63** was initially carried out according to the procedure documented in the group by Dr Daniel Kovacs.[42, 61] The reaction was carried out using hydrogen gas and palladium on carbon in ethanol for 5 days, with crude ^{1}H NMR spectroscopy suggesting poor conversion to the aniline (36-40%). Considering the poor conversion, an alternative route for nitro to aniline reduction was carried out using tin and HCl to produce tin chloride *in situ*, using a low concentration of HCl (2 M) to avoid the deprotection of the *tert*-butyl protecting groups. Mass spectrometry of the crude reaction after 2 hours suggested that the nitro was fully converted to the amine. The crude ^{1}H NMR spectrum of the tin/HCl reaction confirmed full conversion of the nitro compound and the integrals for the aromatic region (2 H) and aliphatic region (48 H for the cyclen ring protons and 54 H for the *tert*-butyl protons) appeared correct, despite a difference in shift to that previously reported – this is proposed to be due to a difference in pH affecting the chemical shifts. The success of the tin/HCl reaction was confirmed by subsequent TFA deprotection of the *tert*-butyl groups to give the corresponding aniline triacid (see section 4.3.3) whose ^{1}H NMR spectrum matched that reported previously, following purification by precipitation from methanol and diethyl ether.

Prior to attempting to amide couple the aniline triester **63** to Boc-L-leucine, test reactions were carried out on the organic moiety **66**, which was synthesised *via* reduction of the corresponding nitro compound according to the literature procedure (Figure 4.9a).[62] Three different amide coupling conditions were carried out in parallel (detailed in Figure 4.9b) to yield **67**, based on previously reported conditions for amide couplings of anilines.[63, 64] Of these, the most effective conditions were determined to be the use of isobutyl chloroformate

and TEA in dry CH_2Cl_2 at room temperature (condition 3). Reaction of Boc-L-leucine with the NH_2 group of **66** to form the amide over ester formation was validated by the ^1H NMR spectrum in DMSO (Figure 4.9c) displaying 3 distinct OH/NH signals (with the NH of the carbamate attaching the Boc group a doublet due to coupling to the adjacent CH group), rather than the two NH signals expected upon ester formation. Amide formation was also confirmed by subsequent TBDMS protection to give **68** and comparison to the ^1H NMR spectrum of **68** formed in an alternative way (Scheme 4.2).

a)

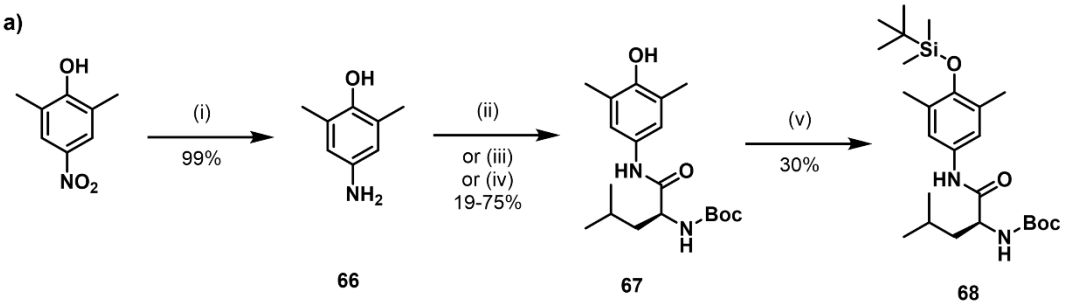

66 67 68

b)

	1	2	3
Reagents	EDC, DMAP, DIPEA, HOBt	Isobutyl chloroformate, TEA	DCC, DMAP
Solvents	MeCN	Dry CH_2Cl_2	
Conditions	rt, 44 h		
Yield / %	19*	75	50

c)

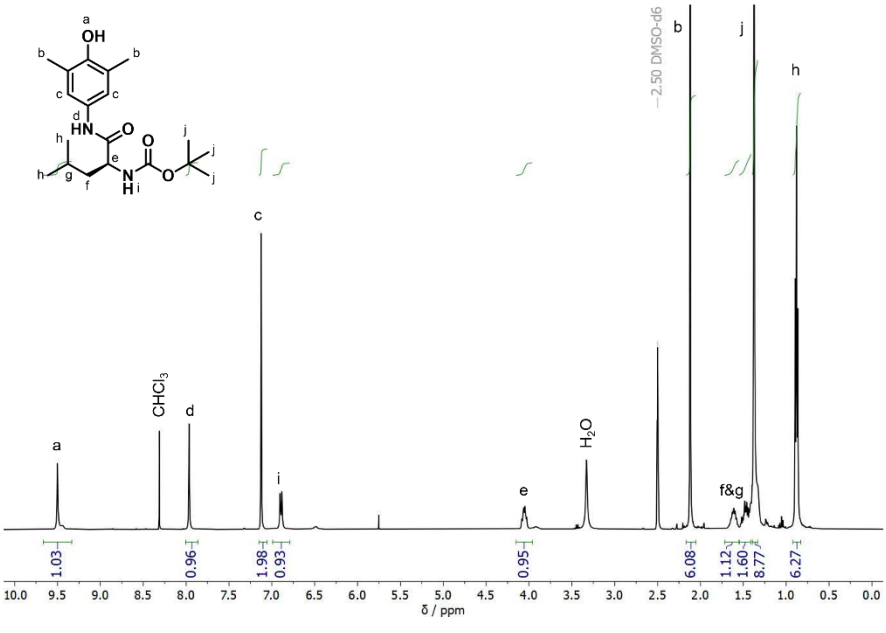

Figure 4.9: a) The synthesis of fragment **66** for amide coupling optimisation of the aniline. Reagents and conditions: i) H_2, palladium on carbon, MeOH, rt, 18 h;[62] ii) Boc-leucine, EDC, HOBt, DMAP, DIPEA, MeCN, rt, 44 h;[63] iii) Boc-leucine, isobutyl chloroformate, TEA, CH_2Cl_2, rt, 44 h;[63, 65] iv) Boc-leucine, DCC, DMAP, CH_2Cl_2, rt, 44 h;[64] v) TBDMSCl, imidazole, DMF, rt, 40 h. b) The different amide coupling conditions used for the synthesis of **67**, where 1=ii, 2=iii and 3=iv. * denotes that the product was columned twice. c) The assigned ^1H NMR spectrum of **67** in DMSO-d_6, containing residual $CHCl_3$ from prior NMR analysis in $CDCl_3$.

Following the success of amide coupling on the organic fragment **66**, the isobutyl chloroformate conditions were employed to attempt the amide coupling of the aniline hexaester **63** with Boc-L-leucine (Scheme 4.1 step vi) to form hexaester **64**. Crude MS analysis of the reaction suggested some product had formed after 24 hours, with appearance of peaks with *m/z* 688 $[M+2H]^{2+}$ and *m/z* 1376 $[M+H]^{+}$, but the reaction appeared to stall after this (according to TLC). The reaction mixture was purified by column chromatography using methanol and CH_2Cl_2 (gradient, 0-20%) to give 8 mg of product (< 12% yield), which was postulated to be impure by LRMS analysis. Analysis of the ^1H NMR spectrum of the resulting material in $CDCl_3$ (Figure 4.10a) was unconvincing due to the number of broad peaks in the aromatic region, however this is often observed for similar compounds due to the fluxional nature of the cyclen rings. Amide coupling of the aniline hexaester **63** with Boc-L-leucine was also carried out using the conditions reported by Mizukami et al.[26] for attachment of leucine to a monometallic terbium complex (without isolation of the intermediate triester), using HBTU, HOBt and DIPEA in dry DMF (Scheme 4.1 step vii). As for the previous attempt, partially impure material was obtained following column chromatography (according to LRMS and TLC analysis) in low yields (< 20%). Analysis of the ^1H NMR spectrum of the resulting material in $CDCl_3$ (Figure 4.10b) appeared, as for the previous conditions, to contain multiple broad peaks in the aromatic region, however the relative integrals appeared to match more closely with those expected. It was concluded that whilst the approach of amide coupling directly onto the previously reported hexaester aniline **63** appeared promising it was difficult to determine the purity of the resulting complex by ^1H NMR analysis. Therefore, synthesis by modification of the arm and subsequent alkylation was determined to be a better route to confirm attachment of the leucine moiety.

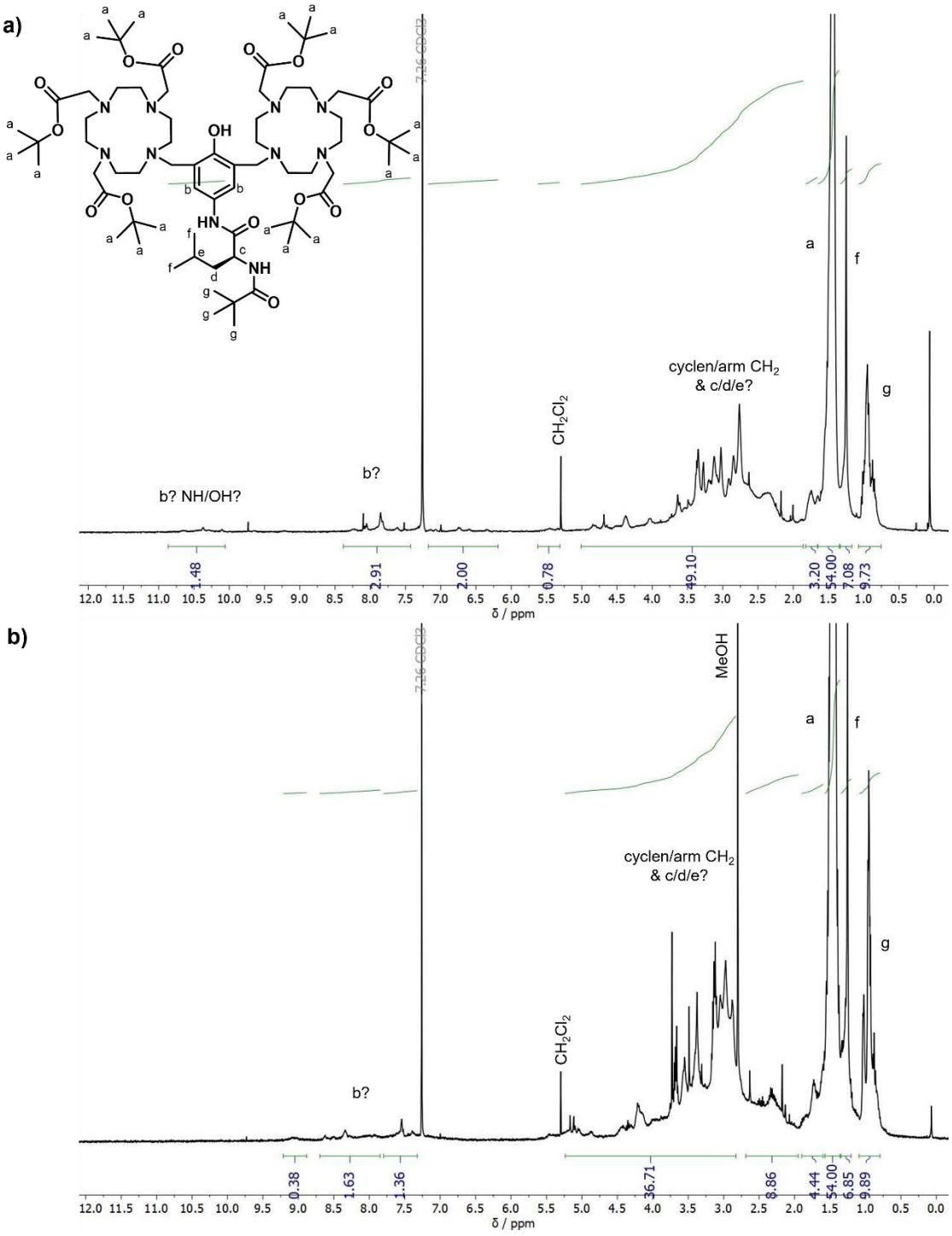

Figure 4.10: The ^{1}H NMR spectra of the combined fractions in $CDCl_3$ from the attempted synthesis of hexaester **64** using two different conditions to give panels a and b, following column chromatography in CH_2Cl_2 and MeOH. Proposed assignments of the peaks are given. a) Material from amide coupling using isobutyl chloroformate and TEA in CH_2Cl_2, b) material from amide coupling using HBTU, HOBt and DIPEA in dry DMF.

Scheme 4.2a highlights the new proposed route using reactions similar to those utilised for the synthesis of the reported bimetallic terbium complexes such as TbTbAzo.

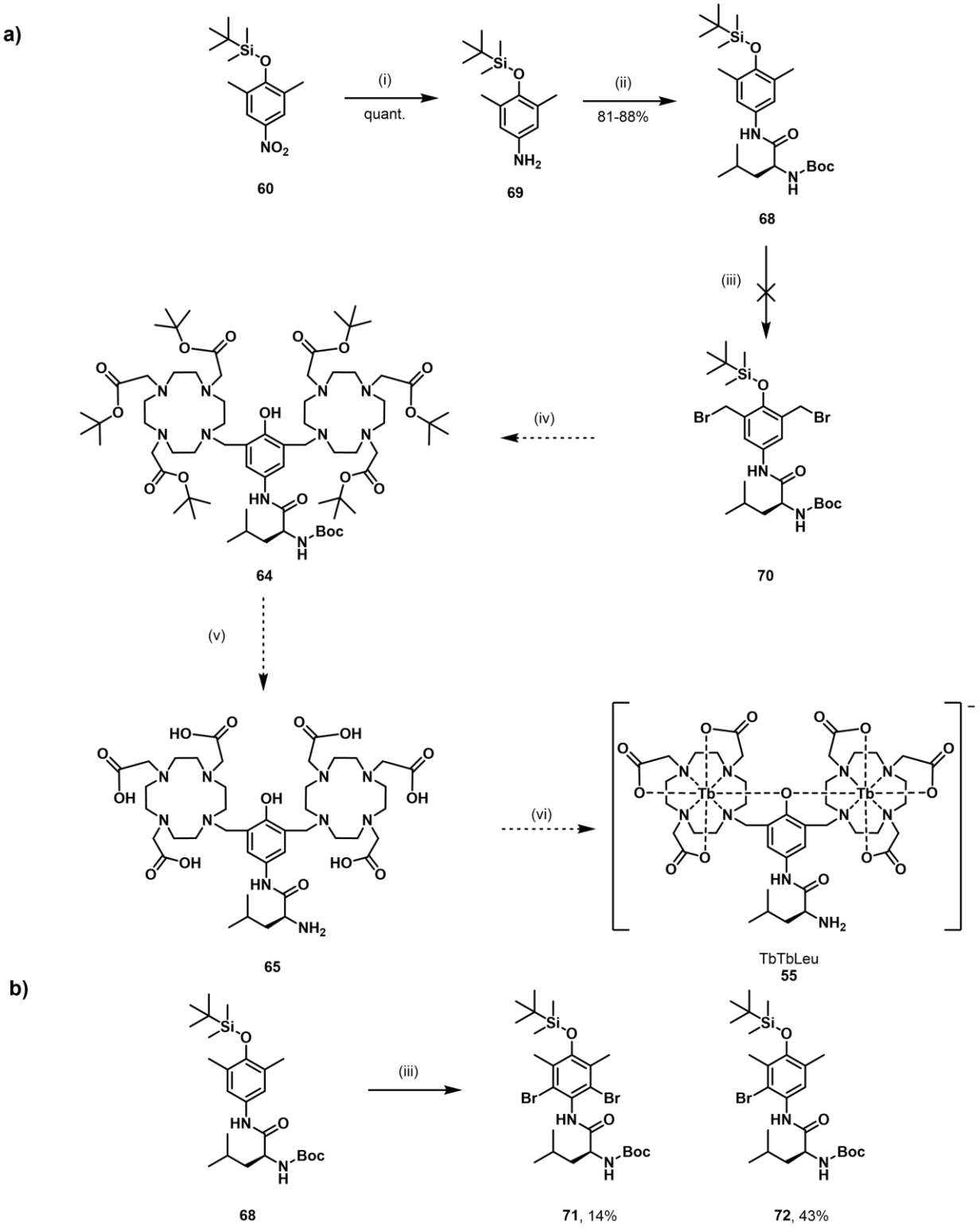

Scheme 4.2: a) The synthesis scheme for TbTbLeu **55** by amide coupling prior to attaching to the DO3A core. Reagents and conditions: i) TBDMSCl, imidazole, DMF, rt, 24 h; ii) Pd/C, H_2, MeOH, rt, 18 h; iii) Boc-leucine, isobutyl chloroformate, TEA, CH_2Cl_2, rt, 40 h; iv) NBS, benzoyl peroxide, CCl_4, 92 °C, 3.5 h; v) **23**, Na_2CO_3, MeCN, 50 °C, 40 h; vi) TFA, CH_2Cl_2, rt, 48 h; vii) $Tb(OTf)_3$, NaOH, MeOH, 50 °C, 3 d. b) The products of bromination of **68** under radical bromination conditions.

TBDMS protection of 2,6-dimethyl-4-nitrophenol to afford **60** was carried out as previously and subsequent reduction of the nitro group to aniline to give **69** was achieved with quantitative conversion using hydrogen and palladium on carbon in methanol, as previously reported.[62] These steps were carried out to ensure reaction with Boc-L-leucine at the aniline rather than the phenol and to corroborate formation of **68** previously. For this route, formation of **68** was carried out by amide coupling of **69** with Boc-L-leucine using isobutyl chloroformate and TEA in dry CH_2Cl_2 and afforded **68** in good yields (80-88%). Radical dibromination using NBS and benzoyl peroxide in CCl_4, as used for the nitro and azobenzene analogues, was attempted to form **70** however this led to bromination on the ring and formation of **71** and **72** (Scheme 4.2b), in yields of 14% and 43% respectively, as evidenced by LRMS, HRMS and analysis of the ^{1}H NMR spectra (Figure 4.11). This result is consistent with previous literature suggestions that electron donating amide or ether groups direct bromination ortho on the ring and radical benzylic bromination products are not observed, even in the presence of ambient light (rather than heat activation of benzoyl peroxide as an initiator, as demonstrated here).[66] No further attempts at bromination were attempted due to the literature precedent for ring bromination of similar substrates.

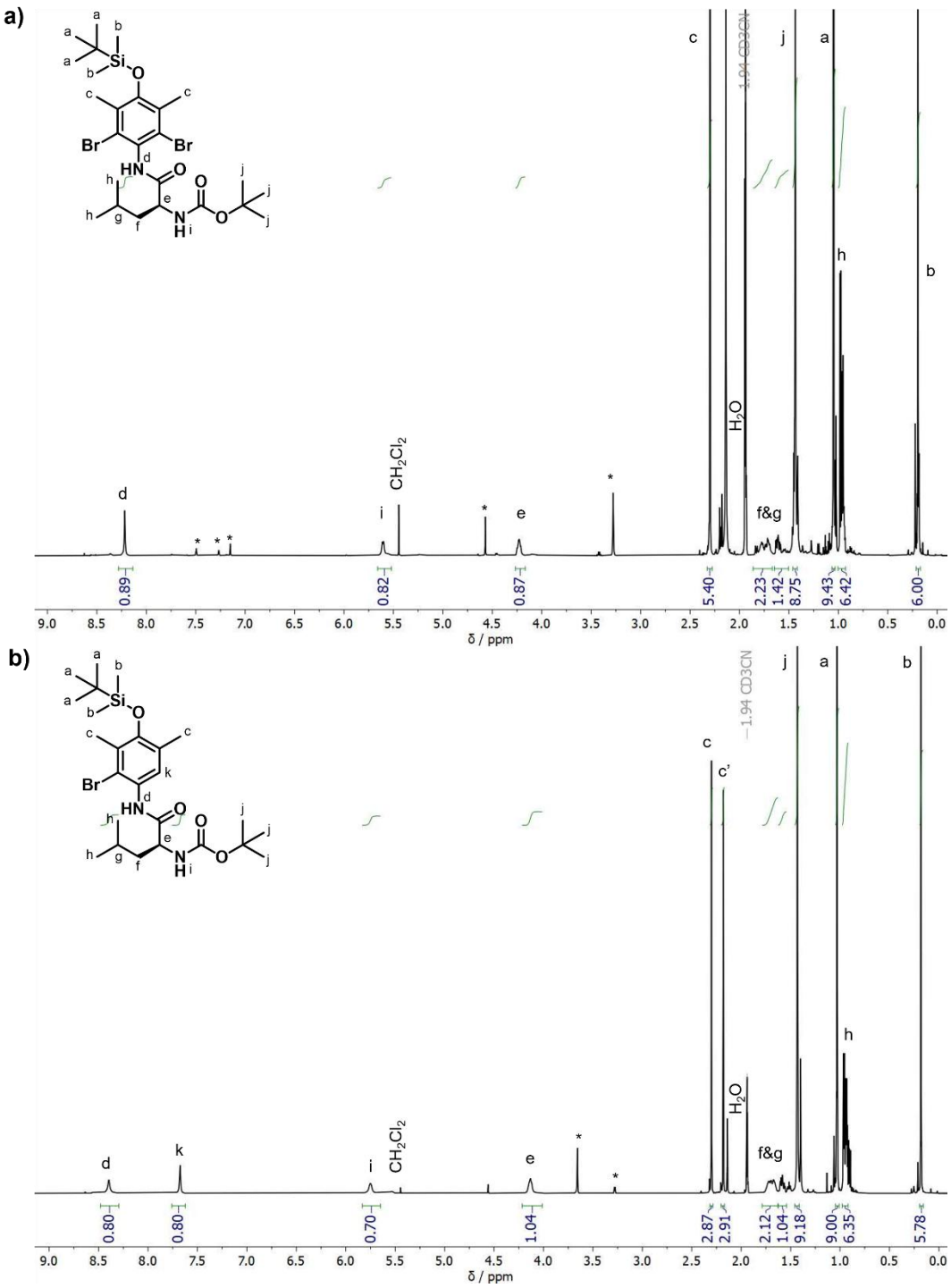

Figure 4.11: The ^{1}H NMR spectra, in MeCN-d_3, of the dibrominated (a, **71**) and monobrominated (b, **72**) products from the reaction of **68** with NBS and benzoyl peroxide in CCl_4. The assignment of peaks is denoted, with * denoting impurities which do not show crosspeaks in the COSY or HSQC spectra to peaks within the desired compound.

One alternative route to install CH_2Z (Z = Cl/Br) groups for attachment of the leucine-containing chromophore that was considered was formylation, or formation of hydroxymethyl groups, following installation of the leucine group (Figure 4.12). Reaction of

4-aminophenol with both Boc-L-leucine and Fmoc-*L*-leucine was carried out as depending on the conditions used for the formylation and subsequent steps different protecting groups may be deprotected during the synthesis. Amide couplings, to give **73** and **74**, were carried out using a variety of literature conditions (Figure 4.12a),[63, 67, 68] with CDI in dry THF producing the highest yield for the Fmoc-*L*-leucine derivative **74**. Formation of the amide rather than the ester is confirmed by ^{1}H NMR analysis of the Fmoc-*L*-leucine compound in DMSO-d_6 due to the presence of 3 OH/NH peaks expected for the amide (compared to two NH/NH_2 peaks expected for the ester) and their high chemical shifts (at 7.58 ppm, 9.16 ppm and 9.73 ppm), with the ^{13}C NMR spectrum showing a characteristic phenol chemical shift of 153.3 ppm.

a)

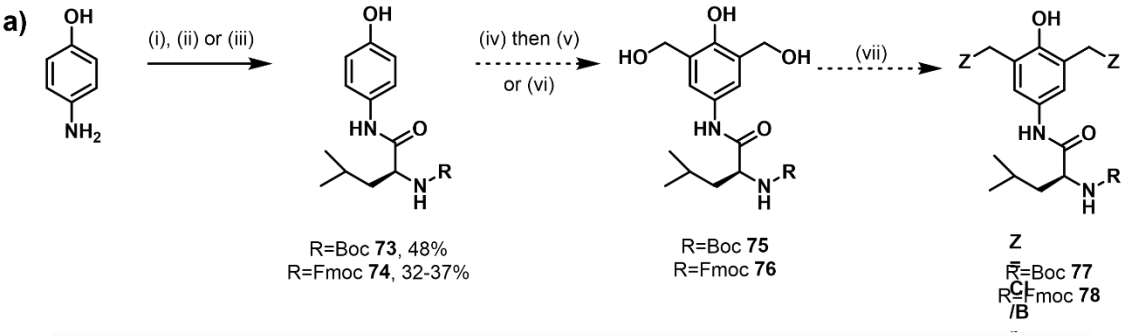

b)

Conditions	Isobutyl chloroformate, TEA, dry CH_2Cl_2, rt, 40 h	DCC, HOBt, TEA, DMF, rt, 17 h	CDI, dry THF, rt, 21 h
Yield with Boc-*L*-leucine / %	48	-	-
Yield with Fmoc-*L*-leucine / %	< 4	32	37

Figure 4.12: a) The proposed synthetic scheme for TbTbLeu via formylation of the organic amide arm to avoid previous bromination issues – steps after halogenation are not reported as they are assumed to be the same as in Scheme 4.2. Reagents and conditions: i) Boc-leucine or Fmoc-leucine, isobutyl chloroformate, TEA, CH_2Cl_2, rt, 40 h; ii) Fmoc-leucine, DCC, HOBt, TEA, DMF, rt, 17 h; iii) Fmoc-leucine, CDI, dry THF, rt, 21 h; iv) HMTA, HCl (1 M), AcOH, 120 °C, 4 h; v) reduction e.g. $NaBH_4$, MeOH, rt, 4 h; vi) Formaldehyde, NaOH, MeOH, 65 °C, 18-40 h; vii) bromination or chlorination e.g. $SOCl_2$, CH_2Cl_2, rt, 2 h. b) Analysis of different amide coupling conditions used to form **73** and **74**, based on literature procedures.[63, 67, 68]

Formation of the desired hydroxymethyl phenol intermediates **75** and **76** were attempted with both the Boc- and Fmoc-protected compounds, using either Duff reaction conditions (which would require subsequent reduction of the aldehyde intermediate) or direct reaction

with formaldehyde in the presence of base,[69-71] however no product was isolated with either condition used, partially due to time constraints. This route was discontinued due to investigation of synthesis of the azobenzene leucine complex, however future work to synthesise the leucine complex could involve subsequent reduction of the crude mixture from the formation the reaction of **74** with HMTA and purification at a later stage before bromination or chlorination, attachment onto the DO3A core, deprotection and lanthanide complexation. TBDMS protection of the phenol using this route may be difficult however it may not be required for alkylation onto the DO3A core, as attachment of a methyl phenol derivative was previously reported without protection of the phenol.[72]

4.3.2 Synthesis of leucine azobenzene complex

Synthesis of the complex TbTbAzoLeu **56** was initially attempted following the route described in Scheme 4.3, involving the formation of the azobenzene group and subsequent attachment of the leucine moiety prior to attachment to the DO3A core. Selective monoprotection of para-phenylenediamine with Fmoc was carried out according to a literature procedure,[73] using Fmoc chloride and DIPEA in CH_2Cl_2, to give **79** in good yields (66-69%). Fmoc was chosen over Boc due to the acidic conditions required for the first step of the azobenzene formation.

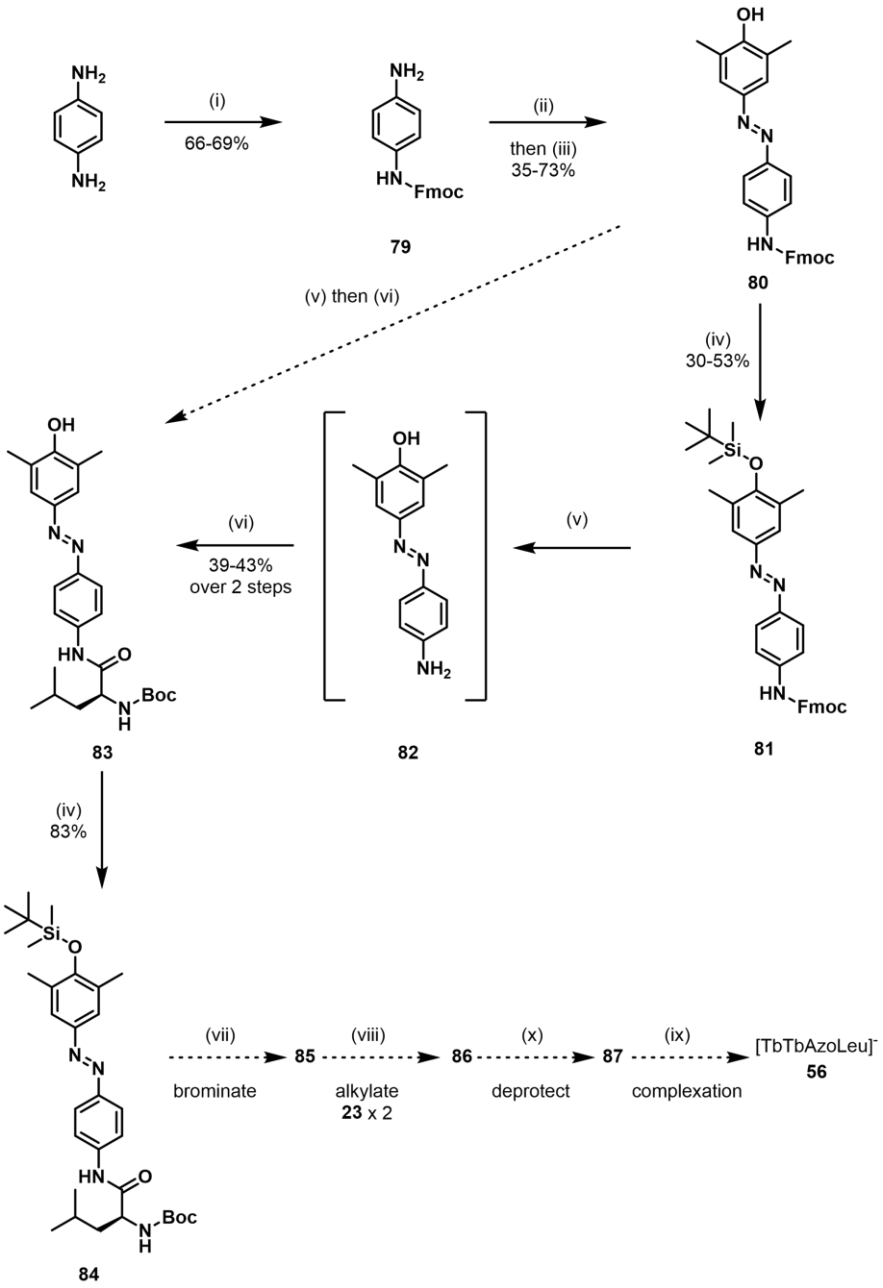

Scheme 4.3: The scheme for the longer synthesis of azobenzene leucine complex TbTbAzoLeu **56**. Reagents and conditions: i) Fmoc chloride, DIPEA, CH_2Cl_2, rt, 2 h; ii) HCl (1 M), $NaNO_2$, H_2O, acetone, 0 °C, 30 min; iii) 2,6-dimethylphenol, NaOH, H_2O, EtOH, rt, 18 h; iv) TBDMSCl, imidazole, DMF, rt, 24-72 h; v) Piperidine, DMF, rt, 1.5 h; vi) Boc-leucine, CDI, dry THF, rt, 48-72 h; vii) NBS, benzoyl peroxide, CCl_4, 90 °C, 3 h; viii) **23**, Na_2CO_3, MeCN, 50 °C, 48 h; ix) TFA, CH_2Cl_2, rt, 24-48 h; x) $Tb(OTf)_3$, NaOH (1 M), H_2O, 50 °C, 4 days.

Diazotisation, using $NaNO_2$ and HCl in water and acetone, of the aniline **79** was carried out and subsequent addition to a basic solution of 2,6-dimethylphenol resulted in formation of the characteristic deep red colour associated with formation of an azobenzene. These conditions employed were similar to those reported by Simms[46] (and others) for the formation of azobenzenes, however the reaction was carried out in a mixture of water and

acetone following the procedure adapted from Zhang *et al.*[74] to aid the solubility of the starting material. This reaction worked to afford the Fmoc protected azobenzene **80** in variable yields (35-73%) on small scale (50-100 mg of **79**) however product was not detected by crude ^{1}H NMR spectra, TLC or LRMS analysis on larger scale (>200 mg of **79**). For scale-up of this reaction multiple smaller batches were carried out (e.g. 3 x 150 mg of **79**) and combined for work-up and purification (by column chromatography using ethyl acetate and PE) to give **80** in decent yields (37-50%), with product formation verified by LRMS (with *m/z* 464 $[M+H]^+$ and *m/z* 949 $[2M+H]^+$ as dominant peaks in the spectra) and HRMS. The variable yields and issues with scale-up for this reaction are proposed to be due to small changes in pH and changes in local pH and solvation, due to the mixture of water and acetone required. The ^{1}H NMR spectrum of **80** (Figure 4.13a) contains a broad peak at 7.5 ppm for two aromatic protons (labelled as e) which appeared unusual, however the COSY spectrum revealed coupling from a sharp doublet at 7.85 ppm and HSQC showed coupling of the broad peak at 7.5 ppm to an aromatic carbon at 119 ppm, which partially validates product formation. Subsequent TBDMS protection of this material afforded **81** in decent yields (30-53%), with formation verified by LRMS (*m/z* 578 $[M+H]^+$ 100% intensity), HRMS and analysis of ^{1}H NMR spectrum (Figure 4.13b) which still contained the broad aromatic peak at 7.5 ppm.

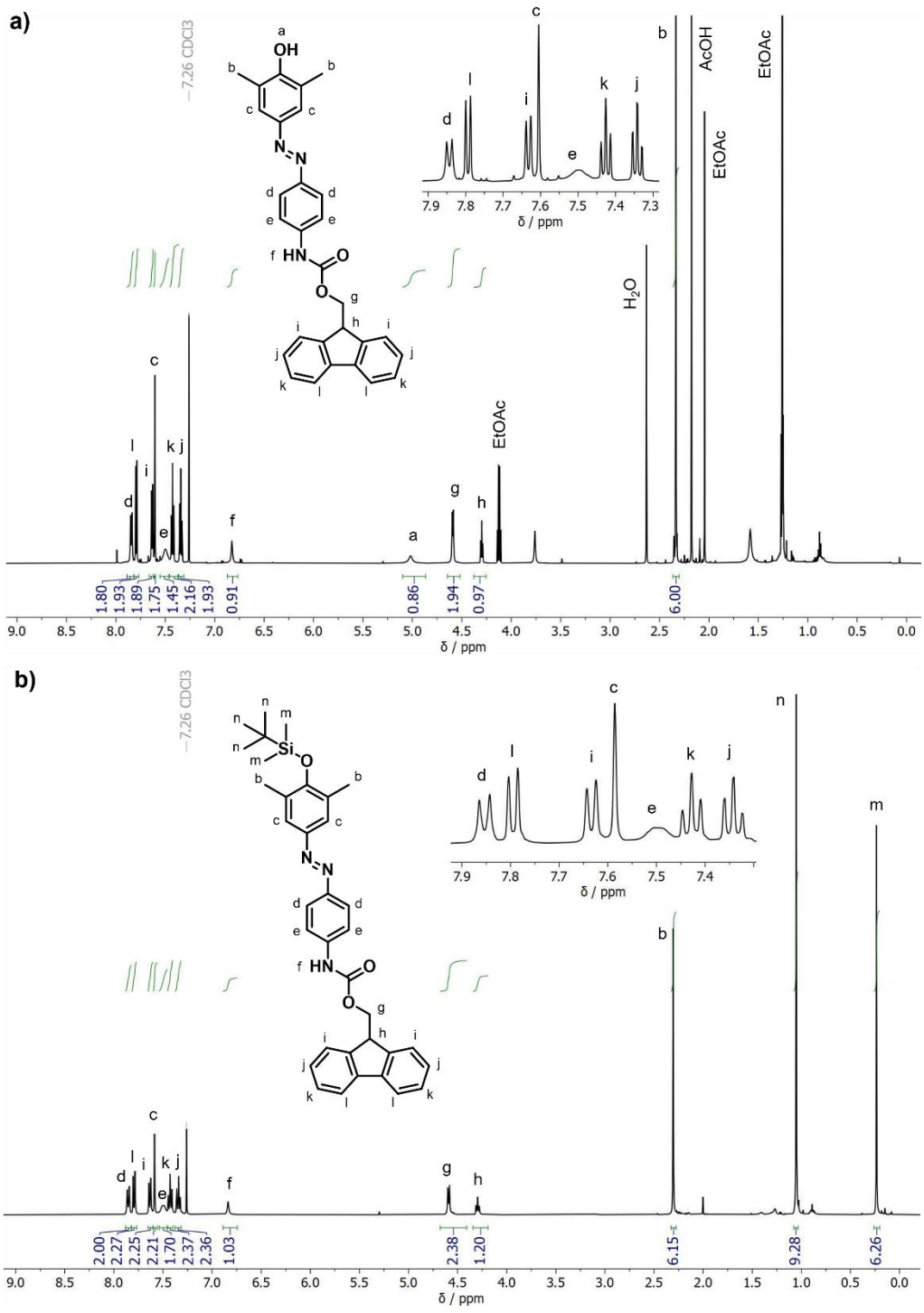

Figure 4.13: The ^{1}H NMR spectra, in $CDCl_3$, of Fmoc-protected azobenzene analogues **80** (panel a) and **81** (panel b). The assignments of the peaks are given, based on 2D NMR spectra. Inset zooms of the aromatic regions clearly show the broad signal observed for environment e.

Formation of the TBDMS protected phenol with the Boc-protected leucine moiety attached **84** was attempted by Fmoc deprotection of **81** and subsequent amide coupling, without purification of the free aniline intermediate. However, crude ^{1}H NMR and LRMS analysis of the intermediate formed following reaction with piperidine in DMF suggested that the

TBDMS and Fmoc groups are both removed, giving intermediate **82** - by LRMS an *m/z* of 264 is observed corresponding to [(**81**-Fmoc-TBDMS)+Na]$^+$ and the ^{1}H NMR spectrum (Figure 4.14a) shows formation of a broad NH_2 peak at 6.4 ppm. Initial amide coupling was attempted using isobutyl chloroformate and TEA in CH_2Cl_2 however only very impure fractions were obtained following column chromatography. Reaction of the deprotected mixture with CDI in dry THF obtained **83** in moderate yields (39-43%) and loss of the amine peak at 6.4 ppm was observed. The obtained orange oil appeared reasonably pure by ^{1}H NMR analysis (Figure 4.14b) in $CDCl_3$. LRMS and HRMS analysis confirmed product formation, with LRMS of product-containing column fractions showing peaks corresponding to [2M+H]$^+$ and [3M+H]$^+$. However, two spots were observed by TLC analysis (EtOAc : PE 1:1, R_f 0.49 and 0.64) which suggests that either a small amount of impurity is present or that the presence of two spots occurs due to the presence of *E/Z* isomers, which was also observed during the formation of the control complex TbTbAzo (albeit only following attachment of the azobenzene species to the DO3A core).

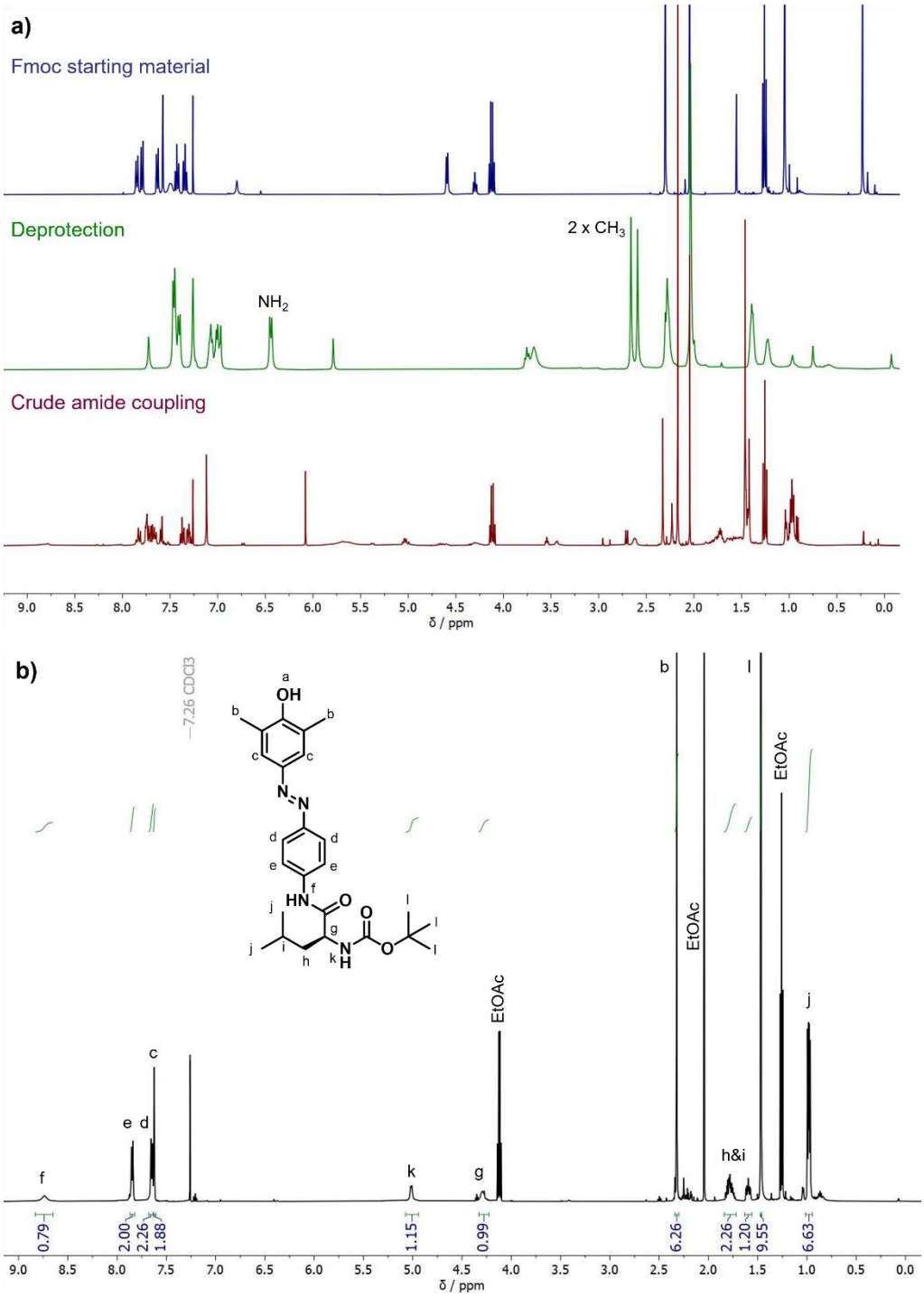

Figure 4.14: a) The stacked ^{1}H NMR spectra, in $CDCl_3$, of the Fmoc- and TBDMS-protected starting material **81** (blue), crude NMR after deprotection by piperidine (green) showing the production of a NH_2 peak (suggesting at least partial formation of **82**), and the crude NMR following the amide coupling (red). b) The ^{1}H NMR spectrum, in $CDCl_3$, of the Boc-protected leucine azobenzene compound **83** isolated from the crude by column chromatography. The assignments of the peaks are given, based on 2D NMR spectra.

The obtained material of **83** was subjected to TBDMS protection conditions to yield **84**, as confirmed by LRMS, HRMS and ^{1}H NMR spectroscopy (Figure 4.15a). The ^{1}H NMR spectra of the resulting orange oil clearly contained the product and confirmed previous amide

formation as the TBDMS-protected product contained two broad singlets corresponding to two NH protons. However, the material showed two spots by TLC analysis and contained excess TBDMSCl or a TBDMS-containing by-product, evidenced by peaks in the ^{1}H NMR spectrum at 0.1 ppm and 0.9 ppm with relative integrals of roughly 6:9.

The impure TBDMS-protected material was subjected to the previously used radical bromination conditions (NBS and benzoyl peroxide in CCl_4 at 90 °C) to determine whether this route is viable, as ring bromination was observed previously for the amide-containing species (see section 4.3.1) whereas the reaction was successful for the simple azobenzene derivative (as previously reported in the literature[42] and shown subsequently in section 4.3.3). The crude ^{1}H NMR spectrum (Figure 4.15b) appeared promising due to the presence of peaks at 4.57 and 4.59 ppm consistent with CH_2Br environments, with partial conversion evident from the remaining CH_3 peaks at around 2.3 ppm. Purification of the crude material, which showed evidence of degradation over time, gave two impure fractions of monobrominated TBDMS-protected compound, confirmed by ^{1}H NMR spectroscopy and LRMS.

These preliminary results for the formation of **84** and proposed formation of **85** in the crude material, prior to degradation, suggests that this may be a viable route to formation of TbTbAzoLeu, however scale-up is difficult and yields are often low (< 50%). A shorter route to TbTbAzoLeu **56** (Scheme 4.4) was also attempted *via* the direct amide coupling of *para*-phenylenediamine with Fmoc-protected leucine and subsequent azobenzene formation, requiring two deprotection steps following attachment to the DO3A core to remove both the Fmoc and *tert*-butyl protecting groups.

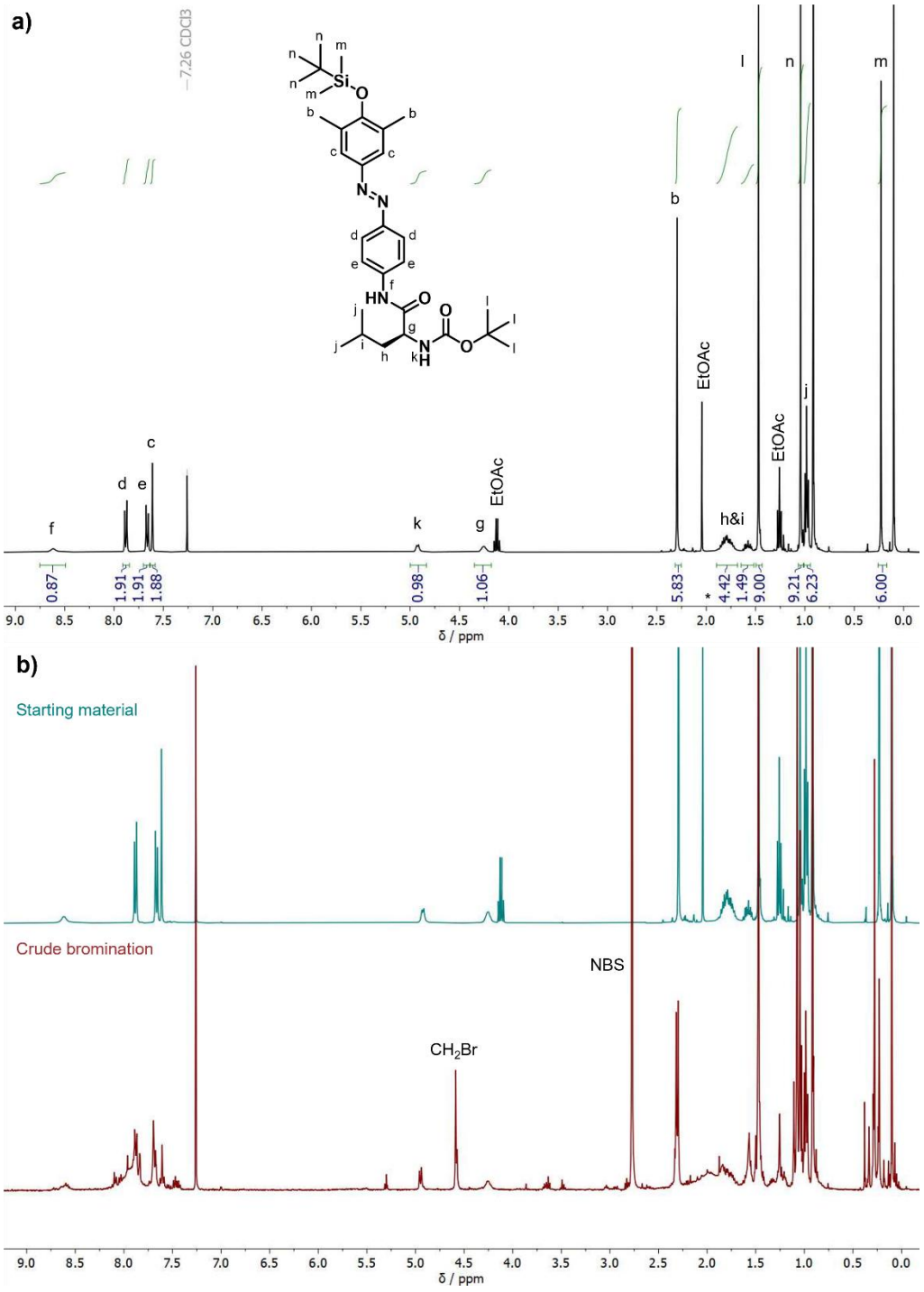

Figure 4.15: a) The ^{1}H NMR spectrum, in $CDCl_3$, of the TBDMS- and Boc-protected azobenzene leucine compound **84**. The assignments of the peaks are given, based on 2D NMR spectra. * denotes a larger integral than expected for the environment – the relative integral appears correct by multiplet analysis. b) The stacked ^{1}H NMR spectra, in $CDCl_3$, from the bromination of **84** to give **85**, showing the starting material (blue) and the crude reaction mixture (red), with the peaks corresponding to CH_2Br environments highlighted.

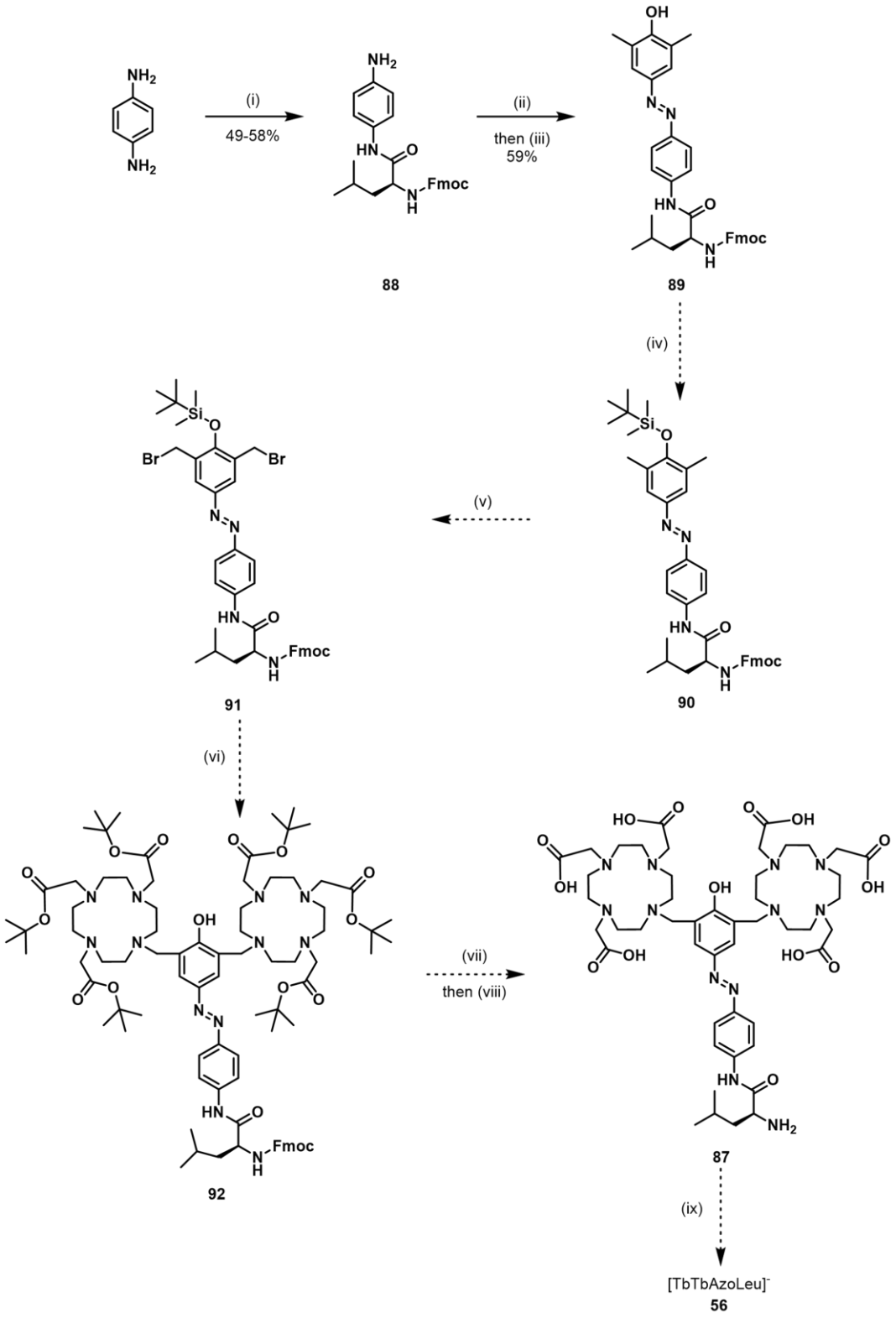

Scheme 4.4: The scheme for the shorter synthesis of azobenzene leucine complex TbTbAzoLeu **56**. Reagents and conditions: i) Fmoc-leucine, DCC, dry THF, rt, 16 h; ii) $NaNO_2$, HCl, H_2O, acetone, 0 °C, 30 min; iii) 2,6-dimethylphenol, NaOH, H_2O, rt, 18 h; iv) TBDMSCl, imidazole, DMF, rt, 96 h; v) NBS, benzoyl peroxide, CCl_4, 90 °C, 3 h; vi) **23**, Na_2CO_3, MeCN, 50 °C, 48 h; vii) Piperidine, DMF, rt, 1 h; viii) TFA, CH_2Cl_2, rt, 24-48 h; x) $Tb(OTf)_3$, NaOH (1 M), H_2O, 50 °C, 3 days.

Amide coupling of para-phenylenediamine and Fmoc-protected leucine was carried out using DCC in dry THF, following an adapted literature procedure for singular reaction of a bisaniline compound with an Fmoc-protected amino acid.[75] This gave **88** in moderate yields (49-58%), confirmed by LRMS, HRMS and ^{1}H NMR spectroscopy (Figure 4.16a) in DMSO-d_6. Diazotisation in a mixture of water and acetone and addition to a basic solution of 2,6-dimethylphenol was carried out on a small scale (190 mg of **88**) to give **89** in moderate yield (59%), confirmed by LRMS, HRMS and ^{1}H NMR spectroscopy (Figure 4.16b). Scale-up of this azobenzene formation reaction (using 400 mg **88**) showed no product formation by LRMS and TLC and, as before, this is attributed to small changes in local pH and solvation. TBDMS protection of **89** proceeded poorly, with poor conversion of the starting material observed, and product isolated (< 5% yield) with the desired mass by LRMS and HRMS (*m/z* 691 $[M+H]^+$) displayed incorrect integrals between the aliphatic and aromatic region of the ^{1}H NMR spectrum.

Overall, this route for the synthesis of TbTbAzoLeu displays some promise however optimisation is required for scale-up of the azobenzene formation step. Future work on this route could involve synthesis of the brominated compound without TBDMS protection of the phenol and subsequent alkylation onto the DO3A core **23**, as alkylation of the DO3A core with a phenolic substituent has been previously reported without protection of the phenol.[72, 76]

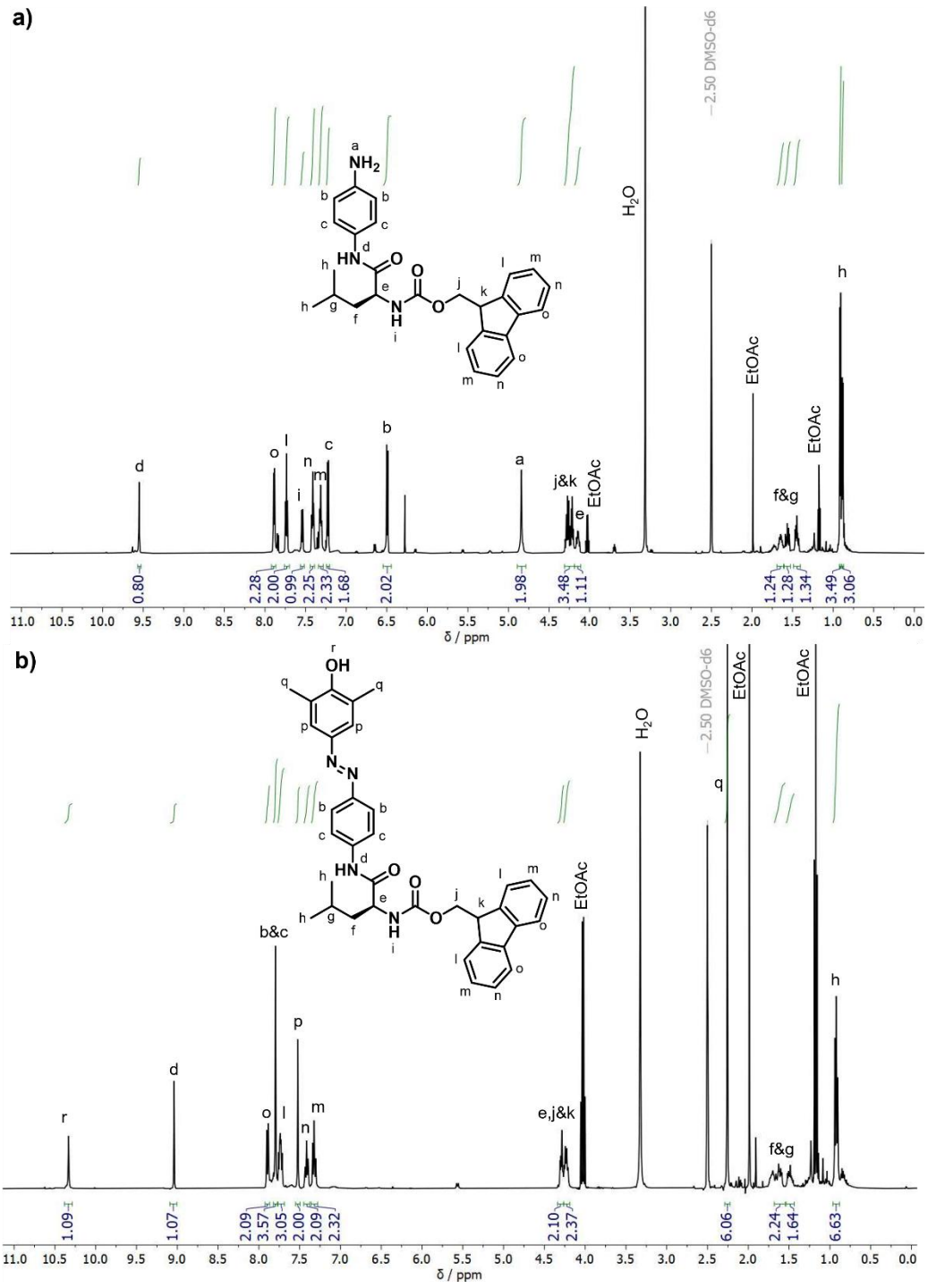

Figure 4.16: The ^{1}H NMR spectra, in DMSO-d_6, of the Fmoc-protected leucine aniline compound **88** (panel a) and the Fmoc-protected leucine azobenzene compound **89** (panel b). The assignments of the peaks are given, based on 2D NMR spectra.

4.3.2.1 Attempted synthesis *via* formation of TbTbOH

Due to unsuccessful attempts to form the desired complex TbTbAzoLeu by synthesis of the ligand and complexation as the final step and uncertainty in the ^{1}H NMR analysis of the formed azobenzenes, synthesis of TbTbAzoLeu following complexation was considered. Placidi *et al*.[77, 78] reported two azo-linked polymetallic lanthanide complexes (termed here as LnLnAzoNO_2, **94**, and Ln_4Azo, **96**) which were synthesised by prior formation of lanthanide complexes and subsequent diazotisation and azobenzene formation, by reaction of a phenol complex (TbTbOH, **93**) with either an organic aniline or another lanthanide complex (**95**, Scheme 4.5). Therefore, it was proposed that a similar route could be followed to synthesise TbTbAzoLeu **56** (Scheme 4.6).

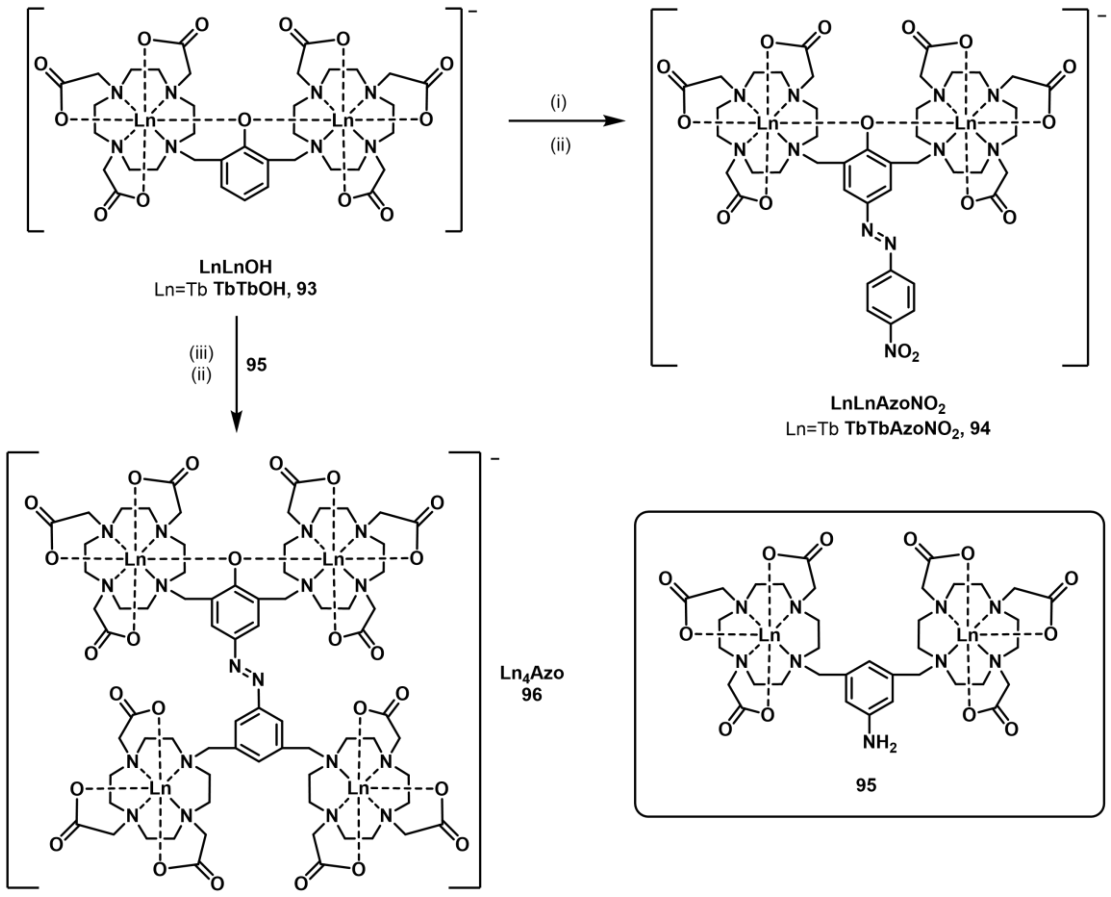

Scheme 4.5: The reported synthesis[77, 78] of two multimetallic azobenzene-containing complexes, LnLnAzoNO_2 and Ln_4Azo. Reagents and conditions: i) $NaNO_2$, 1 M HCl in H_2O, 4-nitroaniline, 0 °C, 10 mins; ii) **93**, 1 M NaOH in H_2O, 0 °C, 30 mins; iii) $NaNO_2$, 1 M HCl in H_2O, **95**, 0 °C, 10 mins.

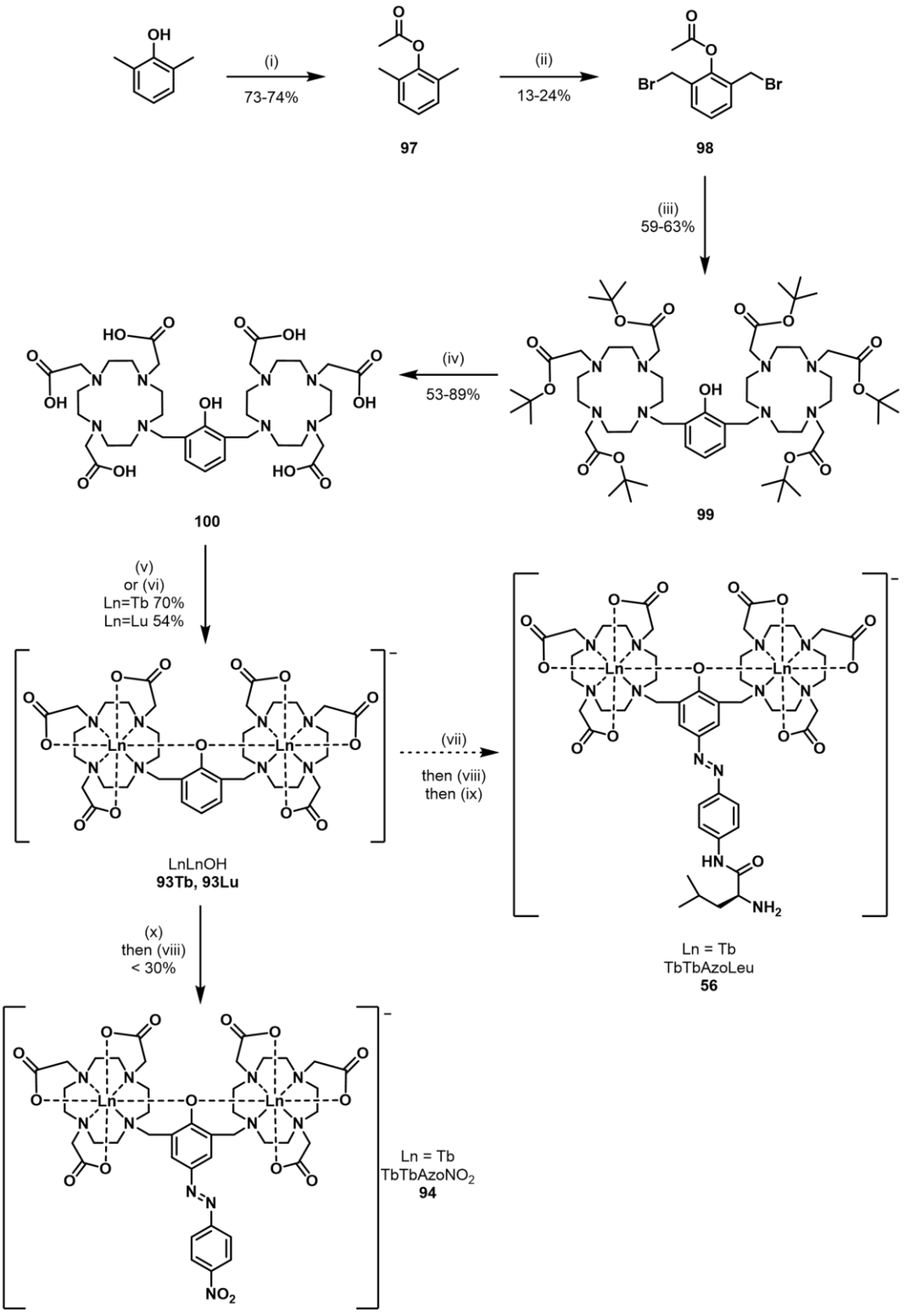

Scheme 4.6: The proposed scheme for the synthesis of azobenzene leucine complex TbTbAzoLeu **57** and the previously reported $TbTbAzoNO_2$ **94**, by azobenzene formation with TbTbOH **93Tb**, according to previously reported procedures.[77, 78] Reagents and conditions: i) Acetic anhydride, 140 °C, 18 h; ii) NBS, benzoyl peroxide, CCl_4, 75 °C, 8-18 h; iii) **23**, Cs_2CO_3, dry MeCN, 82 °C, 47-70 h; iv) TFA, CH_2Cl_2, rt, 20-48 h; v) $Tb(OTf)_3$ or $Lu(OTf)_3$, MeOH, 50 °C, 48-96 h; vi) $Tb(OTf)_3$, MeOH, microwave irradiation, 70 °C, 4 h; vii) **88**, HCl, H_2O, acetone, 0 °C, 30 min; viii) **93**, NaOH, H_2O, rt, 1 h; ix) Piperidine, DMF, rt, 1 h; x) 4-nitroaniline, HCl, H_2O, 0 °C, 30 min.

In contrast to the routes described above which use a TBDMS protecting group on the phenol, synthesis of LnLnOH **93** uses an acetate protecting group which is easily removed during the alkylation step (step iii in Scheme 4.6) however requires harsher conditions to be installed (heating at 140 °C for 18 hours). The acetate precursor **97** was synthesised in good yields (73-74%) and radical bromination using NBS and benzoyl peroxide in CCl_4 afforded the brominated compound **98** in adequate yields (13-24%) following isolation by precipitation from methanol, rather than column chromatography as carried out for other brominated compounds.

To form the hexaester **99**, the brominated compound **98** was reacted with the *tert*-butyl protected DO3A core **23** and initially purified on alumina with CH_2Cl_2 and MeOH, as previously reported.[77] Placidi previously conducted trituration in diethyl ether followed by hexane to further purify the material, therefore this was attempted on the brown oil that resulted after the column purification. The procedure of dissolving the material in diethyl ether and adding hexane as an anti-solvent was carried out twice to yield a brown oil and an orange oil (from the remaining hexane layer), with LRMS suggesting that both fractions contain product and other impurities and fragments (including $[\mathbf{23}+H]^+$). ^{1}H NMR analysis of the two fractions in CD_2Cl_2 (Figure 4.17a) confirmed formation of the desired hexaester compound from the starting bromo compound and the correct relative integrals between the protons of the *tert*-butyl groups, protons of the cyclen rings and the aromatic region, however the aromatic regions of the spectra looked markedly different (Figure 4.17b). The hexane layer contained compound with a dominant triplet (at 6.7 ppm) and doublet (at 7.1 ppm), coupling to each other with a *J*-value of 7.5 Hz, whereas the brown oil contained many broader weaker multiplets in the range 6.4-8.2 ppm. Previous NMR analysis of this triester compound[78] suggested that at room temperature in CD_2Cl_2 the spectrum contained six broad peaks between 6.82 and 7.33 ppm, similar to that observed here in the brown oil, due to the fluxional nature of the compound in solution. Upon heating of the NMR sample to 120 °C it was previously reported that two weak peaks were observed around 6.7 and

7.2 ppm, similar to that observed here for the hexane layer and consistent with the number of aromatic environments expected for the compound.

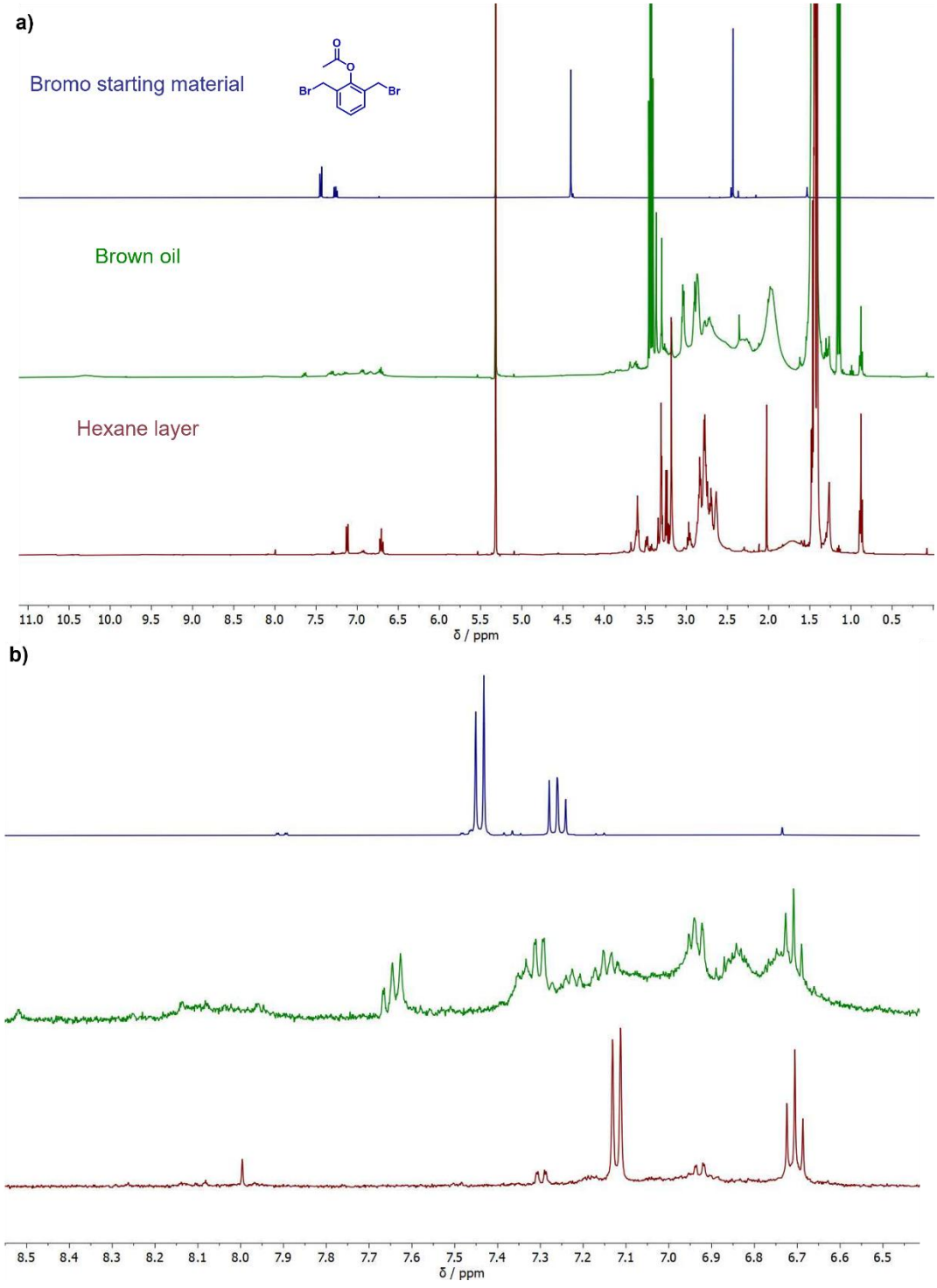

Figure 4.17: a) The stacked ^{1}H NMR spectra at room temperature in CD_2Cl_2 of the bromo starting material **98** (blue) and the two fractions isolated after formation of the hexaester **99**, the brown oil (green) and the hexane layer (red). b) Zoom of the aromatic region, 6.5-8.5 ppm.

Standard TFA in CH_2Cl_2 conditions were used to deprotect the *tert*-butyl groups of the two fractions separately and precipitation from methanol with diethyl ether afforded two batches of the corresponding hexaacid **100** with similar ^{1}H NMR spectra (Figure 4.18). The ^{1}H NMR spectra contain two broad peaks in the region 6.8-7.8 ppm, consistent with that observed previously[78] and suggesting that the fluxional processes of the hexaacids are more rapid than the hexaester precursors.

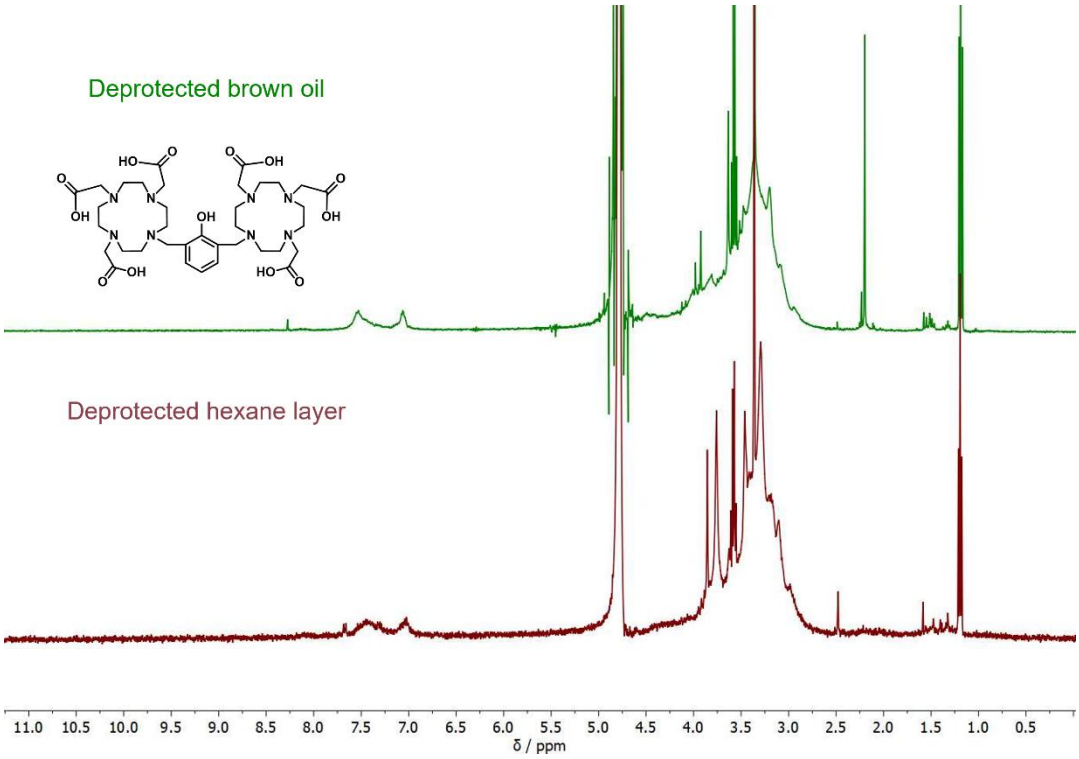

Figure 4.18: The stacked ^{1}H NMR spectra at room temperature in D_2O of the hexaacids **100** formed from deprotection of the brown oil and hexane layer depicted in Figure 4.17.

Despite the similarity in the ^{1}H NMR spectra, the two batches of hexaacid **100** formed were reacted separately with $Tb(OTf)_3$ in methanol at 50 °C (in the absence of any base, as previously reported)[77, 78] to afford the desired intermediate complex TbTbOH **93Tb**. In an attempt to speed up purification, preparative HPLC was initially carried out using various methods, including using neutral and acidic solvents (containing 0.1% formic acid) and various gradients to purify the reaction mixtures obtained. Despite attempted optimisation, messy HPLC traces were observed which hindered product isolation. The product was collected based on purity determined by LCMS analysis and detection of the mass of the

complex in negative mode, however often fragments and adducts were observed, such as the mono Tb-containing complex and methylation of one or multiple acid arms. Due to the issues outlined above, low yields of TbTbOH **93Tb** were recovered from purification by preparative HPLC (< 5%) in lower purity than desired – one sample isolated in this manner is termed TbTbOH batch A and its purity is discussed further later, see Figure 4.21. TbTbOH formation under microwave irradiation was also investigated as an alternative method of synthesis, with microwave irradiation carried out for 4 hours at 70 °C in methanol. Purification of the resulting material by preparative HPLC gave similarly low yields of TbTbOH with lower purity than desired.

Following issues with purification by preparative HPLC, purification of complexes by dialysis was carried out. Three batches of hexaacid were obtained (from three batches of hexaester, Figure A4.1) and analysed by analytical HPLC to determine their purity prior to complexation (Figure 4.19a-c). All batches showed several peaks at short retention times (3-4 min), as expected for a hexaacid, suggesting that multiple conformational isomers are present. The extracted UV trace (from between 3.2-4.5 min, Figure 4.19d-f) for all batches appeared the same and consistent with the UV-Vis spectra reported previously, with a shoulder around 220 nm ($\pi \rightarrow \pi^*$) and a maxima at 280 nm ($n \rightarrow \pi^*$).[78] Batch A of the hexaacid was reacted with $Tb(OTf)_3$ at 50 °C in MeOH for several days and the reaction mixture was subsequently purified by dialysis (1000 Da cut-off), as previously reported,[78] to give TbTbOH **93Tb** batch B. Product formation was confirmed by HRMS analysis (figure A4.2a) and showed no evidence of the monometallic species.

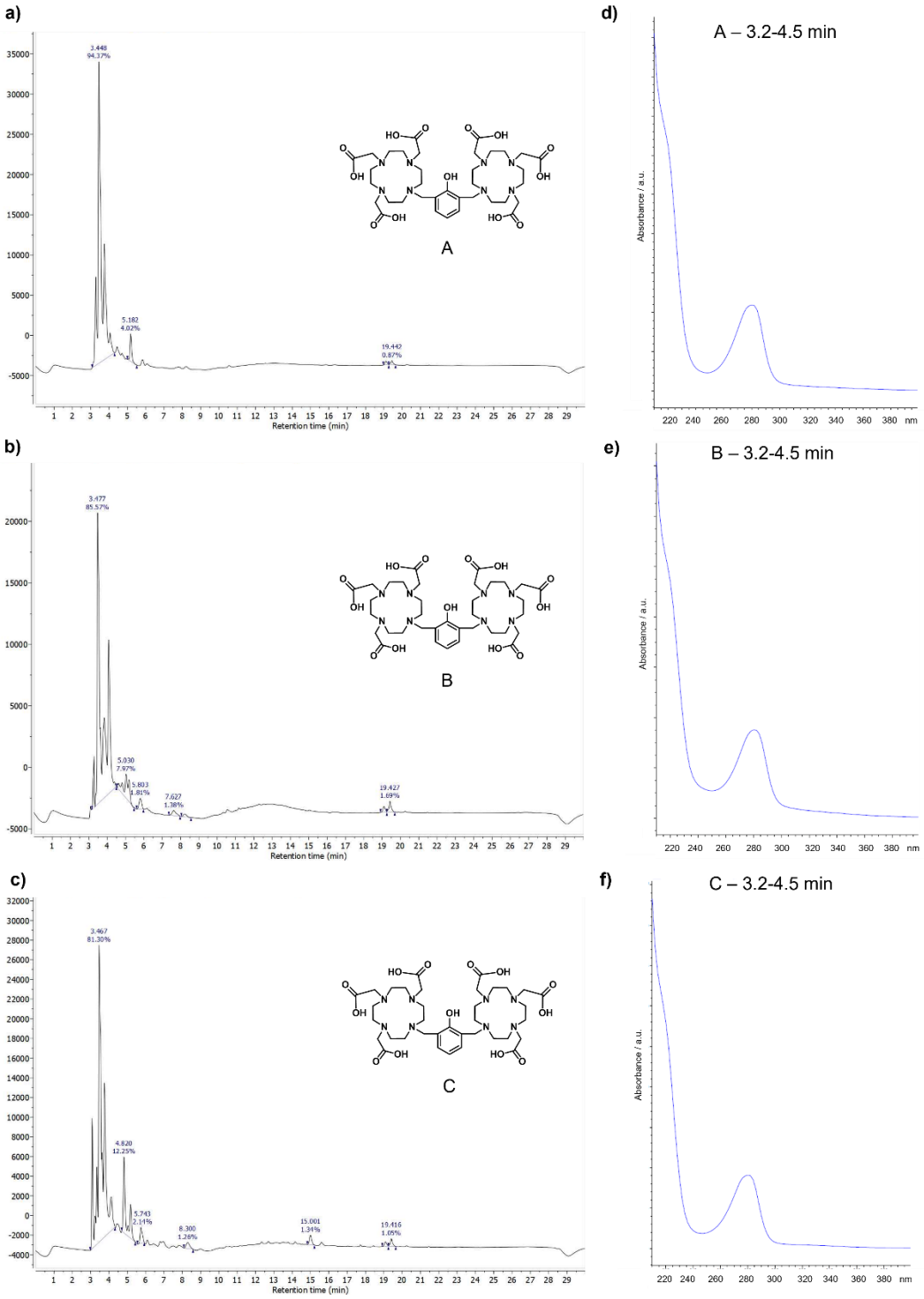

Figure 4.19: a-c) The total absorbance chromatogram from HPLC analysis of the OH ligand **100**, batches A-C (20 µL injection, method 4). d-f) Extracted UV traces, from batches A-C, averaged across the range R_t 3.2-4.5 min.

The ^{1}H NMR spectrum of **93Tb** batch B was measured in D_2O at 500 MHz (Figure 4.20a) and contained approximately 60 peaks (in the region 600 to -600 ppm), most of which appeared sharp, indicative of a rigid structure. There are several possible conformations

for TbTbOH (Figure 4.20b) which could give rise to at least 103 possible peaks (not including the possibility of difference between Δ-SAP-Λ-SAP, Δ-SAP- Δ-SAP and Λ-SAP-Λ-SAP conformations), many of which may overlap or be unresolved in the 50 to -50 ppm region. Variable temperature (VT) NMR could be carried out in the future to deconvolute the spectrum.

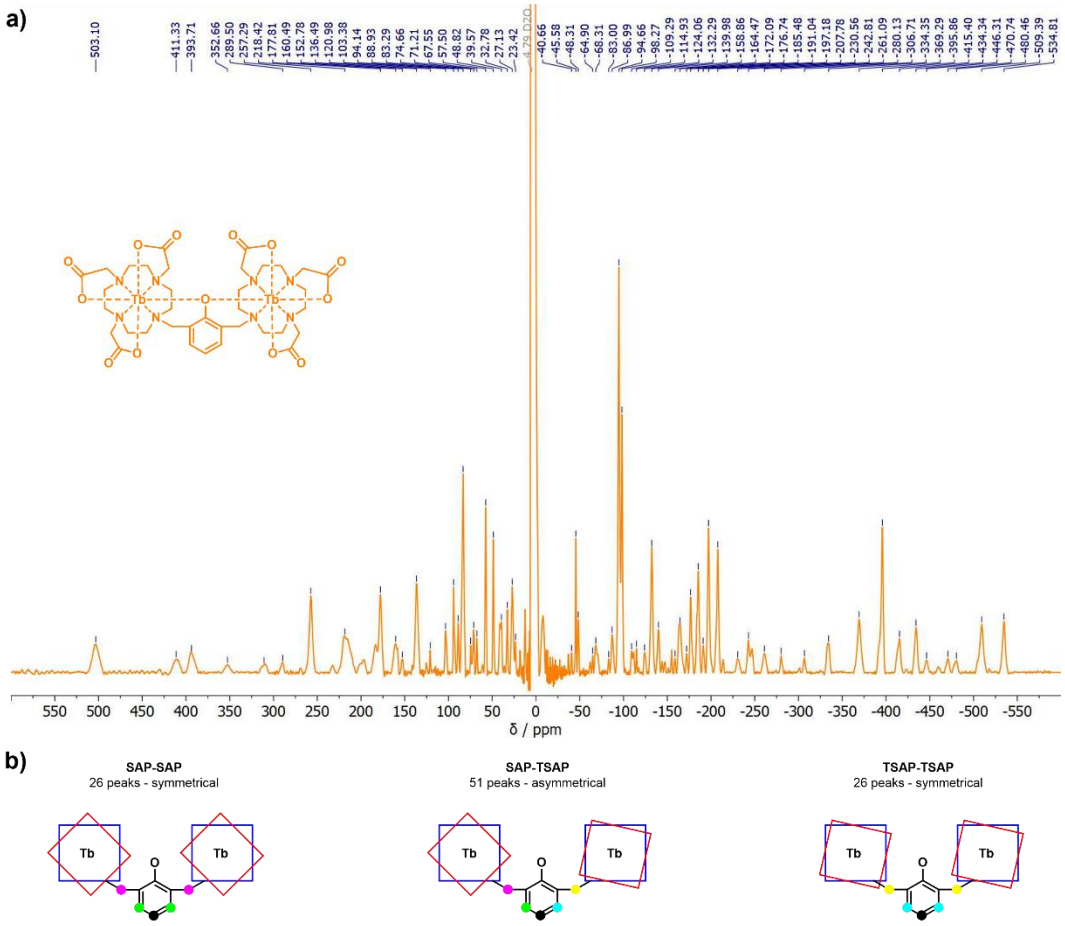

Figure 4.20: a) The ^{1}H NMR spectrum of TbTbOH **93Tb** batch B in D_2O measured at 500 MHz. b) A diagram to show the possible different conformations of TbTbOH and the different possible number of peaks it contributes to the NMR spectrum, with different coloured dots to show different environments for the bridging phenol moiety. This does not take into account possibilities in differing chirality between two SAP or two TSAP conformations.

Analysis of the peaks from the analytical HPLC traces of the two batches of TbTbOH (Figure 4.21) suggests that the final material contains two major species with two different extracted UV traces (with similar spectra observed at different retention times). These different retention times may be observed (under acidic conditions, 0.1% formic acid) due to differences in protonation and interaction of different conformational isomers with the column, as reported previously for other lanthanide complexes.[79] In addition, previous

reports on binuclear lanthanide complexes containing bridging phenol chromophores show that pH-dependent binding of the phenolate arm to the lanthanide centre occurs.[40, 72, 80] From the HPLC traces of TbTbOH reported here, the first species (Figure 4.21c) has an extracted UV trace with maxima around 240 nm (π→π*) and 300 nm (n→π*), whilst the second species (Figure 4.21d) has an extracted UV trace with maxima around 235 nm (π→π*) and 285 nm (n→π*) – these differences may occur due to changes in protonation. Both species have UV traces which exhibit red shifting from the spectrum of the phenol ligand, suggesting that the lanthanide centres present are interacting with the bridging phenol to some extent. The reported UV-Vis spectrum for TbTbOH[78] contains maxima at 238 nm and 290 nm, which suggests that the previously reported TbTbOH contained a mixture of the two species as observed here. Despite the multiple species present, TbTbOH **93Tb** batch B was used for photophysical characterisation for comparison to the previously reported properties. In future, analysis using IR spectroscopy could assist with determining conversion between **99** and **100** and formation of the terbium complex **93Tb**, as changes in the carbonyl stretching frequencies are expected upon removal of the protecting groups and upon complexation – a shift to lower wavenumber is expected due to weakening of the C=O bond.

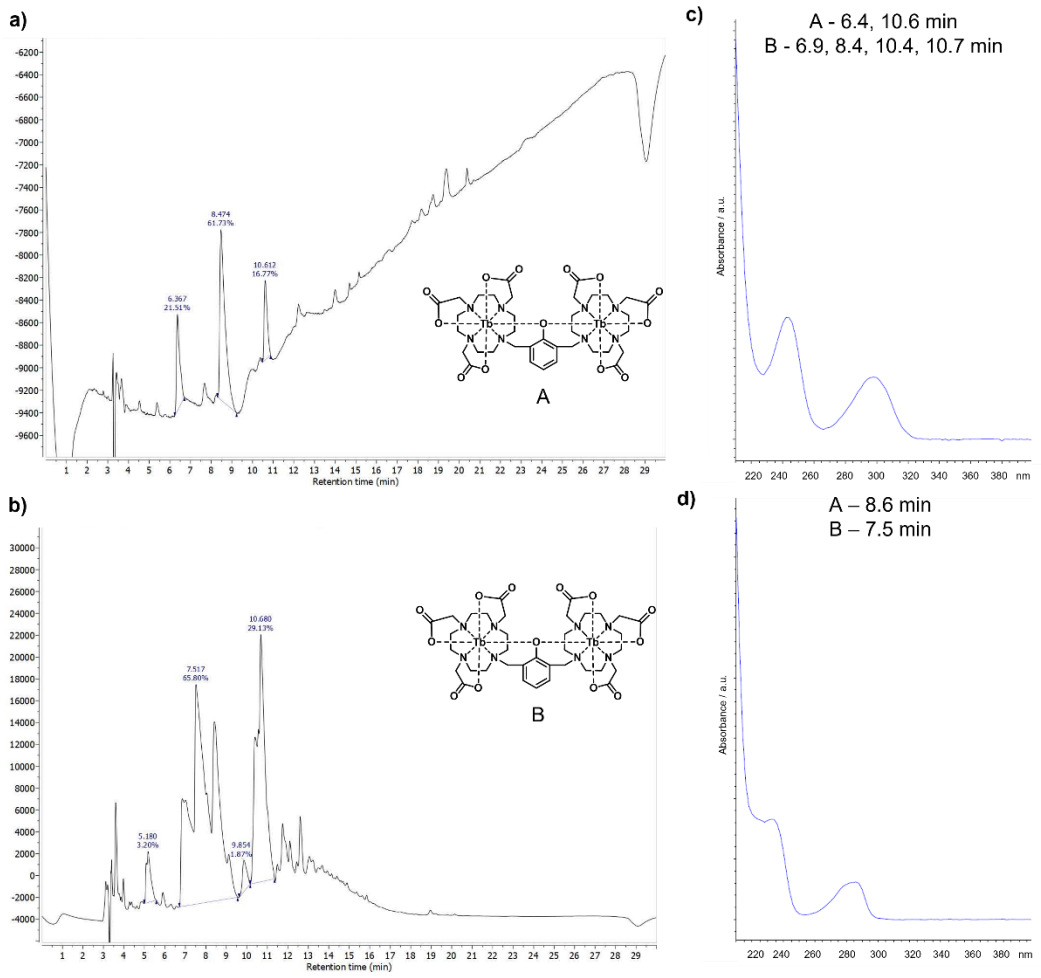

Figure 4.21: a-b) The total absorbance chromatogram from HPLC analysis of two batches of TbTbOH **93Tb**, A and B (20 µL injection, method 4, acidic conditions). c) Extracted UV trace which is representative of the peaks at R_t 6.4 and 10.6 min from batch A and R_t 6.9, 8.4, 10.4 and 10.7 min from batch B. d) Extracted UV trace which is representative of the peaks at R_t 8.6 min from batch A and R_t 7.5 min from batch B.

As the ^{1}H NMR spectrum for the terbium analogue was not previously fully reported, the lutetium analogue LuLuOH **93Lu** was synthesised for ease of comparison as a diamagnetic analogue, using hexaacid **100** batch C. Product formation was validated by HRMS analysis (Figure A4.2b). The sharpness of the aromatic peaks in the ^{1}H NMR spectrum (Figure 4.22) upon complexation indicates that a more rigid structure has been formed, with the splitting pattern of doublet:doublet:triplet observed indicating that each aromatic proton is in a different chemical environment and that the average conformation is not planar – this splitting pattern was observed previously for LuLuOH at 120 °C in DMSO.[78]

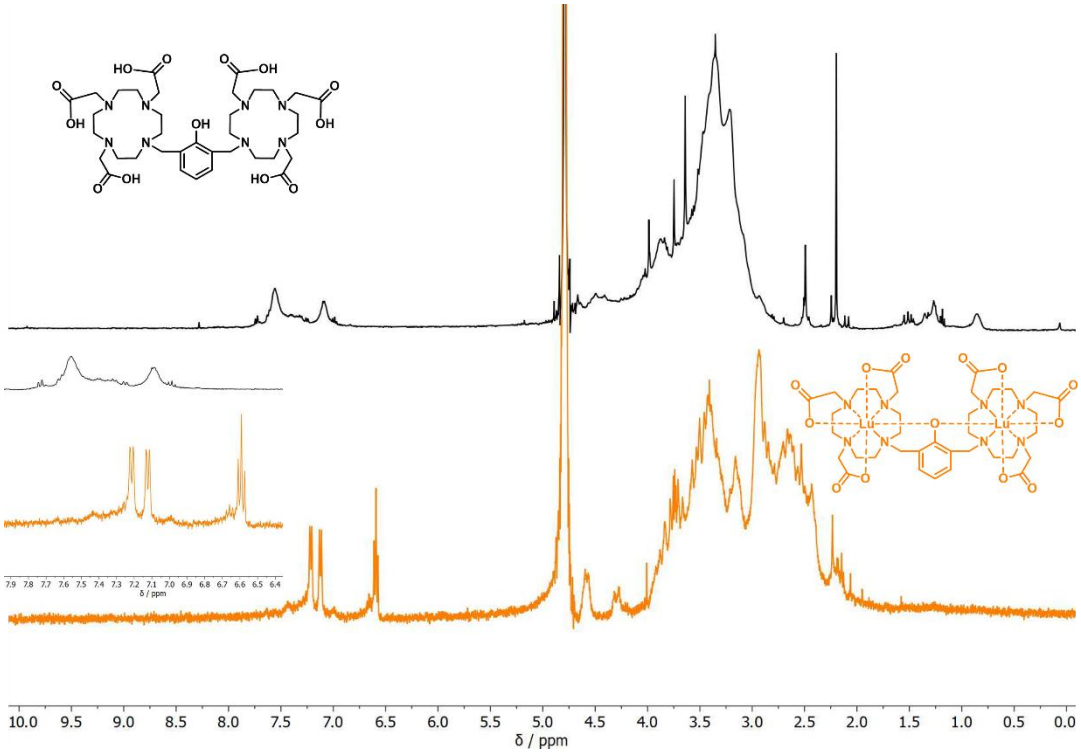

Figure 4.22: The ^{1}H NMR spectra of LuLuOH **93Lu** (orange) compared to its ligand (black) to highlight the change upon complexation – both complexes in D_2O, measured at 400 MHz.

In contrast to TbTbOH batch B, the LuLuOH complex purified by dialysis was determined to be sufficiently pure by analytical HPLC as it contained one major peak (97% pure, Figure 4.23), with the extracted UV trace from R_t 5.9 min (Figure 4.23b) matching the expected UV trace with absorption maxima around 240 nm and 300 nm. This result is consistent with either greater purity of the hexaacid precursor used (resulting in purer LuLuOH than TbTbOH), despite similar analytical HPLC traces of batches A-C of **100** (Figure 4.19), or different ratios of conformations present due to the different sizes of the lanthanide ions – Pope *et al.*[72] reported that a similar ytterbium-containing complex may exist in solution as a species where the bridging phenolate binds only to one of the ytterbium centres.

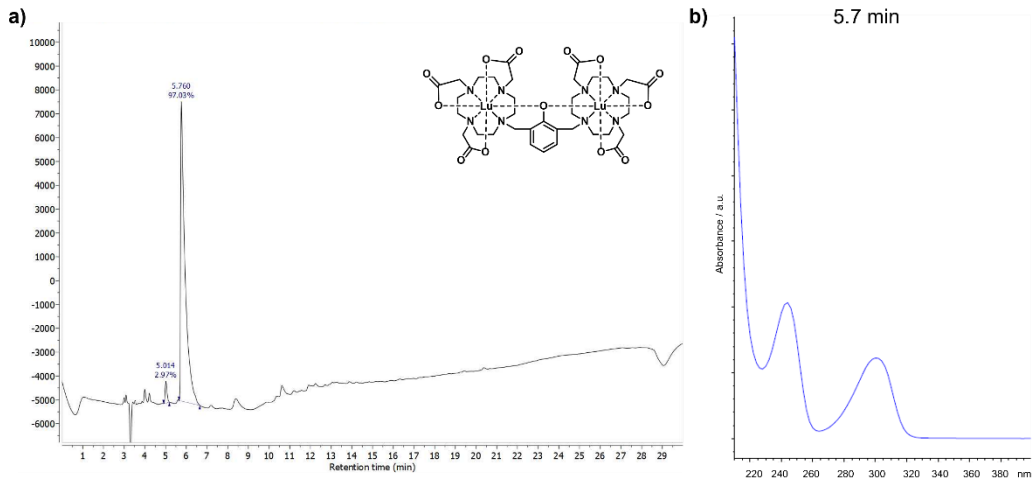

Figure 4.23: a) The total absorbance chromatogram from HPLC analysis of LuLuOH **93Lu** (20 µL injection, method 4). b) Extracted UV trace of the peak at R_t 5.7 min.

Prior to attempting azobenzene formation with TbTbOH and the Fmoc-protected leucine aniline compound **88**, synthesis of TbTbAzoNO_2 **94** was carried out on a 20 mg scale according to the literature procedure, using 1 M HCl.[77, 78] A deep red colour was formed upon addition of the basic phenolate solution to the diazotised 4-nitroaniline solution, indicative of formation of an azobenzene species. The mass of the complex was observed by ESI mass spectrometry, however EI mass spectrometry did not detect the product but detected remaining TbTbOH starting material, suggesting that the azobenzene formation reaction did not proceed to completion. Nevertheless, the reaction mixture was pH adjusted and purified by dialysis (1000 Da molecular weight cut-off) to remove excess small organic reagents and byproducts. Some of the resulting material was not fully soluble in aqueous solution therefore it was collected separately to the soluble fraction and analysed separately, with the water-soluble fraction labelled A and the less soluble fraction labelled B. The resulting yield of complex was low (3 mg, 18%, fraction A and 2 mg, 12%, fraction B) and the material obtained was impure as dialysis cannot remove remaining unreacted TbTbOH. High-resolution mass spectrometry (using ESI, Figure 4.24) detected the desired product (negative mode, *m/z* 1270) in both fractions, however other fragments and impurities were observed including remaining TbTbOH (*m/z* 1121) and TbTbNHNHNO_2 (*m/z* 1272), which may have formed due to photo-induced reduction of the azo N=N bond.

Further analysis using IR spectroscopy could be carried out to confirm presence or reduction of the N=N bond.

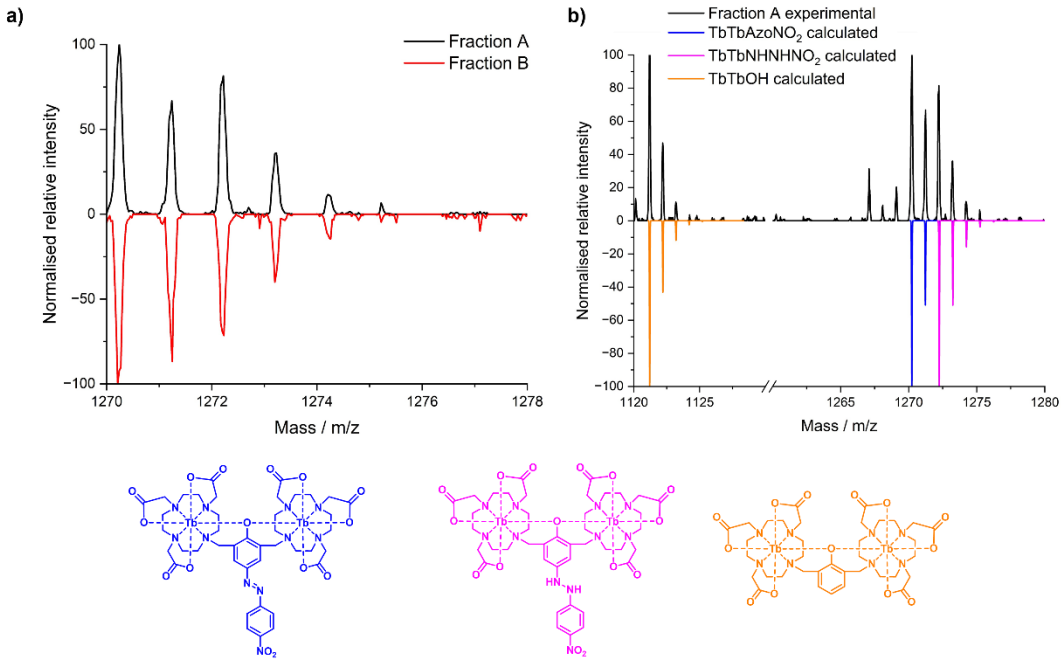

Figure 4.24: Analysis of the negative mode HRMS spectra (ESI) of the synthesised $TbTbAzoNO_2$ **94** fractions. a) Comparison of fraction A (black) and fraction B (red) to show that they appear similar by HRMS. b) Compared of $TbTbAzoNO_2$ **94** fraction A experimental spectrum (black) to the calculated spectra of TbTbOH (orange, **93Tb**), $TbTbNH_2$ (red), $TbTbNHNHNO_2$ (bright pink) and $TbTbAzoNO_2$ (blue). The experimental spectra are normalised to 100 for the peak at 1270 corresponding to $TbTbAzoNO_2$.

To evaluate the level of impurity in the fractions of $TbTbAzoNO_2$ **94** further, analytical HPLC was carried out (method 4) on both fractions, with fraction A dissolved in H_2O and fraction B dissolved in H_2O/MeOH (Figure 4.25). Due to the increased hydrophobicity of the molecule due to the addition of the extra aromatic group, a higher retention time is expected than observed for TbTbOH (**93Tb**, 6-11 minutes) or LuLuOH (**93Lu**, 5 minutes). As predicted, several peaks are observed for both fractions, including peaks with retention times between 14 and 20 minutes.

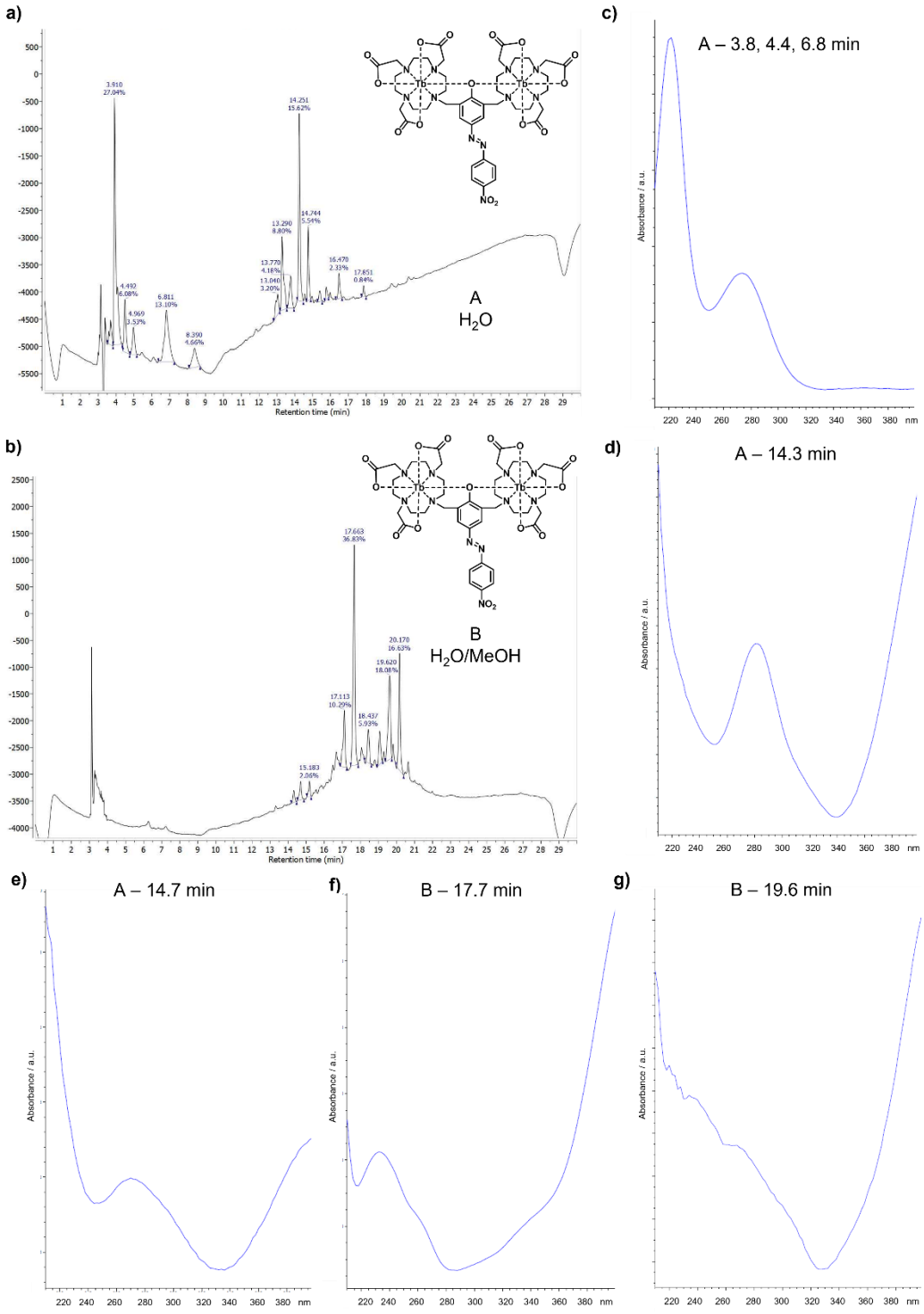

Figure 4.25: a-b) The total absorbance chromatogram from HPLC analysis of two fractions of the synthesised TbTbAzoNO$_2$ **94**, A and B (20 µL injection, method 4), injected in H_2O (A) or H_2O/MeOH (B). c) Extracted UV trace which is representative of the peaks at R_t 3.8, 4.4 and 6.8 min from A. d) Extracted UV trace of the peak at R_t 14.3 min from A. e) Extracted UV trace of the peak at R_t 14.7 min from A. f) Extracted UV trace of the peak at R_t 17.7 min from B. g) Extracted UV trace of the peak at R_t 19.6 min from B. Batch B's HPLC trace contains peaks at 3 minutes however this was found to be due to peaks in the blank run.

Fraction A contained several peaks in the range 3-6 minutes which had an extracted UV trace (Figure 4.25c) similar to that of TbTbOH or its ligand, with maxima at 220 nm and 280

nm. Fraction A and fraction B both contained multiple peaks with retention times above 14 minutes (Figure 4.25d-f) with extracted UV traces containing maxima above 380 nm indicative of azobenzene π→π* transitions. The peak at 14.3 minutes in the HPLC trace of fraction A (Figure 4.25d) matched the reported UV-Vis spectrum of TbTbAzoNO_2 most closely, with maxima observed at approximately 280 nm and above 380 nm (reported shoulders/maxima at 238 nm, 285 nm and 417 nm).[78] Exact comparison to the available UV-Vis spectra was not possible using analytical HPLC as the detector is limited to the range 200-400 nm. Fraction A of the synthesised TbTbAzoNO_2 was used for photophysical characterisation (section 4.3.4) for comparison to its previously reported photophysical properties, TbTbOH **93Tb**, and TbTbAzo **53**, despite its impurities.

The azobenzene formation of TbTbOH **93Tb** with the Fmoc-protected leucine aniline compound **88** to form the desired TbTbAzoLeu complex **56** (after Fmoc deprotection) was attempted both in water only (as for TbTbAzoNO_2) and in a mixture of water and acetone. When the azobenzene formation reaction was carried out in water only no characteristic change in colour to dark red was observed upon addition of the diazotised aniline species to the basic solution of TbTbOH and the mass of the Fmoc-protected TbTbAzoLeu intermediate was not observed by LRMS or HRMS (EI or ESI). Repetition of the reaction in a mixture of water and acetone aided solubility and led to the expected colour change upon addition to the basic TbTbOH solution, however no product was observed by HRMS or LCMS analysis, with only the aniline starting material and TbTbOH observed. The lack of formation of the desired intermediate under these conditions may be due to balancing the issues of solubility with the correct pH and conditions for formation and further optimisation of reaction conditions is required.

4.3.3 Synthesis of control complexes

4.3.3.1 Synthesis and evaluation of the aniline positive control

For use as a positive control for reductive assays and photophysical characterisation, $TbTbNH_2$ **54** was synthesised from the triester intermediate **63** used in the attempted synthesis of the leucine complex (Scheme 4.7). Standard TFA deprotection conditions in CH_2Cl_2 were used to give the amine triacid **101** and subsequent reaction with terbium triflate and purification by dialysis (1000 Da cut-off) yielded the positive control $TbTbNH_2$ **54** as a purple solid in good yields (48%), following the previously reported procedures.[42] Product formation was confirmed by HRMS analysis (Figure A4.2c) and ^{1}H NMR analysis (Figure 4.26).

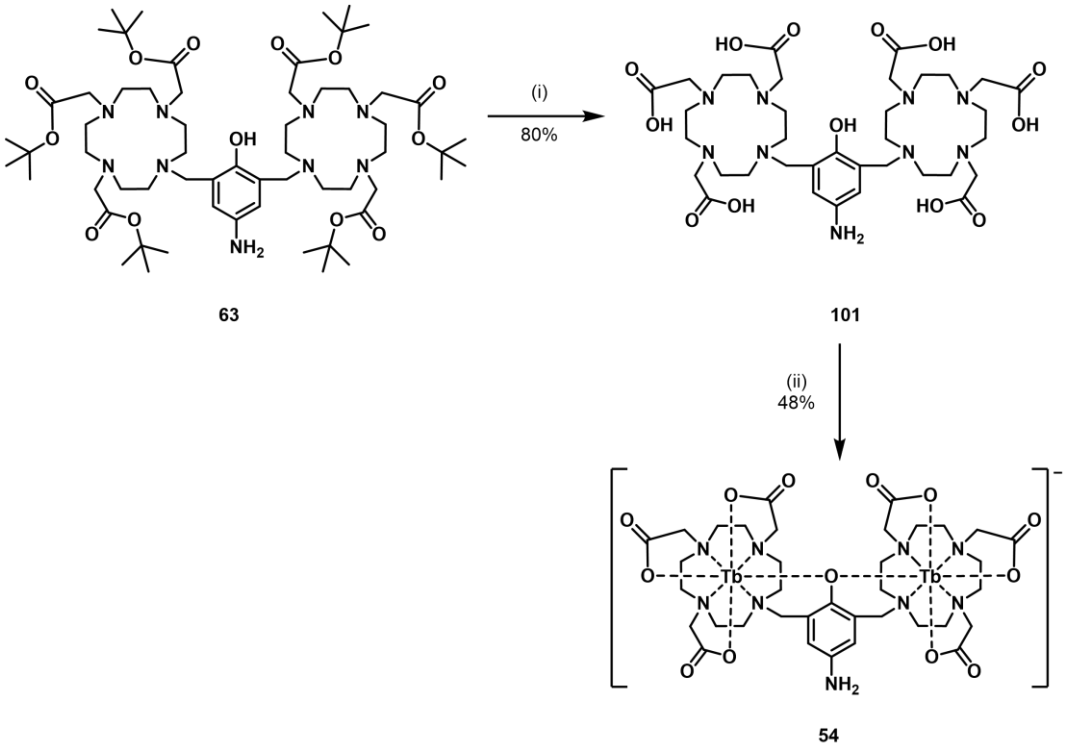

Scheme 4.7: The synthesis of the positive control $TbTbNH_2$ **54**. Reagents and conditions: i) TFA, CH_2Cl_2, rt, 18 h; ii) $Tb(OTf)_3$, NaOH (1 M), H_2O, rt, 4 days.

The ^{1}H NMR spectrum of $TbTbNH_2$ **54** was measured at 500 MHz in D_2O (Figure 4.26, dark red) and compared to that previously reported (Figure 4.26, black) to confirm and evaluate the success of the formation *via* reduction of the nitro group (as opposed to reduction of the azide moiety reported previously). The spectra generally matched well, with some

differences observed which may be due to differences in concentration of the samples and baseline correction and phasing of the spectra. Approximately 50 peaks were observed (excluding any peaks in the 50 to -50 ppm region which may be obscured by phasing of the broad water signal), consistent with a mixture of conformational isomers being present (SAP-SAP, TSAP-TSAP and SAP-TSAP) as observed with TbTbOH. The ^{1}H NMR spectrum of an older sample of $TbTbNH_2$ was evaluated (Figure 4.26, purple) and a large difference in the spectrum was observed, in comparison to other batches, which is expected as aniline complexes are known to undergo slow degradation/oxidation over time, therefore the old sample may contain amounts of nitroso, hydroxylamine and nitro species.

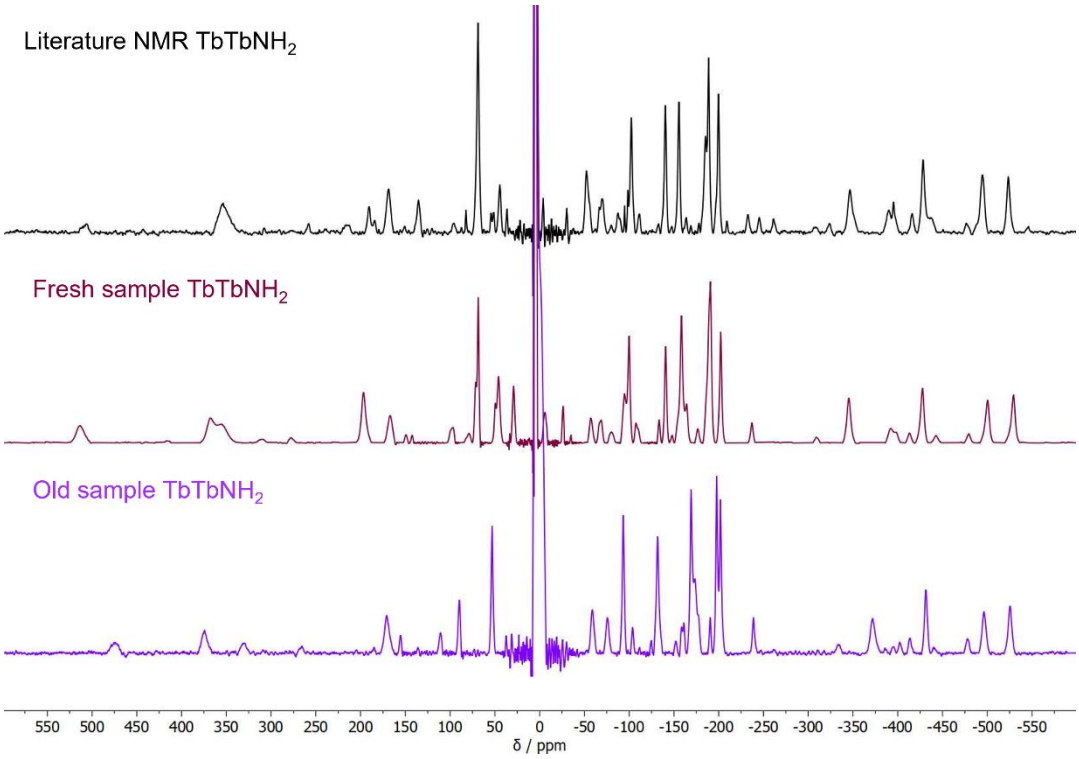

Figure 4.26: The ^{1}H NMR spectra of $TbTbNH_2$ **54** in D_2O measured at 500 MHz, comparing the previously reported spectrum (black), a fresh sample of $TbTbNH_2$ (dark red) and an old sample (purple, NMR carried out several months after synthesis, purification and lyophilisation).

The purity of the resulting $TbTbNH_2$ material was analysed by analytical HPLC using the method reported previously (method 4) for these bimetallic complexes.[42, 46] The HPLC trace suggested that the complex was formed in good purity (92% from the total absorbance chromatogram) with a retention time of 3.3 minutes (Figure 4.27a) and an extracted UV trace (Figure 4.27b) that matched the UV-Vis spectrum reported previously.

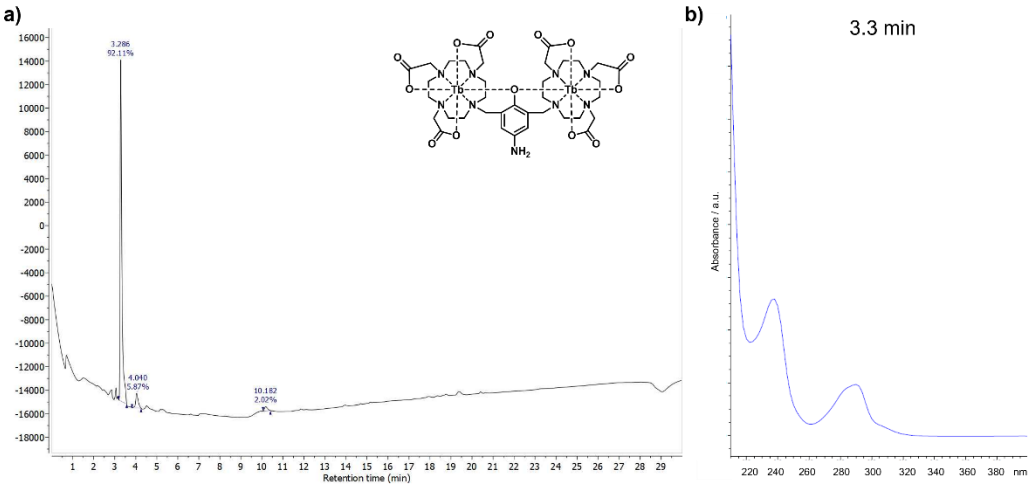

Figure 4.27: a) The total absorbance chromatogram from HPLC analysis of $TbTbNH_2$ **54** (20 µL injection, method 4). b) Extracted UV trace of the peak at R_t 3.3 min.

4.3.3.2 Synthesis and evaluation of the simple azobenzene control

TbTbAzo **53** was synthesised (Scheme 4.8), according to previous procedures,[42, 46] to be used as a control for reductive assays and photophysics. The synthetic route involved the formation of the azobenzene moiety, in water only, to give **102** and subsequent reactions involved TBDMS protection of the alcohol to give **103**, radical bromination to give **104**, alkylation of the DO3A triester **23** to give **105**, deprotection to give the triacid **106** and complexation and purification by dialysis (1000 Da cut-off) to yield TbTbAzo **53** in an overall yield of 3% across 6 steps. Product formation was validated by HRMS analysis (Figure A4.2d). The ^{1}H NMR spectrum of TbTbAzo was not recorded due to low solubility in D_2O, consistent with literature reports.

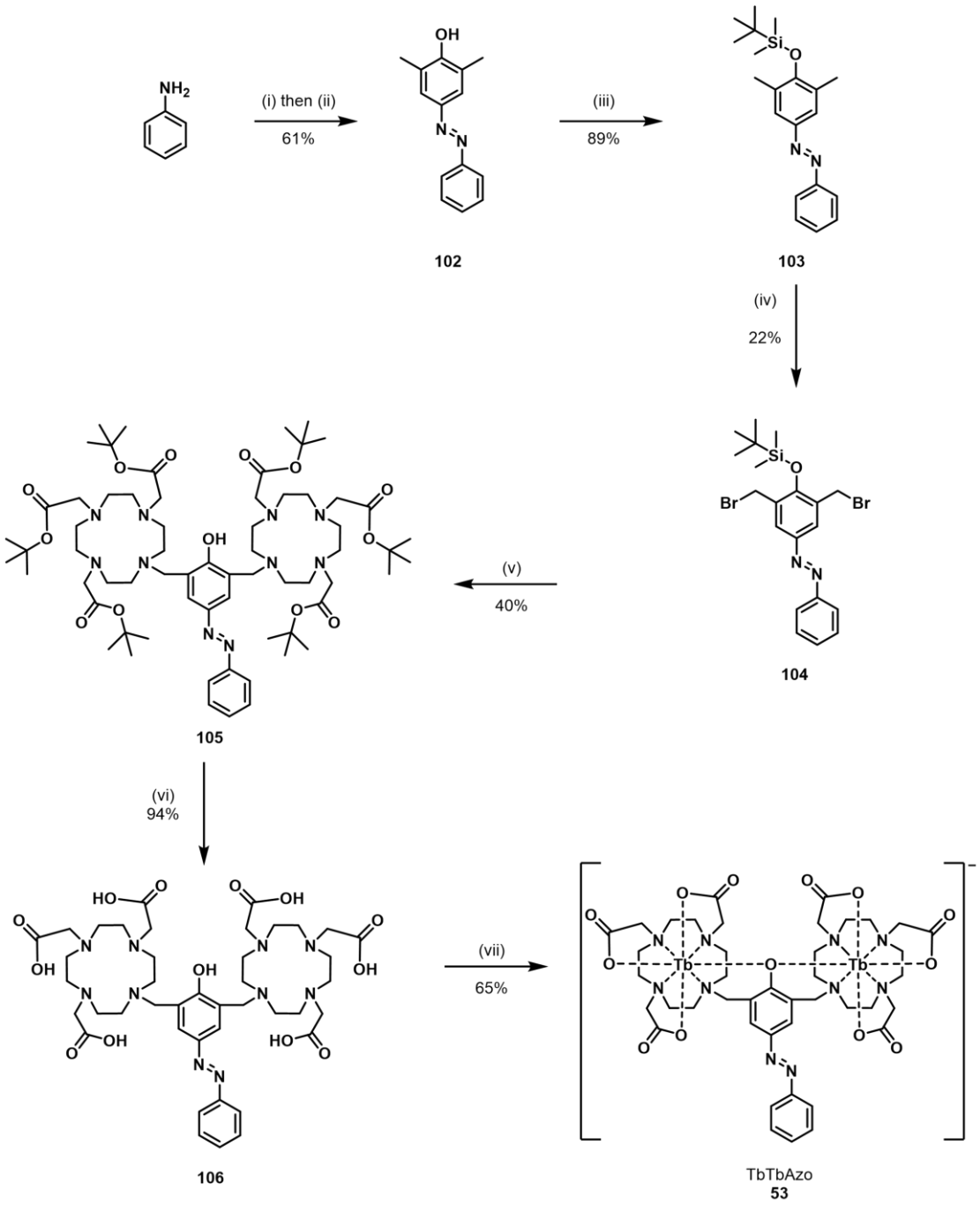

Scheme 4.8: The synthesis of the standard azobenzene complex TbTbAzo **53**, previously reported by Simms et al.[42, 46] Reagents and conditions: i) HCl (1 M), $NaNO_2$, H_2O, 0 °C, 10 min; ii) 2,6-dimethylphenol, NaOH, H_2O, EtOH, rt, 1 h; iii) TBDMSCl, imidazole, DMF, rt, 18 h; iv) NBS, benzoyl peroxide, CCl_4, 92 °C, 3 h; v) **23**, Na_2CO_3, MeCN, 60 °C, 40 h; vi) TFA, CH_2Cl_2, rt, 18 h; vii) $Tb(OTf)_3$, NaOH (1 M), H_2O, 50 °C, 4 days.

The purity of TbTbAzo **53** was evaluated by analytical HPLC (method 4) and was determined to be 95% pure (by total absorbance) with a retention time of 13.8 minutes (Figure 4.28a) and an extracted UV trace (Figure 4.28b) which roughly matched the literature UV-Vis spectrum, with maxima around 270 nm and 370 nm. The literature HPLC trace of TbTbAzo, using the same method, contained two peaks with retention times of 15.3

and 15.5 minutes attributed to the E and Z isomers of the azobenzene moiety.[42, 46] The differences observed here (one peak and shorter retention time) may be attributed to a different ratio of E/Z isomerism or overlapping peaks from E/Z isomers and the shorter retention time may be observed due to use of a new HPLC column. The peak in the total absorbance chromatogram at a retention time of 3.1 minutes is likely an artefact as it was generally removed by subtraction of a blank sample (Figure A4.3), however the peak was still observed at 220 nm – this may be indicative of a small amount of contamination with $TbTbNH_2$ by degradation.

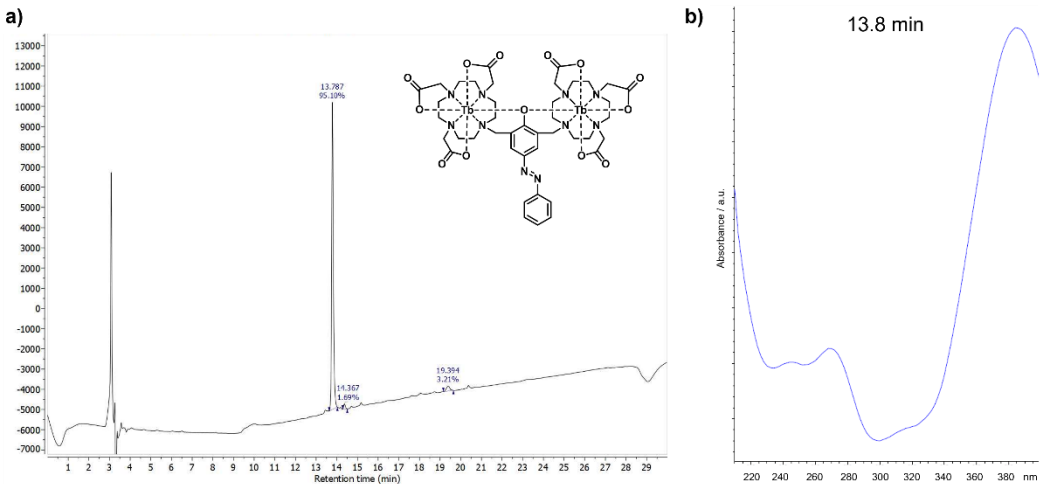

Figure 4.28: a) The total absorbance chromatogram from HPLC analysis of TbTbAzo **53** (20 µL injection, method 4). b) Extracted UV trace of the peak at R_t 13.8 min. The peak at 3 min is mostly an artefact from the lack of blank subtraction but may indicate a small amount of $TbTbNH_2$ present due to degradation.

4.3.4 Photophysical characterisation of bimetallic complexes

Photophysical characterisation of TbTbOH batch B **93Tb**, LuLuOH **93Lu**, $TbTbAzoNO_2$ batch A **94**, $TbTbNH_2$ **54** and TbTbAzo **53** were carried out for validation of their formation by comparison to previously reported data.[42, 77, 78] Measurements were generally carried out at 90 µM in PBS buffer (10 mM, pH 7.4) for comparison to the literature[42] and between complexes, except for lifetime analysis of TbTbOH which was carried out in water for comparison to previous work.[78]

UV-Vis analysis of $TbTbNH_2$ **54** and TbTbAzo **53** (Figure 4.29a) showed similarly shaped spectra to that previously reported, with $TbTbNH_2$ **54** containing two maxima at 248 nm and

310 nm. The spectrum of TbTbAzo contains a maximum at 364 nm, corresponding to the π→π* transition, with a shoulder around 445 nm corresponding to the n→π* transition. The presence of the electron withdrawing azo group in comparison to the electron donating aniline group (para to the phenolate) causes the red shifting of the transitions related to the central aromatic ring. The UV-Vis spectra of TbTbOH **93Tb** (batch B) and LuLuOH **93Lu** (Figure 4.29b) appear similar in shape as expected, with maxima at 236, 288 and 300 nm for TbTbOH or 244 and 296 nm for LuLuOH, consistent with previous reports. The spectrum of LuLuOH shows higher absorbance and more well-defined peaks compared to TbTbOH due to the presence of only one peak in the analytical HPLC trace (compared to over three for TbTbOH), suggestive of the presence of one species. The spectrum of $TbTbAzoNO_2$ **94** (batch A) is also consistent with the literature spectrum, with maxima at 268 nm and approximately 400 nm. The more red-shifted transitions observed for $TbTbAzoNO_2$ **94** compared to TbTbAzo **53** are consistent with introduction of the electron withdrawing nitro group para to the azobenzene linkage. Further analysis (emission spectra) was not carried out on batch A of $TbTbAzoNO_2$ due to its high level of impurity according to analytical HPLC.

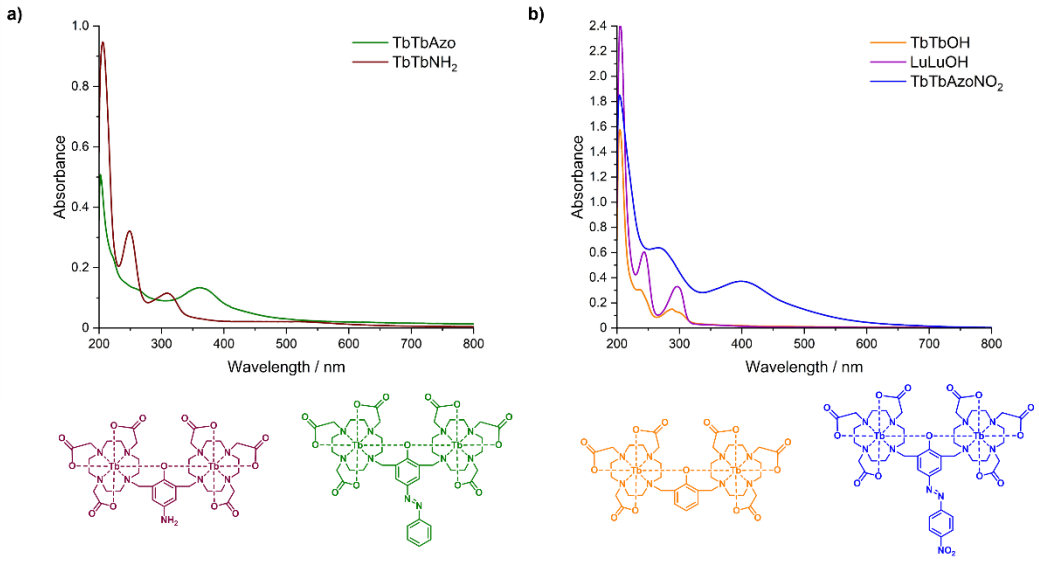

Figure 4.29: The UV-Vis spectra of a) TbTbAzo **53** (green) vs $TbTbNH_2$ **54** (red) and b) TbTbOH **93Tb** (batch B, orange) and LuLuOH **93Lu** (purple) vs $TbTbAzoNO_2$ **94** (batch A, blue) at 90 µM in PBS (10 mM, pH 7.4).

Steady-state emission spectra (Figure 4.30), for comparison between TbTbOH **93Tb**, $TbTbNH_2$ **54** and TbTbAzo **53**, were measured upon excitation at 294 nm (maxima of

TbTbOH chromophore), 318 nm (within the absorbance band of the $TbTbNH_2$ chromophore) and 488 nm (direct terbium excitation, $^5D_4 \leftarrow {}^7F_6$, avoiding excitation of the azobenzene chromophore). As expected from the absorbance spectrum, excitation at 294 nm (Figure 4.30a) gave intense terbium emission from $TbTbNH_2$ **54** and TbTbOH **93Tb** whereas little emission was observed for TbTbAzo **53**. A similar trend was observed upon excitation at 318 nm (Figure 4.30b), however weaker luminescence of $TbTbNH_2$ was observed due to its lower absorbance at this wavelength. Therefore, exciting the chromophores of $TbTbNH_2$ **54** and TbTbOH **93Tb** may be used to sensitise terbium emission. The antenna effect was validated for TbTbOH **93Tb** upon comparison of excitation at 238 nm, 296 nm and 488 nm (Figure A4.4). Excitation of the chromophore of TbTbAzo **53** at 364 nm (π→π*, Figure A4.5) gave weak terbium emission, suggesting that the azobenzene ligand is a poor sensitiser of terbium emission, and the spectrum was dominated by weak ligand fluorescence. Excitation of **53** at 294 nm or 318 nm gave greater emission intensity than excitation at 364 nm, which suggests that a small amount of $TbTbNH_2$ was present in the sample due to degradation. Direct excitation of terbium (488 nm, $^5D_4 \leftarrow {}^7F_6$) gave rise to emission in the case of $TbTbNH_2$ **54** and TbTbOH **93Tb** with almost no emission observed for TbTbAzo **53** and is consistent with the general emission trend $TbTbNH_2$>TbTbOH>TbTbAzo, which is also observed under UV lamp irradiation (254 nm) of the cuvettes (Figure 4.30d). This trend in emission and sensitisation is consistent with a change in triplet energy level of the chromophore based on the electron donating or electron withdrawing power of the substituent para to the coordinating phenol. The time-gated emission spectra upon excitation at 294 nm, 318 nm or 488 nm (Figure A4.6) displayed similar trends in emission intensity.

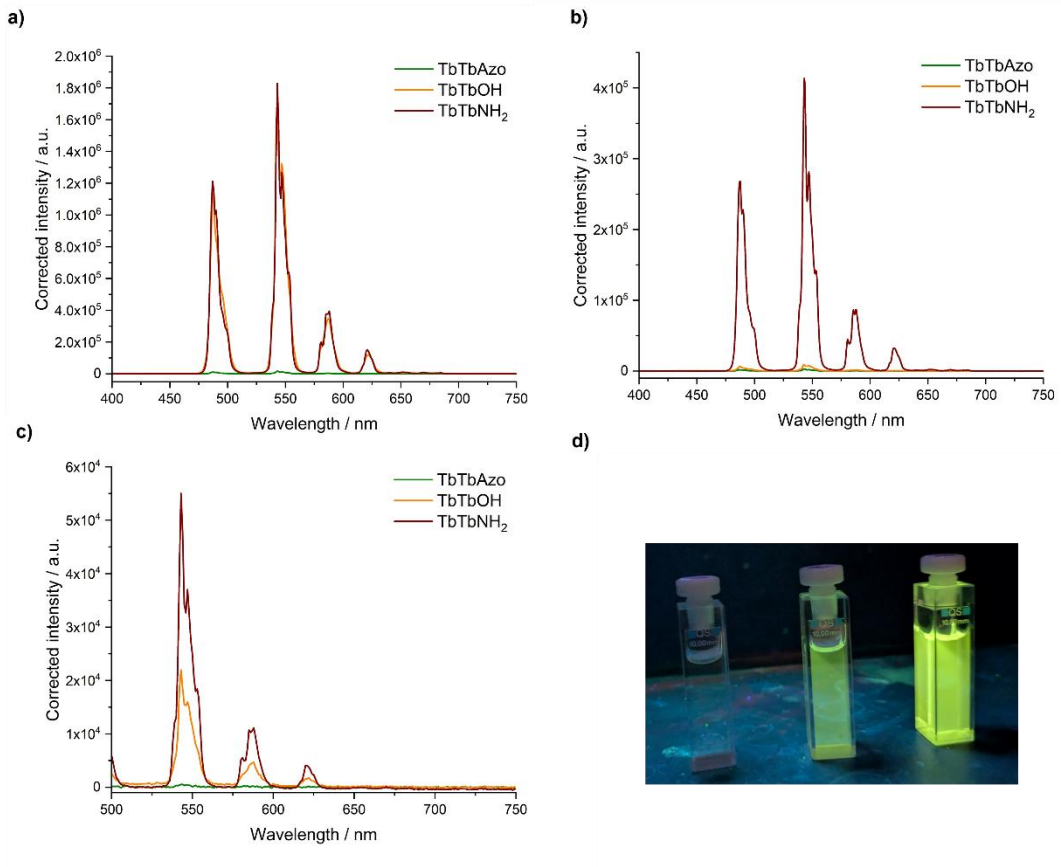

Figure 4.30: Steady state emission spectra of TbTbAzo **53** (red), TbTbOH **93Tb** (orange) and $TbTbNH_2$ **54** (green) at 90 µM in PBS (10 mM, pH 7.4). a) λ_{ex} 294 nm, 400 nm filter, slits 3 / 1 nm; b) λ_{ex} 318 nm, 400 nm filter, slits 1 / 1 nm; c) λ_{ex} 488 nm, 495 nm filter, slits 5 / 1 nm. d) Photo of cuvettes under 254 nm UV lamp, from left to right TbTbAzo, TbTbOH, $TbTbNH_2$.

The excitation spectra of TbTbAzo **53**, $TbTbNH_2$ **54** and TbTbOH **93Tb** were measured, between 240 nm and 450 nm, whilst monitoring the 545 nm transition ($^5D_4 \rightarrow {}^7F_5$) and the normalised excitation spectra were compared to their normalised UV-Vis spectra (Figure 4.31) to examine the effect of ligand sensitisation on terbium emission. The excitation spectrum of TbTbAzo **53** (Figure 4.31a) showed that no terbium emission is observed due to sensitisation of the azobenzene ligand and any emission may occur due to presence of a small amount of $TbTbNH_2$ **54** impurity, due to the peak at 300 nm. This is consistent with the greater steady-state emission observed upon excitation at 294 nm and 318 nm compared to previous reports[42] and a very small amount of $TbTbNH_2$ **54** present in the sample could cause large changes in the spectra due to its high reported quantum yield (45% upon excitation at 310 nm).[42] The excitation spectra of $TbTbNH_2$ **54** (Figure 4.31b) and TbTbOH **93Tb** (Figure 4.31c) overlay well with their absorbance spectra, giving further

evidence that the chromophores can efficiently sensitise terbium by energy transfer processes. The excitation spectrum of TbTbOH (Figure 4.31c) suggests that it contains multiple species but only one species can sensitise terbium, consistent with previous findings on the multiple possible species of $LnLnNH_2$.[80]

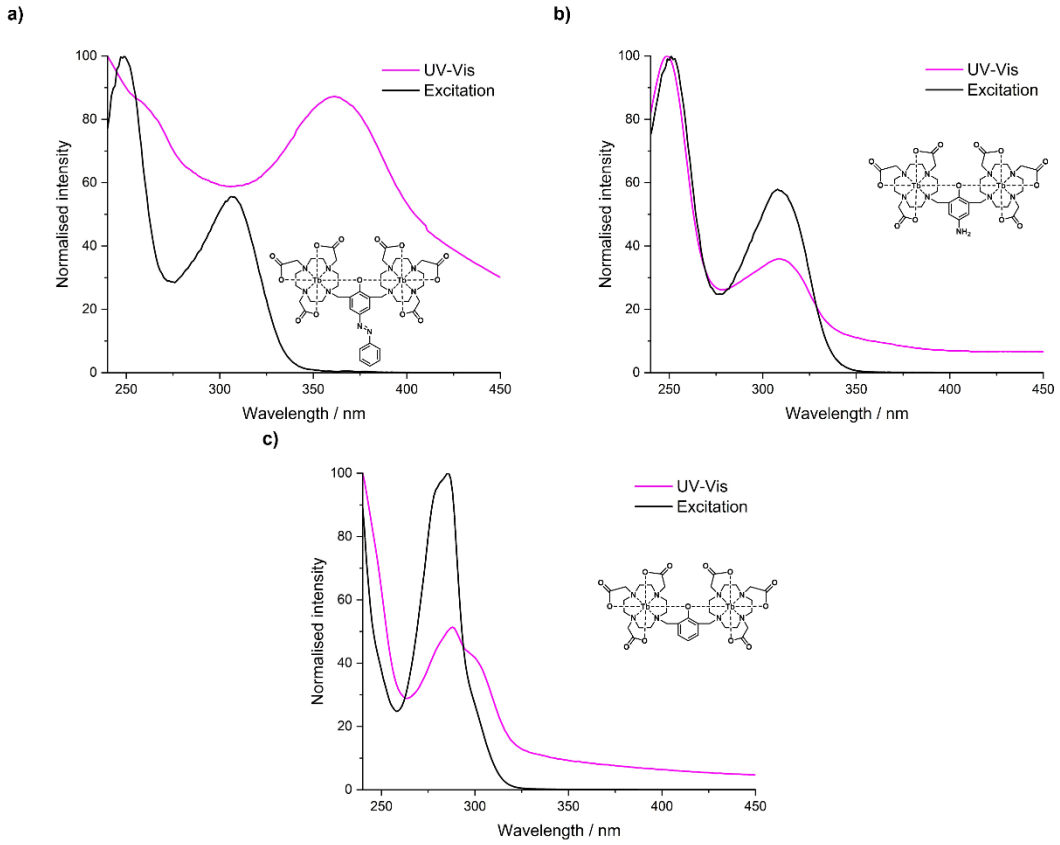

Figure 4.31: The UV-Vis (pink) and excitation (black) spectra of a) TbTbAzo **53**, b) $TbTbNH_2$ **54**, and c) TbTbOH **93Tb**. All complexes 90 µM in PBS (10 mM, pH 7.4), λ_{em} 545 nm, λ_{ex} 240-450 nm, 400 nm filter, a) slits 1 / 10 nm, b) slits 1 / 1 nm, c) slits 1 / 3 nm.

The luminescence lifetimes of TbTbAzo **53**, $TbTbNH_2$ **54** and TbTbOH **93Tb** (monitoring at 545 nm, $^5D_4 \rightarrow {}^7F_5$) were evaluated at 90 µM in water (for TbTbOH) or PBS (10 mM, pH 7.4) upon excitation of the ligand or direct metal excitation, plotted against a logarithmic scale and compared to previous reported values (Figure 4.32). Upon analysis of fitting to monoexponential and biexponential decays, all exhibited biexponential decay profiles (based on visual analysis of suitability of fit and the adjusted R^2 values which are reported in the figure caption), which may be attributed to the presence of multiple species and impurities. The measured long components of the lifetimes are within error of each other

(2.40-2.61 ms) suggesting that the emissive terbium centres are in similar environments. The long component of the lifetimes of TbTbAzo is postulated to arise from the small amount of $TbTbNH_2$ impurity present (which causes most of the luminescence intensity) and the short component is due to the TbTbAzo (more consistent with the previously reported lifetime of 1.0 ms).

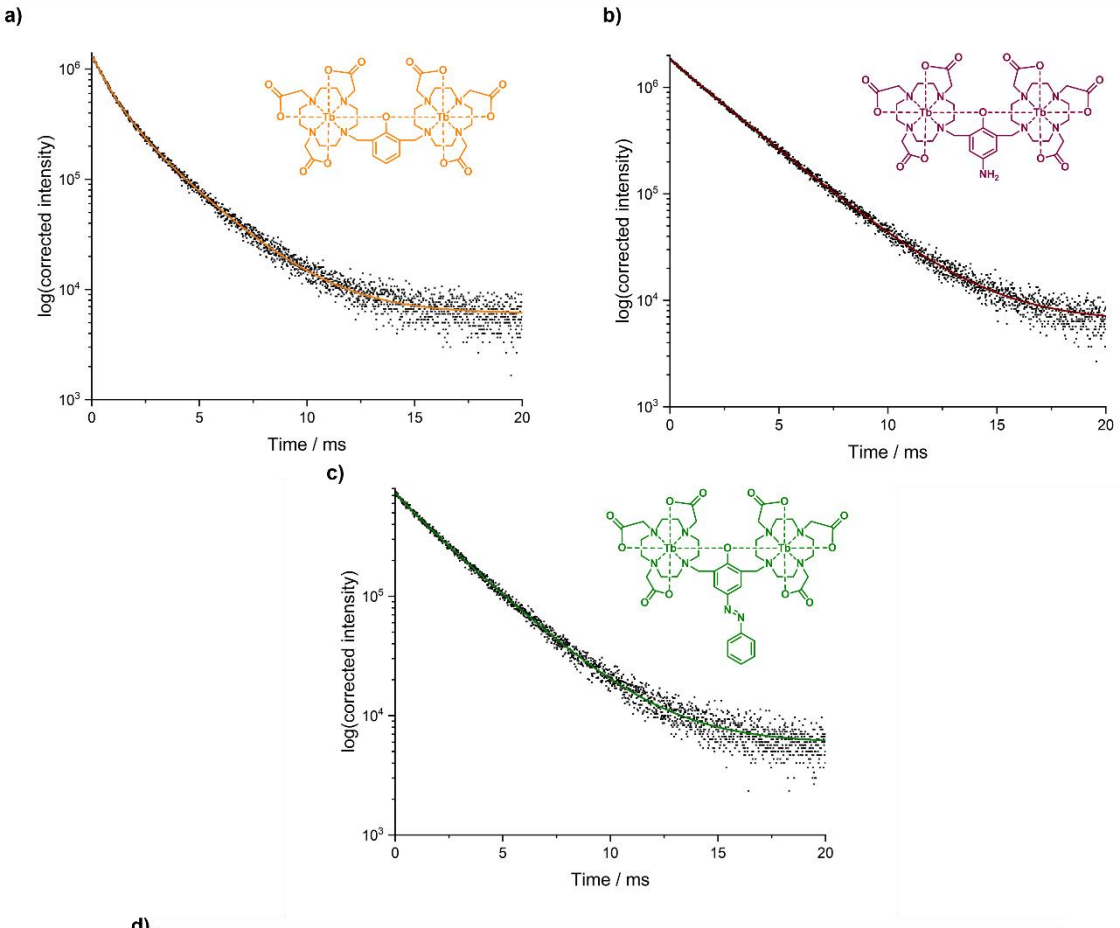

d)

Complex	λ_{ex} / nm	Lifetimes / ms (contribution to decay / %)	
TbTbAzo 53	294	2.61 (91)	0.71 (9)
	488	2.52 (90)	0.70 (10)
$TbTbNH_2$ 54	294	2.60 (95)	0.72 (5)
TbTbOH 93Tb	286	2.40 (62)	0.78 (58)

Figure 4.32: Lifetimes (averages of 3 scans) of a) TbTbOH **93Tb** in H_2O, λ_{ex} 286 nm, λ_{em} 545 nm; b) $TbTbNH_2$ **54** in PBS, λ_{ex} 294 nm, λ_{em} 545 nm; c) TbTbAzo **53** in PBS, λ_{ex} 294 nm, λ_{em} 545 nm. All complexes measured at 90 µM, 400 nm filter, flash count 5, sample window 1 ms, 61 ms per flash. a) slits 4 / 1 nm, R^2 0.999; b) slits 5 / 1 nm, R^2 0.999; c) slits 20 / 2 nm, R^2 0.998. d) Analysis of lifetime data (all fitted to biexponential decay, percentage contribution of each component to overall decay given in brackets).

4.4 Synthesis of alkylated azobenzene complexes

Synthesis of the hexyl and dodecyl azobenzene complexes, **57** and **58**, was attempted according to Scheme 4.9, in order to investigate the effect of modifying hydrophobicity on cell uptake of the previously reported terbium azobenzene complex.

Alkylation of 4-nitrophenol, using the corresponding iodoalkane to give **107** and **108**, was carried out following a procedure reported for alkylation using iodohexane.[81] The resulting alkylated nitro compound was purified by column chromatography and the yield of the dodecyl substrate (69-72%) was lower than that of the corresponding hexyl derivative (87-91%), likely due to solubility issues. Reduction of the nitro group to the corresponding aniline was carried out using tin and HCl and the aniline generated (**109** and **110**) was used immediately in the azobenzene forming step to avoid degradation. The diazotisation step was carried out in a mixture of water and acetone, instead of just water as carried out for TbTbAzo, following the procedure adapted from Zhang *et al.*[74] to aid the solubility of the starting material and increase the yield (55-62% yield for **111** compared to 42% yield in water only). Initial attempts at TBDMS protection of the phenols **111** and **112** appeared promising – purification of **113** resulted in a 38% yield and the crude ^{1}H NMR for **114** contained characteristic peaks (see chapter VI).

Further synthesis was planned to proceed similarly to the synthesis of the other bimetallic complexes, involving radical bromination, alkylation of the DO3A triester **23**, deprotection of the *tert*-butyl protecting groups and complexation and purification by dialysis. However, this was not carried out due to lack of time and solubility concerns with the dodecyl substrate.

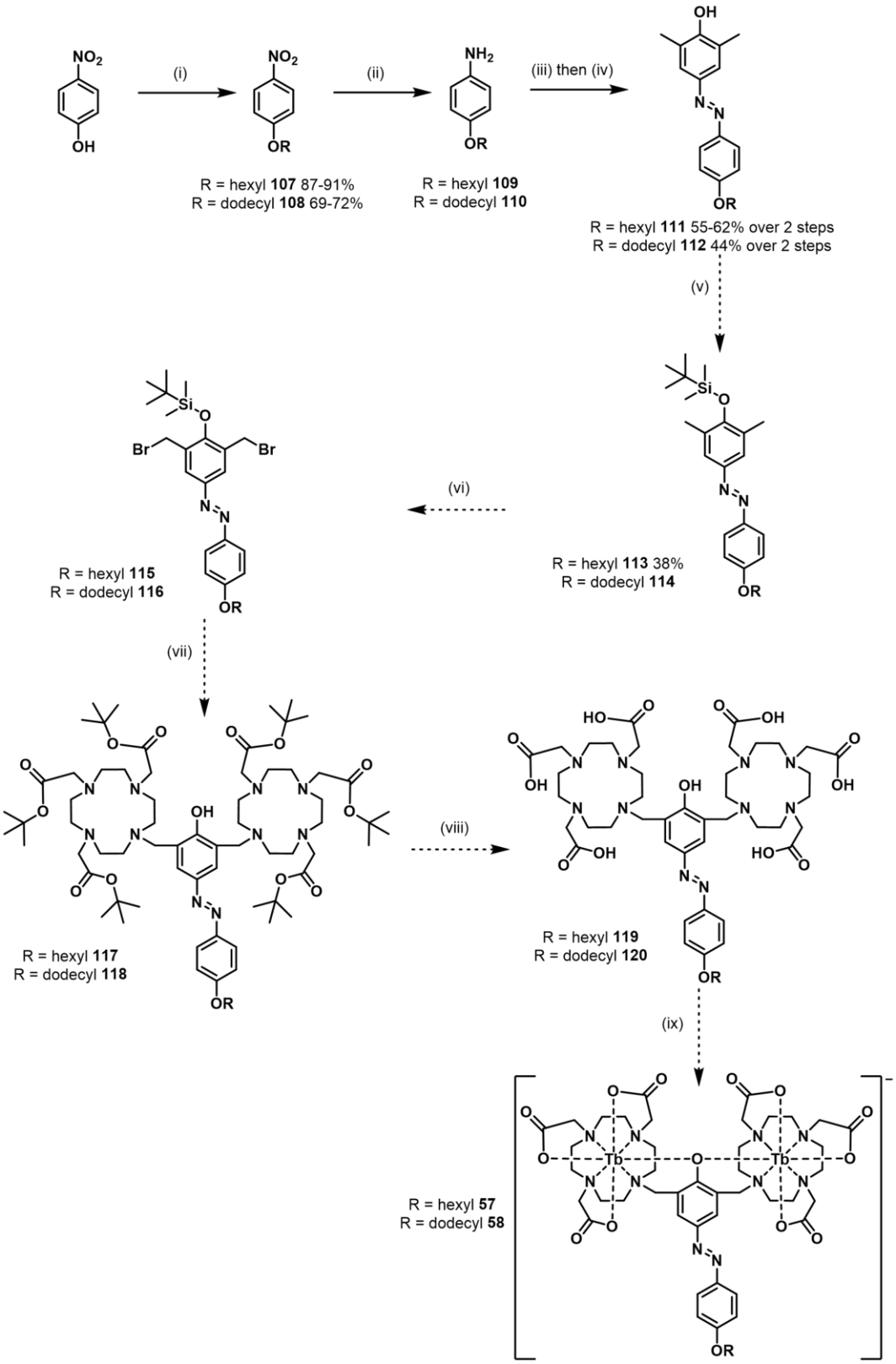

Scheme 4.9: The proposed synthetic scheme for the synthesis of alkylated azobenzene complexes **57** and **58**. Reagents and conditions: i) Iodoalkane, K_2CO_3, dry MeCN, 90 °C, 18-24 h; ii) Sn, HCl (3 M), EtOH, 80 °C, 2 h; iii) $NaNO_2$, H_2O, HCl (12 M), acetone, 0 °C, 30 min; iv) 2,6-dimethylphenol, NaOH, H_2O, 0 °C to rt, 18 h; v) TBDMSCl, imidazole, DMF, rt, 48 h; vi) NBS, benzoyl peroxide, CCl_4, 90 °C, 3 h; vii) **23**, Na_2CO_3, MeCN, 50 °C, 48 h; viii) TFA, CH_2Cl_2, rt, 18 h; ix) $Tb(OTf)_3$, NaOH (1 M), H_2O, 50 °C, 4 days.

4.5 Conclusions and future work

In conclusion, the attachment of leucine or another amino acid for cell targeting or expansion of this work is a promising route to aid the cell permeability of activatable lanthanide complexes. Development of amino acid containing or derivatised azobenzene lanthanide complexes is more synthetically challenging than their unsubstituted derivatives, however some promising routes have been explored to expand the group's knowledge in this area and act as a basis for future work on the development for cell permeable lanthanide complexes. In particular, synthesis of TbTbLeu **55** *via* direct amide coupling onto the aniline hexaester should be further investigated and the synthesis of TbTbAzoLeu **56** following either of the routes involving azobenzene formation and amide coupling prior to complexation may be optimised to increase yields to enable formation of the desired complex. Other methods for attachment of the leucine amino acid or short peptide sequences should be investigated, such as attachment of a DO3A derivative to a solid support for peptide elongation by solid-phase peptide synthesis (SPPS)[82] or attachment of a DO3A amine compound to a polystyrene resin by an amide-containing linker which may be used for peptide synthesis and subsequently cleaved.[24] In addition, synthesis of the complex TbTbAzoNH_2 (**59**, Figure 4.8b) should be carried out in parallel with the synthesis of TbTbAzoLeu for use as a control for activation of TbTbAzoLeu in the presence of LAP or other aminopeptidases. The activation of TbTbLeu and TbTbAzoLeu should be monitored (by luminescence spectroscopy and HPLC) in the presence of zinc and NH_4Cl, LAP, HSA and urate or ascorbate prior to evaluation of cell permeability. The cell permeability of these lanthanide complexes should be assessed by ICP-MS and time-gated imaging techniques, including fluorescence lifetime imaging microscopy (FLIM) and phosphorescence lifetime imaging microscopy (PLIM), in addition to the use of standard confocal microscopy techniques.

Further work is also required for the synthesis of alkyl-appended azobenzene complexes **57** and **58**, with preliminary synthesis appearing promising. This work is lower priority than

attachment of amino acids or peptide chains as modification of the hydrophobicity of the complex may have little effect on cell permeability, based on prior literature, or may cause attachment to cell membranes with the lanthanide centre facing into the extracellular medium or formation of micelles (as the complexes will have a hydrophilic head and long hydrophobic tail). Whilst the attachment of lanthanide complexes to the outer of cells may be interesting for increasing the relaxivity of gadolinium complexes, this would not aid the development of biologically applicable redox activatable lanthanide complexes. These complexes are also likely to have poor solubility in aqueous media so would need to be analysed diluted from stock solutions in DMSO. Their hydrophobicity, relative to the non-alkylated analogues, could be analysed by chromlogD to asses any effect of lipophilicity on cell uptake. To prevent alkyl-appended complexes from getting stuck in the cell membrane, bimetallic complexes should be designed to contain an alkyl linker between the macrocycle and the activatable azobenzene moiety, however with this design smaller changes in properties upon activation is likely.

In addition to exploration of the strategies mentioned above, alternative methods to aid cell permeability could be investigated. Attachment of a single leucine residue could be expanded by investigation of attachment of other, charged, amino acid residues or CPPs. The design of a series of complexes with short peptide chains (3-5 amino acids) attached to the azobenzene could be utilised to investigate any effect of overall charge and hydrophobicity on the uptake of these bimetallic azobenzene lanthanide complexes. Vesicle encapsulation and attachment to an antibody are other strategies which have been successfully employed in the literature for transport of compounds into the cell. Successful imaging of lanthanide complexes *in cellulo* has been previously achieved with many cationic complexes, therefore this strategy should be explored further by swapping the carboxylate arms for amides, which could also be derivatised with amino acids to aid uptake.

4.6 References

1. C. P. Montgomery, B. S. Murray, E. J. New, R. Pal and D. Parker, *Accounts of Chemical Research*, 2009, **42**, 925–937.
2. E. J. New and D. Parker, *Organic & Biomolecular Chemistry*, 2009, **7**, 851–855.
3. E. J. New, A. Congreve and D. Parker, *Chemical Science*, 2010, **1**, 111–118.
4. E. Mathieu, A. Sipos, E. Demeyere, D. Phipps, D. Sakaveli and K. E. Borbas, *Chemical Communications*, 2018, **54**, 10021–10035.
5. S. Pandya, J. Yu and D. Parker, *Dalton Transactions*, 2006, DOI: 10.1039/B514637B, 2757–2766.
6. F. Kielar, G.-L. Law, E. J. New and D. Parker, *Organic & Biomolecular Chemistry*, 2008, **6**, 2256–2258.
7. F. Kielar, A. Congreve, G.-l. Law, E. J. New, D. Parker, K.-L. Wong, P. Castreño and J. de Mendoza, *Chemical Communications*, 2008, DOI: 10.1039/B803864C, 2435–2437.
8. C. Alexander, Z. Guo, P. B. Glover, S. Faulkner and Z. Pikramenou, *Chemical Reviews*, 2025, **125**, 2269–2370.
9. A. J. Hall, A. G. Robertson, R. W. Baker, L. R. Hill and L. M. Rendina, *Chemical Communications*, 2023, **59**, 12511–12514.
10. J. L. Major and T. J. Meade, *Accounts of Chemical Research*, 2009, **42**, 893–903.
11. K. M. Stewart, K. L. Horton and S. O. Kelley, *Organic & Biomolecular Chemistry*, 2008, **6**, 2242–2255.
12. H. Zhang, Y. Zhang, C. Zhang, H. Yu, Y. Ma, Z. Li and N. Shi, *Pharmaceutics*, 2023, **15**.
13. A. Gori, G. Lodigiani, S. G. Colombarolli, G. Bergamaschi and A. Vitali, *ChemMedChem*, 2023, **18**, e202300236.
14. H. Derakhshankhah and S. Jafari, *Biomedicine & Pharmacotherapy*, 2018, **108**, 1090–1096.
15. R. Brock, *Bioconjugate Chemistry*, 2014, **25**, 863–868.
16. A. R. Chabukswar, S. C. Jagdale and P. M. Gandhi, *Journal of Drug Delivery and Therapeutics*, 2019, **9**, 252–256.
17. M. Wang, K. P. Rakesh, J. Leng, W.-Y. Fang, L. Ravindar, D. Channe Gowda and H.-L. Qin, *Bioorganic Chemistry*, 2018, **76**, 113–129.
18. N. Vale, A. Ferreira, J. Matos, P. Fresco and M. J. Gouveia, *Molecules*, 2018, **23**.
19. M. Tomi, M. Mori, M. Tachikawa, K. Katayama, T. Terasaki and K.-i. Hosoya, *Investigative Ophthalmology & Visual Science*, 2005, **46**, 2522–2530.
20. P. Häfliger and R. P. Charles, *Int J Mol Sci*, 2019, **20**.
21. G. Gyimesi and M. A. Hediger, *Molecules*, 2023, **28**.
22. T. Terai, K. Kikuchi, S.-y. Iwasawa, T. Kawabe, Y. Hirata, Y. Urano and T. Nagano, *Journal of the American Chemical Society*, 2006, **128**, 6938–6946.
23. H. Jeong, X. Wu, J.-S. Lee and J. Yoon, *TrAC Trends in Analytical Chemistry*, 2023, **168**, 117335.
24. S. Laine, J.-F. Morfin, M. Galibert, V. Aucagne, C. S. Bonnet and É. Tóth, *Molecules*, 2021, **26**.
25. F. Wang, S. Hu, Q. Sun, Q. Fei, C. Ma, C. Lu, J. Nie, Z. Chen, J. Ren, G.-R. Chen, G. Yang, X.-P. He and T. D. James, *ACS Applied Bio Materials*, 2019, **2**, 4904–4910.
26. S. Mizukami, K. Tonai, M. Kaneko and K. Kikuchi, *Journal of the American Chemical Society*, 2008, **130**, 14376–14377.
27. L. Holden, C. S. Burke, D. Cullinane and T. E. Keyes, *RSC Chemical Biology*, 2021, **2**, 1021–1049.
28. C. Yao, J. Zuo, P. Wu, J. Liu, J. Pan, E. Zhu, H. Feng, K. Zhang and Z. Qian, *Talanta*, 2024, **275**, 126105.
29. V. Fernández-Moreira, F. L. Thorp-Greenwood, A. J. Amoroso, J. Cable, J. B. Court, V. Gray, A. J. Hayes, R. L. Jenkins, B. M. Kariuki, D. Lloyd, C. O. Millet, C. F. Williams and M. P. Coogan, *Organic & Biomolecular Chemistry*, 2010, **8**, 3888–3901.
30. F. R. Svensson, M. Matson, M. Li and P. Lincoln, *Biophysical Chemistry*, 2010, **149**, 102–106.
31. C. Caporale, A. M. Ranieri, S. Paternoster, C. A. Bader, M. Falasca, S. E. Plush, D. A. Brooks, S. Stagni and M. Massi, *Journal*, 2020, **8**.
32. F. Kielar, L. Tei, E. Terreno and M. Botta, *Journal of the American Chemical Society*, 2010, **132**, 7836–7837.
33. A. J. Hall, A. G. Robertson, L. R. Hill and L. M. Rendina, *Scientific Reports*, 2021, **11**, 598.
34. Q. Zheng, H. Dai, M. E. Merritt, C. Malloy, C. Y. Pan and W.-H. Li, *Journal of the American Chemical Society*, 2005, **127**, 16178–16188.
35. K. Sénéchal-David, S. J. A. Pope, S. Quinn, S. Faulkner and T. Gunnlaugsson, *Inorganic Chemistry*, 2006, **45**, 10040–10042.
36. T. J. Sørensen, M. Tropiano, O. A. Blackburn, J. A. Tilney, A. M. Kenwright and S. Faulkner, *Chemical Communications*, 2013, **49**, 783–785.
37. M. S. Tremblay and D. Sames, *Chemical Communications*, 2006, DOI: 10.1039/B607949K, 4116–4118.
38. S. Faulkner and S. J. A. Pope, *Journal of the American Chemical Society*, 2003, **125**, 10526–10527.
39. F.-F. Chen, Z.-Q. Chen, Z.-Q. Bian and C.-H. Huang, *Coordination Chemistry Reviews*, 2010, **254**, 991–1010.
40. O. A. Blackburn, M. Tropiano, L. S. Natrajan, A. M. Kenwright and S. Faulkner, *Chemical Communications*, 2016, **52**, 6111–6114.
41. S. Shinoda, A. Mizote, M. Eiraku Masaki, M. Yoneda, H. Miyake and H. Tsukube, *Inorganic Chemistry*, 2011, **50**, 5876–5878.
42. C. H. Simms, D. Kovacs, L. Hacker, E. T. Sarson, D. Sokolova, K. E. Christensen, A. Khrapichev, L. A. W. Martin, K. Vincent, S. J. Conway, E. M. Hammond, M. J. Langton and S. Faulkner, *Chemistry – A European Journal*, 2025, **n/a**, e202404748.

43. K. Yao, G. Karunanithy, A. Howarth, P. Holdship, A. L. Thompson, K. E. Christensen, A. J. Baldwin, S. Faulkner and N. J. Farrer, *Dalton Transactions*, 2021, **50**, 8761–8767.
44. L. S. Natrajan, A. J. L. Villaraza, A. M. Kenwright and S. Faulkner, *Chemical Communications*, 2009, DOI: 10.1039/B913702E, 6020–6022.
45. T. J. Sørensen and S. Faulkner, *Accounts of Chemical Research*, 2018, **51**, 2493–2501.
46. C. H. Simms, University of Oxford, 2024.
47. Y. Xu, Y. Tang and Q. Li, *Advanced Functional Materials*, 2025, **35**, 2416359.
48. Y. Zhao, Q. Huang and Y. Liu, *ChemBioChem*, 2024, **25**, e202400635.
49. A. Negi, C. Kieffer and A. S. Voisin-Chiret, *ChemistrySelect*, 2022, **7**, e202200981.
50. M. Zhu and H. Zhou, *Organic & Biomolecular Chemistry*, 2018, **16**, 8434–8445.
51. C. H. Simms, V. R. M. Nielsen, T. J. Sørensen, S. Faulkner and M. J. Langton, *Physical Chemistry Chemical Physics*, 2024, **26**, 18683–18691.
52. M. Cieslikiewicz-Bouet, S. V. Eliseeva, V. Aucagne, A. F. Delmas, I. Gillaizeau and S. Petoud, *RSC Advances*, 2019, **9**, 1747–1751.
53. A. Guesdon-Vennerie, P. Couvreur, F. Ali, F. Pouzoulet, C. Roulin, I. Martínez-Rovira, G. Bernadat, F.-X. Legrand, C. Bourgaux, C. L. Mazars, S. Marco, S. Trépout, S. Mura, S. Mériaux and G. Bort, *Nature Communications*, 2022, **13**, 4102.
54. A. Khan, *Chemical Communications*, 2024, **60**, 6591–6602.
55. D. Xiao, L. Liu, F. Xie, J. Dong, Y. Wang, X. Xu, W. Zhong, H. Deng, X. Zhou and S. Li, *Angewandte Chemie International Edition*, 2024, **63**, e202310318.
56. X.-b. Zhao, W. Ha, K. Gao and Y.-p. Shi, *Analytical Chemistry*, 2020, **92**, 9039–9047.
57. Y. Zhang, W. Zhao, Y. Chen, H. Yuan, H. Fang, S. Yao, C. Zhang, H. Xu, N. Li, Z. Liu, Z. Guo, Q. Zhao, Y. Liang and W. He, *Nature Communications*, 2021, **12**, 2772.
58. W. Piao, S. Tsuda, Y. Tanaka, S. Maeda, F. Liu, S. Takahashi, Y. Kushida, T. Komatsu, T. Ueno, T. Terai, T. Nakazawa, M. Uchiyama, K. Morokuma, T. Nagano and K. Hanaoka, *Angewandte Chemie International Edition*, 2013, **52**, 13028–13032.
59. I. Regeni and S. Bonnet, *Nature Reviews Chemistry*, 2025, **9**, 365–377.
60. R. K. Wilharm, M. R. Gau, D. Trauner and E. J. Schelter, *Journal of the American Chemical Society*, 2025, **147**, 27143–27147.
61. D. Kovacs, unpublished work.
62. S. B. M Kretschmer, S. Woltersdorf, C. B. Rödl, D. Vogt, A.-K. Häfner, D. Steinhilber, H. Stark and B. Hofmann, *Future Medicinal Chemistry*, 2016, **8**, 149–164.
63. A. K. Ghosh and D. Shahabi, *Tetrahedron Letters*, 2021, **63**, 152719.
64. M. A. Alisi, M. Brufani, N. Cazzolla, F. Ceccacci, P. Dragone, M. Felici, G. Furlotti, B. Garofalo, A. La Bella, O. Lanzalunga, F. Leonelli, R. Marini Bettolo, C. Maugeri, L. M. Migneco and V. Russo, *Tetrahedron*, 2012, **68**, 10180–10187.
65. J. Chen, S. P. Corbin and N. J. Holman, *Organic Process Research & Development*, 2005, **9**, 185–187.
66. A. Podgoršek, S. Stavber, M. Zupan and J. Iskra, *Tetrahedron Letters*, 2006, **47**, 1097–1099.
67. C. Descôteaux, K. Brasseur, V. Leblanc, S. Parent, É. Asselin and G. Bérubé, *Steroids*, 2012, **77**, 403–412.
68. T. M. Vishwanatha, N. Narendra, B. Chattopadhyay, M. Mukherjee and V. V. Sureshbabu, *The Journal of Organic Chemistry*, 2012, **77**, 2689–2702.
69. S. Albedyhl, Marie T. Averbuch-Pouchot, C. Belle, B. Krebs, Jean L. Pierre, E. Saint-Aman and S. Torelli, *European Journal of Inorganic Chemistry*, 2001, **2001**, 1457–1464.
70. L. F. Lindoy, *Synthesis*, 1998, **1998**, 1029 – 1032.
71. C. Lindler, East Carolina University, 2014.
72. S. J. A. Pope, A. M. Kenwright, S. L. Heath and S. Faulkner, *Chemical Communications*, 2003, DOI: 10.1039/B303012A, 1550–1551.
73. T. Kline, M. Y. Torgov, B. A. Mendelsohn, C. G. Cerveny and P. D. Senter, *Molecular Pharmaceutics*, 2004, **1**, 9–22.
74. L. Zhang, Z. Tang, L. Hou, Y. Qu, Y. Deng, C. Zhang, C. Xie and Z. Wu, *Analyst*, 2020, **145**, 1641–1645.
75. M. Bortolus, G. Ribaudo, A. Toffoletti, D. Carbonera and G. Zagotto, *Photochemical & Photobiological Sciences*, 2019, **18**, 2199–2207.
76. E. Forster, Masters in Chemistry, University of Oxford, 2025.
77. M. P. Placidi, A. J. L. Villaraza, L. S. Natrajan, D. Sykes, A. M. Kenwright and S. Faulkner, *Journal of the American Chemical Society*, 2009, **131**, 9916–9917.
78. M. P. Placidi, University of Manchester, 2009.
79. M. Main, J. S. Snaith, M. M. Meloni, M. Jauregui, D. Sykes, S. Faulkner and A. M. Kenwright, *Chemical Communications*, 2008, DOI: 10.1039/B810083G, 5212–5214.
80. V. R. M. Nielsen, C. H. Simms, D. Kovacs, M. F. Allen, M. J. Langton, S. Faulkner and T. J. Sørensen, *Chemistry – A European Journal*, 2025, DOI: https://doi.org/10.1002/chem.202502305, e02305.
81. S. Avvakumova, P. Fezzardi, L. Pandolfi, M. Colombo, F. Sansone, A. Casnati and D. Prosperi, *Chemical Communications*, 2014, **50**, 11029–11032.
82. B. Yoo, V. R. Sheth and M. D. Pagel, *Tetrahedron Letters*, 2009, **50**, 4459–4462.

5. Chapter V: Conclusions and Future Work

This project aimed to design new organic and lanthanide-based tools for cancer imaging purposes, with a focus on redox activatable probes for selective imaging, for application in diagnosis and prognosis evaluation. Whilst none of the reported compounds were tested *in vivo*, this work acts as proofs-of-concept for development of novel activatable imaging probes and their challenges in design and synthesis.

Chapter II described the synthesis, photophysical characterisation and activation of a series of fluorophores (DCM-OH, resorufin and Me-Tokyo Green) appended to the activatable tetrafluoroaryl azide moiety, to determine whether activation under hypoxia and X-ray irradiation occurs in the same way. Development of these profluorophores highlighted the challenges of probe design, as the overall water solubility of the profluorophore is crucial for activation and use in biological applications, and the nature of the fluorophore and the linker between the fluorophore and activatable group partially dictate level of activation. It was found that the resorufin tetrafluoroaryl azide profluorophore had a tolerable chromlog$D_{7.4}$ value of 6.89 (PFI 10.89), compared with 8.10 for DCM-N_3 (PFI 11.10) which has previously been tested *in cellulo* (despite it being outside the PFI range typically targeted for good ADME properties). This correlated with greater water solubility than the previous DCM-based profluorophores, despite some remaining solubility issues. The resorufin profluorophore exhibited desired poor emission properties at low concentration in PBS, in contrast to the fluorophore resorufin which exhibited bright emission under the same conditions. Activation in the presence of zinc as a chemical reductant showed release of resorufin and an initial corresponding increase in fluorescence emission, with HPLC analysis consistent with 5% release of the active fluorophore. Preliminary testing in the presence of CYP enzymes showed selective release of resorufin (< 2%) under hypoxic conditions, whereas X-ray irradiation up to 60 Gy showed no release of the fluorophore. Further validation of the resorufin profluorophore should be carried out in the presence of

the CYP enzymes under hypoxia and normoxia at lower concentrations (to minimise any effect of precipitation still observed) and activation in the presence of other biological reductants, such as glutathione, should be measured to further validate selectivity. From these data, these tetrafluoroaryl azide profluorophores cannot be used for activation under both hypoxia and X-ray irradiation and further probe design and optimisation is needed to develop selective imaging probes which employ new activatable moieties. These new moieties should allow for selective activation under a variety of conditions and using lower doses of X-ray irradiation, more consistent with those currently used clinically for radiotherapy for treatment of large tumours (< 2 Gy). To increase the level of activation of profluorophores, methyl groups should be added to ether linkages or carbonate or carbamate linkers should be employed over ether linkages, although this will likely decrease their selectivity. To summarise, development of a moiety which may be activated complimentarily under differing conditions (such as hypoxia and X-ray irradiation) would be highly beneficial for clinicians for cancer imaging and treatment, however it requires substantial further work from the field.

In addition to these organic profluorophores, a series of activatable lanthanide complexes (Ln = Eu, Tb, Gd) were designed for optical imaging and MRI applications (chapter III). The lanthanide complexes were ester derivatives of LnDOTA with appended nitrobenzyl, nitroimidazole or benzyl groups as redox activatable moieties (and a negative control). They demonstrated abilities to act as turn-on imaging agents, with an increased in time-gated lanthanide-centred emission intensity observed upon direct excitation of terbium, and turn-on MRI contrast agents, with a small change in relaxivity observed between the activatable gadolinium-containing nitrobenzyl and nitroimidazole complexes and the known MRI contrast agent GdDOTA. The gadolinium nitrobenzyl analogue was previously reported to be selectively activated in the presence of nitroreductases, and both nitrobenzyl and nitroimidazole moieties have been used in the design of many hypoxia-activated prodrugs and profluorophores. Notably, it was determined that activation of these lanthanide

complexes under both chemical and enzymatic conditions suggested that formation of the desired LnDOTA complex occurs primarily due to hydrolysis of the ester bond, with differing rates observed consistent with the different ester groups attached. These complexes were also found to have poor cell permeability. Therefore, the poor selectivity profiles, evidenced by the activation *via* hydrolysis, and the lack of cell permeability precludes the biological applicability of these complexes. To partially overcome these issues and further validate these probes, amide or carbamate linkages could be investigated as alternatives to esters to alter the reactivity and selectivity profiles of activation of these monometallic complexes and further investigation into the enzymatic rates of activation could be carried out by testing the nitroimidazole and benzyl complexes in the presence of the nitroreductase enzyme (and NADH). To aid clinical applicability as activatable MRI contrast agents, relaxivity of any future activatable lanthanide complexes should be evaluated at 11.7 T and also at lower clinically used field strengths, 1.5-3.0 T. Despite the initial promise of these activatable monometallic complexes given the changes in luminescence, relaxivity and the chemical and enzymatic activation observed, further optimisation of complex design is required to obtain imaging probes with the desired characteristics for application *in vivo*, including larger changes in emission intensity upon activation (to remove doubt of evidence of any turn-on effects in the presence of disease markers) and enhanced selectivity.

To attempt to overcome issues with cell permeability, chapter IV highlighted some preliminary work done involving attachment of leucine or alkyl chains to previously a reported bimetallic terbium azobenzene complex to facilitate transport into the cell. The synthetic work carried out highlighted the difficulty in assessment of derivatisation following attachment to the cyclen core and formation of derivatised azobenzene compounds. Nevertheless, the routes explored may be used as foundations for future work on derivatisation of bimetallic complexes to aid cell uptake. Alternative methods for the attachment of leucine, or other amino acids to modulate the charge of the complex such as arginine or lysine, should be investigated, such as amide coupling following attachment of

an azobenzene DO3A precursor to a polystyrene resin to enable late-stage peptide functionalisation. Development of a series of azobenzene bimetallic lanthanide complexes bearing short peptide chains (e.g. 3 amino acids) could be advantageous to explore the effect of charge and hydrophobicity on the uptake of these complexes, or attachment to CPPs could be explored. Cationic complexes could be explored through the use of amide arms, bearing amino acids, to replace the carboxylate arms. Other methods to aid cell uptake of bimetallic activatable lanthanide complexes include vesicle encapsulation, the use of alkyl chains between the macrocycle and activatable group to modify hydrophobicity or attachment to an antibody. Cell permeability of activatable lanthanide complexes should be evaluated by ICP-MS analysis and time-gated measurements such as PLIM, in addition to standard confocal microscopy techniques.

For successful translation of redox activated prodrugs and profluorophores to the clinic, many challenges remain. The success of prodrugs in phase II clinical trials and beyond requires new methodologies for accurate assessment of the level of hypoxia, requiring probes that are sensitive to small changes in oxygen percentage and those that distinguish between transient, persistent and historic hypoxia. The poor vasculature present in hypoxia requires consideration of probe localisation vs activation – if only a small percentage of the probe will reach the desired highly hypoxic region, then a large proportion must be activated for detection. This also highlights the need for imaging techniques with low detection limits whilst ensuring good sensitivity and removal of background signal, such as the use of time-gated microscopy for optical imaging. Optimising the balance between timescale of activation, speed of the imaging technique used and clearance times is also crucial. Further understanding of the biology of hypoxia is needed for greater knowledge of which enzymes and pathways are upregulated, to design probes with good selectivity and avoid side effects. Overall, the future of activatable imaging probes relies on advances in chemistry and biology for the development of highly selective and reversible probes, for cancer

diagnosis and prognosis evaluation, and theranostic probes, for cancer treatment, which may be detected by techniques where the background signal is minimalised.

6. Chapter VI – Experimental Procedures

6.1 General Experimental

Reagents and solvents were obtained from Sigma Aldrich U.K., ChemCruz, Alfa Aesar, Fluorochem and BDH Chemicals and were used without further purification. Dry toluene, dry THF and dry DMF was taken from MBRAUN MB5 Solvent Purification System, and stored over 3 Å molecular sieves, under an inert atmosphere of argon, unless otherwise stated. Dry EtOH and dry MeOH were purchased from Sigma Aldrich U.K. in SureSeal™ bottles and used without further purification.

Concentration *in vacuo* refers to solvent removal under reduced pressure at 40 °C using a Buchi™ rotary evaporator, unless otherwise stated. Brine is a saturated aqueous solution of NaCl. Hexane includes a mixture of hexane isomers. Petroleum ether (PE) refers to the fractions collected between 40–60 °C when distilled. Celite® refers to Celite®545 filter aid, treated with sodium carbonate, flux-calcined, which was purchased from Sigma Aldrich. Deionised H_2O (18.2 Ω) was obtained using an Elix® Essential H_2O purification system. Unless otherwise stated, all reactions were carried out open to air at atmospheric pressure.

Silica gel column chromatography was carried out manually using Merck silica gel (40–63 µm) or using a Biotage® Selekt flash purification system using Biotage® Sfär pre-packed silica columns (10 g, 25 g, 50 g or 100 g, as appropriate) or Modus B series silica or neutral alumina columns (12 g, 25 g or 40 g, as appropriate). The crude compound was either dissolved in analytically pure solvents or dry loaded onto silica and eluted with solvents as supplied.

Melting points were obtained using a Gallenkamp melting point apparatus and are uncorrected. The crystallisation solvent is given in parentheses.

Infrared (IR) spectra were obtained from neat samples or thin liquid films. The spectra were recorded using a Bruker Tensor 27 spectrometer with a diamond ATR module.

Absorption maxima are given in wavenumbers (cm^{-1}) and reported as s (strong), m (medium), or w (weak).

Analytical thin layer chromatography (TLC) was carried out on Merck silica gel 60 F_{254} aluminium-supported thin layer chromatography sheets. Spots were visualised by absorption of UV light (λ_{max} 254 nm and 365 nm), or thermal development after staining with an aqueous solution of potassium permanganate.

^{1}H NMR spectra were recorded using a Bruker AVIII HD 400 nanobay (400 MHz), AVII 500 (500 MHz) or Bruker NEO 600 (600 MHz) spectrometer with broadband helium cryoprobe, using the stated solvent as a reference for internal deuterium lock. The chemical shift data for each signal are given as δ_H in units of parts per million (ppm). The spectra are calibrated using the solvent peak with the data provided by Fulmer *et al.*[1] The multiplicity of each signal is indicated by: s (singlet); br s (broad singlet); d (doublet); t (triplet); q (quartet); m (multiplet) or combinations thereof. The number of protons, n, for a given resonance signal is indicated by nH. Where appropriate, coupling constants (*J*) are expressed in Hz and are recorded to the nearest 0.1 Hz. Identical proton coupling constants (*J*) are averaged in each spectrum and reported to the nearest 0.1 Hz. MestReNova software was used for NMR analysis. ^{1}H NMR spectra were assigned using 2D NMR such as COSY, HSQC and HMBC, as necessary. ‘ar’ refers to aromatic protons.

^{13}C NMR spectra were recorded using a Bruker AVIII HD 400 (101 MHz) or Bruker NEO 600 spectrometer (151 MHz) with broadband proton decoupling, using the stated solvent as a reference for internal deuterium lock. The chemical shift data for each signal are quoted as δ_C in parts per million (ppm). The spectra are calibrated using the solvent peak with the data provided by Fulmer *et al.*[1] The chemical shift is quoted to 1 decimal place, unless two different shifts are indistinguishable, where the shifts are then quoted to 2 decimal places. MestReNova software was used for NMR analysis. ^{13}C NMR spectra were assigned using 2D NMR such as HSQC and HMBC. ‘ar’ refers to aromatic carbons. ^{13}C[^{19}F] denotes fluorine-decoupled carbon NMR spectroscopy.

^{19}F NMR spectra were recorded using a Bruker AVIII HD 400 (376 MHz) or Bruker NEO 600 spectrometer (565 MHz) with broadband proton decoupling, using the stated solvent as a reference for internal deuterium lock. The chemical shift data for each signal are quoted as δ_F in parts per million (ppm). The multiplicity of each signal is indicated by: s (singlet); d (doublet); m (multiplet) or combinations thereof. The number of fluorines, n, for a given resonance signal is indicated by nF. The spectra are uncalibrated. Where appropriate, coupling constants (*J*) are expressed in Hz and are recorded to the nearest 0.1 Hz.

Mass spectra using electrospray ionisation (ESI) were acquired on either an Agilent 6120 (low resolution), H2Os LCT Premier bench-top orthogonal acceleration time-of-flight LC-MS system (low resolution), Thermo Exactive High-Resolution Orbitrap FTMS (high resolution) or BioAccord system (high resolution) from solutions of MeOH, H_2O or MeCN. Mass spectra using electron ionisation (EI) were obtained by Dr Victor Mikhailov using an Agilent 7200 Accurate Mass Q-TOF GC-MS connected to a 7890 GC system, DIP solid/liquid state thermal probe and a CTC Analytics HTS PAL Sample Manager. *m/z* values are reported in Daltons and followed by their percentage abundance in parentheses. Data were processed using MestReNova software. For comparison of experimental HRMS data to theoretical spectra, calculated spectra were produced using Molecular Weight Calculator version 6.50 and data were processed in Origin software.

Specific optical rotations were obtained using a Bellingham + Stanley ADP450 polarimeter, measuring at 589 nm (sodium D line) with a path length of 0.5 dm at 20 °C. The concentration (*c*) is expressed in g / 100 mL (g / 0.1 dm^3). Specific rotations are denoted $[\alpha]_D^T$ (where T denotes the temperature in Celsius) and is calculated using the following equation: $[\alpha]_D{}^T = \frac{\alpha}{lc}$, where α is the observed rotation and l is the path length in dm and c is the concentration in g/mL. For some compounds containing chiral centres, specific optical rotations were not determined, e.g. for compounds not fully soluble in chloroform at 0.5 mg/mL (either particulates in solution or opaque/cloudy suspension), too darkly

coloured for the sample to be see-through in the polarimeter or where not enough pure compound remained for measurement.

Analytical high-performance liquid chromatography (HPLC) was carried out to determine compound purity. Samples (in MeCN or H_2O) were all filtered through a PTFE syringe filter (0.2 µm) or nylon syringe filter (0.45 µm, 13 mm) before injection. HPLC was carried out on an Agilent 1260 Infinity II system with the column oven at 40 °C and UV/Vis detection at 220, 240, 254, 280, 360 and 480 nm, with percentage purity averaged over a minimum of three wavelengths (chosen based on the absorbance spectrum of the compound). A gradient method is used, where solvent A is H_2O with 0.1% formic acid and B is MeCN with 0.1% formic acid. For **methods 1A** and **2A**, a Poroshell 120 EC-C18 reverse phase column (4 µm, 4.6 × 150 mm) was used with a constant flow rate of 1 ml min^{-1}. For **methods 1B**, **2B** and **3**, a Poroshell 120 EC-C18 reverse phase column (4 µm, 4.6 × 100 mm) was used with a constant flow rate of 1 ml min^{-1}. For **method 4**, a Discovery® cyano column (5 µm, 24 cm × 4.6 mm) was used with a constant flow rate of 1 ml min^{-1}, with UV-Vis detection at 220, 240, 254, 272, 280, 360 and 480 nm. HPLC data were processed using MestReNova software.

Table 6.1: The solvent gradient used for Analytical HPLC **method 1.**

Time / min	%A	%B
0.0	95	5
5.0	95	5
10.0	50	50
10.5	5	95
11.0	5	95
11.50	95	5
14.0	95	5

Table 6.2: The solvent gradient used for Analytical HPLC **method 2**.

Time / min	%A	%B
0.0	95	5
1.0	95	5
11.0	5	95
16.0	5	95

Table 6.3: The solvent gradient used for Analytical HPLC **method 3** (for chapter III nitroreductase assay).

Time / min	%A	%B
0.0	95	5
5.0	95	5
10.0	50	50
10.5	5	95
11.0	5	95
11.5	95	5
14.0	95	5

Table 6.4: The solvent gradient used for Analytical HPLC **method 4.**

Time / min	%A	%B
0.0	98	2
5.0	98	2
25.0	0	100
27.0	0	100
29.0	98	2
30.0	98	2

Method 5 was carried out on a PerkinElmer Flexar system with a Binary LC pump and UV/Vis LC detector set at 254 nm. A ZORBAX Rx-Sil column (5 µm, 4.6 x 250 mm) was used with a constant flow rate of 1 ml min^{-1} and an isocratic method of 25 min in CH_2Cl_2:hexane (50:50). HPLC data were processed using Chromera 3.4.4 software.

Method 6 was carried out on a PerkinElmer Flexar system with a Binary LC pump and UV/Vis LC detector set at 254 nm. A SUPELCOSIL™ LC-Si column (5 µm, 4.6 x 250 mm) was used with a constant flow rate of 1 ml min^{-1} and an isocratic method of 25 min in CH_2Cl_2:hexane (50:50). HPLC data were processed using Chromera 3.4.4 software.

Liquid chromatography mass spectrometry (LCMS) was carried out to determine compound purity of more polar compounds. Samples (in MeCN or H_2O) were all filtered through a PTFE syringe filter (0.2 µM) or nylon syringe filter (0.45 µM, 13 mm) before injection. Electrospray ionisation (ESI) liquid chromatography mass spectrometry (LCMS) were acquired using Agilent 1260 Infinity II® fitted with a Quat. Pump (G7111A), autosampler (G7129A), column oven (G7130A), DAD (G7115A) and mass spectrometer (G6125B). The signals acquired were at 254 nm, 365 nm, 220 nm, 450 nm and 280 nm

(with bandwidths of 4 nm and reference wavelength of 800 nm, bandwidth 100 nm). Solvent A is H_2O with 0.1% formic acid and B is MeCN with 0.1% formic acid. LCMS data were processed using Chromera 3.4.4 software and MestReNova software.

Method 1: See Table 6.5 for the solvent gradient. A Poroshell 120 SB-C18 (50 × 2.1 mm, 2.7 µM) column was used, with the column oven at 40 °C, a flow rate of 0.4 mL min^{-1} and injection volumes between 2 µL and 20 µL.

Table 6.5: The solvent gradient used for LCMS **method 1**.

Time / min	%A	%B
0.0	95	5
0.5	95	5
3.5	5	95
6.5	5	95
7.0	95	5
10.0	95	5

Method 2: See Table 6.6 for the solvent gradient. A Poroshell 120 SB-C18 (50 × 2.1 mm, 2.7 µM) column was used, with the column oven at 40 °C, a flow rate of 0.4 mL min^{-1} and injection volumes between 2 µL and 20 µL.

Table 6.6: The solvent gradient used for LCMS **method 2**.

Time / min	%A	%B
0.0	95	5
1.0	95	5
6.0	50	50
6.5	5	95
7.0	5	95
7.5	95	5
10.0	95	5

Methods 3 and 4: See Table 6.7 for the solvent gradient. Method 3: A Poroshell 120 SB-C18 (50 × 2.1 mm, 2.7 µM) column was used, with the column oven at 40 °C, a flow rate of 0.4 mL min^{-1} and injection volumes between 2 µL and 20 µL. Method 4: An InfinityLab Poroshell 120 EC-C18 (4.6 × 100 mm, 4.0 µM) column was used, with the column oven at 40 °C, a flow rate of 0.4 mL min^{-1} and injection volumes between 10 µL and 50 µL.

Table 6.7: The solvent gradient used for LCMS **methods 3 and 4**.

Time / min	%A	%B
0.0	95	5
5.0	95	5
10.0	50	50
10.5	5	95
11.0	5	95
11.50	95	5
14.0	95	5

Semi-preparative high performance liquid chromatography (SP-HPLC) was carried out on an Agilent Infinity II 1260 fitted with a preparatory pump (G7161A), prep sampler (G7157A), VWD (G7114A), fraction collector (G1364E) and a 1 mL sample loop. Complex samples (in MES buffer 0.5 M, filtered through a 0.45 µm nylon syringe filters, for chapter III, or in MeOH, for chapter IV) were purified with sample detection at 254 nm. An Agilent 5 Prep C18 (p/N 446905-702, 50 × 21.2 mm, 5 µL) column was used, with injection volumes between 100 µL and 750 µL.

Method 1: used for nitrobenzyl complexes, where solvent A is H_2O (no additive) and solvent B is MeCN (no additive), flow rate 25 mL min^{-1}.

Table 6.8: The solvent gradient used for SP-HPLC **method 1**.

Time / min	%A	%B
0.0	95	5
4.0	95	5
11.0	50	50
12.0	5	95
14.0	95	5
15.0	95	5

Method 2: used for nitroimidazole complexes, where solvent A is H_2O (no additive) and solvent B is MeCN (no additive), flow rate 15 mL min^{-1}.

Table 6.9: The solvent gradient used for SP-HPLC **method 2**.

Time / min	%A	%B
0.0	95	5
5.0	95	5
7.0	5	95
8.0	5	95
8.5	95	5
9.0	95	5

Method 3: used for benzyl complexes, where solvent A is H_2O (no additive) and solvent B is MeCN (no additive), flow rate 15 mL min^{-1}.

Table 6.10: The solvent gradient used for SP-HPLC **method 3**.

Time / min	%A	%B
0.0	95	5
2.0	95	5
9.0	50	50
11.0	50	50
13.0	5	95
15.0	5	95
16.0	95	5

Method 4: used for TbTbOH, where solvent A is H_2O (0.1% formic acid) and solvent B is MeCN (0.1% formic acid), flow rate 15 mL min^{-1}.

Table 6.11: The solvent gradient used for SP-HPLC **method 4**.

Time / min	%A	%B
0.0	95	5
1.0	95	5
6.0	50	50
7.0	5	95
8.0	5	95
9.0	95	5
10.0	95	5

Method 5: used for TbTbOH, where solvent A is H_2O (no additive) and solvent B is MeCN (no additive), flow rate 15 mL min^{-1}.

Table 6.12: The solvent gradient used for SP-HPLC **method 5**.

Time / min	%A	%B
0.0	95	5
1.0	95	5
7.0	80	20
9.0	80	20
10.0	50	50
11.0	50	50
12.0	95	5
13.0	95	5

UV-Visible spectroscopy was carried out on a Jasco V-770 UV-Visible spectrophotometer running Spectra Manager™ software, with the temperature maintained at 25 °C. Samples were measured in high precision cuvettes from Hellma Analytics (path length 10 mm), using technical grade solvents, and the cuvette was washed with H_2O and EtOH between measurements. Measurements were obtained using Spectra Measurement (with 0.2 or 1 nm interval, analysed at 200 nm min^{-1} or 400 nm min^{-1}) and analysed using Origin™ software.

Fluorescence and **phosphorescence spectroscopy** and **lifetime measurements** were carried out on a Horiba Jobin Yvon FluoroLog® 3-12 equipped with a Hamamatsu R928 detector and a double-grating emission monochromator. Measurements were made with varying slit entrance and exit lengths depending on the sample, as indicated under the relevant spectra. A 2" square unmounted longpass 400 nm filter (FGL400S) or 495 nm filter (FGL495) from Thor labs was used where indicated for the lanthanide complexes. **Degassing measurements** were carried out by purging the sample under a flow of argon for minimum 30 min and transferring the solution inertly to a degassing cuvette, which had been purged by alternating between vacuum and argon three times prior to sample addition. The data was obtained using FluorEssence™ software and processed using Origin™ software. Luminescence data were measured on fluorophores, profluorophores or lanthanide complexes determined to be over 90% pure by ^{1}H NMR, Analytical HPLC or LCMS, unless stated otherwise. Ligands were left under high vacuum for 2 days prior to

luminescent measurements to remove any residual solvent. Cuvettes were cleaned with 25% nitric acid, H_2O and EtOH between lanthanide complexes.

Centrifugation for the purification of compounds was carried out on a Beckman Coulter® Allegra® X-12R Benchtop Centrifuge and centrifugations were performed at 3750 rpm for 5 min at 4 °C. For centrifugation during assays, a Labnet Prism™ Mini Centrifuge was used and centrifugations were performed at 6000 rpm for 4 min.

Buffer preparation

- **Phosphate buffer saline (PBS)** (pH 7.4) for chapters II and III: one phosphate buffered saline tablet (Thermo Scientific™, Oxoid™, BR0014G) was dissolved in deionised H_2O (100 mL) and the pH adjusted to pH 7.4 using NaOH (2M aqueous solution) and HCl (1M aqueous solution).
- **10 mM PBS (pH 7.4)** for chapter IV: to 800 mL deionised H_2O was added NaCl (8.0 g), KCl (0.2 g), KH_2PO_4 (0.245 g) and Na_2HPO_4 (1.44 g). The pH of the solution was adjusted to pH 7.4 using HCl (1M aqueous solution).
- **2-(N-Morpholino)ethanesulfonic acid (MES)** (1M, pH 6.0) for chapter III: 2-(*N*-morpholino)ethanesulfonic acid (MES) monohydrate (5.43 g, 25.0 mmol) was dissolved in deionised H_2O (20 mL) and the pH adjusted to pH 6.0 (tolerance 6.00-6.04) using NaOH (6M aqueous solution). Deionised H_2O was added to give a total volume of 25 mL.
- **Sodium phosphate buffer** (100 mM, pH 7.4) for chapter III hydrogenase assay: Na_2HPO_4 (70 mg) and NaH_2PO_4 (484 mg) were dissolved in deionised H_2O (40 mL) and the pH adjusted to pH 7.4 using NaOH.

pH measurements were determined using a Jenway pH Meter 3305, with an Aldrich glass/calomel combination electrode, or a HI 2210 pH Meter. Calibration for the Jenway pH Meter 3305 was carried out between pH 4.0–7.0 or 7.0–10.0 immediately before use, with buffer solutions of phthalate (pH 4.0), phosphate (pH 7.0) and borate (pH 10.0) from Fisher

Scientific. Electrodes were stored in a 4 M aqueous potassium chloride solution. Calibration for the HI 2210 pH Meter was carried out between pH 4.0-7.0 or 7.0-10.0 immediately before use, using the calibration solutions (pH 4.01, 7.01 and 10.01) from Hanna Instruments. Following use, the electrodes were submerged in the cleaning solution (HI 7061) for at least 20 min then stored in the storage solution (HI 70300), from Hanna Instruments.

Dialysis was carried out using Spectra-Por® Float-A-Lyzer® G2 dialysis membrane tubing made from regenerated cellulose ester (Spectrum Labs®) with a molecular weight cut-off of 500 Da (for EuDOTA and TbDOTA) or 1000 Da (for chapter IV complexes). The dialysis tube was activated by 15% EtOH solution in deionised H_2O (10 min, 2 L), and rinsed with deionised H_2O before soaking with deionised H_2O (10 min, 2 L) before use. The deionised H_2O was removed and the complexes (dissolved in deionised H_2O) transferred into the dialysis tube. The dialysis tube was stirred gently for a minimum of 2 days in deionised H2O (2.5 L) and the H_2O replaced a minimum of 6 times.

Cyclic voltammetry (CV)

Cyclic voltammetry measurements were carried out by Euan Sarson. The electrochemical cell consisted of a polyether ether ketone (PEEK) cylinder containing a working electrode of glassy carbon (1 mm diameter), a counter electrode of graphite, and a leak-free Ag/AgCl reference electrode (LF-2-45 model from Alvatek Ltd). The cell was constructed in a N_2 atmosphere in a glove box (O_2 < 2 ppm), using a 1 mM solution of complex dissolved in degassed H_2O containing PBS at pH 7.4 or 100 mM MES and 50 mM NaCl at pH 6.0. After construction, the air-tight electrochemical cell was removed from the glove box and connected to an Autolab potentiostat. Nova 2.1.7 software was used to run the cyclic voltammograms with step potential = −0.00244 V and scan rate = 0.02 Vs^{-1}, cycling thrice. The Ag/AgCl reference electrode was calibrated to vs SHE by measuring the CV of FcMeOH (0.1 mM in 4:1 buffer:EtOH) and comparing to a literature midpoint potential ($E_{1/2}$) value of +420 mV vs SHE for FcMeOH.[2] Cathodic onset potentials were calculated as

follows: the first linear sweep of the voltammogram of the blank (buffer only) was subtracted from the first linear sweep of the voltammogram of the substrate; a linear baseline in a region of no electrochemical activity was applied; the potential at which the difference between the substrate voltammogram minus blank voltammogram current and the baseline current began to increase exponentially, exceeding a threshold value of 10 nA (instrument current resolution 0.0003% of current range), was taken to be the cathodic onset potential.

6.2 Assay conditions

6.2.1 Chemical zinc reduction assay

6.2.1.1 For organic profluorophores – chapter II

The chemical reduction assay protocol was adapted from O'Connor et al.[3]

Method 1: To a 50 µM solution of **1**/**3**/**4** (6 µL from a 5 mM stock solution in DMSO, 0.05 µmol, 1.0 eq.) in IPA (894 µL), aqueous ammonium chloride (10% w/v, 100 µL) was added. Zinc powder (3 mg, 0.05 mmol, 1000 eq.) was then added to the cuvette and the cuvette was physically shaken between obtaining fluorescence spectra at regular intervals (where t = 0 refers to a spectrum obtained before addition of zinc). The start and end timepoints were analysed by HPLC (method 2B, with detection at 220, 240, 280, 360, 368, 442 and 480 nm).

Method 2: Aqueous ammonium chloride (10% *w/v*, 20 µL) was added to a solution of **3**/**4** (1 mg, 0.002 mmol, 1.0 eq., 1 mM) in DMF (2 mL). Zinc powder (5 mg, 0.072 mmol, 36 eq.) was then added and the resulting mixture was stirred at rt for 24 h. Filtered aliquots of 60 µL (to give 20 µM final concentration) were taken at regular time intervals (where t = 0 refers to before the addition of the zinc powder) and added into DMSO:PBS buffer (1:1, 3 mL) for fluorescence and UV-Vis spectroscopy. Aliquots of 50 µL (final concentration 100 µM) were taken at regular timepoints and diluted in MeCN (450 µL) for analysis by HPLC (50 µL injection, method 2B, with detection at 220, 240, 280, 360, 368, 442 and 480 nm). The

fluorescence spectroscopy blank was 80 µL DMF dissolved in 4 mL of a 1:1 solution of DMSO:PBS buffer. At the end of the assay, 0.2 mL of the HPLC aliquots (in MeCN) were diluted with 0.2 mL PBS and incubated at 37 °C overnight. The incubation in PBS had no effect on the HPLC traces and level of fragmentation observed. For use as a positive control, the corresponding fluorophore (**5/6**) was analysed at 20 µM in DMSO:PBS 1:1 for fluorescence and UV-Vis spectroscopy and at 50 µM in MeCN:PBS for HPLC analysis. Adapted literature procedure.[4]

Method 3 - HPLC: Aqueous ammonium chloride (10% *w/v*, 38 µL) was added to a solution of **15**/**16**/resorufin/Me-Tokyo Green (400 µL from a 1 mM stock solution in DMSO, to give a concentration of 100 µM) in DMF (3562 µL). Zinc powder (1 mg, 38 eq.) was then added and the resulting mixture was stirred at rt for 24 h. At specified time intervals, aliquots (100 µL) were taken, 450 µL PBS buffer (pH 7.4) and 450 µL MeCN was added and the solution was filtered through a PTFE syringe filter. The samples were analysed by HPLC at 480 nm (50 µL injection, final concentration 10 µM, method 2B). t = 0 refers to an aliquot taken before the addition of zinc. At the end of the assay, HPLC samples were added to 0.5 mL PBS and evaluation with pH paper indicated their pH to be between 7 and 8. Overnight incubation in PBS had no effect on the HPLC traces and level of fragmentation observed. For use a positive controls, resorufin and Me-Tokyo Green were dissolved in DMF and NH_4Cl as above and diluted with MeCN:PBS as above for HPLC analysis. Adapted literature procedure.[4]

Method 4 – fluorescence: Aqueous ammonium chloride (10% *w/v*, 38 µL) was added to a solution of **15**/**16**/resorufin/Me-Tokyo Green (400 µL from a 1 mM stock solution in DMSO, to give a concentration of 100 µM) in DMF (3562 µL). Zinc powder (1 mg, 38 eq.) was then added and the resulting mixture was stirred at rt for 24 h. At specified time intervals, aliquots (40 µL) were taken, PBS buffer (2 mL, pH 7.4) was added and the solution was filtered through a PTFE syringe filter. The filter was washed with MeCN (2 mL) and the resulting

solution was analysed by fluorescence spectroscopy (final concentration 1 µM). t = 0 refers to an aliquot taken before the addition of zinc.

Data analysis for methods 3 and 4: Analysis of the fluorescence spectra obtained was carried out in the usual way, using Origin software and subtracting the corrected spectrum of the blank sample (where DMSO was added instead of the desired compound). HPLC spectra analysis was carried out in two ways:

1. Simple HPLC spectra analysis – percentages for each peak were taken directly from the HPLC spectra and plotted against time, using Origin software.
2. Comparative HPLC spectra analysis – the area of a desired peak was divided by the area of that peak for either the t = 0 aliquot (for analysis of loss of the starting azide compound) or the corresponding area of the peak of the corresponding fluorophore analysed at the same time point (for analysis of fluorophore release, to account for any change in the dye over time). This data was plotted as the percentage of compound (remaining or released) over time, using Origin software.

6.2.1.2 For lanthanide complexes – chapter III

The chemical reduction (zinc) assay was carried out by dissolving compound in D_2O and adding 10% *v/v* NH_4Cl solution (10% *w/v* in D_2O) and zinc (38 eq.). The chemical reduction assay protocol was adapted from O'Connor et al.[3]

A stock solution of the europium complex was prepared by dissolving the solid in 3.78 mL D_2O, with 540 µL aliquoted for each reaction. A 10 wt% solution of NH_4Cl in D_2O was prepared and 60 µL was added to the full assay and the NH_4Cl control. Following the addition of zinc powder (38 eq.) to the required solutions, the resulting solutions (prepared as described in

Table 6.13) were heated to 37 °C (using a heat block) for the indicated time and stirred, cooled to rt, filtered (0.45 µm nylon syringe filter) and diluted with D_2O (100 µL). ^1H NMR spectra (for europium complexes and a standard ^1H experiment) were ran at 500 MHz. The

NMR samples were diluted with H_2O for LRMS analysis. For EuNB only, the 6-h timepoint was further analysed by HRMS. The masses used for each europium complex are described in Table 6.14.

Table 6.13: The composition of the solutions prepared and analysed in the chemical reduction assays of the europium complexes. Volumes are given in µL.

Description	**Volume of compound stock**	**Volume of NH_4Cl solution**	**Volume of D_2O**	**Zinc added?**
t = 0 h	540	-	60	No
Timepoints (t = 1, 2, 4, 6 h)	540	60	-	Yes
D_2O control (t = 6 h)	540	-	60	No
NH_4Cl control (t = 6 h)	540	60	-	No

Table 6.14: The masses of complex and zinc powder used for each chemical reduction assay. Time is given in hours.

Europium complex	**Mass of complex in stock solution / mg**	**Mass of complex per vial / mg**	**Mass of zinc for t=1 timepoint / mg**	**Mass of zinc for t=2 timepoint / mg**	**Mass of zinc for t=4 timepoint / mg**	**Mass of zinc for t=6 timepoint / mg**
EuNB (**18a**)	35.6	5.09	18.2	18.4	18.6	18.6
EuNI (**19a**)	39.7	5.67	20.2	20.2	20.4	20.5
EuBn (**22a**)	25.8	4.07	15.6	15.7	15.7	15.9

6.2.2. NaHS reduction assay

All methods are adapted from reported literature procedures.[5]

Method 1: Sodium hydrosulfide hydrate (100 µM in H_2O, 6 µL, at least 7 eq.) was added to a solution of **1** (10 µM, diluted from a 5 mM stock in DMSO, 1.0 eq.) in MeCN/PBS buffer (1:1, buffer pH 7.4, 3 mL). The assay was monitored by fluorescence spectroscopy (λ_{ex} 491 nm, λ_{em} 500–800 nm, slits 5 nm / 2 nm) every 10 min for 1 h, with shaking of the cuvette between timepoints. The 1 h timepoint was further analysed by HPLC (1 mL, 50 µL injection, method 2B, with detection at 220, 240, 280, 360, 450 480, 508 and 550 nm).

Method 2: Sodium hydrosulfide hydrate (100 µM in H_2O, 6–48 µL, at least 7–56 eq.) was added to a solution of **1** (10 µM,* diluted from a 5 mM stock in DMSO, 1.0 eq.) in MeCN/PBS buffer (1:1, buffer pH 7.4, 3 mL) and stirred at rt in a lidded vial for 1 h. The assay was monitored by fluorescence spectroscopy (λ_{ex} 491 nm, λ_{em} 500–800 nm, slits 5 nm / 2 nm) and HPLC (1 mL, 50 µL injection, method 2B, with detection at 220, 240, 280, 360, 450 480, 508 and 550 nm) after 1 h.

Method 3: Sodium hydrosulfide hydrate (100 µM in H_2O, 6–48 µL, at least 7–56 eq.) was added to a solution of **1** (10 µM,* diluted from a 5 mM stock in DMSO, 1.0 eq.) in MeCN (3 mL) and the resulting solution was shaken in a lidded vial for 3 min. The assay was monitored by fluorescence spectroscopy (λ_{ex} 491 nm, λ_{em} 500–800 nm, slits 5 nm / 2 nm) after 3 min.

*Methods 2 and 3 were not carried out as non-diluting titrations, therefore the final concentration of **1** was determined to be 9.8 µM. This was determined to have negligible effect on the fluorescence emission intensity therefore no correction was carried out for the change in concentration.

Method 4: Sodium hydrosulfide hydrate (100 µM in H_2O, 48 µL, at least 56 eq.) was added to a solution of **3**/**4** (10 µM, diluted from a 5 mM stock in DMSO, 1.0 eq.) in MeCN/PBS buffer (1:1, buffer pH 7.4, 3 mL) and stirred at rt in a lidded vial for 1 h. The assay was monitored by fluorescence spectroscopy (λ_{ex} 443 nm, λ_{em} 470–800 nm, slits 5 nm / 2 nm for **3**; λ_{ex} 467 nm, λ_{em} 490–800 nm, slits 10 nm / 2 nm for **4**) and HPLC (1 mL, 50 µL injection, method 2B, with detection at 220, 240, 280, 360, 450 480, 508 and 550 nm) after 1 h.

6.2.3 Enzymatic assays

6.2.3.1 Chapter II – CYP enzyme assays

The procedures were adapted from those previously reported by O'Connor *et al*.[6]

The assays were carried out using the regenerative solutions known as solution A, containing $MgCl_2$, $NADP^+$ and glucose-6-phosphate, and solution B, containing glucose-6-phosphate dehydrogenase, purchased from Corning (cat. no. 451220 and 451200). The enzymes CYP2D6R (CYP2D6R bactosomes, product no. CYP007) and CYP2C9 (CYP2C9HR bactosomes, product no. CYP019) were purchased from BioIVT and exact concentrations of enzyme adjusted for based on their specification sheet.

Calibration curves: For the calibration curves, varying volumes of the compound DMSO stock solution were added to deionised H_2O and 200 µL $KHPO_4$ buffer. Aliquots (50 µL or 100 µL) were added into an equal volume of MeCN, filtered and analysed by HPLC (25 µL injection, method 2B) at 420 nm (for **2**) or 480 nm (for resorufin).

General hypoxia procedure: The oxygen-dependent enzymatic reduction assays were run in a RUSKINN InvivO2® 400 hypoxic Workstation at 37 °C with 0.1-0.4% oxygen and 99.9-99.6% nitrogen. The buffer used in the assays was incubated under the conditions stated previously in the hypoxic workstation for a minimum of 18 h prior to use. To a 2 mL Eppendorf tube, 50 µL of solution A, 10 µL of solution B, $KHPO_4$ buffer (pH 7.4) and the compound DMSO stock solution were added. The Eppendorf was cooled on ice (0-4 °C) and the enzyme was added. The Eppendorf was incubated at 37 °C in the hypoxic workstation for 24 h. Aliquots (50 µL) were taken at desired time intervals, removed from the hypoxic workstation, diluted with MeCN (50 µL) and stored at −20 °C (for up to a week). The samples were thawed, centrifuged at 17,000 *g* at 4 °C for 10 min, the supernatant was removed and analysed by HPLC (25 µL injection) at 420 nm (compound **1**) or 480 nm (compound **15**).

General normoxia procedure: To a 2 mL Eppendorf tube, 50 µL solution A, 10 µL solution B, deionised H_2O, 200 µL $KHPO_4$ buffer (pH 7.4) and the compound DMSO stock solution were added. The Eppendorf was cooled on ice (0-4 °C) and the enzyme was added. The Eppendorf was incubated at 37 °C in a H_2O bath for 24 h. Aliquots (50 µL) were taken at desired time intervals, diluted with MeCN (50 µL) and stored at −20 °C (for up to a week).

The samples were thawed, centrifuged at 17,000 *g* at 4 °C for 10 min, the supernatant was removed and was analysed by HPLC (25 µL injection, method 2B) at 480 nm.

General stability procedure: To a 2 mL Eppendorf tube, 50 µL of solution A, 10 µL of solution B, 730 µL deionised H_2O, 200 µL 0.5 M $KHPO_4$ buffer (pH 7.4) and 10 µL of the compound DMSO stock solution (1 mM, assay concentration 10 µM) were added. The Eppendorf was incubated at 37 °C in a H_2O bath for 24 h. Aliquots (50 µL) were taken at desired time intervals, diluted with MeCN (50 µL) and stored at −20 °C (for up to a week). The samples were centrifuged at 17,000 *g* at 4 °C for 10 min, the supernatant was removed and was analysed by HPLC (25 µL injection, method 2B) at 480 nm.

Volume of reagents used: Conditions 1 and 2 (Table 6.15) were used for the control analysis of DCM-N_3 **1**, whereas conditions 3 and 4 were used for the analysis of profluorophore **15**. The H_2O volume listed is the volume used in hypoxia and normoxia assays, in the stability assay the volume of H_2O was increased to compensate for the loss of the enzyme volume.

Table 6.15: The conditions and volume of reagents used during the enzymatic assays for chapter II.

Condition	**Concentration of DMSO stock solution / mM**	**Stock solution added / µL**	**Assay concentration / µM**	**Enzyme (3.4 nmol/mL)**	**Enzyme added / µL (Concentration / pmol/mL)**	**H_2O / µL**
1	1	1	1	CYP2D6R	27.0 (92)	712
2	1	1	1	CYP2C9HR	27.0 (92)	712
3	10	10	100	CYP2D6R	2.7 (9.2)	727.3
4	10	10	100	CYP2C9HR	2.7 (9.2)	727.3

Data analysis: The concentration of resorufin or compound **2** released was determined directly from the calibration curves (Table 6.16). Consumption of the azide was plotted either as a peak area percentage, in comparison to the t = 0 peak area.

Table 6.16: Volumes of H_2O and DMSO stock solution used for the calibration curves for enzymatic and X-ray irradiation assays for chapter II.

Volume of H2O / µL	798	794	790	786	782
Volume of DMSO stock solution / µL	2	6	10	14	18

Final assay concentration (when DMSO stock 10 mM) / µM	10	30	50	70	90
Final assay concentration (when DMSO stock 2 mM) / µM	2	6	10	14	18

6.2.3.2 Chapter III – nitroreductase enzyme assay

This procedure is adapted from the procedure previously reported[7] and taken from my publication of this work.[8]

The assay was carried out using nitroreductase (NTR) enzyme from *E. coli* (expressed in *E. coli*, >100 units/mg), purchased from Sigma Aldrich, and NADH, purchased from Prozomix (as the disodium salt). The nitroreductase enzyme was prepared by dissolving 25.3 mg of the lyophilised powder (out of 26.6 mg total powder, total containing 1 mg enzyme) in 951 µL H_2O (to give stock solutions of 1 mg/mL), aliquoted (in 100 µL portions), stored at −20 °C and thawed immediately prior to use. NADH was stored at −20 °C and weighed and diluted in H_2O to 5 mM immediately prior to addition to the assay. The lanthanide complexes were stored at −80 °C and weighed and diluted in H_2O to 1 mM immediately prior to addition to the assay.

The assay samples were prepared as described in Table 6.17, with samples prepared by first adding the 0.9% NaCl solution and H_2O, then NADH solution (assay concentration 500 µM) followed by addition of the lanthanide complex stock solution (assay concentration 200 µM). The t = 0 timepoints were taken prior to addition of the NTR enzyme and were taken for all assays. The enzyme solution was added (assay concentration ~32 µg/mL) and the Eppendorfs containing the assays were heated to 37 °C using a H_2O bath. At the indicated timepoints, 100 µL aliquots were taken from each assay, diluted with 100 µL MeCN and centrifuged at 6000 rpm for 4 min. The supernatant was filtered (Nylon syringe filter, 0.45 µM, 13 mm) into HPLC vials (final concentration ~100 µM complex). The assay was monitored by Analytical HPLC (**method 3**, 50 µL injection), with samples injected in the order 1, 4, 2, 3 (see Table 6.17), and analysed using the Agilent HPLC software (with

NaCl/H_2O blank subtraction, for numerical analysis) and MestReNova software (for stacking of the raw spectra, without blank subtraction).

Table 6.17: The volumes of the reagents used for the nitroreductase assay of GdNB.

	1 Full assay	**2 NTR control**	**3 NADH control**	**4 NaCl control**
Lanthanide complex (1 mM) / µL	200	200	200	200
NADH (5 mM) / µL	100	-	100	-
NTR (1 mg/mL) / µL	30	30	-	-
0.9% NaCl solution / µL	670	670	670	670
H2O / µL	-	100	30	130
Total volume / µL	1000	1000	1000	1000

For numerical analysis, the HPLC spectra following blank subtraction (NaCl solution/H_2O/MeCN blank) were used. The concentration of nitrobenzyl alcohol released was calculated by comparing the area of the peak (measured at 269 nm) at 9.6-9.8 min with the control injected at 100 µM. The percentage of GdNB remaining was calculated by comparing the area of the peak (measured at 269 nm) at 8.0–8.1 min to the area of the same peak in the t = 0 sample. The stacked spectra show the uncorrected spectra at 269 nm (no blank subtraction) and any peaks appearing after 12 min are artefacts on the column.

The following controls were also analysed by Analytical HPLC (**method 3,** 50 µL injection): GdNB, at an unspecified concentration, in H_2O, for purity testing, filtered; a HPLC blank where 670 µL 0.9% NaCl solution was added to 330 µL H_2O and 100 µL of this solution was added to 100 µL MeCN and filtered; a NADH blank, with 100 µL of the 5 mM stock solution (in H2O) diluted with 670 µL 0.9% NaCl solution and 230 µL H_2O, and 100 µL of this solution was added to 100 µL MeCN and filtered; nitrobenzyl alcohol (final concentration 100 µM) was prepared from a 10 mM stock solution in DMSO, diluted to 200 µM by adding 20 µL of 10 mM stock solution to 670 µL 0.9% NaCl solution and 310 µL H_2O, and 100 µL of this solution added to 100 µL MeCN and filtered; aminobenzyl alcohol, at an unspecified concentration, in MeOH, filtered.

6.2.3.3 Chapter III – NADH NMR assay

This procedure is taken from my publication on this work.[8]

EuNB (6.3 mg) was dissolved in D_2O (868 µL) to give a 13.3 mM stock solution and an initial ^1H NMR spectra and ^1H NMR for europium spectra was ran. NADH (37.1 mg) was dissolved in D_2O (523 µL) to give a 100 mM stock solution. 200 µL of the NADH stock solution was added to 600 µL of the EuNB solution to give final concentrations of 25 mM NADH and 10 mM EuNB and t = 0 NMR spectra were acquired (15 min following the previous NMR spectra). The NMR tube was heated to 37 °C in a H2O bath for 6 h and NMR spectra (^1H and ^1H for europium) were acquired before heating to 37 °C for a further 18 h (24 h timepoint). Following final NMR analysis in D_2O only, 250 µL MeOD and then a further 650 µL MeOD was added to the NMR tube (to give final 1:1 MeOD:D_2O) to aid solubility of the organic components (likely due to the higher solubility of the high concentration NADH). The controls were as follows: EuDOTA in D_2O; nitrobenzyl alcohol in D_2O and 10% NH_4Cl; and aminobenzyl alcohol in D_2O and 10% NH_4Cl (as used for the chemical reduction assay controls). The percentage of EuDOTA released was calculated by dividing the area of the EuDOTA peak at 33.8 ppm (4H, therefore divided by 4) by the sum of the area of the EuDOTA peak (divided by 4 for 1H) and the corresponding peak of the starting EuNB (1H, 32.5 ppm).

6.2.3.4 Chapter III – hydrogenase enzyme assay

This procedure is adapted from the procedure previously reported[9] and taken from my publication of this work.[8]

An initial study at 24 h in buffer at pH 6 saw complete conversion to EuDOTA for both EuNB and EuNI in the presence and absence of the enzyme, therefore the procedure was optimised to be carried out up to 4 h in buffer at pH 7.4 (based on the PBS stability studies). These assays were carried out by Dr Daria Sokolova or Max Roberts from the Vincent group, University of Oxford, apart from the NMR analysis.

Catalyst preparation and reaction set-up was carried out in a glove box (Glove Box Technology Ltd.) under a protective N*2* atmosphere (O_2 < 3 ppm). Carbon black (BP2000) was brought into a glovebox, suspended in buffer (sodium phosphate buffer, 100 mM, pH 7.4, 20 mg/mL suspension) and was sonicated in the glovebox for 1 h. Overexpressed Hyd-1 (23.1 µL, expressed according to the protocol reported by Sokolova *et al.*[9]) was brought into the glovebox and combined with the sonicated carbon suspension (79.2 µL), removed from the glovebox and immobilised in the fridge (4 °C) for 1 h. The desired complex was dissolved in buffer in the glovebox to make a 10 mM stock solution, which was added to two DrySyn® OCTO tubes–A and B. The immobilised Hyd-1/C was centrifuged in the glovebox, supernatant removed, resuspended in buffer (300 µL) and added to tube A. Tube A contained 1200 µL stock solution of europium complex and 300 µL of Hyd-1/C solution. No catalyst (Hyd-1/C) was added to the control tube B. The DrySyn® OCTO was sealed, removed from the glovebox and connected to H_2 and the samples were stirred at rt for 4 h. Aliquots were taken at the given timepoints (1 h, 2 h and 4 h) and the time when DrySyn® OCTO was not connected to H_2 was not included in the time count. The aliquots were centrifuged (3 min, 14500 rpm), 450 µL supernatant removed, diluted with 50 µL D_2O and measured by ^1H NMR spectroscopy (^1H for europium complexes and ^1H with H2O suppression).

Controls: The ^1H NMR (for europium complexes) spectrum of EuDOTA was measured in D_2O only. The ^1H NMR spectra of nitrobenzyl alcohol and aminobenzyl alcohol were measured following preparation of ~10 mM stock solutions of the compounds in sodium phosphate buffer (pH 7.4) and dilution 10% *v/v* with D_2O. The ^1H NMR spectra of nitroimidazole alcohol and benzyl alcohol were measured in D_2O.

EuNB: t = 0 is the solid dissolved in buffer (to 10 mM) and diluted with 10% *v/v* D_2O.

EuNI: t = 0 is the solid dissolved in D_2O.

EuBn: t = 0 is the solid dissolved in buffer (to 10 mM) and diluted with 10% *v/v* D_2O. Peaks observed in the ^1H spectra in the presence of the Hyd1 enzyme between 3 and 4 ppm (in the assay timepoints) are postulated to arise from residual glycerol from the protein.

6.2.4 X-ray irradiation assay

X-ray irradiation was carried out using a Cs source at the Department of Oncology, University of Oxford. Samples consisted of 20 µL DMSO stock solution (either 10 mM or 2 mM), 520 µL $KHPO_4$ buffer (pH 7.4) and 1460 µL deionised H_2O. The tested compounds were **15** and resorufin (final irradiated concentrations 100 µM and 20 µM, from 10 mM and 2 mM stock solutions respectively). These samples were plated in 6-well plates (one per irradiation dose and one control) and gently shaken to solubilise the compounds. The 6-well plates were incubated overnight at 37 °C in a hypoxia chamber (< 0.1% O_2, Bactron anaerobic chamber) then sealed in hypoxic boxes prior to removal from the hypoxia chamber and irradiation. The plate was either not irradiated (kept in the hypoxic sealed environment), irradiated with 30 Gy over 27 min or irradiated with 60 Gy over 54 min. Each plate was released from the hypoxic environment to normoxia at the same time. Irradiated samples were transferred to glass vials by pipette, frozen by immersion in dry ice, transported to the Department of Chemistry and thawed. Aliquots (50 µL) were injected into MeCN (50 µL) and analysed by HPLC (25 µL injection, method 2B) at 480 nm.

6.2.5 ChromlogD assay

Controls: The calibration mix contained theophylline, phenyl tetrazole, benzimidazole, colchicine, phenyl theophylline, acetophenone, butyrophenone, indole, propiophenone and valerophenone, each 0.5 mg/mL in DMSO. The following control standards were prepared and tested at 1 mg/mL: carbamazepine, budesonide, warfarin, ketoprofen, indomethacin, imipramine, chlorpromazine and nicardipine.

Samples: The DMSO stock solution or solid material (<1 mg) for each tested compound was diluted in either DMSO, MeCN or H_2O (as appropriate) to <1 mM.

Method: The assay was carried out on an Agilent 1260 Infinity II® system with a Poroshell 120 EC-C_{18} column (4 µM, 4.6 × 100 mm, 1 mL min^{-1}), see Table 6.18 for the solvent gradient used. The Chromatographic Hydrophobicity Index (CHI) values were derived directly from the gradient retention times using calibration parameters for the control compounds. The CHI value approximates to the volume % organic concentration when the compound elutes. CHI was linearly transformed into a ChromlogD value by least-square fitting of experimental CHI values using the following formula: ChromlogD = 0.0857*CHI − 2.

Table 6.18: The solvent gradient used for the chromlogD assay, where C = 50 mM NH_4OAc in H_2O and D = MeCN (no additive).

Time / min	%C	%D
0.0	95	5
10.0	5	95
15.0	5	95

6.2.6 Stability measurements for lanthanide complexes

Zinc reduction assay EuNI extra controls: A stock solution of EuNI was prepared by dissolving 11.3 mg of solid in 1.08 mL D_2O. 540 µL of compound stock solution was diluted with either 60 µL D_2O (D_2O only control) or 60 µL NH_4Cl solution (10% wt%) (NH_4Cl control). The resulting solutions were heated to 37 °C in an oil bath with no stirring and analysed by ^1H NMR spectroscopy (^1H for europium complexes and standard ^1H, 500 MHz) at the indicated timepoints (with the time of analysis not included in the assay time).

H_2O rt measurements: 250 µM solutions of TbNI and TbNB were prepared by dilution from a 10 mM stock solution in H2O. The stability in H_2O was analysed by 10 µL injections onto the LCMS (method 3) at given timepoints. The samples were left at rt between injections, with no stirring between timepoints. The stability was analysed by percentage purity of the UV peak corresponding to the desired compound (area of desired peak compared to total area of all peaks), at 254 nm. Data were analysed using MestReNova and processed using Origin™ software.

H_2O 37 °C measurements: 500 µM solutions of TbNI and TbNB were prepared and heated to 37 °C using a H_2O bath with no stirring. At given timepoints, 50 µL aliquots were taken and diluted with 50 µL H_2O to give a final concentration of 250 µM. The samples were analysed by LCMS (method 3). The stability data were analysed and processed as above.

PBS rt measurements: EuNB (6.8 mg) was dissolved in 700 µL PBS buffer (pH 7.4) and analysed by paramagnetic Eu ^{1}H NMR spectroscopy (at 500 MHz) at the indicated time points, with no stirring between timepoints. EuNI (5.2 mg) was dissolved in 700 µL PBS buffer (pH 7.4) and analysed by paramagnetic Eu ^{1}H NMR spectroscopy at the indicated time points, with no stirring between timepoints. For analysis and comparison, EuDOTA (6.3 mg) was dissolved in 700 µL PBS buffer and one paramagnetic Eu ^{1}H NMR spectrum was obtained immediately. The stability/percentage purity was determined by comparing the integral of the peak at 34 ppm (4H) belonging to EuDOTA to the integral of the peak at 33 ppm (1H) belonging to EuNB/EuNI.

6.2.7 Relaxivity measurements

11 T measurements: T_1 measurements were carried out using a Bruker AVIII HD 500 NMR instrument equipped with 5 mm z-gradient broadband X-19F/1H BBFO SMART probe. Samples were prepared between 0 and 1 mM (0.2 mM increments, 200 µL, H_2O), transferred to a capillary tube (~70 µL), flame sealed, transferred to a 5 mm NMR tube and analysed at 298 K. No lock solvent was required. For each concentration, an initial T_1 measurement was carried out using time delays of 0.01, 0.1, 0.5, 1, 5 and 20 s and a more accurate measurement was carried out by measuring at 20–25 time delays (from 0 to 10 s), based on the initial rough T_1 measurement. T_1 data was analysed using TopSpin software and plotted using Origin software.

7 T measurements: Measurements were carried out by Dr Lina Hacker from the Department of Oncology. Relaxivity determination by MRI was conducted using an Agilent 7 T scanner equipped with a DirectDrive console and 400 mT/m imaging gradients (Varian,

UK). The RF coil employed was a 72 mm i.d. birdcage resonator (Rapid Biomedical, Germany). T1 measurements were carried out using an inversion recovery spin-echo sequence with the following parameters: slice thickness of 1 mm, field of view (FoV) of 72 x 72 mm, matrix size of 128 x 128, four averages, TR/TE of 10 s/8 ms, and 12 inversion times (Ti) ranging from 0.01–6.0 s (exponentially spaced). T2 measurements were performed using a spin-echo sequence with the same single-slice sequence as the T1 measurements: slice thickness of 1 mm, FoV of 72 x 72 mm, matrix size of 128 x 128, four averages, TR of 10 s, and 12 echo times (TE) ranging from 8 to 300 ms (exponentially spaced). All samples were placed in 1 mL syringes (Terumo) in a custom-made 3D-printed phantom holder enabling reproducible measurements. Acquired data was analysed using Matlab (version R2022a).

All T_1 measurements were carried out on samples determined to be 95% purity or above by LCMS (method 2).

6.3 Biological Experimental

Biological experiments were carried out by Dr Lina Hacker and Louise Martin from the Department of Oncology, University of Oxford.

Cell culture was carried out using HCT116 cells were cultured in DMEM medium supplemented with 10% FBS at 37°C, 5% CO_2 in a humidified incubator. All cell lines were routinely mycoplasma tested using a HEK-Blue™ detection kit (Invivogen) and found to be negative.

For preparation of samples for **LCMS analysis**, 4.5 million cells were seeded in 10 cm^2 glass dishes and allowed to adhere for 7 h. Cells were treated with the indicated probe concentrations and exposed to hypoxia (<0.1% O_2) for 16 h. Afterwards, cells were washed three times in HEPES inside the hypoxia chamber, scraped into 1 mL of HEPES and spun down. The remaining cell pellet was lysed and evenly resuspended in 200 µL of MeCN: deionised H_2O 1:1 and sonicated for 10 min. Samples were spun down at 4°C at 13,000

rpm for 15 min. The cleared supernatant was carefully removed. The pellet was lysed in 100 µL deionised H_2O, spun down again at 4 °C at 13,000 rpm for 15 min, and the remaining supernatant was added to the prior supernatant. The combined supernatant was centrifuged in an Amicon Ultra Centrifugal Filter (Merck) for 10 min at 4000 g. The resulting filtered supernatant was collected and stored at −80 °C (or on dry ice during transport) prior to analysis by LCMS (method 4).

6.4 Synthesis of Compounds

6.4.1 Compounds from chapter II

2-Methyl-4*H*-chromen-4-one, 7

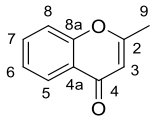

To a solution of 2'-hydroxyacetophenone (3 mL, 24.8 mmol, 1.0 eq.) in EtOAc (120 mL) under a nitrogen atmosphere, Na (1.58 g, 68.7 mmol, 2.8 eq.) was added portion wise. The resulting mixture was stirred at rt for 17 h and the precipitate was filtered and dried under reduced pressure. The precipitate was dissolved in H_2O (50 mL), AcOH (7 mL) added and H_2SO_4 (1.8 mL, 37% in H_2O) added dropwise. The reaction mixture was heated under reflux for 1 h and cooled to ambient temperature. Iced H2O (30 mL) was added portion wise and the pH was adjusted to 7 with solid $NaHCO_3$. The mixture was extracted with toluene (3 × 25 mL) and the organic components were washed with brine (1 × 50 mL), dried over Na_2SO_4, and filtered. The solution was concentrated *in vacuo*, the residue adsorbed onto Celite®, and the product purified using silica gel column chromatography, eluting with EtOAc and PE (isocratic, 25% EtOAc) to afford compound **7** (1.37 g, 35%) as a cream solid: R_f 0.6 (EtOAc : PE 4:1); m.p. 62–64 °C (EtOAc) [lit.[3] 58–60 °C (EtOAc), lit.[10] 55–56 °C, lit.[11] 62–64 °C (hexanes and EtOAc)]; ^{1}H NMR (600 MHz, $CDCl_3$): 2.39 (3H, s, C^9*H*$_3$), 6.18 (1H, s, C^3*H*), 7.37 (1H, dd, J_1 = 7.8, J_2 = 1.0, C^6*H*), 7.41 (1H, dd, J_1 = 8.5, J_2 = 1.0, C^8*H*), 7.61–7.67 (1H, m, C^7*H*), 8.18 (1H, dd, J_1 = 7.8, J_2 = 1.6, C^5*H*); ^{13}C NMR (151 MHz, $CDCl_3$): 20.8 (C^9),

110.7 (C^3), 117.9 (C^8), 123.7 (C^{4a}), 125.1 (C^6), 125.8 (C^5), 133.6 (C^7), 156.7 (C^{8a}), 166.4 (C^2), 178.4 (C^4); LRMS: *m/z* (ESI^+) 161 ($[M+H]^+$, 100%), 183 ($[M+Na]^+$, 40%); Analytical HPLC (method 2B) R_t 6.8 min, >99%. The spectroscopic data are in good agreement with the literature values.[3, 10]

2-(2-Methyl-4*H*-chromen-4-ylidene)malononitrile, 8

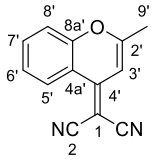

To a solution of **7** (1.30 g, 8.14 mmol, 1.0 eq.) in Ac_2O (8 mL), malononitrile (5.38 g, 81.4 mmol, 10 eq.) was added. The solution was heated under reflux for 5 h, allowed to cool to ambient temperature, MeOH (16 mL) was added and stirred at 50 °C for 30 min. The reaction mixture was concentrated *in vacuo*, and the product crystallised from the residue with Et_2O and recrystallised from MeOH to afford compound **8** (0.93 g, 55%) as a red solid: R_f 0.31 (acetone : PE 1:4); m.p. 185–187 °C (MeOH) [lit.[3] 184–186 °C (MeOH), lit.[12] 187–188 °C, lit.[13] 332–334 °C]; ν_{max} (solid) cm^{-1}: 2214 (C=N, m), 1635 (C=C, s); ^1H NMR (600 MHz, $CDCl_3$): 2.44 (3H, d, J = 0.9, $C^{9'}H_3$), 6.71 (1H, q, J = 0.9, $C^{3'}H$), 7.42–7.48 (2H, m, $C^{6'}H/C^{8'}H$), 7.72 (1H, ddd, J_1 = 8.6, J_2 = 7.1, J_3 = 1.5, $C^{7'}H$), 8.88–8.94 (1H, m, $C^{5'}H$); ^{13}C NMR (151 MHz, $CDCl_3$): 20.5 ($C^{9'}$), 62.4 (C^1), 105.5 ($C^{3'}$), 115.5 (C^2), 116.6 (C^2), 117.6 ($C^{4a'}$), 118.7 ($C^{8'}$), 125.8 ($C^{5'}$), 126.1 ($C^{6'}$), 134.6 ($C^{7'}$), 152.9 ($C^{2'}$), 153.3 ($C^{8a'}$), 161.7 ($C^{4'}$); LRMS: *m/z* (ESI^+) 209.0 ($[M+H]^+$, 93%); Analytical HPLC (method 2B) R_t 9.3 min, >99%. The spectroscopic data are in good agreement with the literature values.[3]

2-Methyl-4*H*-thiochromen-4-one, 9

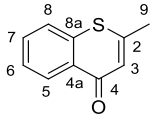

Thiophenol (1.0 mL, 9.8 mmol, 1.0 eq.) was added to polyphosphoric acid (13 mL) at 90 °C. Ethyl acetoacetate (1.3 mL, 10.2 mmol, 1.0 eq.) was added dropwise and the reaction mixture was stirred at 90 °C for 30 min. The reaction mixture was cooled to rt, vigorously

stirred with ice/H_2O and extracted with EtOAc (5 × 50 mL). The organic components were combined and washed with brine (3 × 50 mL), dried over $MgSO_4$, and filtered. The residue was concentrated *in vacuo*, adsorbed onto Celite® and purified using flash silica gel column chromatography, eluting with PE and EtOAc (gradient, 0–30% EtOAc) to yield compound **9** as a yellow solid (221 mg, 13%): R_f 0.35 (EtOAc : PE 1:3); m.p. 74–78 °C (EtOAc) [lit.[14] 103–104 °C, lit.[15, 16] 101–103 °C (benzene and PE)]; v_{max} (solid) cm^{-1}: 1704 (C=O, m), 1614 (C=C, m), 1592 (C=C, s); ^{1}H NMR (400 MHz, $CDCl_3$) 2.47 (3H, d, *J* = 1.0, C^9H_3), 6.85 (1H, q, *J* = 1.0, C^3H), 7.50 (1H, ddd, J_1 = 8.1, J_2 = 6.7, J_3 = 1.7, C^6H), 7.45–7.62 (2H, m, C^7H/C^8H), 8.49 (1H, ddd, J_1 = 8.1, J_2 = 1.5, J_3 = 0.8, C^5H); HRMS *m/z* (ESI^+) [Found: 177.0368, $C_{10}H_8OS$ requires $[M+H]^+$ 177.0369]; LRMS *m/z* (ESI^+): 107 ($[M+H]^+$, 100%). These data are in good agreement with the available literature values.[16-21]

2-(2-Methyl-4*H*-thiochromen-4-ylidene)malononitrile, 10

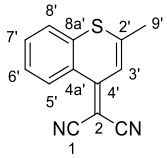

To a solution of **9** (0.26 g, 1.48 mmol, 1.0 eq.) in Ac_2O (5.2 mL), malononitrile (0.98 g, 14.8 mmol, 10 eq.) was added. The solution was heated under reflux for 2 h, allowed to cool to ambient temperature, MeOH (7.8 mL) was added and stirred at 55 °C for 2 h. The reaction mixture was concentrated *in vacuo*, and the product crystallised from the residue with Et_2O and recrystallised from MeOH to afford compound **10** (0.180 g, 54%) as a dark red solid: R_f 0.17 (acetone : PE 1:4); m.p. 178–180 °C (decomposition, MeOH); v_{max} (solid) cm^{-1}: 2953 (C-H, w), 2206 (C≡N, m), 2192 (C≡N, m), 1583 (C=C, s); ^{1}H NMR (400 MHz, $CDCl_3$): 2.53 (3H, d, *J* = 1.1, $C^{9'}H_3$), 7.41 (1H, q, *J* = 1.1, $C^{3'}H$), 7.54–7.62 (1H, m, $C^{8'}H$), 7.62–7.66 (2H, m, $C^{6'}H$/$C^{7'}H$), 8.94 (dt, 1H, J_1 = 8.2, J_2 = 1.1, C^6H); ^{13}C NMR (125 MHz, $CDCl_3$): 23.6 ($C^{9'}$), 68.3 (C^1), 104.0 ($C^{3'}$), 115.8 (C^2), 117.1 ($C^{4a'}$), 120.8 ($C^{8'}$), 125.0 ($C^{5'}$), 127.2 ($C^{6'}$), 128.6, 131.9 ($C^{7'}$), 136.2, 149.0, 156.1 ($C^{4'}$); HRMS *m/z* (ESI^+) [Found: 225.0479, $C_{13}H_8N_2S$ requires $[M+H]^+$ 225.0481]; LRMS *m/z* (ESI^+): 225 ($[M+H]^+$,

100%); Analytical HPLC (Method 2B) R_t 10.6 min, >99%. These data are in good agreement with the available literature values.[17, 20]

4-Azido-2,3,5,6-tetrafluorobenzaldehyde, 11

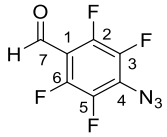

NaN_3 (0.90 g, 13.9 mmol, 1.1 eq.) was added to a solution of pentafluorobenzaldehyde (2.47 g, 12.6 mmol, 1.0 eq.) in acetone (20 mL) and H_2O (7.5 mL) and the mixture was refluxed for 7 h. The resulting solution was cooled to rt and diluted with H_2O (20 mL). The solution was extracted with Et_2O (3 × 30 mL), the organic phase was dried over $MgSO_4$ and the solution was concentrated *in vacuo*. The resulting residue was adsorbed onto Celite® and purified by flash silica column chromatography, eluting with EtOAc and PE (1–15% EtOAc), to yield **11** as an off-white solid (1.76 g, 64%): R_f 0.31 (EtOAc : PE 5:95); ^{1}H NMR (400 MHz, acetone-d_6) 10.23 (1H, p, *J* = 1.2, C^7*H*); ^{13}C NMR (151 MHz, $CDCl_3$): 110.9 (t, *J* = 10.7, C^1), 126.36 (tt, J_1 = 11.6, J_2 = 3.8, C^4), 139.4-141.4 (m, C^3/C^5), 146.2-148.3 (m, C^2/C^6), 181.8 (p, *J* = 3.2, CHO); ^{19}F NMR (377 MHz, acetone-d_6) −153.64 – −154.08 (2F, m, C^3*F*/C^5*F*), −147.66 – −148.41 (2F, m, C^2*F*/C^6*F*); Analytical HPLC (method 2B) R_t 9.0 min, 96.4%. These data are in good agreement with the available literature values.[22]

(4-Azido-2,3,5,6-tetrafluorophenyl)methanol, 12

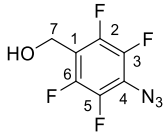

To a solution of **11** (0.786 g, 3.59 mmol, 1.0 eq.) in AcOH (12.0 mL) under argon, $Me_2NH{\cdot}BH_3$ (0.242 g, 4.32 mmol, 1.2 eq.) was added and the reaction mixture was stirred at rt for 2 h. H_2O (50 mL) was added and the mixture was extracted with Et_2O (3 × 40 mL). The combined organic phases were washed with 15% Na_2CO_3 (2 × 50 mL) and brine (1 × 50 mL), dried over $MgSO_4$ and concentrated *in vacuo*. The resulting residue was adsorbed onto Celite® and purified by flash silica column chromatography, eluting with EtOAc and PE

(isocratic, 15% EtOAc) to yield **12** as a yellow solid (0.639 g, 80%): R_f 0.35 (EtOAc : PE 1:5); m.p. 40–42 °C (EtOAc) [lit.[23] 68-71 °C (hexane and Et_2O), lit.[24] 67-68 °C (sublimation)]; v_{max} (solid) cm^{-1}: 3384 (O-H, w br), 2126 (N=N=N, m), 1655 (C=C, m), 1484 (C-F, s); ^1H NMR (600 MHz, $CDCl_3$) 2.08 (1H, br s, OH), 4.78 (2H, s, C^7H_2); ^{19}F NMR (565 MHz, $CDCl_3$) −151.82 (2F, dd, J_1 = 21.3, J_2 = 10.6, C^3F/C^5F), −144.72 (2F, dd, J_1 = 21.3, J_2 = 10.6, C^2F/C^4F); ^{13}C NMR (151 MHz, $CDCl_3$) 52.8 (C^7), 114.3 (C^1), 120.2 (C^4), 140.5 (dt, J_1 = 250.3, J_2 = 3.6, C^3/C^5), 145.4 (dt, J_1 = 268.2, J_2 = 4.3, C^2/C^6); LRMS *m/z* (ESI^+/EI/ACPI): mass not found; Analytical HPLC (method 2B): R_t 8.1 min, >99%. These data are in good agreement with the available literature values.[22, 23, 25]

4-((4-Azido-2,3,5,6-tetrafluorobenzyl)oxy)benzaldehyde, 14, *via* 1-azido-4-(chloromethyl)-2,3,5,6-tetrafluorobenzene, 13

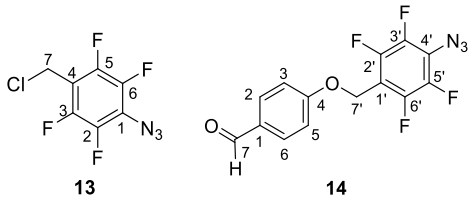

Step 1 - To a solution of **12** (0.64 g, 2.9 mmol, 1.0 eq.) in CH_2Cl_2 (7.0 mL) cooled to 0 °C in an ice-H_2O bath, thionyl chloride (7.0 mL, 96 mmol, 33 eq.) was added dropwise. The reaction mixture was warmed to rt, stirred for 2 h, then concentrated *in vacuo* to yield 1-azido-4-(chloromethyl)-2,3,5,6-tetrafluorobenzene, **13**, as a yellow solid (0.67 g): R_f 0.84 (EtOAc : PE 1:3). This compound was used without further purification and characterisation.

Step 2 - 13 (0.63 g, 2.6 mmol, 1.0 eq.), 4-hydroxybenzaldehyde (0.32 g, 2.6 mmol, 1.0 eq.), caesium chloride (1.7 g, 5.3 mmol, 2 eq.) and TBAI (0.97 g, 2.6 mmol, 1.0 eq.) were dissolved in DMF (35 mL) at 0 °C under an argon atmosphere. The reaction mixture was warmed to rt and stirred for 3 h then diluted with saturated ammonium chloride solution (100 mL). The mixture was extracted with EtOAc (3 × 50 mL) and the organic components were washed with saturated sodium bicarbonate solution (3 × 100 mL) and H_2O (2 × 100 mL) then dried over $MgSO_4$, filtered and concentrated *in vacuo*. The resulting residue was adsorbed onto Celite® and purified by flash silica column chromatography, eluting with

EtOAc and PE (gradient, 5–10% EtOAc) to yield **14** as a colourless solid (101 mg, 17%): R_f 0.44 (EtOAc : PE 1:3); m.p. 75–77 °C (EtOAc); ν_{max} (solid) cm^{-1}: 2128 (N=N=N, m), 1693 (C=O, m), 1603 (C=C, m), 1497 (C-F, s), 1253 (C-O, m); ^{1}H NMR (400 MHz, $CDCl_3$) 5.19 (2H, t, $J_{H\text{-}F}$ = 1.5, $C^{7'}H_2$), 7.02–7.13 (2H, m, C^3H/C^5H), 7.82–7.94 (2H, m, C^2H/C^6H), 9.92 (1H, s, C^7H); ^{1}H NMR (600 MHz, acetone-d_6) 5.39 (2H, t, J_F = 1.5, $C^{7'}H_2$), 7.21–7.28 (2H, m, C^3H/C^5H), 7.90–7.96 (2H, m, C^2H/C^6H), 9.94 (1H, s, C^7H); ^{13}C NMR (151 MHz, acetone-d_6) 58.8 ($C^{7'}$), 111.1 (t, $J_{H\text{-}F}$ = 17.9, $C^{1'}$), 116.1 (C^3/C^5), 122.1-122.6 (m, $C^{1'}$), 132.1 (C^1), 132.7 (C^2/C^6), 141.7 (ddd, J_1 = 248.0, J_2 = 16.4, J_3 = 3.8, $C^{3'}/C^{5'}$), 146.6 (dddd, J_1 = 248.0, J_2 = 12.1, J_3 = 7.7, J_4 = 4.0, $C^{2'}/C^{6'}$), 163.9 (C^4), 191.3 (C^7); ^{19}F NMR (376 MHz, acetone-d_6) −151.76 – −150.59 (2F, m, $C^{3'}F/C^{5'}F$), −143.51 – −141.26 (2F, m, $C^{2'}F/C^{4'}F$); HRMS *m/z* (ESI^+) [Found: 326.0545, $C_{14}H_7F_4N_3O_2$ requires $[M+H]^+$ 326.0547]; LRMS *m/z* (ESI^+) 326.4 ($[M+H]^+$, 85%); Analytical HPLC (method 2B) R_t 10.6 min, 97.8%.

(*E*)-2-(2-(4-((4-Azido-2,3,5,6-tetrafluorobenzyl)oxy)styryl)-4*H*-chromen-4-ylidene)malononitrile, 3

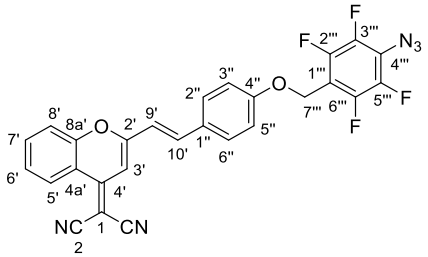

To a solution of **8** (47 mg, 0.23 mmol, 1.0 eq.) and **14** (80 mg, 0.25 mmol, 1.1 eq.) in dry EtOH (8 mL), piperidine (0.09 mL, 0.91 mol, 4 eq.) was added. The solution was heated under reflux for 7 h, cooled to rt, filtered and dried under reduced pressure, washed with dry EtOH and recrystallised from EtOH to give a brown solid, **3** (82 mg, 69%): R_f 0.50 (EtOAc : PE 1:3); m.p. 166 °C (decomposition, EtOH); ν_{max} (solid) cm^{-1}: 2207 (C≡N, m), 2136 (N=N=N, m), 1627 (C=C, m), 1596 (C=C, s), 1557 (C=C, m), 1490 (C-F, m), 1239 (C-O, w); ^{1}H NMR (600 MHz, CD_2Cl_2) 5.19 (2H, t, $J_{H\text{-}F}$ = 1.4, $C^{7''}H_2$), 6.78 (1H, d, J = 16.0, $C^{9'}H$), 6.86 (1H, s, $C^{3'}H$), 7.02–7.07 (2H, m, $C^{3''}H/C^{5''}H$), 7.48 (1H, ddd, J_1 = 8.5, J_2 = 7.2, J_3 = 1.3, $C^{6'}H$), 7.57–7.62 (3H, m, $C^{8'}H/C^{2''}H/C^{6''}H$), 7.65 (1H, d, J = 16.0, $C^{10'}H$), 7.77 (1H,

ddd, J_1 = 8.5, J_2 = 7.2, J_3 = 1.5, $C^{7'}H$), 8.90 (1H, dd, J_1 = 8.4, J_2 = 1.5, $C^{5'}H$); ^{13}C NMR (151 MHz, CD_2Cl_2) 58.2 ($C^{7'''}$), 62.6 (C^{1}), 106.9 ($C^{3'}$), 110.5 (t, J = 17.6, $C^{1'''}$), 115.8 ($C^{3''}$/$C^{5''}$), 116.2 (C^{2}), 117.4 (C^{2}), 117.5 ($C^{9'}$), 118.3 ($C^{4a'}$), 119.0 ($C^{10'}$), 121.2–121.7 (m, $C^{4'''}$), 126.1 ($C^{5'}$), 126.2 ($C^{6'}$), 129.1 ($C^{8'}$), 130.1 ($C^{2''}$/$C^{6''}$), 135.1 ($C^{7'}$), 138.6 ($C^{1''}$), 141.0 (d, J_{C-F} = 250.4, $C^{2'''}$/$C^{6'''}$), 146.1 (d, J_{C-F} = 250.5, $C^{3'''}$/$C^{5'''}$), 152.9 ($C^{4'}$), 153.3 ($C^{8a'}$), 158.3 ($C^{2'}$), 160.3 ($C^{4''}$); ^{19}F NMR (565 MHz, CD_2Cl_2) −152.35 (2F, dd, J_1 = 21.2, J_2 = 10.0, $C^{3''}F$/$C^{4''}F$), −143.47 (2F, dd, J_1 = 22.0, J_2 = 10.0, $C^{2''}F$/$C^{6''}F$); HRMS *m/z* (ESI^+) [Found: 516.1075, $C_{27}H_{13}F_4N_5O_2$ requires $[M+H]^+$ 516.1078]; LRMS *m/z* (ESI^+) 487 ($[M-N_2]^+$, 5%), 516 ($[M+H]^+$, 7%); Analytical HPLC (method 1A) R_t 12.9 min, 96.8%; Analytical HPLC (method 5) R_t 12.9 min, 98.5%.

(*E*)-2-(2-(4-((4-Azido-2,3,5,6-tetrafluorobenzyl)oxy)styryl)-4*H*-thiochromen-4-ylidene)malononitrile, 4

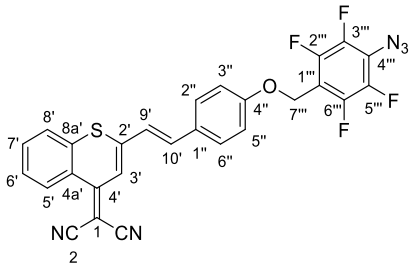

To a solution of **10** (33 mg, 0.15 mmol, 1.0 eq.) and **14** (53 mg, 0.16 mmol, 1.1 eq.) in dry EtOH (8 mL), piperidine (0.06 mL, 0.61 mol, 4.1 eq.) was added. The solution was heated under reflux for 5 h, cooled to rt, filtered and dried under reduced pressure, washed with dry EtOH and recrystallised from EtOH. The resulting residue was adsorbed onto Celite® and purified by flash silica column chromatography, eluting with CH_2Cl_2 and hexane (gradient, 10–100% CH_2Cl_2) to give a pink solid, **4** (23 mg, 39%): R_f 0.39 (EtOAc : PE 1:3); m.p. 155 °C (decomposition, CH_2Cl_2); ν_{max} (solid) cm^{-1}: 2926 (C-H, w), 2207 (C≡N, m), 2123 (N=N=N, m), 1572 (C=C, m), 1537 (C=C, m), 1493 (C-F, m), 1232 (C-O, m); ^1H NMR (600 MHz, CD_2Cl_2) 5.18 (2H, t, J = 1.5, $C^{7''}H_2$), 7.01-7.06 (2H, m, $C^{3''}H$/$C^{5''}H$), 7.09 (1H, d, J = 16.1, $C^{10'}H$), 7.29 (1H, d, J = 16.1, $C^{9'}H$), 7.55-7.59 (3H, m, $C^{3'}H$/$C^{2''}H$/$C^{6''}H$), 7.59-7.62 (1H, m, $C^{6'}H$) 7.66 (1H, ddd, J_1 = 8.2, J_2 = 7.1, J_3 = 1.3, $C^{8'}H$), 7.73 (1H, dd, J_1 = 8.0, J_2 = 1.5,

C$^{7'}$*H*), 8.89 (1H, dd, J_1 = 8.4, J_2 = 1.3, C$^{5'}$*H*); ^{13}C[^{19}F] NMR (126 MHz, CD_2Cl_2) 58.1 (C$^{7''}$), 67.3 (C^{1}), 110.5 (C$^{1'''}$), 115.8 (C$^{3''}$/C$^{5''}$), 116.3 (C^{2}), 117.6 (C^{2}), 121.6 (C$^{3'}$), 124.1 (C$^{10'}$), 125.9 (C$^{8a'}$), 127.9 (C$^{7'}$), 128.5 (C$^{6'}$), 128.6 (C$^{5'}$), 129.2 (C$^{1''}$), 129.8 (C$^{2''}$/C$^{6''}$), 132.3 (C$^{8'}$), 135.4 (C$^{4a'}$), 136.9 (C$^{9'}$), 140.9 (C$^{3'''}$/C$^{5'''}$), 146.1 (C$^{2'''}$/C$^{6'''}$), 148.0 (C$^{2'}$), 156.3 (C$^{4'}$), 160.1 (C$^{4''}$); ^{19}F NMR (376 MHz, CD_2Cl_2) −152.29 – −152.42 (2F, m, C$^{3'''}$*F*/C$^{5'''}$*F*), −142.89 – −143.77 (2F, m, C$^{2'''}$*F*/C$^{6'''}$*F*); HRMS mass not found; LRMS *m/z* (ESI$^+$) 503 ([M-N_2]$^+$, 3%), 532 ([M+H]$^+$, 5%); Analytical HPLC (method 1A) R_t 13.2 min, 98.8%; Analytical HPLC (method 1B) 14.2 min, 97.8%; analytical HPLC (method 6) R_t 5.6 min, >99%.

(*E*)-2-(2-(4-Hydroxystyryl)-4*H*-chromen-4-ylidene)malononitrile, 5

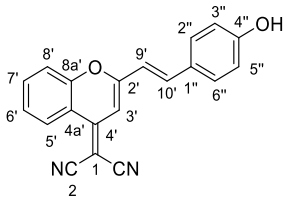

To a solution of **8** (0.105 g, 0.504 mmol, 1.0 eq.) and 4-hydroxybenzaldehyde (0.074 g, 0.606 mmol, 1.2 eq.) in toluene (12.5 mL), AcOH (0.20 mL) and piperidine (0.20 mL, 2.02 mmol, 4 eq.) were added dropwise. The reaction mixture was heated under reflux for 16 h, cooled to ambient temperature and concentrated *in vacuo*. The resulting residue was adsorbed onto Celite® and purified by silica gel column chromatography, eluting with acetone and PE (gradient, 10–50% acetone). The resulting product was recrystallised from anhydrous EtOH to yield compound **5** as a dark brown solid (19 mg, 12%): R_f 0.11 (acetone : PE 1:4); m.p. 230–232 °C (EtOH) [lit.[12] 148–149 °C, lit.[26] 260-262 °C (acetone)]; ν_{max} (solid) cm^{-1}: 3620 (O-H, w br), 3003 (C-H, w), 2254 (C≡N, s), 1443 (C-F, m), 1376 (C-H, m), 1040 (C-O, m); ^{1}H NMR (400 MHz, $(CD_3)_2CO$): 6.92 (1H, s, C$^{3'}$*H*), 6.94 (2H, dt, J_1 = 8.6, J_2 = 4.5, C$^{3''}$*H*/C$^{5''}$*H*), 7.21 (1H, dd, J_1 = 15.7, J_2 = 3.4, C$^{9'}$*H*), 7.60 (1H, ddd, J_1 = 8.4, J_2 = 7.2, J_3 = 1.3, C$^{6'}$*H*), 7.64–7.71 (2H, m, C$^{2''}$*H*/C$^{6''}$*H*), 7.74–7.77 (1H, m, C$^{8'}$*H*), 7.79 (1H, d, *J* = 15.7, C$^{10'}$*H*), 7.91 (1H, ddd, J_1 = 8.4, J_2 = 7.2, J_3 = 1.5, C$^{7'}$*H*,), 8.87 (1H, dd, J_1 = 8.4, J_2 = 1.4, C$^{5'}$*H*); ^{13}C NMR (151 MHz, $(CD_3)_2CO$): 61.8 (C^{1}), 106.7 (C$^{3'}$), 116.6 (C$^{9'}$), 117.0 (C$^{3''}$/C$^{5''}$), 118.0 (C^{2}), 118.6 (C$^{4a'}$), 120.0 (C$^{8'}$), 126.2 (C$^{5'}$), 126.9 (C$^{6'}$), 128.0 (C$^{1''}$), 131.2

($C^{2''}$/$C^{6''}$), 136.0 ($C^{6'}$), 140.2 ($C^{10'}$), 153.5 ($C^{4'}$), 153.9 ($C^{8a'}$), 159.9 ($C^{2'}$), 160.9 ($C^{4''}$); HRMS *m/z* (ESI^+) [Found: 313.0971, $C_{20}H_{12}N_2O_2$ requires $[M+H]^+$ 313.0971]; LRMS *m/z* (ESI^+): 313 ($[M+H]^+$, 5%), 335 ($[M+Na]^+$, 6%); analytical HPLC (method 2B) R_t 10.2 min, 97.9%. These data are in good agreement with the reported values.[26]

(*E*)-2-(2-(4-Hydroxystyryl)-4*H*-thiochromen-4-ylidene)malononitrile, 6

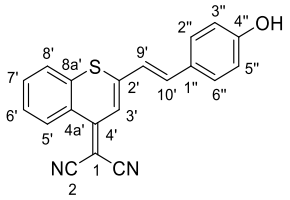

To a solution of **10** (58.6 mg, 0.261 mmol, 1.0 eq.) and 4-hydroxybenzaldehyde (38.5 mg, 0.315 mmol, 1.2 eq.) in toluene (10.0 mL), AcOH (0.1 mL) and piperidine (0.1 mL, 1.01 mmol, 3.9 eq.) were added dropwise. The reaction mixture was heated under reflux for 16 h, cooled to ambient temperature and concentrated *in vacuo*. The resulting residue was adsorbed onto Celite® and purified by silica gel column chromatography, eluting with acetone and PE (gradient, 10–100% acetone). The resulting product was recrystallised from EtOH to yield compound **6** as a red solid (17 mg, 20%): R_f 0.16 (acetone : PE 1:4); m.p. 263–265 °C (EtOH); v_{max} (solid) cm^{-1}: 3650 (O-H, w br), 2254 (C≡N, s), 1444 (C-F, m), 1376 (C-H, m); ^{1}H NMR (600 MHz, $(CD_3)_2CO$): 6.90–6.96 (2H, m, $C^{2''}H$/$C^{6''}H$), 7.41 (1H, d, *J* = 16.1, $C^{9'}H$), 7.48 (1H, d, *J* = 16.1, $C^{10'}H$), 7.59 (1H, s, $C^{3'}H$), 7.65–7.69 (2H, m, $C^{3''}H$/$C^{5''}$-*H*), 7.71 (1H, ddd, J_1 = 8.6, J_2 = 7.0, J_3 = 1.4, $C^{6'}H$), 7.77–7.83 (1H, m, $C^{7'}H$), 7.93 (1H, dd, J_1 = 8.1, J_2 = 1.4, $C^{8'}H$), 8.01 (1H, s, $C^{4''}OH$), 8.88 (1H, dd, J_1 = 8.4, J_2 = 1.3, $C^{5'}H$); ^{13}C NMR (151 MHz, $(CD_3)_2CO$): 67.5 (C^1), 115.6 (C^2), 116.0 ($C^{2''}$/$C^{6''}$), 117.1 (C^2), 120.4 ($C^{3'}$), 122.7 ($C^{9'}$), 125.3 ($C^{8a'}$), 127.1 ($C^{1''}$), 127.8 ($C^{8'}$), 128.0 ($C^{5'}$), 128.2 ($C^{6'}$), 130.0 ($C^{3''}$/$C^{5''}$), 132.3 ($C^{7'}$), 134.9 ($C^{4a'}$), 137.5 ($C^{10'}$), 148.6 ($C^{2'}$), 155.8 ($C^{4'}$), 159.7 ($C^{4''}$); HRMS *m/z* (ESI^+) [Found: 329.0737, $C_{20}H_{12}N_2OS$ requires $[M+H]^+$ 329.0743];LRMS *m/z* (ESI^+): 329 ($[M+H]^+$, 2%), 351 ($[M+Na]^+$, 4%); analytical HPLC (method 2B) R_t 10.4 min, 98.1%.

(*E*)-2-(2-(4-Aminostyryl)-4*H*-chromen-4-ylidene)malononitrile, 2

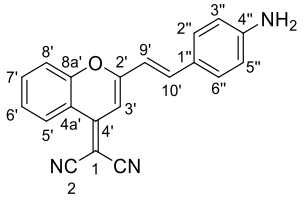

To a solution of **8** (0.13 g, 0.63 mmol, 1.0 eq.) and 4-acetamidobenzaldehyde (0.11 g, 0.67 mmol, 1.1 eq.) in anhydrous toluene (5 mL), AcOH (0.03 mL) and piperidine (0.03 mL) were added dropwise. The reaction mixture was heated to reflux for 3 h, cooled to ambient temperature, filtered and dried under reduced pressure. The resulting residue was suspended in concentrated aqueous HCl (20 mL, 37%) and EtOH (30 mL), heated under reflux for 2 h, cooled to ambient temperature, the pH adjusted to ~7 using saturated aqueous sodium bicarbonate solution and solid K_2CO_3 and the solvent was removed *in vacuo*. The organic components were extracted with EtOAc (3 × 100 mL), dried over $MgSO_4$ and concentrated *in vacuo*. The resulting residue was adsorbed onto Celite® and purified by flash silica gel column chromatography eluting with acetone and PE (gradient, 20–40% acetone), then further purified by flash silica gel column chromatography eluting with CH_2Cl_2 (100%), to yield compound **2** (92 mg, 47%) as a dark red solid: R_f 0.83 (acetone : PE 2:5); m.p. 240–242 °C (CH_2Cl_2) [lit.[27] 243–245 °C, lit.[3] 262–265 °C (toluene)]; ^{1}H NMR (400 MHz, DMSO-d_6): 6.02 (2H, s, C$^{4''}$N*H*$_2$), 6.61–6.69 (2H, m, C$^{3''}$*H*/C$^{5''}$*H*), 6.87 (1H, s, C$^{3'}$*H*), 7.09 (1H, d, *J* = 15.8, C$^{9'}$*H*), 7.49 (2H, d, *J* = 8.7, C$^{2''}$*H*/C$^{6''}$*H*), 7.59 (1H, ddd, J_1 = 8.4, J_2 = 7.1, J_3 = 1.3, C$^{6'}$*H*), 7.65 (1H, d, *J* = 15.8, C$^{10'}$*H*), 7.77 (1H, dd, J_1 = 8.4, J_2 = 1.3, C$^{8'}$*H*), 7.89 (1H, ddd, J_1 = 8.6, J_2 = 7.2, J_3 = 1.5, C$^{7'}$*H*), 8.72 (1H, dd, J_1 = 8.4, J_2 = 1.3, C$^{5'}$*H*); ^{13}C NMR (101 MHz, DMSO-d_6): 57.7 (C^1), 105.2 (C$^{3'}$), 112.8 (C$^{9'}$), 114.4 (C$^{3''}$/C$^{5''}$), 117.0 (C^2), 117.6 (C$^{4a'}$), 119.4 (C$^{5'}$), 122.9 (C$^{1''}$), 125.0 (C$^{8'}$), 126.4 (C$^{6'}$), 131.2 (C$^{2''}$/C$^{6''}$), 135.6 (C$^{7'}$), 141.4 (C$^{10'}$), 152.45 (C$^{4''}$), 152.52 (C$^{8a'}$), 153.2 (C$^{4'}$), 160.3 (C$^{2'}$); LRMS *m/z* (ESI$^+$): 312 ([M+H]$^+$, 100%); Analytical HPLC (method 2B) R_t 10.4 min, >99%. These data are in good agreement with the reported values.[3]

(*E*)-2-(2-(4-Azidostyryl)-4*H*-chromen-4-ylidene)malononitrile, 1

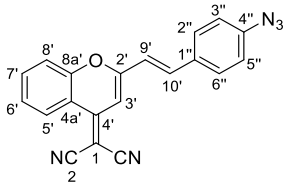

To a solution of **2** (26 mg, 0.08 mmol, 1.0 eq.) in HCl (5 mL, 5 M in H_2O) at 0 °C, $NaNO_2$ (29 mg, 0.42 mmol, 5 eq.) in H2O (0.3 mL) was added dropwise and stirred for 10 min. NaN_3 (110 mg, 1.60 mmol, 21.0 eq.) in H_2O (0.9 mL) was added dropwise and the resulting mixture was stirred at 0–5 °C for 1 h. The organic components were extracted with EtOAc (2 × 50 mL), dried over $MgSO_4$ and concentrated *in vacuo*. The resulting residue was adsorbed onto Celite® and purified by flash silica gel column chromatography, eluting with acetone and PE (20–60% acetone), to yield compound **1** (10 mg, 38%) as an orange solid: R_f 0.40 (acetone : PE 2:8); m.p. 180 °C (decomposition, acetone) [lit.[27] 244–245 °C, lit.[3] 188–189 °C (acetone)]; v_{max} (solid) cm^{-1}: 2207 (C≡N, m), 2121 (N=N, m), 1632 (C=C, m); ^{1}H NMR (400 MHz, acetone-d_6) 6.99 (1H, s, C$^{3'}$*H*), 7.15–7.22 (2H, m, C$^{2''}$*H*/C$^{6''}$*H*), 7.41 (1H, d, *J* = 16.1, C$^{10'}$*H*), 7.62 (1H, ddd, J_1 = 8.4, J_2 = 7.1, J_3 = 1.5, C$^{6'}$*H*), 7.77 (1H, dd, J_1 = 8.4, J_2 = 1.3, C$^{8'}$*H*), 7.81-7.87 (3H, m, C$^{3''}$*H*/C$^{5''}$*H*/C$^{9'}$*H*), 7.93 (1H, ddd, J_1 = 8.6, J_2 = 7.2, J_3 = 1.5, C$^{7'}$*H*), 8.87 (1H, dd, J_1 = 8.6, J_2 = 1.5, C$^{5'}$*H*); ^{13}C NMR (515 MHz, acetone-d_6) 61.9 (C^1), 106.7 (C$^{3'}$), 115.4 (C^2), 116.9 (C^2), 117.6 (C$^{4a'}$), 119.0 (C$^{8'}$), 119.1 (C$^{9'}$), 119.7 (C$^{3''}$/C$^{5''}$), 125.2 (C$^{5'}$), 126.0 (C$^{7'}$), 129.8 (C$^{2''}$/C$^{6''}$), 132.3 (C$^{1''}$), 135.1 (C$^{6'}$), 137.7 (C$^{10'}$), 141.9 (C$^{4''}$), 152.6 (C$^{8a'}$), 152.7 (C$^{4'}$), 158.1 (C$^{2'}$); LRMS *m/z* (ESI, EI, ACPI): mass not found; Analytical HPLC (method 2B) R_t 12.2 min, 97.4%. These data are in good agreement with the reported values.[3, 27, 28]

7-((4-Azido-2,3,5,6-tetrafluorobenzyl)oxy)-3*H*-phenoxazin-3-one, 15

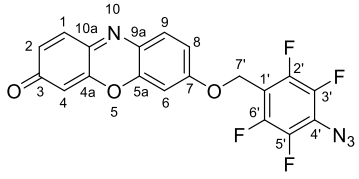

Step 1 - To a solution of **12** (61 mg, 0.28 mmol, 1.0 eq.) in CH_2Cl_2 (1.0 mL) cooled to 0 °C in an ice-H_2O bath, thionyl chloride (0.68 mL, 9.4 mmol, 33 eq.) was added dropwise. The reaction mixture was warmed to rt, stirred for 2 h, then concentrated *in vacuo* to yield **13** as a yellow oil (56 mg), which was used without further purification.

Step 2 – **13** (56 mg, 0.23 mmol, 1.0 eq.), resorufin (50 mg, 0.24 mmol, 1.0 eq.), caesium carbonate (160 mg, 0.48 mmol, 2 eq.) and TBAI (90 mg, 0.23 mmol, 1.0 eq.) were dissolved in dry DMF (5 mL) at 0 °C under an argon atmosphere. The reaction mixture was warmed to rt and stirred for 20 h, then further tetrabutylammonium iodide (90 mg, 0.23 mmol, 1.0 eq.) was added. The reaction mixture was stirred at rt for 4 h then diluted with saturated ammonium chloride solution (75 mL). The mixture was extracted with EtOAc (4 × 50 mL) and the organic components were washed with saturated sodium bicarbonate solution (6 × 50 mL) and H_2O (3 × 50 mL) then dried over Na_2SO_4, filtered and concentrated *in vacuo*. The resulting residue was adsorbed onto Celite® and purified by silica column chromatography, eluting with EtOAc and PE (gradient, 15–100% EtOAc) to yield compound **15** as an orange solid (40 mg, 42%): R_f 0.54 (EtOAc : PE 1:1); m.p. 150 °C (decomposition, EtOAc); ν_{max} (solid) cm^{-1}: 2130 (N=N, m), 1619 (C=O, m), 1567 (C=C, m), 1493 (C-F, s); ^{1}H NMR (400 MHz, $CDCl_3$) 5.21 (2H, s, $C^{7'}H_2$), 6.34 (1H, d, J = 2.0, C^4H), 6.85 (1H, dd, J_1 = 9.8, J_2 = 2.0, C^2H), 6.91 (1H, d, J = 2.7, C^6H), 6.98 (1H, dd, J_1 = 8.9, J_2 = 2.7, C^8H), 7.43 (1H, d, J = 9.8, C^1H), 7.74 (1H, d, J = 8.9, C^9H); ^{13}C[^{19}F] NMR (126 MHz, $CDCl_3$) 58.3 ($C^{7'}$), 101.3 (C^6), 107.1 (C^4), 109.2 ($C^{1'}$), 113.8 (C^8), 121.7 ($C^{6'}$), 129.0 (C^{5a}), 131.9 (C^9), 134.6 (C^2), 134.9 (C^1), 140.6 ($C^{3'}$/$C^{5'}$), 145.6 (C^{9a}), 145.8 ($C^{2'}$/$C^{4'}$), 146.4 (C^{4a}), 149.8 (C^{10a}), 161.7 (C^7), 186.5 (C^3); ^{19}F NMR (376 MHz, $CDCl_3$) −151.08 (2F, dd, J_1 = 22.6, J_2 = 7.5, $C^{3'}F$/$C^{5'}F$), −142.47 (2F, dd, J_1 = 21.7, J_2 = 11.2, $C^{2'}F$/$C^{6'}F$); HRMS *m/z* (ESI^+) [Found: 417.0602, $C_{19}H_8F_4N_4O_3$ requires $[M+H]^+$ 417.0605]; LRMS *m/z* (ESI^+) 417 ($[M+H]^+$, 39%), 833 ($[2M+H]^+$, 40%); Analytical HPLC (method 2B) R_t 10.8 min, 94.6%; Analytical HPLC (method 1B) R_t 12.0 min, 94.1%.

6-((4-Azido-2,3,5,6-tetrafluorobenzyl)oxy)-9-(o-tolyl)-3*H*-xanthen-3-one, 16

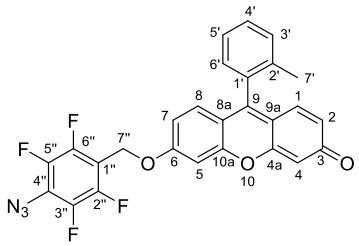

Me-Tokyo Green was synthesised by Dr Antoine Wallabregue, University of Oxford, as described previously.[29]

Step 1 – To a solution of **12** (89 mg, 0.40 mmol, 1.0 eq.) in CH_2Cl_2 (1.0 mL) cooled to 0 °C in an ice-H_2O bath, thionyl chloride (1.0 mL, 13.8 mmol, 35 eq.) was added dropwise. The reaction mixture was warmed to rt, stirred for 2 h, then concentrated *in vacuo* to yield **13** as a yellow oil (90 mg), which was used without further purification.

Step 2 – 13 (90 mg, 0.38 mmol, 1.0 eq.), Me-Tokyo green (110 mg, 0.37 mmol, 1.0 eq.), caesium carbonate (250 mg, 0.76 mmol, 2 eq.) and TBAI (280 mg, 0.76 mmol, 2 eq.) were dissolved in dry DMF (6 mL) at 0 °C under an argon atmosphere. The reaction mixture was warmed to rt and stirred for 22 h then diluted with saturated ammonium chloride solution (75 mL). The mixture was extracted with EtOAc (4 × 50 mL) and the organic components were washed with saturated sodium bicarbonate solution (6 × 50 mL) and H_2O (3 × 50 mL) then dried over Na_2SO_4, filtered and concentrated *in vacuo*. The resulting residue was adsorbed onto Celite® and purified by silica column chromatography, eluting with EtOAc and PE (gradient, 15–100% EtOAc). The resulting residue was dissolved in chloroform (2.5 mL) and precipitated by adding hexane (50 mL). The precipitation procedure was repeated twice and the filtrate was concentrated *in vacuo* to yield compound **16** as an orange solid (20 mg, 11%): R_f 0.24 (EtOAc : PE 1:1); m.p. 145 °C (decomposition, hexane); ν_{max} (solid) cm^{-1}: 2124 (N=N=N, m), 1644 (C=O, m), 1600 (C=C, s), 1498 (C-F, m); ^{1}H NMR (400 MHz, acetone-d_6) 2.11 (3H, s, $C^{7'}H_3$), 5.46 (2H, t, J = 1.5, $C^{7''}H_2$), 6.20 (1H, d, J = 1.9, C^4H), 6.41 (1H, dd, J_1 = 9.8, J_2 = 1.9, C^2H), 6.91 (1H, d, J = 9.8, C^1H), 6.96 (1H, dd, J_1 = 8.8, J_2 = 2.4, C^7H), 7.01 (1H, d, J = 8.8, C^8H), 7.25–7.33 (2H, m, C^5H/$C^{3'}H$), 7.40-7.56 (3H,

m, $C^{4'}H/C^{5'}H/C^{6'}H$); ^{13}C NMR (151 MHz, acetone-d_6) 18.7 ($C^{7'}$), 58.2 ($C^{7''}$), 101.5 (C^{5}), 105.1 (C^{4}), 109.8 (t, J = 17.8, $C^{1''}$), 113.5 (C^{7}), 114.9 (C^{8a}), 118.5 (C^{9a}), 121.3-121.9 (m, $C^{4''}$), 126.2 ($C^{4'}$), 129.2 ($C^{3'}$), 129.46 (C^{8}), 129.51 ($C^{6'}$), 130.1 (C^{2}), 130.3 (C^{1}), 130.6 ($C^{5'}$), 132.6 ($C^{2'}$), 136.2 ($C^{1'}$), 140.67 (dd, J_1 = 247.8, J_2 = 16.4, $C^{3''}/C^{5''}$), 143.94-147.29 (m, $C^{2''}/C^{6''}$), 147.9 (C^{9}), 154.2 (C^{10a}), 158.6 (C^{4a}), 162.9 (C^{6}), 184.3 (C^{3}); ^{19}F NMR (376 MHz, acetone-d_6) −153.59 (2F, dd, J_1 = 20.4, J_2 = 10.1, $C^{3'}F/C^{5'}F$), −145.07 (2F, dd, J_1 = 20.4, J_2 = 10.1, $C^{2'}F/C^{6'}F$); HRMS *m/z* (ESI$^+$) [Found: 506.1117, $C_{27}H_{15}F_4N_3O_3$ requires $[M+H]^+$ 506.1122]; LRMS *m/z* (ESI$^+$) 506 ($[M+H]^+$, 100%), 1011 ($[2M+H]^+$, 23%); Analytical HPLC (method 2B) R_t 12.8 min, 95.7%.

4-Azido-2,3,5,6-tetrafluorobenzyl (4-nitrophenyl) carbonate, 17

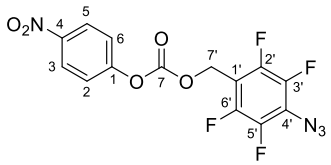

Pyridine (0.62 mL, 7.67 mmol, 5.3 eq.) was added dropwise to a solution of 4-nitrophenyl chloroformate (470 mg, 2.33 mmol, 1.6 eq.) in dry THF (5.0 mL) and stirred at rt for 5 min, under an argon atmosphere over 4 Å molecular sieves. The solution was cooled to 0 °C and a solution of **12** (322 mg, 1.45 mmol, 1.0 eq.) in dry THF (15.0 mL) was added dropwise over 15 min. The resulting solution was warmed to rt and stirred for 72 h, under an argon atmosphere over 4 Å molecular sieves. The THF was removed by concentration *in vacuo* (with temperature maintained below 30 °C) and the resulting residue was dissolved in EtOAc (45 mL). The organic components were washed with H_2O (3 × 15 mL) and brine (1 × 15 mL), dried over $MgSO_4$, filtered and concentrated *in vacuo* (with temperature maintained below 30 °C). The resulting residue was adsorbed onto Celite® and purified by silica column chromatography, eluting with EtOAc and hexane (isocratic, 10% EtOAc), to yield compound **17** as a pale-yellow solid (165 mg, 29%): R_f 0.31 (EtOAc : PE 1:9); m.p. 61–64 °C; v_{max} (solid) cm^{-1}: 2123 (N=N=N, m), 1782 (C=O, m), 1654 (C=C, m), 1492 (C-F, m). 1168 (C-O, s); ^{1}H NMR (600 MHz, $CDCl_3$): 5.40 (2H, t, J = 1.4, $C^{7'}H_2$), 7.37–7.42 (2H,

m, C^{2}*H*/C^{6}*H*), 8.29 (2H, dd, J_1 = 9.3, J_2 = 2.3, C^{3}*H*/C^{5}*H*); ^{13}C NMR (151 MHz, $CDCl_3$): 57.7 (C$^{7'}$), 107.9 (t, J = 17.4, C$^{1'}$), 121.7 (C^{2}/C^{6}), 121.9 (tt, J_1 = 11.7, J_2 = 3.3, C$^{4'}$), 125.4 (C^{3}/C^{5}), 140.5 (dddd, J_1 = 250.8, J_2 = 15.5, J_3 = 3.0, J_4 = 2.8, C$^{3'}$/C$^{5'}$), 145.6 (C^{4}), 145.7 (dddd, J_1 = 252.2, J_2 =12.5 , J_3 = 7.4, J_4 = 4.3, C$^{2'}$/C$^{6'}$), 152.0 (C^{7}), 155.2 (C^{1}); ^{19}F NMR (565 MHz, $CDCl_3$) −151.07 (2F, dd, J_1 = 21.4, J_2 = 10.6, C$^{3'''}$*F*/C$^{5'''}$*F*), −141.84 (2F, dd, J_1 = 21.4, J_2 = 10.6, C$^{2'''}$*F*/C$^{6'''}$*F*); LRMS *m/z* (ESI^{+}/EI/ACPI): mass not detected; Analytical HPLC (method 2B) R_t 10.9 min, 98.2%. These data are in good agreement with the available reported values.[30]

4-Azido-2,3,5,6-tetrafluorobenzyl (3-oxo-3*H*-phenoxazin-7-yl) carbonate

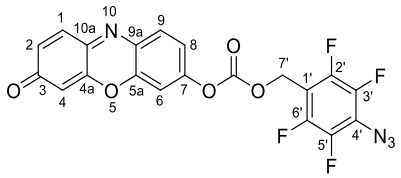

Pyridine (12 µL, 0.15 mmol, 2.5 eq.) was added dropwise to a solution of resorufin (18 mg, 0.084 mmol, 1.4 eq.) and DMAP (1.1 mg, 0.009 mmol, 0.15 eq.) in dry DMF (12.0 mL) and stirred at rt for 5 min, under an argon atmosphere. The resulting solution was added dropwise to a solution of **17** (23 mg, 0.059 mmol, 1.0 eq.) in dry DMF (2.0 mL) over 4 Å molecular sieves (200 mg) and stirred at rt for 19 h under an argon atmosphere. Pyridine (6 µL, 0.075 mmol, 1.25 eq.) was added dropwise and the resulting solution was stirred at rt for a further 53 h, under an argon atmosphere, then diluted with H_2O (50 mL). The mixture was extracted with EtOAc (3 × 50 mL) and the organic components were washed with saturated sodium bicarbonate solution (3 × 50 mL), H_2O (1 × 50 mL) and brine (1 × 50 mL), then dried over Na_2SO_4, filtered and concentrated *in vacuo* (with the bath maintained below 30 °C). The desired product was not convincingly detected by TLC or ^{1}H NMR spectroscopy (possibly <5% product).

6.4.2 Compounds from chapter III

Tri-*tert*-butyl 2,2',2''-(1,4,7,10-tetraazacyclododecane-1,4,7-triyl)triacetate hydrobromide, 23

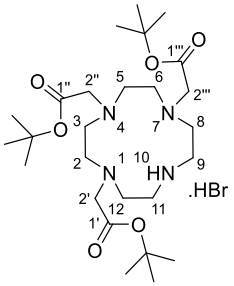

1,4,7,10-tetraazacyclododecane (cyclen, 5.01 g, 29.1 mmol, 1.0 eq.) was dissolved in MeCN (150 mL) and cooled to 0 °C. $NaHCO_3$ (8.09 g, 96.3 mmol, 3.3 eq.) was added and the mixture was stirred for 15 min, before *tert*-butylbromoacetate (14.7 mL, 99.6 mmol, 3.4 eq.) in MeCN (50 mL) was added dropwise over 1 h. The reaction mixture was stirred at 0 °C for 2 h, allowed to warm to rt and stirred and rt for 44 h. The inorganic solids were removed by filtration and the filtrate was concentrated *in vacuo*. The resulting off-white solid was triturated with cold toluene (42 mL), filtered and washed with toluene (2 × 4 mL) to give **23** as a colourless solid (6.87 g, 40%): R_f 0.37 (MeOH : CH_2Cl_2 5:95); m.p. 170–172 °C (toluene) [lit.[31] 176–178 °C, lit.[32] 187–188 °C, lit.[33] 190–191 °C, lit.[34] 178-180 °C]; ^{1}H NMR (400 MHz, DMSO-d_6): 1.38–1.46 (27H, m, 3 × (CH_3)$_3$), 2.62–2.75 (8H, m, 4 × ring CH_2), 2.80–2.88 (4H, m, 2 × ring CH_2), 2.94–3.03 (4H, m, 2 × ring CH_2), 3.35 (2H, s, arm CH_2), 3.41 (4H, s, 2 × arm CH_2), 8.80 (2H, br s, NH_2^+); LRMS *m/z* (ESI$^+$) 495 ([M-tBu-Br]$^+$, 61%), 515 ([M-Br]$^+$, 100%), 1111 ([2M-Br]$^+$, 94%). These data are in good agreement with the reported values.[31-35]

4'-Nitrobenzyl 2-bromoacetate, 24

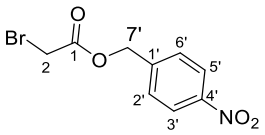

To a suspension of 4-nitrobenzyl alcohol (2.00 g, 13.1 mmol, 1.0 eq.) and $NaHCO_3$ (3.34 g, 39.8 mmol, 3.0 eq.) in MeCN (20 mL), bromoacetyl bromide (1.50 mL, 17.2 mmol, 1.3 eq.)

dissolved in MeCN (6.0 mL) was added dropwise at 0 °C. The resulting suspension was warmed to 45 °C and stirred for a further 18 h, cooled to rt, filtered through Celite®, washed with CH_2Cl_2 and the filtrate was concentrated *in vacuo*. The resulting material was adsorbed onto Celite® and purified by silica column chromatography, eluting with EtOAc and PE (gradient, 0–15% EtOAc), and then was crystallised from Et_2O/hexane to yield compound **24** as a colourless solid (1.99 g, 55%): R_f 0.29 (PE : EtOAc 4:1); m.p. 43–45 °C (hexane); ν_{max} (solid) cm^{-1}: 1753 (C=O, s), 1517 (N-O, s), 1151 (C-O, s); ^{1}H NMR (400 MHz, $CDCl_3$): 3.91 (2H, s, C^2H_2), 5.30 (2H, s, $C^{7'}H_2$), 7.51–7.57 (2H, m, $C^{2'}H/C^{6'}H$), 8.20–8.28 (2H, m, $C^{3'}H/C^{5'}H$); ^{13}C NMR (151 MHz, $CDCl_3$): 25.4 (C^2), 66.4 ($C^{7'}$), 124.1 ($C^{3'}/C^{5'}$), 128.7 ($C^{2'}/C^{6'}$), 142.2 ($C^{1'}$), 148.1 ($C^{4'}$), 167.0 (C^1); LRMS not detected by ESI/EI/APCI. These data are in good agreement with the reported values.[7]

Tri-*tert*-butyl 2,2',2''-(10-(2-((4-nitrobenzyl)oxy)-2-oxoethyl)-1,4,7,10-tetraazacyclododecane-1,4,7-triyl)triacetate, 25

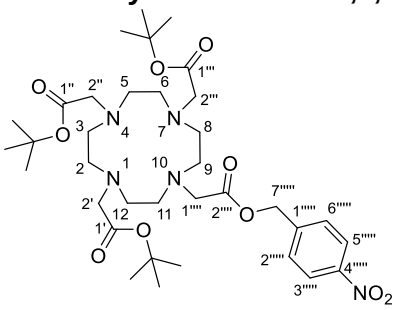

23 (1.35 g, 2.27 mmol, 1.0 eq.) and $NaHCO_3$ (584 mg, 6.95 mmol, 3.0 eq.) was added to a solution of **24** (812 mg, 2.96 mmol, 1.3 eq.) in dry MeCN (20.0 mL) under an argon atmosphere. The resulting suspension was stirred at 80 °C for 39 h, cooled to rt, filtered through Celite®, washed with CH_2Cl_2 and the filtrate was concentrated *in vacuo*. The resulting material was adsorbed onto Celite® and purified by silica column chromatography, eluting with EtOH and $CHCl_3$ (gradient, 0–15% EtOH), to yield **25** as an off-white foam (1.48 mg, 92%): R_f 0.36 ($CHCl_3$: EtOH 8:2); ν_{max} (solid) cm^{-1}: 1726 (C=O, s), 1627 (C=C, m), 1522 (N-O, s), 1162 (C-O, s); ^{1}H NMR (400 MHz, $CDCl_3$): 1.34 (27H, s, 3 × $C(CH_3)_3$), 1.79–3.52 (24H, m, 4 × $COCH_2$, 8 × ring CH_2), 5.14 (2H, s, $C^{7''''}H_2$), 7.39–7.47 (2H, m, $C^{2''''}H/C^{6''''}H$), 8.02–8.15 (2H, m, $C^{3''''}H/C^{5''''}H$); ^{13}C NMR (151 MHz, $CDCl_3$): 27.7 (3 ×

(CH_3)$_3$), 46.3–53.5 (m, 8 × ring CH_2), 54.8 (arm CH_2), 55.4 (arm CH_2), 55.6 (2 × arm CH_2), 65.2 ($C^{7''''}$), 81.9 (3 × $C(CH_3)_3$), 123.6 ($C^{3''''}$/$C^{5''''}$), 128.7 ($C^{2''''}$/$C^{6''''}$), 142.3 ($C^{1''''}$), 147.6 ($C^{4''''}$), 172.7 ($C^{1'}$/$C^{1''}$/$C^{1'''}$), 172.9 (2 × $C^{1'}$/$C^{1''}$/$C^{1'''}$), 173.4 ($C^{2'''}$); HRMS *m/z* (ESI^+) [Found: 708.4188, $C_{35}H_{57}N_5O_{10}$ requires $[M+H]^+$ 708.4178]; LRMS *m/z* (ESI^+) 708 ($[M+H]^+$, 90%), 730 ($[M+Na]^+$, 94%); LCMS (method 1) R_t 3.9 min, 89.4%. These data are generally in good agreement with the reported values.[7]

General TFA deprotection procedure

The corresponding *tert*-butyl protecting compound was dissolved in CH_2Cl_2 and the same volume of TFA was added (overall c_{SM} 30–90 mM, 150–400 eq.). The resulting solution was stirred at rt for 18–72 h. The resulting solution was concentrated *in vacuo* and washed with CH_2Cl_2, repeated twice with CH_2Cl_2 and then three times with MeOH. The resulting residue was dissolved in a minimum amount of MeOH, Et_2O was added until a precipitate formed. The precipitate was typically isolated by centrifugation (3750 rpm, 5 min, 4 °C or 6000 rpm, 5 min, rt). The precipitation procedure was repeated twice and the resulting solid was collected in MeOH then concentrated *in vacuo* to give the product.

2,2',2''-(10-(2-((4-Nitrobenzyl)oxy)-2-oxoethyl)-1,4,7,10-tetraazacyclododecane-1,4,7-triyl)triacetic acid, 26

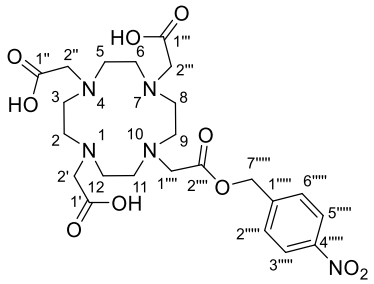

The reaction was carried out following the general TFA deprotection procedure, left to stir at rt for 43 h, using **25** (1.71 g, 2.41 mmol, 1.0 eq.), CH_2Cl_2 (70.0 mL) and TFA (70.0 mL, 915 mmol, 380 eq.) to give **26** as an off-white solid (1.01 g, 78%): m.p. 205 °C (decomposition, MeOH); ν_{max} (solid) cm^{-1}: 3448 (O-H, br, w), 1727 (C=O, m), 1676 (C=O, m), 1636 (C=C, m), 1522 (N-O, m), 1349 (O-H, m) 1189 (C-O, s); ^1H NMR (400 MHz, D_2O): 2.92–3.27 (8H, m, 4 × ring C*H*$_2$), 3.39–3.60 (8H, m, 4 × ring C*H*$_2$), 3.62–4.00 (8H, m, 4 ×

COC*H*$_2$), 5.35 (2H, s, C$^{7''''}$*H*$_2$), 7.62–7.68 (2H, m, C$^{2''''}$*H*/C$^{6''''}$*H*), 8.24–8.30 (2H, m, C$^{3''''}$*H*/C$^{5''''}$*H*); ^{13}C NMR (151 MHz, D_2O): 48.7 (ring CH_2), 51.9 (ring CH_2, arm CH_2), 53.7 (arm CH_2), 56.6 (arm CH_2), 66.6 (C$^{7''''}$), 124.4 (C$^{3''''}$/C$^{5''''}$), 129.5 (C$^{2''''}$/C$^{6''''}$), 143.8 (C$^{1''''}$), 148.0 (C$^{4''''}$), 170.5 (C$^{1'}$/C$^{1''}$/C$^{1'''}$), 172.5 (C$^{2'''}$), 174.5 (C$^{1'}$/C$^{1''}$/C$^{1'''}$); HRMS *m/z* (ESI$^+$) [Found: 540.2314, $C_{23}H_{33}N_5O_{10}$ requires $[M+H]^+$ 540.2300]; LRMS *m/z* (ESI$^+$) 540 ($[M+H]^+$, 97%), 562 ($[M+Na]^+$, 44%); LCMS (method 2) R_t 2.4 min, 98.6%. These data are generally in good agreement with the reported values.[7]

General lanthanide complexation procedure for chapter III

The corresponding lanthanide triflate (1.00-1.12 eq.) was added to a solution of the triacid (1.0 eq.) in MES buffer (1M, pH 6.0, c_{SM} ~65 mM) and the resulting solution was stirred at rt for 1–1.5 h, until the reaction was deemed complete by LCMS analysis (method 2). The reaction mixture was diluted by H_2O (same as or larger volume than MES buffer), filtered (nylon syringe filter, 0.45 µM, 13 mm) and purified by semi-preparative HPLC (method 1 for nitrobenzyl complexes, method 2 for nitroimidazole complexes and method 3 for benzyl complexes). The complexes were recovered as colourless solids from H_2O/MeCN mixtures by lyophilisation.

Europium nitrobenzyl complex (EuNB), 18a

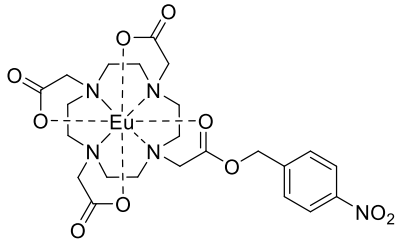

The reaction was carried out following the general lanthanide complexation procedure, using **26** (76.6 mg, 142 µmol, 1.0 eq.) and europium triflate (90.4 mg, 151 µmol, 1.06 eq.) in MES buffer (2.70 mL). The reaction was left at rt for 1 h, purified by semi-preparative HPLC method 1 and lyophilised for 2 days to yield compound **18a** as a colourless solid (65.4 mg, 66%): ^{1}H NMR (400 MHz, D_2O):* −19.4, −17.1, −16.0, −14.5, −13.5, −12.7, −10.3, −9.4, −8.9, −8.6, −8.0, −6.8, −6.2, −6.1, −3.9, −1.1, −0.5, −0.3, 0.2, 3.3, 7.0, 7.8, 8.3, 9.2,

10.6, 24.5, 25.0, 25.8, 32.7, 33.8; HRMS *m/z* (ESI^+) [Found: 690.1275, $C_{23}H_{30}N_5O_{10}Eu$ requires $[M+H]^+$ 690.1278]; LRMS *m/z* (ESI^+) 712 ($[M+Na]^+$, 10%); LCMS (method 2) R_t 2.5 min, 95.4%; Analytical HPLC (method 1A) R_t 9.1 min, 96.3%. *^{1}H NMR contains ~2% EuDOTA so total purity ~93%, all peaks reported including EuDOTA.

Terbium nitrobenzyl complex (TbNB), 18b

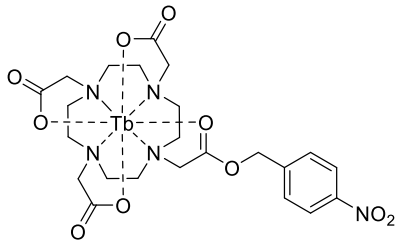

The reaction was carried out following the general lanthanide complexation procedure, using **26** (76.0 mg, 141 µmol, 1.0 eq.) and terbium triflate (90.0 mg, 149 µmol, 1.06 eq.) in MES buffer (2.15 mL). The reaction was left at rt for 1 h, purified by semi-preparative HPLC method 1 and lyophilised for 2 days to give compound **18b** as a colourless solid (42.6 mg, 47%): ^{1}H NMR (400 MHz, D_2O):* −416.7, −398.2, −336.0, −326.9, −305.1, −186.6, −153.7, −118.6, −99.3, −96.8, −95.7, −92.3, −69.5, −65.1, −43.6, −35.7, −32.4, −18.3, −15.8, −14.0, −2.0, −0.45, 1.0, 1.4, 14.5, 82.8, 136.1, 148.0, 159.6, 214.1, 228.4, 293.7; HRMS *m/z* (ESI^+) [Found: 696.1319, $C_{23}H_{30}N_5O_{10}Tb$ requires $[M+H]^+$ 696.1319]; LRMS *m/z* (ESI^+) 696 ($[M+H]^+$, 37%), 718 ($[M+Na]^+$, 100%), 1413 ($[2M+Na]^+$, 59%); LCMS (method 2) R_t 2.8 min, 95.1%; Analytical HPLC (method 1A) R_t 9.0 min, 94.5%.

*^{1}H NMR contains 5% TbDOTA, therefore total purity ~90%, all peaks reported including TbDOTA.

Gadolinium nitrobenzyl complex (GdNB), 18c

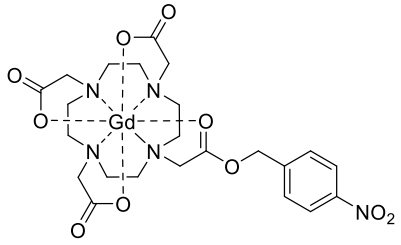

The reaction was carried out following the general lanthanide complexation procedure, using **26** (97.9 mg, 181 µmol, 1.0 eq.) and gadolinium triflate (116 mg, 192 µmol, 1.06 eq.) in MES buffer (2.80 mL). The reaction was left at rt for 1 h, purified by semi-preparative HPLC method 1 and lyophilised for 2 days to give compound **18c** as a colourless solid (54.1 mg, 43%): HRMS *m/z* (ESI^+) [Found: 695.1310, $C_{23}H_{30}N_5O_{10}Gd$ requires $[M+H]^+$ 695.1307]; LRMS *m/z* (ESI^+) 608 (100%), 717 ($[M+Na]^+$, 4%); LCMS (method 2) R_t 2.15 min, 97.2%; Analytical HPLC (method 1A) R_t 9.1 min, 96.1%.

Ethyl 2-amino-1-methyl-1*H*-imidazole-5-carboxylate, 27

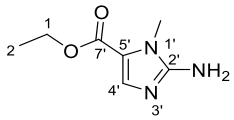

To a suspension of sarcosine ethyl ester hydrochloride (4.00 g, 26.0 mmol, 1.0 eq.) and ethyl formate (14.6 mL, 182 mmol, 7.0 eq.) in dry THF (45 mL) and EtOH (6.5 mL), NaH (60% dispersion in mineral oil, 4.19 g, 105 mmol, 4.0 eq.) was added portion-wise at 0 °C. The reaction mixture was warmed to rt and stirred for 3 h. The resulting yellow suspension was concentrated *in vacuo* and the resulting solid was triturated with hexane (2 × 75 mL), the hexane decanted and the resulting solid concentrated *in vacuo*. The light-yellow solid was suspended in EtOH (80 mL) and concentrated aqueous HCl (37%, 16 mL) was added dropwise, then the suspension was heated under reflux for 2 h. The reaction mixture was filtered whilst hot, washed with hot EtOH (2 × 30 mL) and the filtrate was concentrated *in vacuo* to leave an aqueous solution, which was diluted with EtOH (70 mL) and H_2O (30 mL). The pH of the resulting green solution was adjusted to 3-4 using aqueous NaOH (2 M). Cyanamide (2.20 g, 52.2 mmol, 2.0 eq.) was added and the resulting solution was heated

under reflux for 1.5 h, then cooled to rt and concentrated *in vacuo* until approximately 1/8th of the original volume. The pH was adjusted to 8-9 using solid K_2CO_3, resulting in the formation of a precipitate. The solid was removed by filtration, washed with saturated aqueous $NaHCO_3$ (2 × 20 mL) and H2O (20 mL) and dried *in vacuo* to yield compound **27** as a yellow solid (2.18 g, 48%): R_f 0.34 (MeOH : CH_2Cl_2 1:9); m.p. 150–152 °C (H_2O) [lit.[36] 130–133 °C (H_2O)]; ^{1}H NMR (400 MHz, $CDCl_3$): 1.33 (3H, t, *J* = 7.1, C^2*H*$_3$), 3.68 (3H, s, N$^{1'}$C*H*$_3$), 4.27 (2H, q, *J* = 7.1, C^1*H*$_2$), 7.43 (1H, s, C$^{4'}$*H*); LRMS *m/z* (ESI$^+$) 170 ([M+H]$^+$, 100%). These data are generally in good agreement with the reported values.[36, 37]

Ethyl 1-methyl-2-nitro-1*H*-imidazole-5-carboxylate, 28

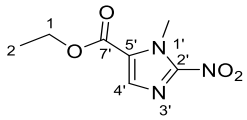

A solution of **27** (2.89 g, 17.1 mmol, 1.0 eq.) in AcOH (58.0 mL) was added dropwise at 0 °C to a solution of $NaNO_2$ (11.8 g, 171 mmol, 10 eq.) in H_2O (27.0 mL) and the resulting solution was stirred at 0 °C for 1 h, then warmed to rt and stirred for 3 h. The resulting mixture was extracted with CH_2Cl_2 (3 × 100 mL) and the organic components were washed with saturated aqueous sodium sulfite (200 mL) and brine (200 mL), dried over $MgSO_4$, filtered and concentrated *in vacuo*. The resulting residue was dissolved in CH_2Cl_2 and purified by silica column chromatography, eluting with CH_2Cl_2, to yield compound **28** as a yellow solid (1.96 g, 58%): R_f 0.86 (MeOH : CH_2Cl_2 2:98); m.p. 50–52 °C (CH_2Cl_2) [lit.[36] 56–58 °C (CH_2Cl_2), lit.[38] 65–66 °C]; ^{1}H NMR (400 MHz, $CDCl_3$): 1.40 (3H, t, *J* = 7.1, C^2*H*$_3$), 4.34 (3H, s, N$^{1'}$C*H*$_3$), 4.40 (2H, q, *J* = 7.1, C^1*H*$_2$), 7.74 (1H, s, C^4*H*); LRMS *m/z* (ESI$^+$) 200 ([M+H]$^+$, 100%), 222 ([M+Na]$^+$, 89%). These data are generally in good agreement with the reported values.[36, 38]

(1-Methyl-2-nitro-1*H*-imidazol-5-yl)methanol, 29

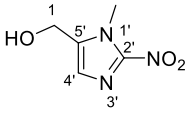

A suspension of $NaBH_4$ (335 mg, 8.50 mmol, 3.0 eq.) in dry EtOH (9.3 mL) was added dropwise at 0 °C to a solution of compound **28** (570 mg, 2.90 mmol, 1.0 eq.) in dry THF (14.7 mL) and MeOH (0.97 mL). The resulting solution was stirred at 0 °C for 3 h, then further $NaBH_4$ (335 mg, 8.0 mmol, 3.0 eq.) in dry EtOH (10.0 mL) was added dropwise, as the reaction was not complete by TLC analysis. After a further 3 h, MeOH (15.0 mL) was added and the resulting solution was stirred at 0 °C for a further 30 min, then acidified to pH 7 using 1 M aqueous HCl and concentrated *in vacuo* to leave an aqueous solution. The aqueous solution was extracted with EtOAc (3 × 40 mL) and the organic components were washed with saturated aqueous $NaHCO_3$ (120 mL), dried over Na_2SO_4, filtered and concentrated *in vacuo*. The resulting residue was adsorbed onto Celite® and purified by silica column chromatography, eluting with MeOH and CH_2Cl_2 (gradient, 2–3% MeOH), to yield compound **29** as a pale-yellow solid (239 mg, 53%): R_f 0.32 (MeOH : CH_2Cl_2 2:98); m.p. 120–122 °C (MeOH) [lit.[36] 141–143 °C (EtOAc), lit.[38] 142–144 °C]; ^{1}H NMR (400 MHz, DMSO-d_6): 3.91 (3H, s, N$^{1'}$C*H*$_3$), 4.54 (2H, s, C^1*H*$_2$), 5.49 (1H, s, O*H*), 7.11 (1H, d, *J* = 0.6, C$^{4'}$*H*); LRMS *m/z* (ESI$^+$) 158 ([M+H]$^+$, 100%). These data are generally in good agreement with the reported values.[36, 38]

(1-Methyl-2-nitro-1*H*-imidazol-5-yl)methyl 2-bromoacetate, 30

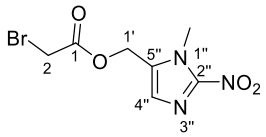

Procedure adapted from Kovacs *et al*.[39]

To a solution of compound **29** (97.3 mg, 0.619 mmol, 1.0 eq.) in CH_2Cl_2 (4.13 mL) and DMF (4.13 mL) at 0 °C, 2,6-di-tertbutylpyridine (0.41 mL, 1.90 mmol, 3.1 eq.) was added and the resulting solution was stirred at 0 °C for 10 min. Bromoacetyl bromide (0.07 mL,

0.804 mmol, 1.3 eq.) was added and the resulting solution was warmed to rt and stirred for a further 16 h then the solvent was reduced *in vacuo*. The resulting mixture was diluted with Et_2O (90 mL) and the organic components were washed with 0.5 M LiCl solution (3 × 30 mL), dried over Na_2SO_4, filtered and concentrated *in vacuo*. The resulting residue was adsorbed onto Celite® and purified by silica column chromatography, eluting with EtOAc and PE (isocratic, 40% EtOAc), to yield compound **30** as a yellow solid (138 mg, 80%): R_f 0.21 (EtOAc : PE 4:6); m.p. 63–65 °C (EtOAc); ν_{max} (thin film) cm^{-1}: 1746 (C=O, s), 1541 (N-O, m), 1282 (C-O, s); ^{1}H NMR (600 MHz, CD_3CN): 3.93 (3H, s, $N^{1''}C\mathit{H_3}$), 3.97 (2H, s, $C^2\mathit{H_2}$), 5.23 (2H, s, $C^{1'}\mathit{H_2}$), 7.19 (1H, s, $C^{4''}\mathit{H}$); ^{13}C NMR (151 MHz, MeCN-d_3): 27.1 ($N^{1''}\mathit{C}$), 35.2 (C^2), 57.6 ($C^{1'}$), 130.1 ($C^{4''}$), 133.1 ($C^{5''}$), 147.7 ($C^{2''}$), 167.7 (C^1); HRMS *m/z* (ESI^+) [Found: 277.9775, $C_7H_8BrN_3O_4$ requires $[M+H]^+$ 277.9771]; LRMS *m/z* (ESI^+) 278 ($[M+H]^+$, ^{79}Br, 14%), 280 ($[M+H]^+$, ^{81}Br, 12%), 577 ($[2M+Na]^+$, $^{79}Br^{79}$Br, 38%), 579 ($[2M+Na]^+$, $^{79}Br^{81}$Br, 66%), 581 ($[2M+Na]^+$, $^{81}Br^{81}$Br, 39%); LCMS (method 1) R_t 3.6 min, 91.5%.

Tri-tert-butyl 2,2',2''-(10-(2-((1-methyl-2-nitro-1H-imidazol-5-yl)methoxy)-2-oxoethyl)-1,4,7,10-tetraazacyclododecane-1,4,7-triyl)triacetate, 31

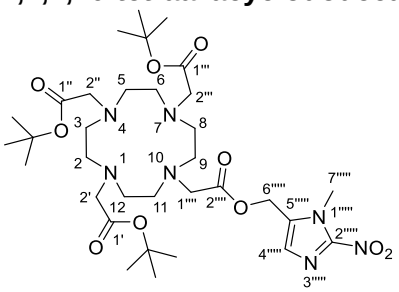

23 (516 mg, 0.866 mmol, 1.0 eq.) and $NaHCO_3$ (219 mg, 2.61 mmol, 3.0 eq.) was added to a solution of **30** (314 mg, 1.13 mmol, 1.3 eq.) in MeCN (14.0 mL). The resulting suspension was stirred at 80 °C for 42 h, cooled to rt, filtered through Celite®, washed with CH_2Cl_2 and the filtrate was concentrated *in vacuo*. The resulting material was adsorbed onto Celite® and purified by silica column chromatography, eluting with EtOH and chloroform (gradient, 0–20% EtOH), resulting in an orange foam **31** (510 mg, 83%) which was stored at −20 °C: R_f 0.33 (EtOH : chloroform 2:8); ν_{max} (solid) cm^{-1}: 1725 (C=O, s), 1536 (N-O, w), 1227 (C-O, s); ^{1}H NMR (400 MHz, $CDCl_3$): 1.24–1.46 (27H, m, 3 × $C(C\mathit{H_3})_3$), 1.54-2.78 (16H, m, 8

× ring C*H*$_2$), 2.98-3.51 (8H, m, 4 × COC*H*$_2$), 4.07 (3H, s, C$^{7''''''}$*H*$_3$), 5.31 (2H, s, C$^{6''''''}$*H*$_2$), 7.06 (1H, s, C$^{4''''''}$*H*); ^{1}H NMR (600 MHz, CD_3CN): 1.29–1.54 (27H, s, 3 × C(C*H*$_3$)$_3$), 1.99–3.49 (24H, m, 4 × COC*H*$_2$, 8 × ring C*H*$_2$), 3.91–3.97 (3H, m, C$^{7''''''}$*H*$_3$), 5.15–5.30 (2H, m, C$^{6''''''}$*H*$_2$), 7.12–7.19 (1H, s, C$^{4''''''}$*H*); ^{13}C NMR (151 MHz, CD_3CN): 28.2 (3 × (*C*H$_3$)$_3$), 35.1 (*C*$^{7''''''}$), 47.9–50.2 (m, ring *C*H$_2$), 52.1–54.5 (m, ring *C*H$_2$), 55.5 (arm *C*H$_2$), 56.3 (arm *C*H$_2$), 56.5 (arm *C*H$_2$), 62.0 (arm *C*H$_2$), 82.8 (3 × *C*(CH$_3$)$_3$), 130.3 (C$^{4''''''}$), 133.4 (C$^{5''''''}$), 147.5 (C$^{2''''''}$), 167.9 (C$^{2''''}$), 174.1 (C$^{1'}$/C$^{1''}$/C$^{1''''}$), 174.3 (C$^{1'}$/C$^{1''}$/C$^{1''''}$), 174.4 (C$^{1'}$/C$^{1''}$/C$^{1''''}$); HRMS *m/z* (ESI$^+$) [Found: 712.4230, $C_{33}H_{57}N_7O_{10}$ requires $[M+H]^+$ 712.4240]; LRMS *m/z* (ESI$^+$) 712 ($[M+H]^+$, 27%), 734 ($[M+Na]^+$, 100%); LCMS (method 1) R_t 3.6 min, 98.3%.

2,2',2''-(10-(2-((1-Methyl-2-nitro-1*H*-imidazol-5-yl)methoxy)-2-oxoethyl)-1,4,7,10-tetraazacyclododecane-1,4,7-triyl)triacetic acid, 32

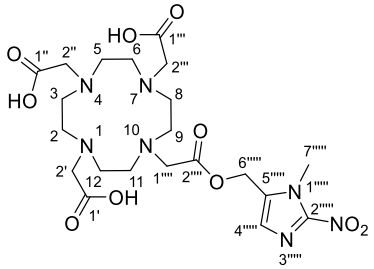

The reaction was carried out following the general TFA deprotection procedure, left to stir at rt for 18 h, using **31** (129 mg, 0.181 mmol, 1.0 eq.) in CH_2Cl_2 (5.2 mL) and TFA (5.2 mL, 68.0 mmol, 376 eq.), to give **32** as an off-white solid (79.5 mg, 81%): ν_{max} (solid) cm^{-1}: 3448 (O-H, br, w), 1727 (C=O, m), 1676 (C=O, m), 1636 (C=C, m), 1522 (N-O, m), 1350 (O-H, m), 1189 (C-O, s); ^{1}H NMR (600 MHz, D_2O): 2.96–3.30 (8H, m, 4 × ring C*H*$_2$), 3.40–3.64 (8H, m, 4 × ring C*H*$_2$), 3.64–3.84 (4H, m, 2 × arm C*H*$_2$), 3.94–4.11 (7H, m, 2 × arm C*H*$_2$, C$^{7''''''}$*H*$_3$), 5.32–5.42 (2H, m, C$^{6''''''}$*H*$_2$), 7.25–7.35 (1H, m, C$^{4''''''}$*H*); ^{13}C NMR (151 MHz, D_2O): 34.9 (C$^{7''''''}$), 48.0–49.2 (m, ring *C*H$_2$), 51.2–52.3 (m, ring *C*H$_2$), 53.0–54.1 (m, arm *C*H$_2$), 55.4–56.2 (m, arm *C*H$_2$), 56.3–56.8 (C$^{6''''''}$), 129.8 (C$^{4''''''}$), 133.6 (C$^{5''''''}$), 146.4 (C$^{2''''''}$), 170.0 (C$^{1'}$/C$^{1''}$/C$^{1''''}$), 172.2 (C$^{2''''}$), 174.5 (C$^{1'}$/C$^{1''}$/C$^{1''''}$); HRMS *m/z* (ESI$^+$) [Found: 544.2347, $C_{21}H_{34}N_7O_{10}$ requires $[M+H]^+$ 544.2362; LRMS *m/z* (ESI$^+$) 544 ($[M+H]^+$, 100%), 566 ($[M+Na]^+$, 31%); LCMS (method 2) R_t 0.6 min, >99%.

Europium nitroimidazole complex (EuNI), 19a

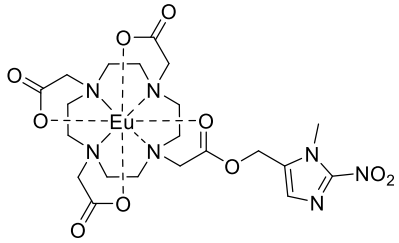

The reaction was carried out following the general lanthanide complexation procedure, using **32** (75.0 mg, 138 µmol, 1.0 eq.) and europium triflate (86.8 mg, 145 µmol, 1.07 eq.) in MES buffer (2.12 mL). The reaction was left at rt for 1 h, purified by semi-preparative HPLC method 2 and lyophilised for 2 days to yield compound **19a** as a colourless solid (36.9 mg, 39%): ^{1}H NMR (400 MHz, D_2O)*: −19.5, −17.2, −16.5, −16.0, −14.6, −12.3, −10.6, −9.5, −9.0, −8.4, −8.0, −7.2, −6.6, −6.3, −5.4, −3.6, −1.0, −0.7, 0.4, 5.7, 7.2, 8.5, 9.3, 10.5, 13.4, 23.8, 25.3, 32.5, 33.8; LRMS *m/z* (ESI$^+$) 715 ([M+Na]$^+$, 9%); HRMS *m/z* (ESI$^+$) [Found: 694.1333, $C_{21}H_{30}N_7O_{10}Eu$ requires [M+H]$^+$ 694.1339]; LCMS (method 2) 1.1 min, 94.5%; Analytical HPLC (method 1A): R_t 3.0 min, 95.1%.

*^{1}H NMR contains 6% EuDOTA, therefore total purity ~89%, all peaks reported including EuDOTA.

Terbium nitroimidazole complex (TbNI), 19b

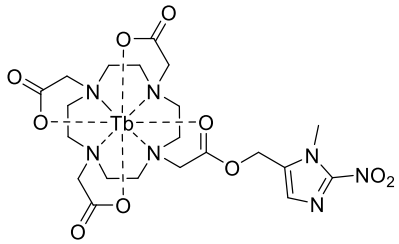

The reaction was carried out following the general lanthanide complexation procedure, using **32** (75.5 mg, 139 µmol, 1.0 eq.) and terbium triflate (88.9 mg, 147 µmol, 1.08 eq.) in MES buffer (2.12 mL). The reaction was left at rt for 1 h, purified by semi-preparative HPLC method 2 and lyophilised for 2 days to yield compound **19b** as a colourless solid (38.6 mg, 40%): ^{1}H NMR (400 MHz, D_2O)*: −417.0, −394.7, −326.7, −322.7, −295.3, −217.9, −194.0, −177.6, −158.6, −117.2, −98.1, −94.7, −91.5, −71.2, −65.8, −62.6, −43.3,

−32.2, −22.2, −19.4, −18.1, −7.9, −5.2, 78.3, 82.5, 95.3, 136.0, 152.7, 169.5, 206.4, 215.4, 220.8, 228.3, 257.5, 303.5; HRMS *m/z* (ESI$^+$) [Found: 700.1357, $C_{21}H_{30}N_7O_{10}Tb$ requires $[M+H]^+$ 700.1380]; LCMS (method 2) R_t 0.7 min, 98.5%; Analytical HPLC (method 1A) R_t 2.9 min, 93.8%.

*^{1}H NMR contains 7% TbDOTA (total purity ~89%), all peaks reported including TbDOTA.

Gadolinium nitroimidazole complex (GdNI), 19c

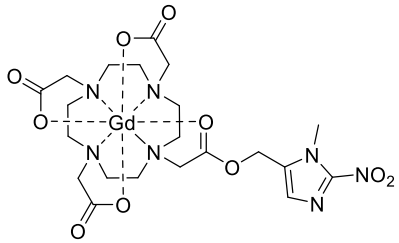

The reaction was carried out following the general lanthanide complexation procedure, using **32** (49.3 mg, 90.7 µmol, 1.0 eq.) and gadolinium triflate (60.0 mg, 99.3 µmol, 1.07 eq.) in MES buffer (1.40 mL). The reaction was left at rt for 1 h, purified by semi-preparative HPLC method 2 and lyophilised to yield compound **19c** as a colourless solid (35.4 mg, 56%): HRMS *m/z* (ESI$^+$) [Found: 721.1167, $C_{21}H_{30}N_7O_{10}Gd$ requires $[M+Na]^+$ 721.1188]; LRMS *m/z* (ESI$^+$) 721 ($[M+Na]^+$, 3%); LCMS (method 2) R_t 1.1 min, 95.3%; Analytical HPLC (method 1A) R_t 3.0 min, 95.6%.

5-Methoxy-2-methyl-1*H*-indole-3-carbaldehyde, 33

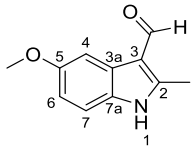

Phosphorus(V) oxychloride (2.20 mL, 23.6 mmol, 1.4 eq.) was added to dry DMF (7.80 mL, 101 mmol, 6 eq.) at 0 °C. The resulting solution was stirred at 0 °C for 10 min to form the presumed Vilsmeier's reagent, which was then added dropwise over 30 min at −10 °C to a solution of 5-methoxy-2-methylindole (2.71 g, 16.8 mmol, 1.0 eq.) in dry DMF (10.4 mL). The resulting solution was stirred for a further 30 min at −10 °C, then warmed to 0 °C and stirred for a further 15 min, before being poured onto a cooled (0 °C) sodium hydroxide

solution (240 mL, 2 M in H_2O). The aqueous layer was extracted with CH_2Cl_2 (3 × 120 mL) and the organic components were washed with brine (120 mL) and 0.5 M LiCl solution (2 × 60 mL), dried over Na_2SO_4, filtered and concentrated *in vacuo*. The resulting dark brown solid was washed with cold EtOAc (4 × 60 mL) to give **33** as a yellow-brown solid (1.85 g, containing product:DMF 3:2 plus small impurities). The solid was re-dissolved in CH_2Cl_2, washed with 0.5 M LiCl solution (2 × 100 mL), dried over Na_2SO_4, filtered and concentrated *in vacuo*. The resulting brown solid was washed with EtOAc to a give **33** as a light-brown solid (943 mg, 30%): R_f 0.18 (EtOAc : hexane 1:1); m.p. 187–189 °C (EtOAc) [lit.[29] 180–183 °C (EtOAc), lit.[40] 198–199 °C, lit.[41] 191–194 °C, lit.[42] 120–122 °C]; ^{1}H NMR (400 MHz, $CDCl_3$): 2.72 (3H, s, C^{2}CH_3), 3.88 (3H, s, OCH_3), 6.88 (1H, dd, J_1 = 8.8, J_2 = 2.5, C^6*H*), 7.23 (1H, d, J = 8.8, C^7*H*), 7.73 (1H, d, J = 2.5, C^4*H*), 8.78 (1H, br s, N*H*), 10.02 (1H, s, C*H*O); LRMS *m/z* (ESI$^+$) 190 ([M+H]$^+$, 78%). These data are generally in good agreement with the reported values.[29, 40-42]

5-Methoxy-1,2-dimethyl-1*H*-indole-3-carbaldehyde, 34

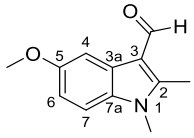

A solution of **33** (897 mg, 4.74 mmol, 1.0 eq.) in dry DMF (6.0 mL) was added dropwise to a suspension of NaH (60% dispersion in mineral oil, 294 mg, 7.34 mmol, 1.5 eq.) in dry DMF (5.5 mL), under an argon atmosphere. The resulting suspension was stirred at rt for 2 h, then cooled to 0 °C. Iodomethane (0.36 mL, 5.80 mmol, 1.2 eq.) was added dropwise and the resulting solution was stirred for a further 2 h at rt. H_2O (50 mL) was added slowly and the aqueous layer was extracted with CH_2Cl_2 (3 × 50 mL). The organic components were washed with H_2O (50 mL), LiCl solution (2 × 50 mL, 0.5 M in H_2O) and brine (50 mL), dried over Na_2SO_4, filtered and concentrated *in vacuo*. The resulting residue was adsorbed onto Celite® and purified by silica column chromatography, eluting with EtOAc and hexane (gradient, 20–100% EtOAc), to yield compound **34** as a yellow solid (686 mg, 71%) : R_f 0.24 (EtOAc : hexane 1:1); m.p. 120–126 °C (EtOAc) [lit.[29] 115–118 °C (EtOAc), lit.[43] 132–

133 °C]; ^{1}H NMR (400 MHz, $CDCl_3$): 2.68 (3H, s, C^2CH_3), 3.71 (3H, s, N^1CH_3), 3.90 (3H, s, OCH_3), 6.92 (1H, dd, J_1 = 8.8, J_2 = 2.5, C^6H), 7.21 (1H, d, J = 8.8, C^7H), 7.78 (1H, d, J = 2.5, C^4H), 10.04 (1H, s, CHO); LRMS *m/z* (ESI$^+$) 176 ([M-CHO]$^+$, 29%), 204 ([M+H]$^+$, 45%), 429 ([2M+Na]$^+$, 100%). These data are generally in good agreement with the reported values.[29, 43]

5-Methoxy-1,2-dimethyl-4,7-dioxo-4,7-dihydro-1*H*-indole-3-carbaldehyde, 37, *via* 5-methoxy-1,2-dimethyl-4-nitro-1*H*-indole-3-carbaldehyde, 35, and 4-amino-5-methoxy-1,2-dimethyl-1*H*-indole-3-carbaldehyde, 36

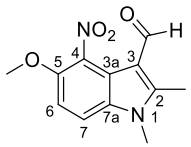

35

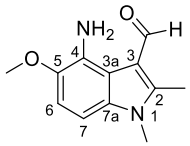

36

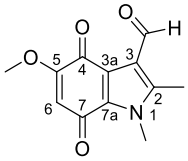

37

Step 1 – A solution of fuming nitric acid (3.1 mL, 74.3 mmol, 22.4 eq.) in AcOH (11.7 mL) was added dropwise to a solution of compound **34** (674 mg, 3.32 mmol, 1.0 eq.) in AcOH (70.0 mL) at 0 °C and the resulting solution was warmed to rt and stirred for a further 3 h. The resulting solution was poured into crushed ice (134 g) and the resulting suspension was stirred for a further 1 h before the yellow precipitated was collected by filtration, washed with H_2O (4 × 150 mL) and dried *in vacuo* to give a mixture of regioisomers containing **35** (710 mg, 100% conversion by ^{1}H NMR, 86% 'yield'), which was used without further purification: LRMS *m/z* (ESI$^+$) 249 ([M+H]$^+$, 2%), 271 ([M+Na]$^+$, 19%), 519 ([2M+Na]$^+$, 85%).

Step 2 - Tin (1.00 g, 8.46 mmol, 5.3 eq.) and aqueous HCl (12.4 mL, 3.0 M, 37.3 mmol, 23.2 eq.) was added to a suspension of compound **35** (400 mg, 1.61 mmol, 1.0 eq., mixture of regioisomers) in EtOH (30.0 mL) and the resulting suspension was heated at 80 °C for 1 h. The resulting suspension was cooled to rt, 100 mL H_2O was added and the mixture was adjusted to pH 8 using solid $NaHCO_3$. The aqueous layer was extracted with chloroform (3 × 100 mL) and the organic components were washed with brine (2 × 50 mL), dried over Na_2SO_4 and concentrated *in vacuo* to give a brown/yellow solid containing **36**

which was used in the next step without further purification: LRMS *m/z* (ESI^+) 219 ($[M+H]^+$, 100%), 459 ($[2M+Na]^+$, 44%).

Step 3 - The resulting solid was dissolved in acetone (100 mL) and to the solution was added Fremy's salt (2.16 g, 8.05 mmol, 5 eq.) in NaH_2PO_4/Na_2HPO_4 buffer (100 mL, 0.4 M in H_2O, pH 6). The resulting solution was stirred at rt for 1 h then concentrated *in vacuo* to remove the acetone and extracted with EtOAc (4 × 75 mL). The organic components were dried over Na_2SO_4, filtered and concentrated *in vacuo*. The resulting residue was adsorbed onto Celite® and purified by silica column chromatography, eluting with acetone and CH_2Cl_2 (gradient, 2.5–10% acetone), to yield compound **37** as an orange solid (202 mg, 46% over 3 steps): R_f 0.52 (acetone : CH_2Cl_2 5:95); m.p. 233–235 °C (CH_2Cl_2, decomposition) [lit.[29] 217–219 °C (acetone), lit.[42] 239–242 °C]; ^{1}H NMR (400 MHz, $CDCl_3$) 2.62 (3H, s, C^2CH_3), 3.85 (3H, s, N^1CH_3), 3.94 (3H, s, OCH_3), 5.70 (1H, s, C^6H), 10.55 (1H, s, CHO); LRMS *m/z* (ESI^+) 234 ($[M+H]^+$, 1%), 489 ($[2M+Na]^+$, 100%). These data are generally in good agreement with the reported values.[29, 43]

3-(Hydroxymethyl)-5-methoxy-1,2-dimethyl-1*H*-indole-4,7-dione, 38

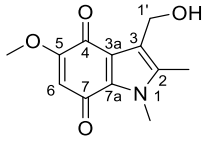

38

$NaBH_4$ (130 mg, 3.44 mmol, 5.2 eq.) was added portion-wise, under a stream of argon, to a suspension of **37** (154 mg, 0.660 mmol, 1.0 eq.) in dry MeOH (12.0 mL) and dry THF (12.0 mL) at 0 °C under an argon atmosphere. The resulting orange suspension was stirred for 45 min, until it became a colourless solution. H_2O (12 mL) was added slowly and the aqueous layer was rapidly extracted with CH_2Cl_2 (3 × 30 mL), dried over Na_2SO_4, filtered and concentrated *in vacuo*. The resulting residue was adsorbed onto Celite® and purified by silica column chromatography, eluting with EtOAc and hexane (gradient, 50–100% EtOAc) then acetone and EtOAc (gradient, 20–50% acetone), to yield compound **38** as a red solid (127 mg, 81%): R_f 0.34 (EtOAc); m.p. 196–198 °C (EtOAc) [lit.[29] 195–198 °C

(EtOAc), lit.[44] 199–200 °C, lit.[43] 215–216 °C]; ^{1}H NMR (400 MHz, $CDCl_3$) 2.23 (3H, s, $C^{2}CH_3$), 3.83 (3H, s, $N^{1}CH_3$), 3.89 (3H, s, OCH_3), 4.62 (2H, d, J = 7.2, $C^{1'}H_2$), 5.64 (1H, s, $C^{6}H$); LRMS *m/z* (ESI^+) 258 ([M+Na]$^+$, 25%), 493 ([2M+Na]$^+$, 100%). These data are generally in good agreement with the reported values.[29, 43, 44]

(5-Methoxy-1,2-dimethyl-4,7-dioxo-4,7-dihydro-1H-indol-3-yl)methyl 2-chloroacetate, 39

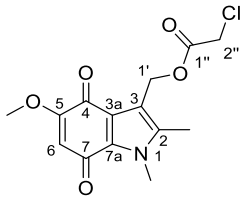

39

This reaction was carried out by Dr Daniel Kovacs. Procedure adapted from Kovacs *et al*.[39]

To a solution of compound **38** (7.0 mg, 29.8 µmol, 1.0 eq.) in CH_2Cl_2 (125 µL) and DMF (125 µL) at 0 °C, 2,6-di-tertbutylpyridine (20.0 µL, 89.3 µmol, 3.0 eq.) was added and the resulting solution was stirred at 0 °C for 10 min. Chloroacetyl chloride (3.0 µL, 37.2 µmol, 1.3 eq.) was added and the resulting solution was warmed to rt and stirred for a further 3 h then the solvent was reduced *in vacuo*. The resulting mixture was diluted brine (1-2 mL), extracted into EtOAc (3 × 2 mL), dried over $MgSO_4$, filtered and concentrated *in vacuo*. The resulting residue was adsorbed onto Celite® and purified by silica column chromatography, eluting with CH_2Cl_2 and Et_2O (gradient, 10–20% CH_2Cl_2), to yield compound **39** as a red solid (8.0 mg, 86%): R_f 0.75 (CH_2Cl_2 : Et_2O 3:2); ^{1}H NMR (400 MHz, $CDCl_3$) 2.29 (3H, s, $C^{2}CH_3$), 3.79 (3H, s, OCH_3), 3.88 (3H, s, $N^{1}CH_3$), 4.03 (2H, s, $C^{2''}H_2$), 5.33 (2H, s, $C^{1'}H_2$), 5.61 (1H, s, $C^{6}H$); ^{13}C NMR (101 MHz, $CDCl_3$): 9.7 ($C^{2}C$), 32.5 ($N^{1}C$), 41.1 ($C^{2''}$), 56.6 ($C^{5}OC$), 58.4 ($C^{1'}$), 106.8 (C^{6}), 114.9 (C^{3a}), 121.8 (C^{3}), 129.4 (C^{7a}), 138.2 (C^{2}), 159.8 (C^{5}), 167.4 ($C^{1''}$), 177.7 (C^{4}), 178.9 (C^{7}).

Tri-*tert*-butyl 2,2',2''-(10-(2-((5-methoxy-1,2-dimethyl-4,7-dioxo-4,7-dihydro-1H-indol-3-yl)methoxy)-2-oxoethyl)-1,4,7,10-tetraazacyclododecane-1,4,7-triyl)triacetate, 40

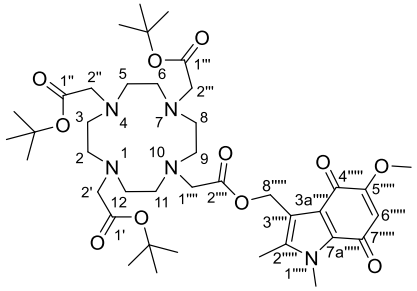

This reaction was carried out by Dr Daniel Kovacs.

23 (10.3 mg, 17.3 µmol, 1.0 eq.) and Na_2CO_3 (4.6 mg, 43.2 µmol, 2.5 eq.) was added to a solution of **39** (7.0 mg, 22.5 µmol, 1.3 eq.) in MeCN (280 µL). The resulting suspension was stirred at 50 °C for 18 h, cooled to rt and concentrated *in vacuo*. The resulting material was adsorbed onto Celite® and purified by silica column chromatography, eluting with MeOH and CH_2Cl_2 (gradient, 0–15% MeOH), resulting in a deep orange solid **40** (14.0 mg, quant.): R_f 0.40 (CH_2Cl_2 : MeOH 2:3); ^{1}H NMR (400 MHz, DMSO-d_6): 1.09–1.59 (27H, m, 3 × C(C*H*$_3$)$_3$), 1.88–2.31 (13H, m, 5 × ring C*H*$_2$, C$^{2''''''}$C*H*$_3$), 2.56–3.23 (14H, m, 3 × ring C*H*$_2$, 4 × arm C*H*$_2$), 3.76 (3H, s, C$^{5''''''}$OC*H*$_3$), 3.82 (3H, s, N$^{1''''''}$C*H*$_3$), 5.23 (2H, s, C$^{8''''''}$*H*$_2$), 5.71–5.82 (1H, m, C$^{6''''''}$*H*); ^{13}C NMR (151 MHz, DMSO-d_6): 9.1 (C$^{2''''''}$*C*), 27.5 (*C*(CH$_3$)$_3$), 32.2 (N$^{1''''''}$*C*), 46.5–53.5 (m, ring *C*H$_2$), 54.5 (C$^{2'}$/C$^{2'''}$), 55.1 (C$^{2''}$), 55.5 (C$^{8''''''}$), 56.4 (C$^{1''''}$), 56.6 (C$^{5''''''}$O*C*), 81.3 (3 × *C*(CH$_3$)$_3$), 106.7 (C$^{6''''''}$), 114.4 (C$^{3a''''''}$), 121.0 (C$^{3''''''}$), 128.3 (C$^{7a''''''}$), 138.6 (C$^{2''''''}$), 159.3 (C$^{5''''''}$), 177.0 (C$^{4''''''}$), 178.3 (C$^{7''''''}$); LRMS *m/z* (ESI$^+$) 790 ([M+H]$^+$, 60%), 812 ([M+Na]$^+$, 100%).

Attempted deprotection of 41

Method 1 (TFA) – The reaction was carried out by Dr Daniel Kovacs, following the general TFA deprotection procedure, and was monitored by TLC and ^{1}H NMR spectroscopy. Degradation was observed after several hours.

Method 2 ($ZnBr_2$) – To a solution of **41** (30.0 mg, 38.0 µmol, 1.0 eq.) in CH_2Cl_2 (1.0 mL), zinc bromide (42.8 mg, 190 µmol, 5.0 eq.) was added and the solution stirred at rt for 30 min, after which a red solid precipitated. The reaction mixture was diluted in H_2O (10

mL) and stirred at rt for a further 1 h. The layers were separated the aqueous layer extracted with CH_2Cl_2 (3 × 10 mL) and concentrated *in vacuo* to give an orange oil. LRMS analysis of the aqueous and organic layers showed that no starting material remained or product was formed and ^{1}H NMR analysis of the organic layer suggested that degradation had occurred.

Method 3 (oxalyl chloride) – To a solution of **41** (20.2 mg, 25.6 µmol, 1.0 eq.) in MeOH (1.2 mL), oxalyl chloride (20.0 µL, 233 µmol, 9.1 eq.) was added and the resulting solution was stirred at rt for 1 h to give a dark orange solution. The reaction mixture was concentrated *in vacuo* to give a red solid. TLC indicated that no starting material remaining and a new orange spot had formed. LRMS analysis suggested that fragmentation had occurred to give the carboxylic acid fragment $[(M\text{-}IQ)+H]^+$ with an *m/z* of 573 (100% intensity). ^{1}H NMR analysis of the crude mixture in $CDCl_3$ showed evidence of organic indolequinone derivatives and in D_2O showed no evidence of triacid formation.

1,4,7-Tribenzyl 1,4,7,10-tetraazacyclododecane-1,4,7-tricarboxylate, 43

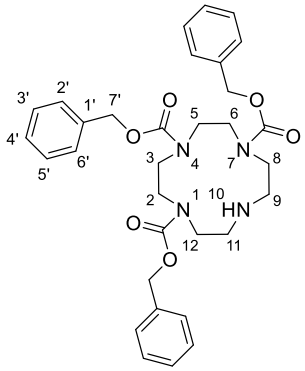

To a solution of 1,4,7,10-tetraazacyclododecane (cyclen, 2.50 g, 14.5 mmol, 1.0 eq.) in CH_2Cl_2 (80 mL), triethylamine (6.00 mL, 43.0 mmol, 3.0 eq.) was added and the resulting solution was stirred at 0 °C for 10 min. Benzyl chloroformate (6.30 mL, 42.0 mmol, 2.9 eq.) was dissolved in DCM (20 mL) and was added dropwise. The resulting solution was warmed to rt and stirred for a further 17 h, then concentrated *in vacuo*. The resulting residue was adsorbed onto Celite® and purified by silica column chromatography, eluting with EtOAc and PE (gradient, 50–100% EtOAc), to yield compound **43** as a colourless oil (3.94 g, 47%): R_f 0.13 (PE : EtOAc 1:1); ν_{max} (thin film) cm^{-1}: 3409 (NH, m), 1698 (C=O, s); ^{1}H

NMR (400 MHz, $CDCl_3$) 0.89 (1H, br s, N*H*), 2.66–2.98 (4H, m, 2 × ring CH_2), 3.20–3.83 (12H, m, 6 × ring CH_2), 4.79–5.22 (6H, m, 3 × OCH_2), 7.15–7.46 (15H, m, 3 × C_6H_5); LRMS *m/z* (ESI^+) 575 ($[M+H]^+$, 93%), 1149 ($[2M+H]^+$, 100%). These data are good agreement with the available literature data.[45, 46]

1,4,7-Tribenzyl 10-(*tert*-butyl) 1,4,7,10-tetraazacyclododecane-1,4,7,10-tetracarboxylate, 44

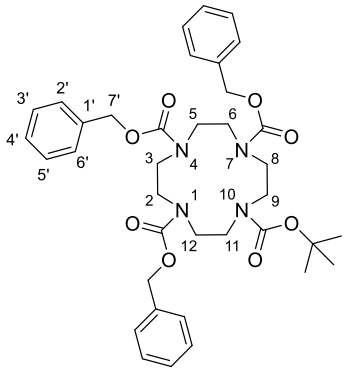

Dry TEA (0.37 mL, 2.70 mmol, 1.3 eq.) was added to a solution of compound **43** (1.20 g, 2.09 mmol, 1.0 eq.) in dry CH_2Cl_2 (14.0 mL) and the resulting solution was stirred at rt for 10 min. Di-*tert*-butyl dicarbonate (0.58 g, 2.70 mmol, 1.3 eq.) was added and the resulting mixture was stirred at rt for 16 h, then concentrated *in vacuo* and stored at −20 °C overnight. The resulting residue was adsorbed onto Celite® and purified by silica column chromatography, eluting with Et_2O and CH_2Cl_2 (gradient, 0–20% Et_2O), to yield compound **44** as a colourless oil (1.16 g, 82%): R_f 0.31 (CH_2Cl_2 : Et_2O 8:2); ν_{max} (thin film) cm^{-1}: 3464 (O-H, br, w), 1694 (C=O, s); ^1H NMR (400 MHz, $CDCl_3$) 1.36 (9H, s, C(CH_3)$_3$), 3.13–3.51 (16H, m, 8 × ring CH_2), 5.00–5.12 (6H, m, 3 × OCH_2), 7.23–7.37 (15H, m, 3 × C_6H_5); LRMS *m/z* (ESI^+) 675 ($[M+H]^+$, 34%), 697 ($[M+Na]^+$, 90%), 1371 ($[2M+H]^+$, 100%). These data are good agreement with the available literature data.[46]

4-((*Tert*-butyldimethylsilyl)oxy)benzaldehyde, 46

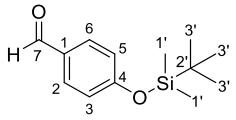

To a solution of 4-hydroxybenzaldehyde (2.52 g, 20.6 mmol, 1.0 eq.) and imidazole (2.11 g, 31.0 mmol, 1.5 eq.) in DMF (30 mL), *tert*-butylchlorodimethylsilane (TBDMSCl, 3.58 g, 23.8 mmol, 1.2 eq.) was added and the resulting solution was stirred at rt for 17 h. The reaction was diluted with Et_2O (50 mL), washed with a brine and H_2O solution (1:1, 150 mL), extracted with Et_2O (2 × 50 mL). The combined organic components were washed with LiCl solution (0.5 M, 100 mL) and brine (100 mL), dried over Na_2SO_4, filtered and concentrated *in vacuo* to give compound **46** as an orange-brown liquid (4.41 g, 90%) which was not purified further: R_f 0.31 (PE : Et_2O 95:5); ^{1}H NMR (400 MHz, $CDCl_3$) 0.25 (6H, s, 2 × C$^{1'}$*H*$_3$), 0.99 (9H, s, 3 × C$^{3'}$*H*$_3$), 6.92–6.96 (2H, m, C^3*H*/C^5*H*), 7.76–7.82 (2H, m, C^2*H*/C^4*H*), 9.89 (1H, s, C^7*H*); LRMS *m/z* (ESI$^+$) 237 ([M+H]$^+$, 100%). These data are good agreement with the available literature data.[47, 48]

(4-((*Tert*-butyldimethylsilyl)oxy)phenyl)methanol, 47

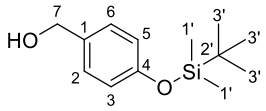

$NaBH_4$ (700 mg, 18.5 mmol, 2 eq.) was added portion-wise to a solution of compound **46** (2.18 g, 9.21 mmol, 1.0 eq.) in MeOH (70.0 mL) and THF (40.0 mL) under an argon atmosphere, at 0 °C. The resulting suspension was warmed to rt after 1 h and stirred at rt for a further 2 h and then quenched with saturated NH_4Cl solution. The resulting suspension was poured into a brine/H2O mixture (1:1, 400 mL), extracted with EtOAc (3 × 250 mL), dried over Na_2SO_4, filtered, concentrated *in vacuo* and stored at −20 °C. The resulting residue was adsorbed onto Celite® and purified by silica column chromatography, eluting with EtOAc and PE (gradient, 10–20% EtOAc), to yield compound **47** as a pale yellow liquid (1.47 g, 67%): R_f 0.51 (PE : EtOAc 6:4); ^{1}H NMR (400 MHz, $CDCl_3$) 0.19 (6H, s, 2 × C$^{1'}$*H*$_3$),

0.98 (9H, s, 3 × C$^{3'}H_3$), 4.61 (2H, s, C$^{7}H_2$), 6.76–6.86 (2H, m, C^{3}H/C^{5}H), 7.19–7.25 (2H, m, C^{2}H/C^{6}H); LRMS *m/z* (ESI$^+$) 239 ([M+H]$^+$, 3%), 261 ([M+Na]$^+$, 41%), 499 ([2M+Na]$^+$, 78%). These data are good agreement with the available literature data.[49-51]

4-((*Tert*-butyldimethylsilyl)oxy)benzyl 2-bromoacetate, 48

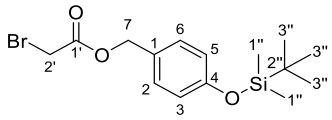

To a solution of compound **47** (793 mg, 3.33 mmol, 1.0 eq.) in CH_2Cl_2 (13.3 mL) and DMF (13.3 mL) at 0 °C, 2,6-di-tertbutylpyridine (1.44 mL, 6.66 mmol, 2.0 eq.) was added and the resulting solution was stirred at 0 °C for 10 min. Bromoacetyl bromide (0.34 mL, 3.90 mmol, 1.2 eq.) was added and the resulting solution was warmed to rt and stirred for a further 18 h then the solvent was reduced *in vacuo*. The CH_2Cl_2 was removed by concentration *in vacuo*. Brine (75 mL) and H2O (75 mL) were added to the resulting solution and the aqueous components were extracted using EtOAc (3 × 50 mL). The organic components dried over Na_2SO_4, filtered and concentrated *in vacuo*. The resulting residue was adsorbed onto Celite® and purified by silica column chromatography, eluting with EtOAc and PE (gradient, 0–10% EtOAc), to yield compound **48** as a colourless liquid (824 mg, 69%): R_f 0.51 (PE : EtOAc 9:1); v_{max} (thin film) cm^{-1}: 1740 (C=O, s), 1611 (C=C, m), 1268 (C-O, s); ^{1}H NMR (400 MHz, $CDCl_3$) 0.20 (6H, s, 2 × C$^{1''}H_3$), 0.98 (9H, s, 3 × C$^{3'}H_3$), 3.85 (2H, s, C$^{2'}H_2$), 5.13 (2H, s, C$^{7}H_2$), 6.80–6.85 (2H, m, C^{3}H/C^{5}H), 7.22–7.26 (2H, m, C^{2}H/C^{6}H); HRMS *m/z* (ESI$^+$) [Found: 381.0510, $C_{15}H_{23}BrO_3Si$ requires [M+Na]$^+$ 381.0492]; LRMS *m/z* (ESI$^+$) 381 ([M+Na]$^+$, ^{79}Br, 59%), 383 ([M+Na]$^+$, ^{81}Br, 60%), 739 ([2M+Na]$^+$, ^{79}Br^{79}Br, 87%), 741 ([2M+Na]$^+$, ^{79}Br^{81}Br, 100%), 743 ([2M+Na]$^+$, ^{81}Br^{81}Br, 90%).

EuDOTA, 21a

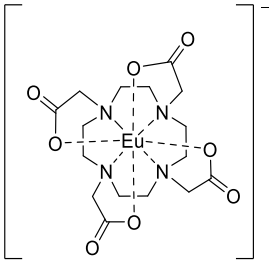

Europium triflate (119 mg, 0.199 mmol, 1.2 eq.) was added to a suspension of DOTA (67.4 mg, 0.167 mmol, 1.0 eq.) in EtOH (0.95 mL) and H_2O (0.95 mL), and the resulting suspension was heated to 40 °C for 17 h. 1M NaOH solution was added portion-wise (1.0 eq. every 30 min, total 0.58 mL, 3.5 eq.) until pH 7 was reached. The resulting suspension was cooled to rt, split into two 1.5 mL Eppendorf tubes, centrifuged for 10 min and the supernatants were filtered (through a Nylon syringe filter), combined and concentrated *in vacuo* to give a colourless solid. The crude residue was redissolved in a minimal amount of H_2O and purified by dialysis (2 weeks, procedure as described in the general experimental), then concentrated *in vacuo* to give compound **21a** as a colourless solid (42.2 mg, 46%): ^{1}H NMR (400 MHz, D_2O): −16.0, −14.6, −8.0, −6.7, −1.1, 33.8 (only SAP isomer reported); HRMS *m/z* (ESI^+) [Found: 577.0769, $C_{16}H_{24}EuN_4O_8$ requires $[(M^-+Na)+H]^+$ 577.0777]; LRMS *m/z* (ESI^+) 577 ($[(M+Na)+H]^+$, 12%), 599 ($[(M+Na)+Na]^+$, 100%). These data are in good agreement with the previously reported values.[52]

TbDOTA, 21b

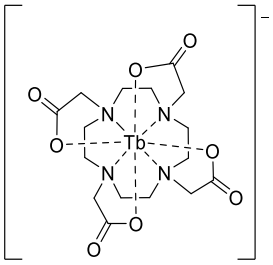

Terbium triflate (133 mg, 0.219 mmol, 1.1 eq.) was added to a solution of DOTA (80.0 mg, 0.198 mmol, 1.0 eq.) in H2O (4.0 mL), and the resulting solution was heated to 40 °C for 19 h. 1 M NaOH solution was added portion-wise (1.0 eq. every 30 min, total 0.50 mL, 2.5 eq.) until pH 7 was reached. The resulting suspension was cooled to rt, filtered (through

a Nylon syringe filter) and concentrated *in vacuo* to give a colourless solid. The crude residue was redissolved in a minimal amount of H_2O and purified by dialysis (2 weeks, procedure as described in the general experimental), then concentrated *in vacuo* to give compound **21b** as a colourless solid (27.6 mg, 25%): ^{1}H NMR (400 MHz, D_2O): −400.3 (SAP, axial ring CH), −240.0 (TSAP), −99.0 (SAP), −95.2 (SAP), −71.5 (TSAP), −69.8 (TSAP), −5.9 (TSAP), 63.6 (TSAP), 84.4 (SAP), 138.4 (SAP), 177.9 (TSAP), 261.9 (SAP, arm CH); HRMS *m/z* (ESI$^+$) [Found: 583.0821, $C_{16}H_{24}TbN_4O_8$ requires $[(M^-+Na)+H]^+$ 583.0818]; LRMS *m/z* (ESI$^+$) 583 ($[(M^-+Na)+H]^+$, 21%), 605 ($[(M^-+Na)+Na]^+$, 100%). These data are in good agreement with the previously reported values.[53]

Tri-*tert*-butyl 2,2',2''-(10-(2-(benzyloxy)-2-oxoethyl)-1,4,7,10-tetraazacyclododecane-1,4,7-triyl)triacetate, 51

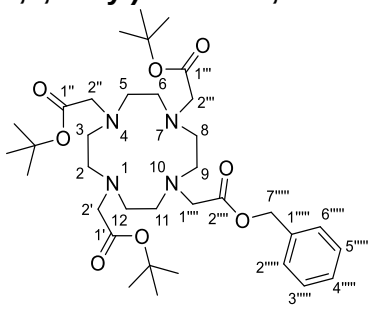

Benzyl 2-bromoacetate (0.40 mL, 2.50 mmol, 1.5 eq.) was added dropwise at 0 °C to a solution of **23** (1.00 g, 1.68 mmol, 1.0 eq.) and K_2CO_3 (1.09 g, 7.89 mmol, 4.7 eq.) in MeCN (20.0 mL). The resulting suspension was stirred at rt for 3 h, filtered, washed with MeCN and the filtrate was concentrated *in vacuo*. The resulting material was dissolved in CH_2Cl_2 and purified by silica column chromatography, eluting with MeOH and CH_2Cl_2 (gradient, 0–10% MeOH), resulting in a yellow oil **51** (1.02 g, 91%) which was stored at −20 °C: R_f 0.18 (MeOH : CH_2Cl_2 5:95); ν_{max} (solid) cm^{-1}: 1727 (C=O, s), 1627 (C=C, w), 1229 (C-O, m), 1162 (C-O, m); ^{1}H NMR (400 MHz, $CDCl_3$): 1.45 (27H, s, 3 × C(C*H*$_3$)$_3$), 1.65–3.44 (24H, m, 4 × arm C*H*$_2$, 8 × ring C*H*$_2$), 5.13 (2H, s, C$^{7''''}$*H*$_2$), 7.28–7.39 (5H, m, C1''''*H*/C$^{2''''}$*H*/C$^{3''''}$*H*/C$^{4''''}$*H*/C$^{5''''}$*H*); ^{13}C NMR (151 MHz, $CDCl_3$): 27.9–28.5 (m, 3 × (*C*H$_3$)$_3$), 50.6–51.5 (ring *C*H$_2$), 51.5–53.5 (ring *C*H$_2$), 55.2 (arm *C*H$_2$), 55.6–56.4 (arm *C*H$_2$), 67.0 (C$^{7''''}$), 81.9–82.0 (m, 3 × *C*(CH$_3$)$_3$), 128.3–128.9 (C$^{2''''}$/C$^{3''''}$/C$^{4''''}$/C$^{5''''}$/C$^{6''''}$), 135.4 (C$^{1''''}$),

173.2 ($C^{1'}/C^{1''}/C^{1'''}$), 173.3 ($C^{1'}/C^{1''}/C^{1'''}$), 173.8 ($C^{2''''}$); HRMS *m/z* (ESI^+) [Found: 685.4159, $C_{35}H_{58}N_4O_8$ requires $[M+Na]^+$ 685.4147]; LRMS *m/z* (ESI^+) 663 ($[M+H]^+$, 99%), 685 ($[M+Na]^+$, 100%); Analytical HPLC (method 2A) R_t 7.8 min, 95.1%. These data are in good agreement with the available literature values.[54-57]

2,2',2''-(10-(2-(benzyloxy)-2-oxoethyl)-1,4,7,10-tetraazacyclododecane-1,4,7-triyl)triacetic acid, 52

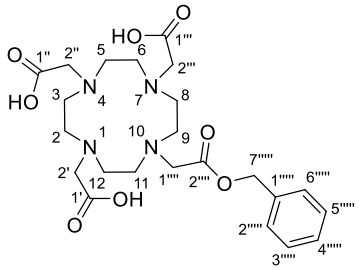

The reaction was carried out following the general TFA deprotection procedure, left to stir at rt for 18 h, using **51** (1.08 g, 1.63 mmol, 1.0 eq.) in CH_2Cl_2 (50.0 mL) and TFA (50.0 mL, 653 mmol, 401.0 eq.), to give **52** as an off-white solid (799 mg, 99%): v_{max} (solid) cm^{-1}: 1779 (C=O, m), 1713 (C=O, m), 1687 (C=C, s), 1386 (O-H, m), 1355 (O-H, m), 1200 (C-O, s); ^1H NMR (400 MHz, D_2O): 2.92–3.24 (8H, m, 4 × ring C*H*$_2$), 3.41–3.54 (8H, m, 4 × ring C*H*$_2$), 3.63–4.02 (8H, m, 4 × arm C*H*$_2$), 5.25 (2H, s, $C^{7''''}H_2$), 7.39-7.53 (5H, m, $C^{2''''}H/C^{3''''}H/C^{4''''}H/C^{5''''}H/C^{6''''}H$); ^{13}C NMR (151 MHz, D_2O): 48.8 (ring *C*H_2), 51.8 (ring *C*H_2), 53.8 (arm *C*H_2), 56.5 (arm *C*H_2), 68.0 ($C^{7''''}$), 129.4 ($C^{2''''}/C^{3''''}/C^{4''''}/C^{5''''}$), 136.1 ($C^{6''''}$), 170.6 ($C^{1'}/C^{1''}/C^{1'''}$), 172.4 ($C^{2'''}$), 174.4 ($C^{1'}/C^{1''}/C^{1'''}$); HRMS *m/z* ($ESI^+$) [Found: 517.2272, $C_{23}H_{34}N_4O_8$ requires $[M+Na]^+$ 517.2269]; LRMS *m/z* (ESI^+) 495 ($[M+H]^+$, 100%), 517 ($[M+Na]^+$, 91%); Analytical HPLC (method 1A) R_t 8.6 min, 92.8%.

Europium benzyl complex (EuBn), 22a

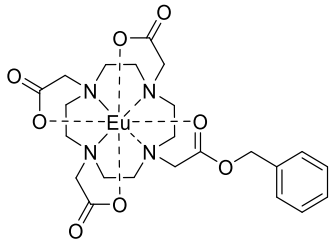

The reaction was carried out following the general lanthanide complexation procedure, using **52** (81.9 mg, 166 µmol, 1.0 eq.) and europium triflate (111 mg, 185 µmol, 1.12 eq.) in MES buffer (2.54 mL, 1 M, pH 6). The reaction was stirred at rt for 1 h, purified by semi-preparative HPLC method 3 and lyophilised for 2 days to yield compound **22a** as a colourless solid (43.2 mg, 41%): ^{1}H NMR (400 MHz, D_2O)*: −19.5, −17.2, −16.2, −15.8, −14.7, −14.2, −13.1, −10.8, −10.1, −9.6, −9.3, −9.1, −8.7, −8.1, −6.8, −6.4, −5.8, −4.1, −0.9, −0.5, 0.4, 3.1, 6.0, 6.2, 6.5, 7.4, 8.0, 8.5, 10.5, 25.5, 25.8, 26.5, 33.0, 34.0; HRMS *m/z* (ESI$^+$) [Found: 645.1420, $C_{23}H_{31}N_4O_8Eu$ requires $[M+H]^+$ 645.1427]; LRMS *m/z* (ESI$^+$) 645 ($[M+H]^+$, 97%), 667 ($[M+Na]^+$, 30%); Analytical HPLC (method 1A) R_t 8.9 min, 99.0%.

*^{1}H NMR contains 2% EuDOTA, therefore total purity ~97%, all peaks reported including EuDOTA.

Terbium benzyl complex (TbBn), 22b

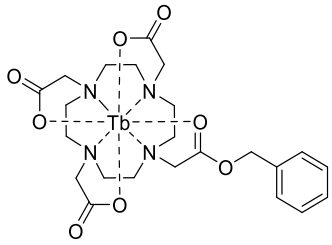

The reaction was carried out following the general lanthanide complexation procedure, using **52** (53.4 mg, 108 µmol, 1.0 eq.) and terbium triflate (66.0 mg, 109 µmol, 1.01.0 eq.) in MES buffer (1.65 mL, 1 M, pH 6). The reaction was stirred at rt for 1 h, purified by semi-preparative HPLC method 3 and lyophilised for 2 days to yield compound **22b** as a colourless solid (27.1 mg, 39%): ^{1}H NMR (400 MHz, D_2O)*: −419.3, −401.4, −344.0, −333.7, −316.8, −182.9, −150.7, −119.6, −99.4, −79.4, −69.0, −67.8, −39.0, −38.7, −37.9, −31.5, −25.5, −20.6, −11.4, −4.3, 12.0, 24.1, 83.8, 147.2, 156.1, 220.9, 233.2, 288.7; HRMS *m/z* (ESI$^+$) [Found: 651.1476, $C_{23}H_{31}N_4O_8Tb$ requires $[M+H]^+$ 651.1468]; LRMS *m/z* (ESI$^+$) 651 ($[M+H]^+$, 100%), 673 ($[M+Na]^+$, 71%); Analytical HPLC (method 1A) R_t 8.8 min, >99%.

*^{1}H NMR contains 1% TbDOTA, therefore total purity ~98%, all peaks reported including TbDOTA.

Gadolinium benzyl complex (GdBn), 22c

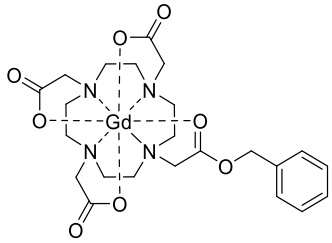

The reaction was carried out following the general lanthanide complexation procedure, using **52** (103 mg, 207 µmol, 1.0 eq.) and gadolinium triflate (138 mg, 228 µmol, 1.1 eq.) in MES buffer (3.20 mL, 1 M, pH 6). The reaction was stirred at rt for 1 h, purified by semi-preparative HPLC method 3 and lyophilised for 2 days to yield compound **22c** as a colourless solid (48.0 mg, 36%): HRMS *m/z* (ESI^+) [Found: 650.1453, $C_{23}H_{31}N_4O_8Gd$ requires $[M+H]^+$ 650.1456]; LRMS *m/z* (ESI^+) 650 ($[M+H]^+$, 14%), 672 ($[M+Na]^+$, 12%), 1299 ($[2M+Na]^+$, 39%), 1321 ($[2M+Na]^+$, 48%); LCMS (method 2) R_t 3.1 min, 97.6%; Analytical HPLC (method 1A) R_t 8.8 min, 98.7%.

6.4.3 Compounds from chapter IV

General synthesis methods for chapter IV

TBDMS protection: The appropriate phenol (1.0 eq.) and imidazole (4.0 eq.) were dissolved in DMF (c_{phenol} = 700 mM), TBDMSCl (2.0 eq.) was added and the resulting solution was stirred at rt for 18–96 h. The reaction mixture was diluted with Et_2O, washed with diluted brine (1:1 brine : H_2O) and re-extracted with Et_2O. The combined organic layers were washed with LiCl solution (0.5 M), dried over $MgSO_4$, filtered and concentrated *in vacuo*. The resulting material was adsorbed onto Celite® and purified by silica column chromatography, eluting with Et_2O and PE (gradient, 0–5% Et_2O) for **60** and **103**, or eluting with EtOAc and PE (gradient, 0–10% EtOAc for **113**, 0–20% EtOAc for **68, 81** and **84**).

Azobenzene formation: The appropriate aniline (1.0 eq.) was dissolved in acetone and H_2O (ratio 3:1, $c_{aniline}$ = 40 mM) and HCl (12 M, 1.0 eq.) was added dropwise. The resulting solution was cooled to 0 °C and a solution of $NaNO_2$ (1.0 eq.) in H_2O (c_{NaNO2} = 1 M) was

added dropwise and the resulting solution was stirred at 0 °C for 30 min. The resulting solution was added dropwise at 0 °C to a solution of 2,6-dimethylphenol (1.2 eq.) and NaOH (2.8 eq.) in H_2O (c_{phenol} = 200 mM) and the resulting solution was allowed to warm to rt, stirring, for 18 h. The reaction mixture was neutralised using AcOH then diluted with H_2O, extracted with EtOAc and the combined organic layers were washed with brine, dried, filtered and concentrated *in vacuo*. The resulting material was adsorbed onto Celite® and purified by silica column chromatography, eluting with EtOAc and PE (gradient 0–50% EtOAc for **89**, 0–20% EtOAc for **80**, 0–10% EtOAc for **111**, isocratic 5% EtOAc for **112**).

Bromination procedure: To a solution of the protected phenol (1.0 eq.) in CCl_4 ($c_{S.M.}$ = 50–100 mM) under argon, NBS (2.1 eq.) and benzoyl peroxide (0.05 eq.) were added. The resulting solution was heated to 90–92 °C for 3.0–3.5 h, cooled to rt, filtered and filtrate was concentrated *in vacuo*. The crude material was stored at −20 °C. The resulting material was dissolved in pentane (**104**) or adsorbed onto Celite® (**61, 71** & **72**) and purified by silica column chromatography, eluting with EtOAc and PE (0–10% EtOAc for **71** & **72**), Et_2O and PE (0–5% Et_2O for **61**) or pentane (isocratic, carried our twice, for **104**). Procedure taken from Simms *et al*.[58, 67]

Alkylation of 4-nitrophenol: 4-nitrophenol (1.0 eq.) and K_2CO_3 (2.0 eq.) were dissolved in dry MeCN (c_{phenol} = 75 mM) under argon and foil and the appropriate iodoalkane (2.0 eq.) was added. The resulting solution was heated to 90 °C with vigorous stirring for 18–24 hrs, then concentrated *in vacuo*, dissolved in CH_2Cl_2, filtered and concentrated *in vacuo*. The resulting material was dissolved in PE (**107**) or adsorbed onto Celite® (**108**) and purified by silica column chromatography, eluting with EtOAc and PE (gradient, 0–10% EtOAc).

Formation of alkylated 4-aminophenol: The appropriate alkylated 4-nitrophenol (1.0 eq.) was dissolved in EtOH (c_{SM} = 54 mM) and HCl (3 M, 23.2 eq.). Tin (5.4 eq.) was added and the resulting suspension was heated to 80 °C for 2 h. The cooled reaction mixture was diluted with H_2O, solid $NaHCO_3$ was added to adjust to pH 8 and the aqueous layer was extracted with EtOAc, dried over $MgSO_4$, filtered and concentrated *in vacuo* to give the

crude aniline, which was used directly in the next step without further purification or characterisation.

***Tert*-butyl(2,6-dimethyl-4-nitrophenoxy)dimethylsilane, 60**

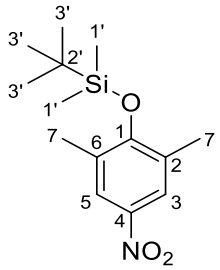

The reaction was carried out according to the general TBDMS protection method, using 2,6-dimethyl-4-nitrophenol (2.03 g, 12.1 mmol), imidazole (3.30 g, 48.5 mmol) and TBDMSCl (3.70 g, 24.6 mmol), yielding **60** as an off-white solid (3.08 g, 90%): R_f 0.68 (PE : Et_2O 95:5); ν_{max} (solid) cm^{-1}: 1580 (C=C, m), 1510 (N-O, m), 1251 (Si-CH_3, s); ^{1}H NMR (400 MHz, $CDCl_3$): 0.24 (6H, s, 2 × $C^{1'}H_3$), 1.03 (9H, s, 3 × $C^{3'}H_3$), 2.27 (6H, t, 2 × $C^{7'}H_3$), 7.90 (2H, s, C^3H/C^5H); ^{13}C NMR (101 MHz, $CDCl_3$): -2.7 ($C^{1'}$), 18.1 (C^7), 19.0 ($C^{2'}$), 26.1 ($C^{3'}$), 124.5 (C^3/C^5), 129.8 (C^2/C^4), 141.6 (C^4), 158.4 (C^1); HRMS *m/z* (ESI^+) [Found: 282.1517, $C_{14}H_{23}NO_3Si$ requires $[M+H]^+$ 282.1520]; LRMS *m/z* (ESI^+) 585 ($[2M+Na]^+$, 100%). These data are in good agreement with the available literature values.[58]

(2,6-Bis(bromomethyl)-4-nitrophenoxy)(tert-butyl)dimethylsilane, 61

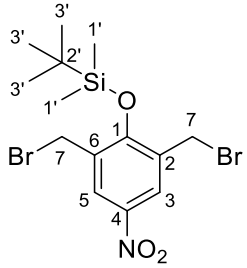

The reaction was carried out according to the general bromination procedure, using **60** (1.51 g, 5.37 mmol), NBS (2.04 g, 11.5 mmol) and benzoyl peroxide (90.7 mg, 281 µmol), yielding **61** as an off-white solid (783 mg, 33%): R_f 0.30 (pentane : Et_2O 95:5); ν_{max} (solid) cm^{-1}: 1593 (C=C, m), 1522 (N-O, m), 1266 (Si-CH_3, m); ^{1}H NMR (400 MHz, $CDCl_3$): 0.35 (6H, s, 2 × $C^{1'}H_3$), 1.10 (9H, s, 3 × $C^{3'}H_3$), 4.50 (4H, s, 2 × C^7H_2), 8.28 (2H, s, C^3H/C^7H);

^{13}C NMR (151 MHz, $CDCl_3$): -3.1 ($C^{1'}$), 19.1 ($C^{2'}$), 26.1 ($C^{3'}$), 27.3 (C^7), 127.5 (C^3/C^5), 130.8 (C^2/C^6), 142.2 (C^4), 156.4 (C^1); LRMS *m/z* (ESI^+) 438 ($[M+H]^+$, 8%). These data are in good agreement with the available literature values.[58]

Nitro triester, 62

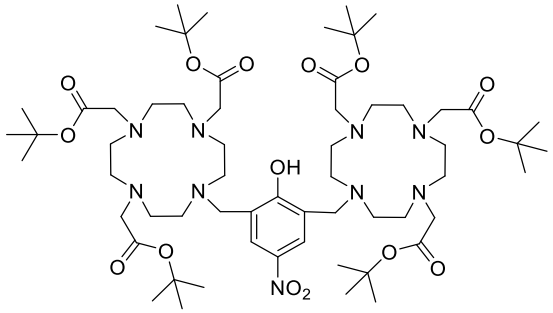

To a solution of DO3A triester **23** (500 mg, 0.839 mmol, 1.8 eq.) in MeCN (9.0 mL), Na_2CO_3 (152 mg, 1.43 mmol, 3.0 eq.) was added and **61** (209 mg, 0.476 mmol, 1.0 eq.) in MeCN (3.0 mL) was added. The resulting solution was heated to 50 °C for 43 h, cooled to rt, filtered and the filtrated was concentrated *in vacuo*. The crude material was stored at −20 °C. The resulting material was dissolved in CH_2Cl_2 and purified by silica column chromatography, eluting with MeOH and CH_2Cl_2 (gradient, 0–10% MeOH), to yield **62** as a bright yellow oil (316 mg, 56%): R_f 0.26 (CH_2Cl_2 : MeOH 95:5); ν_{max} (solid) cm^{-1}: 3435 (O-H, w br), 1725 (C=O, s), 1594 (N-O, w), 1369 (O-H, m), 1279 (C-O, s); ^{1}H NMR (400 MHz, $CDCl_3$): 1.17–1.57 (54H, m, 6 × C(C*H*$_3$)$_3$), 1.76–4.54 (48H, m, 16 × ring C*H*$_2$, 8 × arm C*H*$_2$), 7.69–8.29 (2H, m, 2 × ar *H*); HRMS *m/z* (ESI^+) [Found: 1192.7818, $C_{60}H_{105}N_9O_{15}$ requires $[M+H]^+$ 1192.7803]; LRMS *m/z* (ESI^+) 596 ($[M+2H]^{2+}$, 100%), 1192 ($[M+H]^+$, 95%), 1214 ($[M+Na]^+$, 68%). These data are in decent agreement with the available literature values.[58]

Aniline triester, 63

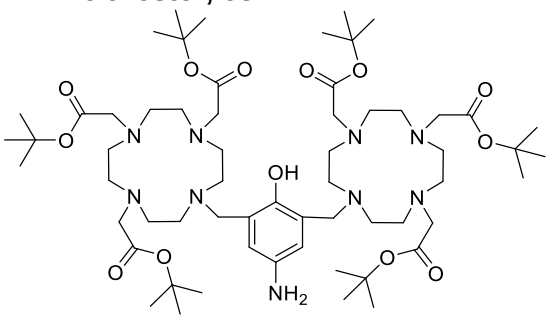

To a solution of **62** (47.4 mg, 39.7 µmol, 1.0 eq.) in EtOH (4.0 mL), HCl (2M, 0.5 mL, 1.00 mmol, 25.2 eq.) and tin (26.6 mg, 224 µmol, 5.6 eq.) were added and the resulting suspension was heated to 80 °C for 2 h. The resulting suspension was cooled to rt, diluted with H2O (10 mL) and solid $NaHCO_3$ was added to adjust to pH 8. The organic components were extracted with $CHCl_3$ (3 × 10 mL), washed with brine (20 mL), dried, filtered and concentrated *in vacuo* to yield **63** as a yellow-orange oil (44 mg, 95%) which was stored at −20 °C under argon and not purified further: ^{1}H NMR (400 MHz, $CDCl_3$): 1.44 (54H, s, 6 × C(C*H*$_3$)$_3$), 2.53–4.85 (48H, m, 16 × ring C*H*$_2$, 8 × arm C*H*$_2$), 6.50–7.11 (2H, m, 2 × ar *H*); HRMS *m/z* (ESI$^+$) [Found: 1162.8073, $C_{60}H_{107}N_9O_{13}$ requires $[M+H]^+$ 1162.8061]; LRMS *m/z* (ESI$^+$) 582 ($[M+2H]^{2+}$, 100%), 1162 ($[M+H]^+$, 90%). These data are in decent agreement with the available literature values.[58]

Leucine amide triester, 64

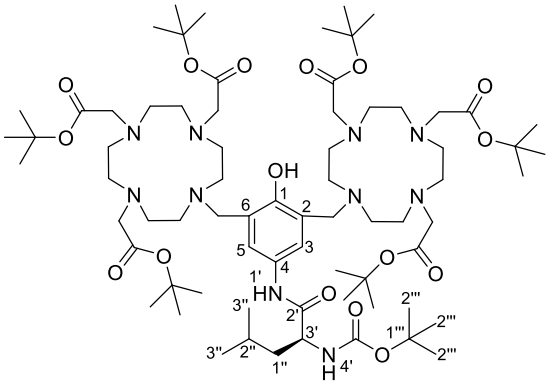

Method 1 - TEA (14.4 µL, 103 µmol, 3.0 eq.) and isobutyl chloroformate (5.90 µL, 1.50 µmol, 1.5 eq.) were added to a solution of Boc-*L*-leucine (9.7 mg, 41.9 µmol, 1.2 eq.) dissolved in dry CH_2Cl_2 (0.5 mL) under argon and the resulting solution was stirred for

5 min. **63** (40.0 mg, 34.4 µmol, 1.0 eq.) was added and the resulting solution was stirred under argon at rt for 48 h. The resulting solution was diluted with CH_2Cl_2 (5 mL), washed with H_2O (5 mL) and brine (2 × 5 mL), dried over $MgSO_4$, filtered and concentrated *in vacuo*. The resulting material was dissolved in a minimal volume of CH_2Cl_2 and purified by silica column chromatography, eluting with MeOH and CH_2Cl_2 (gradient, 0–20% MeOH), to yield **64** (impure) as a yellow solid (8.0 mg, 17%): R_f 0.17 (CH_2Cl_2 : MeOH 9:1); ^{1}H NMR (400 MHz, $CDCl_3$): 0.74–1.06 (9H, m, 3 × $C^{2'''}H_3$), 1.25 (6H, s, 2 × $C^{3''}H_3$), 1.36–1.64 (54H, m, 6 × $C(CH_3)_3$), 1.63–1.85 (3H, m, $C^{1''}H/C^{2''}H$), 1.85–5.02 (48 H, m, 16 × ring CH_2, 8 × arm CH_2), 7.44–8.50 (2H, m, C^3H/C^5H), 10.00–10.75 (1H, m, O*H*); ^{1}H NMR (600 MHz, MeCN-d_3): 0.90–0.97 (6H, m), 1.34–1.55 (63H, m), 1.55–1.73 (3H, m), 2.14–4.55 (49H, m), 5.75–6.58 (1H, m), 6.77–8.11 (2H, m), 8.69–10.69 (1H, m); HRMS *m/z* (ESI^+) [Found: 1375.9464, $C_{71}H_{126}N_{10}O_{16}$ requires $[M+H]^+$ 1375.9426]; LRMS *m/z* (ESI^+) 688 ($[M+2H]^{2+}$, 100%), 1375 ($[M+H]^+$, 100%).

Method 2 – HBTU (33.5 mg, 88.3 µmol, 3.0 eq.), HOBt (9.10 mg, 67.3 µmol, 2.3 eq.) and DIPEA (20 µL, 115 µmol, 3.8 eq.) were added to a solution of Boc-L-leucine (15.2 mg, 65.7 µmol, 2.2 eq.) in dry DMF (1.0 mL) under argon. **63** (34.8 mg, 29.9 µmol, 1.0 eq.) was added and the resulting solution was stirred under argon at rt for 26 h. The resulting solution was diluted with Et_2O (20 mL), washed with LiCl solution (0.5 M), re-extracted with Et_2O (20 mL), the combined organic layers dried over $MgSO_4$, filtered and concentrated *in vacuo*. The resulting material was dissolved in a minimal volume of CH_2Cl_2 and purified by silica column chromatography, eluting with MeOH and CH_2Cl_2 (gradient, 0–15% MeOH), to yield **64** (impure) as a yellow solid (8.2 mg, 20%): ^{1}H NMR (400 MHz, $CDCl_3$): 0.78–1.08 (9H, m, 3 × $C^{2'''}H_3$), 1.27 (6H, s, 2 × $C^{3''}H_3$), 1.36–1.57 (54H, m, 6 × $C(CH_3)_3$), 1.60–2.63 (13H, m, $C^{1''}H/C^{2''}H$, ring CH_2, arm CH_2), 2.83–5.23 (37 H, m, ring CH_2, arm CH_2), 7.31–9.20 (2H, m, $C^3H/C^5H/OH$); LRMS *m/z* (ESI^+) 688 ($[M+2H]^{2+}$, 74%), 1375 ($[M+H]^+$, 42%).

4-amino-2,6-dimethylphenol, 66

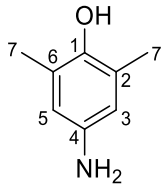

To a solution of 4-nitro-2,6-dimethylphenol (912 mg, 5.46 mmol, 1.0 eq.) in MeOH (15.0 mL) under argon, palladium on carbon (160 mg, 1.51 mmol, 0.28 eq.) was added. The argon atmosphere was replaced with hydrogen gas and the resulting suspension was stirred for 18 h. The resulting suspension was filtered over Celite®, washed with MeOH and concentrated *in vacuo* to yield **66** as a dark purple solid (747 mg, 99%) which was not purified further: R_f 0.00 (pentane); ^{1}H NMR (400 MHz, $CDCl_3$): 2.17 (6H, s, 2 × C^7H_3), 3.58 (2H, br s, NH_2), 6.37 (2H, s, C^3H/C^5H); HRMS *m/z* (ESI^+) [Found: 138.0916, $C_8H_{11}NO$ requires $[M+H]^+$ 138.0913]; LRMS *m/z* (ESI^+) 138 ($[M+H]^+$, 100%). These data are in agreement with the reported values.[59]

***Tert*-butyl (S)-(1-((4-hydroxy-3,5-dimethylphenyl)amino)-4-methyl-1-oxopentan-2-yl)carbamate, 67**

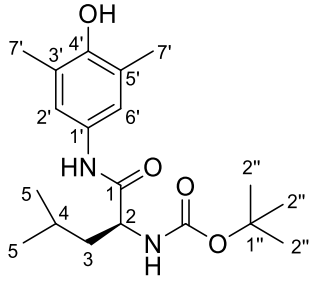

Method 1 – Boc-L-leucine (202 mg, 874 µmol, 1.2 eq.), DMAP (89.3 mg, 731 µmol, 1.0 eq.), DIPEA (640 µL, 3.67 mmol, 5.1 eq.), EDC (144 mg, 751 µmol, 1.1 eq.) and HOBt (10.2 mg, 75.5 µmol, 0.1.0 eq.) were added to **66** (98.2 mg, 716 µmol, 1.0 eq.) was dissolved in MeCN (7.5 mL) purged with argon and the resulting solution was stirred at rt for 44 h. The resulting solution was concentrated *in vacuo*, diluted with EtOAc (100 mL), washed with a saturated solution of $NaHCO_3$ (100 mL), re-extracted with EtOAc (100 mL) and the combined organic layers were dried over $MgSO_4$, filtered and concentrated *in vacuo*. The resulting material was adsorbed onto Celite® and purified by silica column

chromatography, eluting with EtOAc and PE (gradient, 0–50% EtOAc), then purified further by silica column chromatography, eluting with EtOAc and PE (gradient, 0–20% EtOAc), to yield **71** as an orange oil (47.2 mg, 19%): $[\alpha]_D^{20}$ = −40.4 (*c* 0.5, $CHCl_3$).

Method 2 – TEA (310 µL, 2.22 mmol, 3.0 eq.) and isobutyl chloroformate (130 µL, 1.14 mmol, 1.5 eq.) were added to a solution of Boc-L-leucine (209 mg, 905 µmol, 1.2 eq.) dissolved in dry CH_2Cl_2 (7.5 mL) under argon and the resulting solution was stirred at rt for 5 min. **66** (102 mg, 745 µmol, 1.0 eq.) was added and the resulting solution was stirred at rt for a further 44 h. The resulting solution was diluted with CH_2Cl_2, washed with H_2O (20 mL) and brine (2 × 20 mL) and the organic components were dried over $MgSO_4$, filtered and concentrated *in vacuo*. The resulting material was adsorbed onto Celite® and purified by silica column chromatography, eluting with EtOAc and PE (gradient, 0–20% EtOAc), to yield **67** as an orange oil (196 mg, 75%): $[\alpha]_D^{20}$ = −52.5 (*c* 0.5, $CHCl_3$)

Method 3 – DMAP (186 mg, 1.52 mmol, 2.0 eq.) and DCC (309 mg, 1.50 mmol, 2.0 eq.) were added to a solution of Boc-L-leucine (207 mg, 893 µmol, 1.2 eq.) dissolved in dry CH_2Cl_2 (4.5 mL) under argon and the resulted suspension was stirred at rt for 5 min. **66** (103 mg, 751 µmol, 1.0 eq.) was added and the resulting solution was stirred at rt for a further 44 h. The resulting solution was diluted with CH_2Cl_2, filtered and the filtrate was washed with a saturated solution of NH_4Cl (20 mL) then brine (20 mL) and the organic components were dried over $MgSO_4$, filtered and concentrated *in vacuo*. The resulting material was adsorbed onto Celite® and purified by silica column chromatography, eluting with EtOAc and PE (gradient, 0–20% EtOAc), to yield **67** as an orange oil (133 mg, 50%): $[\alpha]_D^{20}$ = −34.0 (*c* 0.5, $CHCl_3$).

R_f 0.63 (PE:EtOAc 1:1); ^{1}H NMR (600 MHz, $CDCl_3$): 0.96 (6H, t, *J* 5.9, 2 × C^5H_3), 1.45 (9H, s, 3 × $C^{2''}H_3$), 1.49–1.59 (1H, m, C^3H), 1.65–1.83 (2H, m, C^3H /C^4H), 2.20 (6H, s, 2 × $C^{7'}H_3$), 4.20 (1H, br s, C^2H), 4.94 (1H, br s, OCON*H*C^2), 7.11 (2H, s, $C^{2'}H$/$C^{6'}H$), 8.00 (1H, br s, C^1ON*H*); ^{1}H NMR (600 MHz, DMSO-d_6): 0.86–0.91 (6H, m, 2 × C^5H_3), 1.35–1.43 (10H, m, 3 × $C^{2''}H_3$ and C^3H), 1.44–1.53 (1H, m, C^3H), 1.56–1.67 (1H, m, C^4H), 2.12 (6H, s, 2 ×

$C^{7'}H_3$), 4.04–4.09 (1H, m, C^2H), 6.88 (1H, d, J = 8.1, C^2NH), 7.13 (2H, s, $C^{2'}H/C^{6'}H$), 7.96 (1H, s, C^1ONH), 9.50 (1H, s, OH); ^{13}C NMR (151 MHz, $CDCl_3$): 16.2 ($C^{7'}$), 23.1 (C^5), 25.0 (C^4), 28.5 ($C^{2''}$), 40.9 (C^3), 53.8 (C^2), 80.5 ($C^{1''}$), 120.9 ($C^{2'}/C^{6'}$), 123.7 ($C^{3'}/C^{5'}$), 130.2 ($C^{1'}$), 149.3 ($C^{4'}$), 156.3 (NH*C*OO), 171.0 (C^1); ^{13}C NMR (151 MHz, DMSO-d_6): 17.2 ($C^{7'}$), 22.1 (C^5), 23.4 (C^5), 24.8 (C^4), 28.7 ($C^{2''}$), 41.4 (C^3), 53.9 (C^2), 78.4 ($C^{1''}$), 120.2 ($C^{2'}/C^{6'}$), 124.8 ($C^{3'}/C^{5'}$), 131.2 ($C^{1'}$), 149.5 ($C^{4'}$), 155.8 (NH*C*OO), 171.3 (C^1); HRMS *m/z* (ESI$^+$) [Found: 351.2265, $C_{19}H_{30}N_2O_4$ requires $[M+H]^+$ 351.2278]; LRMS *m/z* (ESI$^+$) 351 ($[M+H]^+$, 46%), 701 ($[2M+H]^+$, 100%), 723 ($[2M+Na]^+$, 85%), 1051 ($[3M+H]^+$, 14%), 1073 ($[3M+Na]^+$, 35%).

4-((*Tert*-butyldimethylsilyl)oxy)-3,5-dimethylaniline, 69

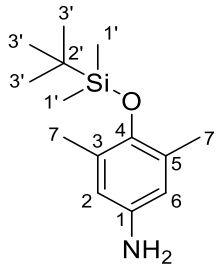

To a solution of **60** (1.00 g, 3.55 mmol, 1.0 eq.) in MeOH (150 mL) under argon, palladium on carbon (111 mg, 1.04 mmol, 0.3 eq.) was added. The argon atmosphere was replaced with hydrogen gas and the resulting suspension was stirred for 18 h. The resulting suspension was filtered over Celite®, washed with MeOH and concentrated *in vacuo* to yield **69** as a red oil (887 mg, 99%) which was not purified further: ^{1}H NMR (400 MHz, $CDCl_3$): 0.16 (6H, s, 2 × $C^{1'}H_3$), 1.02 (9H, s, 3 × $C^{3'}H_3$), 2.14 (6H, s, 2 × C^7H_3), 3.30 (2H, s, NH_2), 6.34 (2H, s, C^2H/C^6H); ^{13}C NMR (151 MHz, $CDCl_3$): −3.0 ($C^{1'}$), 18.0 (C^7), 18.9 ($C^{2'}$), 26.3 ($C^{3'}$), 115.9 (C^2/C^6), 129.3 (C^3/C^5), 140.0 (C^1), 144.9 (C^4); HRMS *m/z* (ESI$^+$) [Found: 503.3490, $C_{14}H_{25}NOSi$ requires $[2M+H]^+$ 503.3484]; LRMS *m/z* (ESI$^+$) 252 ($[M+H]^+$, 85%), 503 ($[2M+H]^+$, 100%).

***Tert*-butyl (S)-(1-((4-((*tert*-butyldimethylsilyl)oxy)-3,5-dimethylphenyl)amino)-4-methyl-1-oxopentan-2-yl)carbamate, 68**

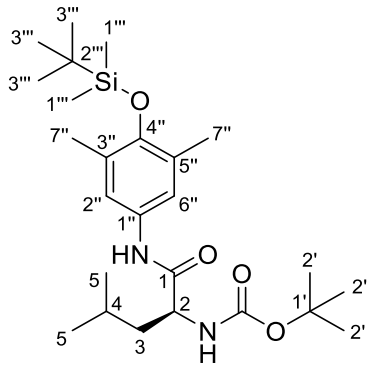

Method 1 - The reaction was carried out according to the general TBDMS protection method, for 40 h, using **67** (138 mg, 394 µmol), imidazole (109 mg, 1.60 mmol) and TBDMSCl (119 mg, 790 µmol), yielding **68** as an off-white solid (55.3 mg, 30%).

Method 2 - Isobutyl chloroformate (310 µL, 2.71 mmol, 1.5 eq.) and TEA (750 µL, 5.38 mmol, 3.0 eq.) were added to a solution of Boc-L-leucine (495 mg, 2.14 mmol, 1.2 eq.) in CH_2Cl_2 (25.0 mL) under argon and the resulting solution was stirred at rt for 5 min. **69** (447 mg, 1.78 mmol, 1.0 eq.) dissolved in CH_2Cl_2 (5.0 mL) was added and the resulting solution was stirred under argon at rt for a further 40 h. The resulting solution was diluted with CH_2Cl_2 (70 mL), washed with H_2O (100 mL) and brine (100 mL), dried over $MgSO_4$, filtered and concentrated *in vacuo*. The resulting material was adsorbed onto Celite® and purified by silica column chromatography, eluting with EtOAc and PE (gradient, 0–10% EtOAc), to yield **72** as a colourless foam (656 mg, 79%): R_f 0.88 (PE : EtOAc 1:1); $[\alpha]_D^{20}$ = −19.2 (*c* 0.5, $CHCl_3$); ^{1}H NMR (600 MHz, $CDCl_3$): 0.16 (6H, s, 2 × $C^{1'''}H_3$), 0.96 (6H, dd, J_1 = 7.8, J_2 = 6.4, 2 × C^5H_3), 1.02 (9H, s, 3 × $C^{3'''}H_3$), 1.45 (9H, s, 3 × $C^{2'}H_3$), 1.50–1.57 (1H, m, C^3H), 1.68–1.81 (2H, m, C^3H/C^4H), 2.17 (6H, s, 2 × $C^{7''}H_3$), 4.16–4.27 (1H, m, C^2H), 4.97 (1H, d, *J* = 8.3, OCON*H*C^2), 7.12 (2H, s, $C^{2''}H$/$C^{6''}H$), 8.03 (1H, s, C^1ON*H*); ^{13}C NMR (151 MHz, $CDCl_3$): −2.9 ($C^{1'''}$), 18.0 ($C^{7''}$), 18.9 ($C^{2'''}$), 22.3 (C^5), 23.1 (C^5), 25.0 (C^4), 26.2 ($C^{3'''}$), 28.5 ($C^{2'}$), 41.1 (C^3), 53.9 (C^2), 80.5 ($C^{1'}$), 120.6 ($C^{2''}$/$C^{6''}$), 129.1 ($C^{3''}$/$C^{5''}$), 131.1 ($C^{1''}$), 149.0 ($C^{4''}$), 156.2 (C^2NCOO), 170.6 (C^1); HRMS *m/z* (ESI^+) [Found: 465.3141,

$C_{25}H_{44}N_2O_4Si$ requires $[M+H]^+$ 465.3143]; LRMS *m/z* (ESI$^+$) 465 ($[M+H]^+$, 80%), 929 ($[2M+H]^+$, 95%), 1393 ($[3M+H]^+$, 56%).

***Tert*-butyl (S)-(1-((2,6-dibromo-4-((tert-butyldimethylsilyl)oxy)-3,5-dimethylphenyl)amino)-4-methyl-1-oxopentan-2-yl)carbamate, 71, and *tert*-butyl (S)-(1-((2-bromo-4-((tert-butyldimethylsilyl)oxy)-3,5-dimethylphenyl)amino)-4-methyl-1-oxopentan-2-yl)carbamate, 72**

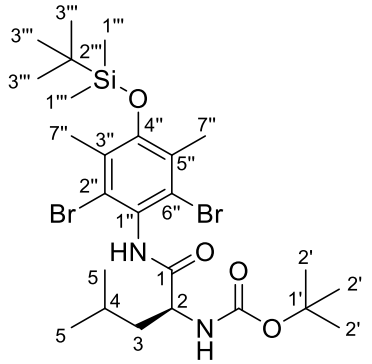

71

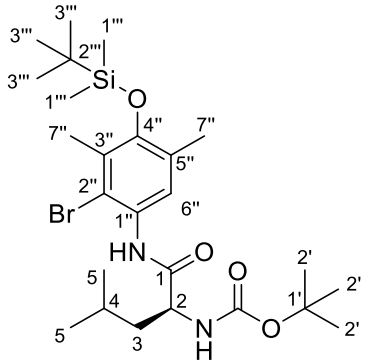

72

The reaction was carried out according to the general bromination procedure, using **68** (633 mg, 1.36 mmol), NBS (509 mg, 2.86 mmol) and benzoyl peroxide (23.4 mg, 72.5 µmol), yielding **71** as yellow oil (121 mg, 14%) and **72** as a yellow solid (320 mg, 43%).

71: R_f 0.24 (PE : EtOAc 9:1); $[\alpha]_D^{20}$ = −53.2 (*c* 0.5, $CHCl_3$); ^{1}H NMR (600 MHz, MeCN-d_3): 0.19 (6H, s, 2 × C$^{1'''}$*H*$_3$), 0.91–1.01 (6H, m, 2 × C^5*H*$_3$), 1.05 (9H, s, 3 × C$^{3'''}$*H*$_3$), 1.43 (9H, s, 3 × C$^{2'}$*H*$_3$), 1.49–1.64 (1H, m, C^3*H*), 1.66–1.85 (2H, m, C^3*H*/C^4*H*), 2.30 (6H, s, 2 × C$^{7''}$*H*$_3$), 4.23 (1H, td, J_1 = 9.5, J_2 = 4.8, C^2*H*), 5.61 (1H, d, *J* = 8.3, OCON*H*C^2), 8.22 (1H, s, C^{1}ON*H*); ^{13}C NMR (101 MHz, MeCN-d_3): −3.0 (C$^{1'''}$), 19.2 (C$^{2'''}$), 19.6 (C$^{7''}$), 21.9 (C^5), 23.3 (C^5), 25.6 (C^4), 26.3 (C$^{3'''}$), 28.7 (C$^{2'}$), 41.7 (C^3), 54.4 (C^2), 80.0 (C$^{1'}$), 125.4 (C$^{2''}$/C$^{6''}$), 130.0 (C$^{1''}$), 130.3 (C$^{3''}$/C$^{5''}$), 152.5 (C$^{4''}$), 156.7 (C^{2}N*C*OO), 172.5 (C^1); HRMS *m/z* (ESI$^+$) [Found: 621.1351, $C_{25}H_{42}Br_2N_2O_4Si$ requires $[M+H]^+$ 621.1353]; LRMS *m/z* (ESI$^+$) 621 ($[M+H]^+$, ^{79}Br^{79}Br, 9%), 623 ($[M+H]^+$, ^{79}Br^{81}Br, 23%), 625 ($[M+H]^+$, ^{81}Br^{81}Br, 14%), 1245 ($[2M+H]^+$, 100%), 1247 ($[2M+H]^+$, 99%).

72: R_f 0.33 (PE : EtOAc 9:1); $[\alpha]_D^{20}$ = −42.0 (*c* 0.5, $CHCl_3$); ^{1}H NMR (600 MHz, MeCN-d_3): 0.18 (6H, s, 2 × C$^{1'''}$*H*$_3$), 0.91–0.98 (6H, m, 2 × C^5*H*$_3$), 1.03 (9H, s, 3 × C$^{3'''}$*H*$_3$), 1.43 (9H, s,

3 × C$^{2'}$*H$_3$*), 1.54–1.62 (1H, m, C^3*H*), 1.63–1.78 (2H, m, C^3*H*/C^4*H*), 2.18 (3H, s, C$^{8''}$*H$_3$*), 2.30 (3H, s, C$^{7''}$*H$_3$*), 4.10–4.17 (1H, m, C^2*H*), 5.75 (1H, s, OCON*H*C^2), 7.68 (1H, s, C$^{6''}$*H*), 8.40 (1H, s, C^{1}ON*H*); ^{13}C NMR (101 MHz, MeCN-d$_3$): −2.9 (C$^{1'''}$), 18.2 (C$^{8''}$), 19.25 (C$^{7''}$), 19.31 (C$^{2'''}$), 21.8 (C^5), 25.7 (C^4), 26.4 (C$^{3'''}$), 28.6 (C$^{2'}$), 41.3 (C^3), 55.2 (C^2), 80.3 (C$^{1'}$), 117.2 (C$^{2''}$), 124.0 (C$^{6''}$), 129.3 (C$^{5''}$), 130.2 (C$^{3''}$), 130.6 (C$^{1''}$), 150.2 (C$^{4''}$), 156.8 (C^{2}N*C*OO), 172.2 (C^1); HRMS *m/z* (ESI$^+$) [Found: 543.2235, $C_{25}H_{43}BrN_2O_4Si$ requires [M+H]$^+$ 543.2248]; LRMS *m/z* (ESI$^+$) 543 ([M+H]$^+$, ^{79}Br, 28%), 545 ([M+H]$^+$, ^{81}Br, 44%), 1085 ([2M+H]$^+$, ^{79}Br^{79}Br, 68%), 1087 ([2M+H]$^+$, ^{79}Br^{81}Br, 100%), 1089 ([2M+H]$^+$, ^{81}Br^{81}Br, 77%).

***Tert*-butyl (S)-(1-((4-hydroxyphenyl)amino)-4-methyl-1-oxopentan-2-yl)carbamate, 73**

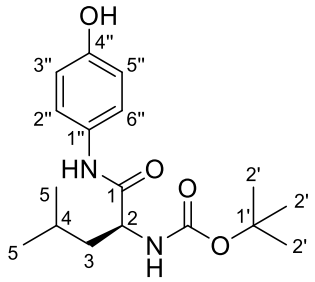

Isobutyl chloroformate (480 µL, 4.19 mmol, 1.5 eq.) and TEA (1.15 mL, 8.25 mmol, 3.0 eq.) were added to a solution of Boc-L-leucine (766 mg, 3.31 mmol, 1.2 eq.) in CH_2Cl_2 (30.0 mL) under argon and the resulting solution was stirred at rt for 5 min. 4-aminophenol (304 mg, 2.78 mmol, 1.0 eq.) was added and the resulting solution was stirred under argon at rt for a further 40 h. The resulting solution was diluted with CH_2Cl_2, washed with H_2O (30 mL) and brine (30 mL), dried over $MgSO_4$, filtered and concentrated *in vacuo*. The resulting material was adsorbed onto Celite® and purified by silica column chromatography, eluting with EtOAc and PE (gradient, 0–30% EtOAc), to yield **73** as a pink foam (431 mg, 48%): R_f 0.53 (PE : EtOAc 1:1); $[\alpha]_D^{20}$ = −57.2 (*c* 0.5, $CHCl_3$); ^{1}H NMR (600 MHz, $CDCl_3$): 0.95 (6H, dd, J_1 = 11.0, J_2 = 6.3, 2 × C^5*H$_3$*), 1.42 (9H, s, 3 × C$^{2'}$*H$_3$*), 1.54–1.63 (1H, m, C^3*H*), 1.67–1.78 (2H, m, C^3*H*/C^4*H*), 4.22–4.36 (1H, m, C^2*H*), 5.17 (1H, s, C^{2}N*H*), 6.50 (1H, s, O*H*), 6.67 (2H, d, *J* = 8.5, C$^{3''}$*H*/C$^{5''}$*H*), 7.22 (2H, d, *J* = 8.5, C$^{2''}$*H*/C$^{6''}$*H*), 8.51 (1H, s, C^{1}N*H*); ^{13}C NMR (151 MHz, $CDCl_3$): 22.0 (C^5), 23.1 (C^5), 25.0 (C^4), 28.5 (C$^{2'}$), 41.2 (C^3), 53.9 (C^2), 80.7 (C$^{1'}$), 115.8 (C$^{3''}$/C$^{5''}$), 122.4 (C$^{2''}$/C$^{6''}$), 130.3 (C$^{1''}$), 153.2 (C$^{6''}$), 156.5 (C^{2}N*C*OO), 171.4 (C^1);

HRMS *m/z* (ESI^+) [Found: 645.3878, $C_{17}H_{26}N_2O_4$ requires $[2M+H]^+$ 645.3858]; LRMS *m/z* (ESI^+) 323 ($[M+H]^+$, 5%), 645 ($[2M+H]^+$, 100%), 667 ($[2M+Na]^+$, 82%), 989 ($[3M+H]^+$, 56%).

(9*H*-Fluoren-9-yl)methyl (S)-(1-((4-hydroxyphenyl)amino)-4-methyl-1-oxopentan-2-yl)carbamate, 74

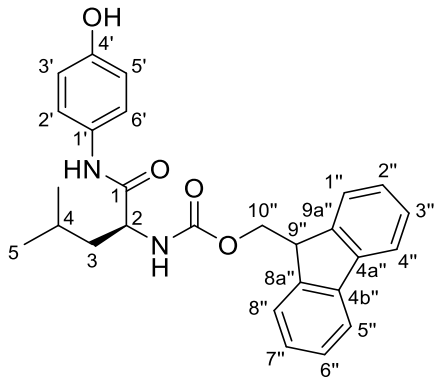

Method 1 - Isobutyl chloroformate (480 µL, 4.19 mmol, 1.5 eq.) and TEA (1.15 mL, 8.25 mmol, 3.0 eq.) were added to a solution of Fmoc-L-leucine (1.18 g, 3.33 mmol, 1.2 eq.) in CH_2Cl_2 (30.0 mL) under argon and the resulting solution was stirred at rt for 5 min. 4-aminophenol (302 mg, 2.77 mmol, 1.0 eq.) was added and the resulting solution was stirred under argon at rt for a further 40 h. The resulting solution was diluted with CH_2Cl_2, washed with H_2O (10 mL) and brine (10 mL), dried over $MgSO_4$, filtered and concentrated *in vacuo*. The resulting material was adsorbed onto Celite® and purified by silica column chromatography, eluting with EtOAc and PE (gradient, 0–50% EtOAc), to yield **81** as a dark brown solid (47.0 mg, impure, < 4%).

Method 2 – DCC (198 mg, 958 µmol, 1.1 eq.) and HOBt (132 mg, 977 µmol, 1.1 eq.) were added to a solution of Fmoc-L-leucine (305 mg, 863 µmol, 1.0 eq.) in DMF (2.0 mL) and stirred at rt for 5 min. TEA (130 µL, 933 µmol, 1.1 eq.) was added to a solution of 4-aminophenol (100 mg, 916 µmol, 1.1 eq.) in DMF (2.0 mL) and stirred at rt for 5 min, then the resulting solution was added to the Fmoc-L-leucine solution and stirred at rt for a further 17 h. The resulting solution was diluted with EtOAc (20 mL) and H_2O (20 mL), washed with H_2O (20 mL × 3), dried over $MgSO_4$, filtered and concentrated *in vacuo*. The resulting material was adsorbed onto Celite® and purified by silica column chromatography, eluting

with EtOAc and PE (gradient, 0–30% EtOAc), to yield **74** as a dark brown solid (123 mg, 32%).

Method 3 – CDI (155 mg, 956 µmol, 1.1 eq.) was added to a solution of Fmoc-L-leucine (302 mg, 855 µmol, 1.0 eq.) in dry THF (2.0 mL) under argon and the resulting solution was stirred at rt for 1.5 h. 4-aminophenol (100 mg, 916 µmol, 1.1 eq.) was added and the resulting solution was stirred at rt under argon for a further 19 h. The resulting solution was concentrated *in vacuo*, diluted with EtOAc (10 mL), washed with saturated $NaHCO_3$ solution (10 mL) and H_2O (10 mL), dried over $MgSO_4$, filtered and concentrated *in vacuo*. The resulting material was adsorbed onto Celite® and purified by silica column chromatography, eluting with EtOAc and PE (gradient, 0–30% EtOAc), to yield **74** as a dark brown solid (141 mg, 37%).

R_f 0.47 (PE:EtOAc 1:1); ^{1}H NMR (600 MHz, DMSO-d_6): 0.90 (6H, dd, J_1 = 16.1, J_2 = 6.6, 2 × C^5H_3), 1.40–1.53 (1H, m, C^3H), 1.54–1.69 (2H, m, C^3H/C^4H), 4.16 (1H, ddd, J_1 = 10.1, J_2 = 8.3, J_3 = 5.3, $C^{9''}H$), 4.19–4.32 (3H, m, C^2H/$C^{10''}H_2$), 6.65–6.71 (2H, m, $C^{3'}H$/$C^{5'}H$), 7.32 (2H, dt, J_1 = 7.7, J_2 = 3.8, $C^{2''}H$/$C^{7''}H$), 7.35–7.39 (2H, m, $C^{2'}H$/$C^{6'}H$), 7.41 (2H, td, J_1 = 7.4, J_2 = 3.0, $C^{3''}H$/$C^{6''}H$), 7.58 (1H, d, J = 8.2, C^2NH), 7.73 (2H, t, J = 7.3, $C^{1''}H$/$C^{8''}H$), 7.89 (2H, d, J = 7.6, $C^{4''}H$/$C^{5''}H$), 9.16 (1H, s, O*H*), 9.73 (1H, s, C^1ONH); ^{13}C NMR (151 MHz, DMSO-d_6): 21.5 (C^5), 23.0 (C^5), 24.3 (C^4), 40.8 (C^3), 46.7 ($C^{9''}$), 53.7 (C^2), 65.6 ($C^{10''}$), 115.0 ($C^{3'}$/$C^{5'}$), 120.1 ($C^{4''}$/$C^{5''}$), 121.0 ($C^{2'}$/$C^{6'}$), 125.3 ($C^{1''}$/$C^{8''}$), 127.0 ($C^{2''}$/$C^{7''}$), 127.6 ($C^{3''}$/$C^{6''}$), 130.6 ($C^{1'}$), 140.7 ($C^{4a''}$/$C^{4b''}$), 143.8 ($C^{8a''}$/$C^{9a''}$), 153.3 ($C^{4'}$), 156.0 (C^2NCOO), 170.7 (C^1); HRMS *m/z* (ESI^+) [Found: 445.2133, $C_{27}H_{28}N_2O_4$ requires $[M+H]^+$ 445.2122]; LRMS *m/z* (ESI^+) 445 ($[M+H]^+$, 88%), 467 ($[M+Na]^+$, 78%), 889 ($[2M+H]^+$, 80%), 911 ($[2M+Na]^+$, 100%), 1355 ($[3M+Na]^+$, 22%).

Attempts of further reaction of 73 and 74

Method 1 (Duff reaction) – Procedure adapted from Lindler.[61] The protected leucine compound (1.0 eq, **73** or **74**) was suspended in AcOH (c_{SM} ~300 mM), HMTA (2.0 eq.) was added and the resulting suspension heated to 120 °C for 3 h. The resulting suspension was

cooled to rt, HCl (1 M in H_2O, 2.0 eq.) was added and heated to 120 °C for a further 30 min. The resulting suspension was cooled to rt, diluted with H_2O, extracted with Et_2O and washed with H_2O and saturated aqueous $NaHCO_3$ solution, dried over $MgSO_4$, filtered and concentrated *in vacuo*. For the Boc-protected compound no change was observed by TLC. For the Fmoc-protected compound a change was observed by TLC, producing a spot on the baseline (in various TLC solvents) but no product was observed by LRMS analysis. Further reaction (reduction to form the desired hydroxymethyl compounds **75/76**) was not carried out.

Method 2 (formaldehyde) – Procedure adapted from Albedyhl *et al*.[60] The protected leucine compound (1.0 eq., **73** or **74**) was dissolved in MeOH (c_{SM} 50 mM) under argon and to this NaOH solution (25% in H_2O, 1.0 eq.) and formaldehyde (1.0 eq.) were added at 0 °C. The resulting solution was heated to 65 °C for 18 h, cooled to rt, adjusted to pH 5 using AcOH (33% in H_2O) and concentrated *in vacuo*. The resulting material was diluted in H_2O, extracted with EtOAc, dried over $MgSO_4$, filtered and concentrated *in vacuo*. No product was convincingly detected by LRMS, TLC or ^{1}H NMR analysis.

(9H-fluoren-9-yl)methyl (4-aminophenyl)carbamate, 79

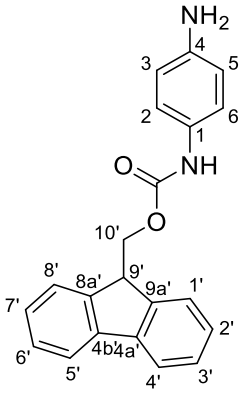

DIPEA (2.56 mL, 14.7 mmol, 3.0 eq.) then Fmoc-chloride (1.27 g, 4.90 mmol, 1.0 eq.) were added to a solution of phenylenediamine (528 mg, 4.88 mmol, 1.0 eq.) in CH_2Cl_2 (30 mL) at 0 °C under argon. The resulting solution was warmed to rt and stirred for 2 h, then filtered to collect the precipitate. The white solid was suspended in CH_2Cl_2 : hexane 1:1 (50 mL), filtered and dried to yield **79** as a white solid (1.07 g, 70%): ^{1}H NMR (600 MHz, DMSO-d_6):

4.23–4.32 (1H, m, $C^{9'}H$), 4.33–4.52 (2H, m, $C^{10'}H_2$), 4.78 (2H, s, NH_2), 6.48 (2H, d, J = 8.2, C^3H/C^5H), 7.04–7.14 (2H, m, C^2H/C^6H), 7.30–7.39 (2H, m, $C^{2'}H/C^{7'}H$), 7.39–7.46 (2H, m, $C^{3'}H/C^{6'}H$), 7.74 (2H, d, J = 7.4, $C^{1'}H/C^{8'}H$), 7.90 (2H, d, J = 7.6, $C^{4'}H/C^{5'}H$), 9.20 (1H, s, CONH); ^{13}C NMR (101 MHz, $CDCl_3$): 46.7 ($C^{9'}$), 65.4 ($C^{10'}$), 114.0 (C^3/C^5), 120.1 ($C^2/C^6/C^{4'}/C^{5'}$), 125.2 ($C^{1'}/C^{8'}$), 127.1 ($C^{2'}/C^{7'}$), 127.6 ($C^{3'}/C^{6'}$), 128.0 (C^1), 140.8 ($C^{4a'}/C^{4b'}$), 143.8 ($C^{8a'}/C^{9a'}$), 144.4 (C^4), 153.7 (O*C*ONH); HRMS *m/z* (ESI$^+$) [Found: 331.1435, $C_{21}H_{18}N_2O_2$ requires $[M+H]^+$ 331.1441]; LRMS *m/z* (ESI$^+$) 331 ($[M+H]^+$, 35%), 661 ($[2M+H]^+$, 100%), 991 ($[3M+H]^+$, 34%). These data are in decent agreement with the previously reported literature.[62, 63]

(9H-fluoren-9-yl)methyl (E)-(4-((4-hydroxy-3,5-dimethylphenyl)diazenyl)phenyl)carbamate, 80

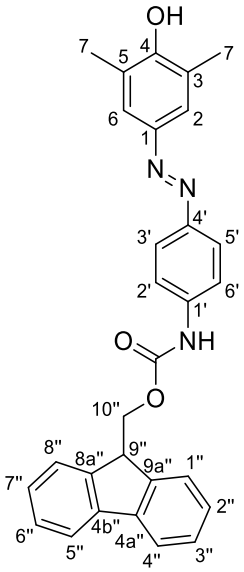

The reaction was carried out according to the general azobenzene formation method, using **79** (153 mg, 462 µmol), HCl (12 M, 40 µL, 480 µmol), $NaNO_2$ (34.5 mg, 500 µmol), 2,6-dimethylphenol (70.2 mg, 575 µmol) and NaOH (50.8 mg, 1.27 mmol, 2.8 eq.), yielding **80** as a red solid (75.6 mg, 35%): R_f 0.11 (PE : EtOAc 9:1); ^{1}H NMR (600 MHz, $CDCl_3$): 2.34 (6H, s, 2 × C^7H_3), 4.30 (1H, t, J = 6.4, $C^{9''}H$), 4.59 (2H, d, J = 6.4, $C^{10''}H_2$), 5.02 (1H, s, OH), 6.82 (1H, s, NH), 7.29–7.39 (2H, m, $C^{2''}H/C^{7''}H$), 7.39–7.46 (2H, m, $C^{3''}H/C^{6''}H$), 7.47–7.55 (2H, m, $C^{2'}H/C^{6'}H$), 7.61 (2H, s, C^2H/C^6H), 7.62–7.66 (2H, m, $C^{1''}H/C^{8''}H$), 7.80 (2H, d, J = 7.6, $C^{4''}H/C^{5''}H$), 7.87 (2H, J = 8.6, $C^{3'}H/C^{5'}H$); ^{13}C NMR (151 MHz, $CDCl_3$): 16.1 (C^7),

47.3 ($C^{9''}$), 67.2 ($C^{10''}$), 118.8 ($C^{2'}$/$C^{6'}$), 120.2 ($C^{4''}$/$C^{5''}$), 123.67 (C^{3}/C^{5}), 123.69 (C^{2}/C^{6}), 123.8 ($C^{3'}$/$C^{5'}$), 125.1 ($C^{1''}$/$C^{8''}$), 127.3 ($C^{2''}$/$C^{7''}$), 128.0 ($C^{3''}$/$C^{6''}$), 139.7 ($C^{1'}$), 141.6 ($C^{4a''}$/$C^{4b''}$), 143.8 ($C^{8a''}$/$C^{9a''}$), 146.5 (C^{1}), 149.0 ($C^{4'}$), 153.3 (O*C*ONH), 155.0 (C^{4}); HRMS *m/z* (ESI^+) [Found: 464.1969, $C_{29}H_{25}N_3O_3$ requires $[M+H]^+$ 464.1969]; LRMS *m/z* (ESI^+) 464 ($[M+H]^+$, 100%).

Note: for scale-up of this reaction, three reactions on 150 mg scale were carried out separately then combined for work-up and purification.

(9H-fluoren-9-yl)methyl (E)-(4-((4-((tert-butyldimethylsilyl)oxy)-3,5-dimethylphenyl)diazenyl)phenyl)carbamate, 81

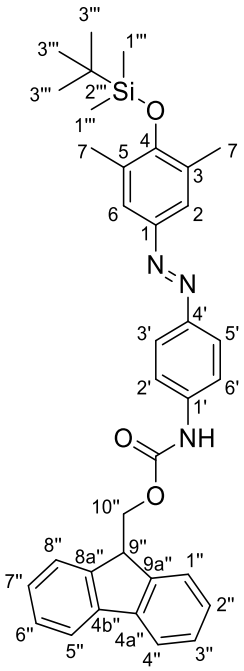

The reaction was carried out according to the general TBDMS protection method, for 72 h, using **80** (65.3 mg, 141 µmol), imidazole (40.1 mg, 589 µmol) and TBDMSCl (42.6 mg, 283 µmol), yielding **81** as an orange solid (24.0 mg, 30%): R_f 0.82 (PE : EtOAc 1:1); ^{1}H NMR (600 MHz, $CDCl_3$): 0.24 (6H, s, 2 × $C^{1'''}H_3$), 1.05 (9H, s, 3 × $C^{3'''}H_3$), 2.31 (6H, s, 2 × $C^{7}H_3$), 4.30 (1H, t, *J* = 6.5, $C^{9''}H$), 4.59 (2H, d, *J* = 6.5, $C^{10''}H_2$), 6.84 (1H, s, N*H*), 7.31–7.37 (2H, m, $C^{2''}H$/$C^{7''}H$), 7.39–7.45 (2H, m, $C^{3''}H$/$C^{6''}H$), 7.45–7.55 (2H, m, $C^{2'}H$/$C^{6'}H$), 7.59 (2H, s, $C^{2}H$/$C^{6}H$), 7.61–7.66 (2H, m, $C^{1''}H$/$C^{8''}H$), 7.76–7.82 (2H, m, $C^{4''}H$/$C^{5''}H$), 7.83–7.88 (2H, m, $C^{3'}H$/$C^{5'}H$); ^{13}C NMR (151 MHz, $CDCl_3$): −2.7 ($C^{1'''}$), 18.1 (C^{7}), 19.0 ($C^{2'''}$), 26.2 ($C^{3'''}$), 47.3 ($C^{9''}$), 67.2 ($C^{10''}$), 118.8 ($C^{2'}$/$C^{6'}$), 120.2 ($C^{4''}$/$C^{5''}$), 123.6 (C^{2}/C^{6}), 123.8 ($C^{3'}$/$C^{5'}$), 125.1

($C^{1''}$/$C^{8''}$), 127.3 ($C^{2''}$/$C^{7''}$), 128.0 ($C^{3''}$/$C^{6''}$), 129.5 (C^{3}/C^{5}), 139.8 ($C^{1'}$), 141.5 ($C^{4a''}$/$C^{4b''}$), 143.8 ($C^{8a''}$/$C^{9a''}$), 147.1 (C^{1}), 149.0 ($C^{4'}$), 153.2 (O*C*ONH), 155.2 (C^{4}); HRMS *m/z* (ESI^+) [Found: 578.2848, $C_{35}H_{39}N_3O_3Si$ requires $[M+H]^+$ 578.2833]; LRMS *m/z* (ESI^+) 578 ($[M+H]^+$, 100%).

***Tert*-butyl (*S,E*)-(1-((4-((4-hydroxy-3,5-dimethylphenyl)diazenyl)phenyl)amino)-4-methyl-1-oxopentan-2-yl)carbamate, 83, *via* 82**

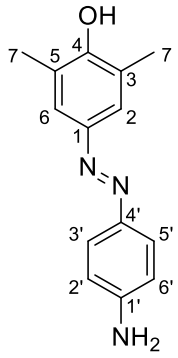

82

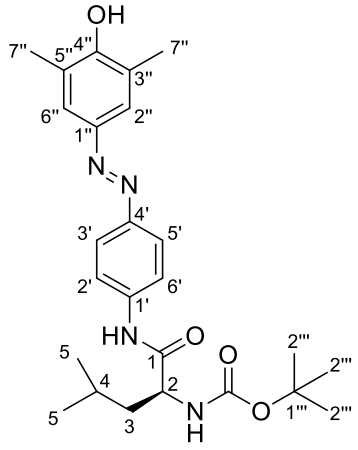

83

Step 1 - 81 (174 mg, 302 µmol, 1.0 eq.) was dissolved in DMF (6.0 mL), piperidine (150 µL, 1.52 mmol, 5.1 eq.) was added and the resulting solution was stirred at rt for 1 h under nitrogen. The resulting solution was diluted with H_2O, extracted with EtOAc, dried over $MgSO_4$, filtered and concentrated *in vacuo* to give **82** as the major product. LRMS *m/z* (ESI^+) 264 ($[M+H]^+$, 100%), 356 ($[M+TBDMS+H]^+$, 2%).

Step 2 - Boc-L-leucine (68.4 mg, 296 µmol, 1.0 eq.) was dissolved in dry THF (1.5 mL) under argon. CDI (48.1 mg, 297 µmol, 1.0 eq.) was added and the resulting solution was stirred at rt under argon for 1 h. The products from step 1 were dissolved in dry THF (1.5 mL) and added and the resulting solution was stirred at rt under argon for 17 h. Boc-L-leucine (68.7 mg, 297 µmol, 1.0 eq.) was dissolved in dry THF (1.0 mL) under argon, CDI (49.2 mg, 303 µmol, 1.0 eq.) was added, the resulting solution was stirred at rt for 1 h and the solution was added to the other solution and the combined solution was stirred at rt for a further 20 h. The resulting solution was concentrated *in vacuo*, diluted in EtOAc, washed with saturated $NaHCO_3$ solution and H_2O, dried over $MgSO_4$, filtered and concentrated *in vacuo*. The resulting material was adsorbed onto Celite® and purified by silica column

chromatography, eluting with EtOAc and PE (gradient, 0–20% EtOAc), to yield **83** as an orange oil (57.6 mg, 43%): ^{1}H NMR (600 MHz, $CDCl_3$): 0.98 (6H, dd, J_1 = 10.1, J_2 = 6.3, 2 × C^{5}*H*$_3$), 1.47 (9H, s, 3 × C$^{2'''}$*H*$_3$), 1.57–1.64 (1H, m, C^{3}*H*), 1.73–1.84 (2H, m, C^{3}*H*/C^{4}*H*), 2.32 (6H, s, 2 × C$^{7''}$*H*$_3$), 4.28 (1H, d, *J* = 11.0, C^{2}*H*), 5.01 (1H, d, *J* = 7.8, C^{2}N*H*), 7.62 (2H, s, C$^{2''}$*H*/C$^{6''}$*H*), 7.65 (2H, d, *J* = 8.6, C$^{2'}$*H*/C$^{6'}$*H*), 7.85 (2H, d, *J* = 8.6, C$^{3'}$*H*/C$^{6'}$*H*), 8.74 (1H, s, N*H*); ^{13}C NMR (151 MHz, $CDCl_3$): 16.0 (C$^{7''}$), 21.9 (C^{5}), 23.0 (C^{5}), 24.8 (C^{4}), 28.3 (C$^{2'''}$), 40.3 (C^{3}), 80.9 (C$^{1'''}$), 119.9 (C$^{2'}$/C$^{6'}$), 123.5 (C$^{3'}$/C$^{5'}$), 123.8 (C$^{2''}$/C$^{6''}$), 123.9 (C$^{3''}$/C$^{5''}$), 139.9 (C$^{1'}$), 145.9 (C$^{1''}$), 148.6 (C$^{4'}$), 155.6 (C$^{4''}$), 156.5 (C^{2}NCOO), 171.0 (C^{1}); HRMS *m/z* (ESI^{+}) [Found: 455.2654, $C_{25}H_{34}N_4O_4$ requires $[M+H]^+$ 455.2653]; LRMS *m/z* (ESI^{+}) 455 ($[M+H]^+$, 14%), 909 ($[2M+H]^+$, 100%), 931 ($[2M+Na]^+$, 16%), 1363 ($[3M+H]^+$, 99%), 1385 ($[3M+Na]^+$, 35%).

***Tert*-butyl *(S,E)*-(1-((4-((4-((*tert*-butyldimethylsilyl)oxy)-3,5-dimethylphenyl)diazenyl)phenyl)amino)-4-methyl-1-oxopentan-2-yl)carbamat*e*, 84**

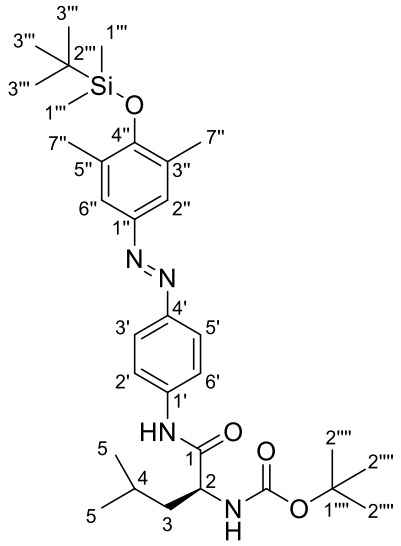

The reaction was carried out according to the general TBDMS protection method, using **83** (43.1 mg, 94.8 µmol), imidazole (29.4 mg, 432 µmol) and TBDMSCl (34.8 mg, 231 µmol) for 24 h then additional imidazole (29.4 mg, 432 µmol) and TBDMSCl (31.8 mg, 211 µmol) were added prior to stirring for a further 72 h. Purification yielded **84** as an orange oil (44.8 mg, impure, < 83%): R_f 0.86 (PE : EtOAc 1:1); ^{1}H NMR (600 MHz, $CDCl_3$): 0.23 (6H, s, 2 × C$^{1'''}$*H*$_3$), 0.98 (6H, t, *J* = 6.4, 2 × C^{5}*H*$_3$), 1.04 (9H, s, 3 × C$^{3'''}$*H*$_3$), 1.47 (9H, s, 3 × C$^{2''''}$*H*$_3$) 1.52–1.65 (1H, m, C^{3}*H*), 1.68–1.90 (2H, m, C^{3}*H*/C^{4}*H*), 2.30 (6H, s, 2 × C$^{7''}$*H*$_3$), 4.25 (1H, s,

C^2H), 4.92 (1H, d, J = 8.0, C^2NH), 7.61 (2H, s, $C^{2''}H/C^{6''}H$), 7.63–7.70 (2H, m, $C^{2'}H/C^{6'}H$), 7.84–7.92 (2H, m, $C^{3'}H/C^{5'}H$), 8.62 (1H, s, C^1NH); ^{13}C NMR (151 MHz, $CDCl_3$): −2.7 ($C^{1'''}$), 18.1 ($C^{7''}$), 19.0 ($C^{2'''}$), 22.1 (C^5), 23.1 (C^5), 25.0 (C^4), 25.8 ($C^{3'''}$), 28.5 ($C^{2''''}$), 40.3 (C^3), 54.0 (C^2), 81.0 ($C^{1''''}$), 120.0 ($C^{2'}/C^{6'}$), 123.6 ($C^{2''}/C^{6''}$), 123.7 ($C^{3'}/C^{5'}$), 129.5 ($C^{3''}/C^{5''}$), 140.0 ($C^{1'}$), 147.1 ($C^{1''}$), 149.4 ($C^{4'}$), 155.3 ($C^{4''}$), 156.5 (C^2NCOO), 170.9 (C^1); HRMS *m/z* (ESI^+) [Found: 569.3543, $C_{31}H_{48}N_4O_4Si$ requires $[M+H]^+$ 569.3519]; LRMS *m/z* (ESI^+) 569 ($[M+H]^+$, 100%), 591 ($[M+Na]^+$, 50%), 1137 ($[2M+H]^+$, 60%), 1159 ($[2M+Na]^+$, 20%).

Attempted bromination of 84 to give 85

84 (34.9 mg, 61.4 µmol, 1.0 eq.) was dissolved in CCl_4 (1.30 mL) and purged under argon. NBS (24.0 mg, 135 µmol, 2.2 eq.) and benzoyl peroxide (1.2 mg, 3.72 µmol, 0.06 eq.) were added and the resulting suspension was heated to 92 °C for 22 h. The resulting suspension was cooled to rt, filtered and the filtrate was concentrated *in vacuo*. The resulting material was adsorbed onto Celite® and purified by silica column chromatography, eluting with EtOAc and PE (gradient, 0–20% EtOAc). The crude ^{1}H NMR spectrum suggested partial conversion to the desired mono-brominated and di-brominated species. Isolated column fractions were impure but contained evidence of the mono-brominated species: HRMS *m/z* (ESI^+) [Found: 647.2628, $C_{31}H_{47}BrN_4O_4Si$ requires $[M+H]^+$ 647.2623]; LRMS *m/z* (ESI^+) 647 ($[M+H]^+$, ^{79}Br, 16%), 649 ($[M+H]^+$, ^{81}Br, 15%), 669 ($[M+Na]^+$, ^{79}Br, 7%), 671 ($[M+H]^+$, ^{81}Br, 10%).

(9*H*-fluoren-9-yl)methyl (*S*)-(1-((4-aminophenyl)amino)-4-methyl-1-oxopentan-2-yl)carbamate, 88

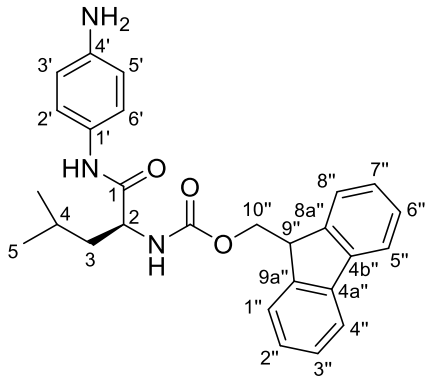

Procedure adapted from Bortolus *et al*.[64] Fmoc-L-leucine (344 mg, 973 µmol, 1.0 eq.) was added to a solution of DCC (214 mg, 1.04 mmol, 1.1 eq.) in dry THF (10.0 mL) and the resulting solution was stirred at rt for 10 min. Phenylenediamine (105 mg, 971 µmol, 1.0 eq.) was added and the resulting suspension was stirred at rt for 16 h. The resulting suspension was filtered and the filtrate was concentrated *in vacuo*. The resulting material was adsorbed onto Celite® and purified by silica column chromatography, eluting with EtOAc and PE (gradient, 0–50% EtOAc), to yield **88** as a pink-red solid (210 mg, 49%): R_f 0.31 (PE : EtOAc 1:1); $[\alpha]_D^{20}$ = −55.2 (*c* 0.5, $CHCl_3$); ^{1}H NMR (600 MHz, DMSO-d_6): 0.90 (6H, dd, J_1 = 17.1, J_2 = 6.6, 2 × C^5H_3), 1.45 (1H, ddd, J_1 = 13.7, J_2 = 8.7, J_3 = 5.2, C^3H), 1.56 (1H, ddd, J_1 = 13.4, J_2 = 10.0, J_3 = 5.2, C^3H), 1.64 (1H, ddt, J_1 = 13.1, J_2 = 8.5, J_3 = 6.5, C^4H), 4.14 (1H, ddd, J_1 = 10.0, J_2 = 8.4, J_3 = 5.2, C^2H), 4.19–4.24 (1H, m, $C^{9''}H$), 4.24–4.32 (2H, m, $C^{10''}H_2$), 4.84 (2H, s, NH_2), 6.47–6.52 (2H, m, $C^{3'}H/C^{5'}H$), 7.20–7.24 (2H, m, $C^{2'}H/C^{6'}H$), 7.28–7.34 (2H, m, $C^{2''}H/C^{7''}H$), 7.39–7.44 (2H, m, $C^{3''}H/C^{6''}H$), 7.54 (1H, d, *J* = 8.4, C^2NH), 7.74 (2H, t, *J* = 7.3, $C^{1''}H/C^{8''}H$), 7.87–7.91 (2H, m, $C^{4''}H/C^{5''}H$), 9.55 (1H, s, C^1NH); ^{13}C NMR (151 MHz, DMSO-d_6): 21.6 (C^5), 23.0 (C^5), 24.3 (C^4), 40.9 (C^3), 46.7 ($C^{9''}$), 53.6 (C^2), 65.5 ($C^{10''}$), 113.7 ($C^{3'}/C^{5'}$), 120.1 ($C^{4''}/C^{5''}$), 121.0 ($C^{2'}/C^{6'}$), 125.3 ($C^{1''}/C^{8''}$), 127.0 ($C^{2''}/C^{7''}$), 127.6 ($C^{3''}/C^{6''}$), 128.9 ($C^{1'}$), 140.7 ($C^{4a''}/C^{4b''}$), 143.8 ($C^{8a''}/C^{9a''}$), 144.8 ($C^{4'}$), 155.9 (C^2NCOO), 170.3 (C^1); HRMS *m/z* (ESI^+) [Found: 444.2294, $C_{27}H_{29}N_3O_3$ requires $[M+H]^+$ 444.2282]; LRMS *m/z* (ESI^+) 444 ($[M+H]^+$, 11%), 887 ($[2M+H]^+$, 91%), 909 ($[2M+Na]^+$, 8%), 1330 ($[3M+H]^+$, 100%).

(9*H*-fluoren-9-yl)methyl (*S*,*E*)-(1-((4-((4-hydroxy-3,5-dimethylphenyl)diazenyl)phenyl)amino)-4-methyl-1-oxopentan-2-yl)carbamate, 89

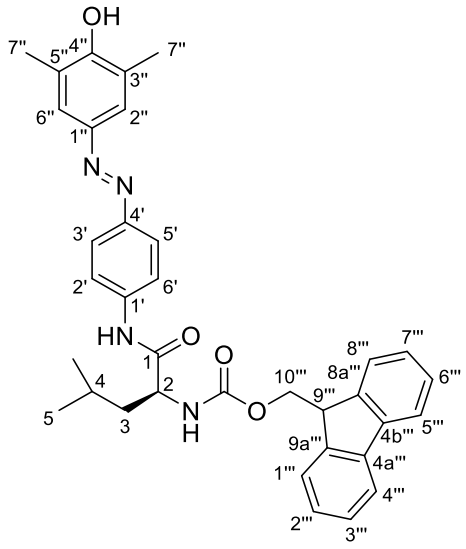

The reaction was carried out according to the general azobenzene formation method, using **88** (192 mg, 433 µmol), HCl (12 M, 40 µL, 480 µmol), $NaNO_2$ (34.4 mg, 499 µmol), 2,6-dimethylphenol (66.4 mg, 544 µmol) and NaOH (63.0 mg, 1.58 mmol, 3.6 eq.), yielding **89** as a red solid (147 mg, 59%): R_f 0.72 (PE : EtOAc 1:1); ^{1}H NMR (600 MHz, DMSO-d_6): 0.92 (6H, dd, J_1 = 12.1, J_2 = 6.6, 2 × C^5*H*$_3$), 1.49 (1H, ddd, J_1 = 13.7, J_2 = 8.8, J_3 = 5.0, C^3*H*), 1.58–1.66 (2H, m, C^3*H*/C^4*H*), 2.26 (6H, s, 2 × C$^{7''}$*H*$_3$), 4.20–4.26 (2H, m, C^2*H*/C$^{9''}$*H*), 4.26–4.33 (2H, m, C$^{10'''}$*H*$_2$), 7.30–7.35 (2H, m, C$^{2'''}$*H*/C$^{7'''}$*H*), 7.39–7.44 (2H, m, C$^{3'''}$*H*/C$^{6'''}$*H*), 7.52 (2H, s, C$^{2''}$*H*/C$^{6''}$*H*), 7.71 (1H, d, J = 8.1, C^{2}N*H*), 7.74 (2H, t, J = 7.5, C$^{1'''}$*H*/C$^{8'''}$*H*), 7.77–7.82 (4H, m, C$^{2'}$*H*/C$^{3'}$*H*/C$^{5'}$*H*/C$^{6'}$*H*), 7.87–7.92 (2H, m, C$^{4'''}$*H*/C$^{5'''}$*H*), 9.03 (1H, s, C^{1}N*H*), 10.32 (1H, s, O*H*); ^{13}C NMR (151 MHz, DMSO-d_6): 16.7 (C$^{7''}$), 21.4 (C^5), 23.0 (C^5), 24.3 (C^4), 46.7 (C$^{9''}$), 53.9 (C^2), 65.6 (C$^{10'''}$), 119.5 (C$^{2'}$/C$^{6'}$), 120.1 (C$^{4'''}$/C$^{5'''}$), 122.9 (C$^{3'}$/C$^{5'}$), 123.0 (C$^{2''}$/C$^{6''}$), 124.9 (C$^{3''}$/C$^{5''}$), 125.3 (C$^{1'''}$/C$^{8'''}$), 127.0 (C$^{2'''}$/C$^{7'''}$), 127.6 (C$^{3'''}$/C$^{6'''}$), 140.70 (C$^{4a'''}$/C$^{4b'''}$), 141.0 (C$^{1'}$), 143.9 (C$^{8a''}$/C$^{9a''}$), 144.9 (C$^{1''}$), 147.8 (C$^{4'}$), 156.1 (C^{2}NH*C*OO), 156.5 (C$^{4''}$), 172.0 (C^1); HRMS *m/z* (ESI$^+$) [Found: 577.2796, $C_{35}H_{36}N_4O_4$ requires [M+H]$^+$ 577.2809]; LRMS *m/z* (ESI$^+$) 577 ([M+H]$^+$, 73%), 599 ([M+Na]$^+$, 18%), 1153 ([2M+H]$^+$, 100%), 1175 ([2M+Na]$^+$, 28%).

2,6-dimethylphenyl acetate, 97

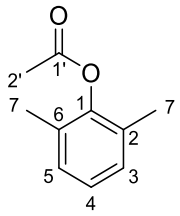

Procedure from Placidi *et al*.[65, 66] 2,6-dimethylphenol (1.04 g, 8.51 mmol, 1.0 eq.) was dissolved in acetic anhydride (4.0 mL, 42.3 mmol, 5.0 eq.) and the resulting solution was heated to 140 °C for 18 h. The resulting solution was cooled to rt, diluted with Et_2O (30 mL), washed with brine (3 × 30 mL), dried over $MgSO_4$, filtered and concentrated *in vacuo*. The resulting material was dissolved in PE and purified by silica column chromatography, eluting with EtOAc and PE (gradient, 0–10% EtOAc), to yield **97** as a colourless liquid (1.04 g, 74%): R_f 0.48 (PE : EtOAc 9:1); ^{1}H NMR (400 MHz, acetone-d_6): 2.14 (6H, s, 2 × C^7H_3), 2.32 (3H, s, $C^{2'}H_3$), 7.00–7.13 (3H, m, C^3H/C^4H/C^5H); ^{13}C NMR (101 MHz, acetone-d_6): 16.3 (C^7), 20.3 ($C^{2'}$), 126.4 (C^4), 129.2 (C^3/C^5), 131.0 (C^2/C^6), 149.4 (C^1), 168.9 ($C^{1'}$); HRMS *m/z* (EI^+) [Found: 164.0835, $C_{10}H_{12}O_2$ requires $[M]^+$ 164.0832]. These data are in good agreement with the reported values.[65]

2,6-bis(bromomethyl)phenyl acetate, 98

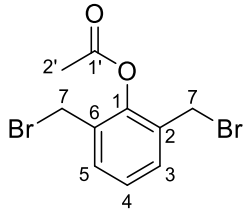

Procedure from Placidi *et al*.[65, 66] NBS (2.00 g, 11.2 mmol, 2.1 eq.) and benzoyl peroxide (150 mg, 464 µmol, 0.09 eq.) was added to a solution of **97** (872 mg, 5.31 mmol, 1.0 eq.) in CCl_4 (11.0 mL) under argon and the resulting solution was heated to 75 °C for 8 h. The resulting solution was cooled to rt, diluted with Et_2O, filtered and the filtrate was concentrated *in vacuo*. The resulting white/yellow solid was partially dissolved in hot MeOH, filtered whilst hot and the resulting filtrate was cooled to rt, producing a white precipitate, which was isolated by vacuum filtration and dried *in vacuo* to yield **98** (226 mg, 13%): R_f

0.43 (PE : EtOAc 9:1); ^{1}H NMR (400 MHz, CD_2Cl_2): 2.43 (3H, s, $C^{2'}H_3$), 4.40 (4H, s, 2 × $C^{7}H_2$), 7.26 (1H, t, *J* = 8.0, $C^{4}H$), 7.44 (2H, d, *J* = 8.0, $C^{3}H$/$C^{5}H$); ^{13}C NMR (101 MHz, CD_2Cl_2): 20.9 ($C^{2'}$), 28.0 (C^{7}), 127.3 (C^{4}), 131.7 (C^{2}/C^{6}), 131.9 (C^{3}/C^{5}), 148.0 (C^{1}), 168.9 ($C^{1'}$); HRMS *m/z* (EI^+) molecular ion not found, -Ac fragment observed, [Found: 277.8949, $C_8H_8Br_2O$ requires $[M\text{-}Ac+H]^+$ 277.8936]. These data are in good agreement with the reported values.[65]

Phenol triester, 99

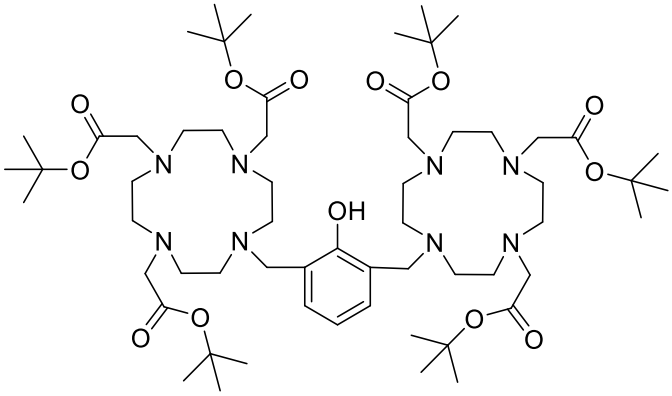

Procedure from Placidi *et al*.[65, 66] **23** (2.33 g, 3.91 mmol, 2.0 eq.) was dissolved in dry MeCN (60.0 mL) under argon and Cs_2CO_3 (3.22 g, 9.87 mmol, 5.0 eq.) was added. **98** (631 mg, 1.96 mmol, 1.0 eq.) was dissolved in dry MeCN (5.0 mL) and added and the resulting suspension was heated to reflux for 70 h. The resulting suspension was filtered to removed inorganic solids and the filtrate was concentrated *in vacuo*. The resulting material was diluted in CH_2Cl_2 (50 mL), washed with brine (3 × 50 mL), dried over $MgSO_4$, filtered and concentrated *in vacuo*. The resulting material was dissolved in CH_2Cl_2 and purified by neutral alumina column chromatography, eluting with MeOH and CH_2Cl_2 (gradient, 0–10% MeOH). The resulting material was partially precipitated from hexane and Et_2O and several fractions were obtained* to yield **99** as an orange oil (1.41 g, 63%*): R_f 0.69 (CH_2Cl_2 : MeOH 9:1, alumina); ^{1}H NMR (600 MHz, CD_2Cl_2): 1.39–1.50 (54H, m, 6 × C(CH_3)$_3$), 2.56–3.71 (48H, m, 16 × ring CH_2, 8 × arm CH_2), 6.61–8.29 (3H, m, 3 × ar *H*); ^{13}C NMR (151 MHz, CD_2Cl_2): 28.0–28.6 (m, CCH_3), 45.7–59.3 (m, ring CH_2, arm CH_2), 80.7–83.3 (CCH_3), 119.3 (ar *C*), 124.0 (ar *C*), 129.0 (ar *C*), 130.8 (ar *C*), 157.5 (ar *C*), 170.6–173.4 (*C*=O); HRMS

m/z (ESI$^+$) [Found: 1147.7999, $C_{60}H_{106}N_8O_{13}$ requires $[M+H]^+$ 1147.7952]; LRMS *m/z* (ESI$^+$) 574 ($[M+2H]^{2+}$, 55%), 1147 ($[M+H]^+$, 100%), 1169 ($[M+Na]^+$, 47%). These data are in good agreement with the reported values.[65]

*Overall yield from 5 isolated fractions of varying purity by ^{1}H NMR spectroscopy taken forward for further reaction.

Phenol triacid, 100

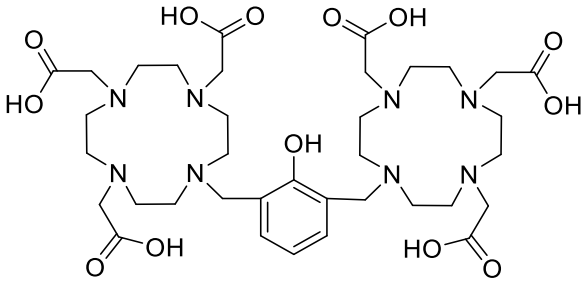

Procedure from Placidi *et al*.[65, 66] The reaction was carried out following the general TFA deprotection procedure, left to stir at rt for 72 h, using **99** (237 mg, 206 µmol, 1.0 eq.) in CH_2Cl_2 (2.4 mL) and TFA (2.4 mL, 31.4 mmol, 152 eq.), to give **100** as a brown solid (149 mg, 89%): ^{1}H NMR (400 MHz, D_2O): 2.78–4.31 (48H, m, 16 × ring C*H*$_2$, 8 × arm C*H*$_2$), 6.81–7.75 (3H, m, 3 × ar *H*); HRMS *m/z* (ESI$^+$) [Found: 811.4205, $C_{36}H_{58}N_8O_{13}$ requires $[M+H]^+$ 811.4196]; LRMS *m/z* (ESI$^+$) 406 ($[M+2H]^+$, 89%), 811 ($[M+H]^+$, 100%), 833 ($[M+Na]^+$, 54%). These data are in decent agreement with the reported values.[65]

TbTbOH, 93Tb

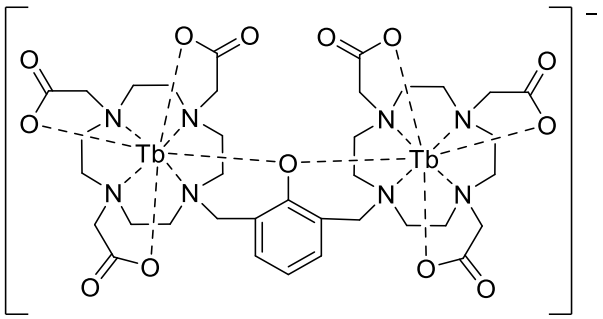

Method 1 (standard complexation and purification by preparative HPLC) – Terbium triflate (156 mg, 257 µmol, 2.5eq.) was added to a solution of **100** (84.6 mg, 104 µmol, 1.0 eq.) in MeOH (1.7 mL) and the resulting solution was heated to 50 °C for 40 h. The resulting

suspension was filtered, concentrated *in vacuo*, and stored at −20 °C prior to purification. The resulting residue was redissolved in MeOH and purified by semi-preparative HPLC method 4 and lyophilised for 2 days to yield **93Tb** as an impure mixture of bimetallic and monometallic terbium complexes (5 mg, < 4%).

Method 2 (microwave complexation and purification by preparative HPLC) – Terbium triflate (189 mg, 312 µmol, 2.4eq.) was added to a solution of **100** (104 mg, 128 µmol, 1.0 eq.) in MeOH (4.0 mL) and the resulting solution was heated to 70 °C for 4 h under microwave irradiation (using a Biotage® Initiator+ fourth generation microwave synthesiser, set for a very high absorption level, microwave irradiation 2.45 GHz). The resulting suspension was concentrated *in vacuo*, and stored at −20 °C prior to purification. The resulting residue was redissolved in MeOH and purified by semi-preparative HPLC method 5 and lyophilised for 2 days to yield **93Tb** (15.1 mg, impure, < 11%).

Note: semi-preparative HPLC method 5 was also used following standard complexation conditions and resulted in similarly poor yields of TbTbOH.

Method 3 (standard complexation and dialysis) - Terbium triflate (192 mg, 317 µmol, 2.5 eq.) was added to a solution of **100** (104 mg, 129 µmol, 1.0 eq.) in MeOH (2.5 mL) and the resulting solution was heated to 50 °C for 120 h. The resulting suspension was filtered and concentrated *in vacuo*. The crude residue was redissolved in a minimal amount of H_2O and purified by dialysis (1000 Da cut-off, procedure as described in the general experimental), then lyophilised for 2 days to give complex **93Tb** as an off-white solid (102 mg, 70%): ^{1}H NMR (500 MHz, D_2O):* 503.1, 411.3, 393.7, 352.7, 310.8, 289.5, 257.3, 218.4, 177.8, 160.5, 152.8, 136.5, 121.0, 103.4, 94.1, 88.9, 83.3, 74.7, 71.2, 67.6, 57.5, -64.9, -68.3, -83.0, -87.0, -94.7, -98.3, -109.3, -114.9, -124.1, -132.3, -140.0, -158.9, -164.5, -172.1, -176.7, -185.5, -191.0, -197.2, -207.8, -230.6, -242.8, -261.1, -280.1 , -306.7, -334.4, -369.3, -395.9, -415.4, -434.3, -446.3, -470.7, -480.5, -509.4, -534.8; HRMS *m/z* (ESI^-) [Found: 1121.2140, $C_{36}H_{51}N_8O_{13}Tb_2$ requires $[M]^-$ 1121.2088].

*Only peaks outside of the range -50 to 50 ppm reported.

LuLuOH, 93Lu

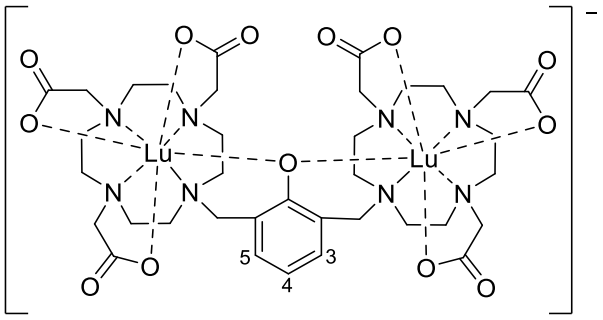

Lutetium triflate (113 mg, 182 µmol, 2.4 eq.) was added to a solution of **100** (60.8 mg, 75.0 µmol, 1.0 eq.) in MeOH (1.5 mL) and the resulting solution was heated to 50 °C for 70 h. The resulting suspension was filtered and concentrated *in vacuo*. The crude residue was redissolved in a minimal amount of H_2O and purified by dialysis (1000 Da cut-off, procedure as described in the general experimental), then lyophilised for 2 days to give complex **93Lu** as an off-white solid (47 mg, 54%): ^{1}H NMR (400 MHz, D_2O): 2.01–3.98 (48H, m, 16 × ring C*H*$_2$, 8 × arm C*H*$_2$), 6.59 (1H, t, *J* = 7.4, C^4*H*), 7.12 (1H, d, *J* = 7.4, C^3*H* or C^5*H*), 7.21 (1H, d, *J* = 7.4, C^3*H* or C^5*H*); HRMS *m/z* (ESI$^-$) [Found: 1153.2398, $C_{36}H_{51}N_8O_{13}Lu_2$ requires [M]$^-$ 1153.2397]; Analytical HPLC (method 4): R_t 5.8 min, 97%.

TbTbAzoNO$_2$, 94

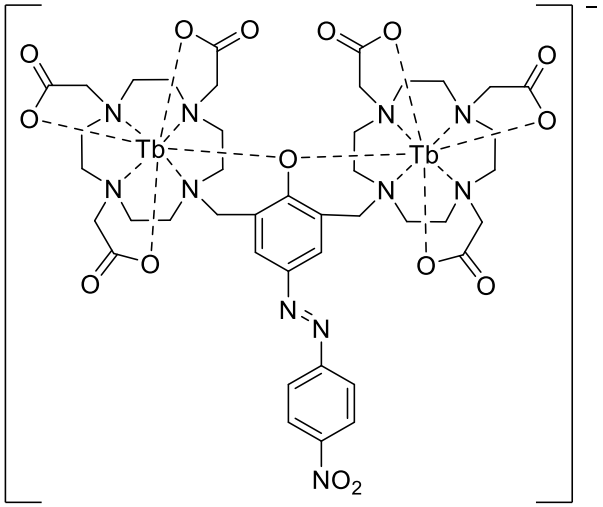

Procedure taken from Placidi.[66] 4-nitroaniline (3.2 mg, 23.2 µmol, 1.8 eq.) was added to a solution of $NaNO_2$ (3.4 mg, 49.3 µmol, 3.8 eq.) in HCl solution (1 M in H_2O, 1.5 mL, 115 eq.)

at 0 °C under nitrogen and stirred for 30 min to give a pale-yellow colour. **93Tb** (14.6 mg, 13.0 µmol, 1.0 eq.) was dissolved in NaOH solution (1 M in H_2O, 1.5 mL, 115 eq.) at 0 °C and this solution was added to the aniline solution at 0 °C, giving a dark red colour, stirred for 30 min, warmed to rt and stirred for a further 1.5 h. The resulting solution was adjusted to pH 7, concentrated *in vacuo* and stored at -20 °C prior to purification. The crude residue was redissolved in a minimal amount of H_2O and purified by dialysis (1000 Da cut-off, procedure as described in the general experimental), then lyophilised for 2 days to give a two fractions (one H_2O soluble and one less H_2O soluble) containing **94** (5 mg, < 30%)* which was determined to be impure by HRMS and HPLC analysis: HRMS *m/z* (ESI^-) [Found: 1270.2350, $C_{42}H_{53}N_{11}O_{15}Tb_2$ requires $[M]^-$ 1270.2313].

*Overall mass of 2 fractions, both impure.

Attempted formation of TbTbAzoLeu, 57

Procedure adapted from Placidi.[66] **88** (19.3 mg, 43.5 µmol, 1.6 eq.) was added to a solution of $NaNO_2$ (6.2 mg, 89.9 µmol, 3.3 eq.) in HCl solution (1 M in H_2O, 3.0 mL, 111 eq.) and acetone (3.0 mL) at 0 °C under nitrogen and stirred for 30 min to give a yellow suspension. **93Tb** (30.3 mg, 27.0 µmol, 1.0 eq.) was dissolved in NaOH solution (1 M in H_2O, 3.0 mL, 111 eq.) at 0 °C and this solution was added to the aniline solution at 0 °C, giving a dark red suspension, stirred for 30 min, warmed to rt and stirred for a further 1.5 h. No product formation was observed by LRMS (ESI or EI), HRMS, LCMS.

Aniline triacid, 101

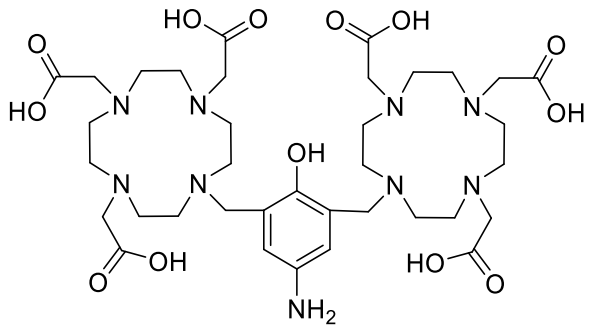

The reaction was carried out following the general TFA deprotection procedure, left to stir at rt for 18 h, using **63** (40.7 mg, 35.0 µmol, 1.0 eq.) in CH_2Cl_2 (900 µL) and TFA (900 µL,

11.8 mmol, 336 eq.) to give **101** as a brown solid (24.1 mg, 80%) which was stored at −20 °C: ^{1}H NMR (400 MHz, D_2O): 2.29–4.44 (48H, m, 16 × ring C*H*$_2$, 8 × arm C*H*$_2$), 7.58 (2H, br s, 2 × ar *H*); HRMS *m/z* (ESI$^+$) [Found: 826.4298, $C_{36}H_{59}N_9O_{13}$ requires $[M+H]^+$ 826.4305]; LRMS *m/z* (ESI$^+$) 826 ($[M+H]^+$, 100%), 848 ($[M+Na]^+$, 25%). These data are in decent agreement with the available literature values.[58]

TbTbNH$_2$, 54

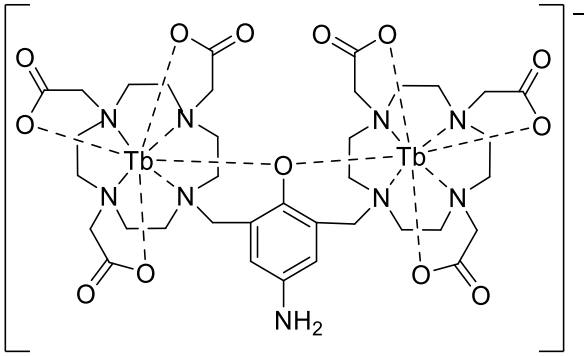

Terbium triflate (156 mg, 257 µmol, 2.6 eq.) was added to a solution of **101** (81.0 mg, 98.1 µmol, 1.0 eq.) in H_2O (2.1 mL) and the resulting solution was heated to 50 °C for 18 h. The resulting solution was cooled to rt then adjusted to pH 7 by addition of 1 M NaOH (3 eq. then 3 eq. then 1.0 eq.) and the resulting suspension was heated to 50 °C for a further 24 h. The resulting suspension was filtered, concentrated *in vacuo*, and stored at −20 °C prior to purification. The crude residue was redissolved in a minimal amount of H_2O and purified by dialysis (1000 Da cut-off, procedure as described in the general experimental), then lyophilised for 2 days to yield **54** as a purple solid (53 mg, 48%): ^{1}H NMR (600 MHz, D_2O):* 513.2, 368.0, 355.7, 310.4, 277.6, 196.8, 167.0, 149.3, 142.4, 97.3, 71.5, 68.6, 49.7, 45.9, -57.2, -68.6, -80.1, -94.7, -99.9, -107.7, -133.4, -140.7, -148.0, -158.4, -164.2, -176.7, -190.3, -202.3, -237.1, -309.4, -345.4, -392.3, -413.2, -427.6, -442.8, -479.3, -500.4, -529.4; HRMS *m/z* (ESI$^-$) [Found: 1136.2211, $C_{36}H_{53}N_9O_{13}Tb_2$ requires $[M]^-$ 1136.2197]; Analytical HPLC (method 4): R_t 3.3 min, 92%.

*Only peaks outside of the range -50 to 50 ppm reported.

(E)-2,6-dimethyl-4-(phenyldiazenyl)phenol, 102

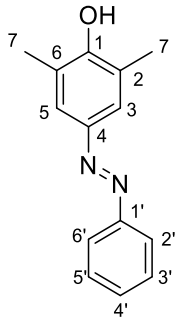

Procedure taken from Simms.[67] To a solution of aniline (1.80 mL, 19.8 mmol, 1.0 eq.) in HCl (1 M, 50 mL) at 0 °C, a solution of sodium nitrite (1.46 g, 21.2 mmol, 1.1 eq.) in H_2O (70 mL) was added dropwise under argon. The resulting solution was stirred at 0 °C for 10 min, then the solution was added dropwise under argon to a solution of 2,6-dimethylphenol (2.45 g, 20.1 mmol, 1.0 eq.) and NaOH (0.84 g, 21.0 mmol, 1.1 eq.) in H_2O (200 mL) and EtOH (70 mL). The resulting solution was stirred at rt for 1 h until a precipitate formed. The precipitate was isolated and dried under vacuum, then dissolved in EtOAc (40 mL), dried over $MgSO_4$ and concentrated *in vacuo* to yield **102** as a dark red solid (2.75 g, 61%): R_f 0.28 (PE : EtOAc 9:1); ν_{max} (solid) cm^{-1}: 3324 (O-H, br w), 1592 (C=C, m), 1313 (C-N, m), 1296 (C-N, s); ^{1}H NMR (400 MHz, DMSO-d_6): 2.27 (6H, s, 2 × C^7H_3), 7.45–7.61 (5H, m, $C^{2'}H$/$C^{3'}H$/$C^{4'}H$/$C^{5'}H$/$C^{6'}H$), 7.77–7.84 (2H, m, C^3H/C^5H); ^{13}C NMR (101 MHz, DMSO-d_6): 16.7 (C^7), 122.0 (C^3/C^5), 123.3 ($C^{2'}$/$C^{6'}$), 124.9 (C^2/C^6), 129.3 ($C^{3'}$/$C^{5'}$), 130.4 ($C^{4'}$), 144.9 (C^4), 152.2 ($C^{1'}$), 157.0 (C^1); HRMS *m/z* (ESI^+) [Found: 227.1181, $C_{14}H_{14}N_2O$ requires $[M+H]^+$ 227.1179]; LRMS *m/z* (ESI^+) 227 ($[M+H]^+$, 100%).

(E)-1-(4-((*Tert*-butyldimethylsilyl)oxy)-3,5-dimethylphenyl)-2-phenyldiazene, 103

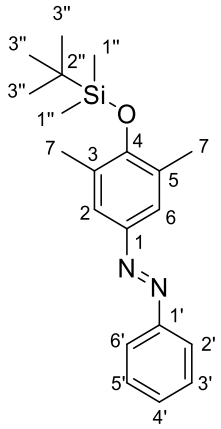

Procedure taken from Simms *et al*.[58, 67] The reaction was carried out according to the general TBDMS protection method, using **102** (2.03 g, 8.97 mmol), imidazole (2.47 g, 36.3 mmol) and TBDMSCl (2.73 g, 18.1 mmol), yielding **103** as an orange/red oil (2.60 g, 85%), which was stored at −20 °C under foil: R_f 0.67 (PE : Et_2O 95:5); ν_{max} (solid) cm^{-1}: 1586 (C=C, w), 1314 (C-N, m), 1289 (C-N, m), 1255 (Si-CH_3, m), 1121 (Si-O, m); ^{1}H NMR (400 MHz, $CDCl_3$): 0.24 (6H, s, 2 × $C^{1''}H_3$), 1.05 (9H, s, 3 × $C^{3''}H_3$), 2.31 (6H, s, 2 × C^7H_3), 7.43 (1H, tt, J_1 = 7.2, J_2 = 1.3, $C^{4'}H$), 7.50 (2H, tt, J_1 = 7.1, J_2 = 1.2, $C^{3'}H$/$C^{5'}H$), 7.61 (2H, s, C^2H/C^6H), 7.84–7.89 (2H, m, $C^{2'}H$/$C^{6'}H$); ^{13}C NMR (101 MHz, $CDCl_3$): -2.7 ($C^{3''}$), 18.1 (C^7), 19.0 ($C^{2''}$), 26.2 ($C^{3''}$), 122.7 ($C^{2'}$/$C^{6'}$), 123.8 (C^2/C^6), 129.2 ($C^{3'}$/$C^{5'}$), 129.5 ($C^{4'}$), 130.4 (C^3/C^5), 147.1 (C^1), 153.0 ($C^{1'}$), 155.4 (C^4); HRMS *m/z* (ESI$^+$) [Found: 341.2047, $C_{20}H_{28}N_2OSi$ requires $[M+H]^+$ 341.2044]; LRMS *m/z* (ESI$^+$) 341 ($[M+H]^+$, 100%), 703 ($[2M+Na]^+$, 56%). These data are in good agreement with the available literature values.[58]

(E)-1-(3,5-Bis(bromomethyl)-4-((tert-butyldimethylsilyl)oxy)phenyl)-2-phenyldiazene, 104

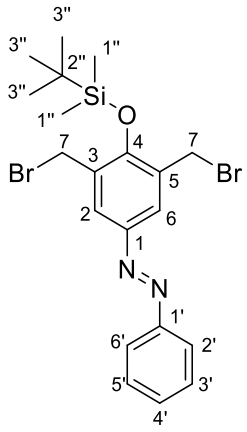

The reaction was carried out according to the general bromination procedure, using **103** (948 mg, 2.78 mmol), NBS (1.05 g, 5.90 mmol) and benzoyl peroxide (49.4 mg, 0.153 mmol), yielding **104** as an orange solid (309 mg, 22%), which was stored at −20 °C under foil: R_f 0.44 (PE : Et_2O 95:5); ^{1}H NMR (600 MHz, $CDCl_3$): 0.34 (6H, s, 2 × $C^{1''}H_3$), 1.11 (9H, s, 3 × $C^{3''}H_3$), 4.58 (4H, s, 2 × C^7H_2), 7.44–7.49 (1H, m, $C^{4'}H$), 7.49–7.55 (2H, m, $C^{3'}H$/$C^{5'}H$), 7.86–7.93 (2H, m, $C^{2'}H$/$C^{6'}H$), 7.99 (2H, s, C^2H/C^6H); ^{13}C NMR (101 MHz, $CDCl_3$): -3.1 ($C^{1''}$), 19.1 ($C^{2''}$), 26.2 ($C^{3''}$), 28.8 (C^7), 122.9 ($C^{2'}$/$C^{6'}$), 126.9 (C^2/C^6), 129.3 ($C^{3'}$/$C^{5'}$), 130.2 (C^3/C^5), 131.1 ($C^{4'}$), 147.4 (C^1), 152.7 ($C^{1'}$), 153.5 (C^4); HRMS *m/z* (ESI^+) [Found: 497.0261, $C_{20}H_{26}Br_2N_2OSi$ requires $[M+H]^+$ 497.0254]; LRMS *m/z* (ESI^+) 497 ($[M+H]^+$, $^{79}Br^{79}Br$, 47%), 499 ($[M+H]^+$, $^{79}Br^{81}Br$, 93%), 501 ($[M+H]^+$, $^{81}Br^{81}Br$, 52%). These data are in good agreement with the available literature values.[58]

Azobenzene triester, 105

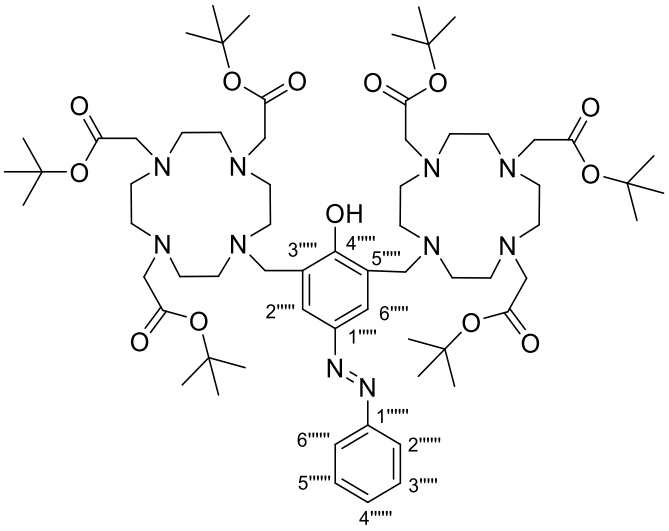

Procedure taken from Simms *et al*.[58, 67] **104** (291 mg, 0.584 mmol, 1.0 eq.) in MeCN (2.0 mL) was added to a suspension of **23** (631 mg, 1.06 mmol, 1.8 eq.) and Na_2CO_3 (241 mg, 2.28 mmol, 3.9 eq.) in MeCN (15.5 mL) and the resulting suspension was heated to 60 °C for 40 h. The resulting suspension was cooled to rt, filtered and the filtrate was concentrated *in vacuo*. The resulting material was dissolved in CH_2Cl_2:MeCN 8:2 and purified by silica column chromatography, eluting with CH_2Cl_2, MeCN, IPA and MeOH (gradient, CH_2Cl_2:MeCN:IPA:MeOH 8:2:0:0 → 6:4:0:0 → 6:3:1 → 6:2:2:0 → 6:2:1:1 → 6:2:0:2). The resulting material was concentrated *in vacuo*, redissolved in $CHCl_3$, filtered (Nylon syringe filter) and concentrated *in vacuo* to afford **105** as an orange-red solid (289 mg, 40%), which was stored at −20 °C under foil: R_f 0.20 and 0.30 (CH_2Cl_2:MeCN:IPA:MeOH 60:28:8:4); ^{1}H NMR (400 MHz, $CDCl_3$): 1.22–1.65 (54H, m, 6 × C(C*H*$_3$)$_3$), 2.06–4.10 (48H, m, 8 × arm C*H*$_2$, 16 × ring C*H*$_2$), 7.32–7.48 (3H, m, $C^{3'''''}H$/$C^{4'''''}H$/$C^{5'''''}H$), 7.72–7.89 (2H, m, $C^{2'''''}H$/$C^{6'''''}H$), 8.00–8.25 (2H, m, $C^{2'''''}H$/$C^{6'''''}H$), 9.09 (1H, br s, O*H*); ^{13}C NMR (151 MHz, $CDCl_3$): 27.9–28.5 (m, 6 × C(*C*H$_3$)$_3$), 47.3-58.4 (ring/arm *C*H$_2$), 82.2–82.9 (m, 6 × *C*(CH$_3$)$_3$), 122.2 ($C^{3'''}$/$C^{5'''}$), 122.7 ($C^{2'''''}$/$C^{6'''''}$), 126.2 ($C^{2''''}$/$C^{6''''''}$), 128.8 ($C^{3''''''}$/$C^{5''''''}$), 130.7 ($C^{4''''''}$), 147.5 ($C^{1''''}$), 152.7 ($C^{1''''''}$), 157.0 ($C^{4''''}$), 170.7 (*C*OO), 172.4 (*C*OO), 173.4 (*C*OO); HRMS *m/z* (ESI$^+$) [Found: 1251.8335, $C_{66}H_{111}N_{10}O_{13}$

requires $[M+H]^+$ 1251.8327]; LRMS *m/z* (ESI^+) 626 ($[M+2H]^+$, 100%), 1252 ($[M+H]^+$, 99%). These data are in decent agreement with the available literature values.[58]

Azobenzene triacid, 106

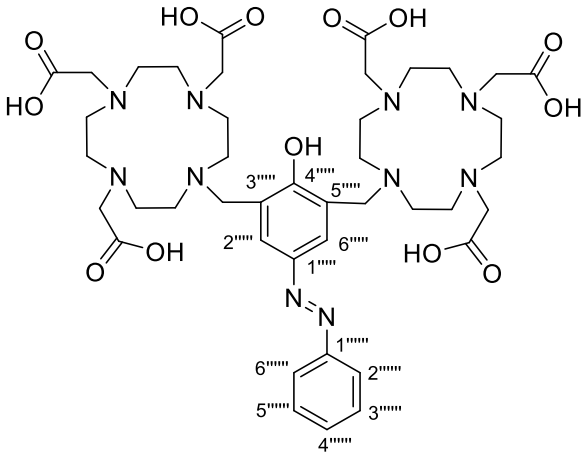

The reaction was carried out following the general TFA deprotection procedure, left to stir at rt for 18 h, using **105** (108 mg, 86.1 mmol, 1.0 eq.) in CH_2Cl_2 (1.9 mL) and TFA (1.9 mL, 24.8 mmol, 289 eq.), to give **106** as a red solid (74.2 mg, 94%): which was stored at −20 °C under foil: ^{1}H NMR (400 MHz, D_2O): 2.81–4.62 (48H, m, 8 × arm C*H*$_2$, 16 × ring C*H*$_2$), 7.58–7.68 (3H, m, $C^{3'''''}H/C^{4'''''}H/C^{5'''''}H$), 7.87–7.96 (2H, m, $C^{2'''''}H/C^{6'''''}H$), 8.05-8.19 (2H, s, $C^{2'''''}H/C^{6'''''}H$); HRMS *m/z* (ESI^+) [Found: 915.4585, $C_{42}H_{62}N_{10}O_{13}$ requires $[M+H]^+$ 915.4571]; LRMS *m/z* (ESI^+) 458 ($[M+2H]^{2+}$, 14%), 915 ($[M+H]^+$, 64%), 937 ($[M+Na]^+$, 100%). These data are in good agreement with the available literature values.[58]

TbTbAzo, 53

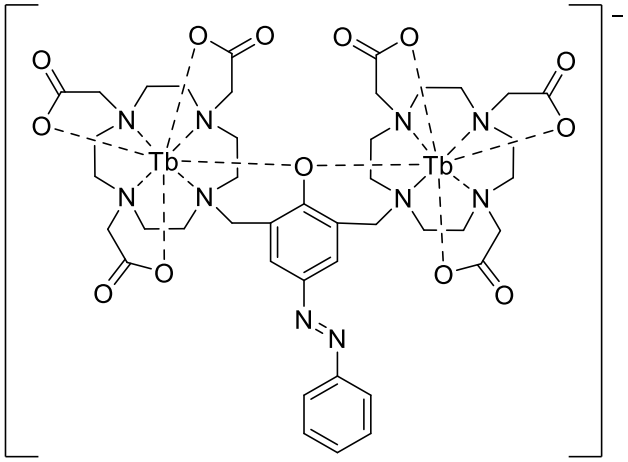

Terbium triflate (60.0 mg, 99.0 µmol, 2.4 eq.) was added to a solution of **106** (37.4 mg, 40.9 µmol, 1.0 eq.) in H_2O (820 µL) and the resulting solution was heated to 50 °C for 18 h. The resulting solution was cooled to rt then adjusted to pH 7 by addition of 1 M NaOH (3 eq. then 3 eq. then 1.0 eq.) and the resulting suspension was heated to 50 °C for a further 72 h. The resulting suspension was filtered, concentrated *in vacuo*, and stored at −20 °C prior to purification. The crude residue was redissolved in a minimal amount of H_2O and purified by dialysis (1000 Da cut-off, procedure as described in the general experimental), then lyophilised for 2 days to yield **53** as an orange solid (32.6 mg, 65%): HRMS *m/z* (ESI^-) [Found: 1225.2496, $C_{42}H_{56}N_{10}O_{13}Tb_2$ requires $[M+H]^-$ 1225.2463]; Analytical HPLC (method 4) R_t 13.8 min, 95%.

1-(hexyloxy)-4-nitrobenzene, 107

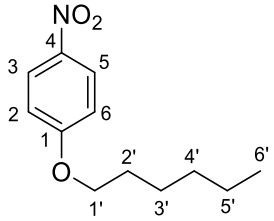

The reaction was carried out according to the general 4-nitrophenol alkylation method, using 4-nitrophenol (1.51 g, 10.8 mmol), K_2CO_3 (3.00 g, 21.7 mmol) and 1-iodohexane (4.60 g, 21.7 mmol), yielding **107** as a yellow oil (2.20 g, 91%): R_f 0.80 (PE : EtOAc 1:1); ν_{max} (solid) cm^{-1}: 1594 (C=C, s), 1514 (N-O, s), 1265 (C-O, s); ^1H NMR (400 MHz, $CDCl_3$): 0.88–0.97 (3H, m, $C^{6'}H_3$), 1.30–1.40 (4H, m, $C^{4'}H_2/C^{5'}H_2$), 1.40–1.52 (2H, m, $C^{3'}H_2$), 1.77–1.86 (2H, m, $C^{2'}H_2$), 4.05 (2H, t, $C^{1'}H_2$), 6.94 (2H, dt, J_1 = 10.4, J_2 = 3.4, C^2H/C^6H), 8.19 (2H, dt, J_1 = 10.4, J_2 = 3.4, C^3H/C^5H); ^{13}C NMR (151 MHz, $CDCl_3$): 14.2 ($C^{6'}$), 22.7 ($C^{5'}$), 25.7 ($C^{3'}$), 29.1 ($C^{2'}$), 31.6 ($C^{4'}$), 69.1 ($C^{1'}$), 114.5 (C^2/C^6), 126.1 (C^3/C^5), 141.5 (C^4), 164.4 (C^1); HRMS *m/z* (ESI^+) [Found: 224.1274, $C_{12}H_{17}NO_3$ requires $[M+H]^+$ 224.1281]; LRMS *m/z* (ESI^+) 224 ($[M+H]^+$, 89%), 469 ($[2M+Na]^+$, 100%).

1-(dodecyloxy)-4-nitrobenzene, 108

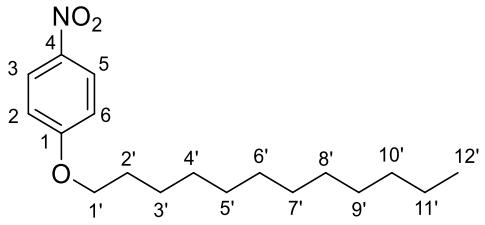

The reaction was carried out according to the general 4-nitrophenol alkylation method, using 4-nitrophenol (1.51 g, 10.8 mmol), K_2CO_3 (2.99 g, 21.6 mmol) and 1-iododododecane (6.39 g, 21.6 mmol), yielding **108** as a pale yellow solid (2.31 g, 69%): R_f 0.85 (PE : EtOAc 1:1); ν_{max} (solid) cm^{-1}: 1594 (C=C, m), 1514 (N-O, m), 1264 (C-O, s); ^{1}H NMR (400 MHz, $CDCl_3$): 0.83–0.93 (3H, m, $C^{12'}H_3$), 1.16–1.40 (16H, m, 8 × alkyl CH_2), 1.41–1.52 (2H, m, $C^{3'}H_2$), 1.76–1.87 (2H, m, $C^{2'}H_2$), 4.04 (2H, t, J = 6.5, $C^{1'}H_2$), 6.94 (2H, dt, J_1 = 10.4, J_2 = 3.4, C^2H/C^6H), 8.19 (2H, dt, J_1 = 10.4, J_2 = 3.4, C^3H/C^5H); ^{13}C NMR (101 MHz, $CDCl_3$): 14.3 ($C^{12'}$), 22.8, 26.1 ($C^{3'}$), 29.1 ($C^{2'}$), 29.45 (alkyl CH_2), 29.49 (alkyl CH_2), 29.67 (alkyl CH_2), 29.71 (alkyl CH_2), 29.78 (alkyl CH_2), 29.79 (alkyl CH_2), 32.1 (alkyl CH_2), 69.1 ($C^{1'}$), 114.6 (C^2/C^6), 126.1 (C^3/C^5), 141.5 (C^4), 164.4 (C^1); HRMS *m/z* (ESI^+) [Found: 330.2029, $C_{18}H_{29}NO_3$ requires $[M+Na]^+$ 330.2040]; LRMS *m/z* (ESI^+) 637 ($[2M+Na]^+$, 100%).

4-(hexyloxy)aniline, 109

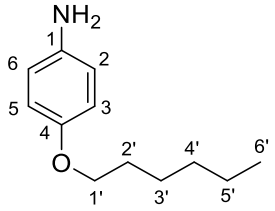

The reaction was carried out according to the general alkylated 4-aminophenol method, using **107** (599 mg, 2.68 mmol), HCl (3 M, 21.0 mL, 63.0 mmol) and tin (1.71 g, 14.4 mmol), yielding **109** as an orange oil (453 mg, 87%). The aniline was used directly without further purification or characterisation: ^{1}H NMR (400 MHz, $CDCl_3$): 0.90 (3H, t, J = 7.0, $C^{6'}H_3$), 1.27–1.39 (4H, m, $C^{4'}H_2/C^{5'}H_2$), 1.43 (2H, tt, J_1 = 8.6, J_2 = 5.5, $C^{3'}H_2$), 1.67–1.79 (2H, m, $C^{2'}H_2$), 3.40 (2H, br s, NH_2), 3.88 (2H, t, J = 6.6, $C^{1'}H_2$), 6.62–6.66 (2H, m, C^3H/C^5H), 6.71–6.77 (2H, m, C^2H/C^6H); ^{13}C NMR (151 MHz, $CDCl_3$): 14.0 ($C^{6'}$), 22.6 ($C^{5'}$), 25.8 ($C^{3'}$), 29.4

($C^{2'}$), 31.6 ($C^{4'}$), 68.8 ($C^{1'}$), 115.7 (C^{2}/C^{6}), 116.4 (C^{3}/C^{5}), 139.8 (C^{1}), 152.4 (C^{4}); LRMS *m/z* (ESI^{+}) 194 ($[M+H]^{+}$, 82%).

4-(dodecyloxy)aniline, 110

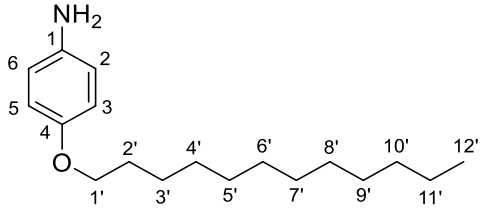

The reaction was carried out according to the general alkylated 4-aminophenol method, using **108** (600 mg, 1.95 mmol), HCl (3 M, 15.1 mL, 63.0 mmol) and tin (1.25 g, 10.5 mmol), yielding **110** as a pale pink/orange solid (512 mg, 99%). The aniline was used directly without further purification or characterisation: ^{1}H NMR (400 MHz, $CDCl_3$): 0.88 (3H, t, *J* = 6.6, $C^{12'}H_3$), 1.20–1.37 (16H, m, 8 × alkyl CH_2), 1.38–1.49 (2H, m, $C^{3'}H_2$), 1.68–1.79 (2H, m, $C^{2'}H_2$), 3.40 (2H, br s, NH_2), 3.87 (2H, t, *J* = 6.6, $C^{1'}H_2$), 6.58–6.68 (2H, m, $C^{3}H$/$C^{5}H$), 6.70–6.78 (2H, m, $C^{2}H$/$C^{4}H$); ^{13}C NMR (151 MHz, $CDCl_3$): 14.1 ($C^{12'}$), 22.7 (alkyl CH_2), 26.1 ($C^{3'}$), 29.36 (alkyl CH_2), 29.45 ($C^{2'}$), 29.61 (alkyl CH_2), 29.62 (alkyl CH_2), 29.65 (alkyl CH_2), 29.68 (alkyl CH_2), 31.9 ($C^{10'}$), 68.7 ($C^{1'}$), 115.7 (C^{2}/C^{6}), 116.4 (C^{3}/C^{5}), 139.8 (C^{1}), 152.4 (C^{4}); LRMS *m/z* (ESI^{+}) 555 ($[2M+H]^{+}$, 100%), 577 ($[2M+Na]^{+}$, 23%).

(E)-4-((4-(hexyloxy)phenyl)diazenyl)-2,6-dimethylphenol, 111

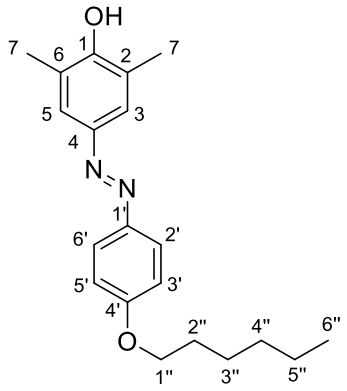

The reaction was carried out according to the general azobenzene formation method, using **109** (253 mg, 1.31 mmol), HCl (12 M, 110 µL, 1.32 mmol), $NaNO_2$ (92.3 mg, 1.34 mmol), 2,6-dimethylphenol (196 mg, 1.60 mmol) and NaOH (147 mg, 3.67 mmol), yielding **111** as

a dark red solid (233 mg, 55%): R_f 0.21 (PE : EtOAc 9:1); v_{max} (solid) cm^{-1}: 1602 (C=C, m), 1581 (C=C, m), 1320 (C-N, m), 1293 (C-N, m), 1252 (C-O, s); ^{1}H NMR (400 MHz, DMSO-d_6): 0.89 (3H, td, J_1 = 6.1, J_2 = 2.9, $C^{6''}H_3$), 1.25–1.37 (4H, m, $C^{4''}H_2$/$C^{5''}H_2$), 1.37–1.48 (2H, m, $C^{3''}H_2$), 1.68–1.79 (2H, m, $C^{2''}H_2$), 2.25 (6H, s, 2 × C^7H_3) 4.05 (2H, t, J = 6.5, $C^{1''}H_2$), 7.04–7.11 (2H, m, $C^{3'}H$/$C^{5'}H$), 7.50 (2H, s, C^3H/C^5H), 7.74–7.82 (2H, m, $C^{2'}H$/$C^{6'}H$), 8.98 (1H, s, O*H*); ^{13}C NMR (151 MHz, DMSO-d_6): 13.9 ($C^{6''}$), 16.7 (C^7), 22.1 ($C^{4''}$), 25.2 ($C^{3''}$), 28.6 ($C^{2''}$), 31.0 ($C^{5''}$), 67.9 ($C^{1''}$), 122.9 (C^2/C^6), 123.8 (C^3/C^5), 124.8 ($C^{2'}$/$C^{6'}$), 144.9 (C^4), 146.2 ($C^{1'}$), 156.3 (C^1), 160.6 ($C^{4'}$); HRMS *m/z* (ESI^+) [Found: 327.2070, $C_{20}H_{26}N_2O_2$ requires $[M+H]^+$ 327.2067]; LRMS *m/z* (ESI^+) 327 ($[M+H]^+$, 100%).

(E)-4-((4-(dodecyloxy)phenyl)diazenyl)-2,6-dimethylphenol, 112

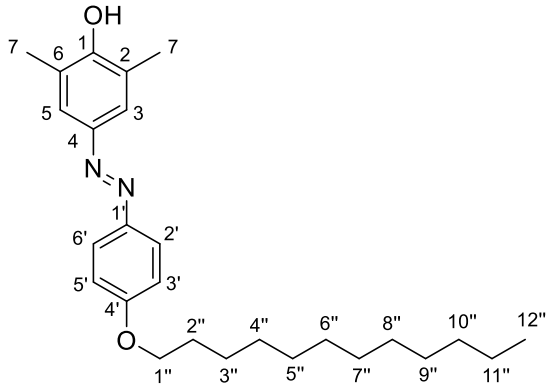

The reaction was carried out according to the general azobenzene formation method, using **110** (186 mg, 0.669 mmol), HCl (12 M, 60.0 µL, 0.720 mmol), $NaNO_2$ (47.3 mg, 0.686 mmol), 2,6-dimethylphenol (99.0 mg, 0.810 mmol) and NaOH (74.9 mg, 1.87 mmol), yielding **112** as a red solid (120 mg, 44%): R_f 0.31 (PE : EtOAc 9:1); v_{max} (solid) cm^{-1}: 1597 (C=C, m), 1583 (C=C, m), 1337 (C-N, w), 1251 (C-O, m); ^{1}H NMR (600 MHz, DMSO-d_6): 0.85 (3H, t, J = 6.9, $C^{12''}H_3$), 1.21–1.37 (16H, m, 8 × alkyl CH_2), 1.38–1.46 (2H, m, $C^{3''}H_2$), 1.70–1.76 (2H, m, $C^{2''}H_2$), 2.25 (6H, s, 2 × C^7H_3), 4.05 (2H, t, J = 6.5, $C^{1''}H_2$), 7.04–7.10 (2H, m, $C^{3'}H$/$C^{5'}H$), 7.50 (2H, s, C^3H/C^5H), 7.75–7.80 (2H, m, $C^{2'}H$/$C^{6'}H$), 8.96 (1H, s, O*H*); ^{13}C NMR (151 MHz, DMSO-d_6): 14.4 ($C^{12''}$), 17.2 (C^7), 22.6 ($C^{10''}$), 25.9 ($C^{3''}$), 29.06 ($C^{2''}$), 29.17 (alkyl CH_2), 29.18 (alkyl CH_2), 29.44 (alkyl CH_2), 29.48 (alkyl CH_2), 29.50 (alkyl CH_2), 31.8 ($C^{10''}$), 68.3 ($C^{1''}$), 115.4 ($C^{3'}$/$C^{5'}$), 123.4 (C^3/C^5), 124.3 ($C^{2'}$/$C^{6'}$), 125.3 (C^2/C^6), 145.4 (C^4),

146.7 ($C^{1'}$), 156.8 (C^{1}), 161.0 ($C^{4'}$); HRMS *m/z* (ESI^+) [Found: 411.2999, $C_{26}H_{38}N_2O_2$ requires $[M+H]^+$ 411.3006]; LRMS *m/z* (ESI^+) 411 ($[M+H]^+$, 100%).

(E)-1-(4-((tert-butyldimethylsilyl)oxy)-3,5-dimethylphenyl)-2-(4-(hexyloxy)phenyl)diazene, 113

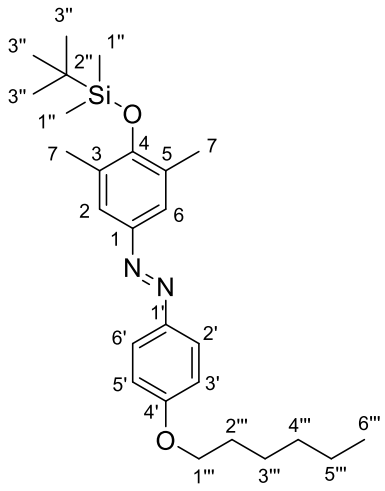

The reaction was carried out according to the general TBDMS protection method, for 40 h, using **111** (137 mg, 0.419 mmol, 1.0 eq.), imidazole (115 mg, 1.69 mmol, 4.0 eq.) and TBDMSCl (254 mg, 1.68 mmol, 4.0 eq.), yielding **113** as an yellow/orange oil (69.8 mg, impure, < 38%), which was stored at −20 °C under foil: R_f 0.74 (PE : EtOAc 9:1); ν_{max} (solid) cm^{-1}: 1600 (C=C, m), 1313 (C-N, m), 1290 (C-N, m), 1251 (Si-CH_3, C-O, s), 1120 (Si-O, m); ^1H NMR (400 MHz, DMSO-d_6): 0.23 (6H, s, 2 × $C^{1''}H_3$), 0.86–0.91 (3H, m, $C^{6'''}H_3$), 1.01 (9H, s, $C^{3''}H_3$), 1.21–1.38 (4H, m, $C^{4'''}H_2$/$C^{5'''}H_2$), 1.38–1.50 (2H, m, $C^{3'''}H_2$), 1.69–1.79 (2H, m, $C^{2'''}H_2$), 2.26 (6H, s, $C^{7}H_3$), 4.01–4.14 (2H, m, $C^{1'''}H_2$), 7.02–7.16 (2H, m, $C^{3'}H$/$C^{5'}H$), 7.54 (2H, s, $C^{2}H$/$C^{6}H$), 7.73–7.89 (2H, m, $C^{2'}H$/$C^{6'}H$); HRMS *m/z* (ESI^+) [Found: 441.2946, $C_{26}H_{40}N_2O_2Si$ requires $[M+H]^+$ 441.2932]; LRMS *m/z* (ESI^+) 441 ($[M+H]^+$, 100%).

(E)-1-(4-((tert-butyldimethylsilyl)oxy)-3,5-dimethylphenyl)-2-(4-(dodecyloxy)phenyl)diazene, 114

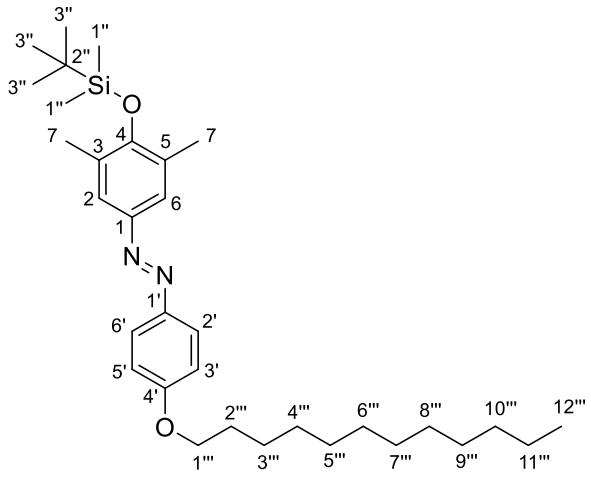

The reaction was carried out according to the general TBDMS protection method, for 44 h, using **112** (115 mg, 279 µmol, 1.0 eq.), imidazole (78.3 mg, 1.15 mmol, 4.0 eq.) and TBDMSCl (84.0 mg, 557 µmol, 2.0 eq.), to give crude material of **114** which was not purified further: R_f 0.73 (PE : EtOAc 9:1); v_{max} (solid) cm^{-1}: 1600 (C=C, m), 1315 (C-N, m), 1250 (Si-CH_3, s), 1146 (Si-O, m); ^{1}H NMR (600 MHz, $CDCl_3$): 0.23 (6H, s, 2 × $C^{1''}H_3$), 0.89 (3H, d, J = 6.9, $C^{12'''}H_3$), 1.05 (9H, s, 3 × $C^{3''}H_3$), 1.23–1.32 (16H, m, 8 × alkyl CH_2), 1.44–1.50 (2H, m, $C^{3'''}H_2$), 1.78–1.85 (2H, m, $C^{2'''}H_2$), 2.30 (6H, s, 2 × C^7H_3), 4.03 (2H, t, J = 6.6, $C^{1''}H_2$), 6.96–7.01 (2H, m, $C^{3'}H$/$C^{5'}H$), 7.58 (2H, s, C^2H/C^6H), 7.85–7.90 (2H, m, $C^{2'}H$/$C^{6'}H$); HRMS *m/z* (ESI^+) [Found: 525.3889, $C_{32}H_{52}N_2O_2Si$ requires $[M+H]^+$ 525.3871]; LRMS *m/z* (ESI^+) 525 ($[M+H]^+$, 100%).

6.5 References

1. G. R. Fulmer, A. J. M. Miller, N. H. Sherden, H. E. Gottlieb, A. Nudelman, B. M. Stoltz, J. E. Bercaw and K. I. Goldberg, *Organometallics*, 2010, **29**, 2176–2179.
2. P. Rodriguez-Maciá, A. Dutta, W. Lubitz, W. J. Shaw and O. Rüdiger, *Angewandte Chemie International Edition*, 2015, **54**, 12303–12307.
3. L. J. O'Connor, I. N. Mistry, S. L. Collins, L. K. Folkes, G. Brown, S. J. Conway and E. M. Hammond, *ACS Central Science*, 2017, **3**, 20–30.
4. E. D. D. Calder, A. Skwarska, D. Sneddon, L. K. Folkes, I. N. Mistry, S. J. Conway and E. M. Hammond, *Tetrahedron*, 2020, **76**, 131170.
5. Y. Zheng, M. Zhao, Q. Qiao, H. Liu, H. Lang and Z. Xu, *Dyes and Pigments*, 2013, **98**, 367–371.
6. L. J. O'Connor, C. Cazares-Körner, J. Saha, C. N. G. Evans, M. R. L. Stratford, E. M. Hammond and S. J. Conway, *Nature Protocols*, 2016, **11**, 781–794.
7. Y. Liu, L. Zhang, M. Nazare, Q. Yao and H.-Y. Hu, *Acta Pharmaceutica Sinica B*, 2018, **8**, 401–408.
8. C. A. Foster, D. Sneddon, L. Hacker, E. T. Sarson, M. Robertson, D. Sokolova, L. A. W. Martin, M. F. Allen, A. Khrapichev, K. A. Vincent, E. M. Hammond, S. J. Conway and S. Faulkner, *Inorganic Chemistry*, 2025, DOI: 10.1021/acs.inorgchem.5c00199.

9. D. Sokolova, T. C. Lurshay, J. S. Rowbotham, G. Stonadge, H. A. Reeve, S. E. Cleary, T. Sudmeier and K. A. Vincent, *Nature Communications*, 2024, **15**, 7297.
10. A. Y. Shaw, C.-Y. Chang, H.-H. Liau, P.-J. Lu, H.-L. Chen, C.-N. Yang and H.-Y. Li, *European Journal of Medicinal Chemistry*, 2009, **44**, 2552–2562.
11. M.-Y. Chang, M.-C. Tsai and C.-Y. Lin, *RSC Advances*, 2021, **11**, 11655–11662.
12. S. V. Mulay, Y. Kim, K. J. Lee, T. Yudhistira, H.-S. Park and D. G. Churchill, *New Journal of Chemistry*, 2017, **41**, 11934–11940.
13. I. Zeid, H. A. El-Bary, S. Yassin and M. Zahran, *Liebigs Annalen der Chemie*, 1984, **1984**, 186–190.
14. H. Nakazumi, T. Ueyama, Kitao and Teijiro, *Journal of Heterocyclic Chemistry*, 1984, **21**, 193–196.
15. M. H. Holshouser, L. J. Loeffler and I. H. Hall, *Journal of Medicinal Chemistry*, 1981, **24**, 853–858.
16. M. H. Holshouser, L. J. Loeffler and I. H. Hall, *J Med Chem*, 1981, **24**, 853–858.
17. X. Zeng, Z. Chen, L. Tang, H. Yang, N. Liu, H. Zhou, Y. Li, J. Wu, Z. Deng, Y. Yu, H. Deng, X. Hong and Y. Xiao, *Chemical Communications*, 2019, **55**, 2541–2544.
18. Y. Zhang, H. Tanimoto, Y. Nishiyama, T. Morimoto and K. Kakiuchi, *Synlett*, 2012, **2012**, 367–370.
19. P. Kumar and M. S. Bodas, *Tetrahedron*, 2001, **57**, 9755–9758.
20. J. Huang, Y. Jiang, J. Li, J. Huang and K. Pu, *Angewandte Chemie International Edition*, 2021, **60**, 3999–4003.
21. D. Zhao, B. Beiring and F. Glorius, *Angewandte Chemie International Edition*, 2013, **52**, 8454–8458.
22. K. Strømgaard, D. R. Saito, H. Shindou, S. Ishii, T. Shimizu and K. Nakanishi, *Journal of Medicinal Chemistry*, 2002, **45**, 4038–4046.
23. H. Inada, K. Furukawa, M. Shibuya and Y. Yamamoto, *Chemical Communications*, 2019, **55**, 15105–15108.
24. J. F. W. Keana and S. X. Cai, *The Journal of Organic Chemistry*, 1990, **55**, 3640–3647.
25. C. Yang, Y. Yang, Y. Li, Q. Ni and J. Li, *Journal of the American Chemical Society*, 2022, DOI: 10.1021/jacs.2c10177.
26. L. O'Connor, Doctor of Philosophy, University of Oxford, 2016.
27. W. Sun, J. Fan, C. Hu, J. Cao, H. Zhang, X. Xiong, J. Wang, S. Cui, S. Sun and X. Peng, *Chemical Communications*, 2013, **49**, 3890–3892.
28. C. Cazares-Körner, I. M. Pires, I. D. Swallow, S. C. Grayer, L. J. O'Connor, M. M. Olcina, M. Christlieb, S. J. Conway and E. M. Hammond, *ACS Chemical Biology*, 2013, **8**, 1451–1459.
29. A. L. D. Wallabregue, H. Bolland, S. Faulkner, E. M. Hammond and S. J. Conway, *Journal of the American Chemical Society*, 2023, DOI: 10.1021/jacs.2c12493.
30. S. S. Matikonda, J. M. Fairhall, F. Fiedler, S. Sanhajariya, R. A. J. Tucker, S. Hook, A. L. Garden and A. B. Gamble, *Bioconjugate Chemistry*, 2018, **29**, 324–334.
31. F. Wan, M. Liu, J. Zhang, Y. Li and L. Jiang, *Research on Chemical Intermediates*, 2015, **41**, 5109–5119.
32. S. N. A. Jenie, S. M. Hickey, Z. Du, D. Sebben, D. A. Brooks, N. H. Voelcker and S. E. Plush, *Inorganica Chimica Acta*, 2017, **462**, 236–240.
33. B. Jagadish, G. L. Brickert-Albrecht, G. S. Nichol, E. A. Mash and N. Raghunand, *Tetrahedron Letters*, 2011, **52**, 2058–2061.
34. A. Dadabhoy, S. Faulkner and P. G. Sammes, *Journal of the Chemical Society, Perkin Transactions 2*, 2002, DOI: 10.1039/B104541P, 348–357.
35. S. Mizukami, K. Tonai, M. Kaneko and K. Kikuchi, *Journal of the American Chemical Society*, 2008, **130**, 14376–14377.
36. L. J. O'Connor, C. Cazares-Körner, J. Saha, C. N. G. Evans, M. R. L. Stratford, E. M. Hammond and S. J. Conway, *Organic Chemistry Frontiers*, 2015, **2**, 1026–1029.
37. C. Rufer, H. J. Kessler and E. Schroeder, *Journal of Medicinal Chemistry*, 1971, **14**, 94–96.
38. B. Cavalleri, R. Ballotta, V. Arioli and G. Lancini, *Journal of Medicinal Chemistry*, 1973, **16**, 557–560.
39. D. Kovacs, D. Phipps, A. Orthaber and K. E. Borbas, *Dalton Transactions*, 2018, **47**, 10702–10714.
40. B. Huang, A. Desai, S. Tang, T. P. Thomas and J. R. Baker, Jr., *Organic Letters*, 2010, **12**, 1384–1387.
41. K. Torisu, K. Kobayashi, M. Iwahashi, H. Egashira, Y. Nakai, Y. Okada, F. Nanbu, S. Ohuchida, H. Nakai and M. Toda, *European Journal of Medicinal Chemistry*, 2005, **40**, 505–519.
42. B. Huang, S. Tang, A. Desai, X.-m. Cheng, A. Kotlyar, A. V. D. Spek, T. P. Thomas and J. R. Baker, *Bioorganic & Medicinal Chemistry Letters*, 2009, **19**, 5016–5020.
43. M. A. Naylor, M. Jaffar, J. Nolan, M. A. Stephens, S. Butler, K. B. Patel, S. A. Everett, G. E. Adams and I. J. Stratford, *Journal of Medicinal Chemistry*, 1997, **40**, 2335–2346.
44. A. S. Cotterill, C. J. Moody, R. J. Mortimer, C. L. Norton, N. O'Sullivan, M. A. Stephens, N. R. Stradiotto, E. Swann and I. J. Stratford, *Journal of Medicinal Chemistry*, 1994, **37**, 3834–3843.
45. S. C. Burdette and S. J. Lippard, *Inorganic Chemistry*, 2002, **41**, 6816–6823.
46. K.-L. N. A. Finney, A. C. Harnden, N. J. Rogers, P. K. Senanayake, A. M. Blamire, D. O'Hogain and D. Parker, *Chemistry – A European Journal*, 2017, **23**, 7976–7989.
47. H. Azuma, K. Miyasaka, T. Yokotani, T. Tachibana, A. Kojima-Yuasa, I. Matsui-Yuasa and K. Ogino, *Bioorganic & Medicinal Chemistry*, 2006, **14**, 1811–1818.
48. Y. Kaburagi, H. Osajima, K. Shimada, H. Tokuyama and T. Fukuyama, *Tetrahedron Letters*, 2004, **45**, 3817–3821.
49. A. B. Smith, J. B. Sperry and Q. Han, *The Journal of Organic Chemistry*, 2007, **72**, 6891–6900.
50. P. Tagliatesta, D. Giovannetti, A. Leoni, M. G. P. M. S. Neves and J. A. S. Cavaleiro, *Journal of Molecular Catalysis A: Chemical*, 2006, **252**, 96–102.

51. Abu T. Khan, S. Ghosh and Lokman H. Choudhury, *European Journal of Organic Chemistry*, 2004, **2004**, 2198–2204.
52. M. S. Thomsen, P. R. Nawrocki, N. Kofod and T. J. Sørensen, *European Journal of Inorganic Chemistry*, 2022, **2022**, e202200334.
53. S. Aime, M. Botta and G. Ermondi, *Inorganic Chemistry*, 1992, **31**, 4291–4299.
54. S. Mizukami, R. Takikawa, F. Sugihara, Y. Hori, H. Tochio, M. Wälchli, M. Shirakawa and K. Kikuchi, *Journal of the American Chemical Society*, 2008, **130**, 794–795.
55. R. C. Strauch, D. J. Mastarone, P. A. Sukerkar, Y. Song, J. J. Ipsaro and T. J. Meade, *Journal of the American Chemical Society*, 2011, **133**, 16346–16349.
56. Y. Yamakoshi, H. Qiao, A. N. Lowell, M. Woods, B. Paulose, Y. Nakao, H. Zhang, T. Liu, S. Lund-Katz and R. Zhou, *Chemical Communications*, 2011, **47**, 8835–8837.
57. C. Wängler, B. Wängler, M. Eisenhut, U. Haberkorn and W. Mier, *Bioorganic & Medicinal Chemistry*, 2008, **16**, 2606–2616.
58. C. H. Simms, D. Kovacs, L. Hacker, E. T. Sarson, D. Sokolova, K. E. Christensen, A. Khrapichev, L. A. W. Martin, K. Vincent, S. J. Conway, E. M. Hammond, M. J. Langton and S. Faulkner, *Chemistry – A European Journal*, 2025, **n/a**, e202404748.
59. S. B. M Kretschmer, S. Woltersdorf, C. B. Rödl, D. Vogt, A.-K. Häfner, D. Steinhilber, H. Stark and B. Hofmann, *Future Medicinal Chemistry*, 2016, **8**, 149–164.
60. S. Albedyhl, Marie T. Averbuch-Pouchot, C. Belle, B. Krebs, Jean L. Pierre, E. Saint-Aman and S. Torelli, *European Journal of Inorganic Chemistry*, 2001, **2001**, 1457–1464.
61. C. Lindler, East Carolina University, 2014.
62. T. Kline, M. Y. Torgov, B. A. Mendelsohn, C. G. Cerveny and P. D. Senter, *Molecular Pharmaceutics*, 2004, **1**, 9–22.
63. N. Tran-Hoang and T. Kodadek, *ACS Combinatorial Science*, 2018, **20**, 55–60.
64. M. Bortolus, G. Ribaudo, A. Toffoletti, D. Carbonera and G. Zagotto, *Photochemical & Photobiological Sciences*, 2019, **18**, 2199–2207.
65. M. P. Placidi, A. J. L. Villaraza, L. S. Natrajan, D. Sykes, A. M. Kenwright and S. Faulkner, *Journal of the American Chemical Society*, 2009, **131**, 9916–9917.
66. M. P. Placidi, University of Manchester, 2009.
67. C. H. Simms, University of Oxford, 2024.

A. Appendix

A1 Extra Figures

A1.2 Chapter II

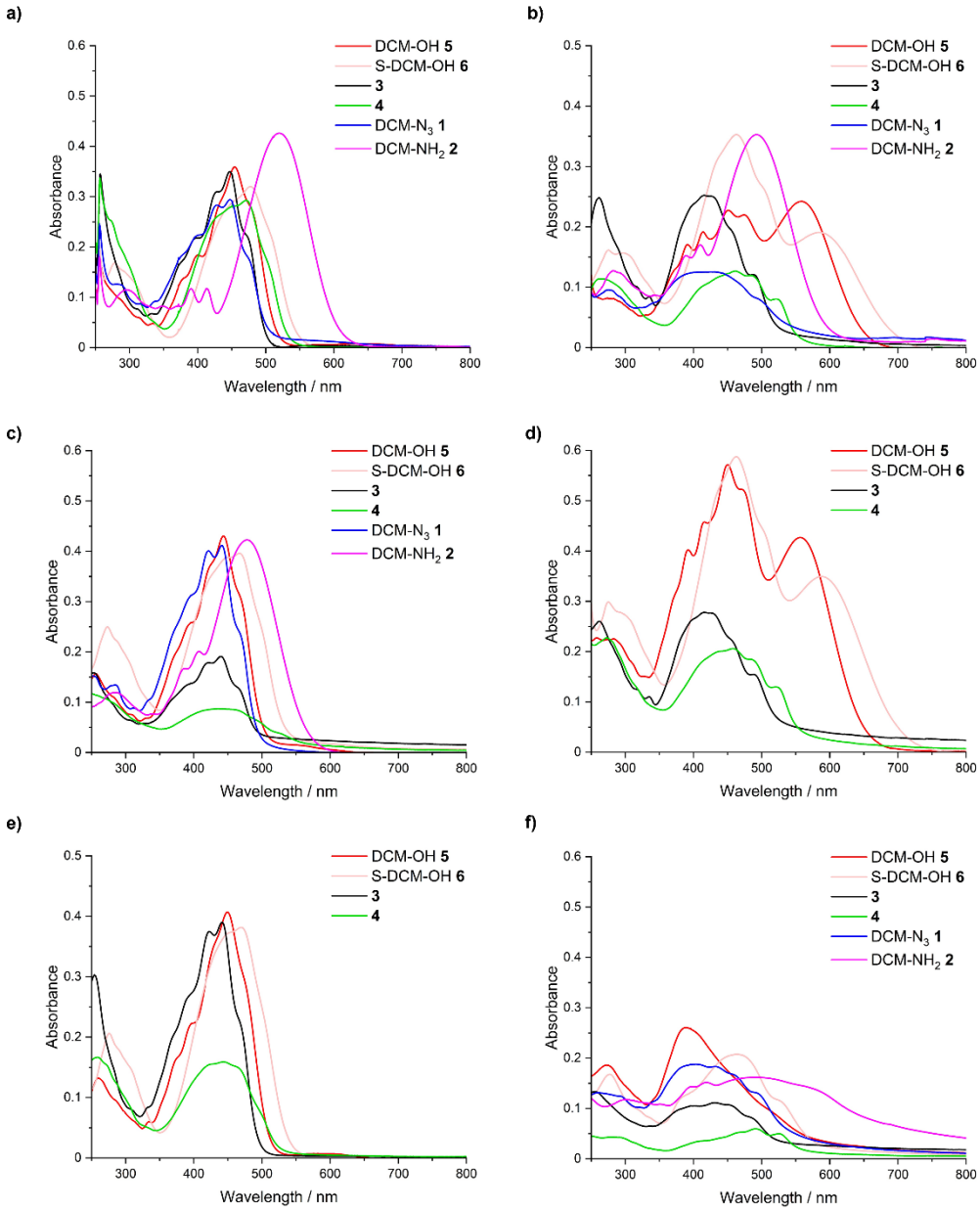

Figure A2.1: The UV-Vis spectra of compounds 1-6 in various solvent systems. a) DMSO at 10 µM, b) DMSO:PBS (1:1 v/v, buffer pH 7.4) at 10 µM, c) MeCN:PBS (1:1 v/v, buffer pH 7.4) at 10 µM, d) DMSO:PBS (1:1 v/v, buffer pH 7.4). at 20 µM, e) IPA at 10 µM, f) PBS at 20 µM.

Table A2.1: A summary of the profiles of the UV-Vis spectra of compounds **1-6** in various solvents, 10-20 μM.

Compound	Solvent	Concentration / μM	λ_{max} / nm	Absorbance at λ_{max}
3	DMSO	10	447	0.35
	DMSO:PBS 1:1	10	415	0.26
	DMSO:PBS 1:1	20	415	0.28
	IPA	15	442	0.39
	MeCN:PBS 1:1	10	440	0.19
	H_2O	10	428	0.27
	PBS	20	430	0.11
4	DMSO	10	470	0.29
	DMSO:PBS 1:1	10	462	0.13
	DMSO:PBS 1:1	20	462	0.20
	IPA	15	444	0.16
	MeCN:PBS 1:1	10	438	0.09
	H_2O	10	432	0.13
	PBS	20	492	0.06
5 DCM-OH	DMSO	10	454	0.36
	DMSO:PBS 1:1	10	450 556	0.26 0.22
	DMSO:PBS 1:1	20	450 556	0.57 0.43
	IPA	15	450	0.41
	MeCN:PBS 1:1	10	443	0.43
	H_2O	10	386	0.11
	PBS	20	388 520	0.26 0.09
6 DCM-OH	DMSO	10	477	0.32
	DMSO:PBS 1:1	10	464 584	0.36 0.19
	DMSO:PBS 1:1	20	464 584	0.59 0.35
	IPA	15	470	0.38
	MeCN:PBS 1:1	10	467	0.40
	H_2O	10	464	0.13
	PBS	20	465 530	0.21 0.11
1 DCM-N_3	DMSO	10	447	0.29
	DMSO:PBS 1:1	10	420	0.13
	MeCN:PBS 1:1	10	441	0.41
	PBS	20	405	0.19
2 DCM-NH_2	DMSO	10	518	0.43
	DMSO:PBS 1:1	10	492	0.35
	MeCN:PBS 1:1	10	478	0.42
	PBS	20	491	0.16

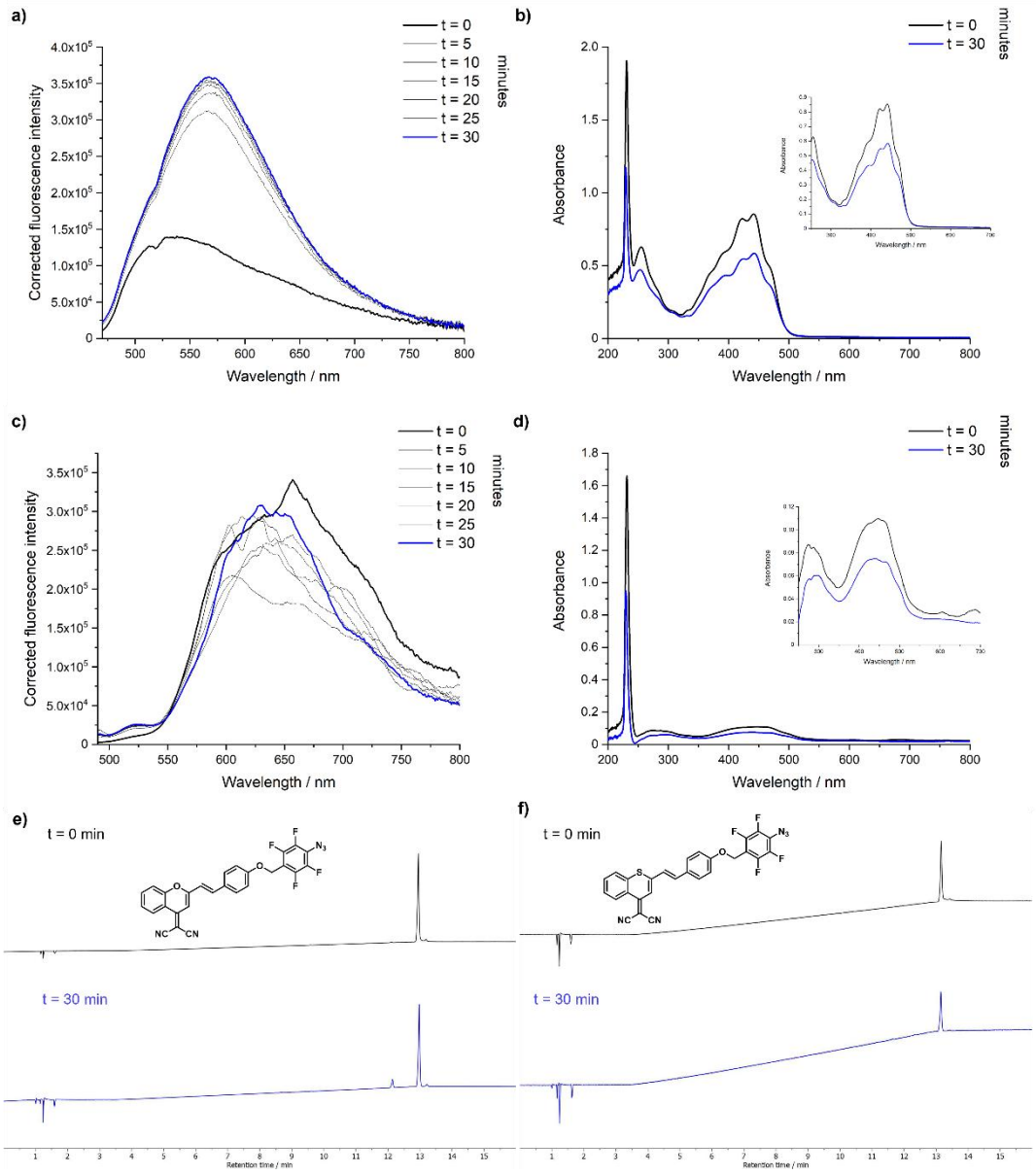

Figure A2.2: Results of the zinc assay of compounds **3** (panels a, b and e) and **4** (panels c, d and f) according to method 1 (50 µM in IPA). a) Fluorescence spectra, λ_{ex} 450 nm, λ_{em} 470-800 nm, slits 5 nm / 2 nm. b and d) UV-Vis spectra over time. c) Fluorescence spectra, λ_{ex} 470 nm, λ_{em} 490-800 nm, slits 10 nm / 2 nm. e and f) HPLC analysis (method 1B) showing the change in the HPLC trace over time, analysed at 480 nm.

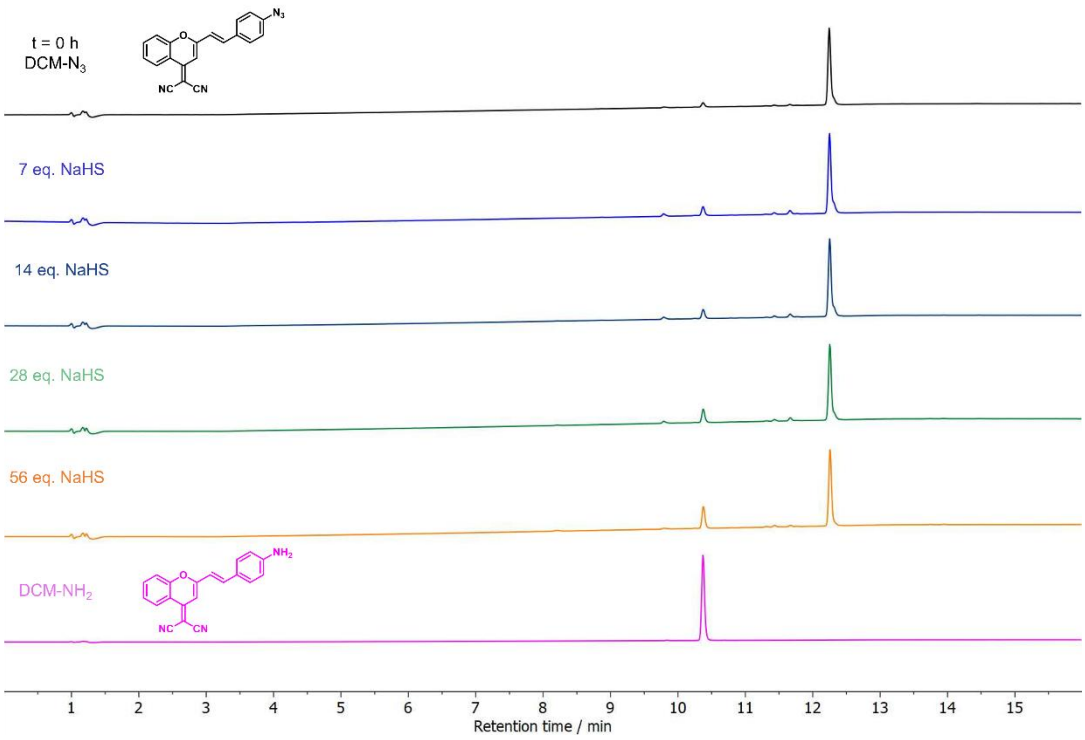

Figure A2.3: Results of the analytical HPLC analysis (at 480 nm) of DCM-N_3 in the presence of 7-56 equivalents of NaHS (NaHS assay method 2).

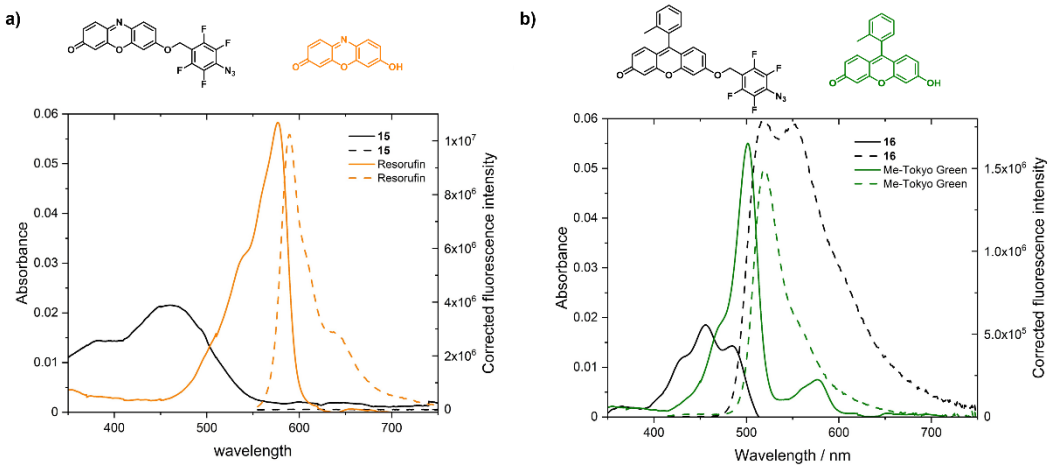

Figure A2.4: The UV-Vis spectra (solid lines) and fluorescence emission spectra (dashed lines) of a) profluorophore **15** (black) vs resorufin (orange) and b) profluorophore **16** (black) vs Me-Tokyo Green (green), measured at 1 µM in MeCN:PBS 1:1 (PBS pH 7.4). For panel a fluorescence emission, λ_{ex} 540 nm, λ_{em} 555-800 nm, slits 2 nm / 1 nm; for panel b fluorescence emission, λ_{ex} 400 nm, λ_{em} 415-800 nm, slits 2 nm / 2 nm.

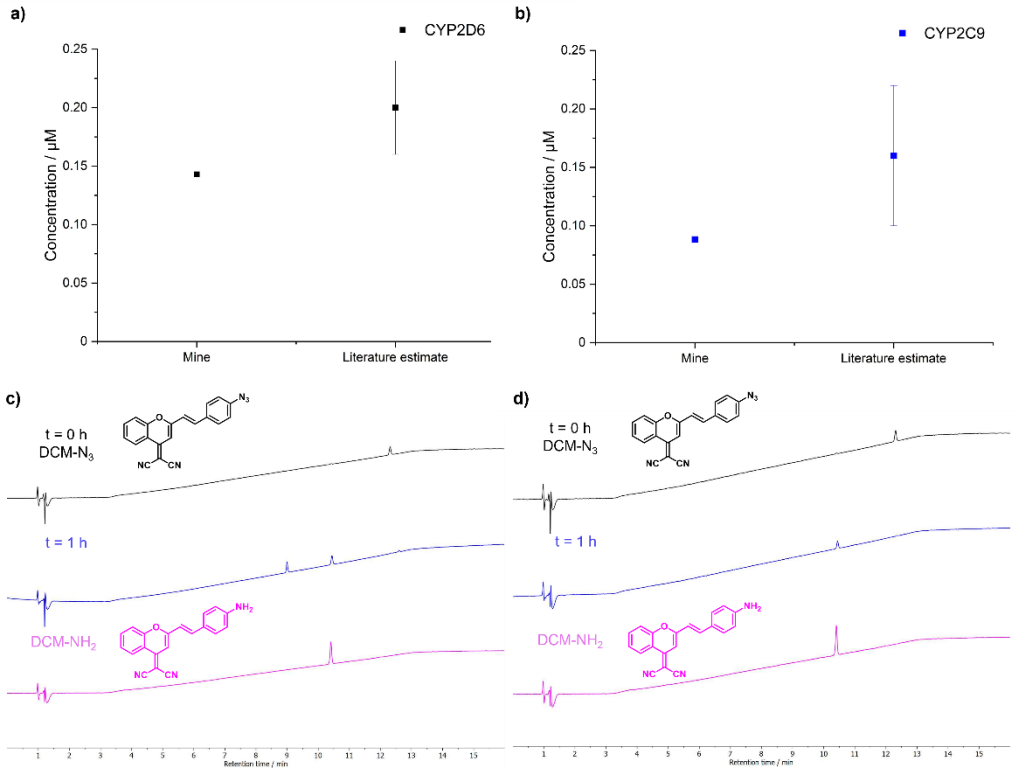

Figure A2.5: a and b) Comparison of the release of DCM-NH_2 observed from DCM-N_3 in the presence of CYP2D6 (panel a) or CYP2C9 (panel b), in comparison to that observed in the literature, by comparison to a calibration curve of DCM-NH_2 in H_2O/$KHPO_4$ buffer. c and d) HPLC analysis of the enzyme assays of DCM-N_3 after 1 hour (blue), in comparison to DCM-N_3 (0.5 µM, black) and DCM-NH_2 (0.5 µM, pink), analysed at 480 nm.

A1.3 Chapter III

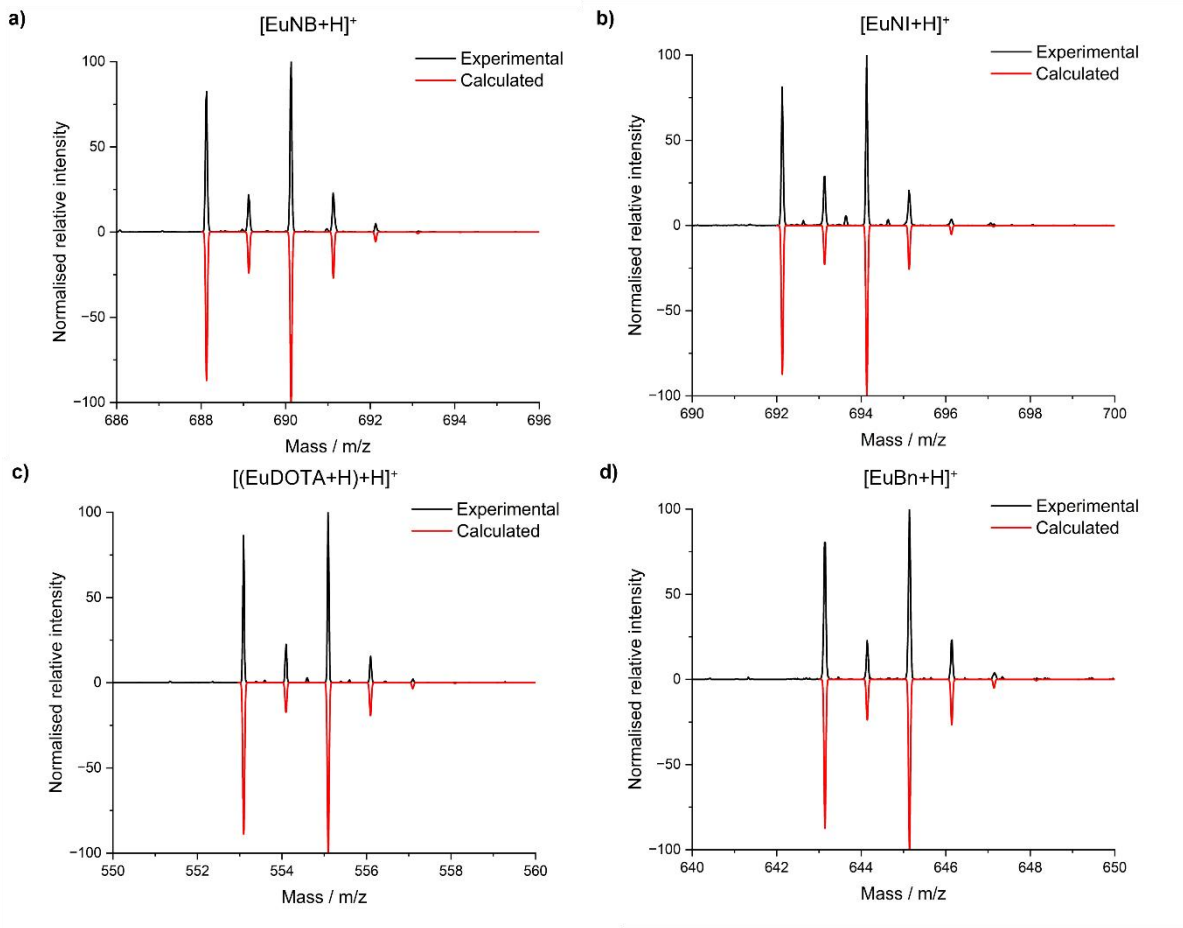

Figure A3.1: High resolution mass spectrometry (HRMS) analysis of the EuNB **18a** (a), EuNI **19b** (b), [EuDOTA]$^-$ **21a** (c) and EuBn **22a** (d) complexes (experimental, black) in comparison to the calculated spectra (red), highlighting the distinct isotopic pattern for europium.

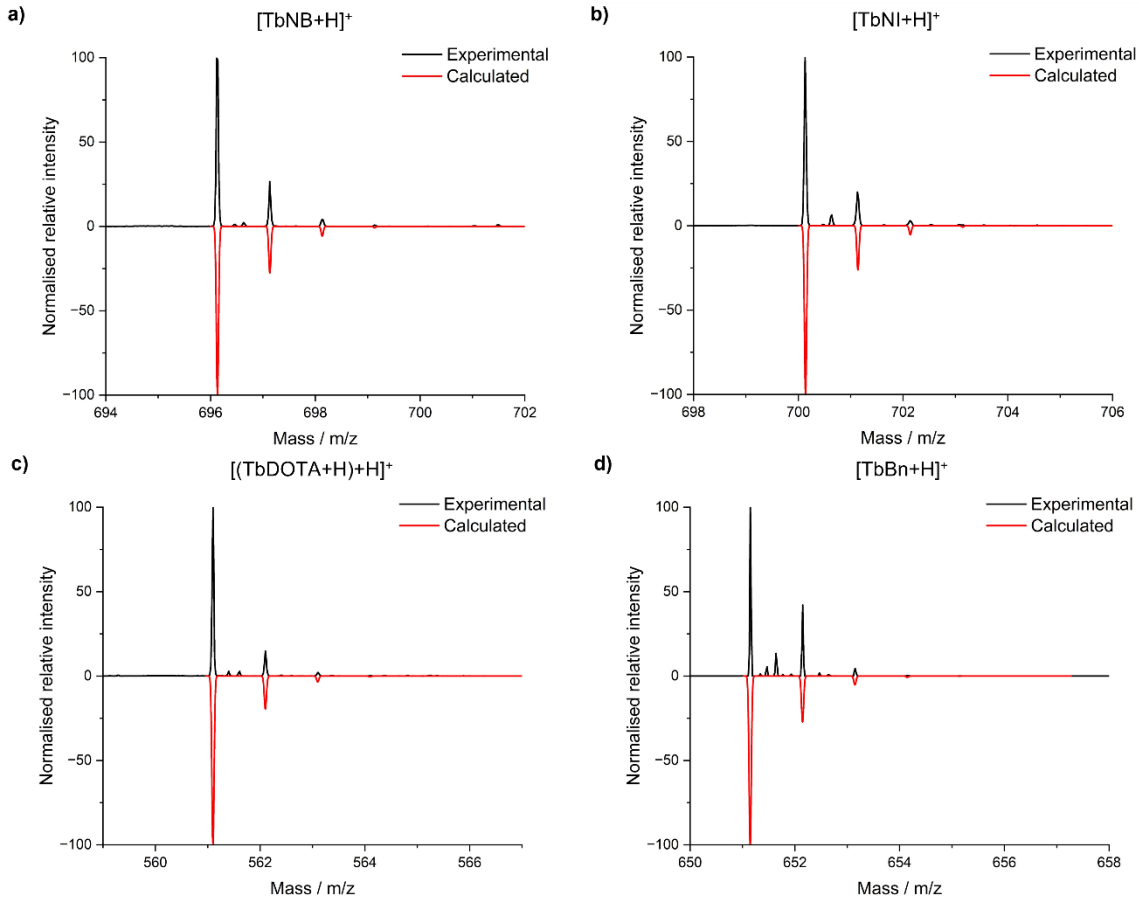

Figure A3.2: High resolution mass spectrometry (HRMS) analysis of the TbNB **18b** (a), TbNI **19b** (b), $[TbDOTA]^-$ **21b** (c) and TbBn **22b** (d) complexes (experimental, black) in comparison to the calculated spectra (red), highlighting the distinct isotopic pattern for terbium.

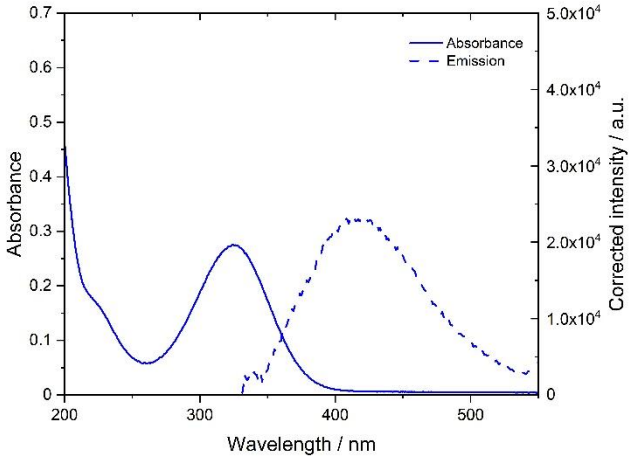

Figure A3.3: The UV-Visible spectra (solid lines) and steady-state emission spectra (dotted lines) of NI ligand (**32**, blue – λ_{ex} 300 nm) 29 nm / 1 nm, integration time 0.5 s, S1 channel.

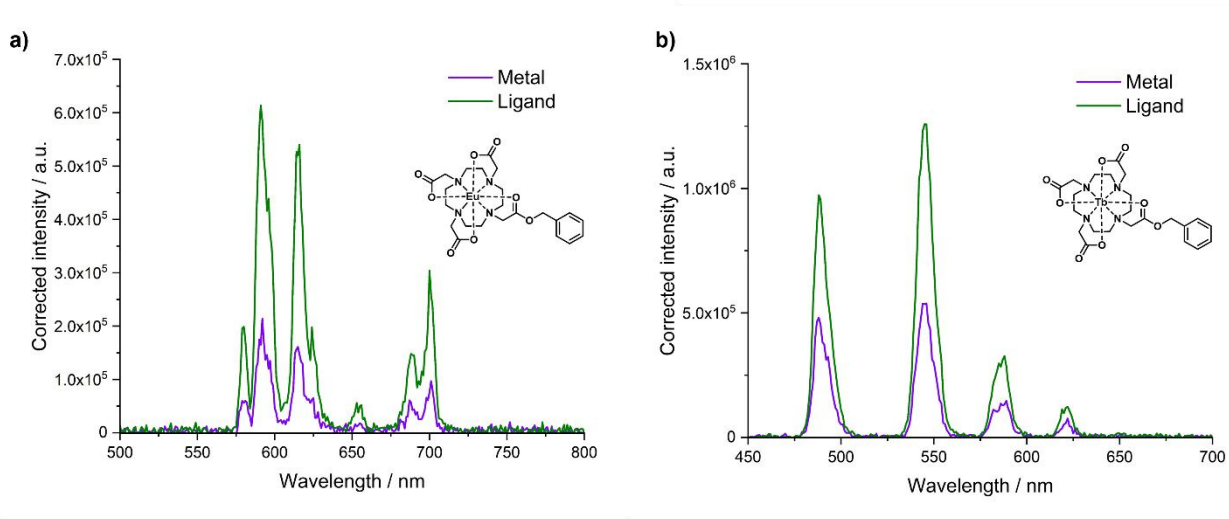

Figure A3.4: The time-gated emission spectra of a) EuBn (**22a**) and b) TbBn (**22b**) at 50 µM upon excitation of the ligand (262 nm, green) or direct metal excitation (397 nm for Eu, 366 nm for Tb, purple).

Table A3.1: Direct excitation lifetime data (λ_{ex} 397 nm for Eu, 366 nm for Tb). All lifetimes are in ms. *Biexponential decay.

	EuNB 18a		**EuNI 19a**				**EuDOTA 21a**	
	τ_{H2O}	τ_{D2O}	τ_{H2O}		τ_{D2O}		τ_{H2O}	τ_{D2O}
n=1	0.63	2.20	0.607		2.46		0.62	2.37
n=2	0.62	2.16	0.607		2.43		0.66	2.32
n=3	0.63	2.20	0.608		2.45		0.66	2.30
	TbNB 18b		**TbNI 19b**				**TbDOTA 21b**	
	τ_{H2O}	τ_{D2O}	τ_{H2O} *		τ_{D2O} *		τ_{H2O}	τ_{D2O}
n=1	1.98	3.35	0.20	2.07	0.24	3.69	2.03	3.68
n=2	1.94	3.36	0.20	2.04	0.23	3.64	2.06	3.51
n=3	1.90	3.37	2.07	2.07	0.23	3.61	2.09	3.55

Table A3.2: Direct excitation lifetime data (λ_{ex} 269 nm for NB, 320 nm for NI). All lifetimes are in ms. *Biexponential decay.

	EuNB 18a		**EuNI 19a**		
	τ_{H2O}	τ_{D2O}	τ_{H2O}		τ_{D2O}
n=1	0.61	2.35	0.59		2.38
n=2	0.61	2.42	0.59		2.40
n=3	0.62	2.43	0.62		2.42
	TbNB 18b		**TbNI 19b**		
	τ_{H2O}	τ_{D2O}	τ_{H2O} *		τ_{D2O}
n=1	1.93	3.75	0.25	2.05	3.79
n=2	1.94	3.74	0.23	2.06	3.51
n=3	1.92	3.75	0.21	2.06	3.54

Table A3.3: Cathodic onset potentials of 1 mM TbNB (**18b**), TbNI (**19b**) and TbBn (**22b**) in the buffer mentioned, measured at ambient temperature by Euan Sarson.

Complex	Cathodic onset potential vs SHE / mV	
	PBS (pH 7.4)	MES (pH 6.0)
TbNB 18b	-356	-217
TbNI 19b	-236	-119
TbBn 22b	-	-

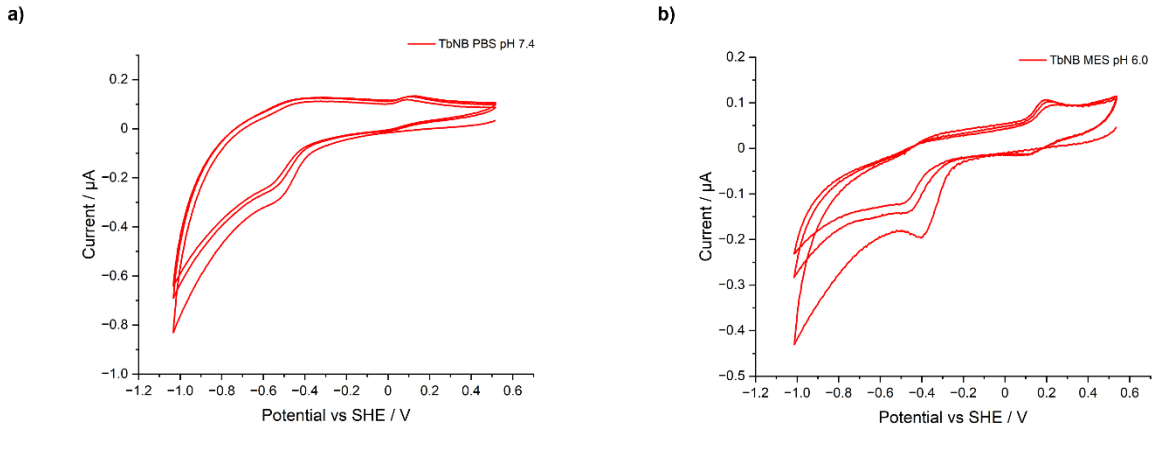

Figure A3.5: Cyclic voltammograms of TbNB (**18b**) in a) PBS at pH 7.4, b) in MES at pH 6, showing 3 cycles. Measurements carried out by Euan Sarson.

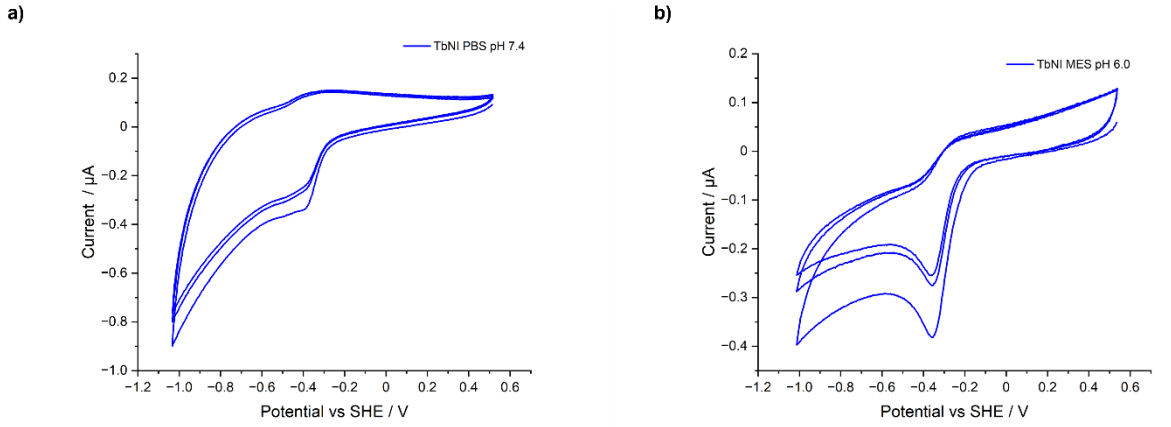

Figure A3.6: Cyclic voltammograms of TbNI (**19b**) in a) PBS at pH 7.4, b) in MES at pH 6, showing 3 cycles. Measurements carried out by Euan Sarson.

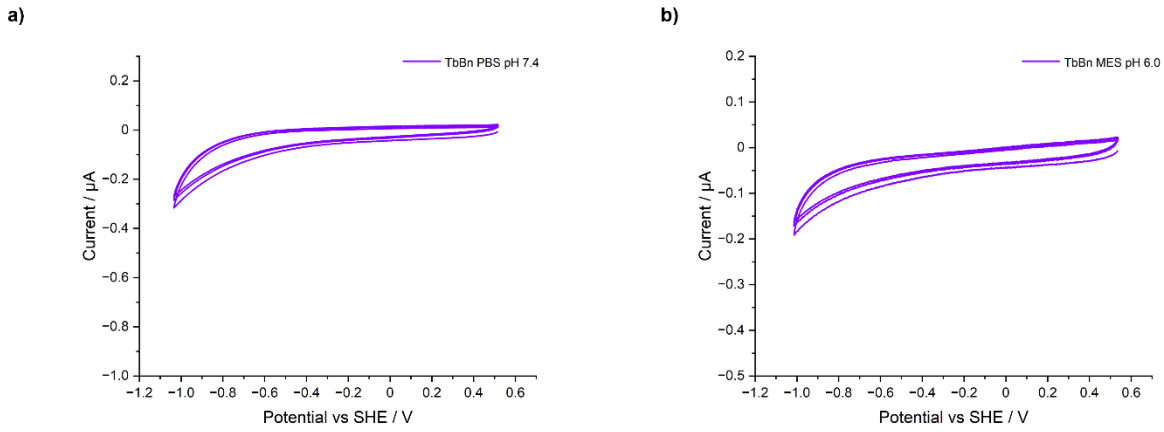

Figure A3.7: Cyclic voltammograms of TbBn (**22b**) in a) PBS at pH 7.4, b) in MES at pH 6, showing 3 cycles. Measurements carried out by Euan Sarson.

A1.4 Chapter IV

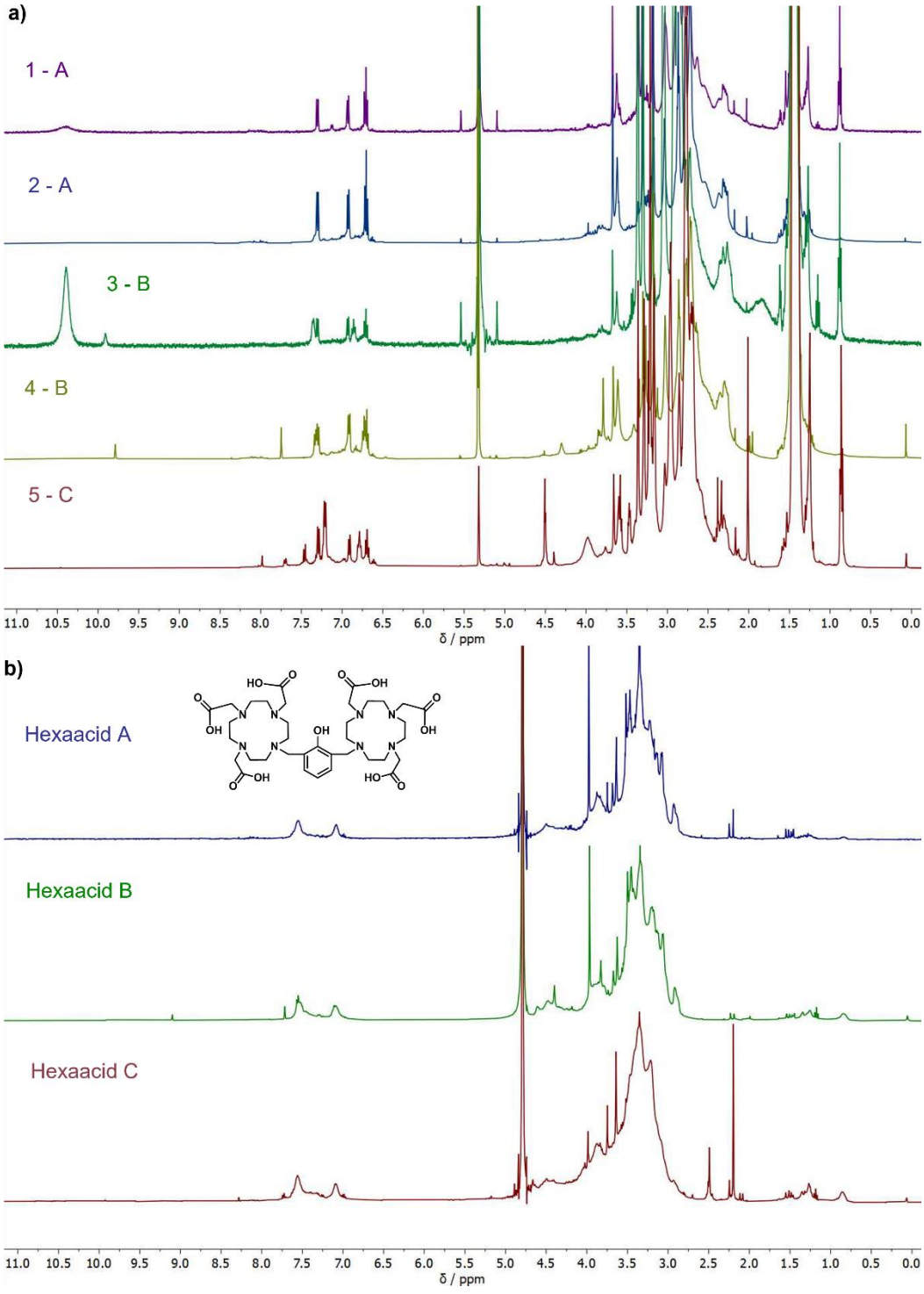

Figure A4.1: a) The stacked ^{1}H NMR spectra, in CD_2Cl_2 at room temperature, of the 5 fractions of hexaester **99** isolated, labelled as the hexaester fraction number (1-5) and a letter (A-C) to denote which fractions were combined. b) The stacked ^{1}H NMR spectra, measured in D_2O at room temperature, of the hexaacids **100** formed from deprotection of the hexaesters shown in panel a.

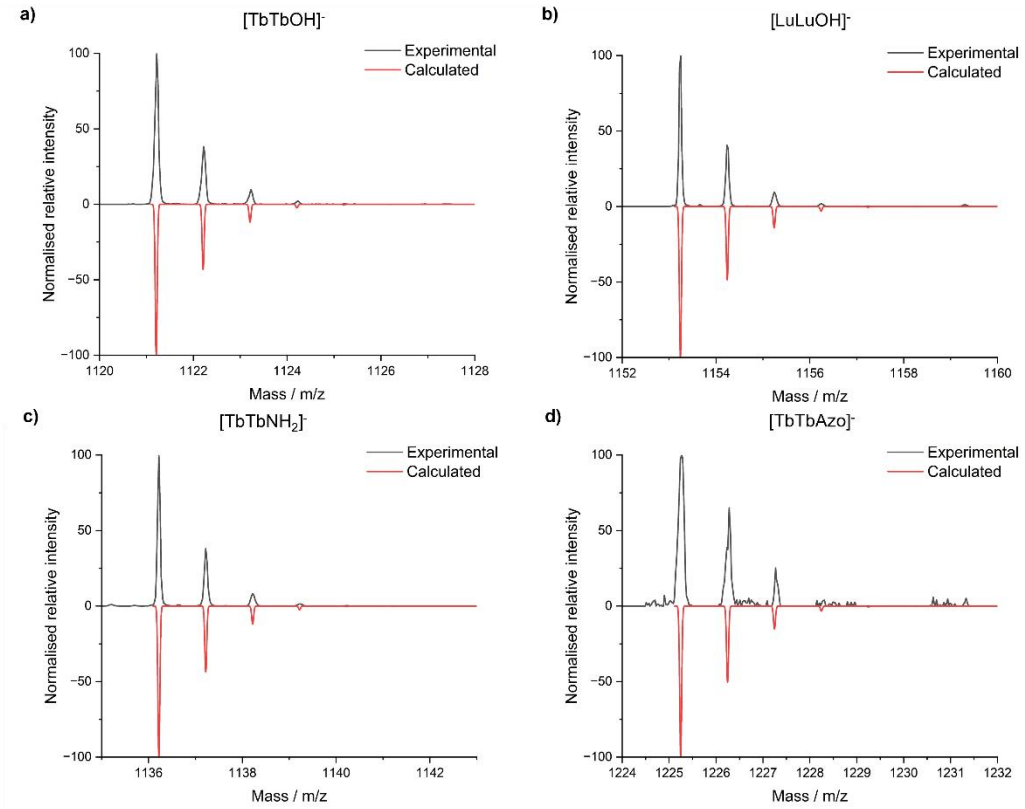

Figure A4.2: High resolution mass spectrometry (HRMS) analysis of the TbTbOH **93Tb** (a), LuLuOH **93Lu** (b), $TbTbNH_2$ **54** (c) and TbTbAzo **53** (d) complexes (experimental, black) in comparison to the calculated spectra (red).

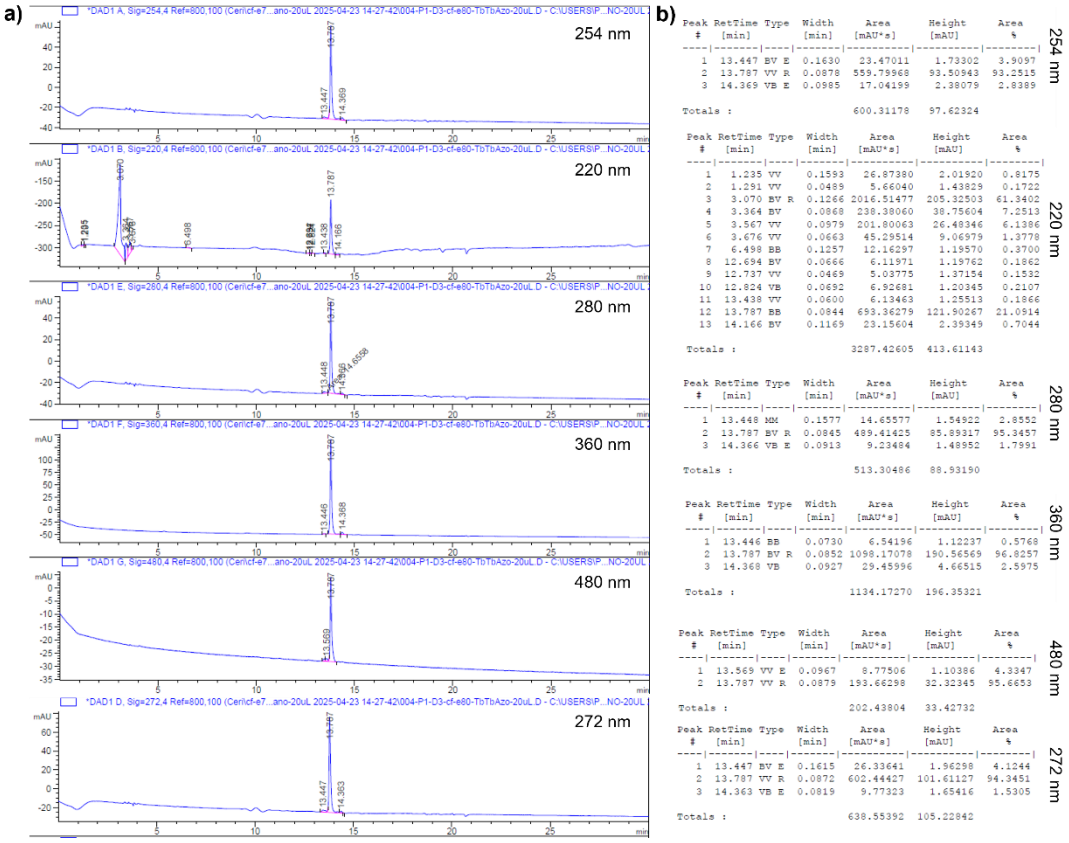

Figure A4.3: The HPLC analysis of TbTbAzo **53** (20 µL, method F) after blank subtraction. a) The traces at 254 nm, 220 nm, 280 nm, 360 nm, 480 nm and 272 nm after blank subtraction. b) Tables of purity analysis from the traces, based on area percentages. The purity is 83% averaged across all 6 wavelengths or 95% averaged across 5 wavelengths.

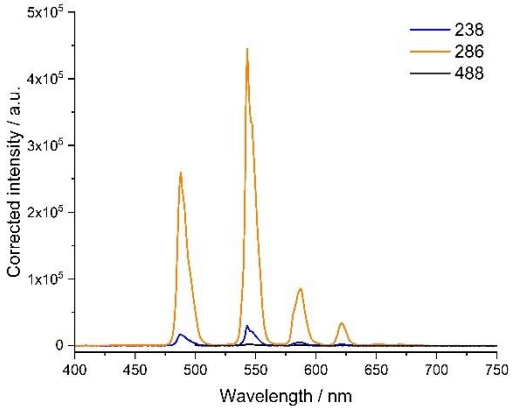

Figure A4.4: Steady state emission spectra of TbTbOH **93Tb**, at 90 µM in H_2O, upon excitation at 238 nm (blue, ligand π→π*), 286 (orange, ligand n→π*) and 488 (black, direct terbium excitation). 400 nm filter for a and b, 495 nm filter for c, slits 2 / 1 nm.

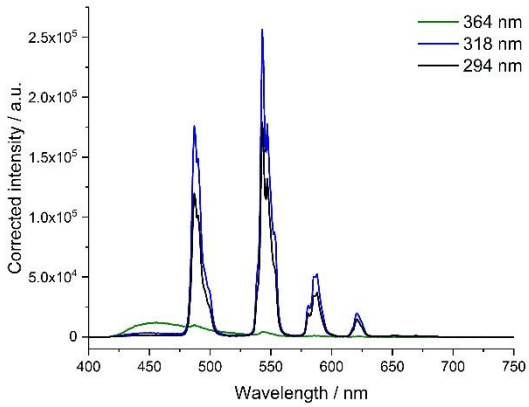

Figure A4.5: Comparison of steady state emission of TbTbAzo **53**, 90 µM in PBS, upon excitation at 364 nm (red, ligand π-π*), 318 (blue) and 294 (black). 400 nm filter, slits 10 / 1 nm.

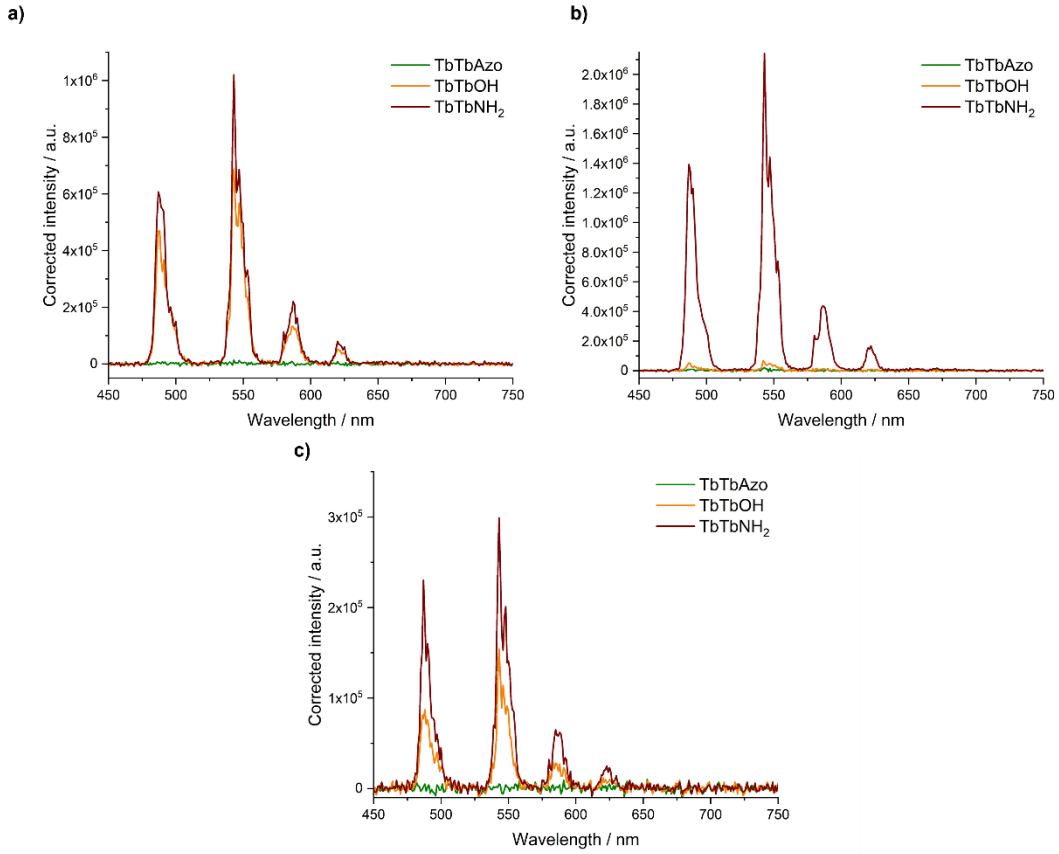

Figure A4.6: Time gated emission spectra of TbTbAzo **53** (red), TbTbOH **93Tb** (orange) and $TbTbNH_2$ **54** (green) at 90 µM in PBS (10 mM, pH 7.4), 400 nm filter, flash count 5, 1 ms sample window, 61 ms per flash. a) λ_{em} 294 nm, slits 3 / 1 nm; b) λ_{em} 318 nm, slits 5 / 1 nm; c) λ_{em} 488 nm, slits 5 / 1 nm.

A2 NMR Spectra of Novel and Final Compounds

A2.2 Compounds from chapter II

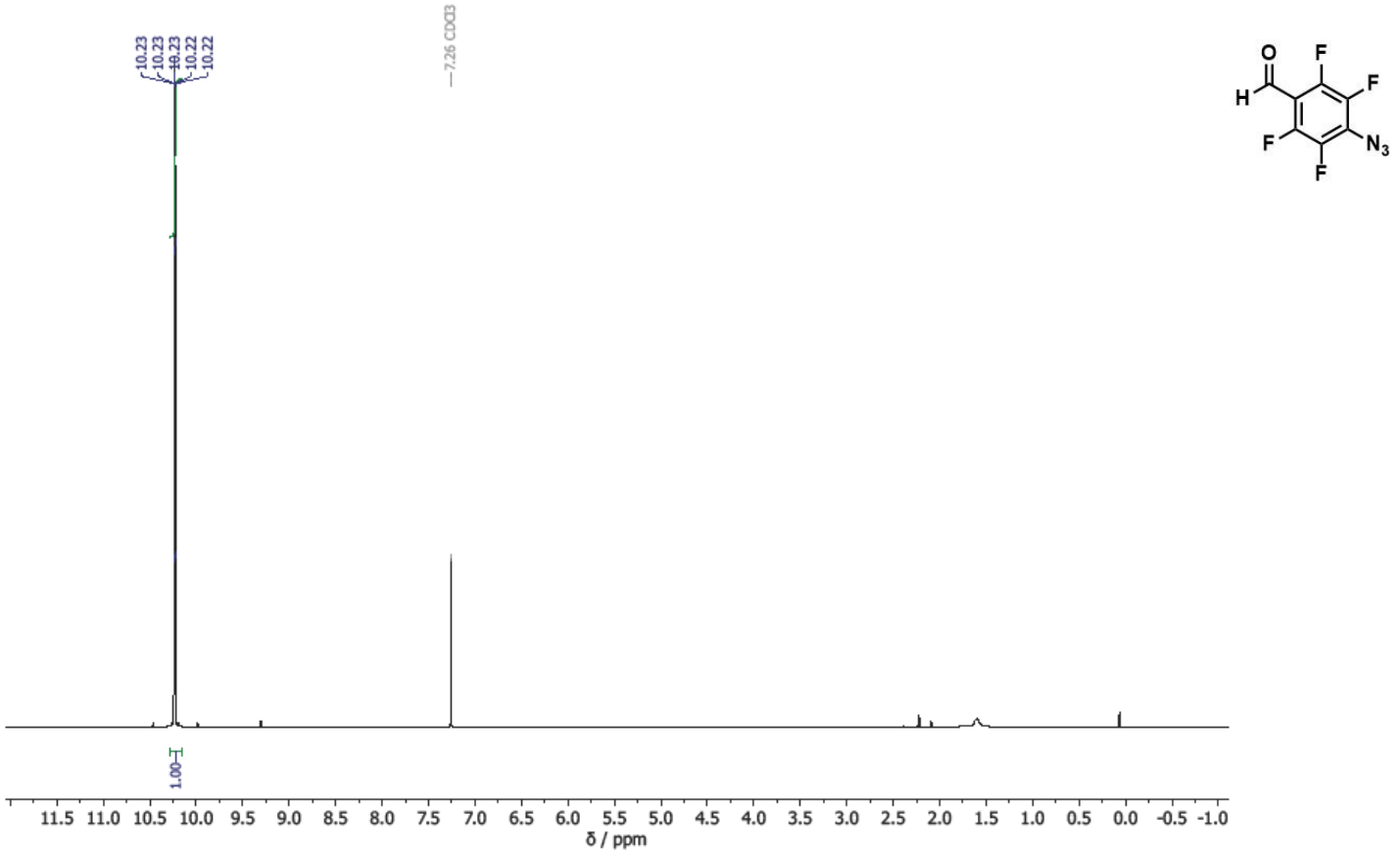

Figure A6.1: The ^{1}H NMR spectrum of 4-azido-2,3,5,6-tetrafluorobenzaldehyde **11** in $CDCl_3$.

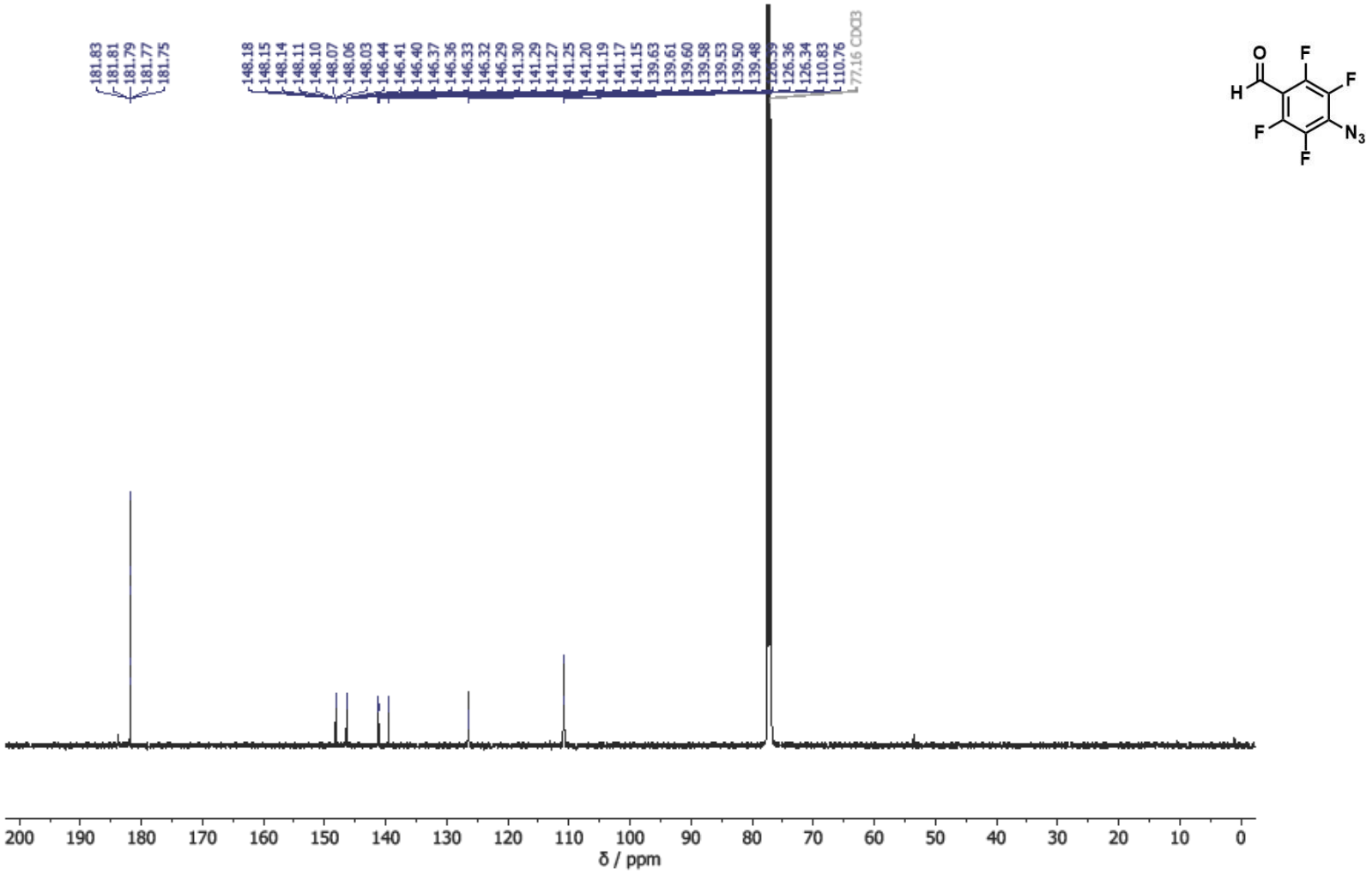

Figure A6.2: The ^{13}C NMR spectrum of 4-azido-2,3,5,6-tetrafluorobenzaldehyde **11** in $CDCl_3$.

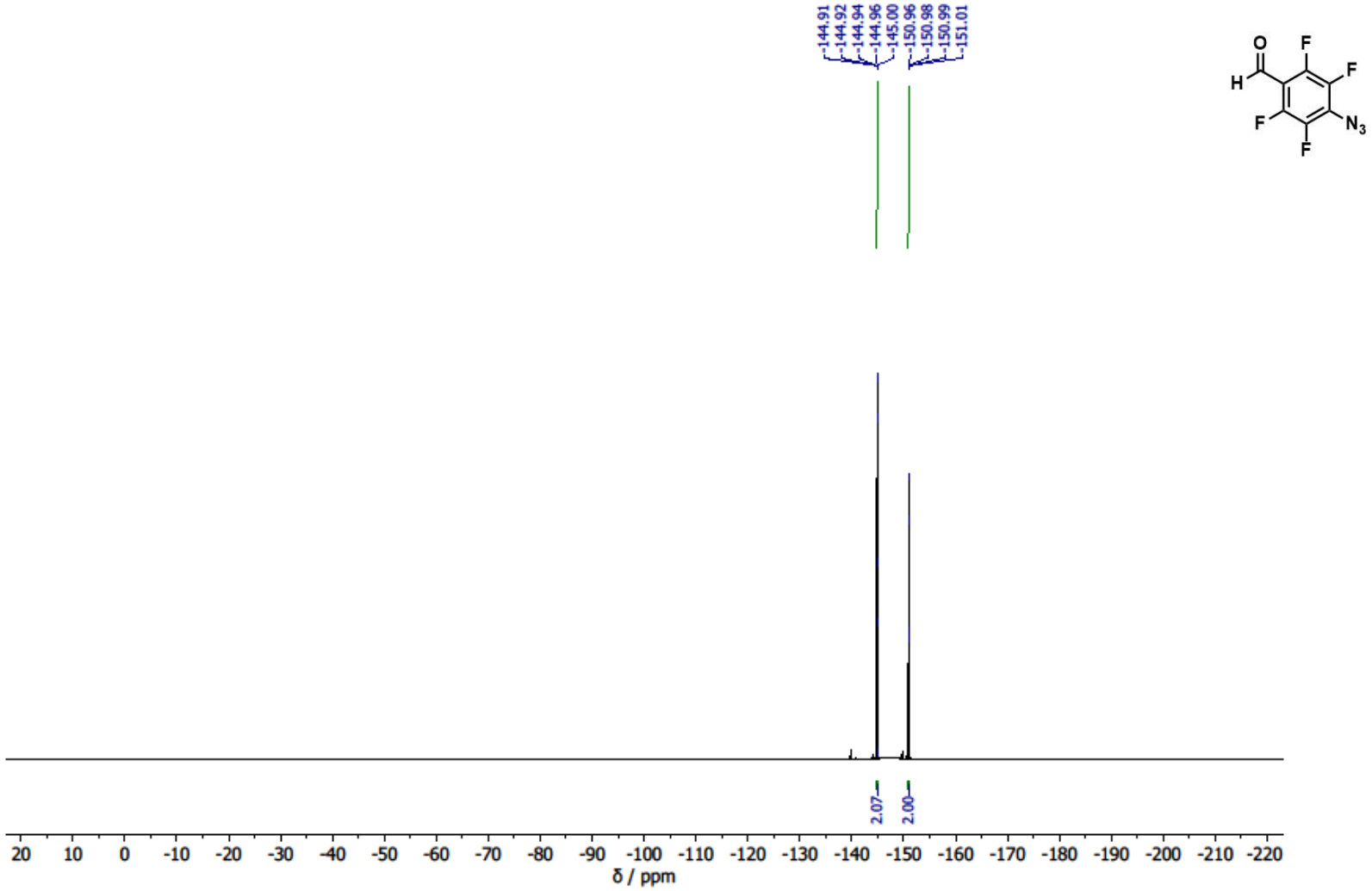

Figure A6.3: The ^{19}F NMR spectrum of 4-azido-2,3,5,6-tetrafluorobenzaldehyde **11** in $CDCl_3$.

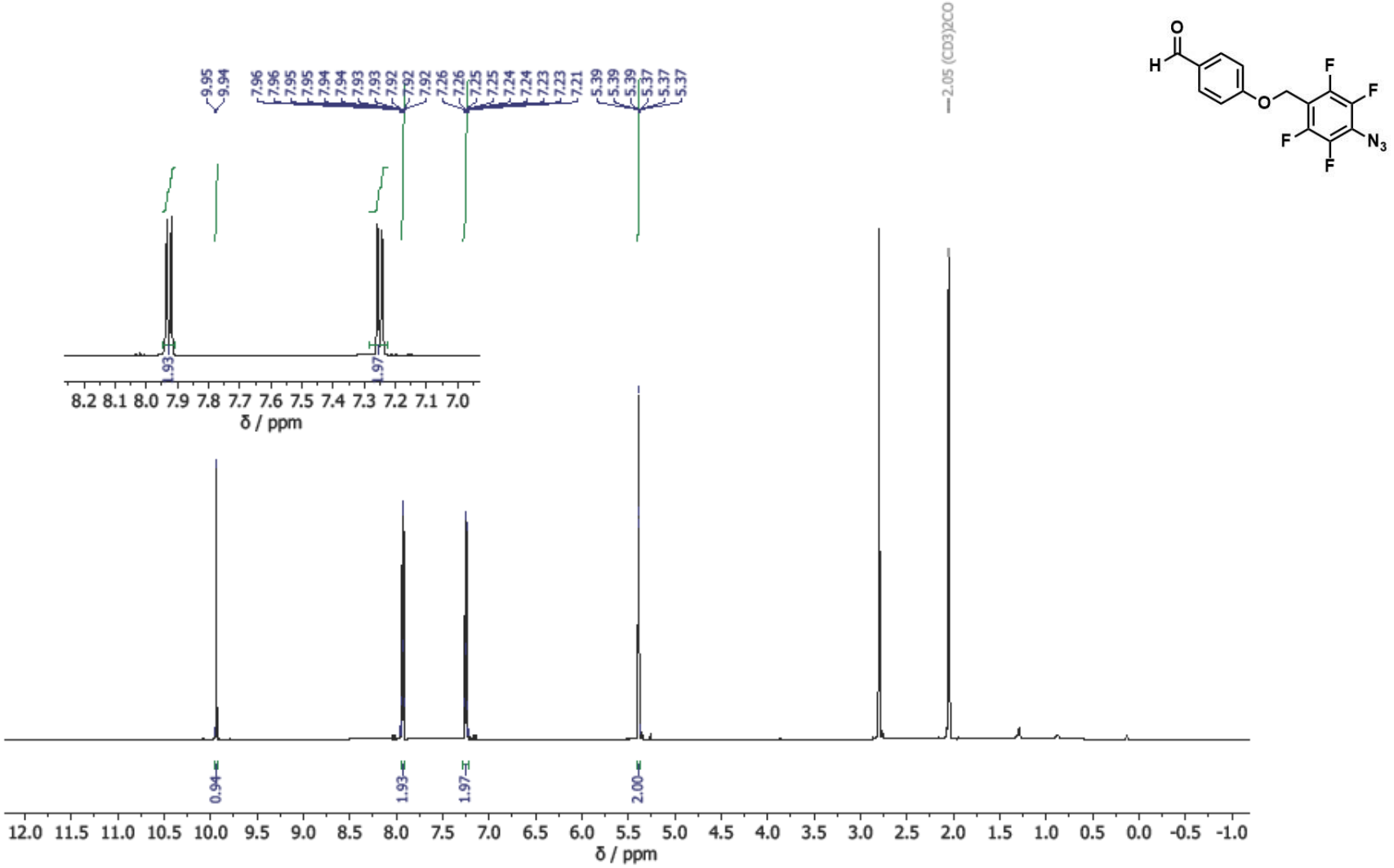

Figure A6.4: The ^{1}H NMR spectrum of 4-((4-azido-2,3,5,6-tetrafluorobenzyl)oxy)benzaldehyde **14** in acetone-d_6.

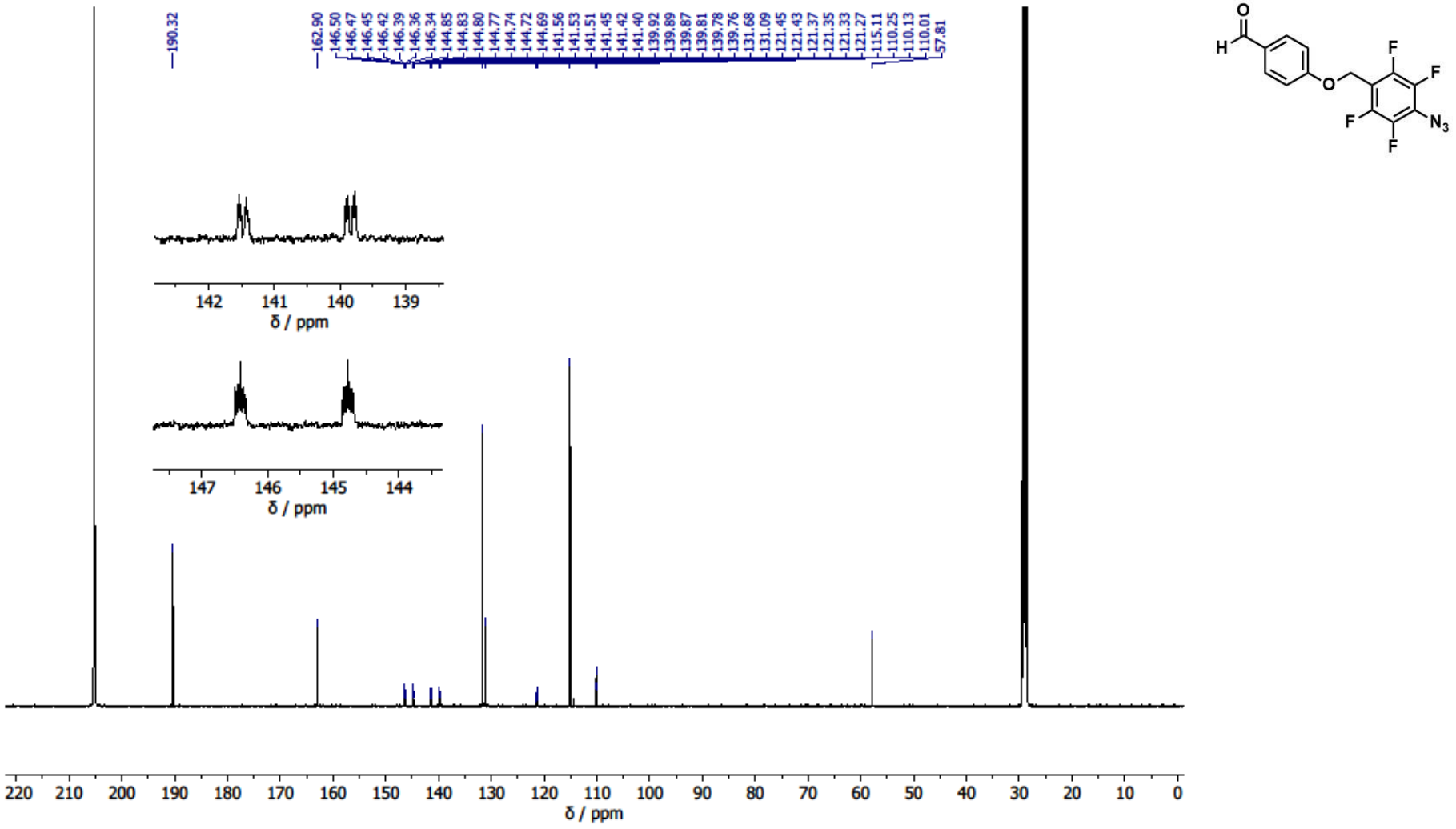

Figure A6.5: The ^{13}C NMR spectrum of 4-((4-azido-2,3,5,6-tetrafluorobenzyl)oxy)benzaldehyde **14** in acetone-d_6.

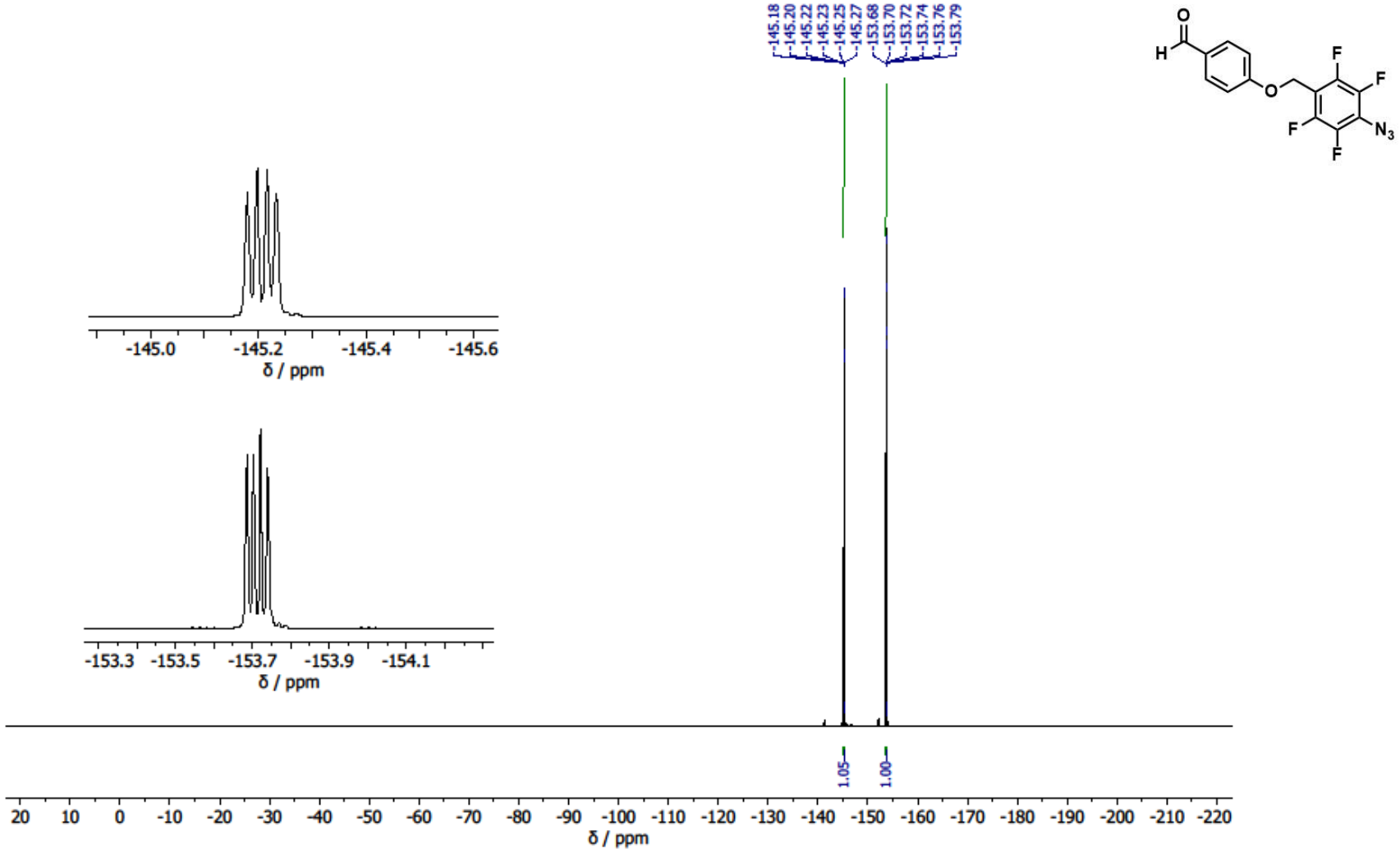

Figure A6.6: The ^{19}F NMR spectrum of 4-((4-azido-2,3,5,6-tetrafluorobenzyl)oxy)benzaldehyde **14** in acetone-d_6.

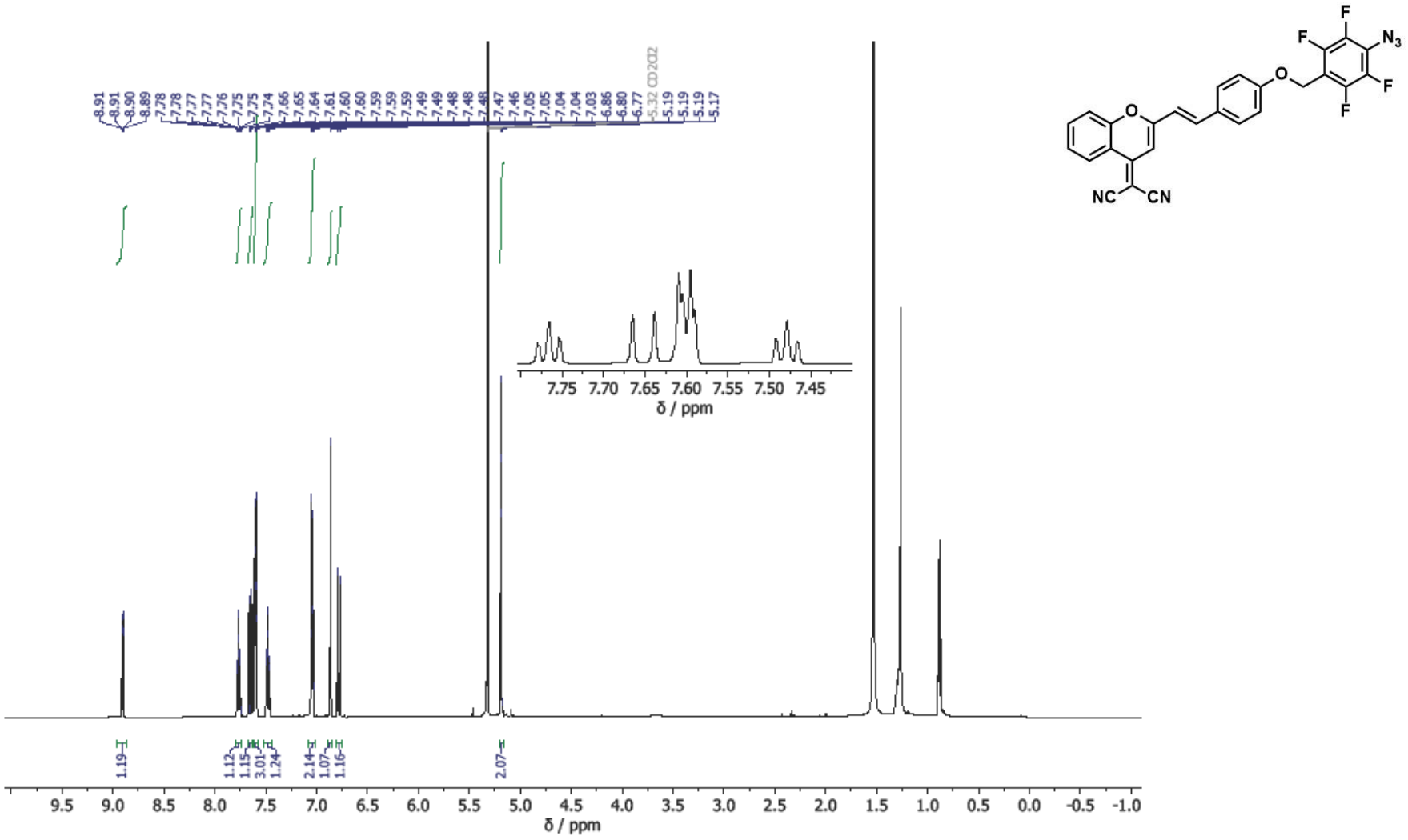

Figure A6.7: The ^{1}H spectrum of (E)-2-(2-(4-((4-azido-2,3,5,6-tetrafluorobenzyl)oxy)styryl)-4H-chromen-4-ylidene)malononitrile **3** in CD_2Cl_2.

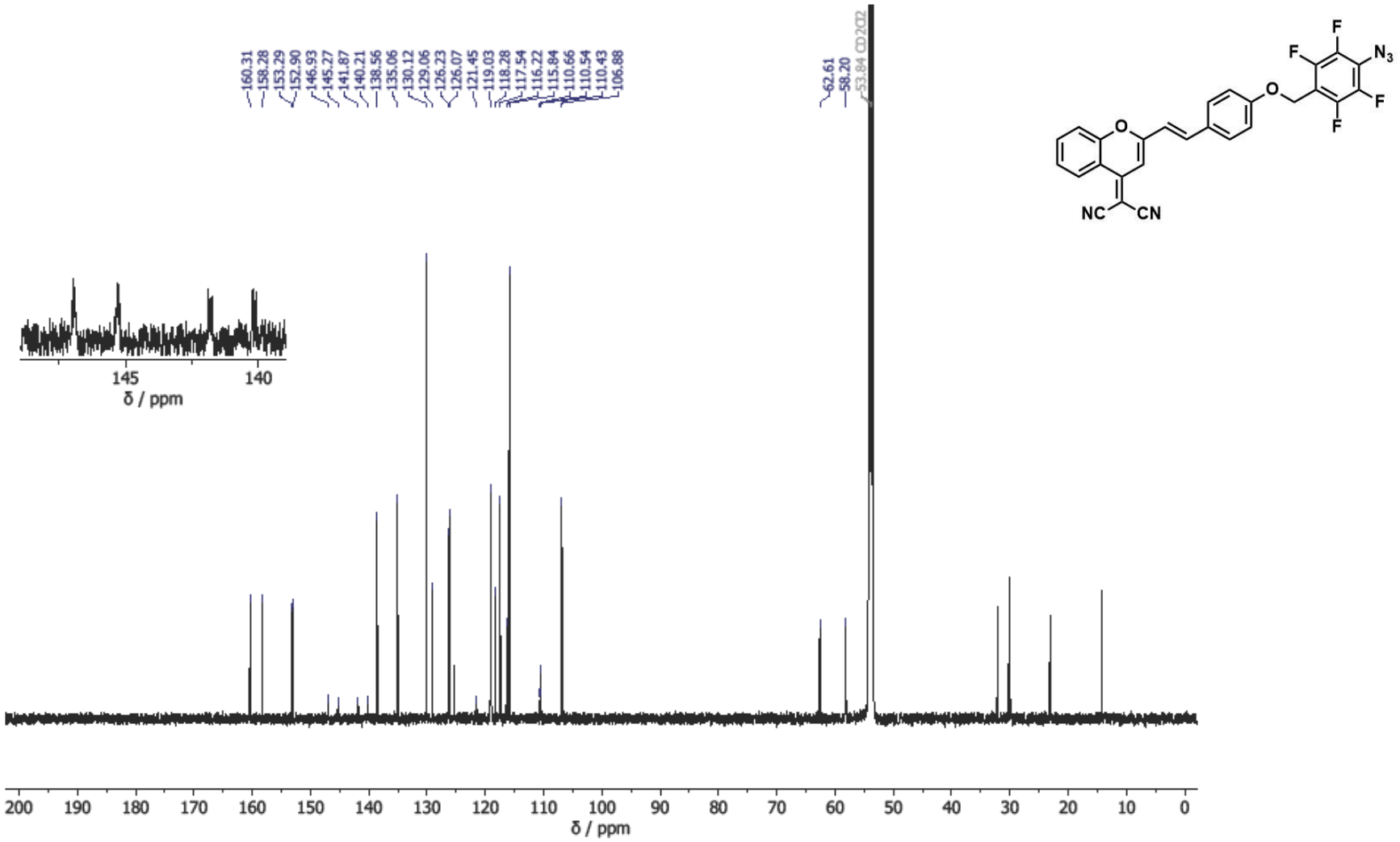

Figure A6.8: The ^{13}C spectrum of (E)-2-(2-(4-((4-azido-2,3,5,6-tetrafluorobenzyl)oxy)styryl)-4H-chromen-4-ylidene)malononitrile **3** in CD_2Cl_2.

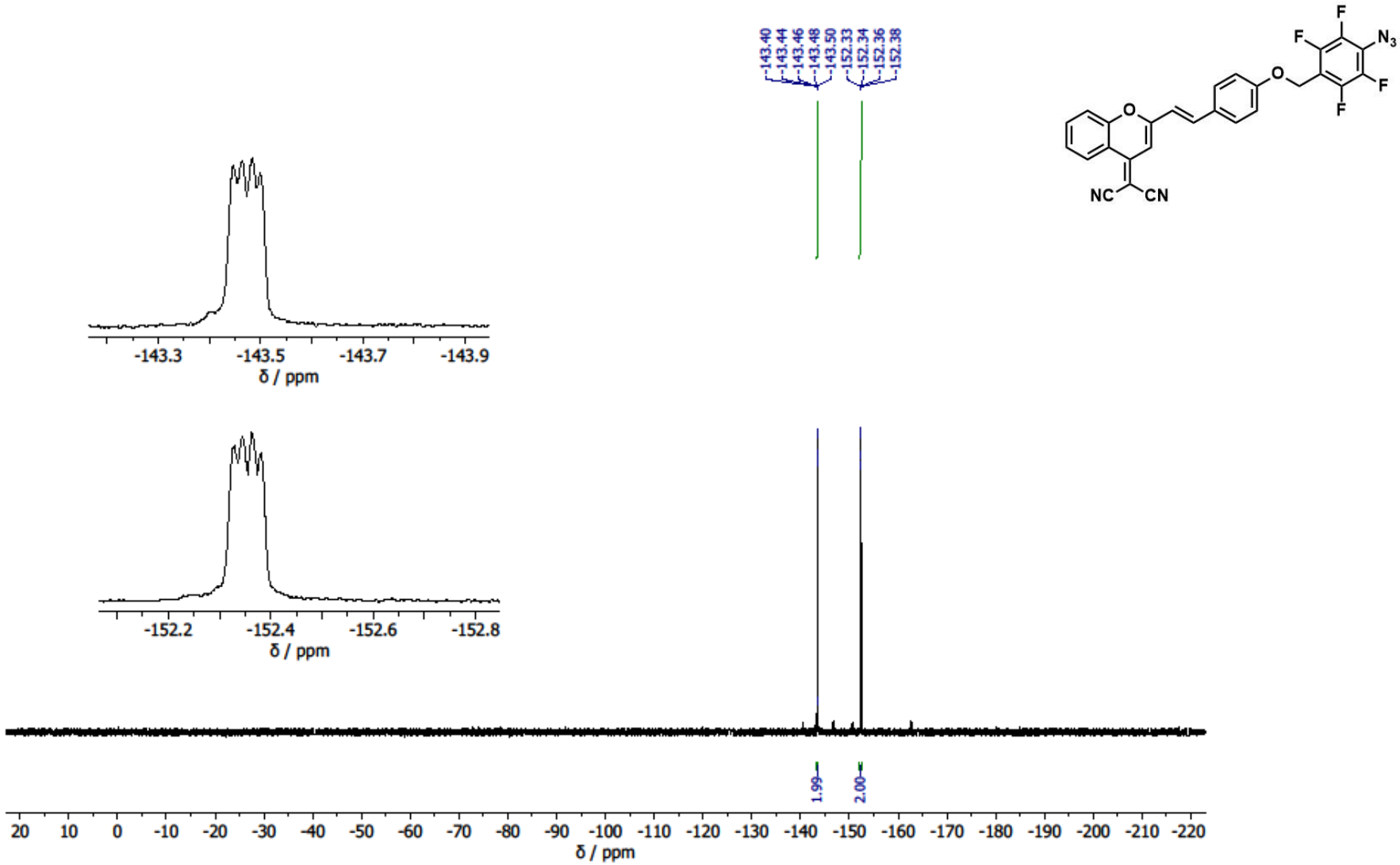

Figure A6.9: The ^{19}F spectrum of (E)-2-(2-(4-((4-azido-2,3,5,6-tetrafluorobenzyl)oxy)styryl)-4H-chromen-4-ylidene)malononitrile **3** in CD_2Cl_2.

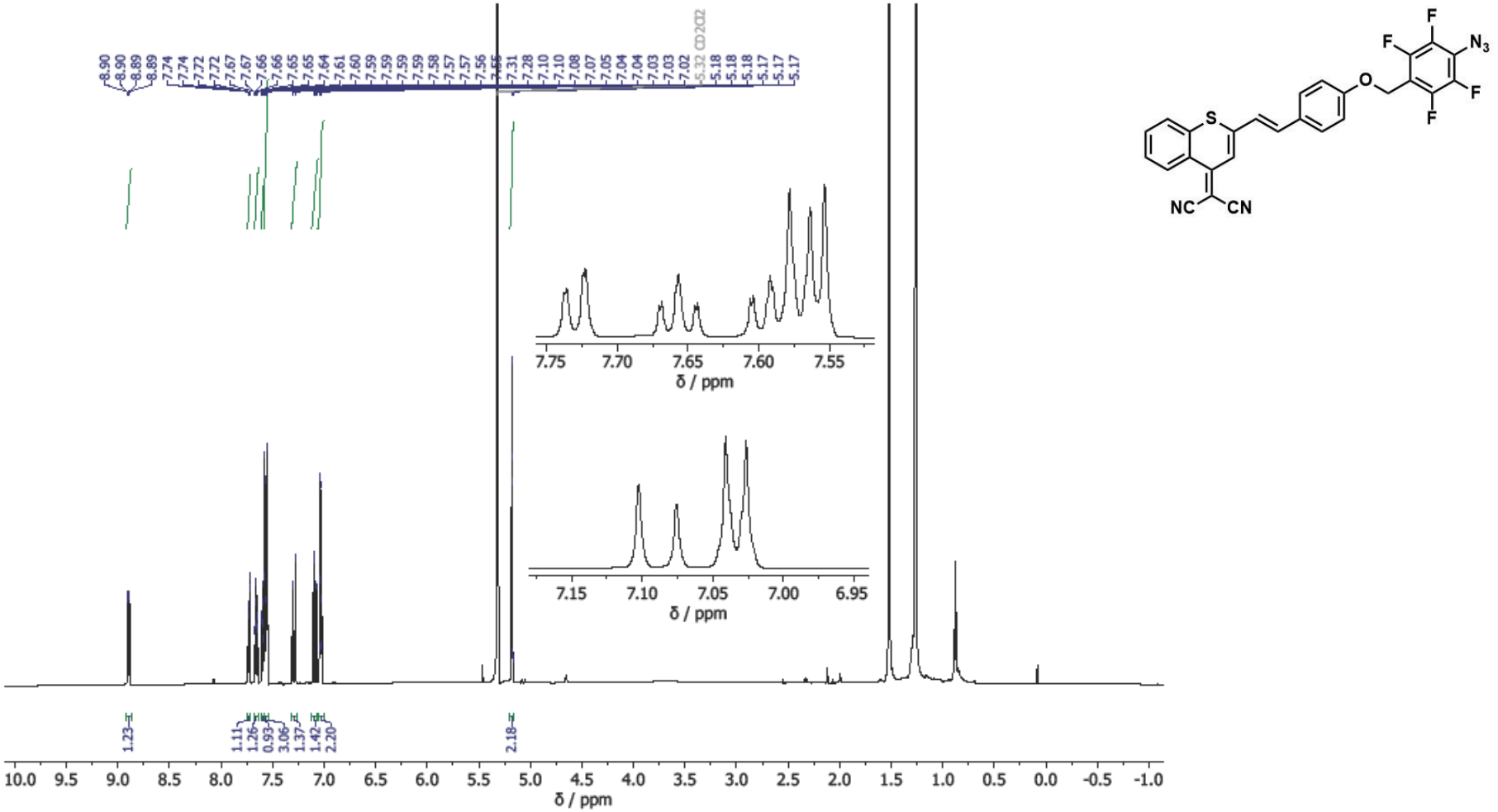

Figure A6.10: The ^{1}H NMR spectrum of (E)-2-(2-(4-((4-azido-2,3,5,6-tetrafluorobenzyl)oxy)styryl)-4H-thiochromen-4-ylidene)malononitrile **4** in CD_2Cl_2.

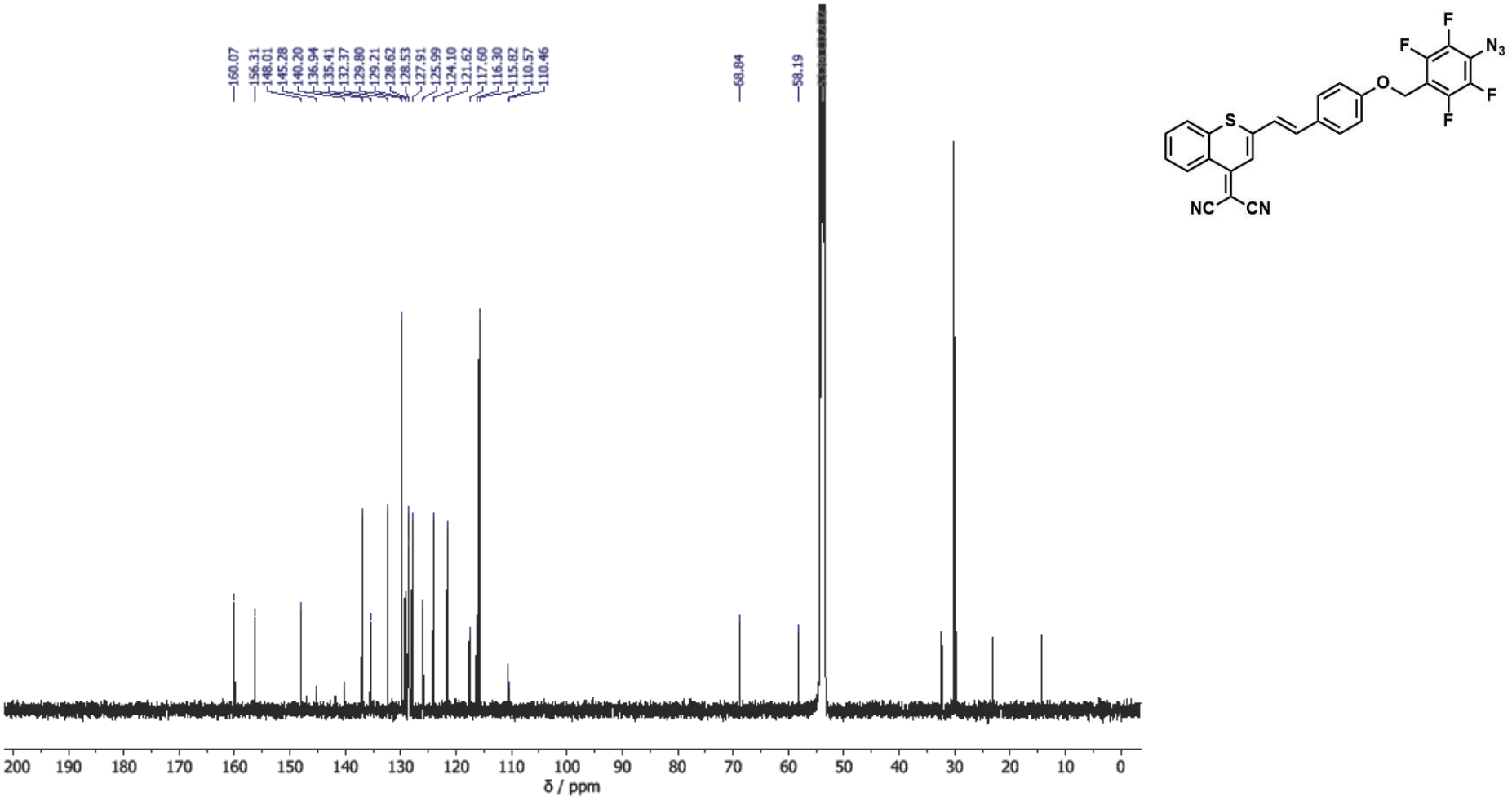

Figure A6.11: The ^{13}C NMR spectrum of (E)-2-(2-(4-((4-azido-2,3,5,6-tetrafluorobenzyl)oxy)styryl)-4H-thiochromen-4-ylidene)malononitrile **4** in CD_2Cl_2.

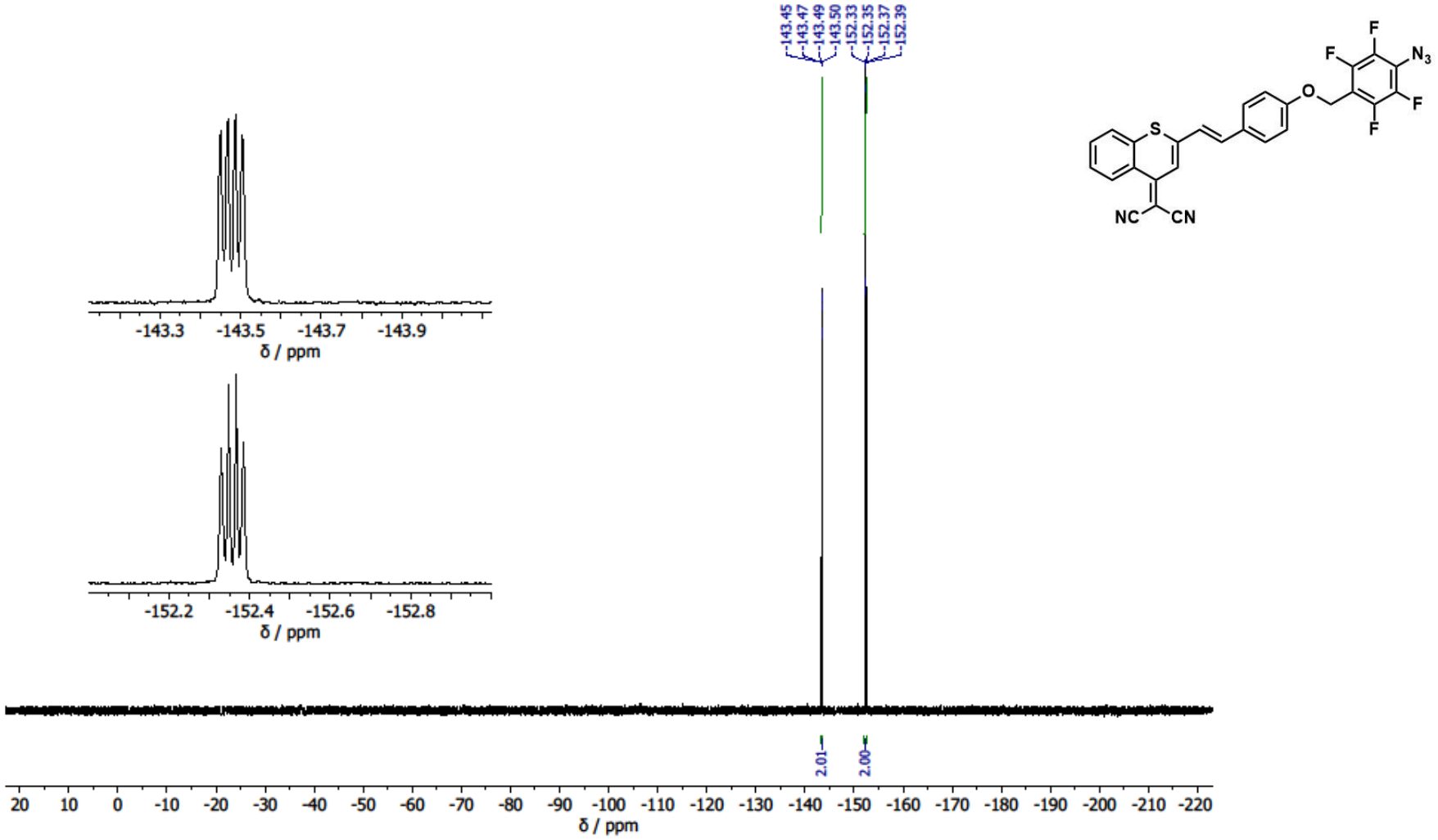

Figure A6.12: The ^{19}F NMR spectrum of (E)-2-(2-(4-((4-azido-2,3,5,6-tetrafluorobenzyl)oxy)styryl)-4H-thiochromen-4-ylidene)malononitrile **4** in CD_2Cl_2.

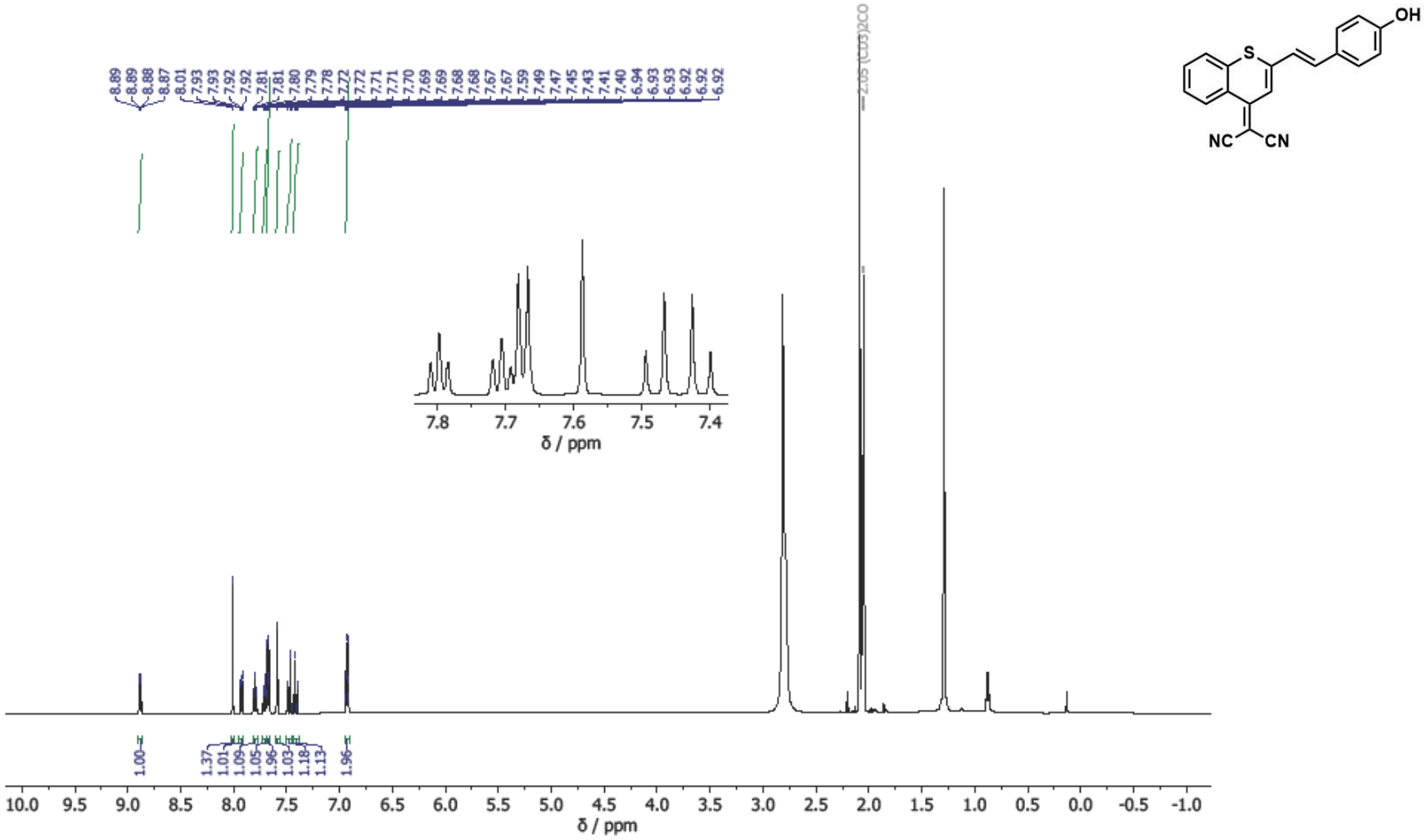

Figure A6.13: The ^{1}H NMR spectrum of (E)-2-(2-(4-hydroxystyryl)-4H-thiochromen-4-ylidene)malononitrile **6** in acetone-d_6.

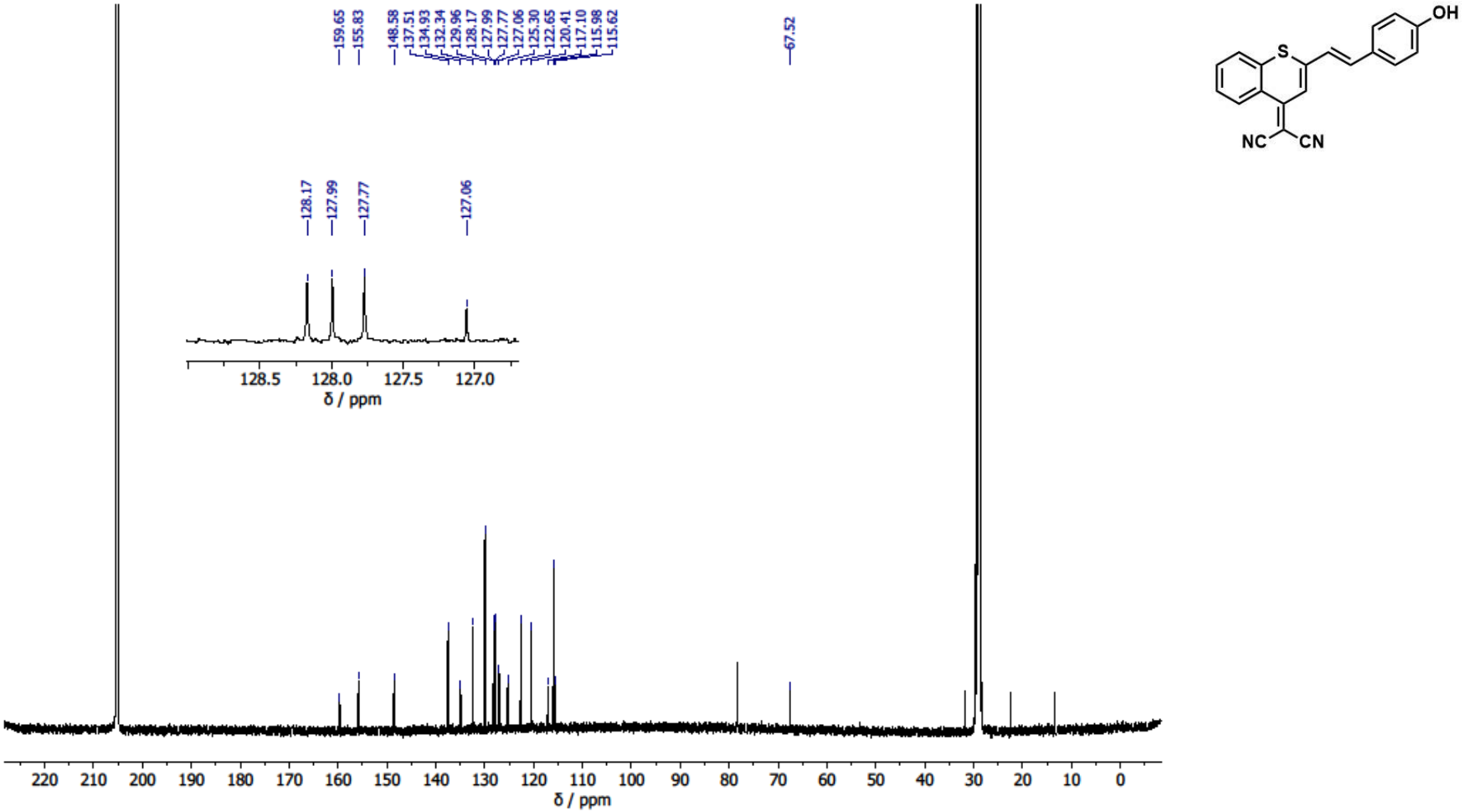

Figure A6.14: The ^{13}C NMR spectrum of (E)-2-(2-(4-hydroxystyryl)-4H-thiochromen-4-ylidene)malononitrile **6** in acetone-d_6.

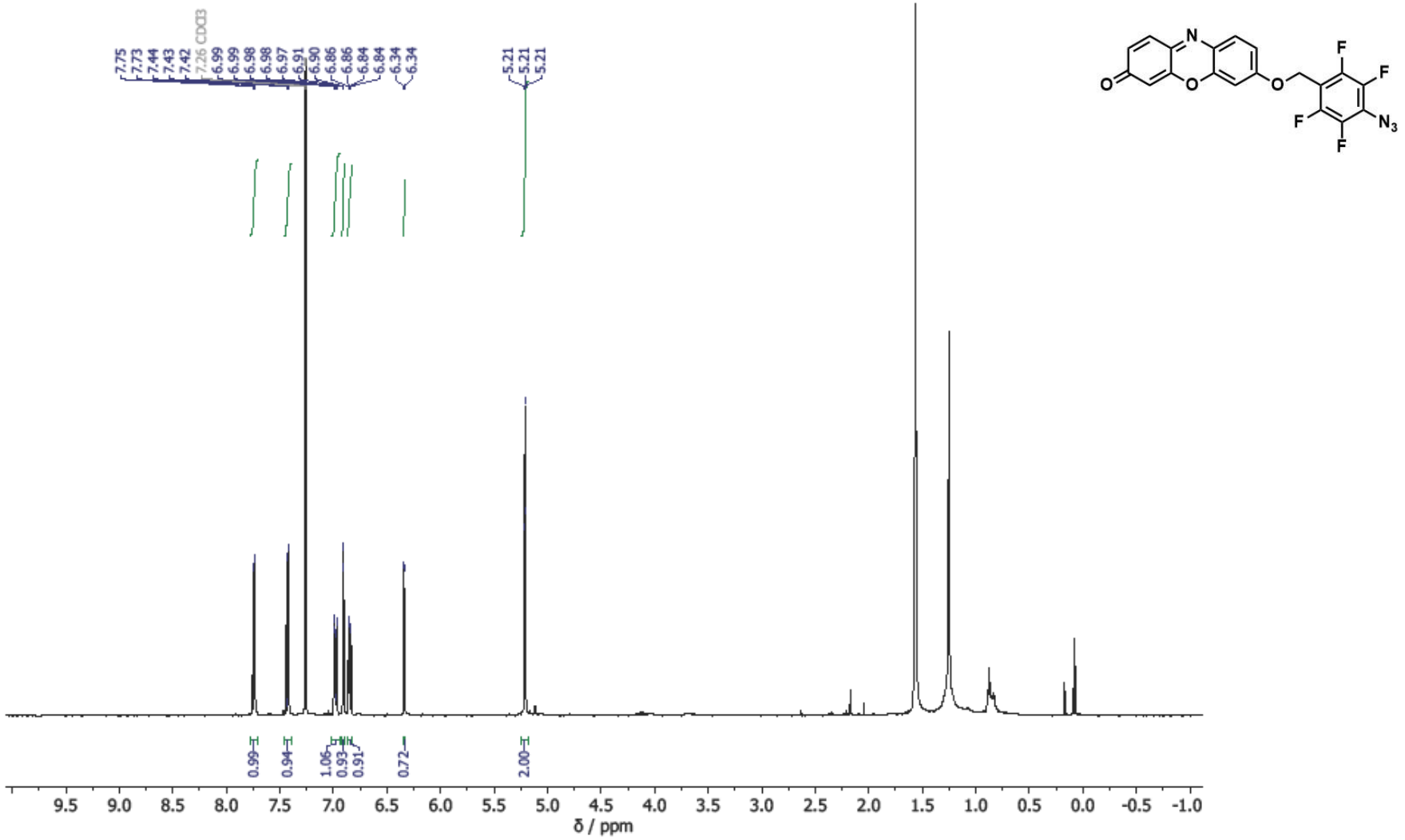

Figure A6.15: The ^{1}H NMR spectrum of 7-((4-azido-2,3,5,6-tetrafluorobenzyl)oxy)-3H-phenoxazin-3-one **15** in $CDCl_3$.

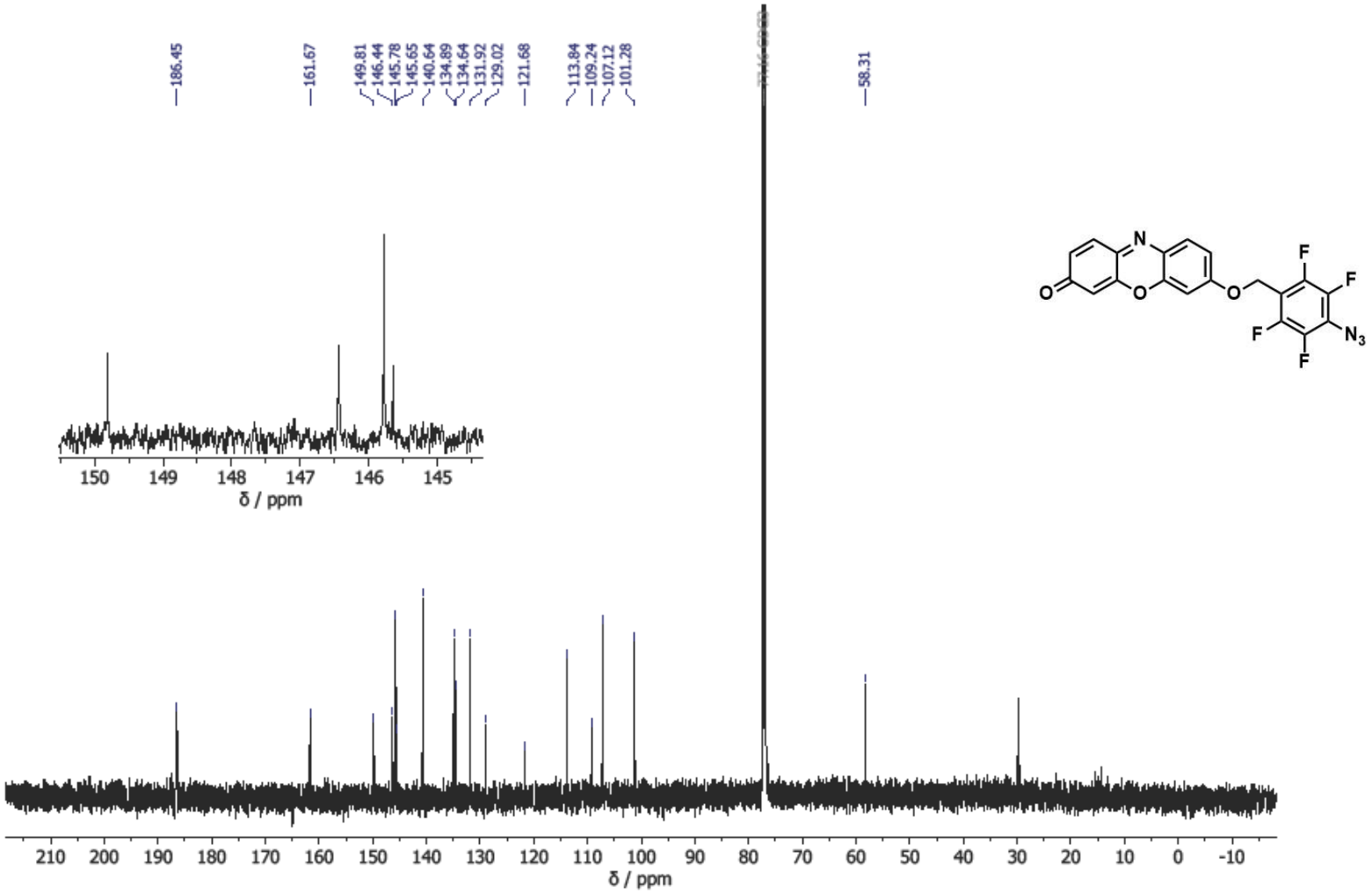

Figure A6.16: The ^{13}C NMR spectrum of 7-((4-azido-2,3,5,6-tetrafluorobenzyl)oxy)-3H-phenoxazin-3-one **15** in $CDCl_3$.

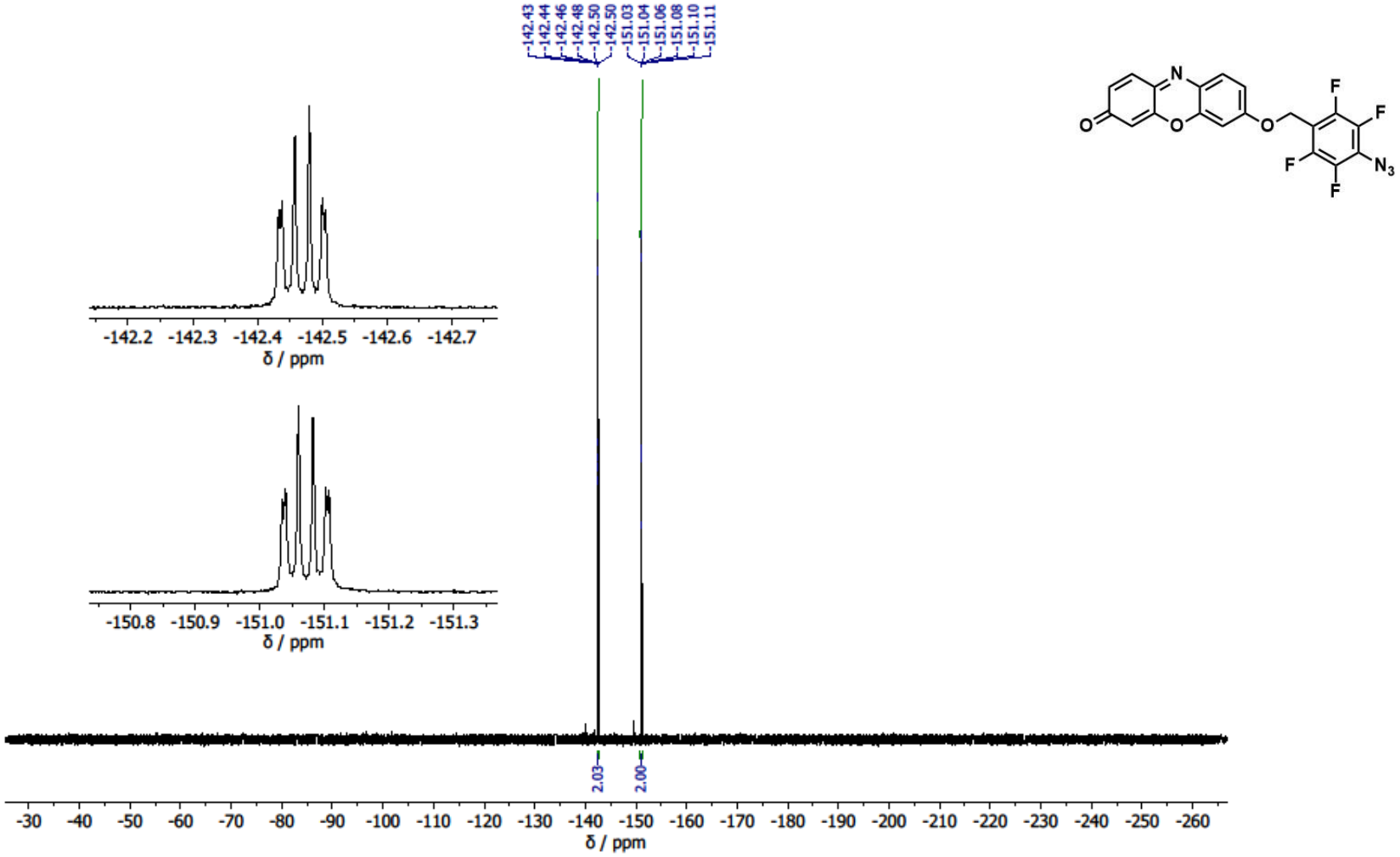

Figure A6.17: The ^{19}F NMR spectrum of 7-((4-azido-2,3,5,6-tetrafluorobenzyl)oxy)-3H-phenoxazin-3-one **15** in $CDCl_3$.

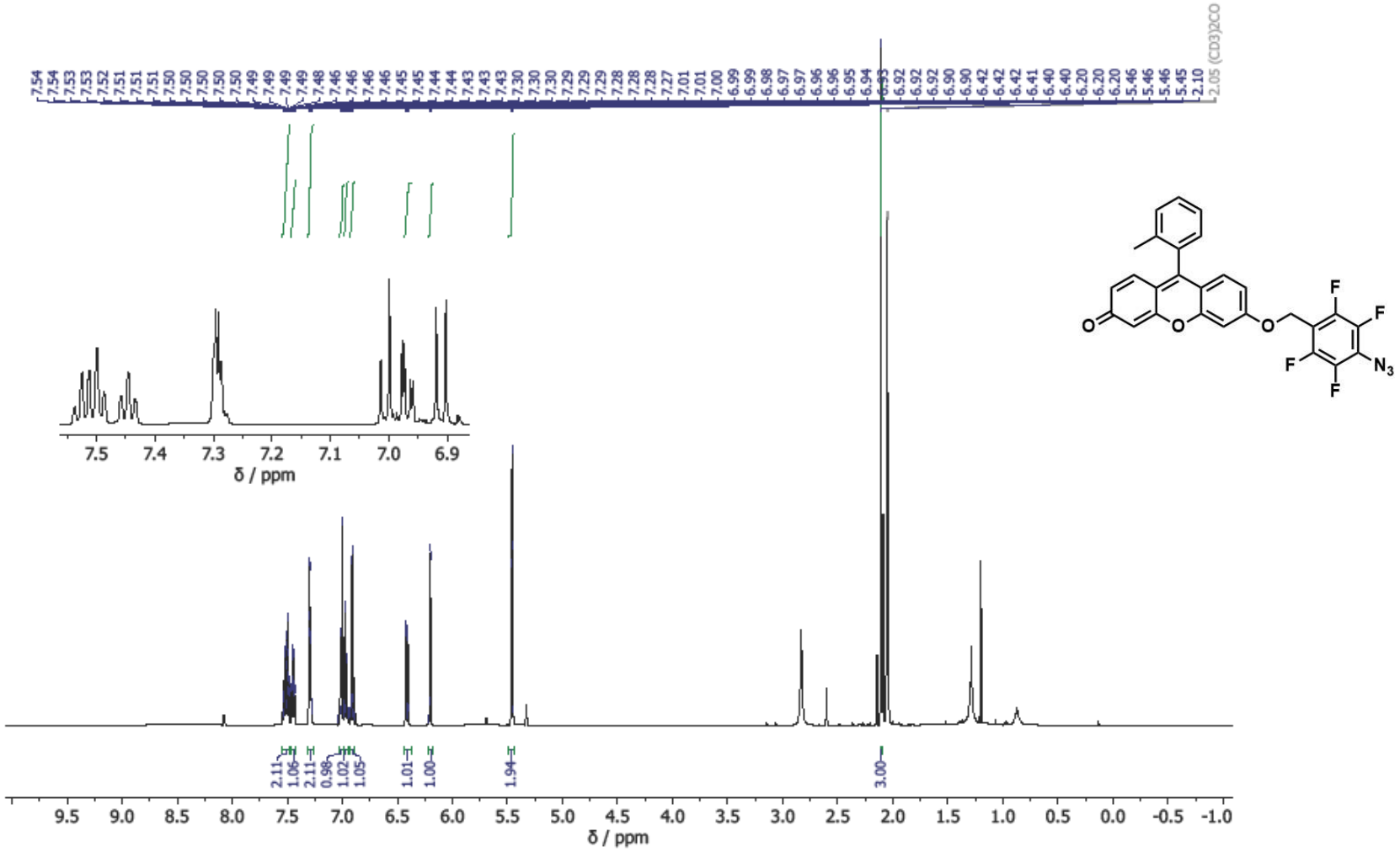

Figure A6.18: The ^{1}H NMR spectrum of 6-((4-azido-2,3,5,6-tetrafluorobenzyl)oxy)-9-(o-tolyl)-3H-xanthen-3-one **16** in acetone-d_6.

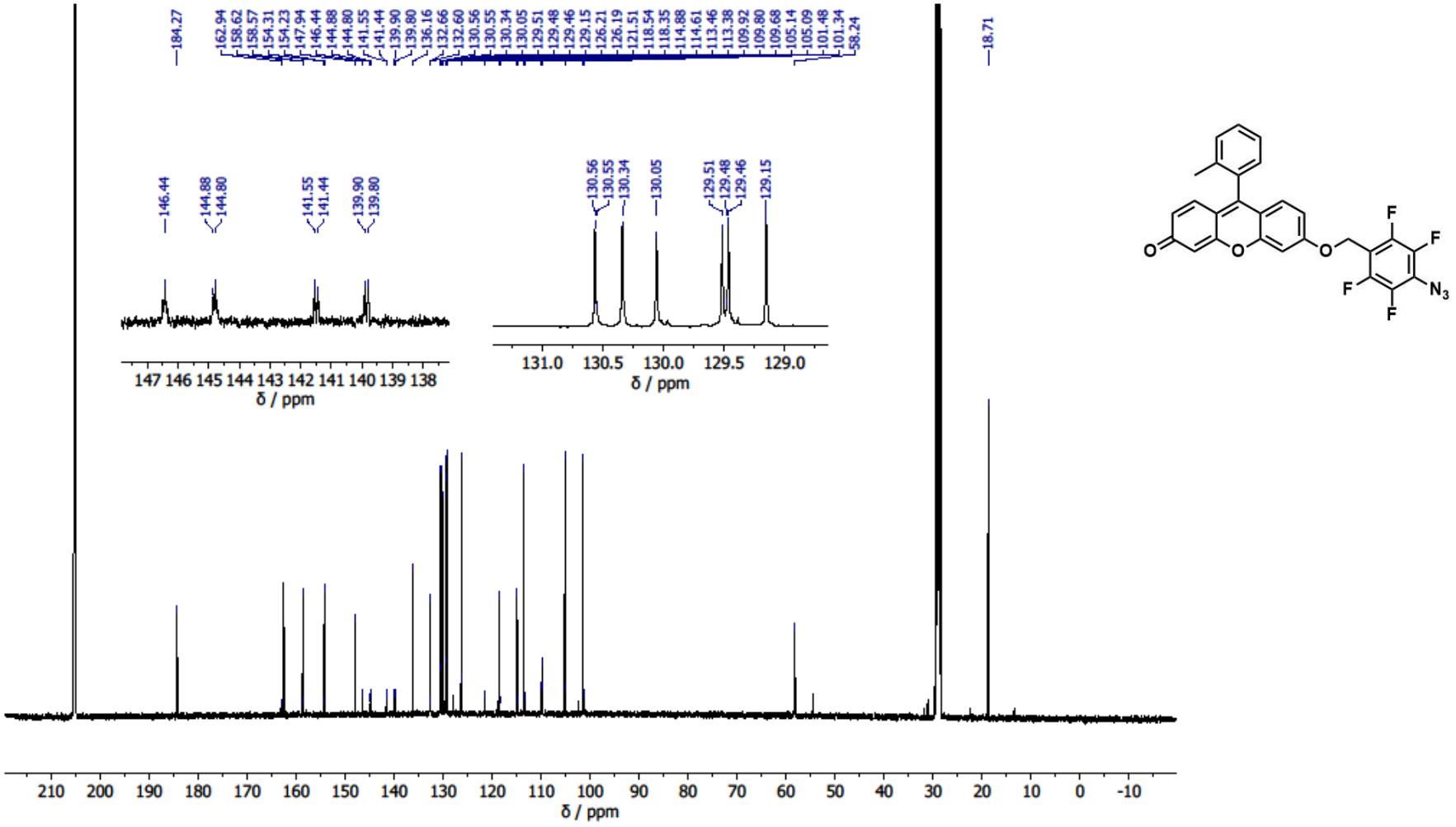

Figure A6.19: The ^{13}C NMR spectrum of 6-((4-azido-2,3,5,6-tetrafluorobenzyl)oxy)-9-(o-tolyl)-3H-xanthen-3-one **16** in acetone-d_6.

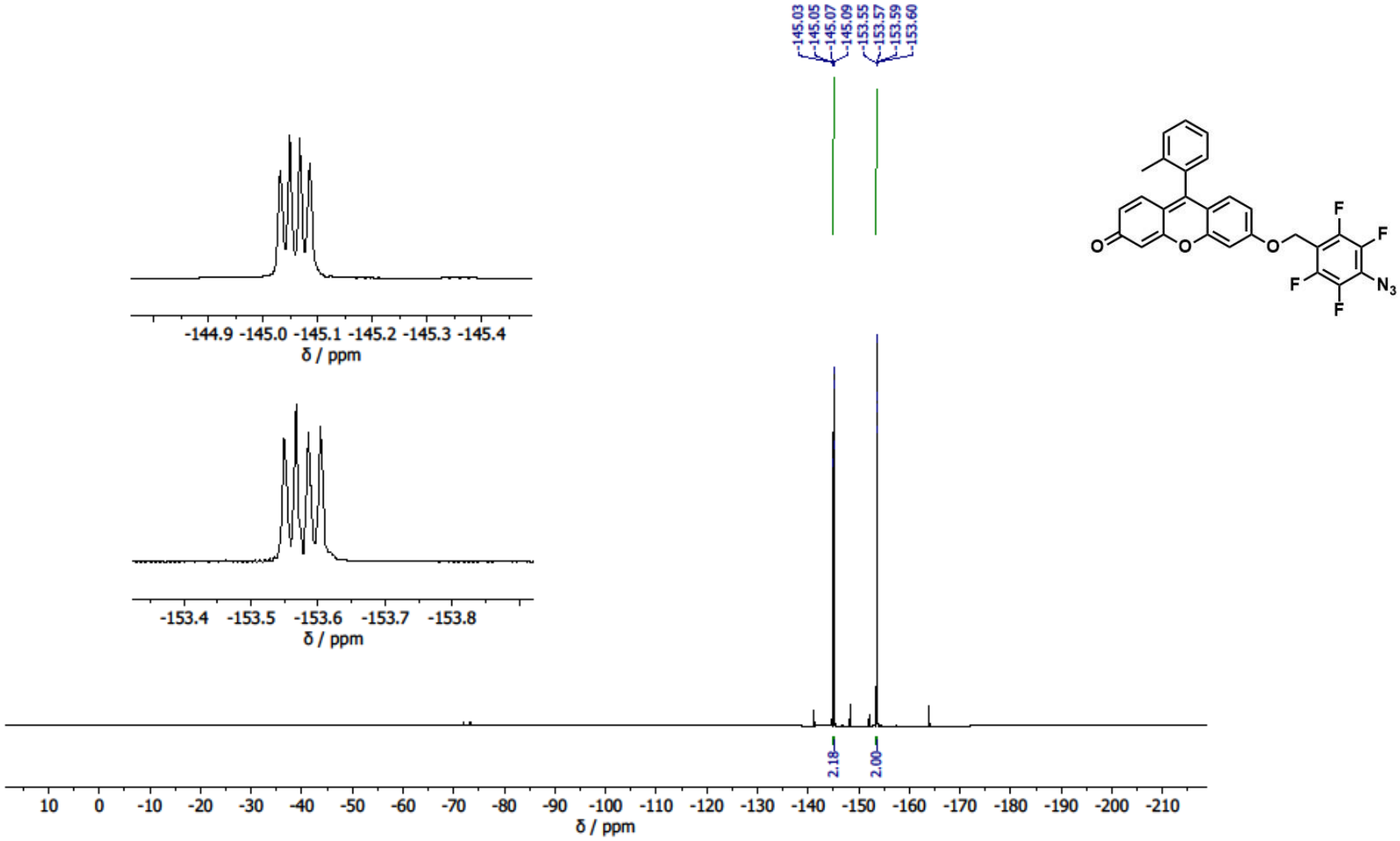

Figure A6.20: The ^{19}F NMR spectrum of 6-((4-azido-2,3,5,6-tetrafluorobenzyl)oxy)-9-(o-tolyl)-3H-xanthen-3-one **16** in acetone-d_6.

A2.3 Compounds from chapter III

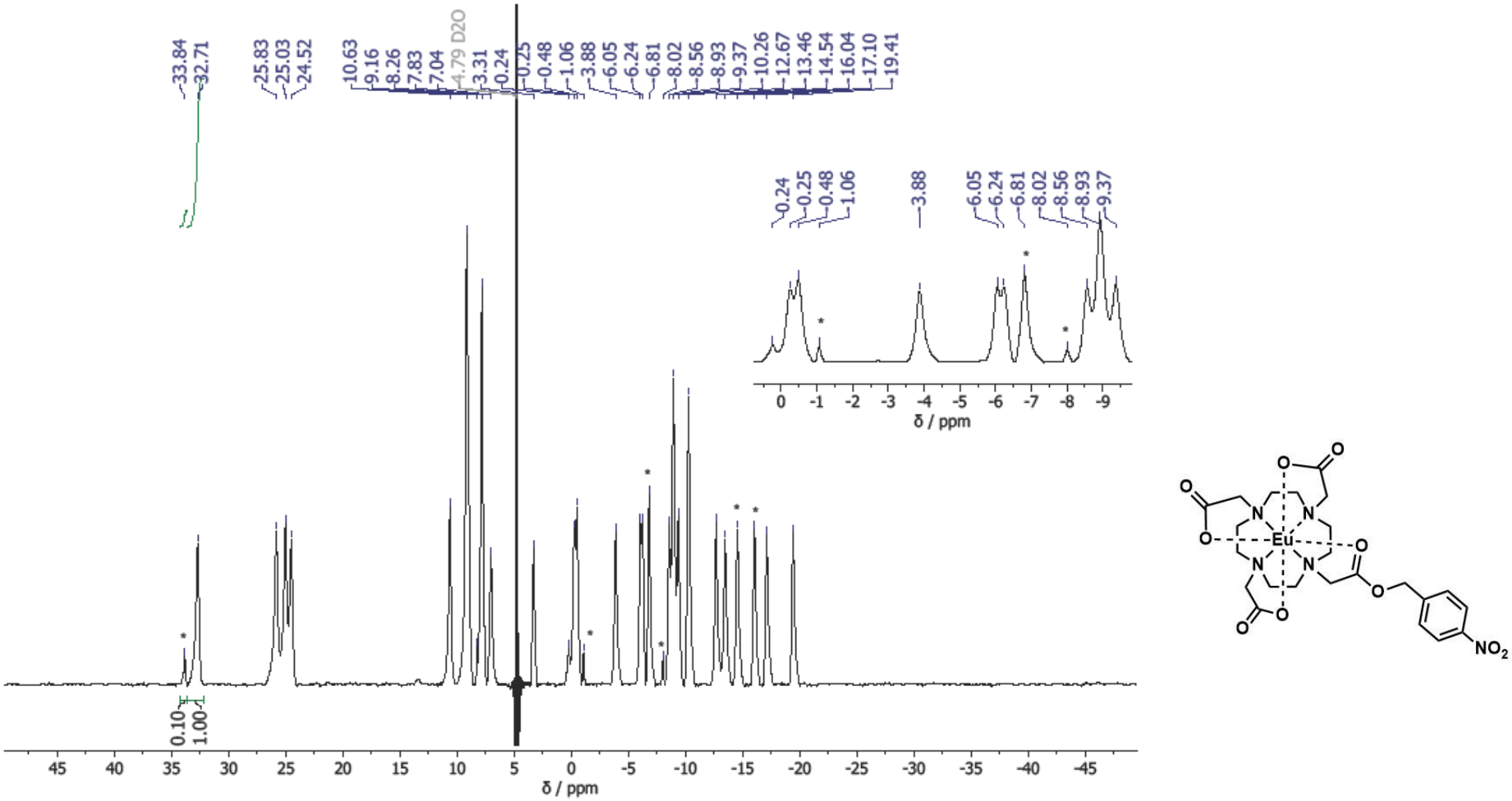

Figure A6.21: The ^{1}H (for europium complexes) NMR spectrum (400 MHz) of EuNB **1*8*a** in D_2O. The stars represent peaks which may arise due to the presence of EuDOTA as an impurity. The integrals suggest that ~2% EuDOTA is present (assuming the EuDOTA peak contains 4 protons due to symmetry and the EuNB peak contains 1 proton).

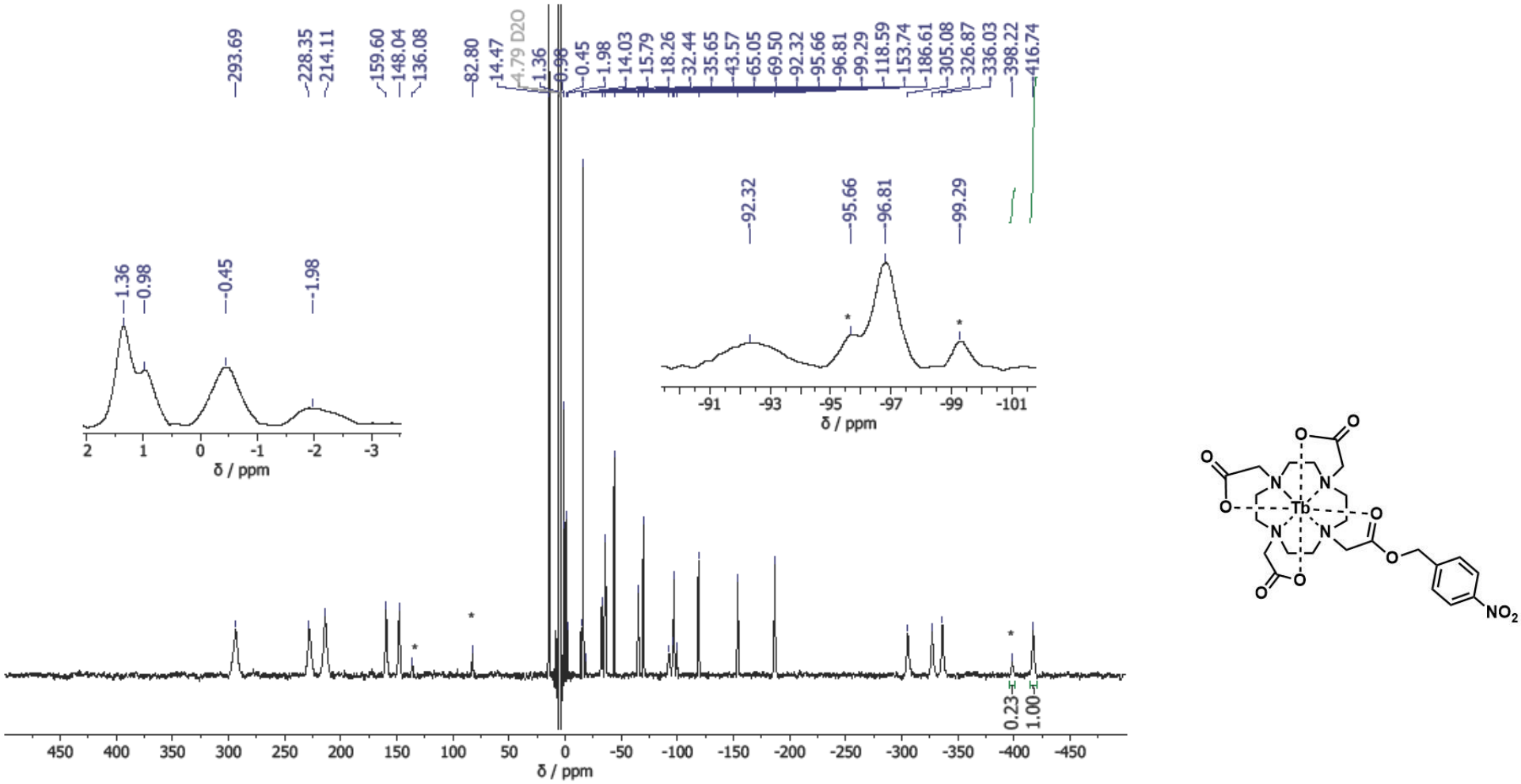

Figure A6.22: The ^{1}H (for terbium complexes) NMR spectrum (400 MHz) of TbNB **18b** in D_2O. The stars represent peaks which may arise due to the presence of TbDOTA as an impurity. The integrals suggest that ~5% TbDOTA is present (assuming the TbDOTA peak contains 4 protons due to symmetry and the TbNB peak contains 1 proton).

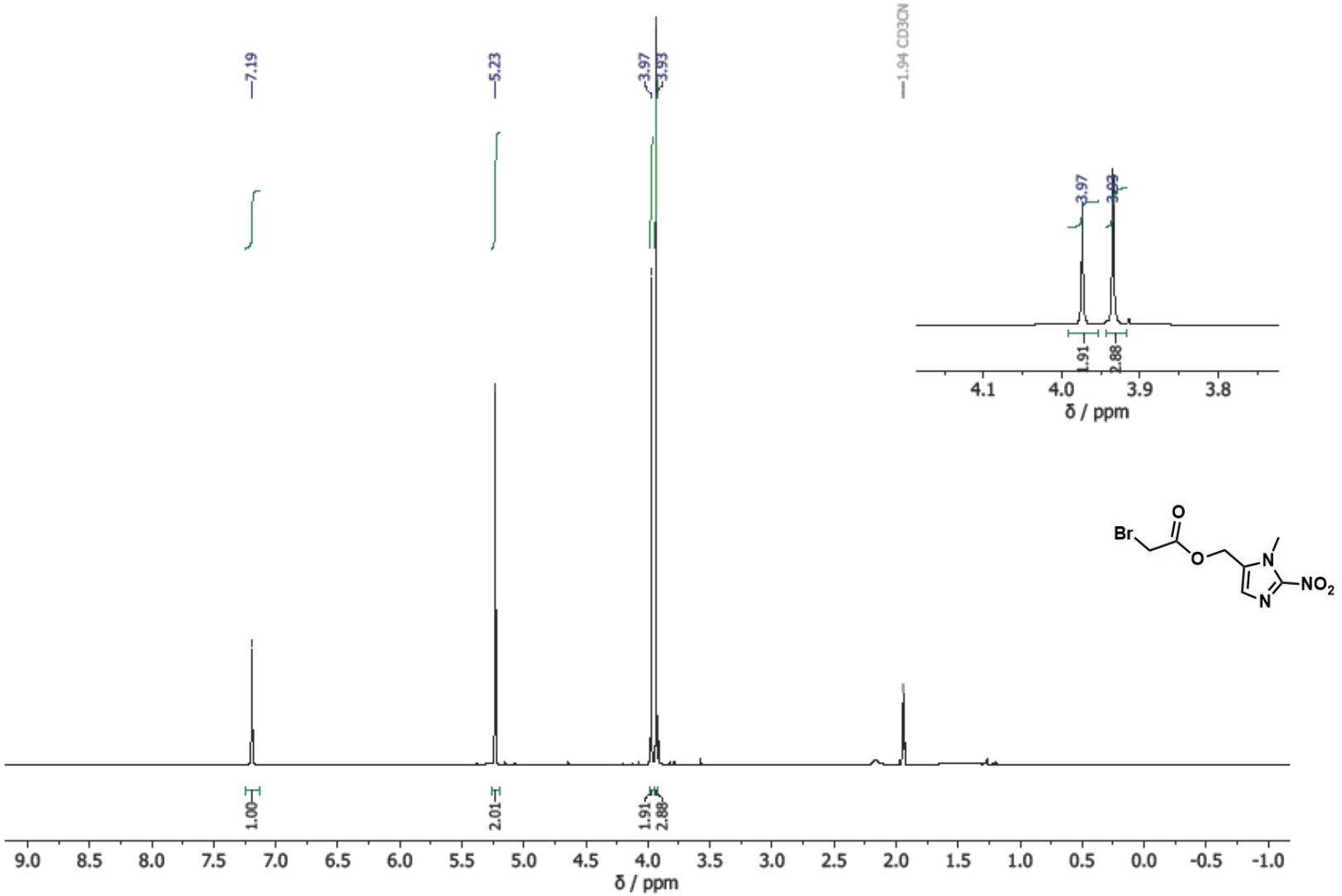

Figure A6.23: The ^{1}H NMR spectrum (600 MHz) of (1-methyl-2-nitro-1H-imidazol-5-yl)methyl 2-bromoacetate **30** in CD_3CN.

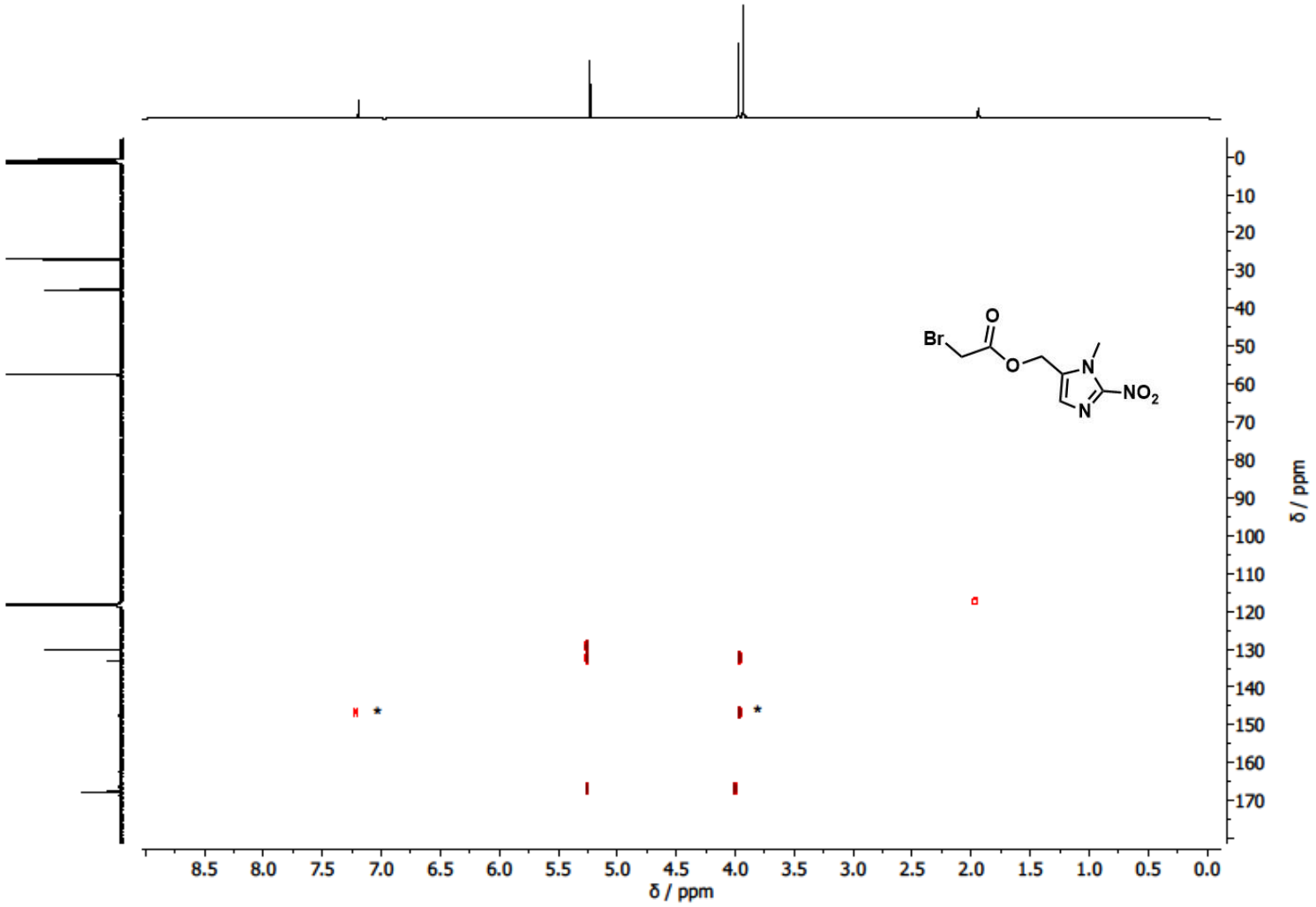

Figure A6.24: The HMBC NMR spectrum of (1-methyl-2-nitro-1H-imidazol-5-yl)methyl 2-bromoacetate **30** in CD_3CN, to prove the presence of the low intensity peaks in the ^{13}C NMR spectrum (highlighted with an asterisk).

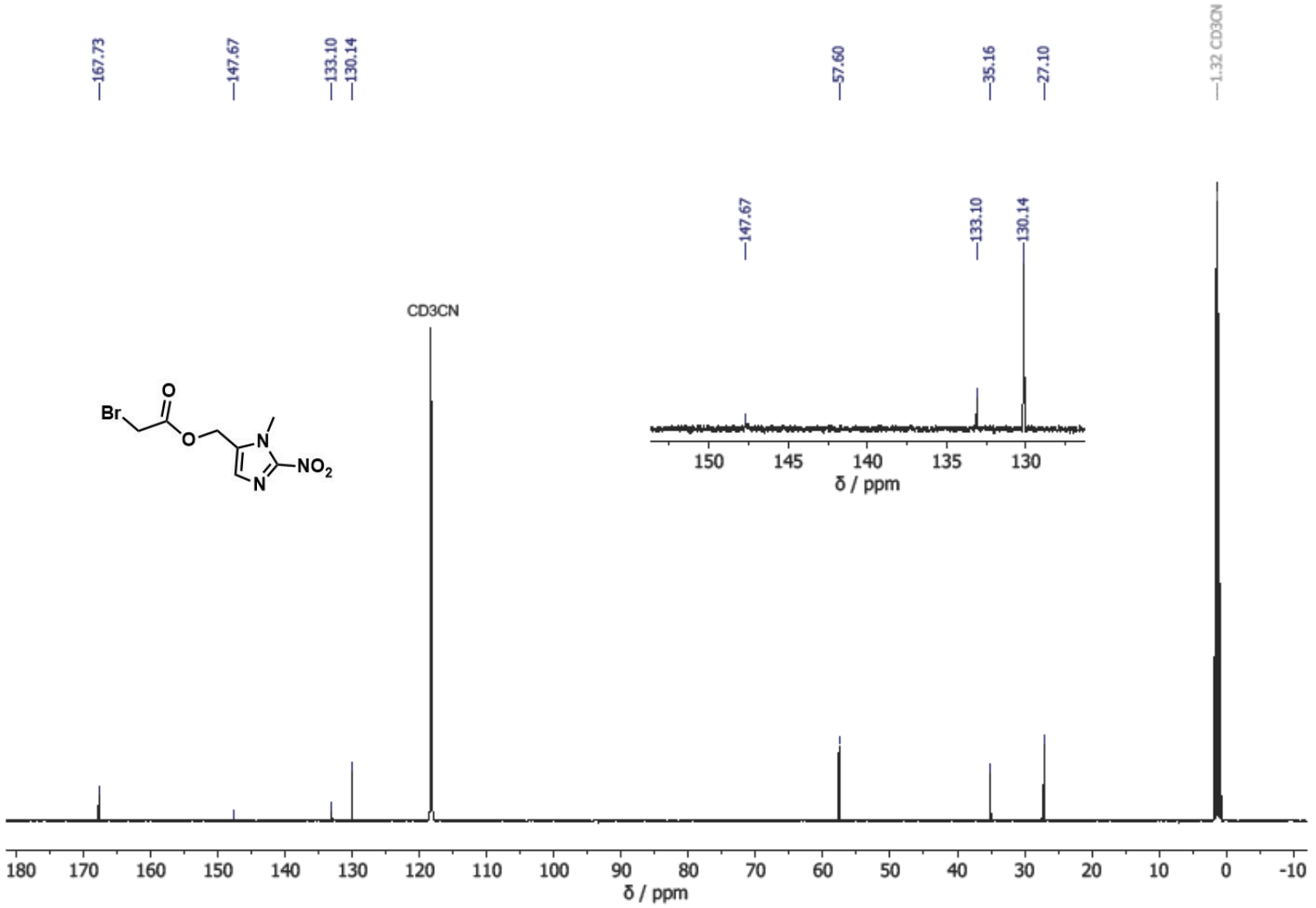

Figure A6.25: The ^{13}C NMR (151 MHz) spectrum of (1-methyl-2-nitro-1H-imidazol-5-yl)methyl 2-bromoacetate **30** in CD_3CN.

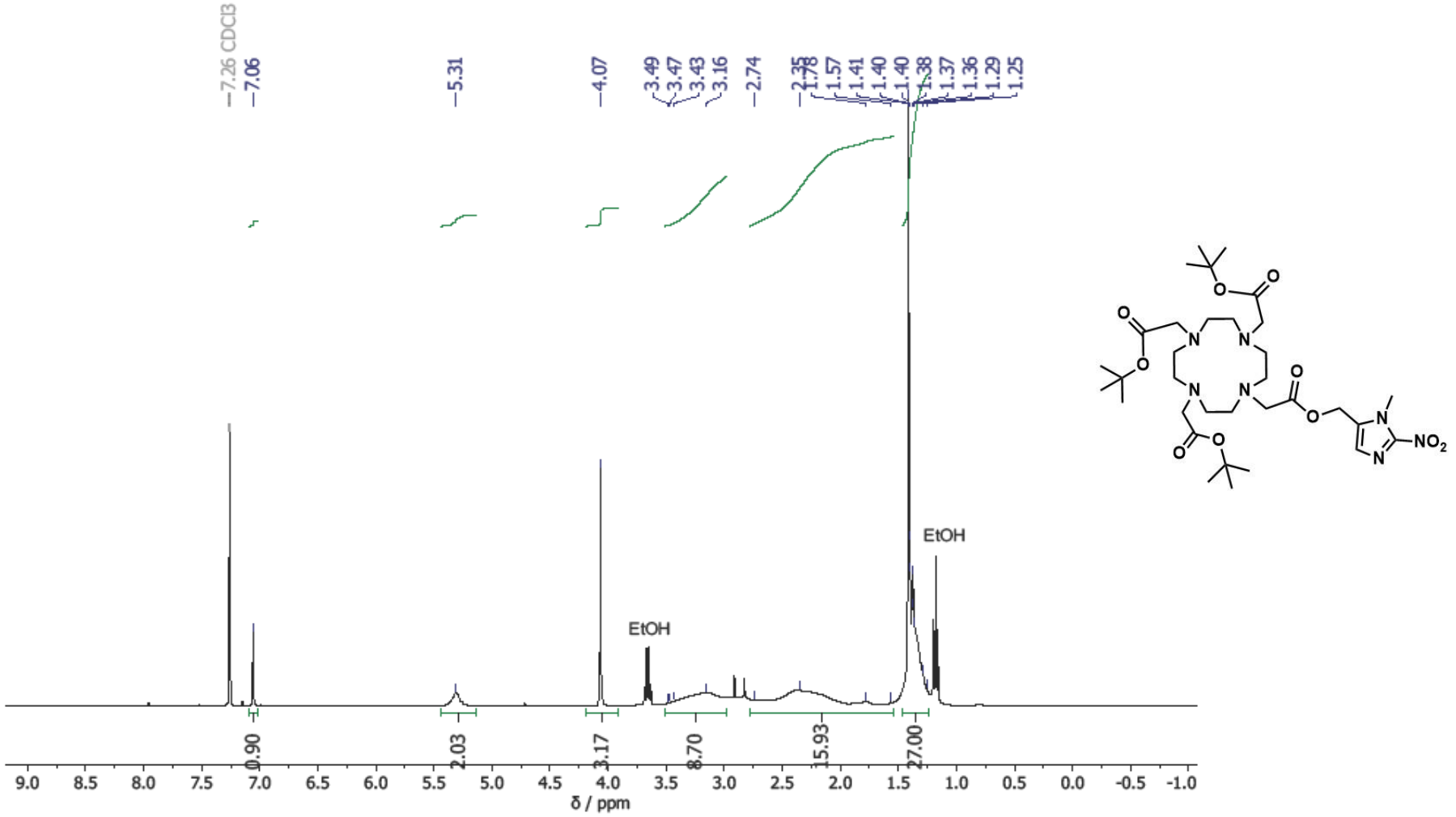

Figure A6.26: The ^{1}H NMR spectrum (400 MHz) of tri-tert-butyl 2,2',2''-(10-(2-((1-methyl-2-nitro-1H-imidazol-5-yl)methoxy)-2-oxoethyl)-1,4,7,10-tetraazacyclododecane-1,4,7-triyl)triacetate **31** in $CDCl_3$.

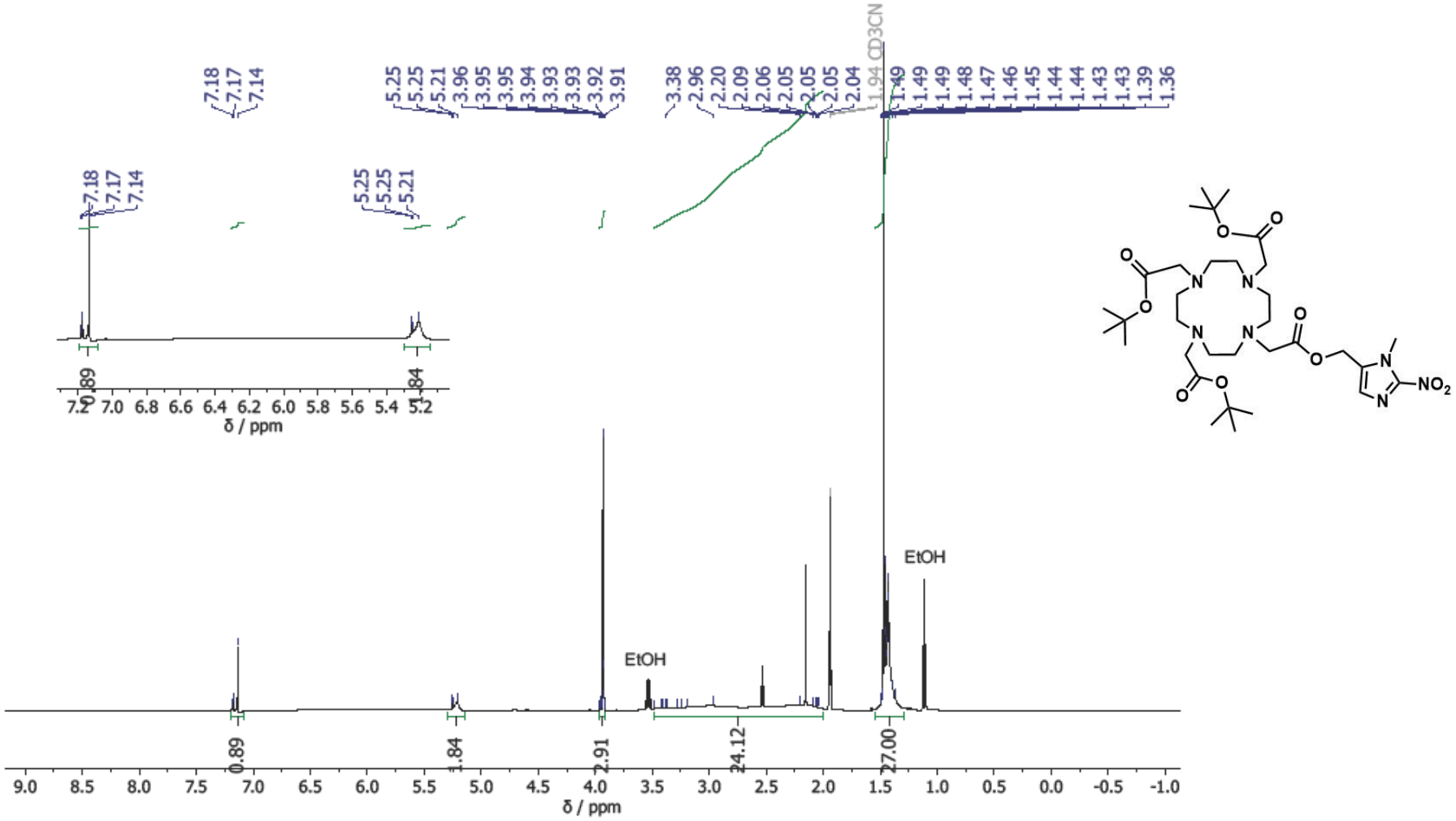

Figure A6.27*:* The ^{1}H NMR spectrum (600 MHz) of tri-tert-butyl 2,2',2''-(10-(2-((1-methyl-2-nitro-1H-imidazol-5-yl)methoxy)-2-oxoethyl)-1,4,7,10-tetraazacyclododecane-1,4,7-triyl)triacetate **31** in CD_3CN.

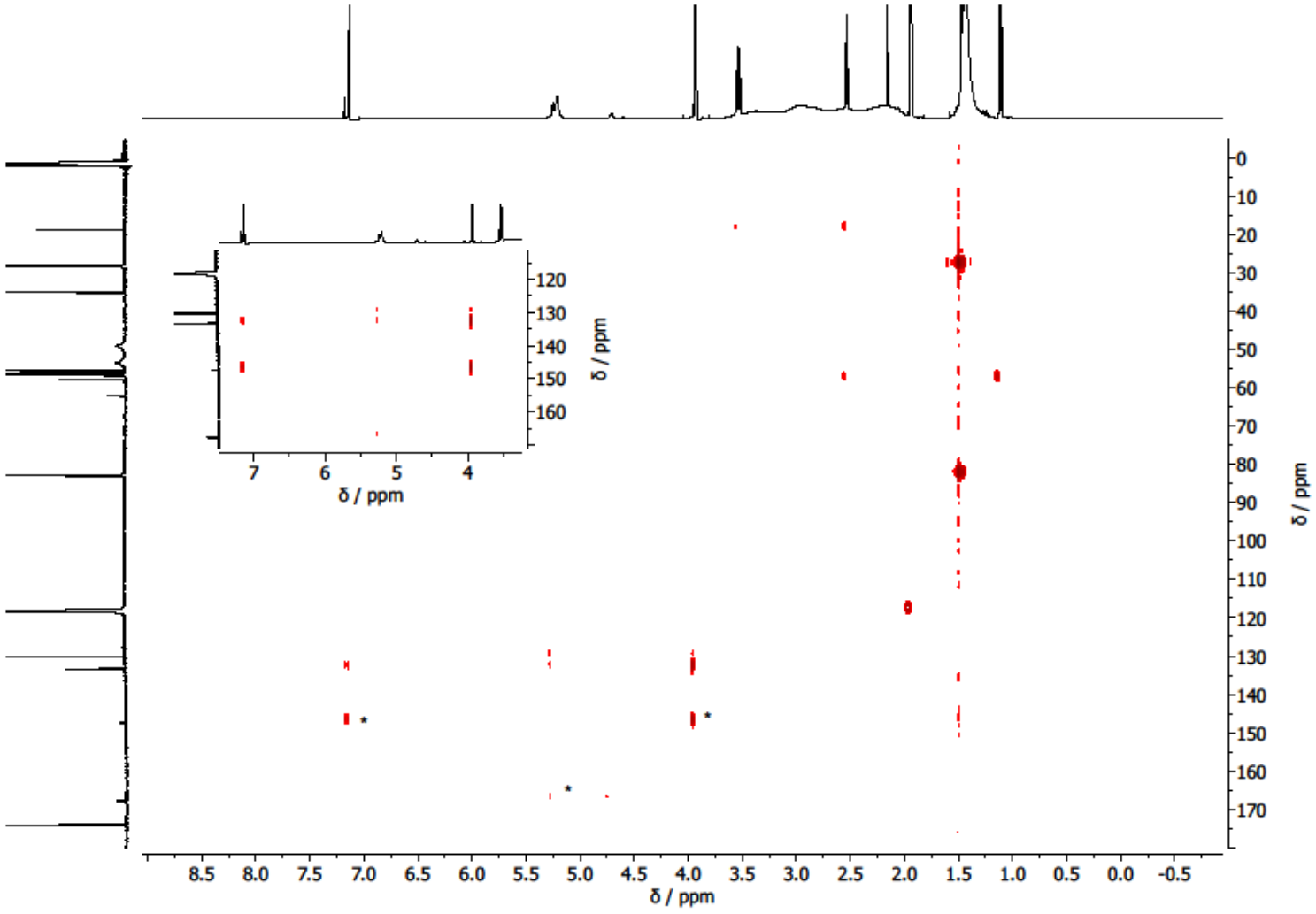

Figure A6.28: The HMBC NMR spectrum of tri-tert-butyl 2,2',2''-(10-(2-((1-methyl-2-nitro-1H-imidazol-5-yl)methoxy)-2-oxoethyl)-1,4,7,10-tetraazacyclododecane-1,4,7-triyl)triacetate **31** in CD_3CN, to prove the presence of the low intensity peaks in the ^{13}C NMR spectrum (highlighted with an asterisk).

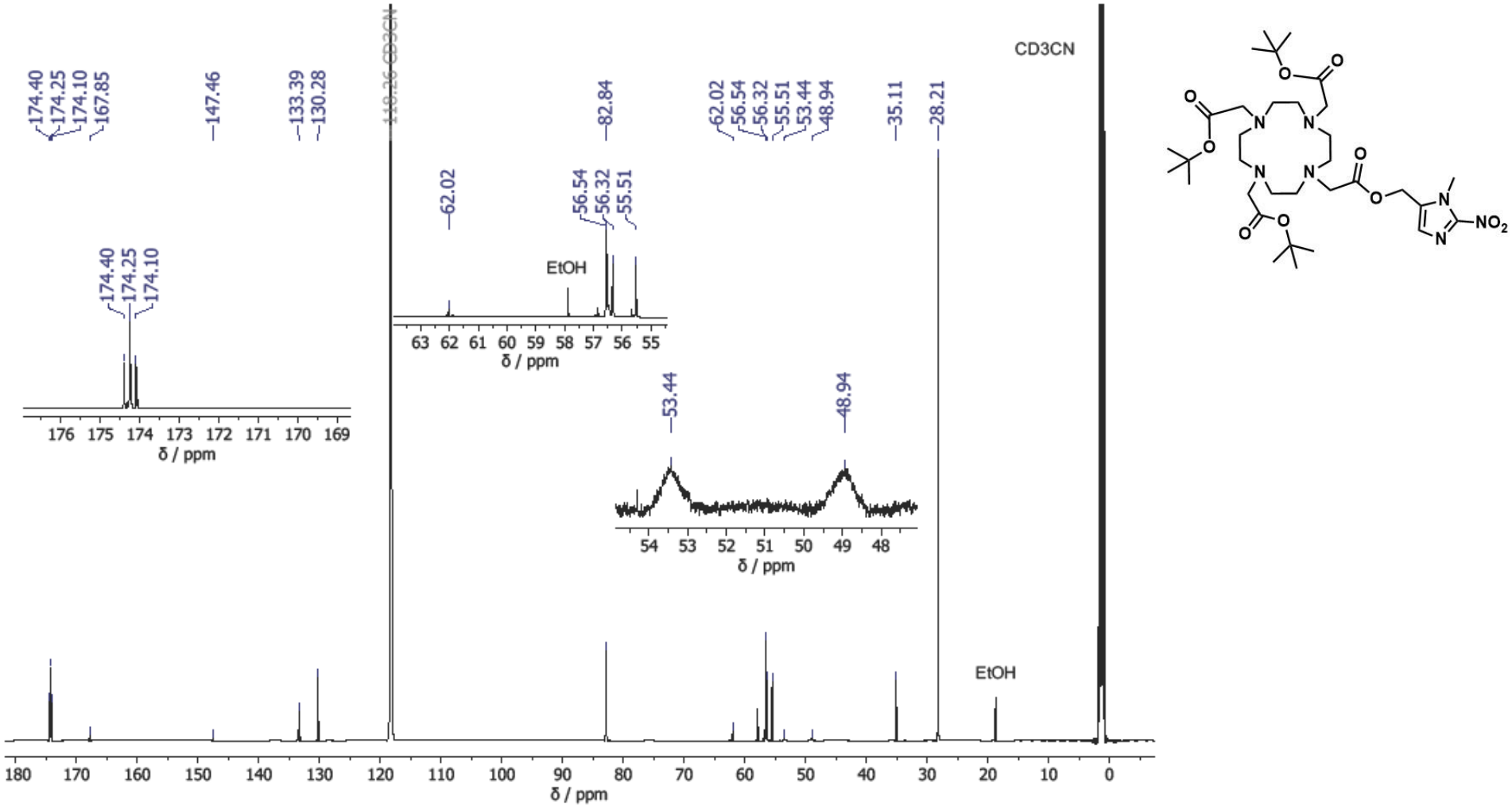

Figure A6.29: The ^{13}C NMR spectrum (151 MHz) of tri-tert-butyl 2,2',2''-(10-(2-((1-methyl-2-nitro-1H-imidazol-5-yl)methoxy)-2-oxoethyl)-1,4,7,10-tetraazacyclododecane-1,4,7-triyl)triacetate **31** in CD_3CN.

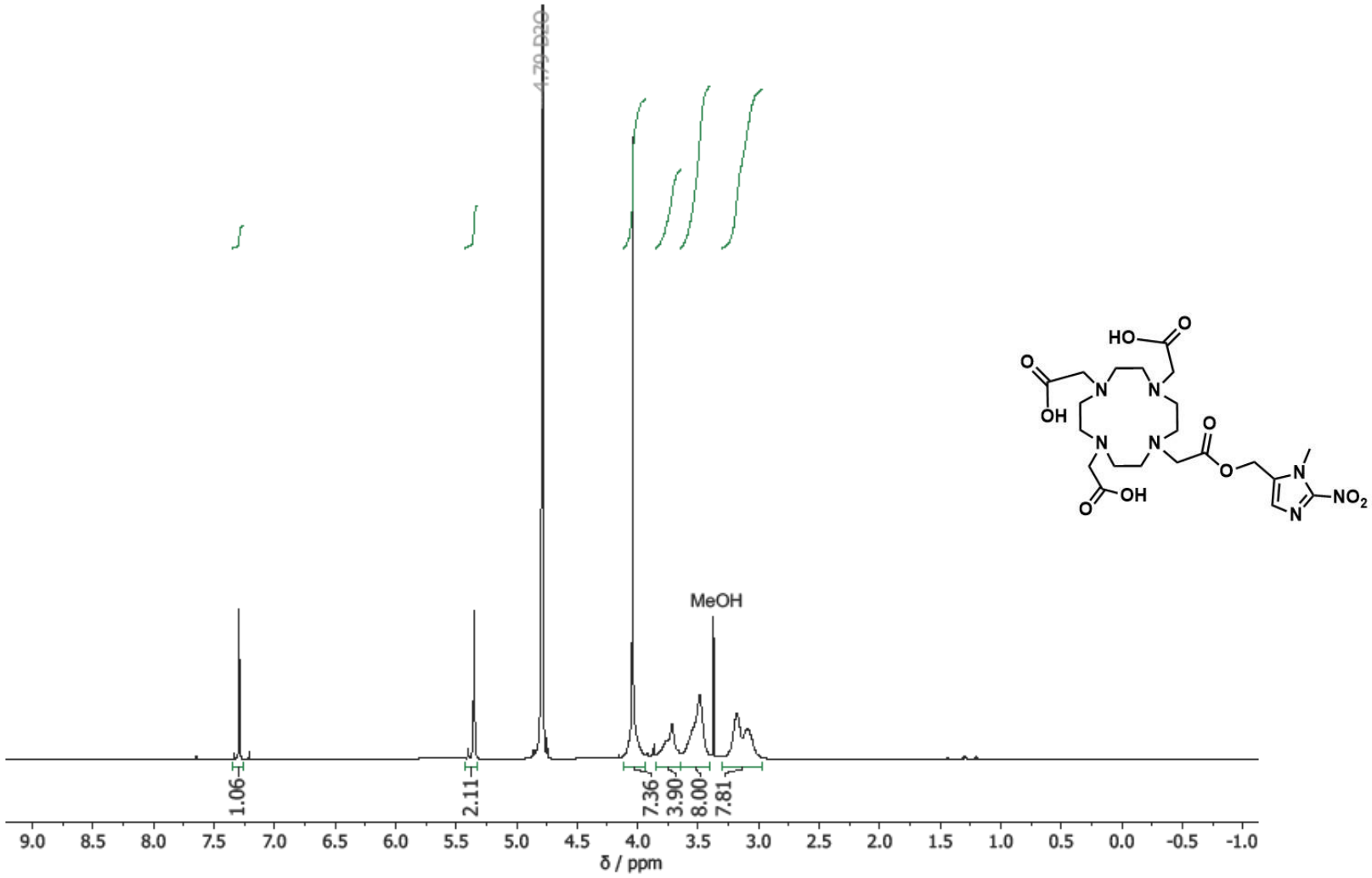

Figure A6.30: The ^{1}H NMR spectrum (600 MHz) of 2,2',2''-(10-(2-((1-methyl-2-nitro-1H-imidazol-5-yl)methoxy)-2-oxoethyl)-1,4,7,10-tetraazacyclododecane-1,4,7-triyl)triacetic acid **32** in D_2O, with residual MeOH remaining for reference in the ^{13}C NMR spectrum.

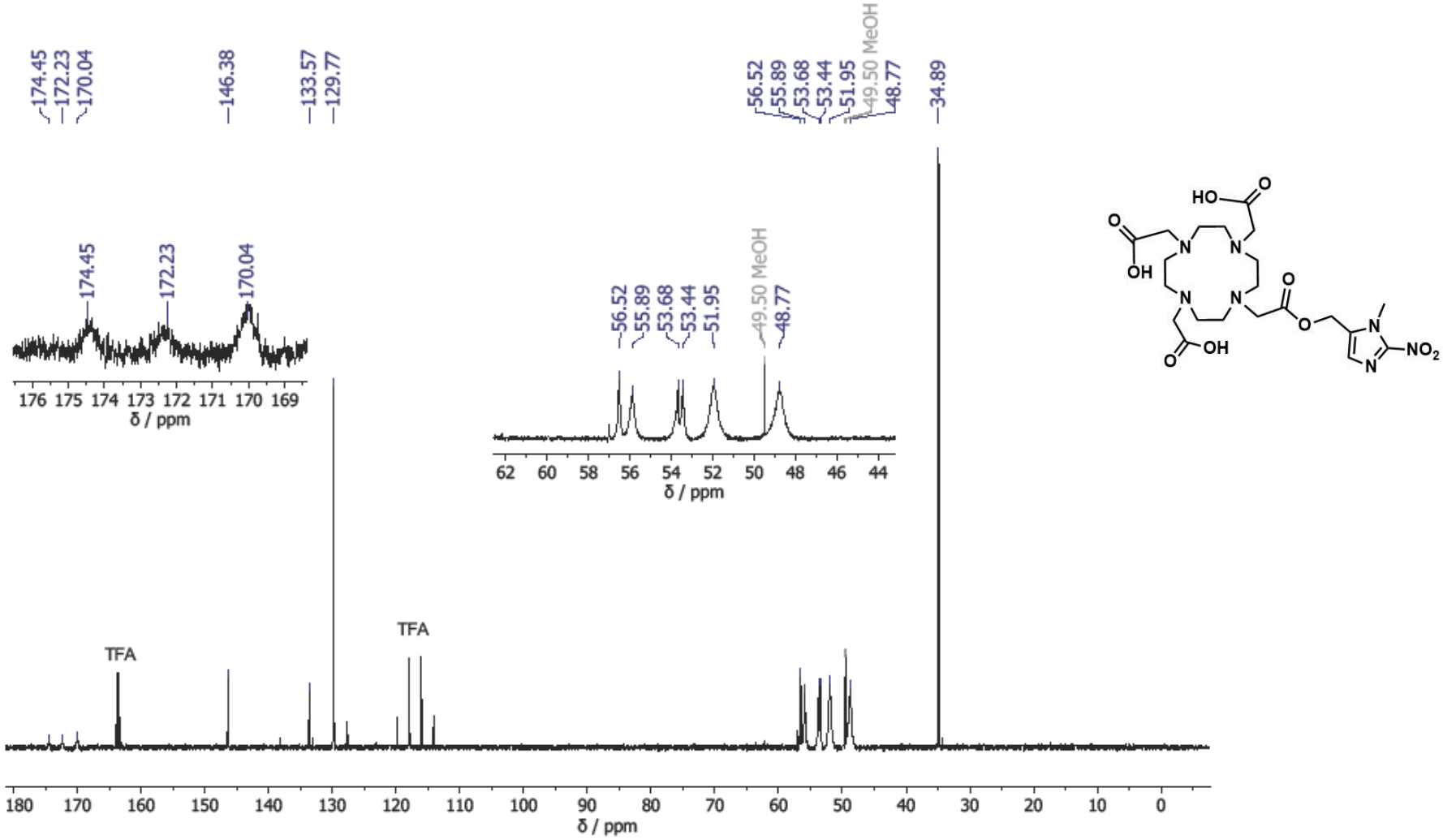

Figure A6.31: The ^{13}C NMR spectrum (151 MHz) of 2,2',2''-(10-(2-((1-methyl-2-nitro-1H-imidazol-5-yl)methoxy)-2-oxoethyl)-1,4,7,10-tetraazacyclododecane-1,4,7-triyl)triacetic acid **32** in D_2O, with residual MeOH remaining for reference.

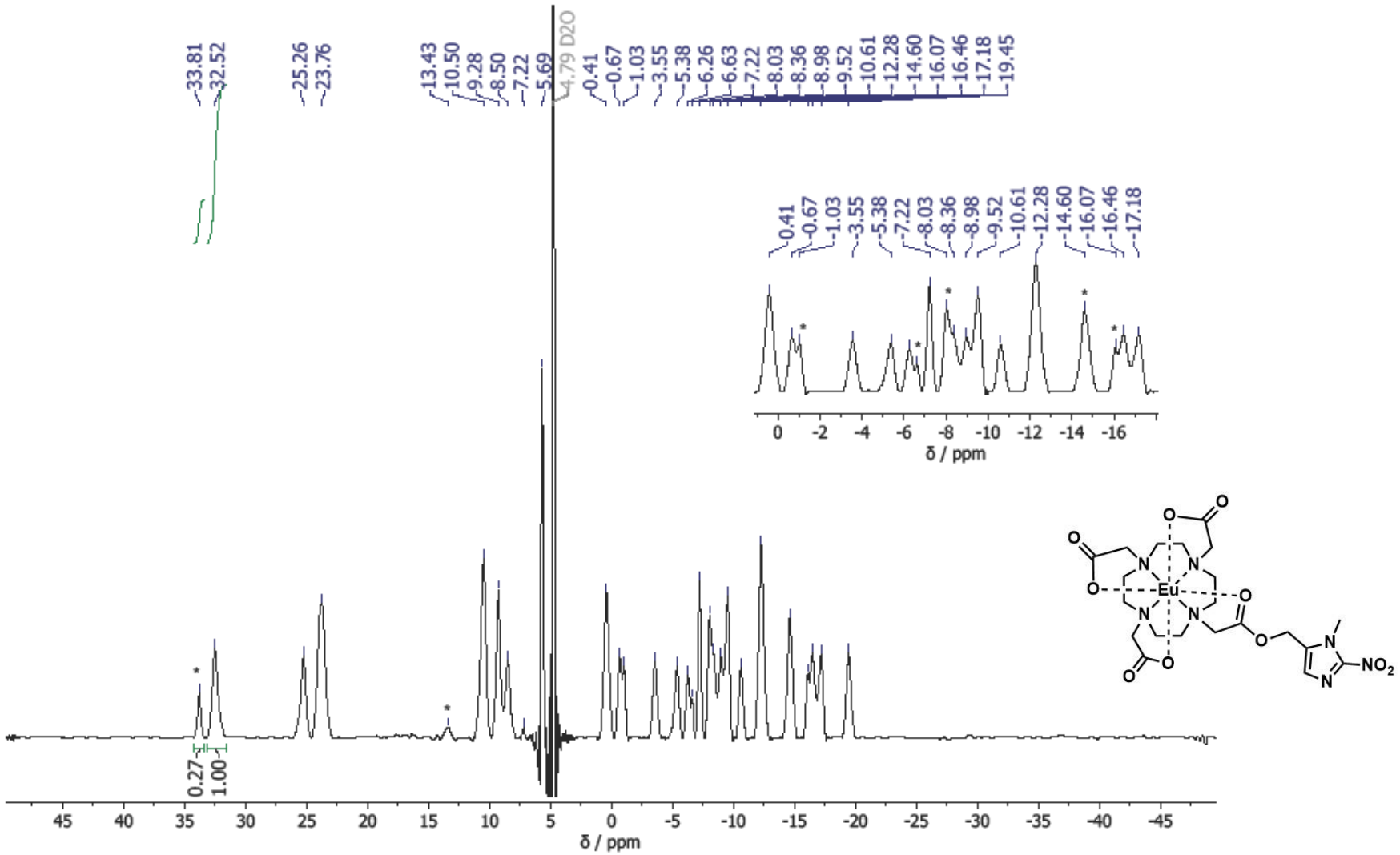

Figure A6.32: The ^{1}H (for europium complexes) NMR spectrum (400 MHz) of EuNI **19a** in D_2O. The stars represent peaks which may arise due to the presence of EuDOTA as an impurity. The integrals suggest that ~6% EuDOTA is present (assuming the EuDOTA peak contains 4 protons due to symmetry and the EuNI peak contains 1 proton).

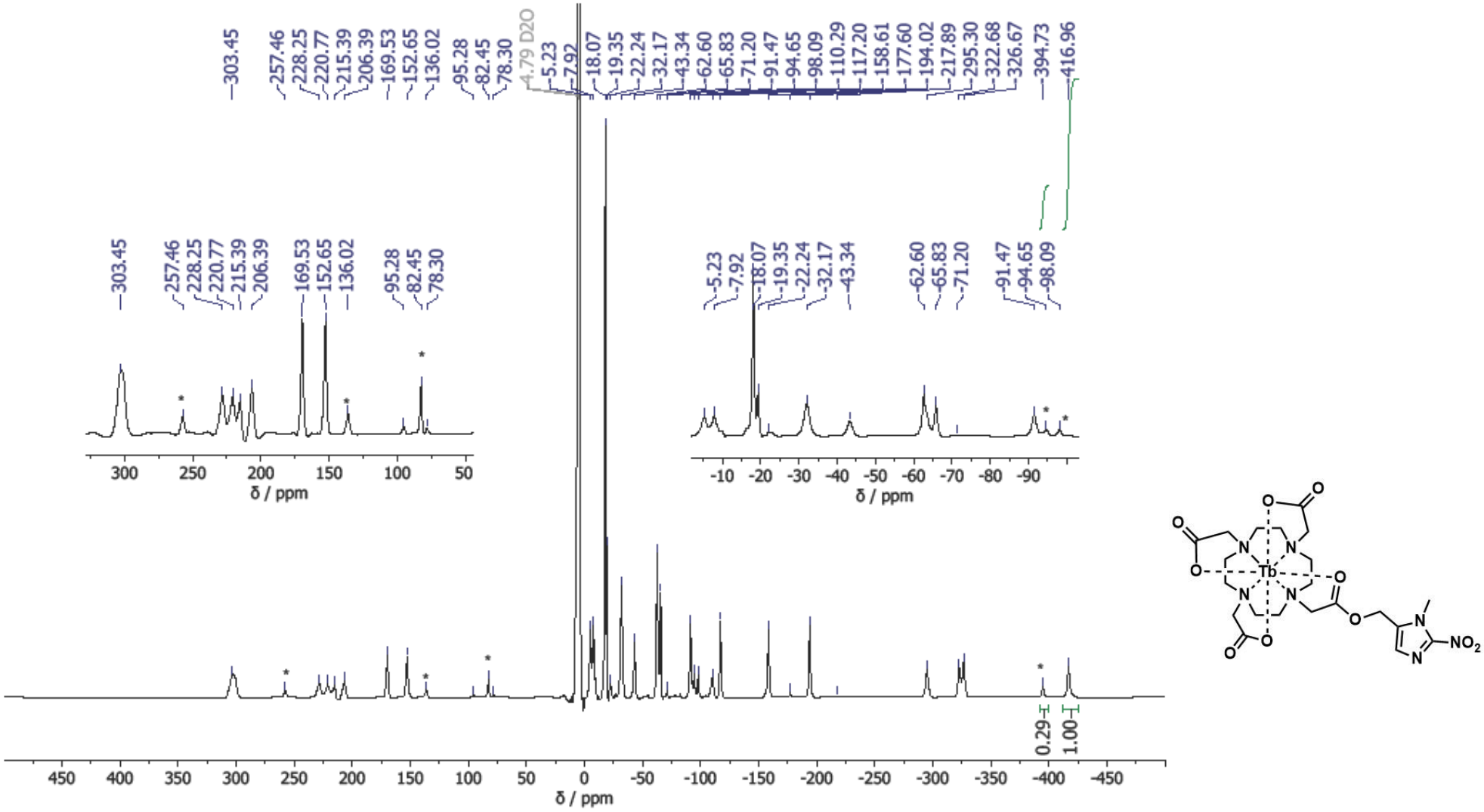

Figure A6.33: The ^{1}H (for terbium complexes) NMR (400 MHz) spectrum of TbNI **19b** in D_2O. The stars represent peaks which may arise due to the presence of TbDOTA as an impurity. The integrals suggest that ~7% TbDOTA is present (assuming the TbDOTA peak contains 4 protons due to symmetry and the TbNI peak contains 1 proton).

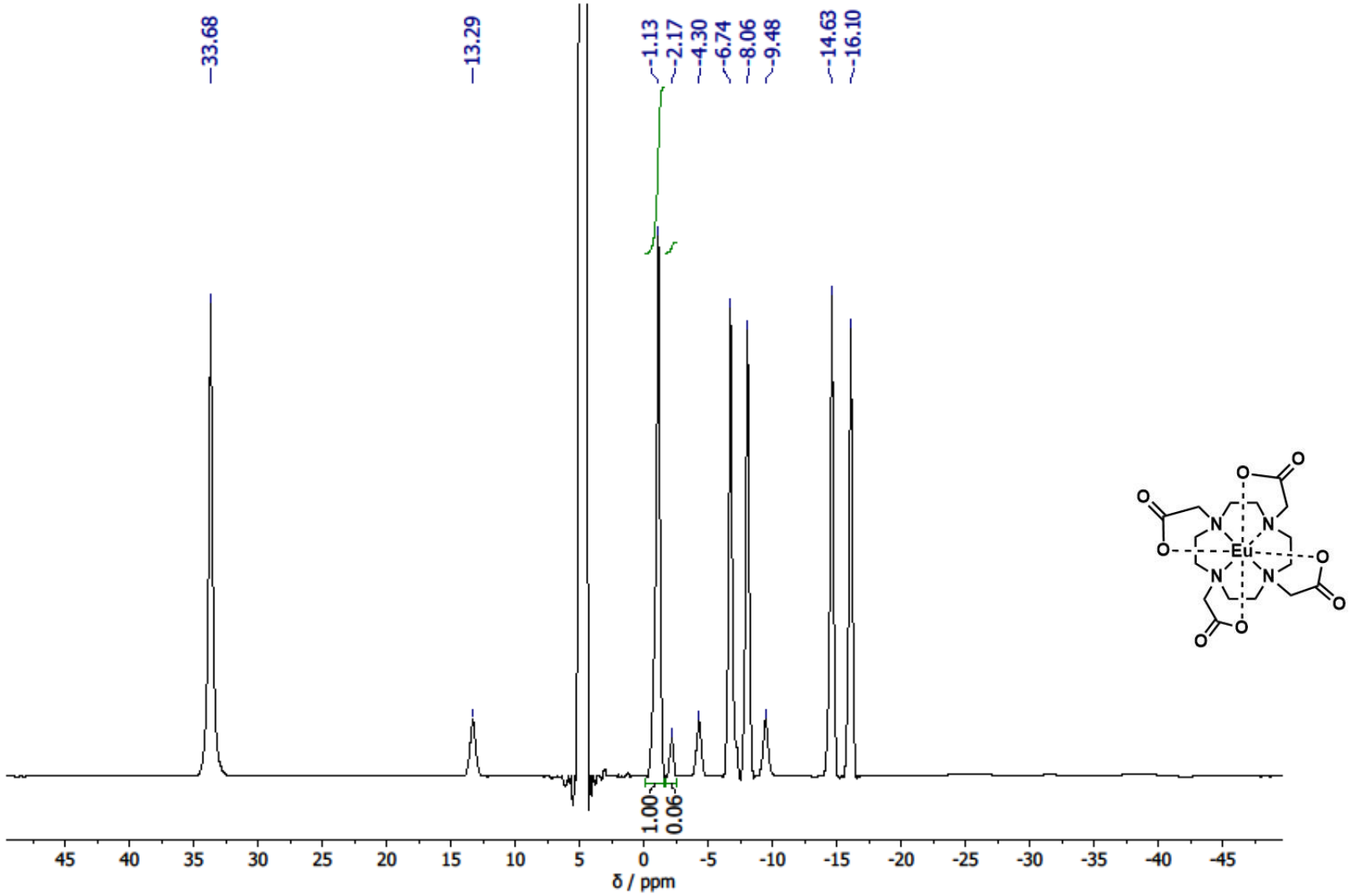

Figure A6.34: The ^{1}H (for europium complexes) NMR spectrum (400 MHz) of EuDOTA **21a** in D_2O. The integrals show the ratio between TSAP and SAP isomers.

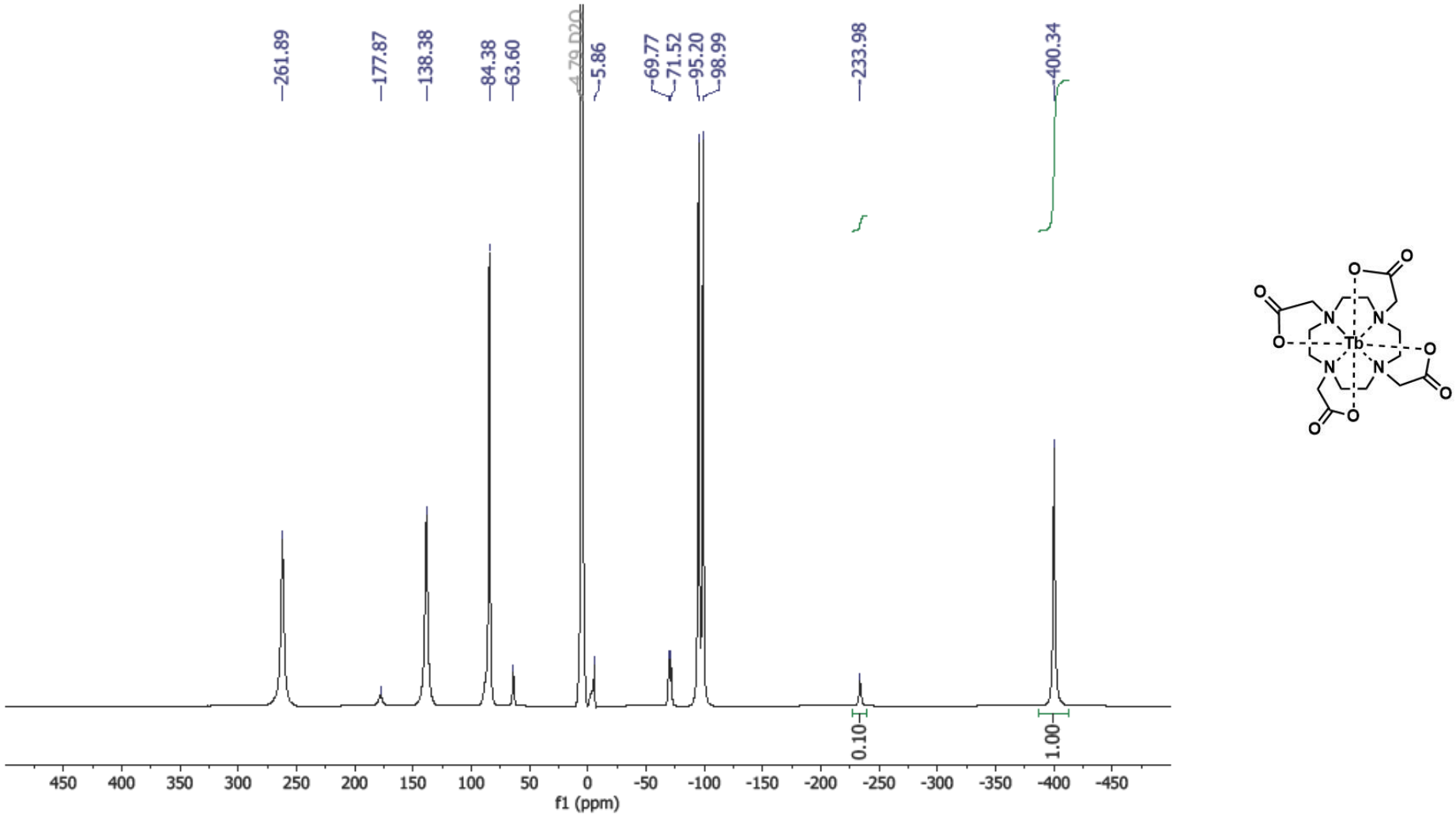

Figure A6.35: The ^{1}H (for terbium complexes) NMR spectrum (400 MHz) of TbDOTA **21b** in D_2O. The integrals show the ratio between TSAP and SAP isomers.

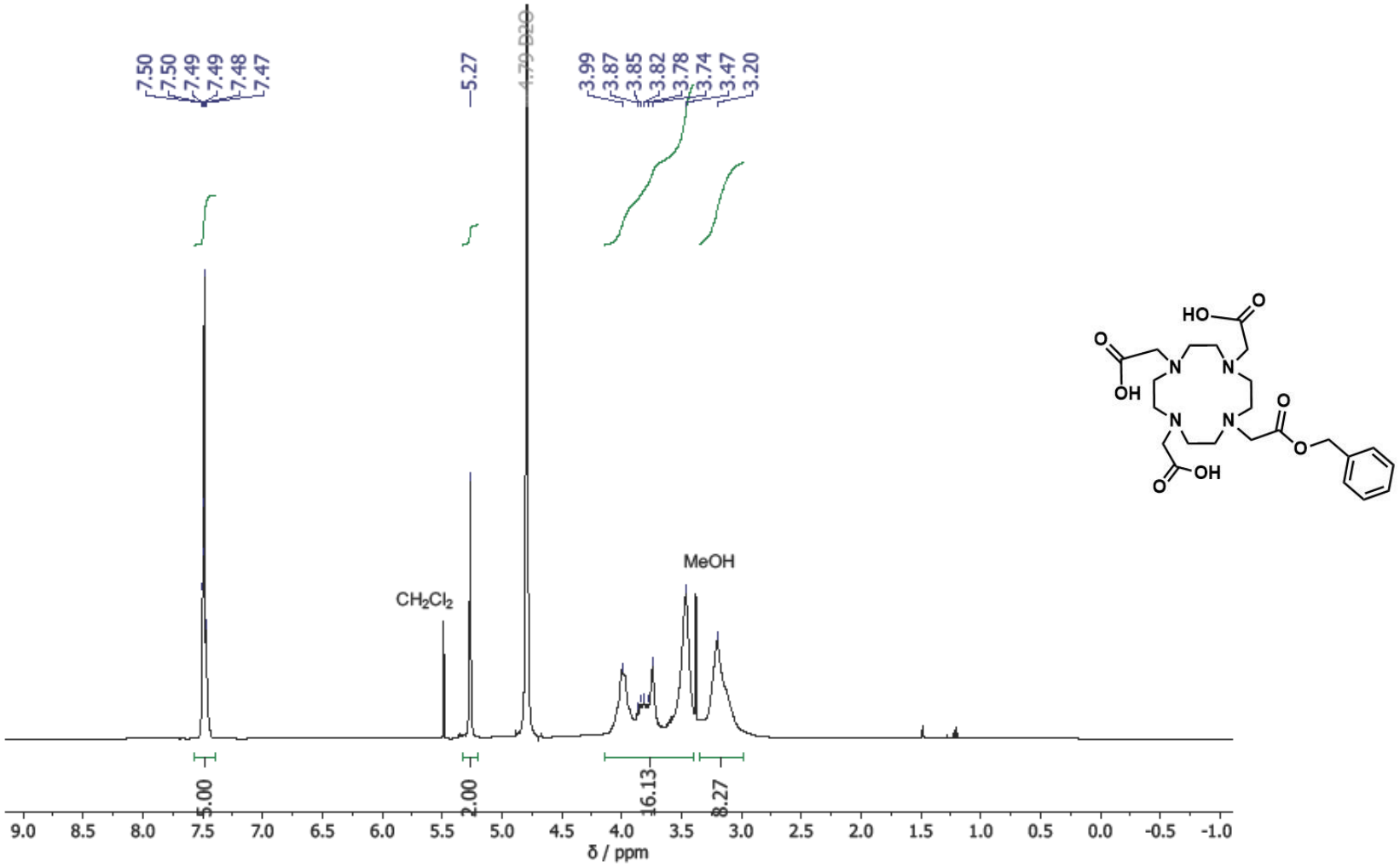

Figure A6.36: The ^{1}H NMR spectrum (400 MHz) of 2,2',2''-(10-(2-(benzyloxy)-2-oxoethyl)-1,4,7,10-tetraazacyclododecane-1,4,7-triyl)triacetic acid, **52** in D_2O, with residual MeOH remaining for reference in the ^{13}C NMR spectrum.

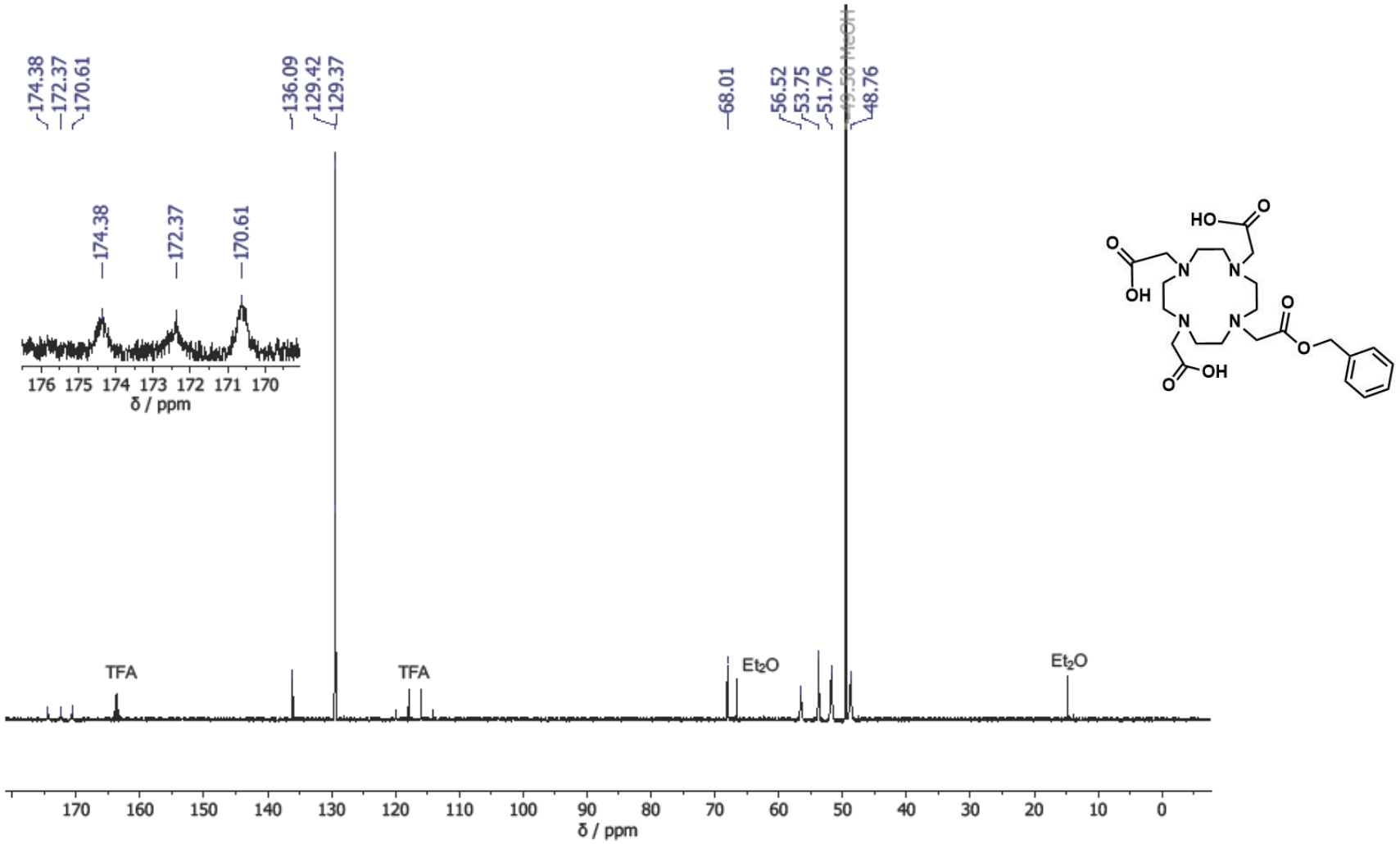

Figure A6.37: The ^{13}C NMR spectrum (151 MHz) of 2,2',2''-(10-(2-(benzyloxy)-2-oxoethyl)-1,4,7,10-tetraazacyclododecane-1,4,7-triyl)triacetic acid, **52** in D_2O, with MeOH remaining for reference.

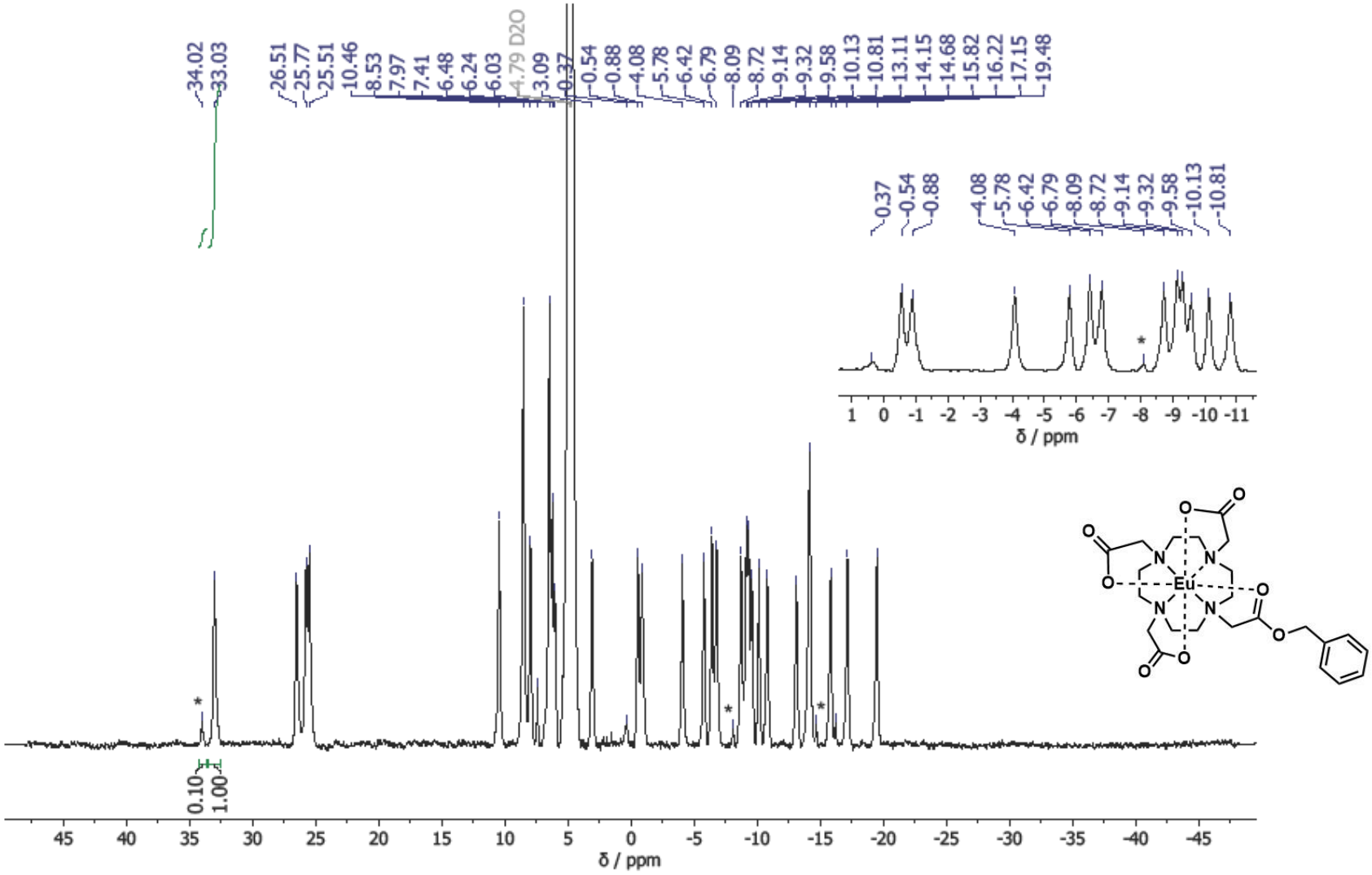

Figure A6.38: The ^{1}H (for europium complexes) NMR spectrum (400 MHz) of EuBn **22a** in D_2O. The stars represent peaks which may arise due to the presence of EuDOTA as an impurity. The integrals suggest that ~2% EuDOTA is present (assuming the EuDOTA peak contains 4 protons due to symmetry and the EuBn peak contains 1 proton).

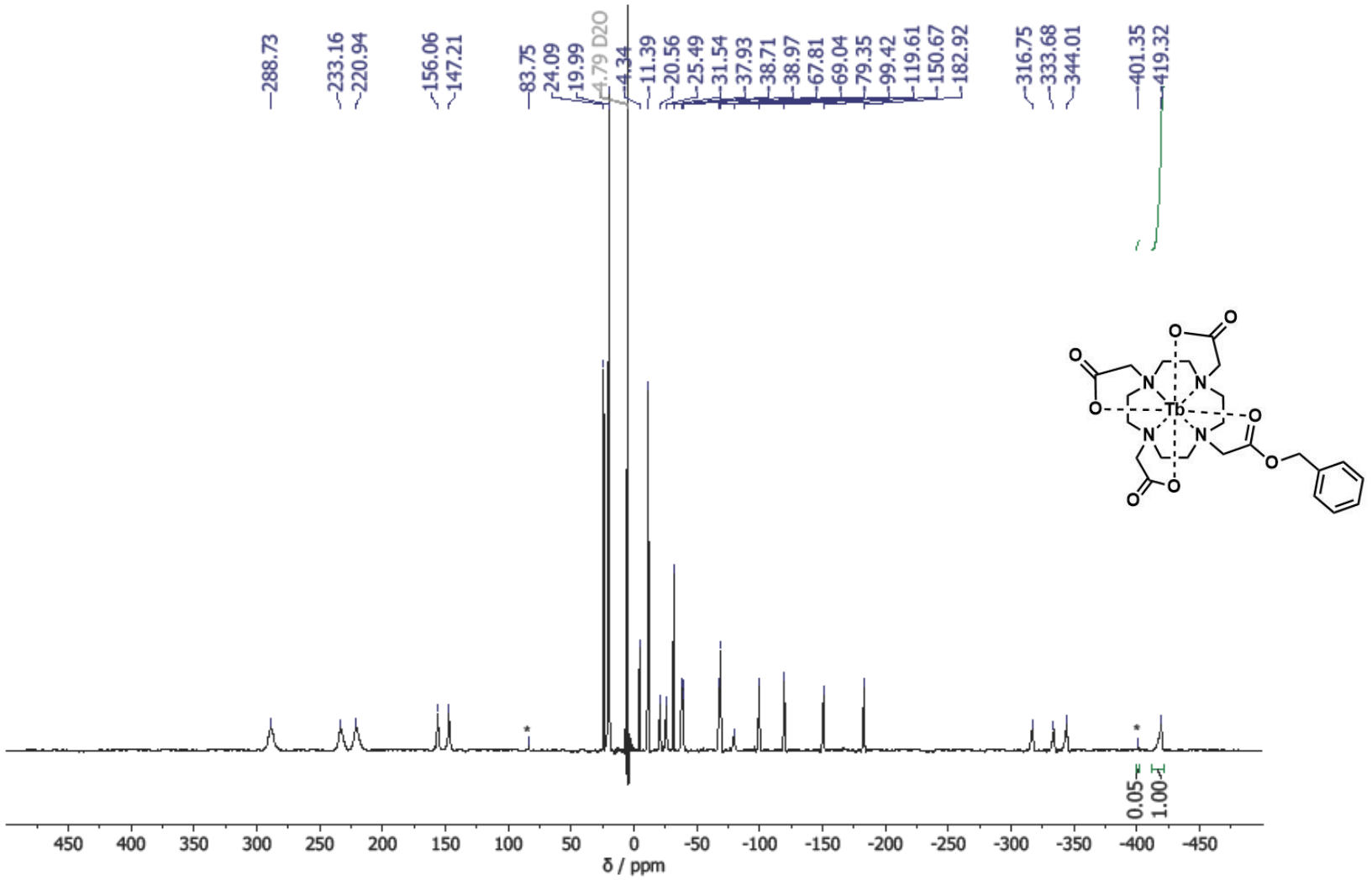

Figure A6.39: The ^{1}H (for terbium complexes) NMR spectrum (400 MHz) of TbBn **22b** in D_2O. The stars represent peaks which may arise due to the presence of TbDOTA as an impurity. The integrals suggest that ~1% EuDOTA is present (assuming the TbDOTA peak contains 4 protons due to symmetry and the TbBn peak contains 1 proton).

A2.4 Compounds from chapter IV

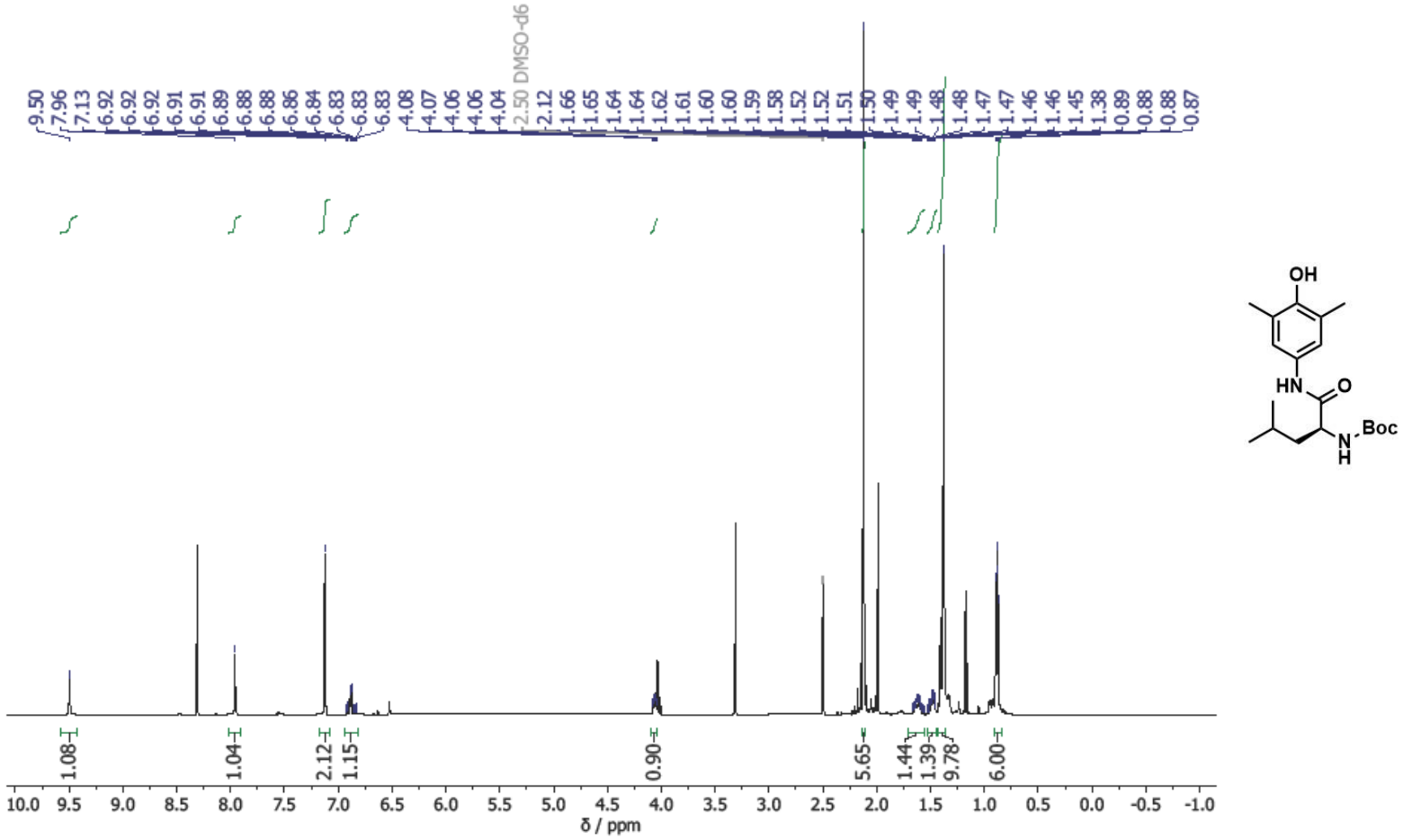

Figure A6.40: The ^{1}H NMR spectrum (600 MHz) *of* tert-butyl (S)-(1-((4-hydroxy-3,5-dimethylphenyl)amino)-4-methyl-1-oxopentan-2-yl)carbamate, **67**, in *DMSO-d*$_6$.

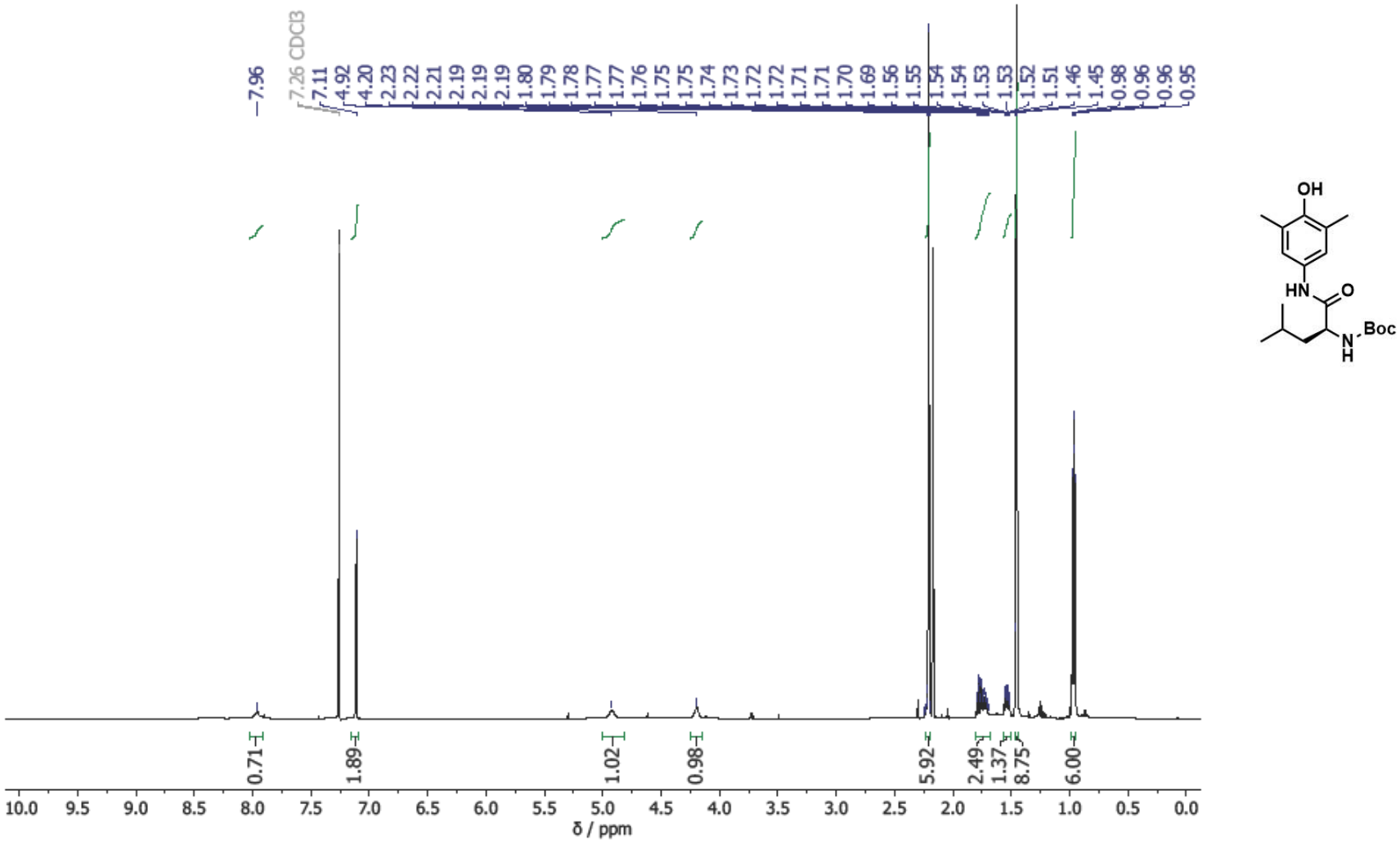

Figure A6.41: The ^{1}H NMR spectrum (600 MHz) *of* tert-butyl (S)-(1-((4-hydroxy-3,5-dimethylphenyl)amino)-4-methyl-1-oxopentan-2-yl)carbamate, **67**, in $CDCl_3$.

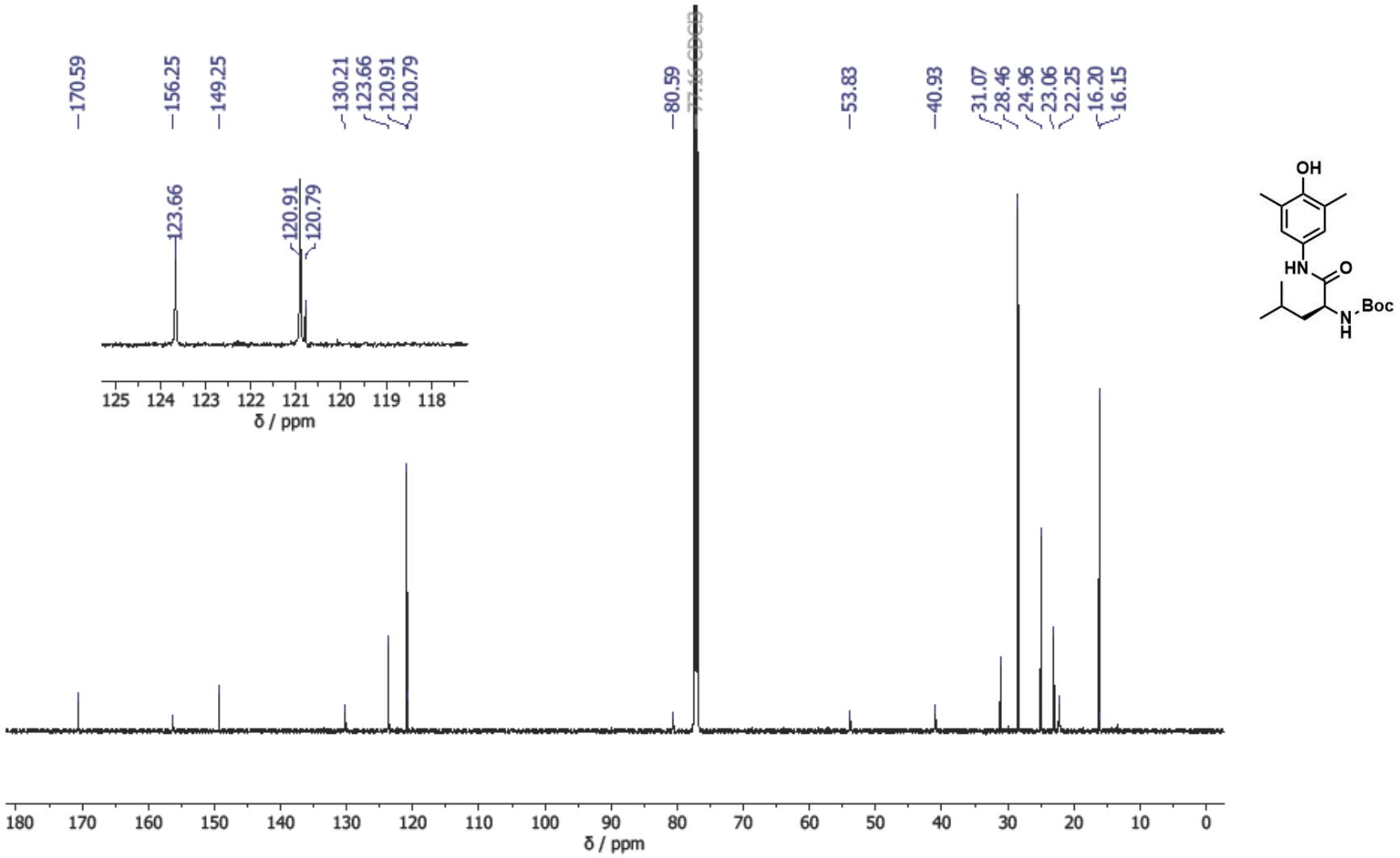

Figure A6.42: The ^{13}C NMR spectrum (600 MHz) *of* tert-butyl (S)-(1-((4-hydroxy-3,5-dimethylphenyl)amino)-4-methyl-1-oxopentan-2-yl)carbamate, **67**, in $CDCl_3$.

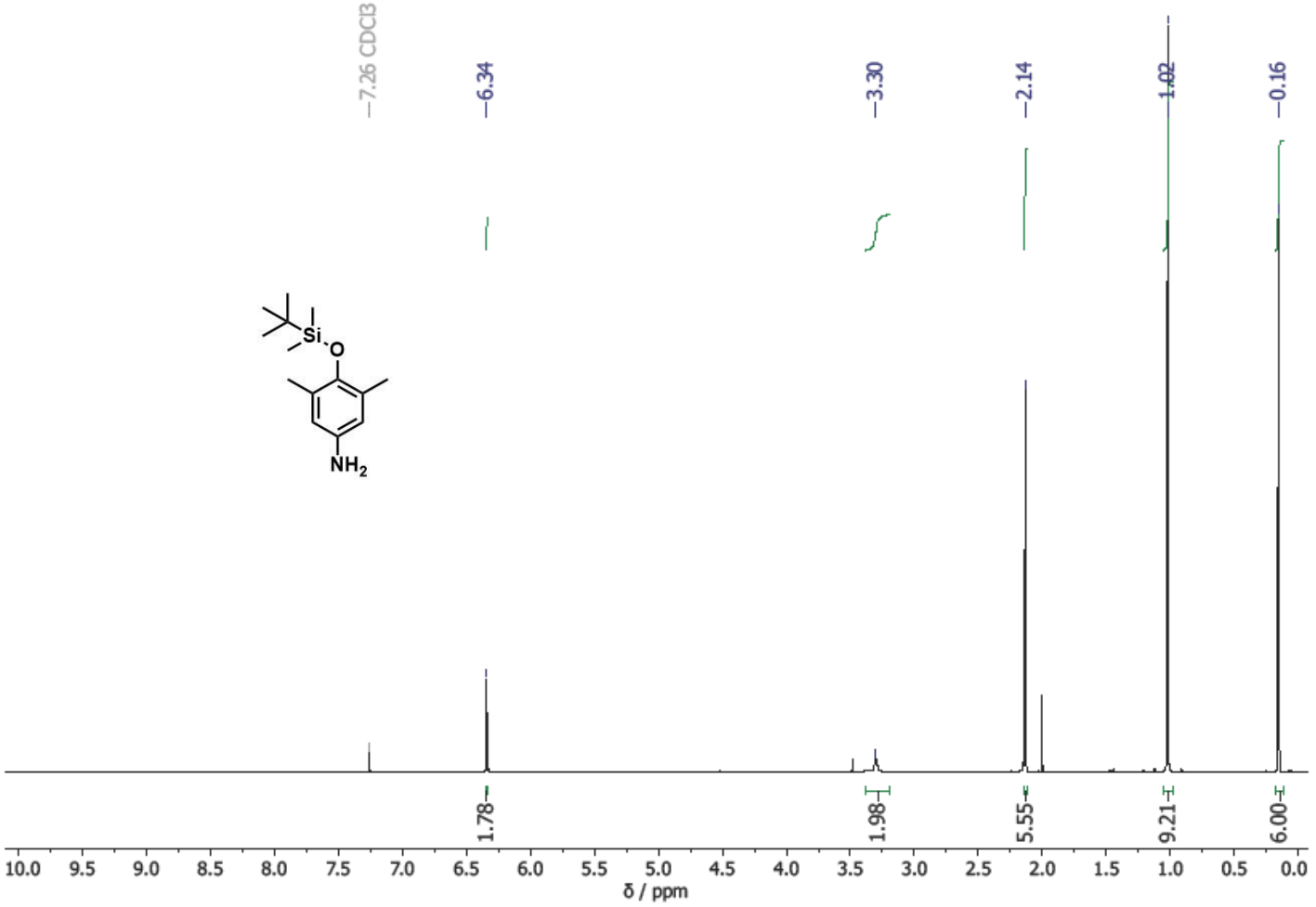

Figure A6.43: The ^{1}H NMR spectrum (600 MHz) of 4-((tert-butyldimethylsilyl)oxy)-3,5-dimethylaniline, **69**, in $CDCl_3$.

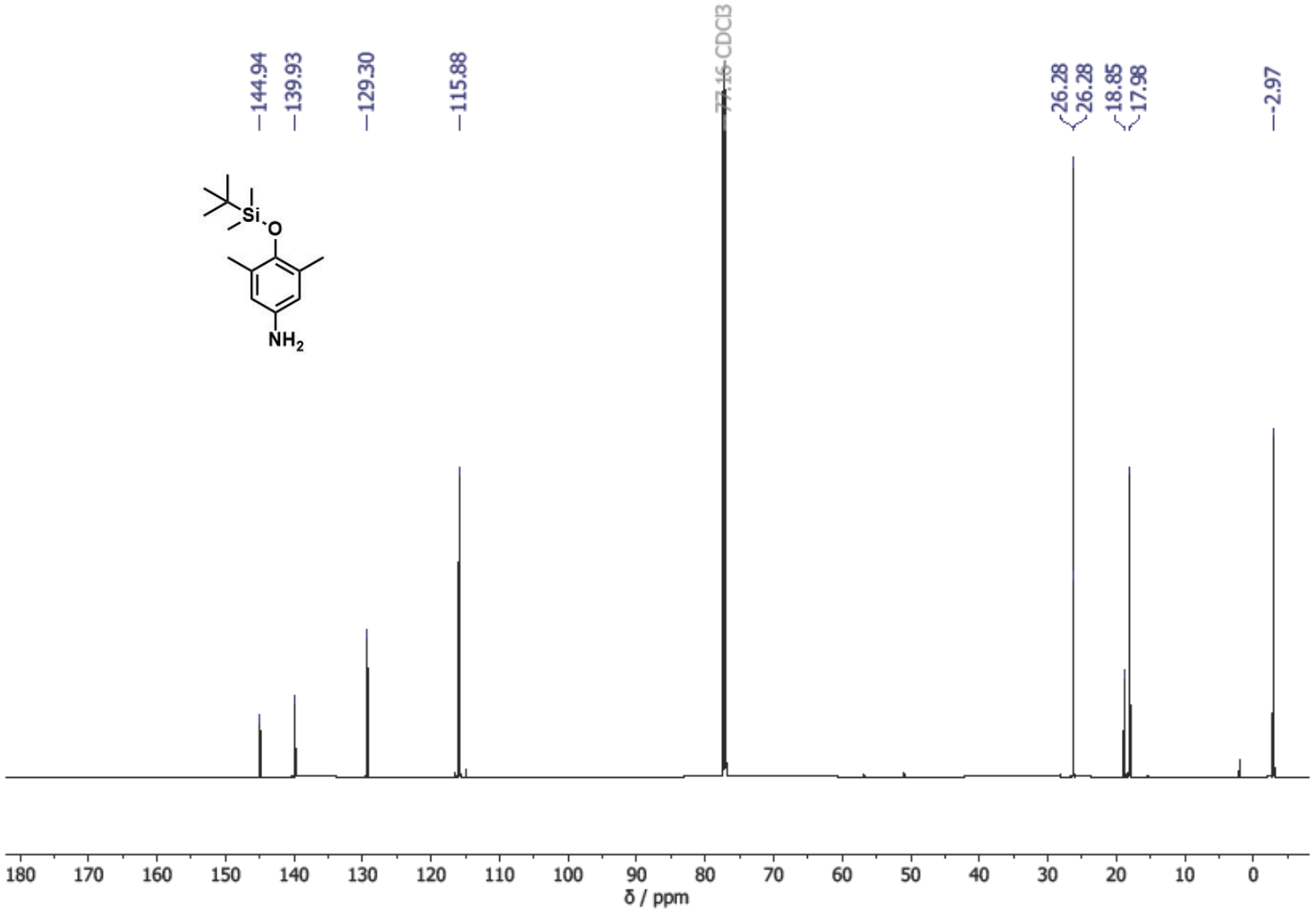

Figure A6.44: The ^{13}C NMR spectrum (151 MHz) of 4-((tert-butyldimethylsilyl)oxy)-3,5-dimethylaniline, **69**, in $CDCl_3$.

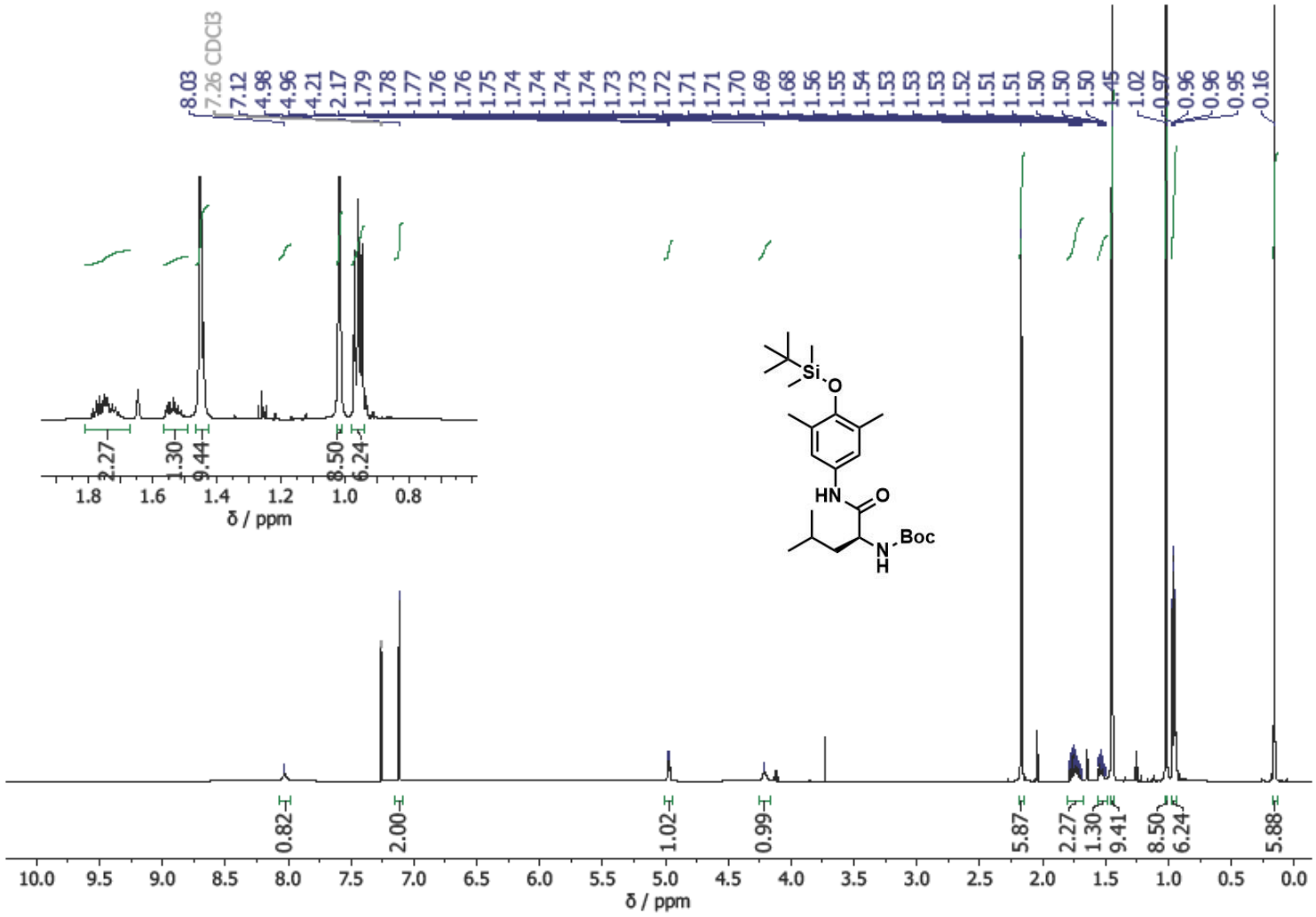

Figure A6.45: The ^{1}H NMR spectrum (600 MHz) of tert-butyl (S)-(1-((4-((tert-butyldimethylsilyl)oxy)-3,5-dimethylphenyl)amino)-4-methyl-1-oxopentan-2-yl)carbamate, **68**, *in* $CDCl_3$.

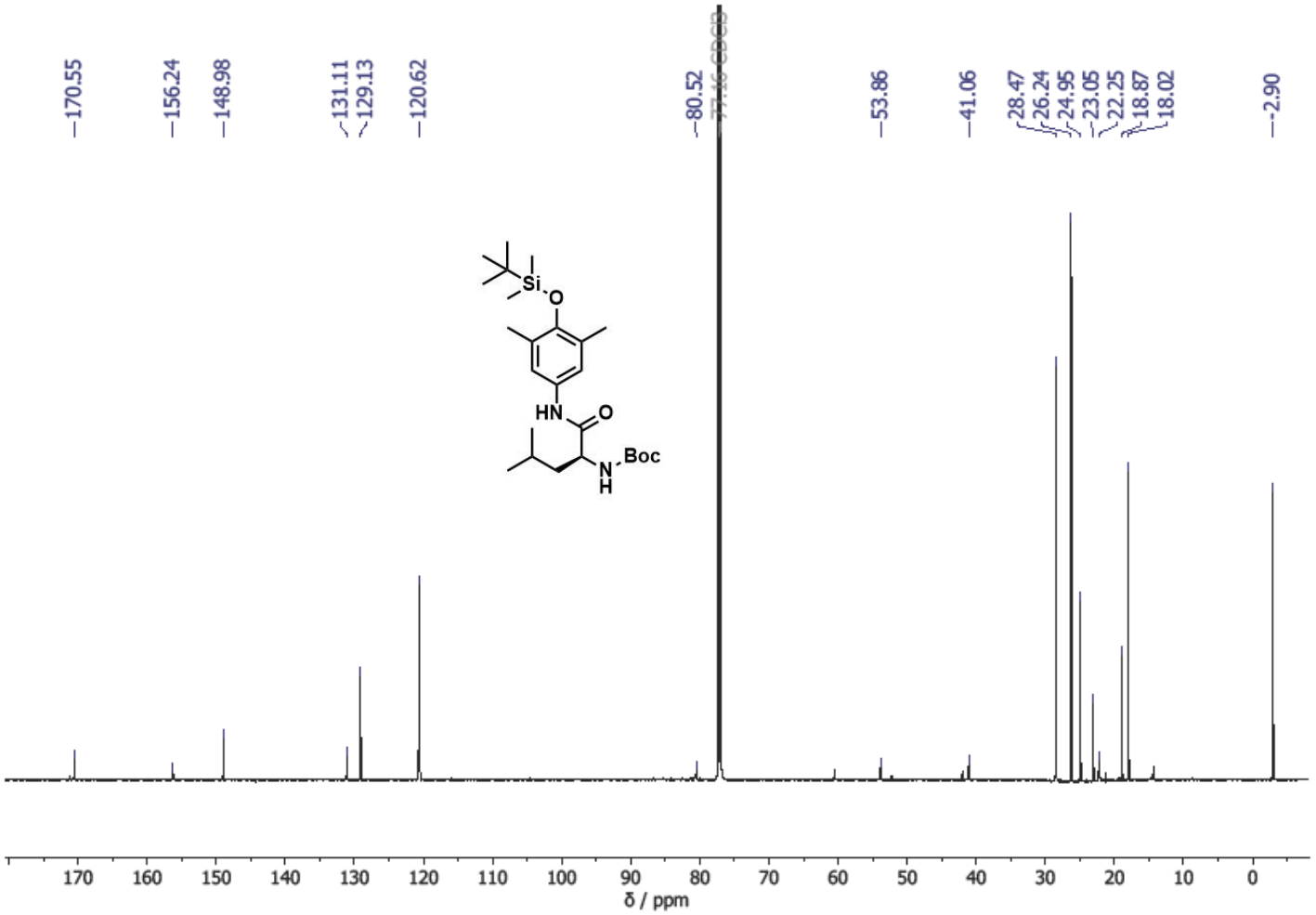

Figure A6.46: The ^{13}C NMR spectrum (151 MHz) of tert-butyl (S)-(1-((4-((tert-butyldimethylsilyl)oxy)-3,5-dimethylphenyl)amino)-4-methyl-1-oxopentan-2-yl)carbamate, **68**, *in $CDCl_3$.*

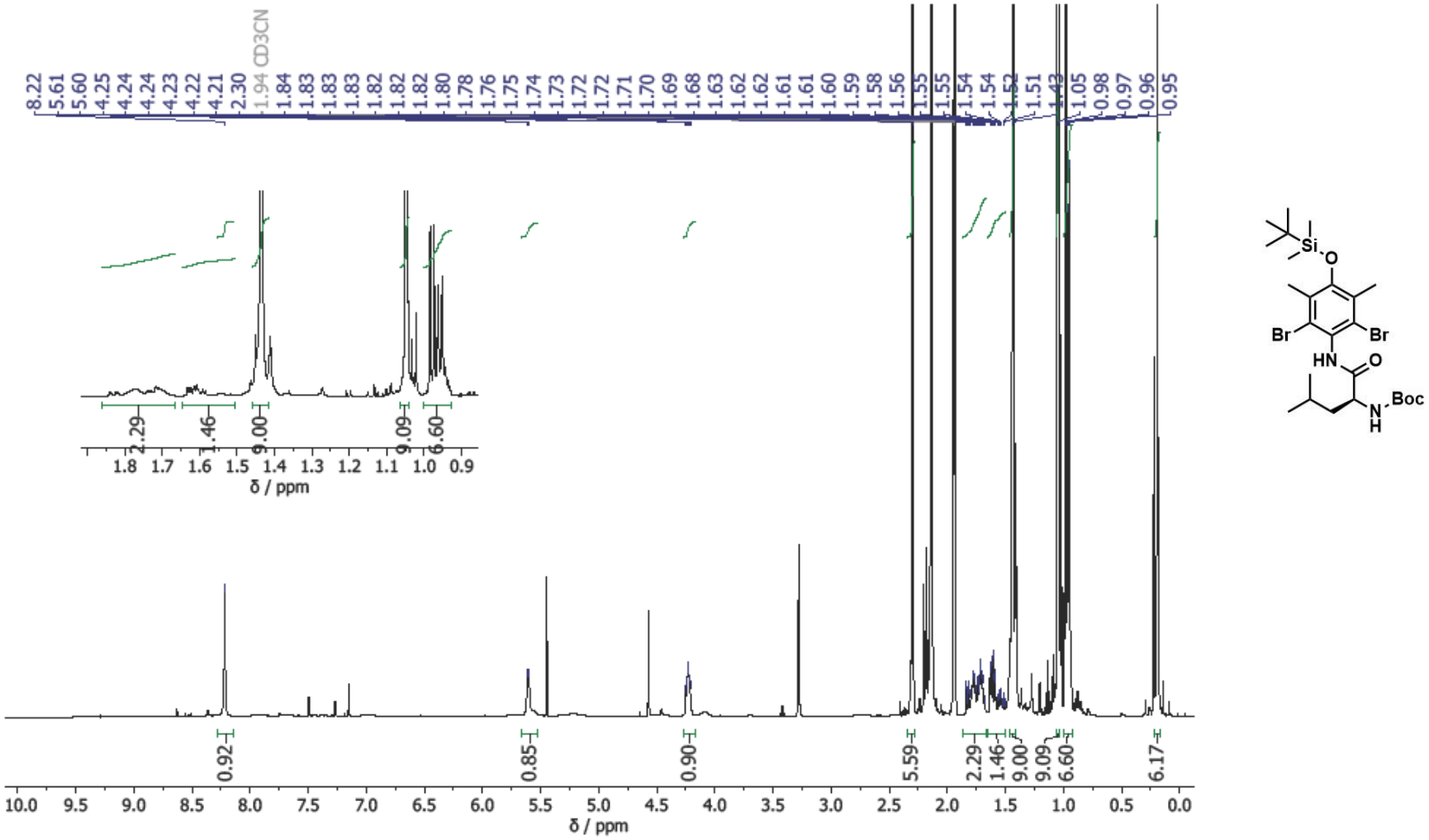

Figure A6.47: The ^{1}H NMR spectrum (600 MHz) of tert-butyl (S)-(1-((2,6-dibromo-4-((tert-butyldimethylsilyl)oxy)-3,5-dimethylphenyl)amino)-4-methyl-1-oxopentan-2-yl)carbamate, **71**, in CD_3CN.

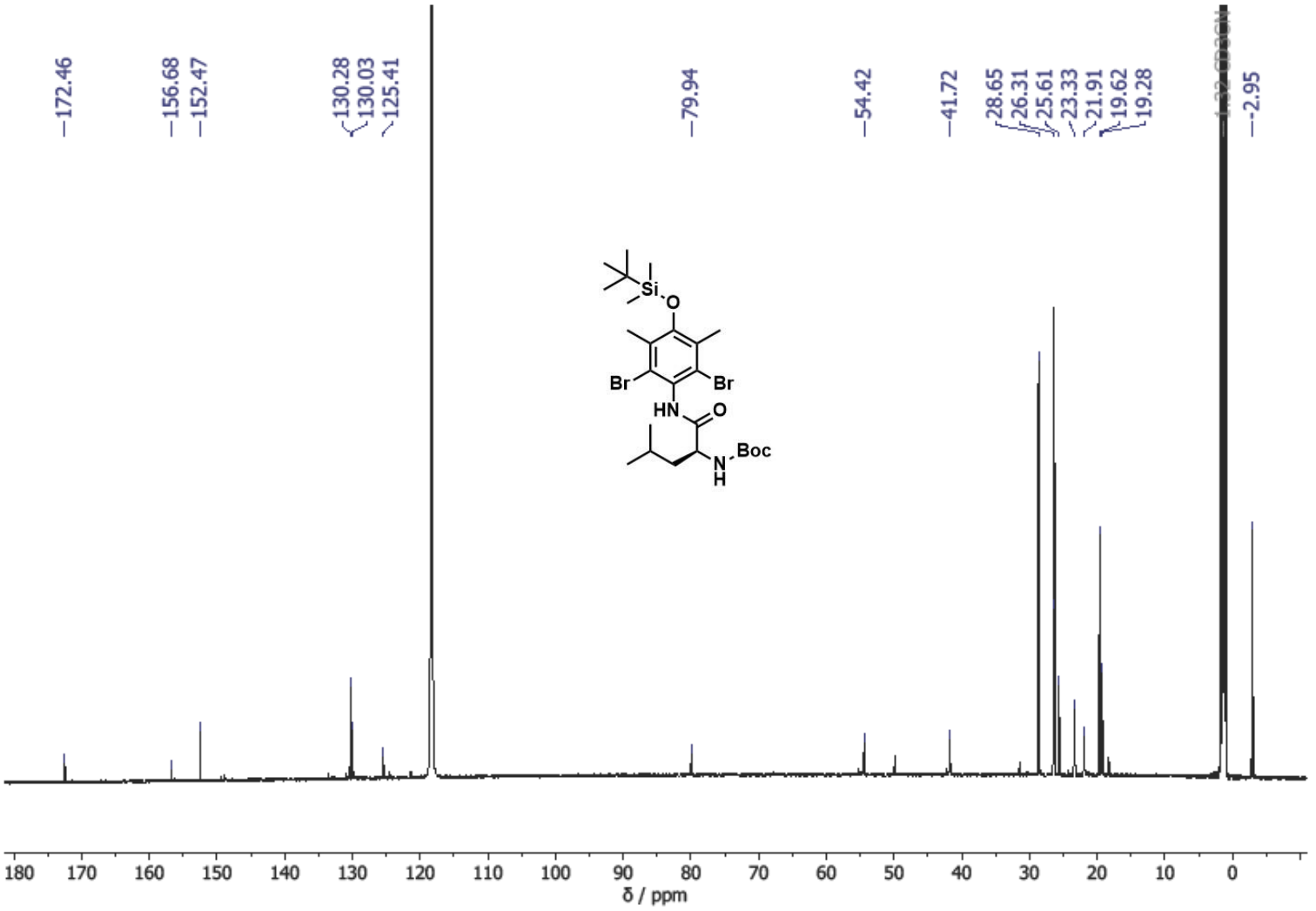

Figure A6.48: The ^{13}C NMR spectrum (151 MHz) of tert-butyl (S)-(1-((2,6-dibromo-4-((tert-butyldimethylsilyl)oxy)-3,5-dimethylphenyl)amino)-4-methyl-1-oxopentan-2-yl)carbamate, **71**, in CD_3CN.

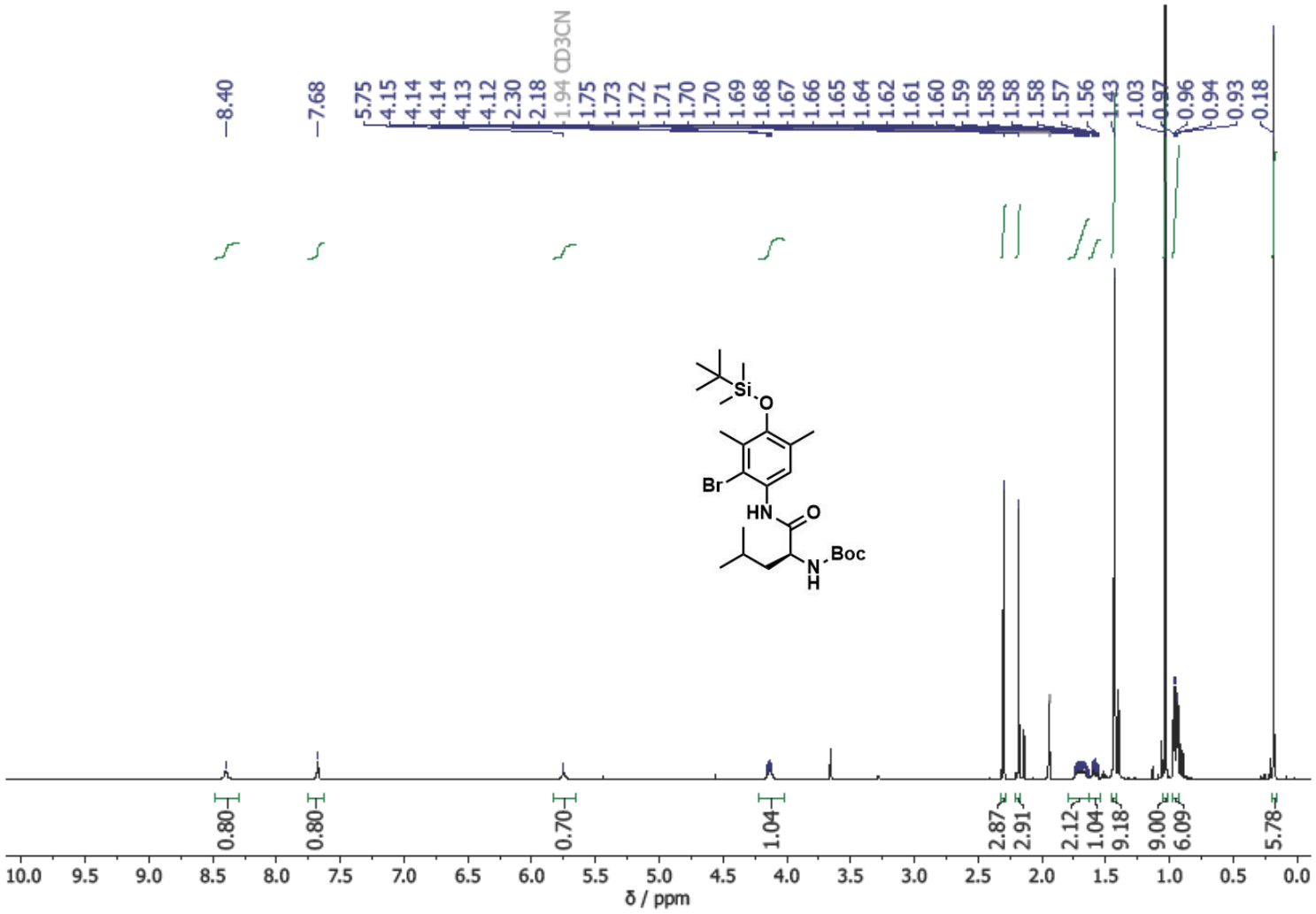

Figure A6.49: The ^{1}H NMR spectrum (600 MHz) of tert-butyl (S)-(1-((2-bromo-4-((tert-butyldimethylsilyl)oxy)-3,5-dimethylphenyl)amino)-4-methyl-1-oxopentan-2-yl)carbamate, **72**, in CD_3CN.

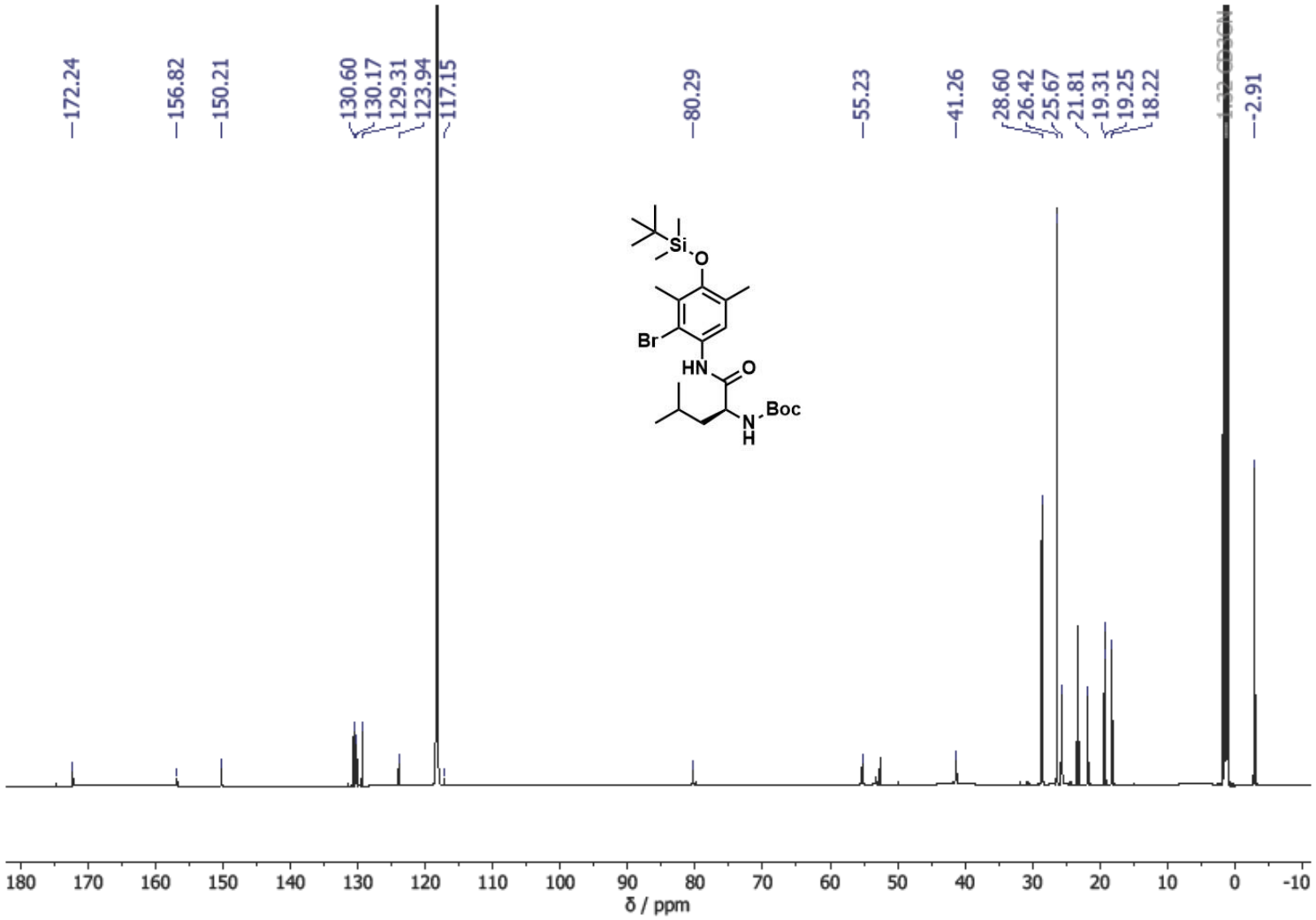

Figure A6.50: The ^{13}C NMR spectrum (151 MHz) of tert-butyl (S)-(1-((2-bromo-4-((tert-butyldimethylsilyl)oxy)-3,5-dimethylphenyl)amino)-4-methyl-1-oxopentan-2-yl)carbamate, **72**, in CD_3CN.

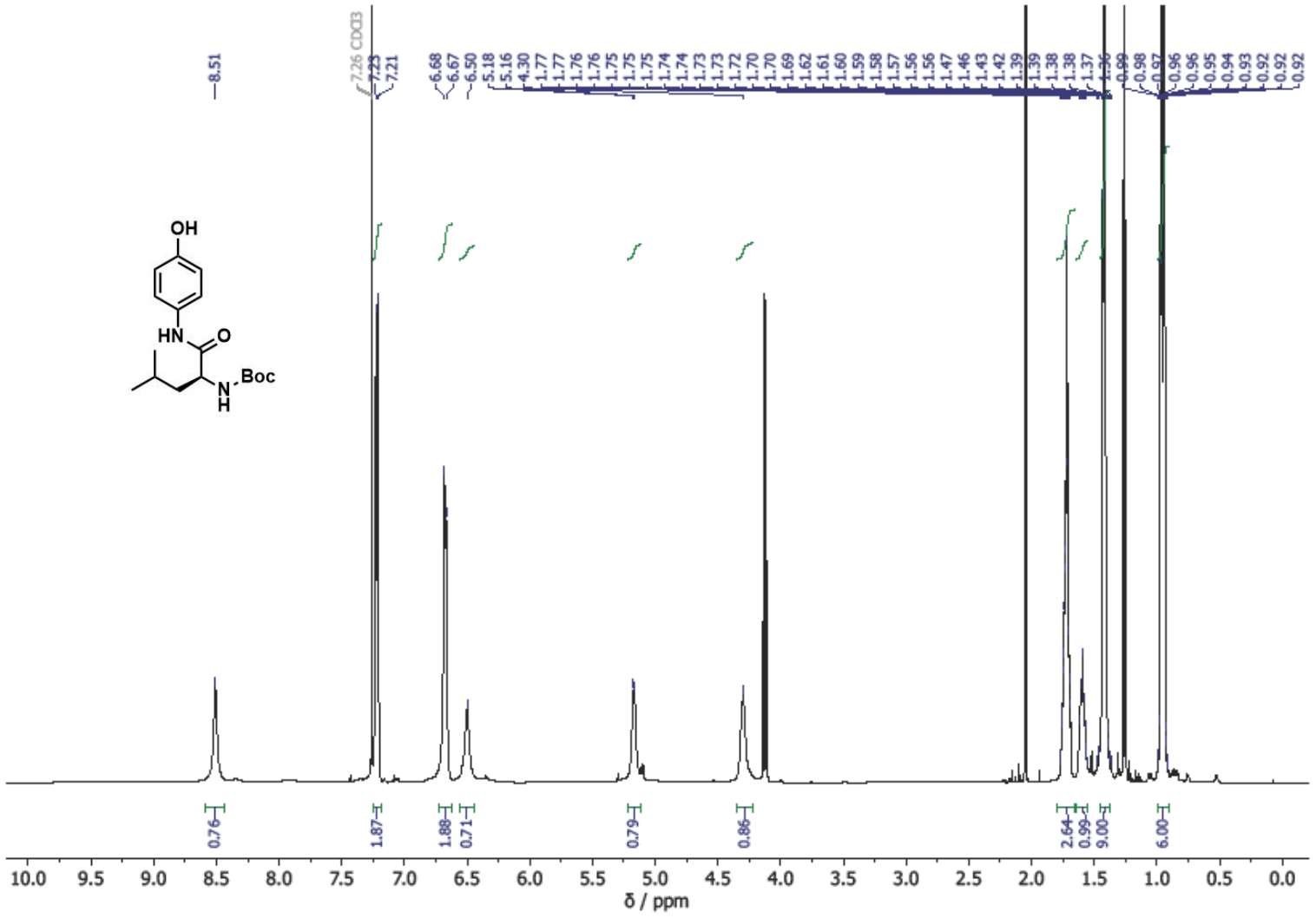

Figure A6.51: The ^{1}H NMR spectrum (600 MHz) of tert-butyl (S)-(1-((4-hydroxyphenyl)amino)-4-methyl-1-oxopentan-2-yl)carbamate, **73**, in $CDCl_3$

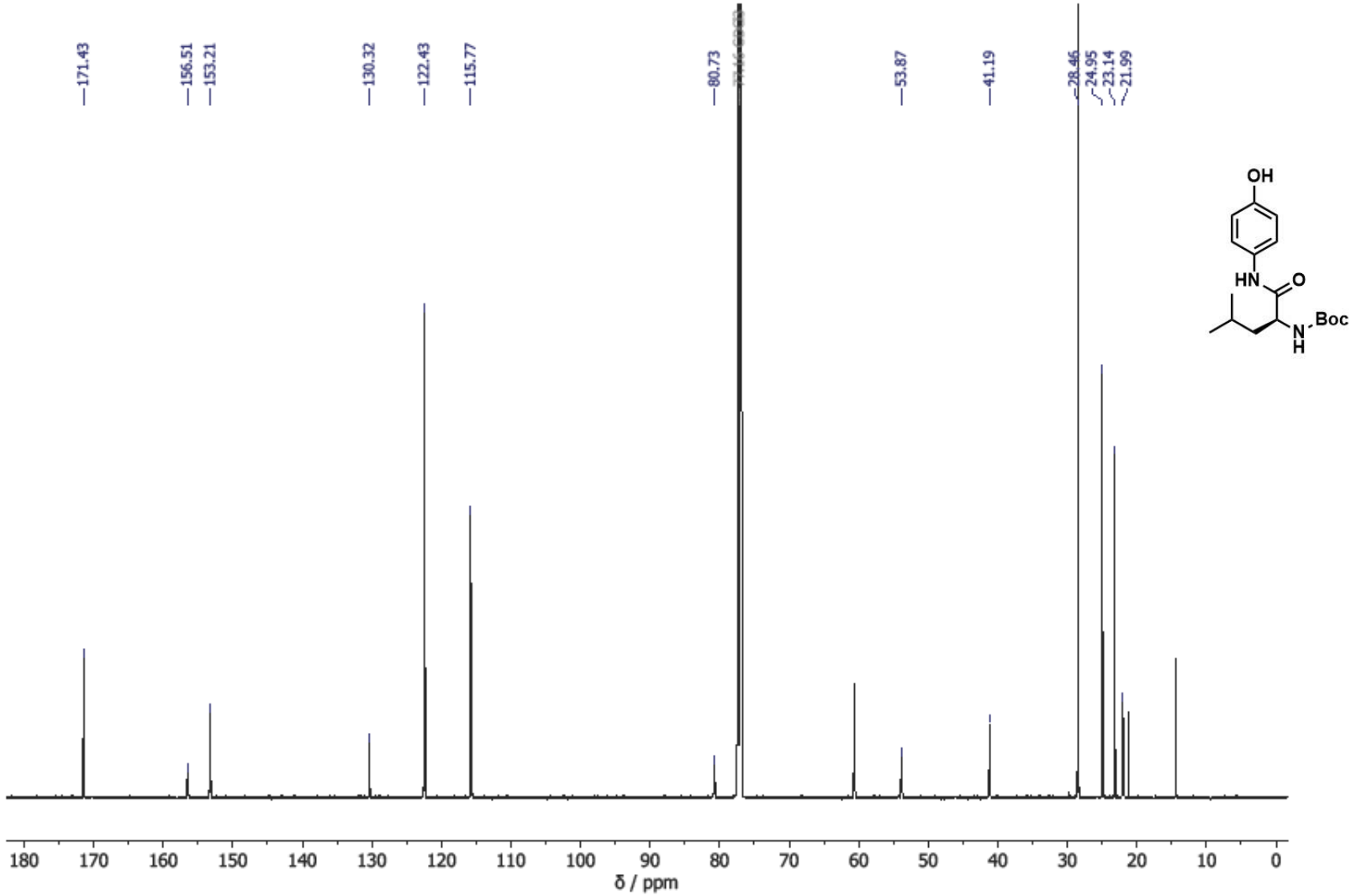

Figure A6.52: The ^{13}C NMR spectrum (151 MHz) of tert-butyl (S)-(1-((4-hydroxyphenyl)amino)-4-methyl-1-oxopentan-2-yl)carbamate, **73**, in $CDCl_3$

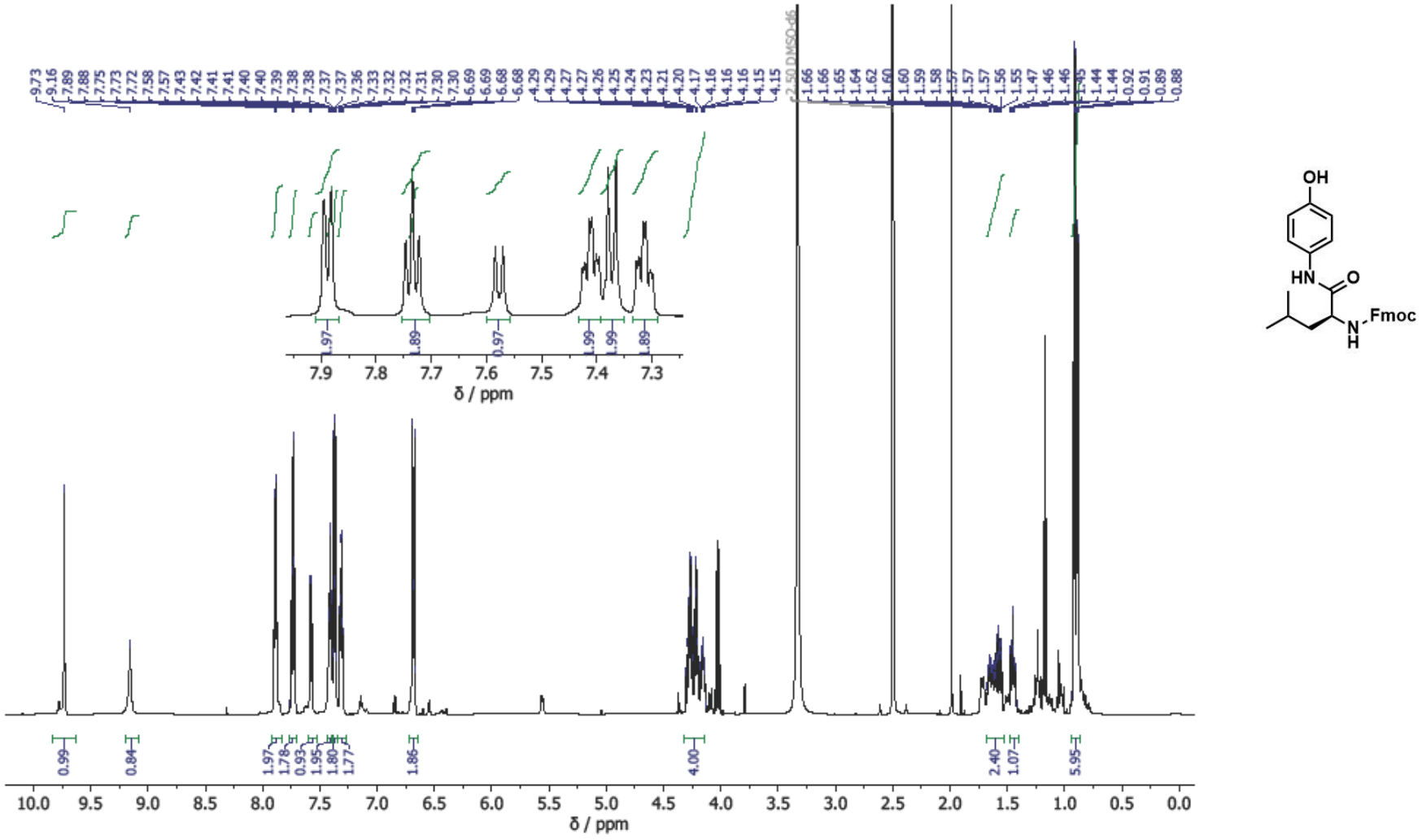

Figure A6.53: The ^{1}H NMR spectrum (600 MHz) of (9H-fluoren-9-yl)methyl (S)-(1-((4-hydroxyphenyl)amino)-4-methyl-1-oxopentan-2-yl)carbamate, **74**, in DMSO-d_6.

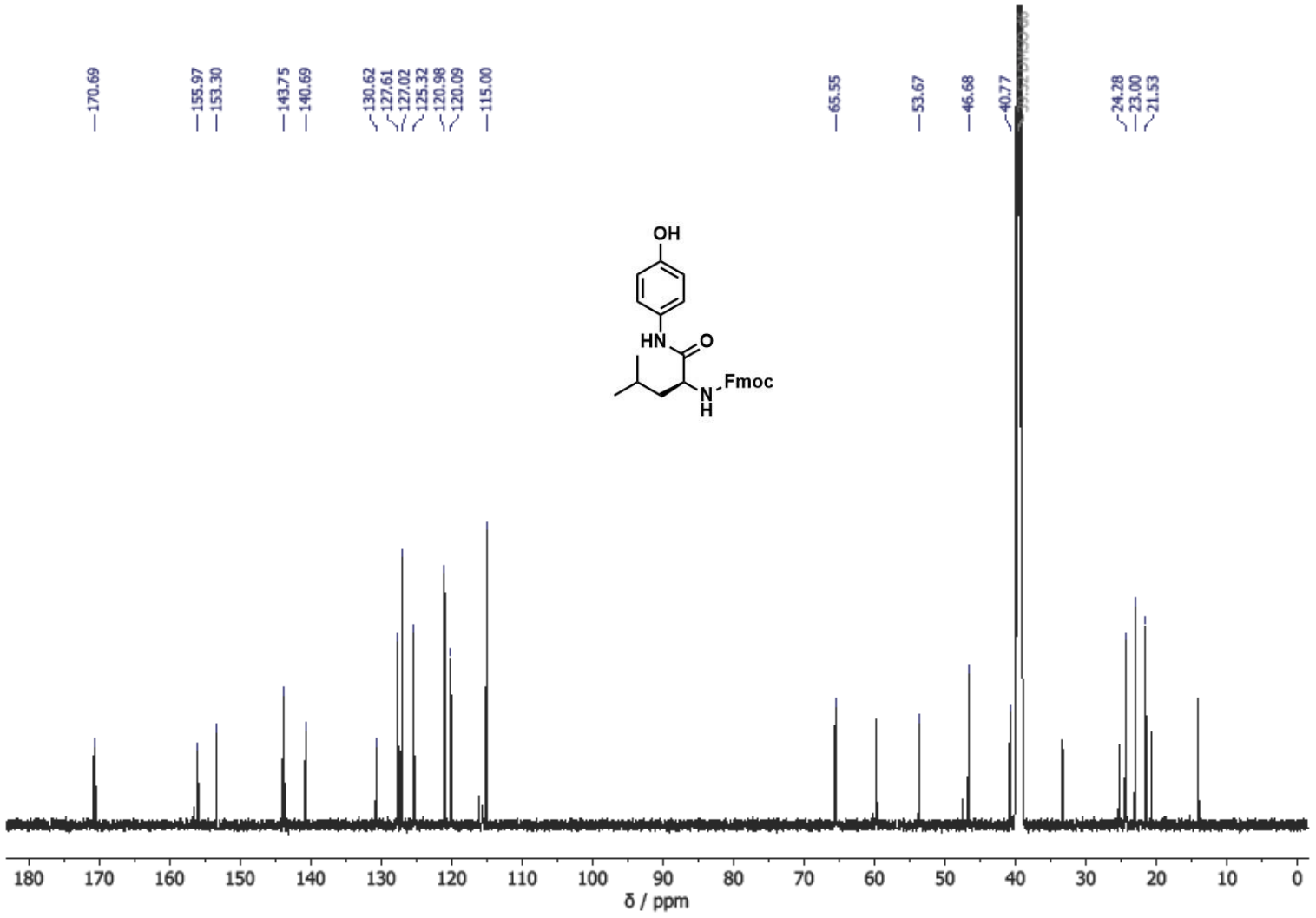

Figure A6.54: The ^{13}C NMR spectrum (151 MHz) of (9H-fluoren-9-yl)methyl (S)-(1-((4-hydroxyphenyl)amino)-4-methyl-1-oxopentan-2-yl)carbamate, **74**, in DMSO-d_6.

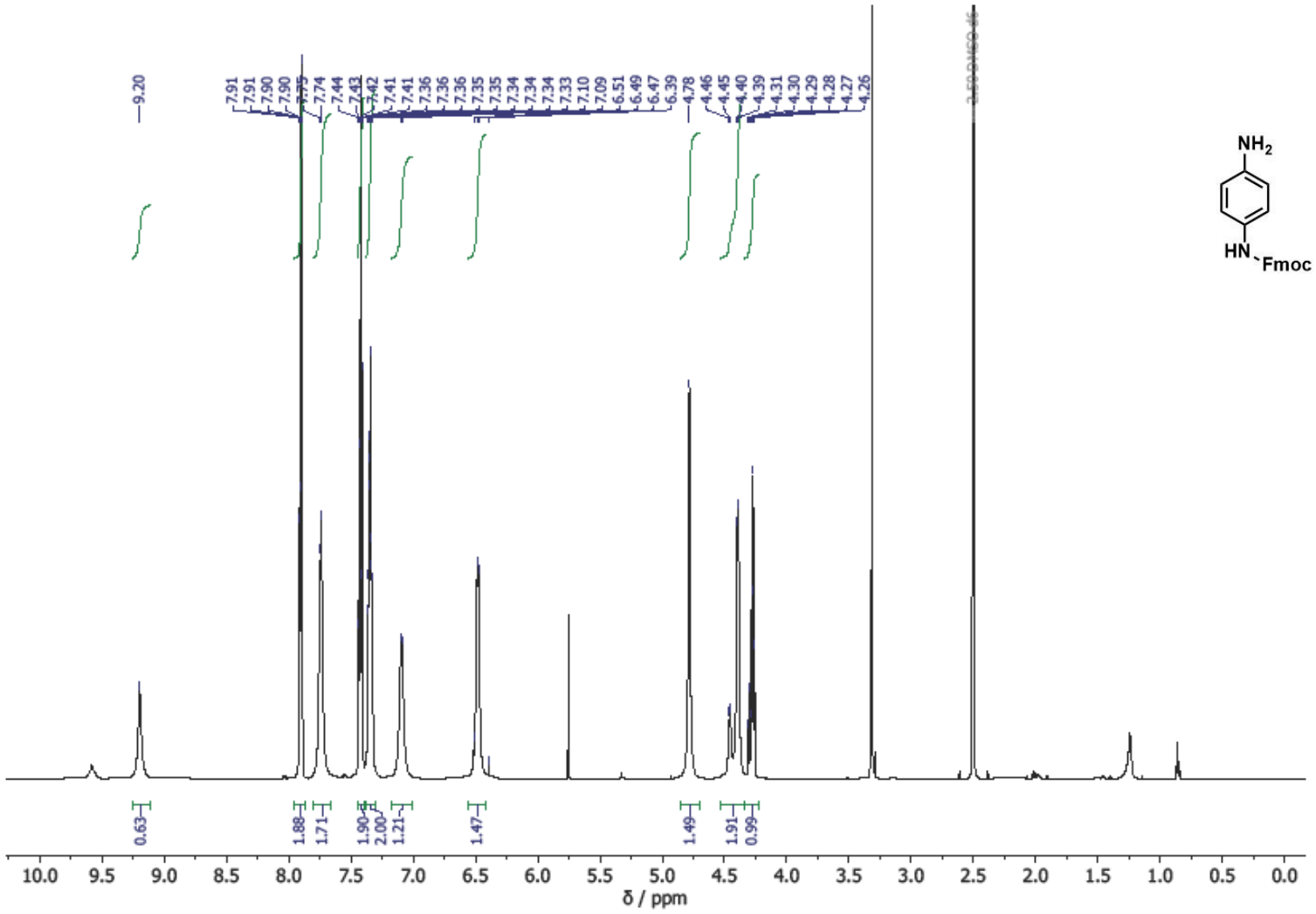

Figure A6.55: The ^{1}H NMR spectrum (600 MHz) of (9H-fluoren-9-yl)methyl (4-aminophenyl)carbamate, **79**, in DMSO-d_6.

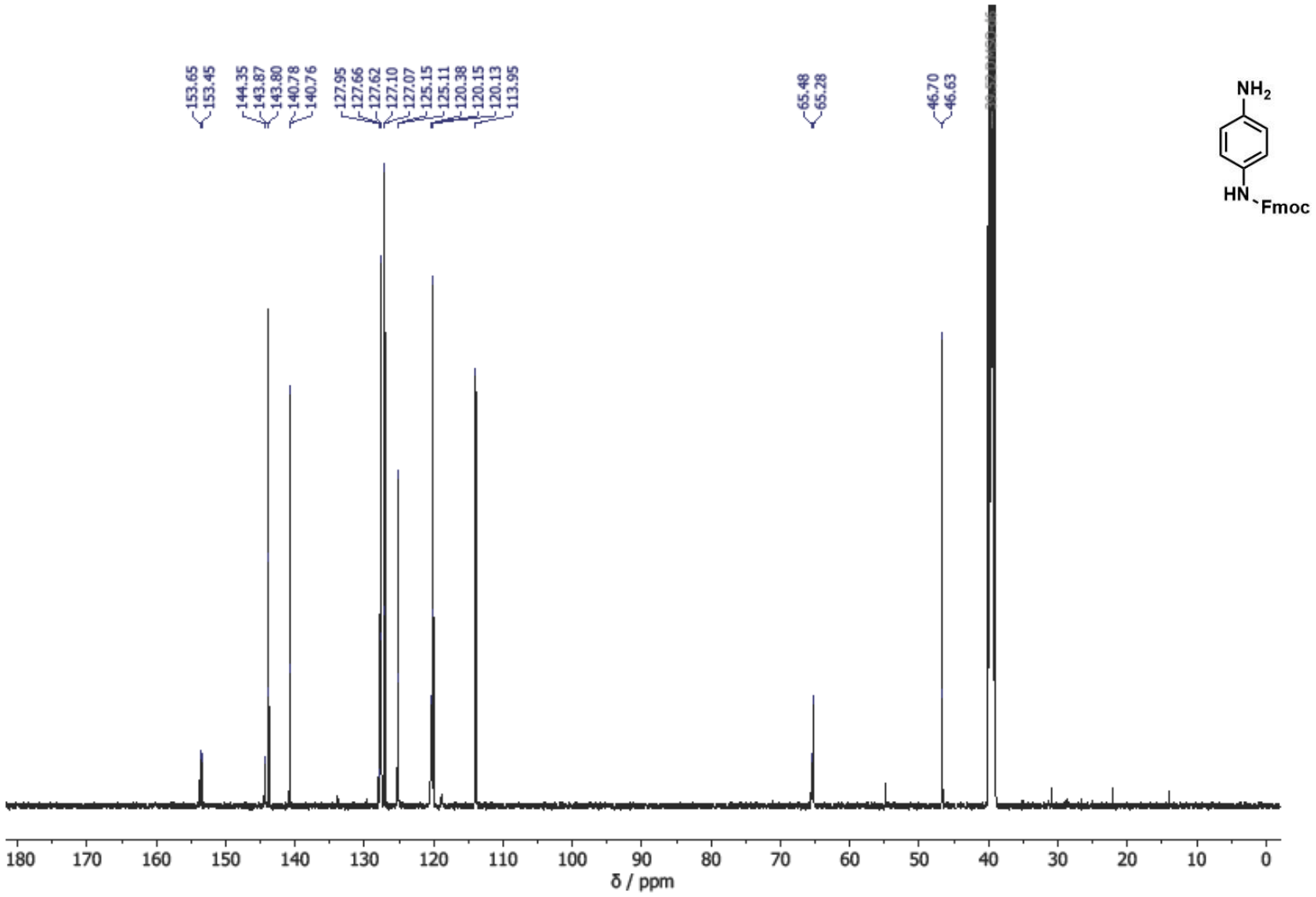

Figure A6.56: The ^{13}C NMR spectrum (151 MHz) of (9H-fluoren-9-yl)methyl (4-aminophenyl)carbamate, **79**, in DMSO-d_6.

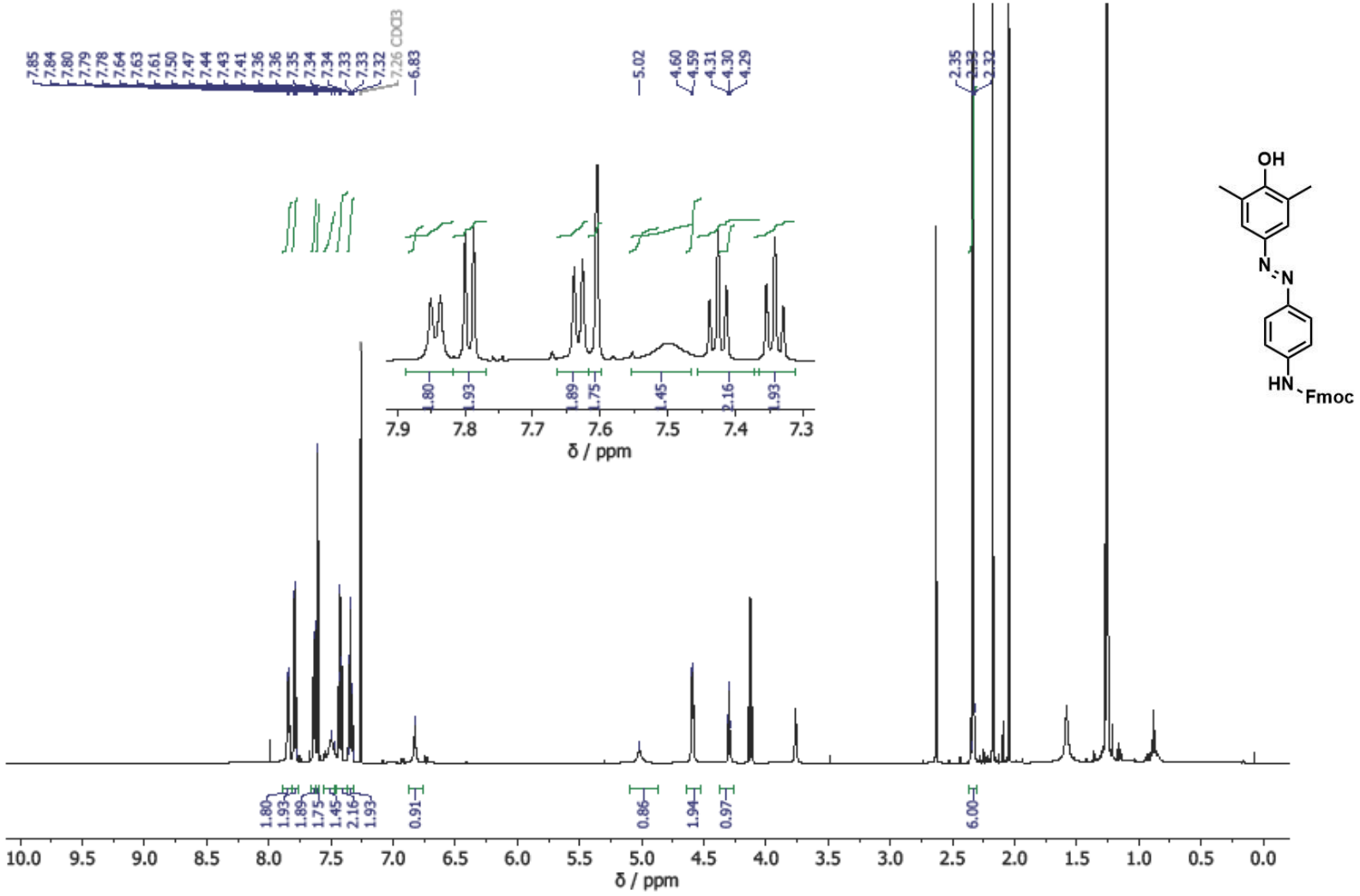

Figure A6.57: *The ^{1}H NMR spectrum (600 MHz) of* (9H-fluoren-9-yl)methyl (E)-(4-((4-hydroxy-3,5-dimethylphenyl)diazenyl)phenyl)carbamate, **80**, *in $CDCl_3$.*

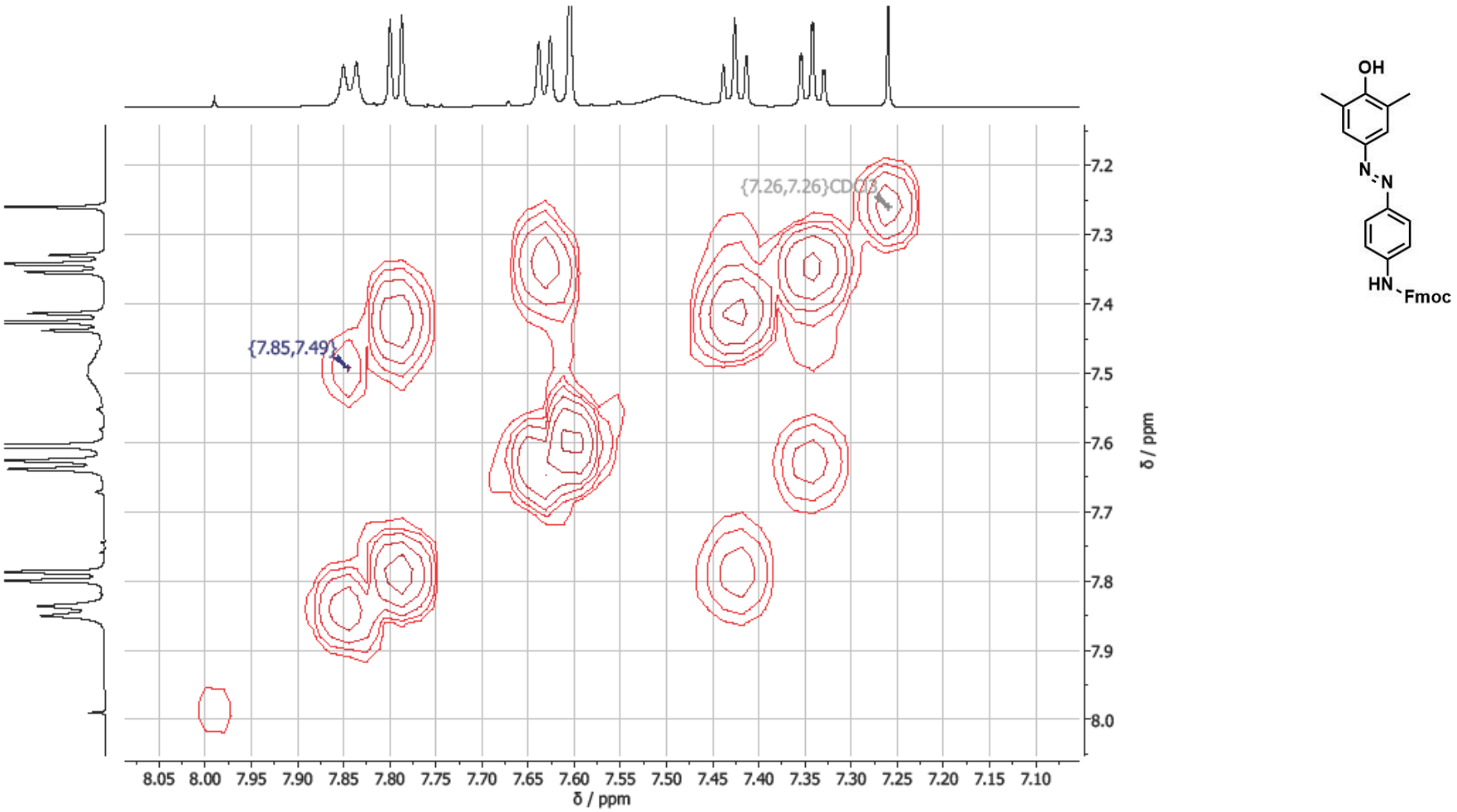

Figure A6.58: The aromatic region of the COSY NMR spectrum (600 MHz) of (9H-fluoren-9-yl)methyl (E)-(4-((4-hydroxy-3,5-dimethylphenyl)diazenyl)phenyl)carbamate, **80**, in $CDCl_3$. The picked peak shows the coupling between the two aromatic regions of the middle aromatic ring.

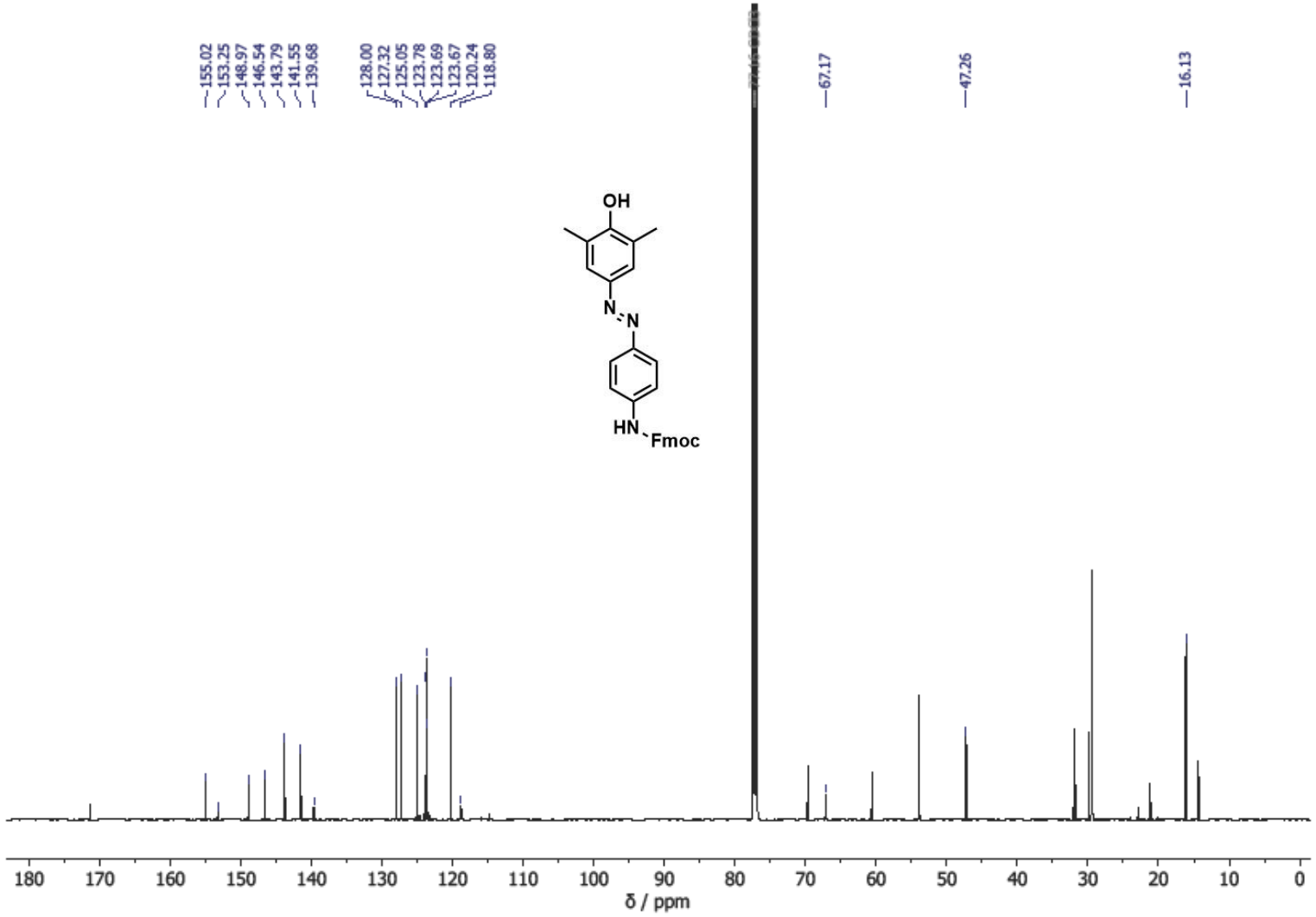

Figure A6.59: The ^{13}C NMR spectrum (151 MHz) of (9H-fluoren-9-yl)methyl (E)-(4-((4-hydroxy-3,5-dimethylphenyl)diazenyl)phenyl)carbamate, **80**, *in $CDCl_3$.*

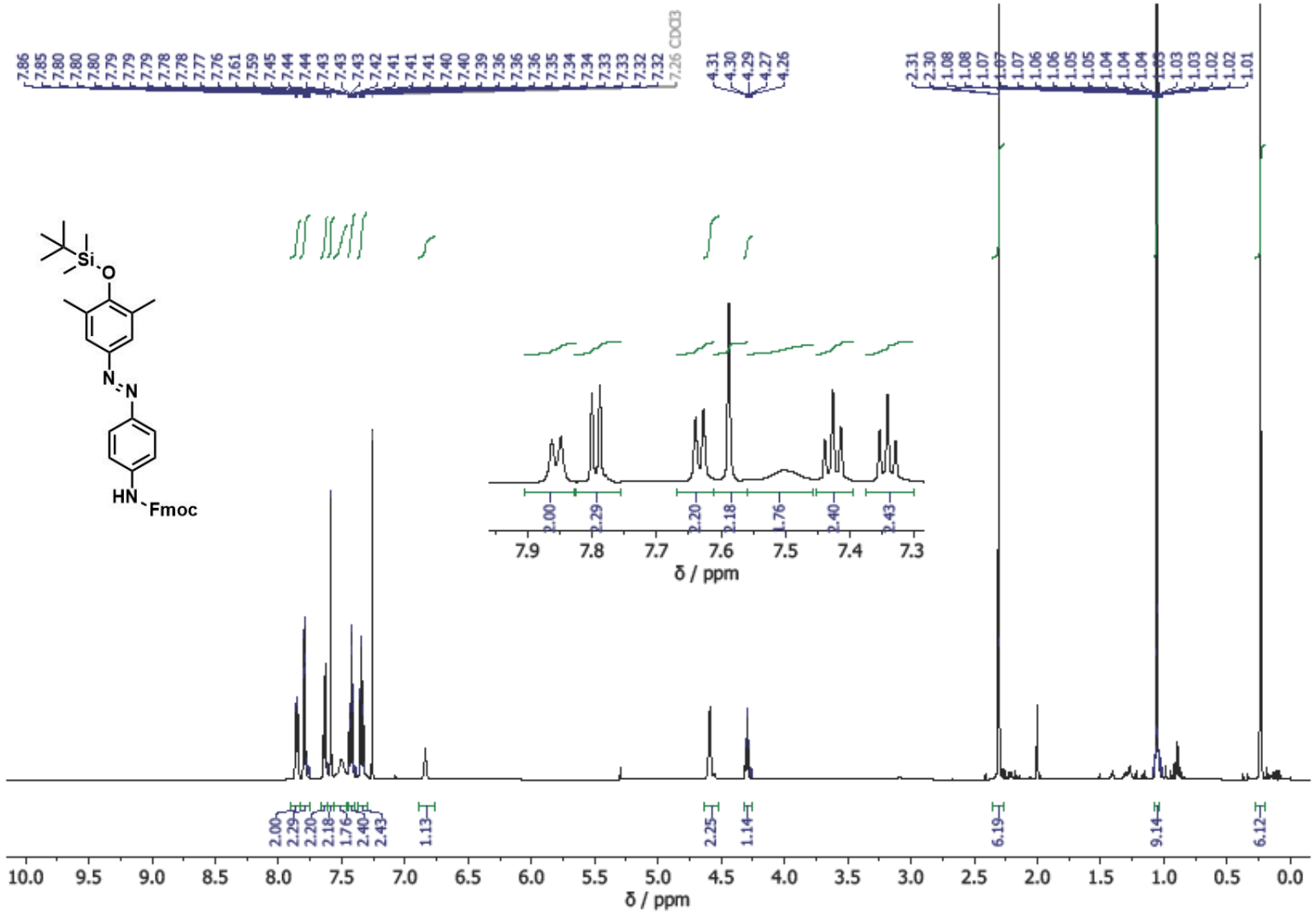

Figure A6.60: The [1]H NMR spectrum (600 MHz) of (9H-fluoren-9-yl)methyl (E)-(4-((4-((tert-butyldimethylsilyl)oxy)-3,5-dimethylphenyl)diazenyl)phenyl)carbamate, **81**, *in* $CDCl_3$.

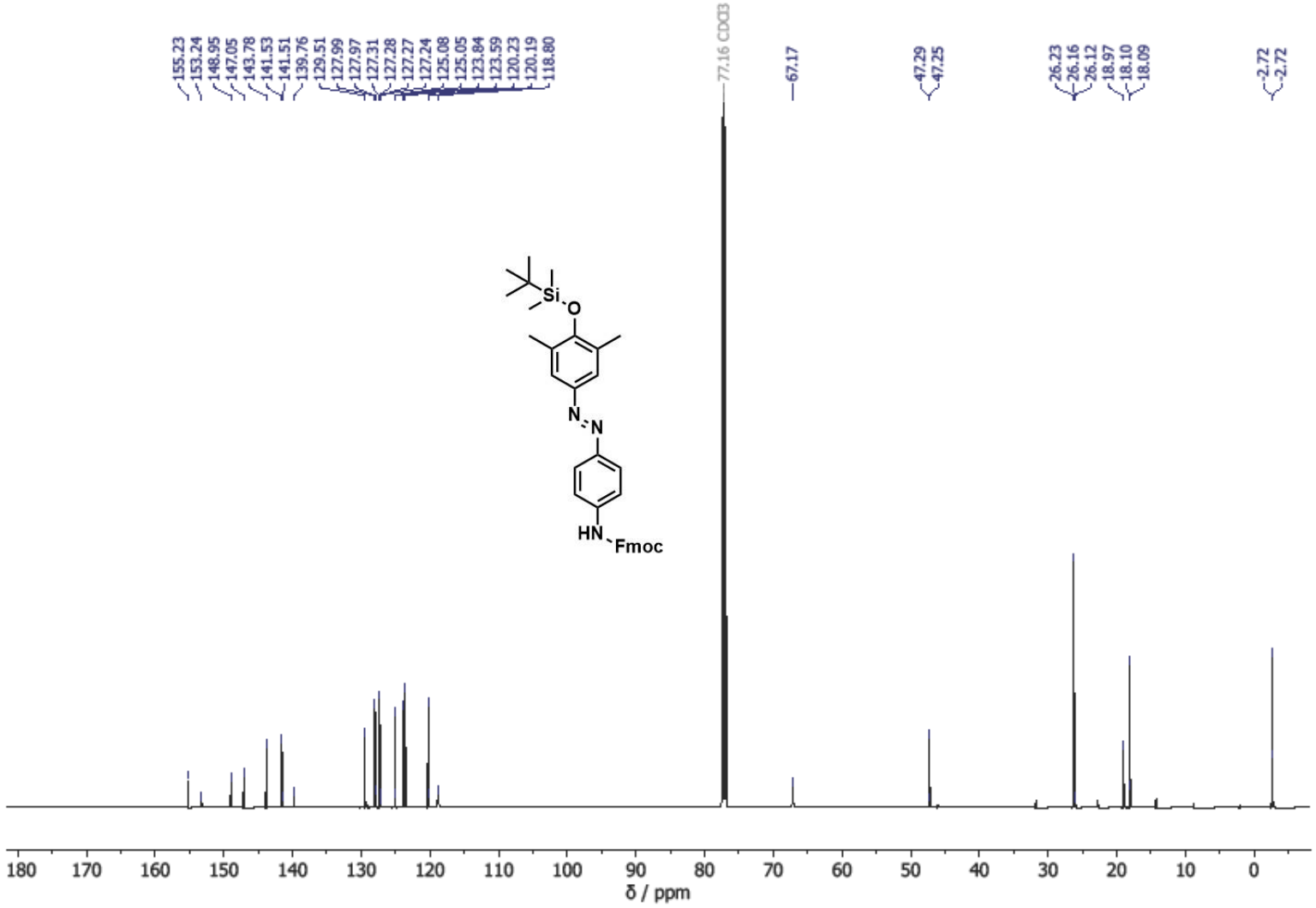

Figure A6.61: The ^{13}C NMR spectrum (600 MHz) of (9H-fluoren-9-yl)methyl (E)-(4-((4-((tert-butyldimethylsilyl)oxy)-3,5-dimethylphenyl)diazenyl)phenyl)carbamate, **81**, *in* $CDCl_3$.

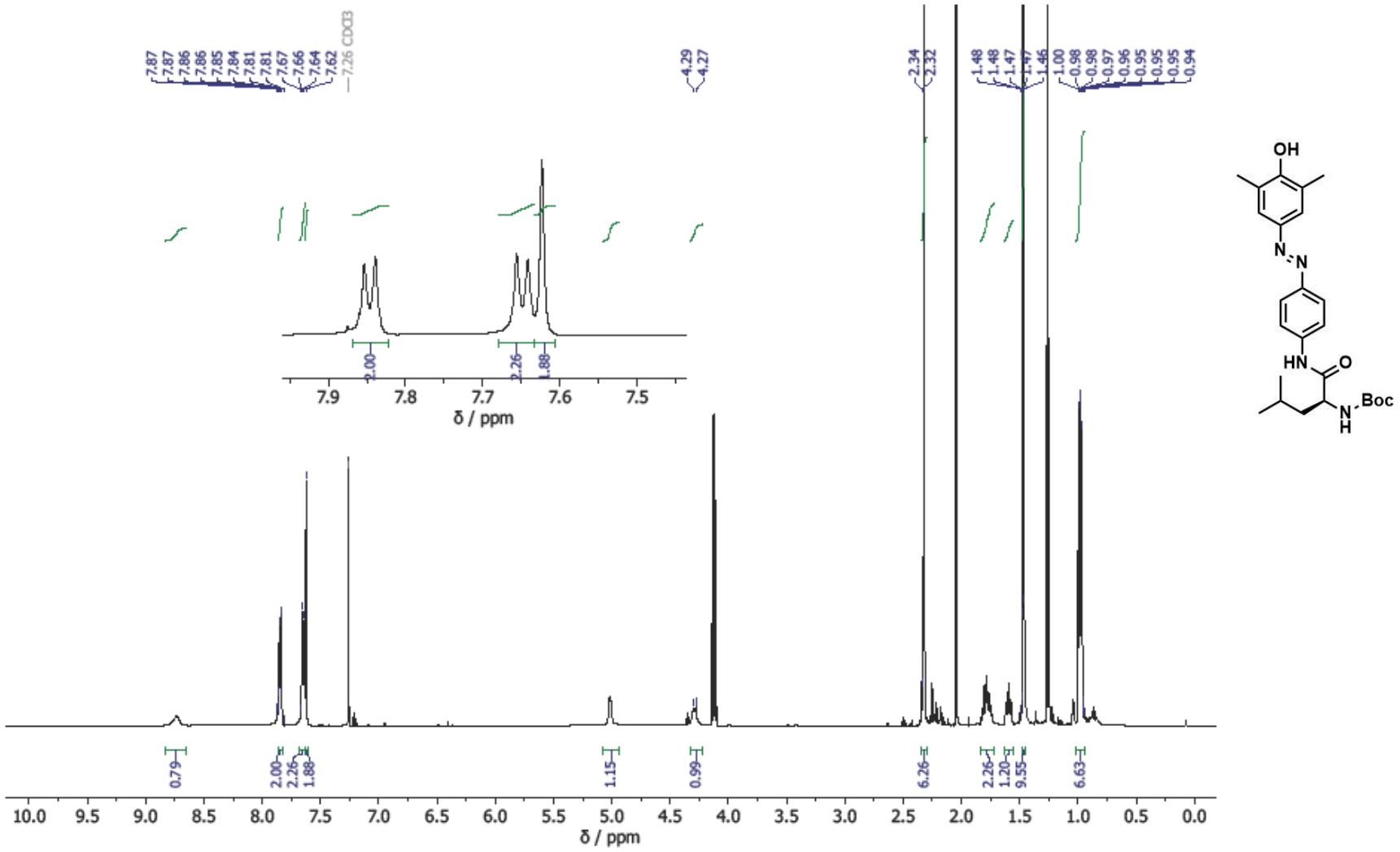

Figure A6.62: The ^{1}H NMR spectrum (600 MHz) of tert-butyl (S,E)-(1-((4-((4-hydroxy-3,5-dimethylphenyl)diazenyl)phenyl)amino)-4-methyl-1-oxopentan-2-yl)carbamate, **83**, in $CDCl_3$.

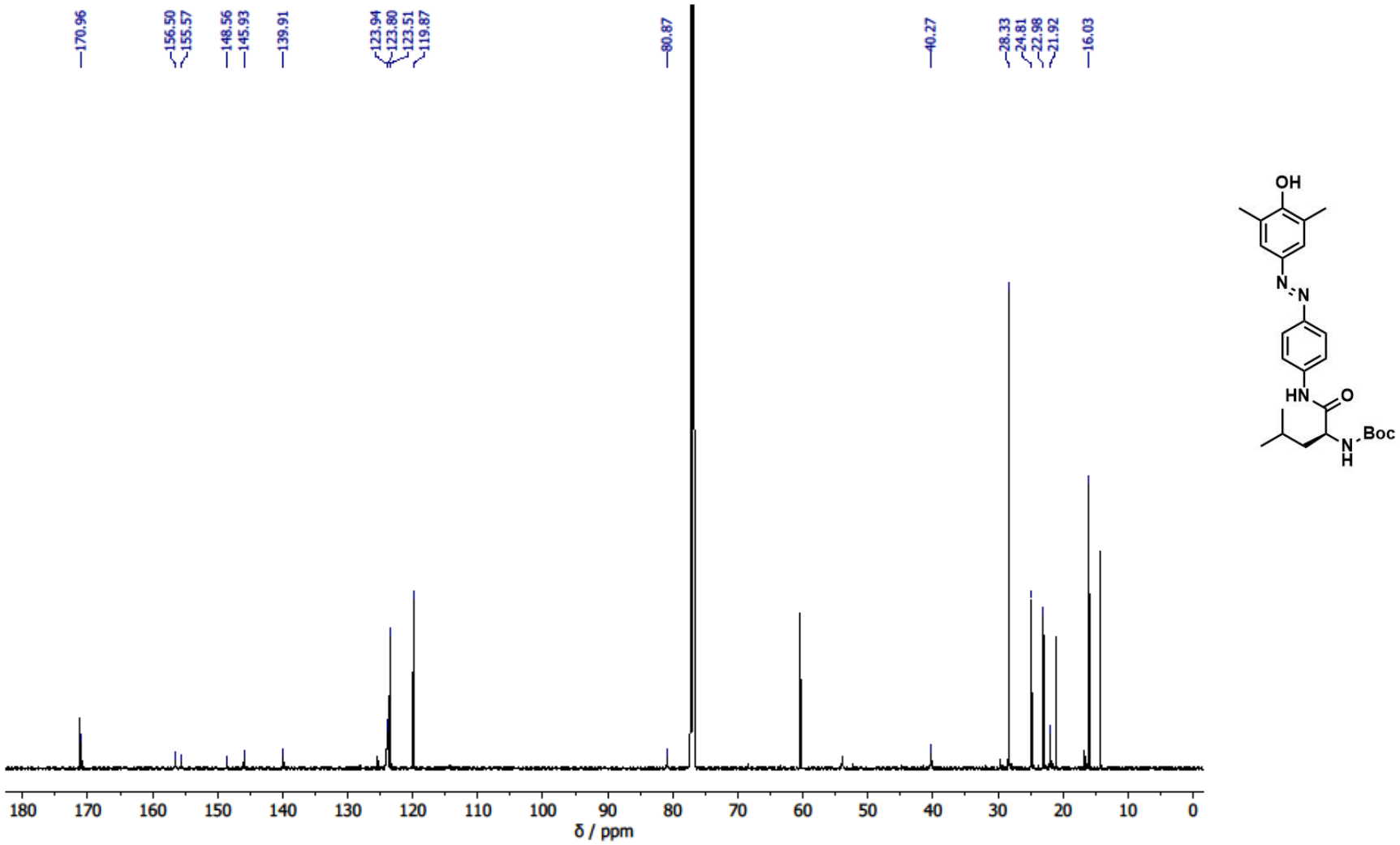

Figure A6.63: The ^{13}C NMR spectrum (151 MHz) of tert-butyl (S,E)-(1-((4-((4-hydroxy-3,5-dimethylphenyl)diazenyl)phenyl)amino)-4-methyl-1-oxopentan-2-yl)carbamate, **83**, in $CDCl_3$.

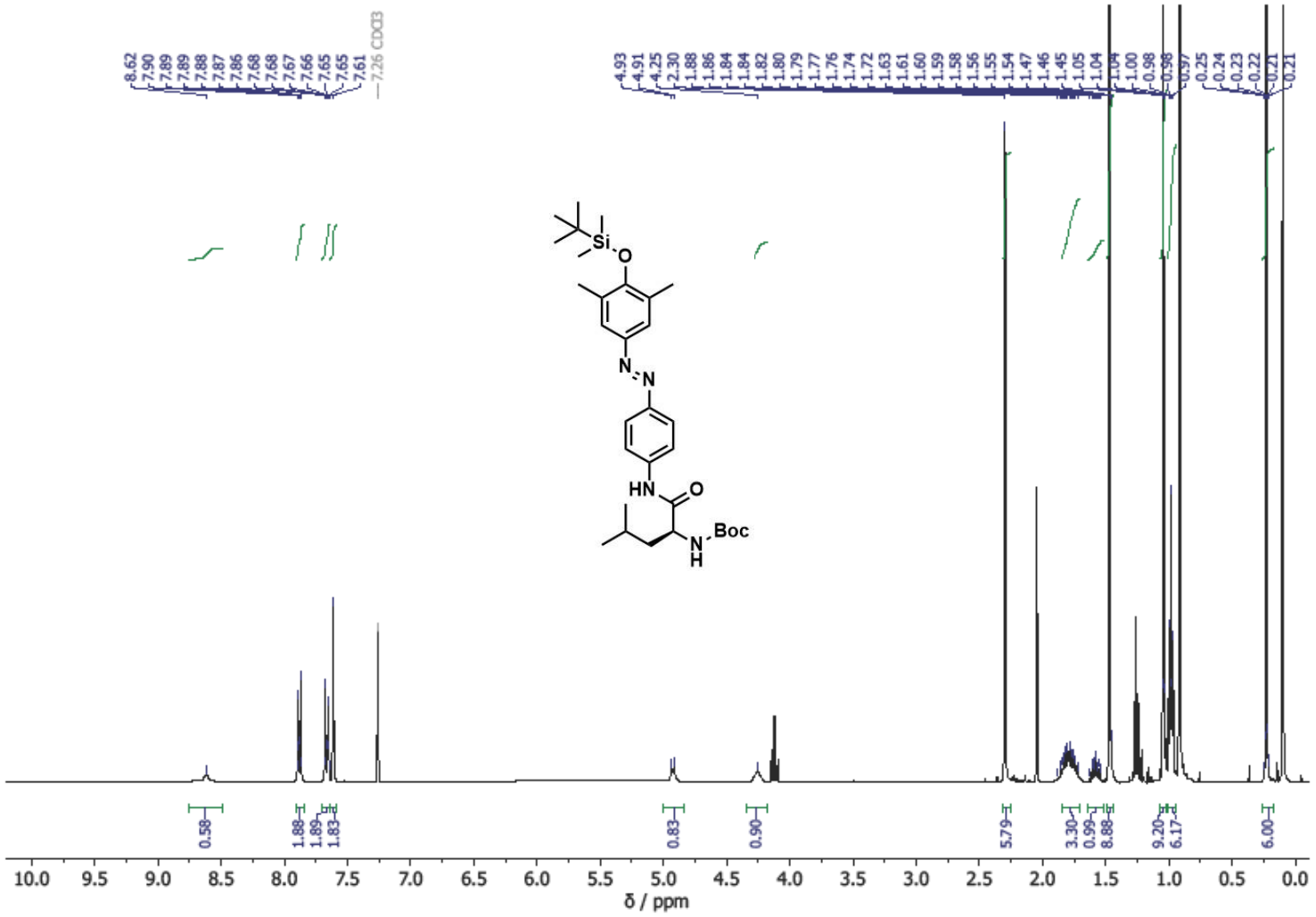

Figure A6.64: The ^{1}H NMR spectrum (600 MHz) of tert-butyl (S,E)-(1-((4-((4-((tert-butyldimethylsilyl)oxy)-3,5-dimethylphenyl)diazenyl)phenyl)amino)-4-methyl-1-oxopentan-2-yl)carbamate, **84**, *in* $CDCl_3$.

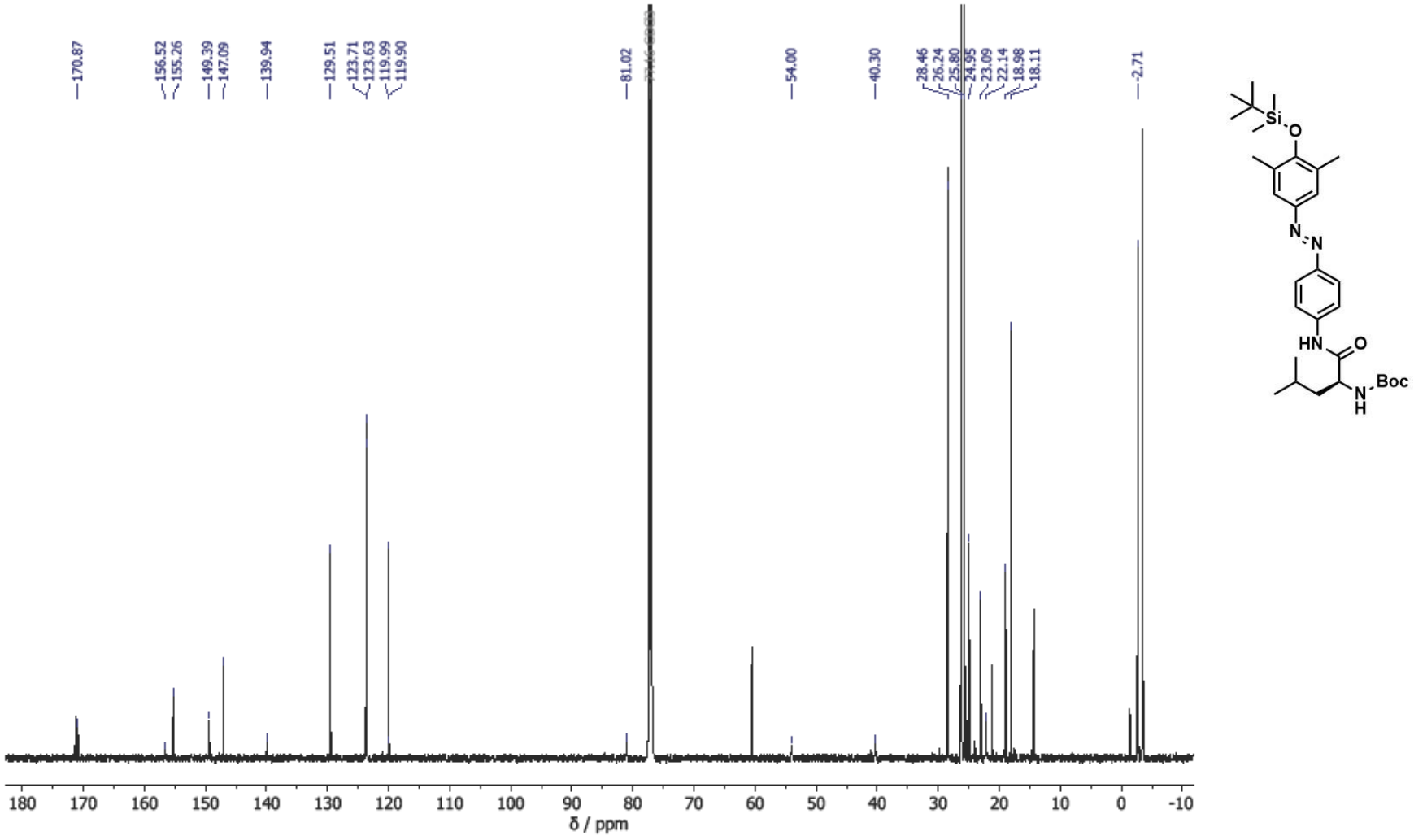

Figure A6.65: The ^{13}C NMR spectrum (151 MHz) of tert-butyl (S,E)-(1-((4-((4-((tert-butyldimethylsilyl)oxy)-3,5-dimethylphenyl)diazenyl)phenyl)amino)-4-methyl-1-oxopentan-2-yl)carbamate, **84**, *in $CDCl_3$.*

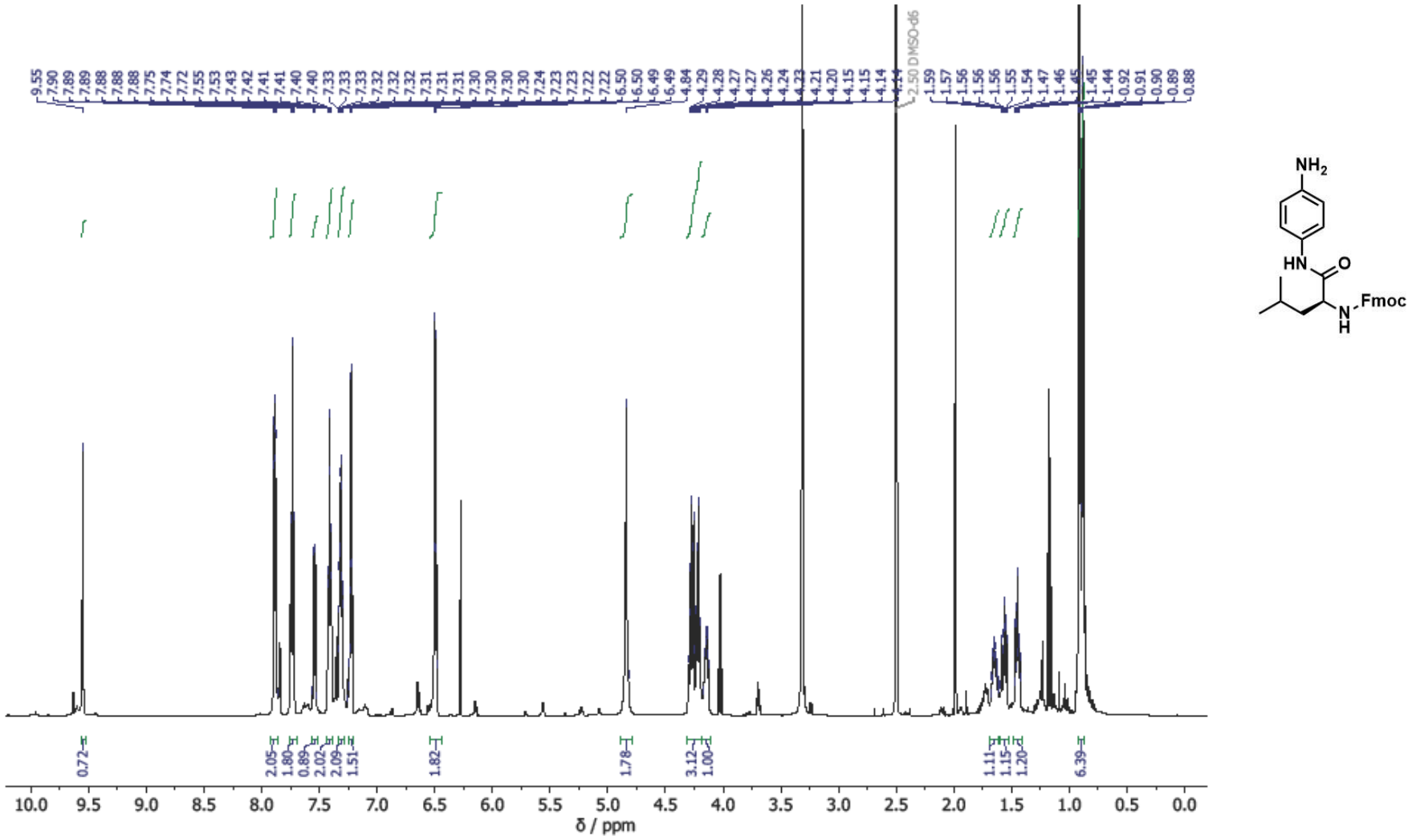

Figure A6.66: The ^{1}H NMR spectrum (600 MHz) of (9H-fluoren-9-yl)methyl (S)-(1-((4-aminophenyl)amino)-4-methyl-1-oxopentan-2-yl)carbamate, **88**, in DMSO-d_6.

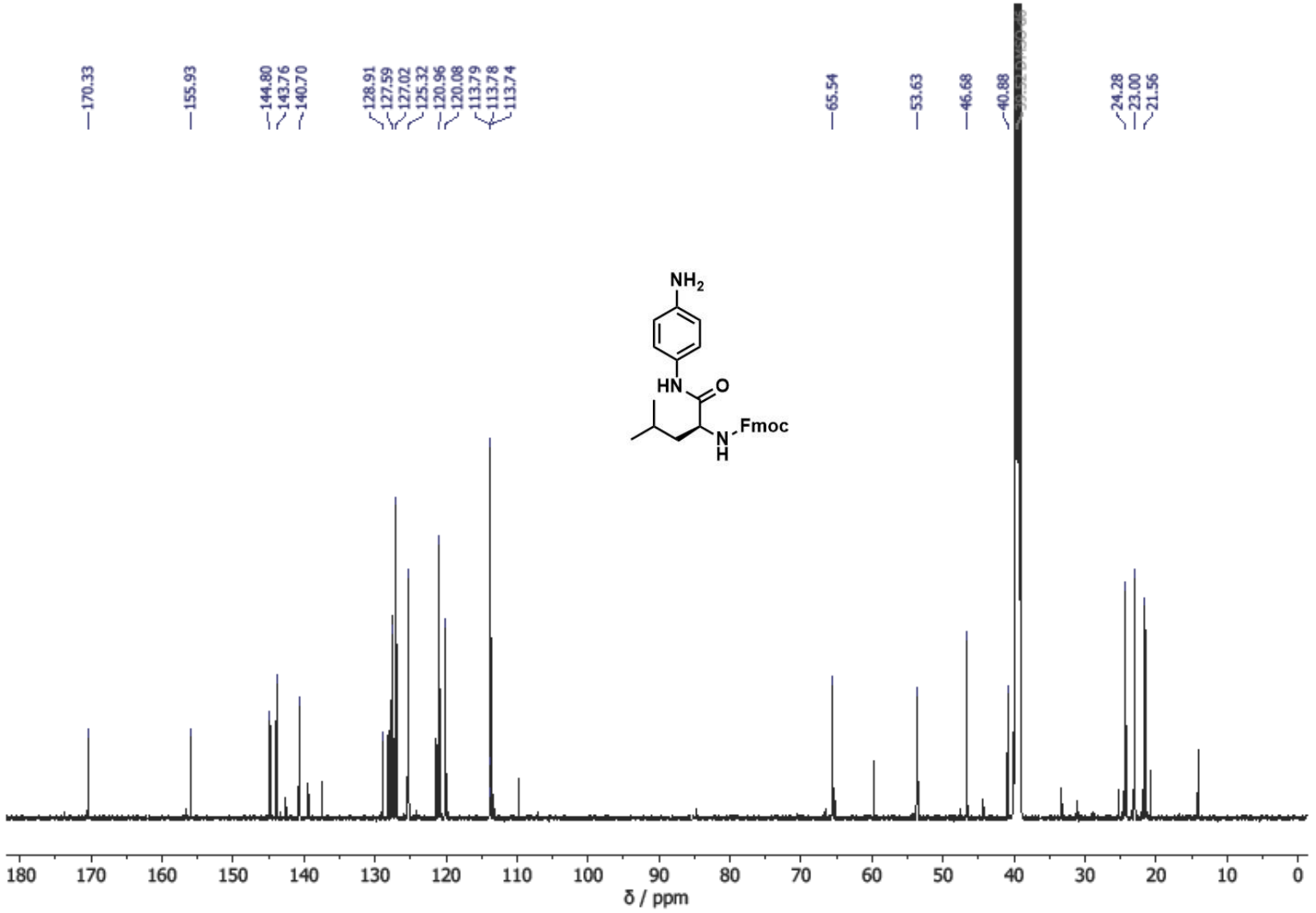

Figure A6.67: The ^{13}C NMR spectrum (151 MHz) of (9H-fluoren-9-yl)methyl (S)-(1-((4-aminophenyl)amino)-4-methyl-1-oxopentan-2-yl)carbamate, **88**, in DMSO-d_6.

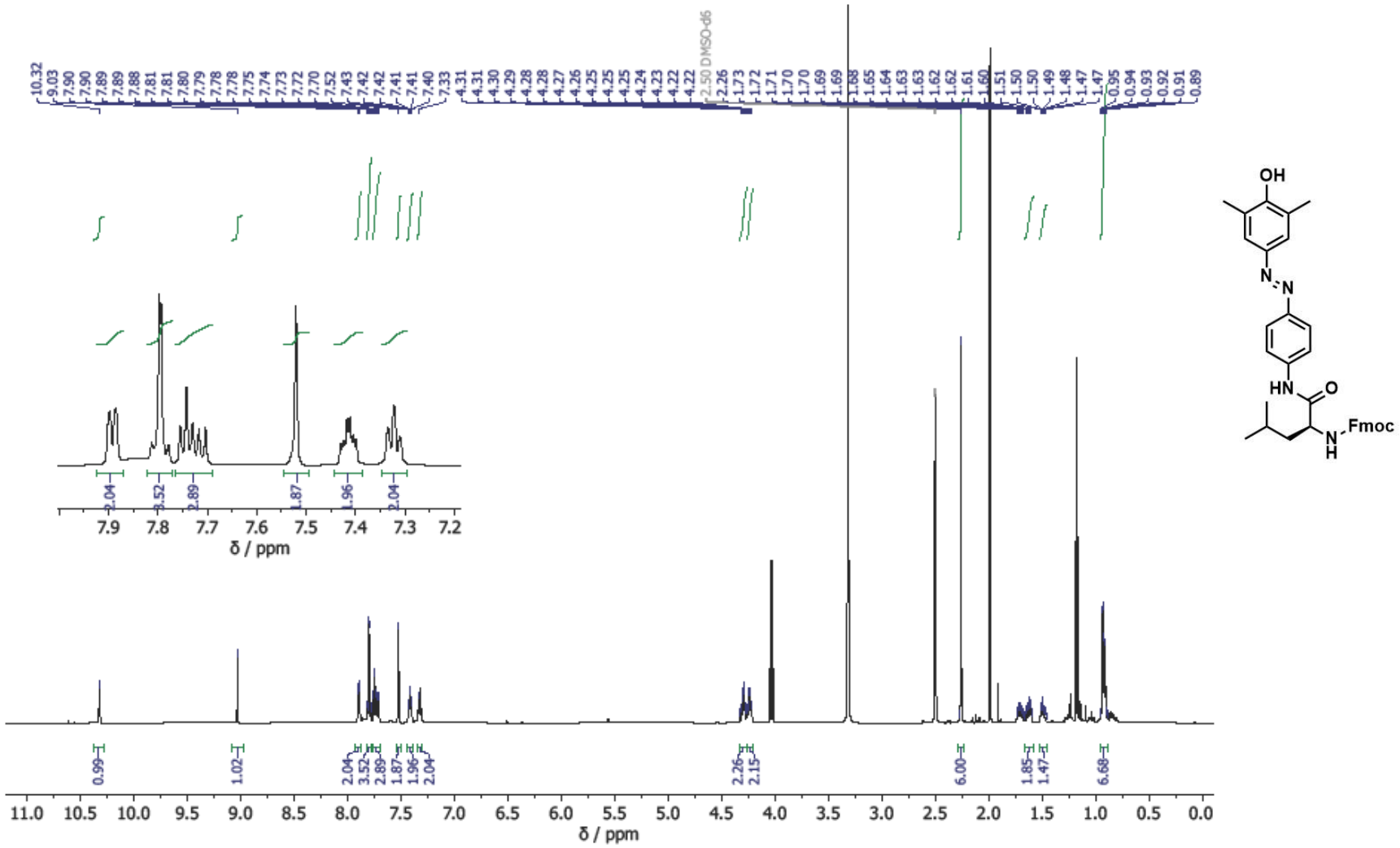

Figure A6.68: *The ^{1}H NMR spectrum (600 MHz) of* (9H-fluoren-9-yl)methyl (S,E)-(1-((4-((4-hydroxy-3,5-dimethylphenyl)diazenyl)phenyl)amino)-4-methyl-1-oxopentan-2-yl)carbamate, **89**, *in DMSO-d_6.*

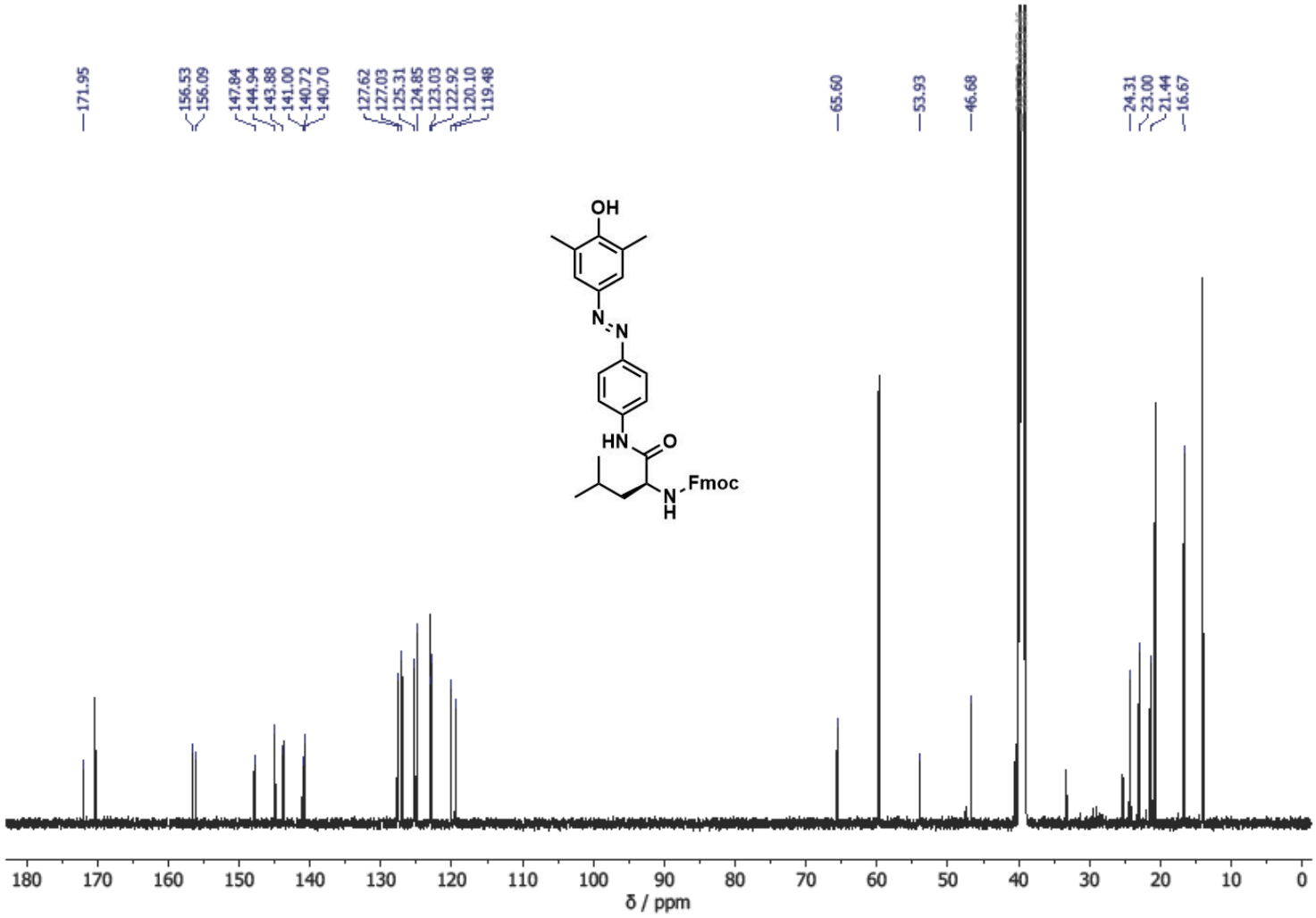

Figure A6.69: *The ^{13}C NMR spectrum (151 MHz) of* (9H-fluoren-9-yl)methyl (S,E)-(1-((4-((4-hydroxy-3,5-dimethylphenyl)diazenyl)phenyl)amino)-4-methyl-1-oxopentan-2-yl)carbamate, **89**, *in DMSO-d_6.*

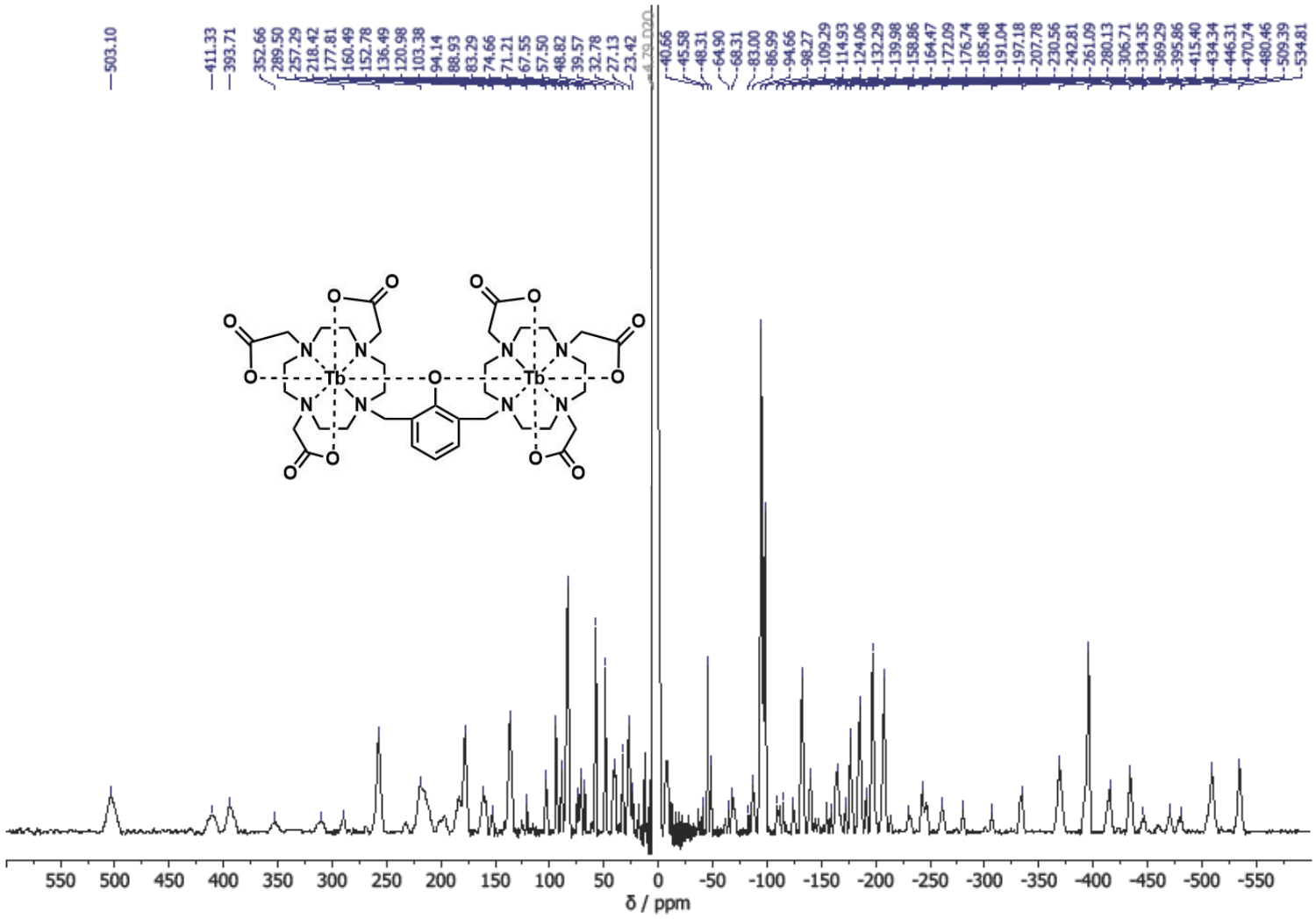

Figure A6.70: The ^{1}H NMR spectrum (500 MHz) of TbTbOH **93Tb** in D_2O.

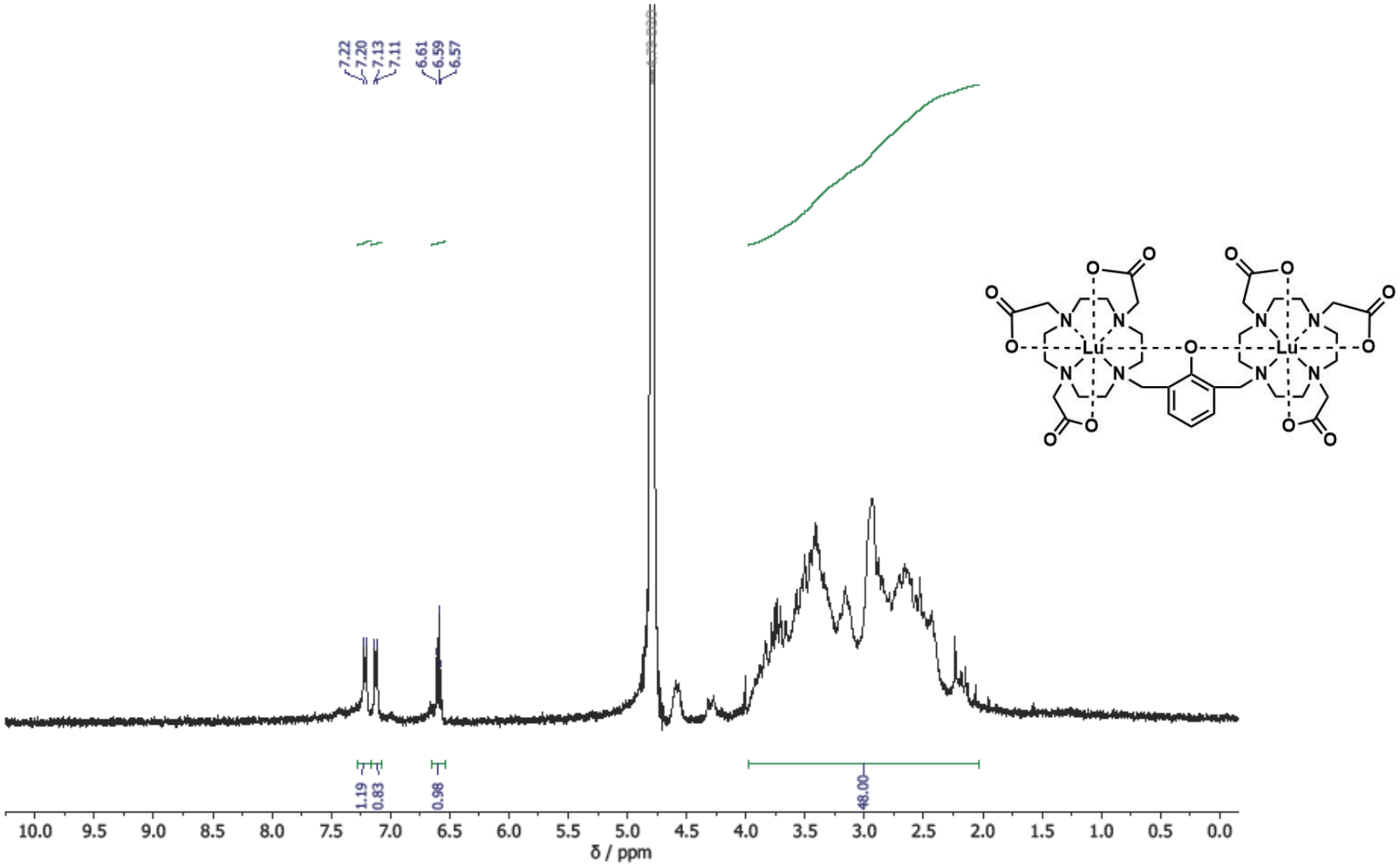

Figure A6.71: The ^{1}H NMR spectrum (500 MHz) of LuLuOH **93Lu** in D_2O.

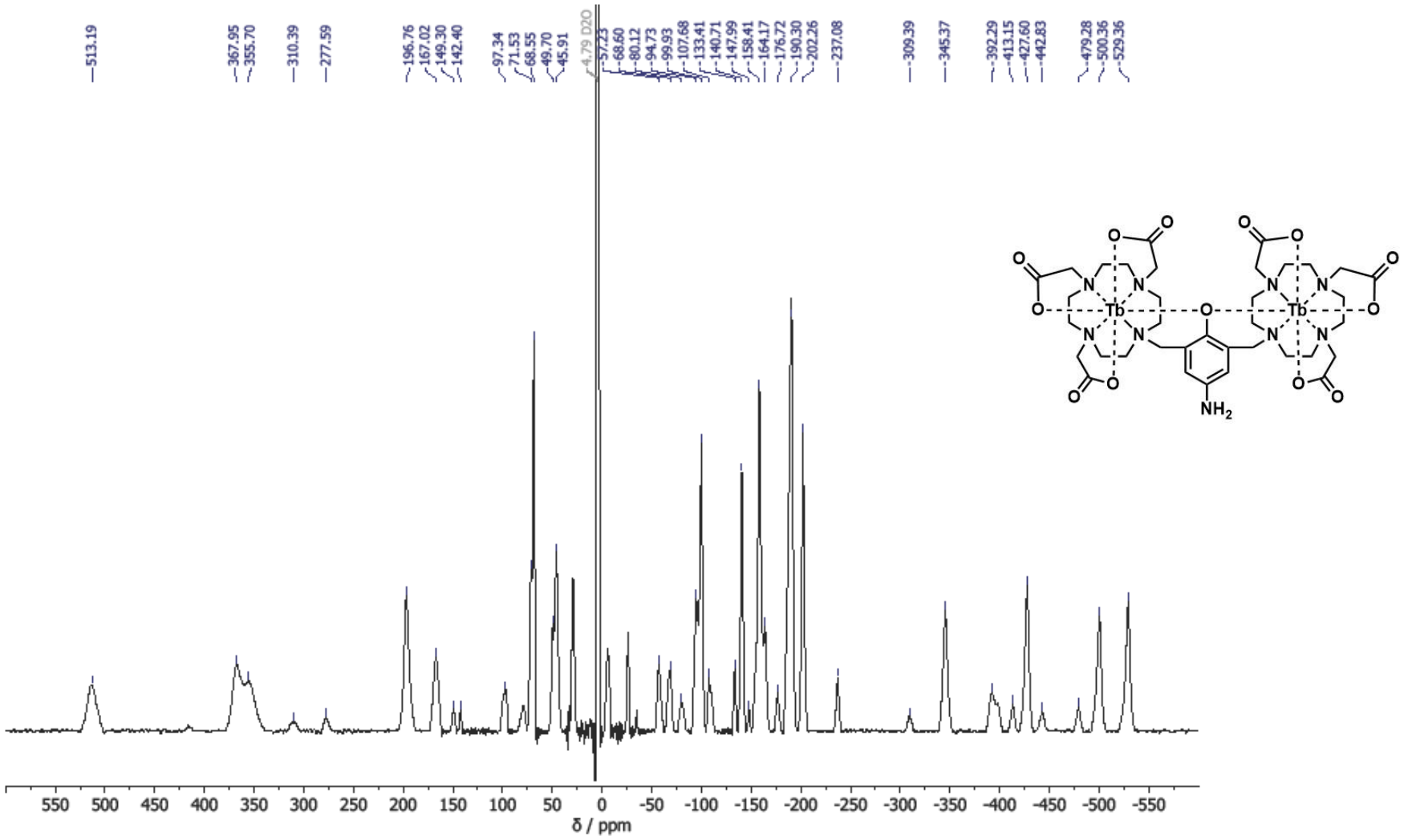

Figure A6.72: The ^{1}H NMR spectrum (500 MHz) of TbTbNH$_2$ **54** in D_2O.

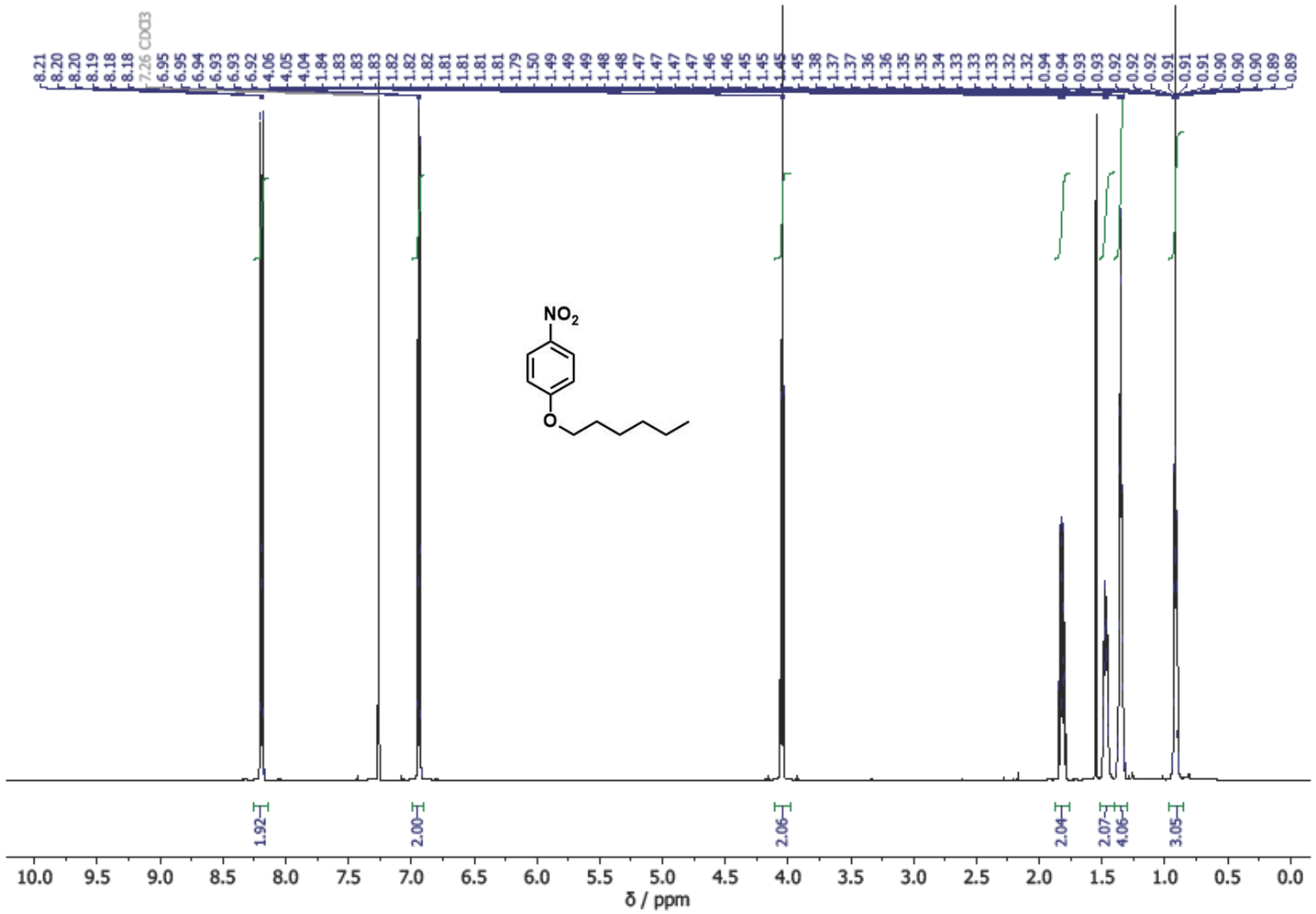

Figure A6.73: The ^{1}H NMR spectrum (600 MHz) of 1-(hexyloxy)-4-nitrobenzene, **107**, in $CDCl_3$.

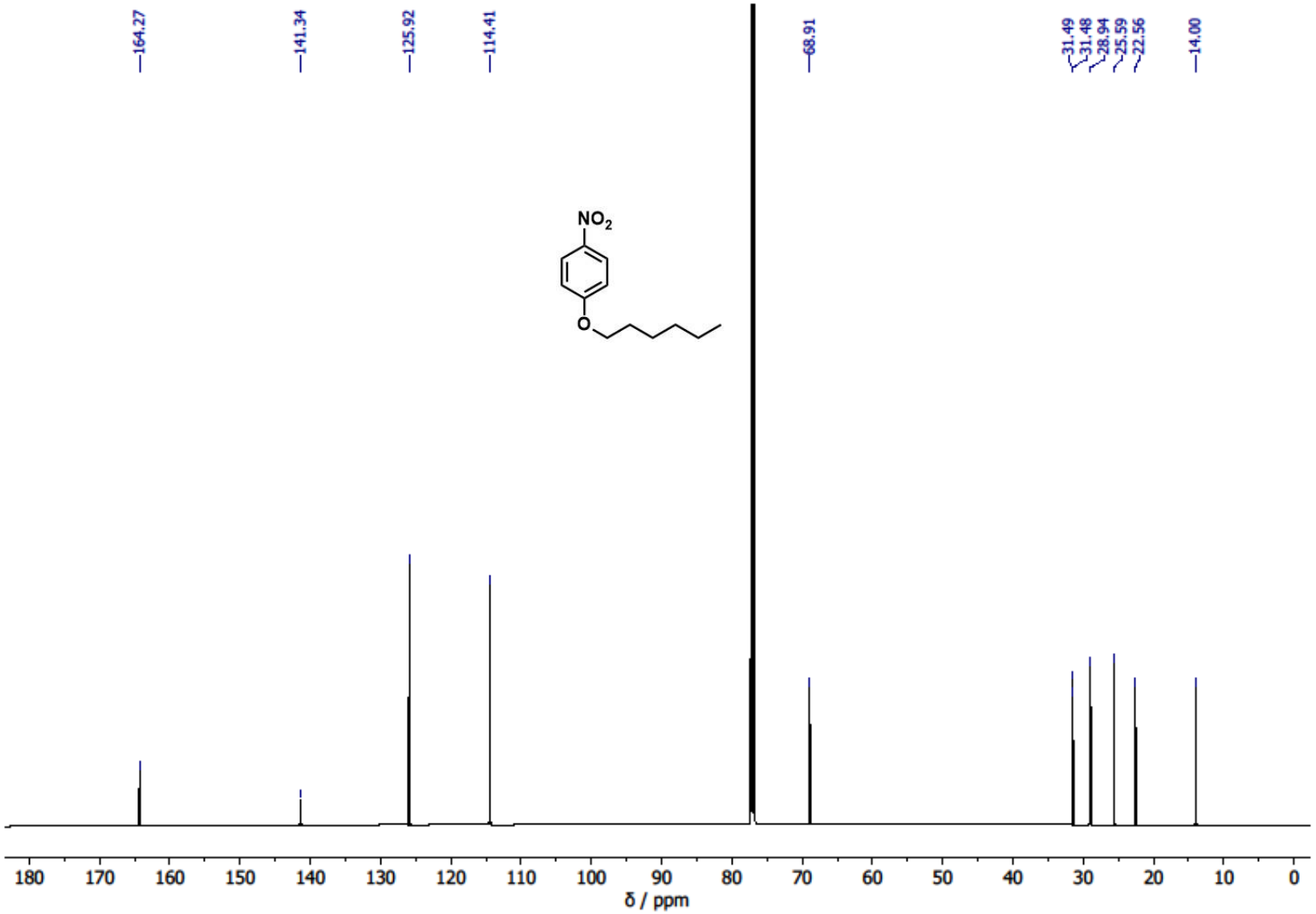

Figure A6.74: The ^{13}C NMR spectrum (151 MHz) of 1-(hexyloxy)-4-nitrobenzene, **107**, in $CDCl_3$.

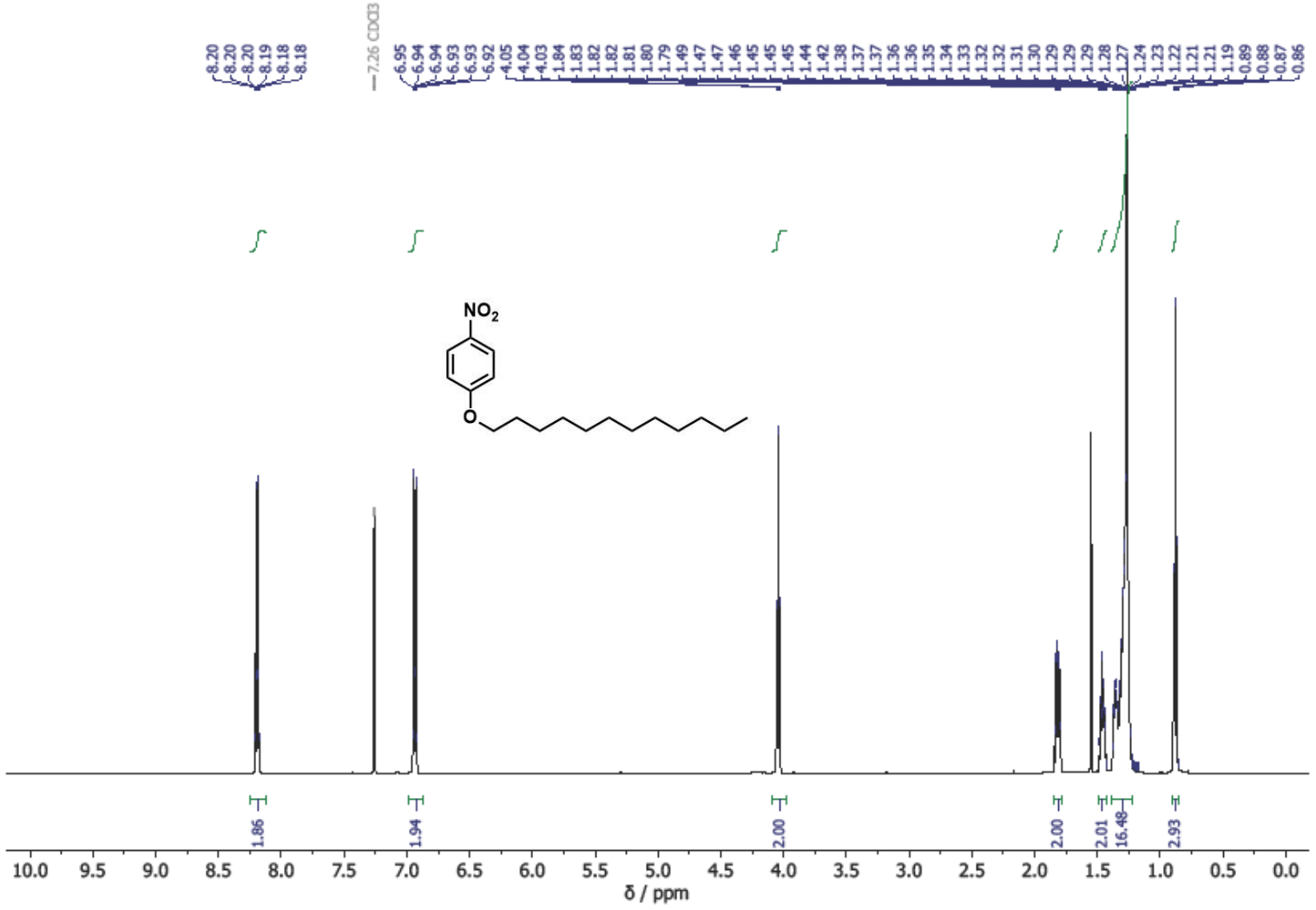

Figure A6.75: The ^{1}H NMR spectrum (600 MHz) of 1-(dodecyloxy)-4-nitrobenzene, **108**, in $CDCl_3$.

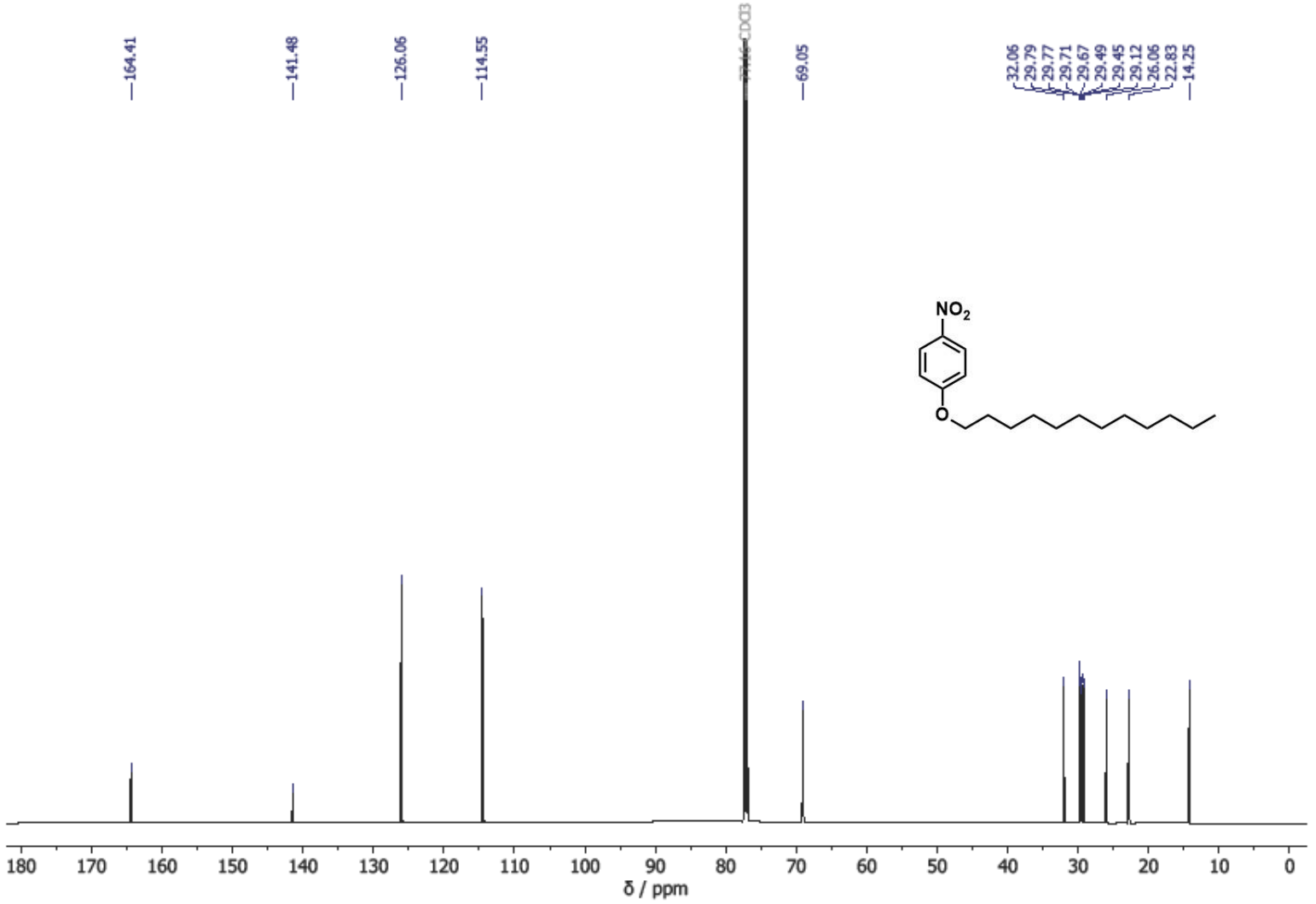

Figure A6.76: The ^{13}C NMR spectrum (151 MHz) of 1-(dodecyloxy)-4-nitrobenzene, **108**, in $CDCl_3$.

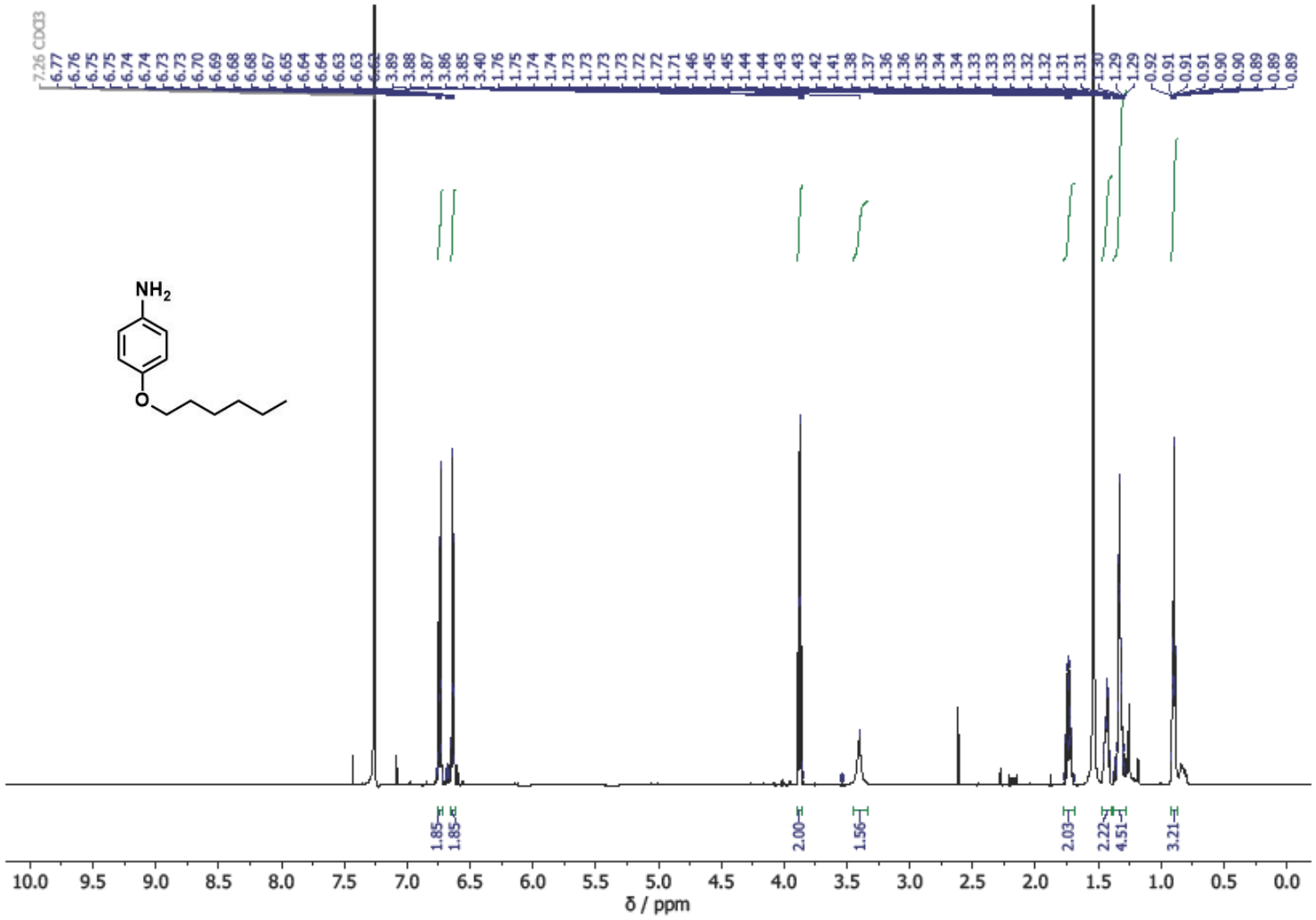

Figure A6.77: The ^{1}H NMR spectrum (600 MHz) of 4-(hexyloxy)aniline, **109**, in $CDCl_3$.

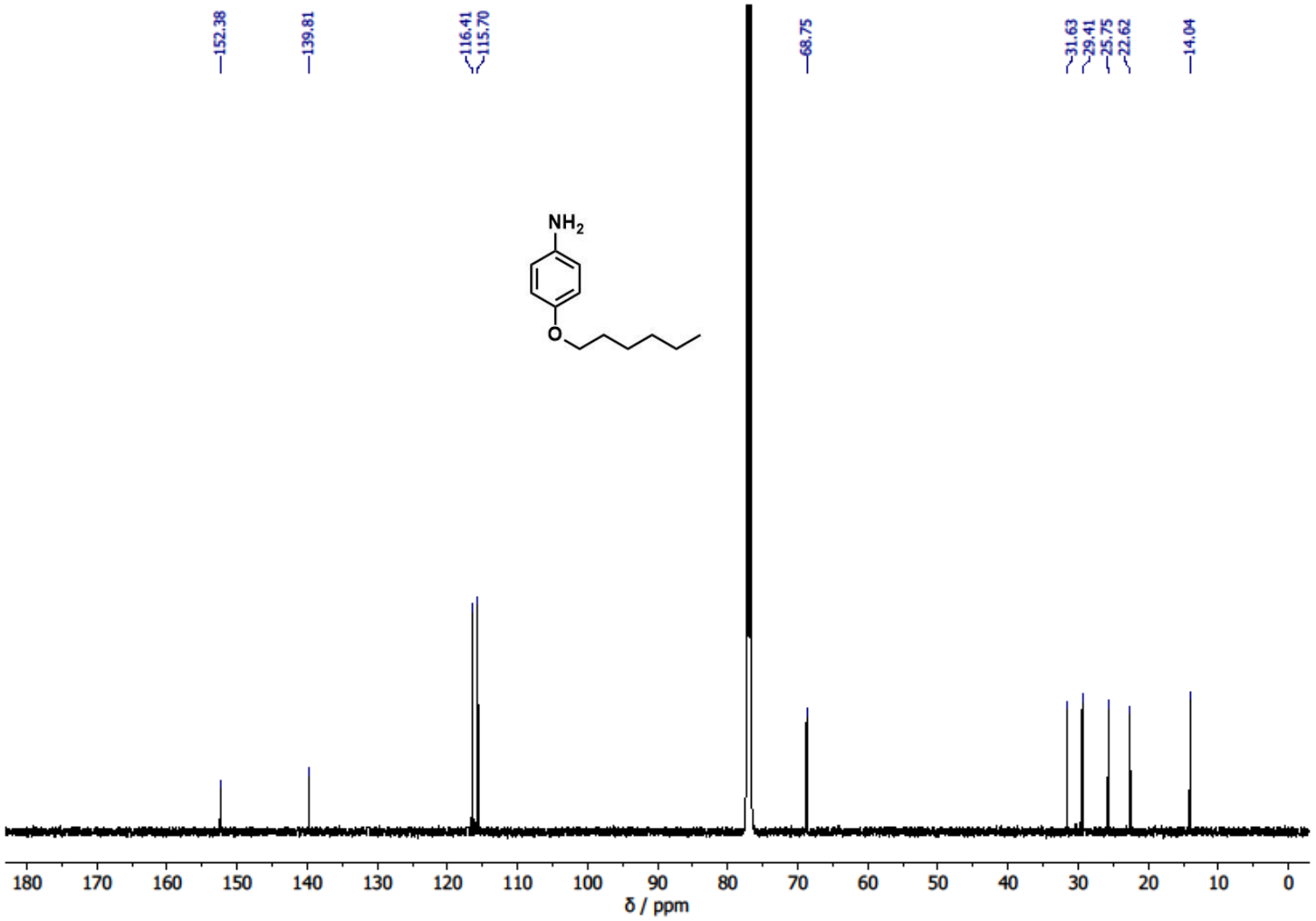

Figure A6.78: The ^{13}C NMR spectrum (151 MHz) of 4-(hexyloxy)aniline, **109**, in $CDCl_3$.

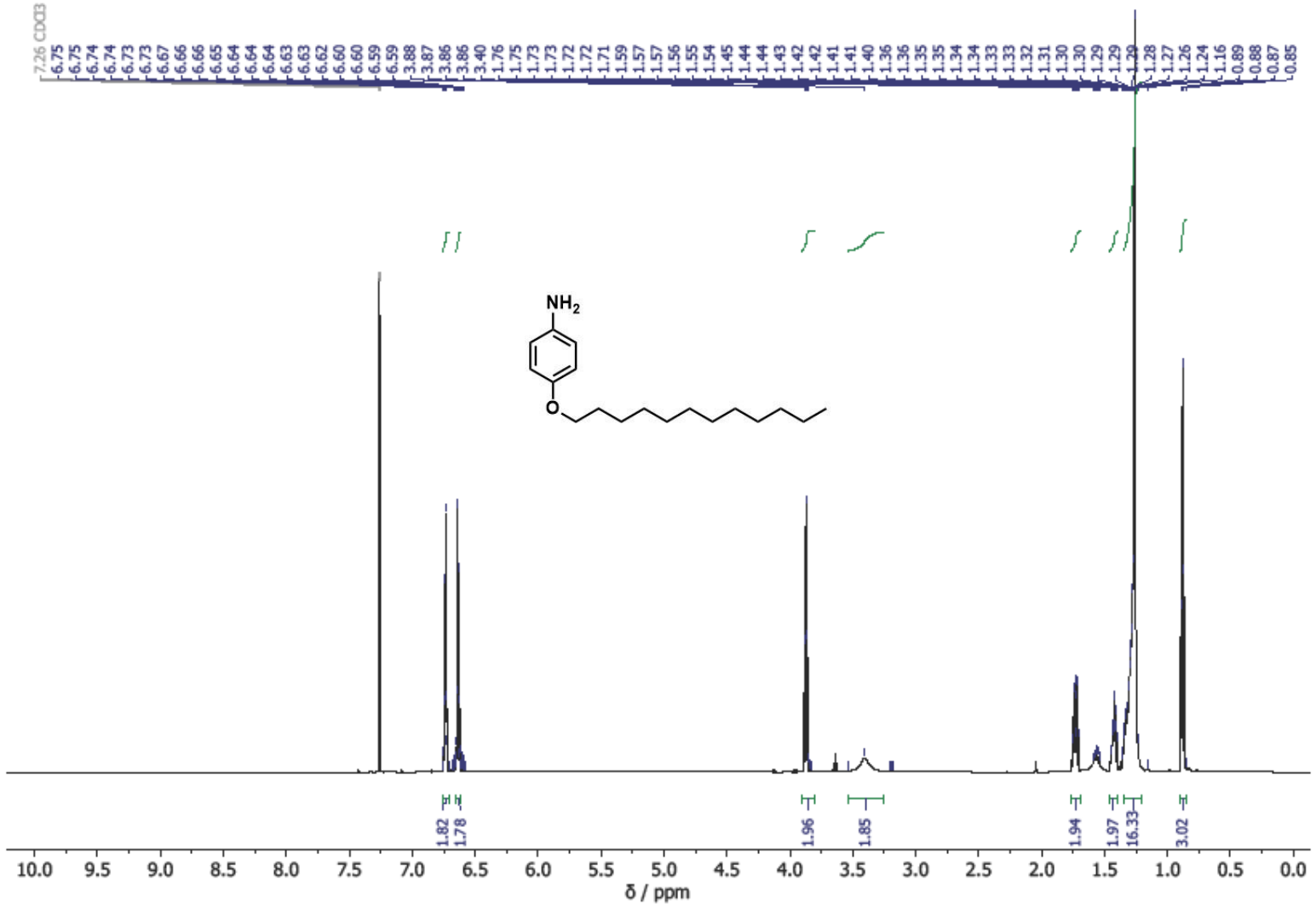

Figure A6.79: The ^{1}H NMR spectrum (600 MHz) of 4-(dodecyloxy)aniline, **110**, in $CDCl_3$.

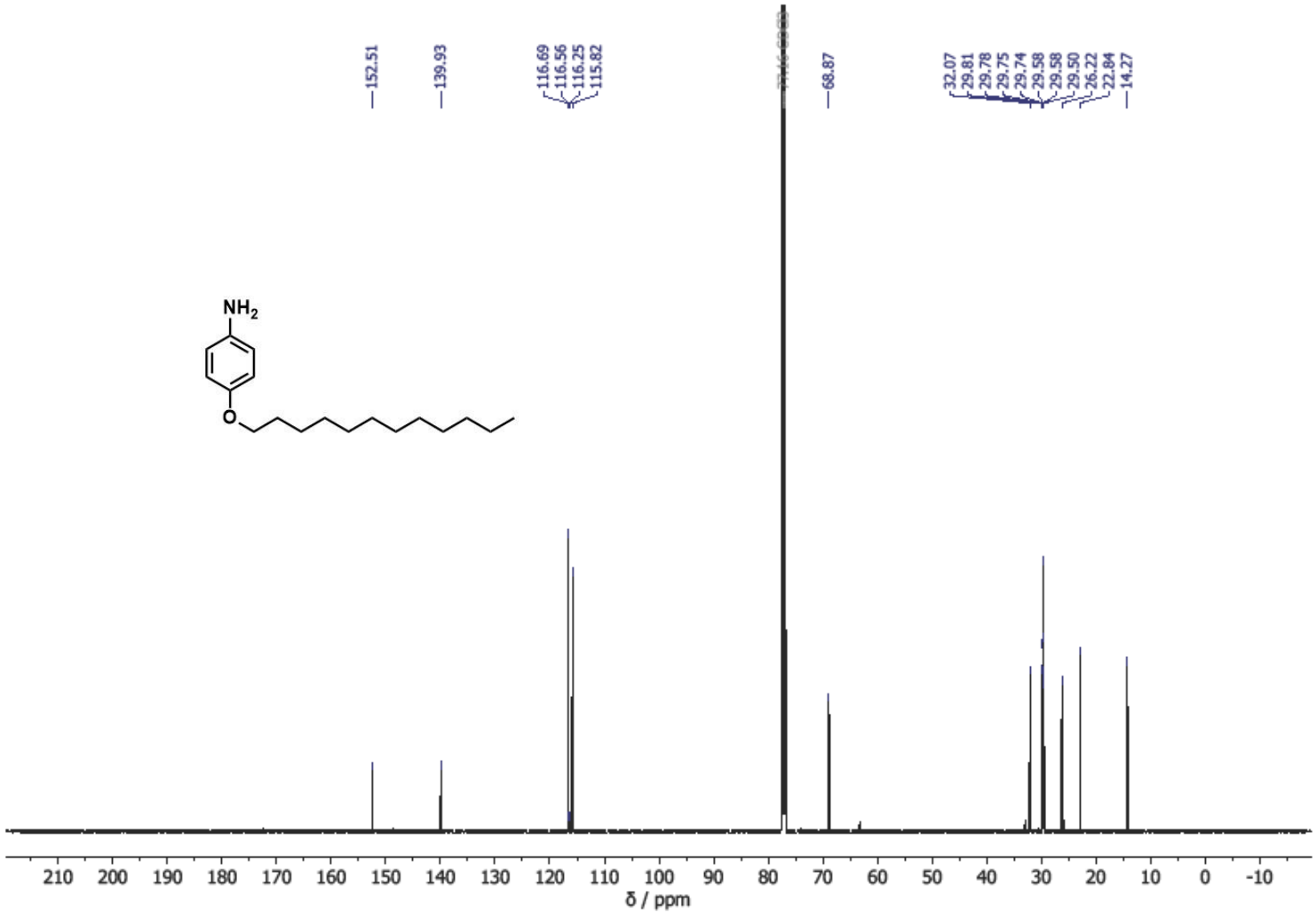

Figure A6.80: The ^{13}C NMR spectrum (151 MHz) of 4-(dodecyloxy)aniline, **110**, in $CDCl_3$.

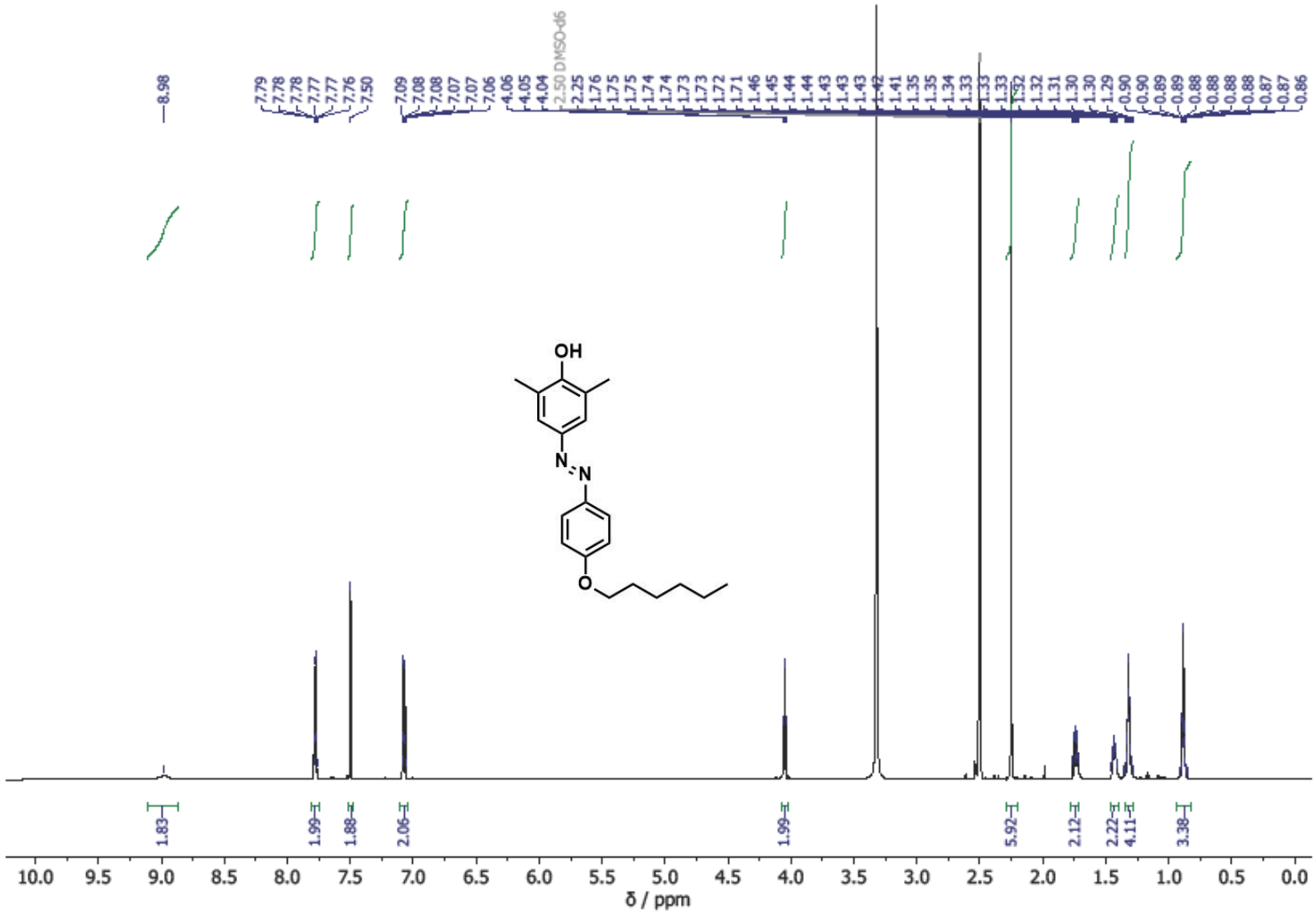

Figure A6.81: The ^{1}H NMR spectrum (600 MHz) of (E)-4-((4-(hexyloxy)phenyl)diazenyl)-2,6-dimethylphenol, **111**, in DMSO-d_6.

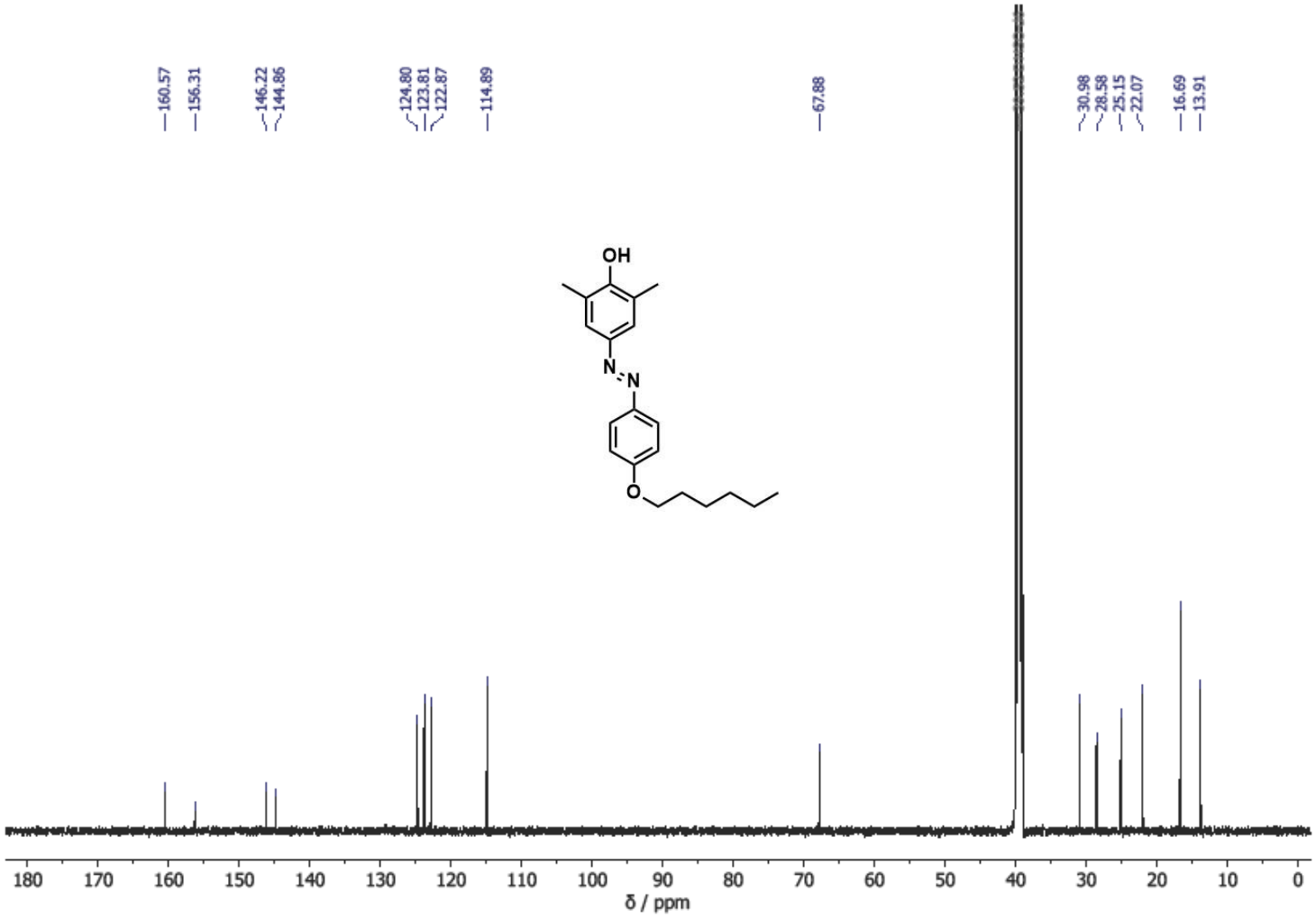

Figure A6.82: The ^{13}C NMR spectrum (151 MHz) of (E)-4-((4-(hexyloxy)phenyl)diazenyl)-2,6-dimethylphenol, **111**, in DMSO-d_6.

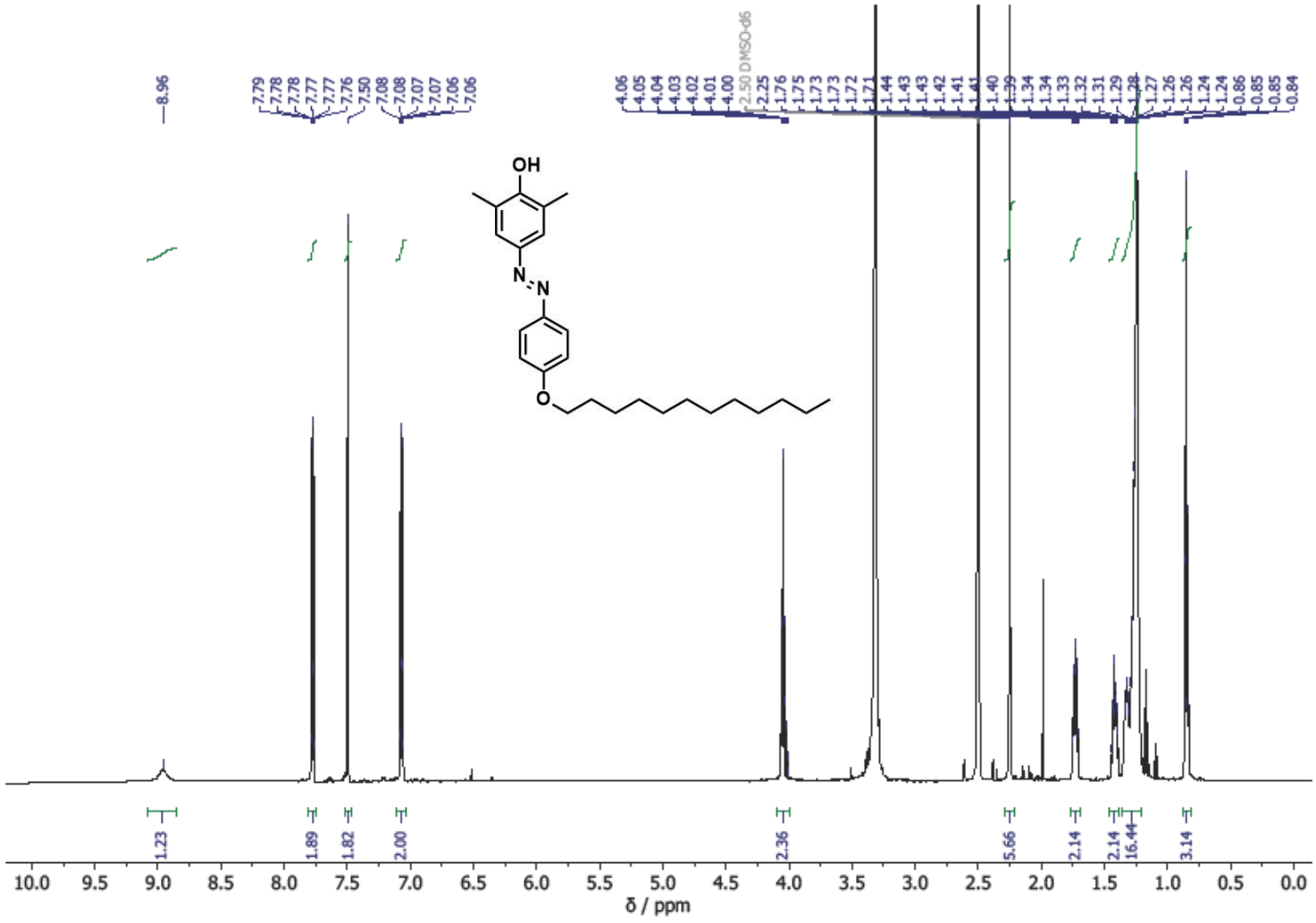

Figure A6.83: The ^{1}H NMR spectrum (600 MHz) of (E)-4-((4-(dodecyloxy)phenyl)diazenyl)-2,6-dimethylphenol, **112**, in DMSO-d_6.

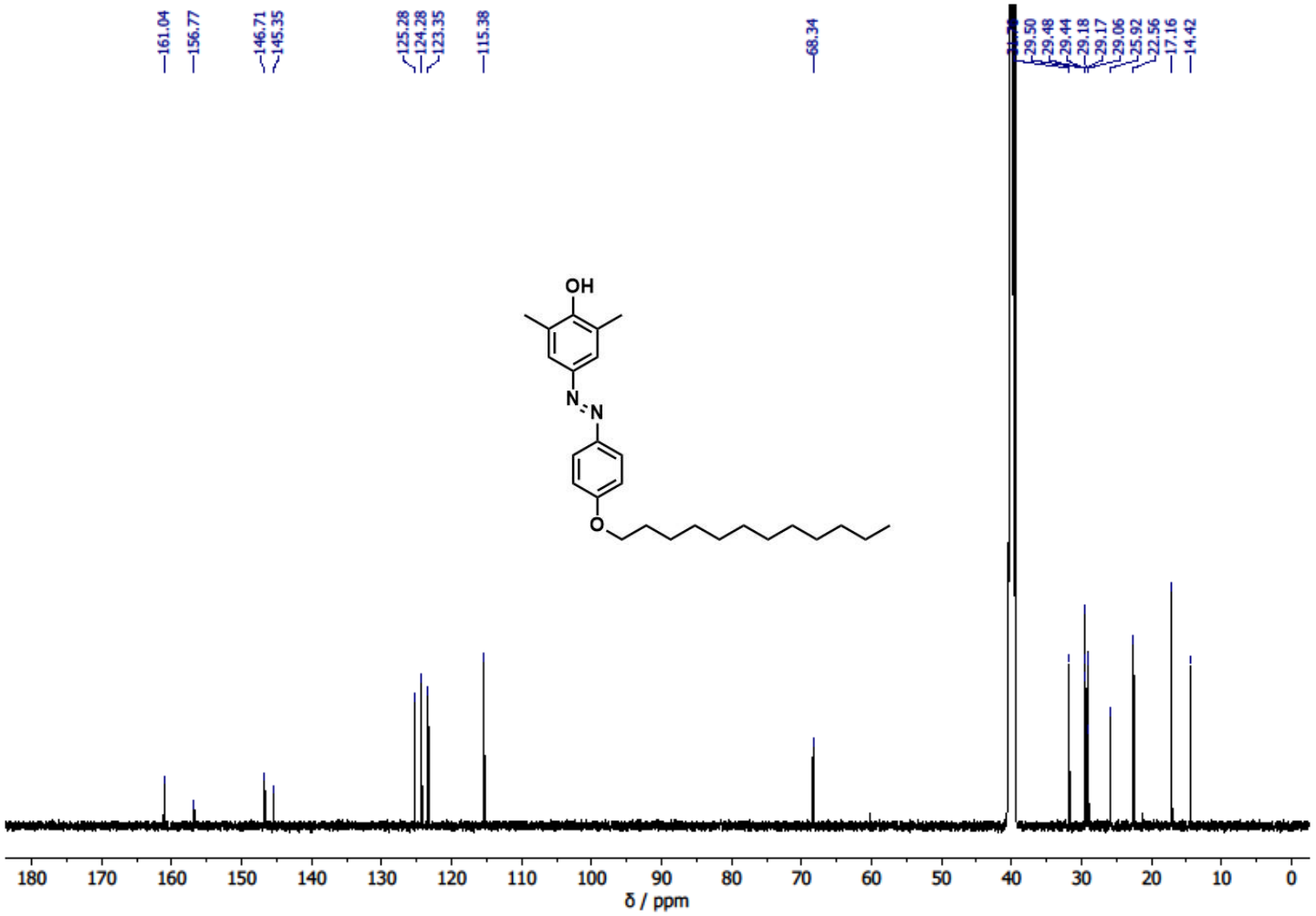

Figure A6.84: The ^{13}C NMR spectrum (151 MHz) of (E)-4-((4-(dodecyloxy)phenyl)diazenyl)-2,6-dimethylphenol, **112**, in DMSO-d_6.

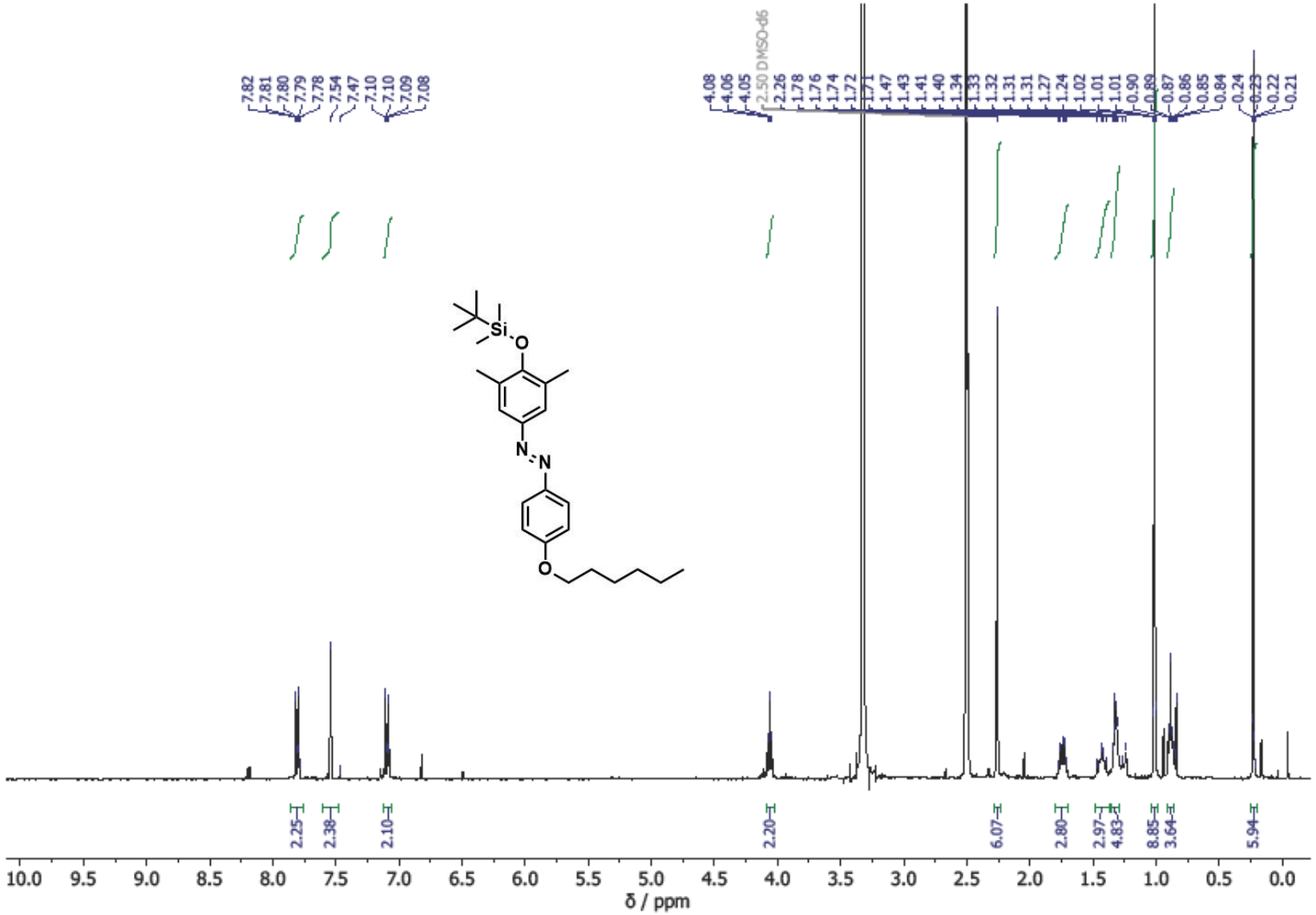

Figure A6.85: *The ^{1}H NMR spectrum (600 MHz) of* (E)-1-(4-((tert-butyldimethylsilyl)oxy)-3,5-dimethylphenyl)-2-(4-(hexyloxy)phenyl)diazene, **113**, *in DMSO-d_6.*

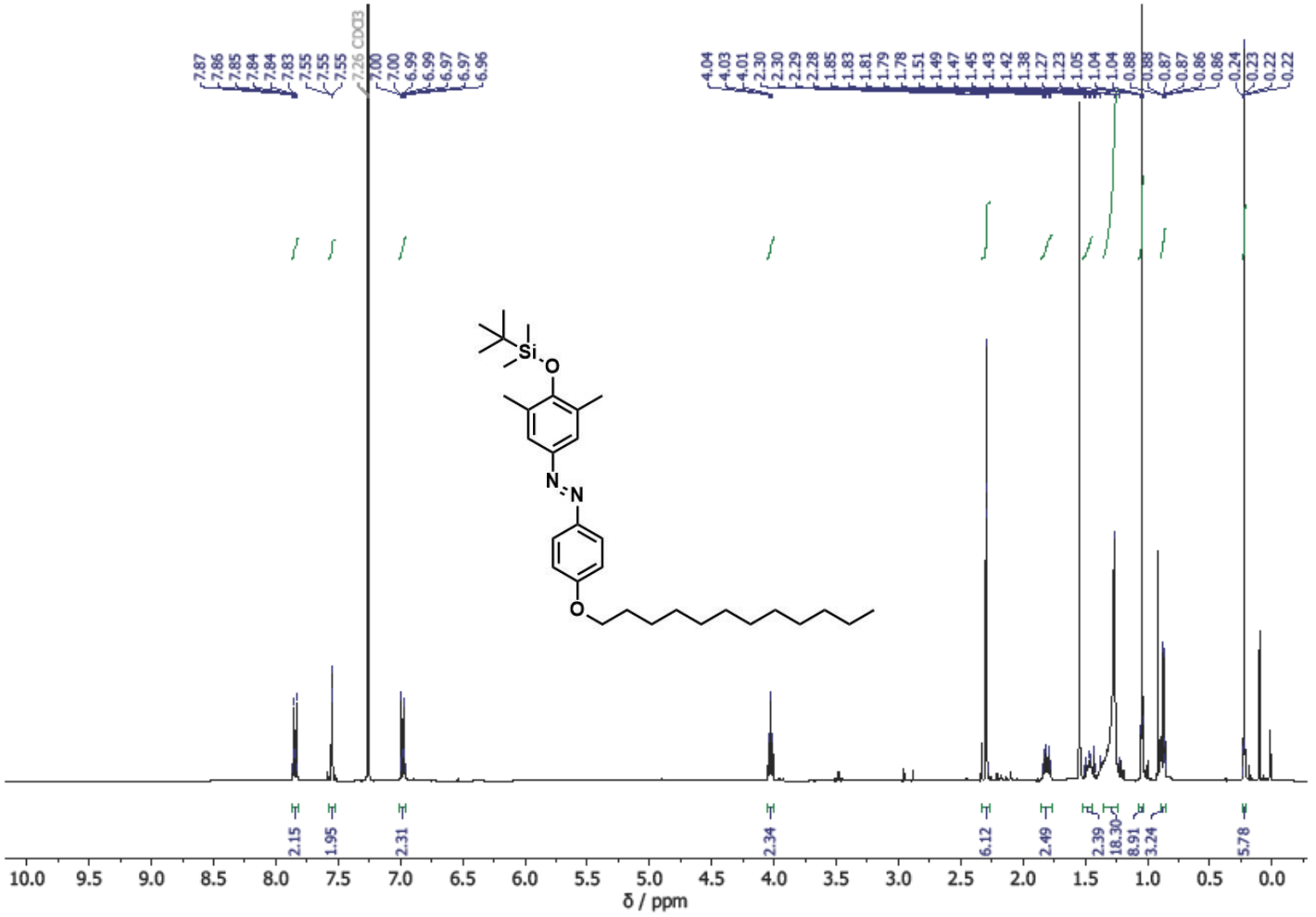

Figure A6.86: The ^{1}H NMR spectrum (600 MHz) of (E)-1-(4-((tert-butyldimethylsilyl)oxy)-3,5-dimethylphenyl)-2-(4-(dodecyloxy)phenyl)diazene, **114**, in DMSO-d_6.

.

A3 HPLC/LCMS Traces of Novel Compounds

A3.2 Compounds from chapter II

(4-Azido-2,3,5,6-tetrafluorophenyl)methanol, **12** – Analytical HPLC method 2B

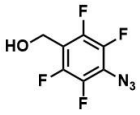

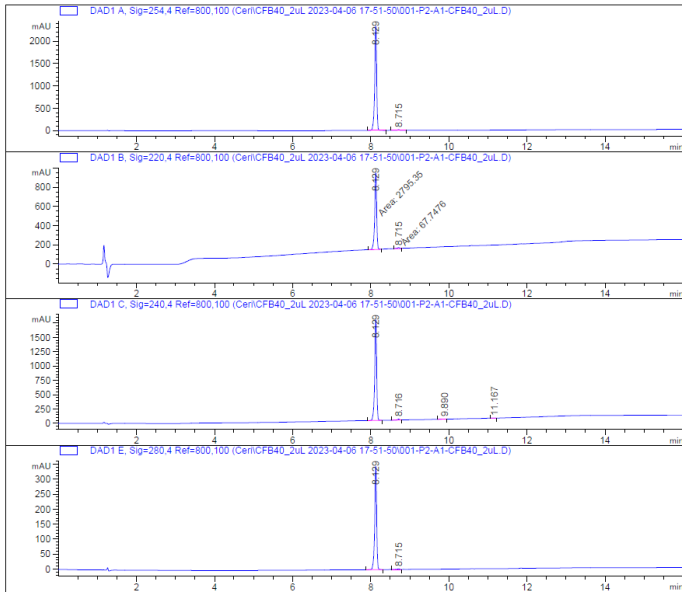

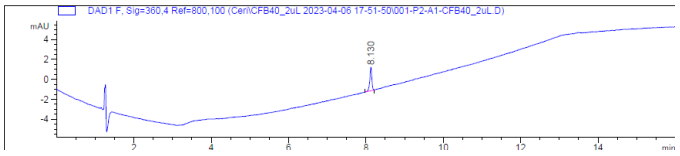

Signal 2: DAD1 B, Sig=220,4 Ref=800,100

Peak #	RetTime [min]	Type	Width [min]	Area [mAU*s]	Height [mAU]	Area %
1	8.129	MM	0.0581	2795.35303	801.95496	97.6338
2	8.715	MM	0.0992	67.74763	11.37673	2.3662
Totals :				2863.10066	813.33169	

Signal 3: DAD1 C, Sig=240,4 Ref=800,100

Peak #	RetTime [min]	Type	Width [min]	Area [mAU*s]	Height [mAU]	Area %
1	8.129	BB	0.0525	6115.44824	1760.77319	98.9207
2	8.716	BB	0.0535	54.20002	15.22609	0.8767
3	9.890	BB	0.0848	6.27580	1.06488	0.1015
4	11.167	BB	0.0494	6.24955	1.94735	0.1011
Totals :				6182.17361	1779.01151	

Signal 4: DAD1 E, Sig=280,4 Ref=800,100

Peak #	RetTime [min]	Type	Width [min]	Area [mAU*s]	Height [mAU]	Area %
1	8.129	BB	0.0524	1194.87354	344.73883	99.3344
2	8.715	BB	0.0565	8.00697	2.05150	0.6656
Totals :				1202.88050	346.79033	

Signal 5: DAD1 F, Sig=360,4 Ref=800,100

Peak #	RetTime [min]	Type	Width [min]	Area [mAU*s]	Height [mAU]	Area %
1	8.130	BB	0.0543	8.56428	2.35988	100.0000
Totals :				8.56428	2.35988	

Signal 1: DAD1 A, Sig=254,4 Ref=800,100

Peak #	RetTime [min]	Type	Width [min]	Area [mAU*s]	Height [mAU]	Area %
1	8.129	BB	0.0528	8171.64014	2334.24829	99.2945
2	8.715	BV R	0.0554	58.06109	15.61044	0.7055
Totals :				8229.70123	2349.85873	

4-((4-Azido-2,3,5,6-tetrafluorobenzyl)oxy)benzaldehyde, **14** – Analytical HPLC method 2B

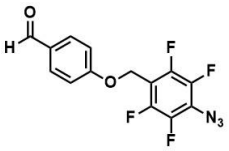

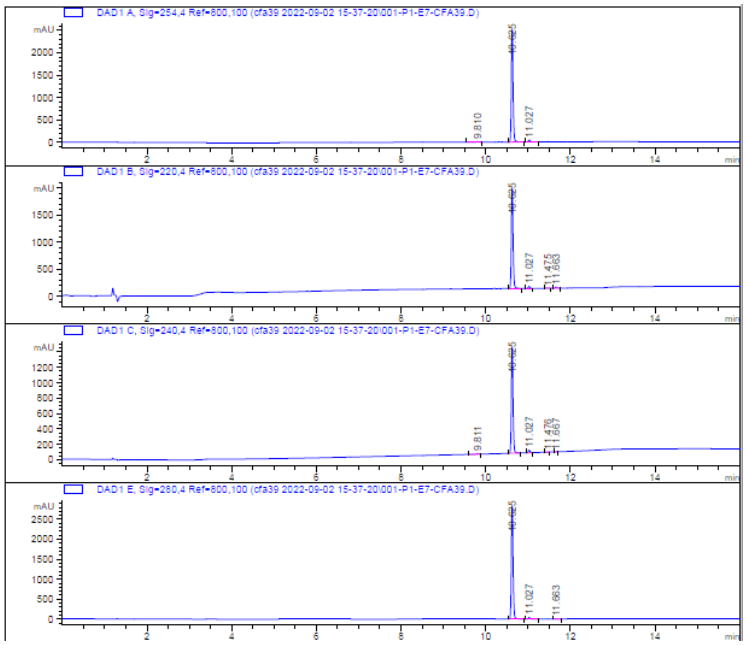

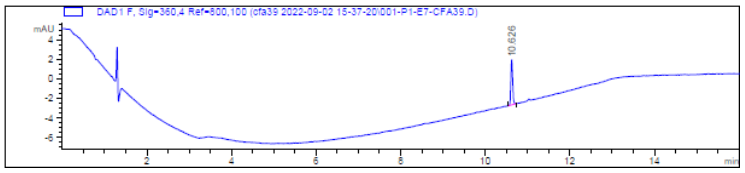

Signal 2: DAD1 B, Sig=220,4 Ref=800,100

Peak #	RetTime [min]	Type	Width [min]	Area [mAU*s]	Height [mAU]	Area %
1	10.625	BB	0.0446	5343.52051	1853.68237	96.9935
2	11.027	BB	0.0420	97.31289	35.42548	1.7664
3	11.475	BB	0.0425	7.60123	2.72898	0.1380
4	11.663	BB	0.0465	60.72025	19.95473	1.1022

Totals : 5509.15487 1911.79156

Signal 3: DAD1 C, Sig=240,4 Ref=800,100

Peak #	RetTime [min]	Type	Width [min]	Area [mAU*s]	Height [mAU]	Area %
1	9.811	VB R	0.0519	22.86426	6.51805	0.5770
2	10.625	BB	0.0434	3839.17773	1380.83252	96.8768
3	11.027	BB	0.0418	90.89201	33.39599	2.2935
4	11.476	BB	0.0370	5.00007	2.08360	0.1262
5	11.667	BB	0.0410	5.01519	1.88876	0.1266

Totals : 3962.94927 1424.71892

Signal 4: DAD1 E, Sig=280,4 Ref=800,100

Peak #	RetTime [min]	Type	Width [min]	Area [mAU*s]	Height [mAU]	Area %
1	10.625	BB	0.0447	8201.75781	2841.28882	98.3480
2	11.027	BV R	0.0428	117.21125	41.67497	1.4055
3	11.663	BB	0.0468	20.55694	6.69301	0.2465

Totals : 8339.52600 2889.65680

Signal 5: DAD1 F, Sig=360,4 Ref=800,100

Peak #	RetTime [min]	Type	Width [min]	Area [mAU*s]	Height [mAU]	Area %
1	10.626	BB	0.0471	13.89082	4.61636	100.0000

Totals : 13.89082 4.61636

Signal 1: DAD1 A, Sig=254,4 Ref=800,100

Peak #	RetTime [min]	Type	Width [min]	Area [mAU*s]	Height [mAU]	Area %
1	9.810	VB R	0.0470	31.00560	10.05614	0.4270
2	10.625	BB	0.0440	7113.01270	2517.48657	97.9644
3	11.027	BV R	0.0427	116.79570	41.70419	1.6086

Totals : 7260.81399 2569.24690

(E)-2-(2-(4-((4-Azido-2,3,5,6-tetrafluorobenzyl)oxy)styryl)-4H-chromen-4-ylidene)malononitrile, **3** – Analytical HPLC method 1A

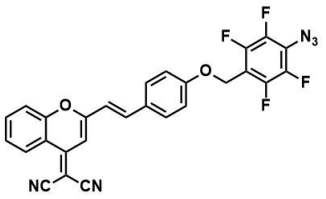

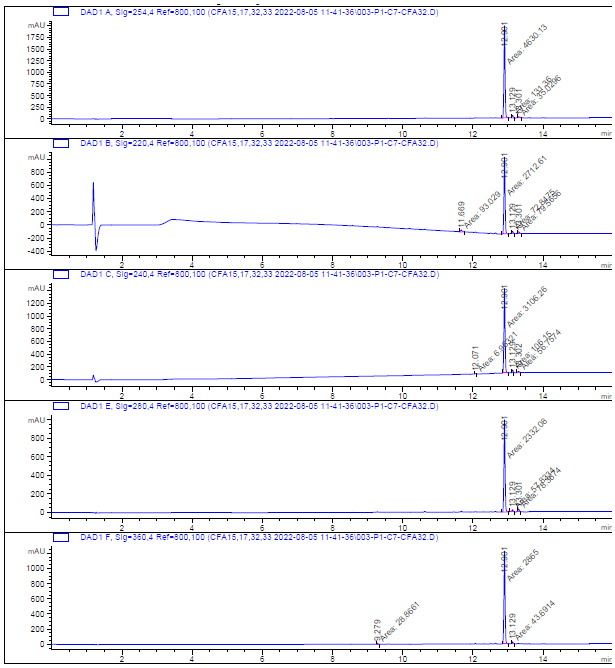

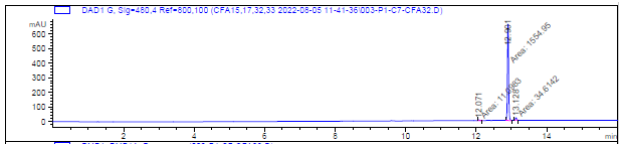

Signal 1: DAD1 A, Sig=254,4 Ref=800,100

Peak #	RetTime [min]	Type	Width [min]	Area [mAU*s]	Height [mAU]	Area %
1	12.901	MM	0.0388	4630.12549	1991.03870	96.5310
2	13.129	MM	0.0391	131.35982	55.94618	2.7387
3	13.301	MM	0.0299	35.02963	19.52798	0.7303
Totals :				4796.51493	2066.51286	

Signal 2: DAD1 B, Sig=220,4 Ref=800,100

Peak #	RetTime [min]	Type	Width [min]	Area [mAU*s]	Height [mAU]	Area %
1	11.669	MM	0.0542	93.02905	28.59451	3.1449
2	12.901	MM	0.0387	2712.61499	1169.29358	91.7026
3	13.129	MM	0.0365	72.84746	33.27833	2.4627
4	13.301	MM	0.0543	79.56564	24.40822	2.6898
Totals :				2958.05714	1255.57464	

Signal 3: DAD1 C, Sig=240,4 Ref=800,100

Peak #	RetTime [min]	Type	Width [min]	Area [mAU*s]	Height [mAU]	Area %
1	12.071	MM	0.0258	6.96321	4.50171	0.2125
2	12.901	MM	0.0387	3106.25830	1337.92383	94.8149
3	13.129	MM	0.0386	106.15047	45.86747	3.2401
4	13.302	MM	0.0554	56.75737	17.08823	1.7325
Totals :				3276.12935	1405.40124	

Signal 4: DAD1 E, Sig=280,4 Ref=800,100

Peak #	RetTime [min]	Type	Width [min]	Area [mAU*s]	Height [mAU]	Area %
1	12.901	MM	0.0389	2332.08105	998.00128	94.4620
2	13.129	MM	0.0422	87.83338	22.83292	2.3431
3	13.301	MM	0.0481	78.36743	27.13682	3.1750
Totals :				2468.28186	1047.97102	

Signal 5: DAD1 F, Sig=360,4 Ref=800,100

Peak #	RetTime [min]	Type	Width [min]	Area [mAU*s]	Height [mAU]	Area %
1	9.279	MM	0.0412	28.86607	11.67163	0.9827
2	12.901	MM	0.0388	2865.00073	1229.15137	97.5300
3	13.129	MM	0.0327	43.69142	22.25632	1.4873
Totals :				2937.55822	1263.07932	

Signal 6: DAD1 G, Sig=480,4 Ref=800,100

Peak #	RetTime [min]	Type	Width [min]	Area [mAU*s]	Height [mAU]	Area %
1	12.071	MM	0.0395	11.09826	4.68805	0.6934
2	12.901	MM	0.0392	1554.94531	661.80328	97.1441
3	13.128	MM	0.0363	34.61415	15.91255	2.1625
Totals :				1600.65772	682.40388	

(E)-2-(2-(4-((4-Azido-2,3,5,6-tetrafluorobenzyl)oxy)styryl)-4H-chromen-4-ylidene)malononitrile, **3** – Analytical HPLC method 5

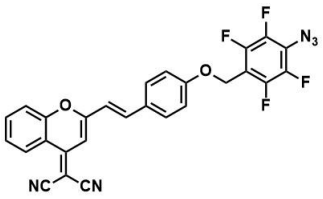

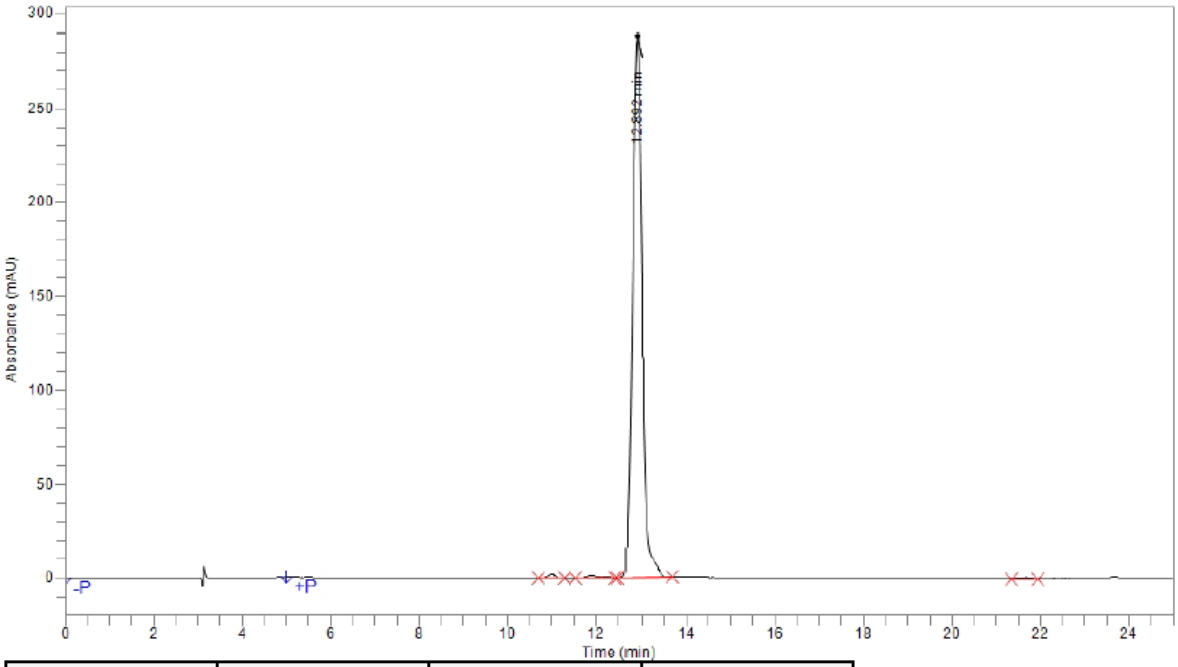

Time	Height	Area	Area %
10.993	2,147.4	26,224.4	0.60
11.896	1,284.1	19,642.2	0.45
12.206	683.5	7,060.6	0.16
12.892	288,529.6	4,271,297.3	98.53
21.665	757.2	10,778.0	0.25
Total		4,335,002.4	100.00

(E)-2-(2-(4-((4-Azido-2,3,5,6-tetrafluorobenzyl)oxy)styryl)-4H-thiochromen-4-ylidene)malononitrile, **4** – Analytical HPLC method 1B

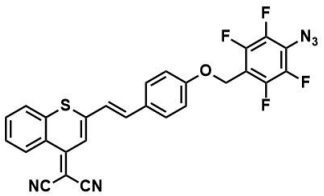

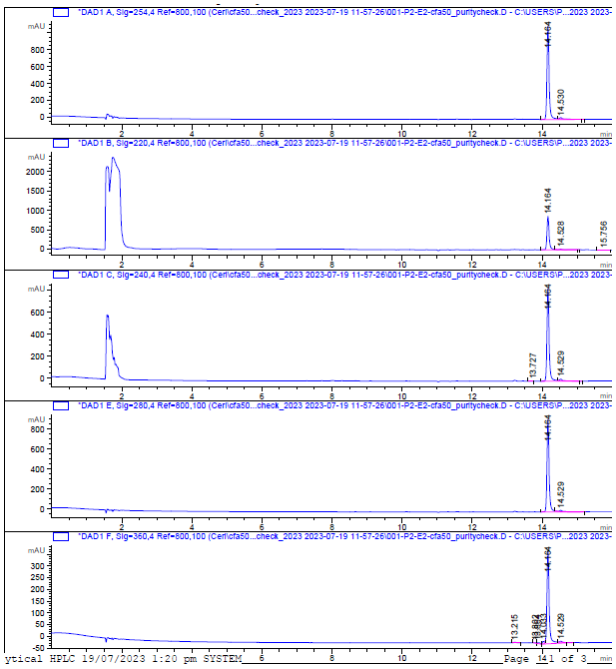

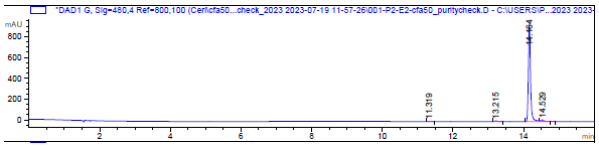

Signal 1: DAD1 A, Sig=254,4 Ref=800,100
Signal has been modified after loading from rawdata file!

Peak #	RetTime [min]	Type	Width [min]	Area [mAU*s]	Height [mAU]	Area %
1	14.164	VV R	0.0664	4893.59863	1108.44824	98.2088
2	14.530	VB E	0.0805	89.25430	15.89187	1.7912
Totals :				4982.85294	1124.34011	

Signal 2: DAD1 B, Sig=220,4 Ref=800,100
Signal has been modified after loading from rawdata file!

Peak #	RetTime [min]	Type	Width [min]	Area [mAU*s]	Height [mAU]	Area %
1	14.164	VV R	0.0667	3846.42358	863.65399	96.4370
2	14.528	VV E	0.1124	121.92646	14.59457	3.0544
3	15.756	BBA	0.1541	20.28659	1.67763	0.5086
Totals :				3988.53664	879.92619	

Signal 3: DAD1 C, Sig=240,4 Ref=800,100
Signal has been modified after loading from rawdata file!

Peak #	RetTime [min]	Type	Width [min]	Area [mAU*s]	Height [mAU]	Area %
1	13.727	VV	0.0945	11.01711	1.57674	0.2870
2	14.164	VV R	0.0666	3745.86890	843.60870	97.5910
3	14.529	VB E	0.0803	81.44930	14.55170	2.1220
Totals :				3838.33531	859.73715	

Signal 4: DAD1 E, Sig=280,4 Ref=800,100
Signal has been modified after loading from rawdata file!

Peak #	RetTime [min]	Type	Width [min]	Area [mAU*s]	Height [mAU]	Area %
1	14.164	VV R	0.0661	4064.97266	925.05890	97.1583
2	14.529	VB E	0.1193	118.89410	13.29459	2.8417
Totals :				4183.86675	938.35349	

Signal 5: DAD1 F, Sig=360,4 Ref=800,100
Signal has been modified after loading from rawdata file!

Peak #	RetTime [min]	Type	Width [min]	Area [mAU*s]	Height [mAU]	Area %
1	13.215	BB	0.0671	12.34341	2.71077	0.6367
2	13.802	BV	0.0601	8.16292	1.75930	0.4211
3	13.864	VB	0.0905	23.05447	3.14734	1.1893
4	14.033	BV E	0.0588	40.65265	10.83762	2.0971
5	14.164	VV R	0.0690	1834.54480	396.52692	94.6344
6	14.529	VB E	0.0660	19.80207	4.44592	1.0215
Totals :				1938.56032	419.42786	

Signal 6: DAD1 G, Sig=480,4 Ref=800,100
Signal has been modified after loading from rawdata file!

Peak #	RetTime [min]	Type	Width [min]	Area [mAU*s]	Height [mAU]	Area %
1	11.319	BB	0.0541	8.60814	2.38373	0.2062
2	13.215	BB	0.0661	33.11863	7.56484	0.7932
3	14.164	BV R	0.0659	4081.19751	935.20435	97.7441
4	14.529	VB E	0.0676	52.46397	11.64057	1.2565
Totals :				4175.38825	956.79348	

(E)-2-(2-(4-((4-Azido-2,3,5,6-tetrafluorobenzyl)oxy)styryl)-4H-thiochromen-4-ylidene)malononitrile, **4** – Analytical HPLC method 6

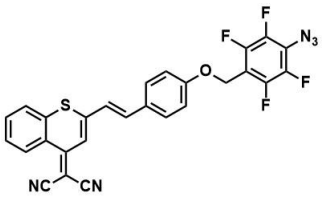

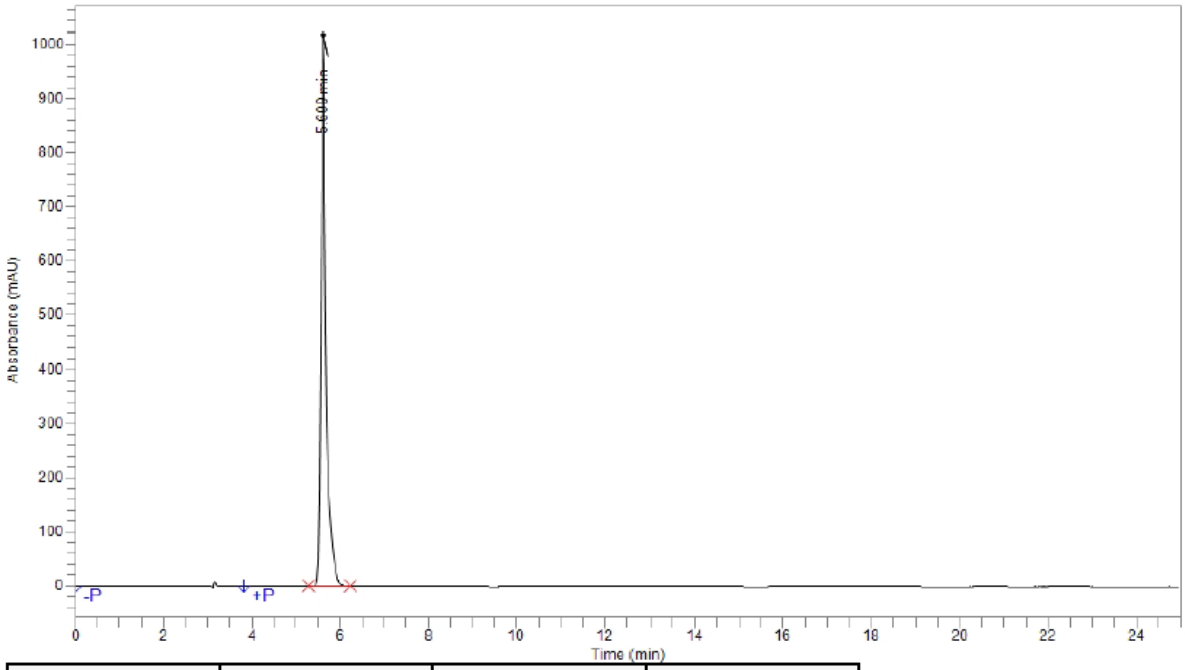

Time	Height	Area	Area %
5.609	1,017,065.5	8,614,783.4	100.00
Total		8,614,783.4	100.00

(E)-2-(2-(4-Hydroxystyryl)-4H-chromen-4-ylidene)malononitrile, **5** – Analytical HPLC method 2B

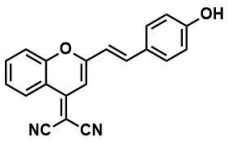

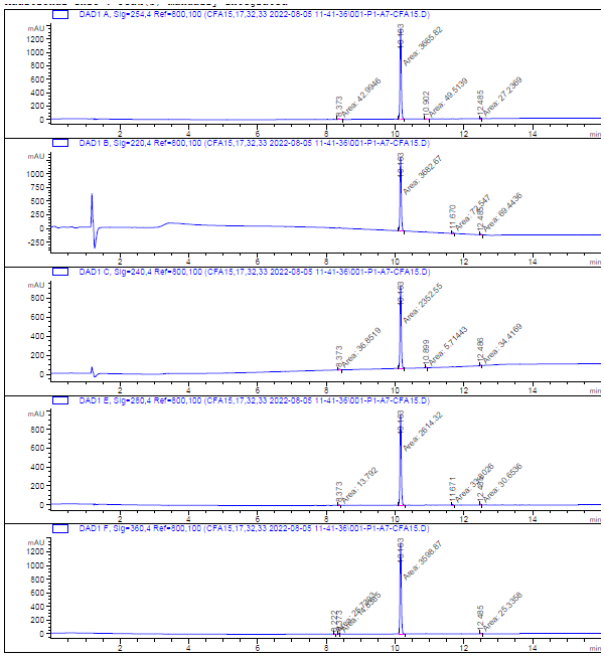

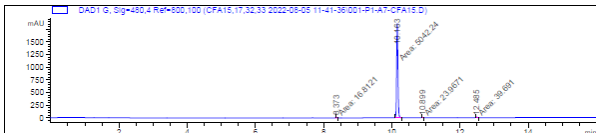

Signal 1: DAD1 A, Sig=254,4 Ref=800,100

Peak #	RetTime [min]	Type	Width [min]	Area [mAU*s]	Height [mAU]	Area %
1	8.373	MM	0.0640	42.99488	11.20048	1.1358
2	10.163	MM	0.0449	3665.82031	1361.67932	96.8368
3	10.902	MM	0.0918	49.51393	8.98545	1.3080
4	12.485	MM	0.0445	27.23688	10.20904	0.7195
Totals :				3785.56570	1392.07426	

Signal 2: DAD1 B, Sig=220,4 Ref=800,100

Peak #	RetTime [min]	Type	Width [min]	Area [mAU*s]	Height [mAU]	Area %
1	10.163	MM	0.0450	3682.67236	1363.25903	96.2875
2	11.670	MM	0.0480	72.54700	25.17624	1.8968
3	12.485	MM	0.0550	69.44357	21.03819	1.8157
Totals :				3824.66293	1409.47346	

Signal 3: DAD1 C, Sig=240,4 Ref=800,100

Peak #	RetTime [min]	Type	Width [min]	Area [mAU*s]	Height [mAU]	Area %
1	8.373	MM	0.0501	96.85188	12.27167	1.5168
2	10.163	MM	0.0449	2352.54517	873.03546	96.8314
3	10.899	MM	0.0273	5.71443	3.48704	0.2352
4	12.486	MM	0.0455	34.41685	12.61118	1.4166
Totals :				2429.52832	901.40535	

Signal 4: DAD1 E, Sig=280,4 Ref=800,100

Peak #	RetTime [min]	Type	Width [min]	Area [mAU*s]	Height [mAU]	Area %
1	8.373	MM	0.0409	13.79198	5.62018	0.5122
2	10.162	MM	0.0448	2614.32153	972.42712	97.0939
3	11.671	MM	0.0571	33.80263	9.85870	1.2554
4	12.485	MM	0.0441	30.65363	11.59134	1.1385
Totals :				2692.56977	999.49734	

Signal 5: DAD1 F, Sig=360,4 Ref=800,100

Peak #	RetTime [min]	Type	Width [min]	Area [mAU*s]	Height [mAU]	Area %
1	8.222	MM	0.0445	25.73929	9.64097	0.7023
2	8.373	MM	0.0362	14.83851	6.81912	0.4049
3	10.163	MM	0.0447	3598.87305	1342.35217	98.2014
4	12.485	MM	0.0339	25.33577	12.45697	0.6913
Totals :				3664.78662	1371.26922	

Signal 6: DAD1 G, Sig=480,4 Ref=800,100

Peak #	RetTime [min]	Type	Width [min]	Area [mAU*s]	Height [mAU]	Area %
1	8.373	MM	0.0313	16.81211	8.95568	0.3282
2	10.163	MM	0.0451	5042.24463	1864.98987	98.4291
3	10.899	MM	0.0420	29.96709	9.81346	0.4679
4	12.485	MM	0.0437	39.69097	15.14488	0.7748
Totals :				5122.71480	1898.60388	

(E)-2-(2-(4-Hydroxystyryl)-4H-thiochromen-4-ylidene)malononitrile, **6** – Analytical HPLC method 2B

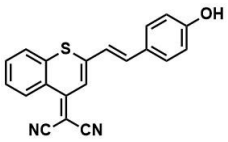

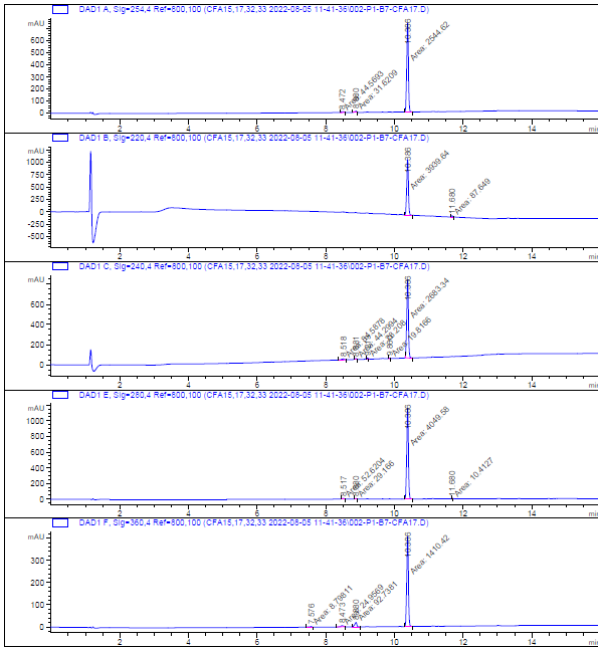

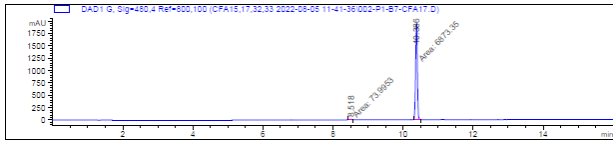

Signal 1: DAD1 A, Sig=254,4 Ref=800,100

Peak #	RetTime [min]	Type	Width [min]	Area [mAU*s]	Height [mAU]	Area %
1	8.472	MM	0.0885	44.56930	8.39222	1.7006
2	8.880	MM	0.0569	31.62092	9.25969	1.2065
3	10.386	MM	0.0574	2544.62085	739.20959	97.0929

Totals : 2620.81107 756.86151

Signal 2: DAD1 B, Sig=220,4 Ref=800,100

Peak #	RetTime [min]	Type	Width [min]	Area [mAU*s]	Height [mAU]	Area %
1	10.386	MM	0.0580	3939.63647	1132.27319	97.8236
2	11.680	MM	0.0508	87.64901	28.77153	2.1764

Totals : 4027.28548 1161.04472

Signal 3: DAD1 C, Sig=240,4 Ref=800,100

Peak #	RetTime [min]	Type	Width [min]	Area [mAU*s]	Height [mAU]	Area %
1	8.518	MM	0.1265	84.58784	11.14497	2.9574
2	8.881	MM	0.0681	44.29943	10.84242	1.5488
3	9.219	MM	0.0500	28.20797	9.39540	0.9862
4	9.860	MM	0.0496	19.81662	6.66113	0.6928
5	10.386	MM	0.0575	2683.34326	778.24646	93.8148

Totals : 2860.25512 816.29038

Signal 4: DAD1 E, Sig=280,4 Ref=800,100

Peak #	RetTime [min]	Type	Width [min]	Area [mAU*s]	Height [mAU]	Area %
1	8.517	MM	0.0574	52.62036	9.00754	1.2705
2	8.880	MM	0.0688	29.16596	7.06058	0.7042
3	10.386	MM	0.0580	4049.58423	1163.98181	97.7739
4	11.680	MM	0.0236	10.41273	7.34762	0.2514

Totals : 4141.78328 1187.39755

Signal 5: DAD1 F, Sig=360,4 Ref=800,100

Peak #	RetTime [min]	Type	Width [min]	Area [mAU*s]	Height [mAU]	Area %
1	7.576	MM	0.0621	8.79811	2.36216	0.5725
2	8.473	MM	0.0756	24.95694	5.50508	1.6238
3	8.880	MM	0.0736	92.73813	21.01088	6.0341
4	10.386	MM	0.0578	1410.41614	406.42374	91.7696

Totals : 1536.90932 435.30185

Signal 6: DAD1 G, Sig=480,4 Ref=800,100

Peak #	RetTime [min]	Type	Width [min]	Area [mAU*s]	Height [mAU]	Area %
1	8.518	MM	0.0986	73.99530	12.50629	1.0651
2	10.386	MM	0.0583	6873.35449	1963.93640	98.9349

Totals : 6947.34979 1976.44270

(*E*)-2-(2-(4-Aminostyryl)-4*H*-chromen-4-ylidene)malononitrile, **2** – Analytical HPLC method 2B

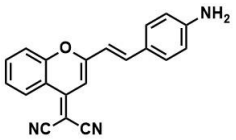

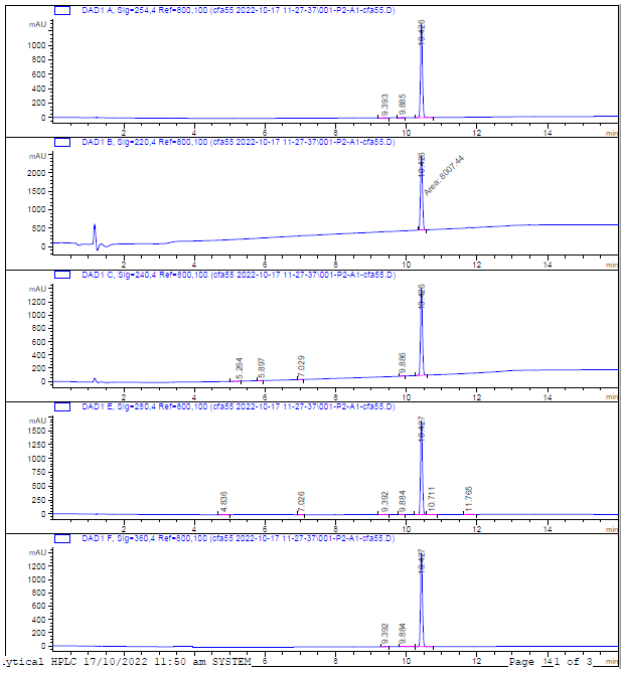

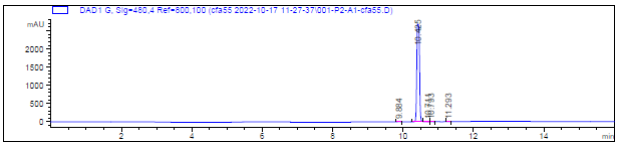

Signal 1: DAD1 A, Sig=254,4 Ref=800,100

Peak #	RetTime [min]	Type	Width [min]	Area [mAU*s]	Height [mAU]	Area %
1	9.393	BB	0.0649	6.93517	1.62159	0.1423
2	9.885	BB	0.0625	24.07160	6.04554	0.4940
3	10.426	BV R	0.0575	4842.24023	1297.90076	99.3637
Totals :				4873.24700	1305.56789	

Signal 2: DAD1 B, Sig=220,4 Ref=800,100

Peak #	RetTime [min]	Type	Width [min]	Area [mAU*s]	Height [mAU]	Area %
1	10.426	MM	0.0668	8007.43652	1998.55566	100.0000
Totals :				8007.43652	1998.55566	

Signal 5: DAD1 F, Sig=360,4 Ref=800,100

Peak #	RetTime [min]	Type	Width [min]	Area [mAU*s]	Height [mAU]	Area %
1	9.392	BB	0.0629	30.34341	7.54532	0.5683
2	9.884	BV R	0.0706	21.39292	4.57045	0.4007
3	10.427	BV R	0.0576	5287.44336	1413.65356	99.0310
Totals :				5339.17969	1425.76933	

Signal 5: DAD1 F, Sig=360,4 Ref=800,100

Peak #	RetTime [min]	Type	Width [min]	Area [mAU*s]	Height [mAU]	Area %
1	9.392	BB	0.0629	30.34341	7.54532	0.5683
2	9.884	BV R	0.0706	21.39292	4.57045	0.4007
3	10.427	BV R	0.0576	5287.44336	1413.65356	99.0310
Totals :				5339.17969	1425.76933	

Signal 6: DAD1 G, Sig=480,4 Ref=800,100

Peak #	RetTime [min]	Type	Width [min]	Area [mAU*s]	Height [mAU]	Area %
1	9.884	BB	0.0614	34.90088	8.96170	0.2419
2	10.425	BV R	0.0864	1.43502e4	2682.26880	99.4541
3	10.711	VV E	0.0703	29.38835	6.20523	0.2037
4	10.793	VB E	0.0501	6.70493	1.95273	0.0465
5	11.293	BV	0.0555	7.76886	2.18255	0.0538
Totals :				1.44289e4	2701.57101	

Signal 6: DAD1 G, Sig=480,4 Ref=800,100

Peak #	RetTime [min]	Type	Width [min]	Area [mAU*s]	Height [mAU]	Area %
1	9.884	BB	0.0614	34.90088	8.96170	0.2419
2	10.425	BV R	0.0864	1.43502e4	2682.26880	99.4541
3	10.711	VV E	0.0703	29.38835	6.20523	0.2037
4	10.793	VB E	0.0501	6.70493	1.95273	0.0465
5	11.293	BV	0.0555	7.76886	2.18255	0.0538
Totals :				1.44289e4	2701.57101	

(E)-2-(2-(4-Azidostyryl)-4H-chromen-4-ylidene)malononitrile, **1** – Analytical HPLC method 2B

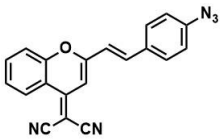

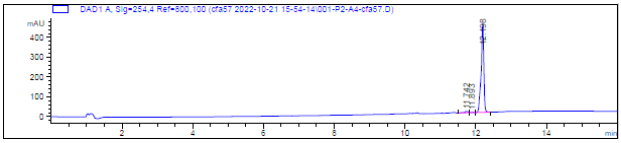

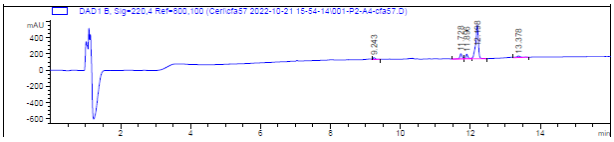

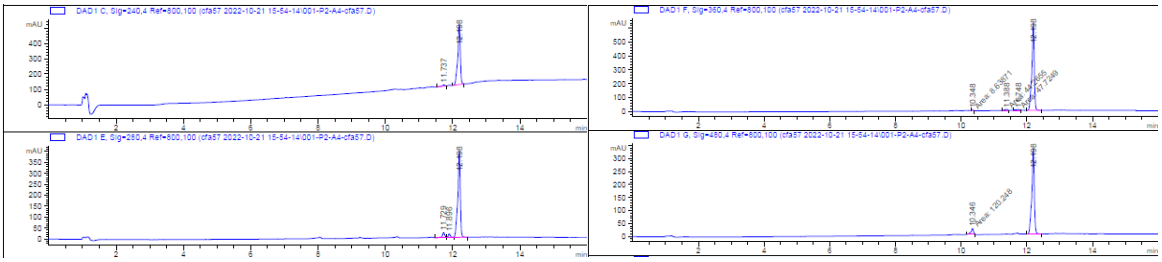

Signal 1: DAD1 A, Sig=254,4 Ref=800,100

Peak #	RetTime [min]	Type	Width [min]	Area [mAU*s]	Height [mAU]	Area %
1	11.742	BV	0.0943	47.86312	7.41905	2.0082
2	11.893	VB	0.0703	9.65047	2.03599	0.4049
3	12.198	BB	0.0732	2325.84131	450.89694	97.5869
Totals :				2383.35490	460.35198	

Signal 2: DAD1 B, Sig=220,4 Ref=800,100

Peak #	RetTime [min]	Type	Width [min]	Area [mAU*s]	Height [mAU]	Area %
1	9.243	VV R	0.0667	98.64544	22.26472	3.3211
2	11.728	BV E	0.0653	279.13229	63.48552	9.3974
3	11.896	VV E	0.0615	232.06340	56.99799	7.8128
4	12.198	VB R	0.0749	2210.04541	416.33081	74.4046
5	13.378	VV R	0.1115	150.42133	17.37007	5.0642

Signal 3: DAD1 C, Sig=240,4 Ref=800,100

Peak #	RetTime [min]	Type	Width [min]	Area [mAU*s]	Height [mAU]	Area %
1	11.737	BB	0.0824	46.87992	8.63140	2.2573
2	12.198	BB	0.0730	2029.91382	394.86185	97.7427
Totals :				2076.79374	403.49325	

Signal 4: DAD1 E, Sig=280,4 Ref=800,100

Peak #	RetTime [min]	Type	Width [min]	Area [mAU*s]	Height [mAU]	Area %
1	11.729	BV E	0.0705	108.58477	22.82509	4.8753
2	11.896	VV E	0.0620	71.20415	16.95105	3.1970
3	12.198	VB R	0.0731	2047.43884	397.20642	91.9277
Totals :				2227.22776	436.98256	

Signal 5: DAD1 F, Sig=360,4 Ref=800,100

Peak #	RetTime [min]	Type	Width [min]	Area [mAU*s]	Height [mAU]	Area %
1	10.348	MM	0.0450	8.63871	3.20149	0.2568
2	11.388	MM	0.0906	44.26547	8.14583	1.3158
3	11.748	MM	0.1187	47.72490	6.70139	1.4186
4	12.198	BB	0.0732	3263.53516	632.27954	97.0088
Totals :				3364.16423	650.32825	

Signal 6: DAD1 G, Sig=480,4 Ref=800,100

Peak #	RetTime [min]	Type	Width [min]	Area [mAU*s]	Height [mAU]	Area %
1	10.346	MM	0.0869	120.24751	23.06853	6.5085
2	12.198	BB	0.0739	1727.29517	331.06699	93.4915
Totals :				1847.54268	354.13551	

7-((4-Azido-2,3,5,6-tetrafluorobenzyl)oxy)-3*H*-phenoxazin-3-one, **15** – Analytical HPLC method 2B

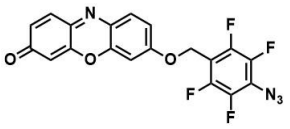

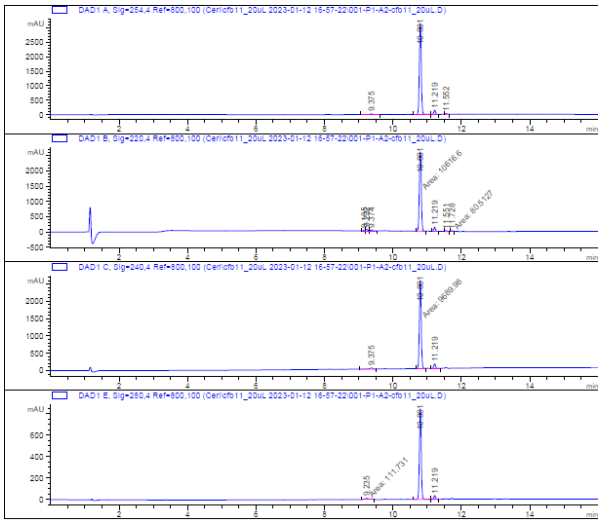

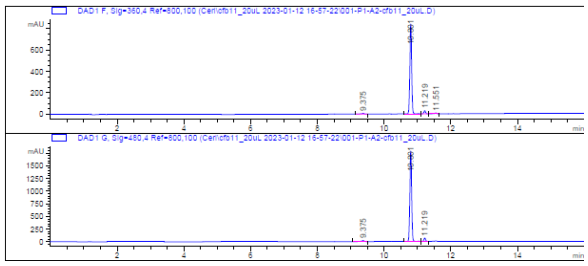

Signal 1: DAD1 A, Sig=254,4 Ref=800,100

Peak #	RetTime [min]	Type	Width [min]	Area [mAU*s]	Height [mAU]	Area %
1	9.375	BV R	0.0833	154.16747	25.58772	1.1726
2	10.801	BV R	0.0617	1.23739e4	3143.59692	94.1132
3	11.219	BB	0.0560	519.65930	144.34367	3.9524
4	11.552	VB	0.0549	100.16459	27.92118	0.7618
Totals :				1.31479e4	3341.44950	

Signal 2: DAD1 B, Sig=220,4 Ref=800,100

Peak #	RetTime [min]	Type	Width [min]	Area [mAU*s]	Height [mAU]	Area %
1	9.165	BV	0.0491	79.68697	25.02843	0.6793
2	9.232	VV	0.0635	222.26479	50.36369	1.8946
3	9.374	VB	0.0701	158.03413	32.27452	1.3471
4	10.801	MM	0.0683	1.06166e4	2591.68091	90.4978
5	11.219	BB	0.0559	475.27875	132.35899	4.0514
6	11.551	VB	0.0548	98.95812	27.65141	0.8435
7	11.728	MM	0.0527	80.51266	25.48124	0.6863
Totals :				1.17313e4	2884.83919	

Signal 6: DAD1 G, Sig=480,4 Ref=800,100

Peak #	RetTime [min]	Type	Width [min]	Area [mAU*s]	Height [mAU]	Area %
1	9.375	BB	0.0749	105.77048	19.94497	1.4877
2	10.801	BV R	0.0590	6758.88674	1784.84802	95.0696

alytical HPLC 18/03/2023 12:13 pm SYSTEM

ta File C:\Users\P...n\1\Data\Ceri\cfb11_20uL 2023-01-12 16-5

mple Name: cfb11_20uL

Peak #	RetTime [min]	Type	Width [min]	Area [mAU*s]	Height [mAU]	Area %
3	11.219	BB	0.0561	244.82652	67.85548	3.4437
Totals :				7109.48275	1872.64847	

Signal 3: DAD1 C, Sig=240,4 Ref=800,100

Peak #	RetTime [min]	Type	Width [min]	Area [mAU*s]	Height [mAU]	Area %
1	9.375	BV R	0.0757	186.49977	34.67928	1.7998
2	10.801	MM	0.0633	9689.97754	2550.24023	93.5117
3	11.219	BV R	0.0561	485.83783	134.57977	4.6885
Totals :				1.03623e4	2719.49929	

Signal 4: DAD1 E, Sig=280,4 Ref=800,100

Peak #	RetTime [min]	Type	Width [min]	Area [mAU*s]	Height [mAU]	Area %
1	9.235	MM	0.1524	111.73144	12.22225	3.2693
2	10.801	BV R	0.0590	3191.57471	842.36896	93.1015
3	11.219	BB	0.0560	124.75192	34.67569	3.6391
Totals :				3428.05807	889.26689	

Signal 5: DAD1 F, Sig=360,4 Ref=800,100

Peak #	RetTime [min]	Type	Width [min]	Area [mAU*s]	Height [mAU]	Area %
1	9.375	BB	0.0751	39.06186	7.33468	1.1651
2	10.801	BV R	0.0588	3173.67358	841.87012	94.6652
3	11.219	BB	0.0562	107.18600	29.66109	3.1972
4	11.551	VB R	0.0619	32.60144	7.77987	0.9724
Totals :				3352.52288	886.64576	

6-((4-Azido-2,3,5,6-tetrafluorobenzyl)oxy)-9-(o-tolyl)-3H-xanthen-3-one, **16** – Analytical HPLC method 2B

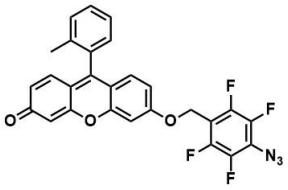

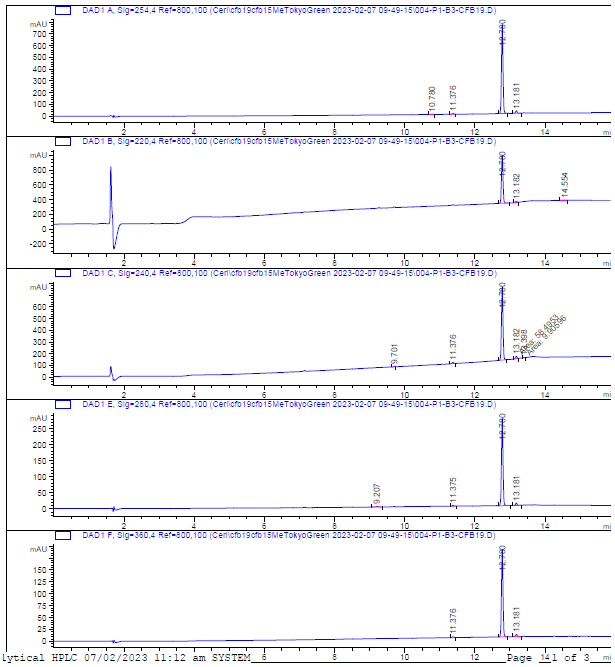

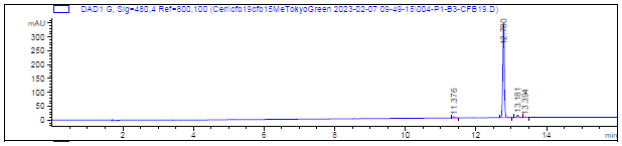

Signal 1: DAD1 A, Sig=254,4 Ref=800,100

Peak #	RetTime [min]	Type	Width [min]	Area [mAU*s]	Height [mAU]	Area %
1	10.780	BB	0.0661	6.46959	1.37040	0.2705
2	11.376	BB	0.0469	23.12614	7.50804	0.9669
3	12.780	BB	0.0463	2291.49219	757.97296	95.8100
4	13.181	BV R	0.0511	70.61725	21.06785	2.9526
Totals :				2391.70517	787.91925	

Signal 2: DAD1 B, Sig=220,4 Ref=800,100

Peak #	RetTime [min]	Type	Width [min]	Area [mAU*s]	Height [mAU]	Area %
1	12.780	BV R	0.0465	1977.80237	650.07349	96.5755
2	13.182	BB	0.0471	51.13506	17.00295	2.4969
3	14.554	BB	0.0678	18.99581	4.27972	0.9276
Totals :				2047.93324	671.35616	

Signal 3: DAD1 C, Sig=240,4 Ref=800,100

Peak #	RetTime [min]	Type	Width [min]	Area [mAU*s]	Height [mAU]	Area %
1	9.701	BB	0.0434	6.03209	2.17293	0.3020
2	11.376	BB	0.0481	32.15347	10.10992	1.6097
3	12.780	BB	0.0462	1890.83386	626.15558	94.6638
4	13.182	MM	0.0495	58.49531	19.67815	2.9285
5	13.398	MM	0.0517	9.90596	3.19277	0.4959
Totals :				1997.42069	661.30934	

Signal 4: DAD1 E, Sig=280,4 Ref=800,100

Peak #	RetTime [min]	Type	Width [min]	Area [mAU*s]	Height [mAU]	Area %
1	9.207	BB	0.0648	9.00806	1.98868	1.0330
2	11.375	BB	0.0469	8.24179	2.67622	0.9451
3	12.780	BB	0.0464	830.35083	273.32123	95.2190
4	13.181	BV R	0.0515	24.44246	7.21495	2.8029
Totals :				872.04314	285.20108	

Signal 5: DAD1 F, Sig=360,4 Ref=800,100

Peak #	RetTime [min]	Type	Width [min]	Area [mAU*s]	Height [mAU]	Area %
1	11.376	BB	0.0460	6.33307	2.11031	1.0995
2	12.780	BB	0.0462	553.67047	183.28223	96.1269
3	13.181	BV R	0.0539	15.97511	4.44952	2.7736
Totals :				575.97865	189.84206	

Signal 6: DAD1 G, Sig=480,4 Ref=800,100

Peak #	RetTime [min]	Type	Width [min]	Area [mAU*s]	Height [mAU]	Area %
1	11.376	BB	0.0467	13.29937	4.34619	1.2336
2	12.780	BB	0.0464	1030.92932	340.05743	95.6237
3	13.181	BV R	0.0529	28.82960	8.22277	2.6741
4	13.394	VB E	0.0512	5.05269	1.46747	0.4687
Totals :				1078.11098	354.09386	

4-Azido-2,3,5,6-tetrafluorobenzyl (4-nitrophenyl) carbonate, **17** – Analytical HPLC method 2B

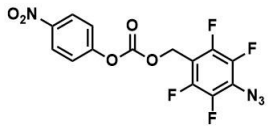

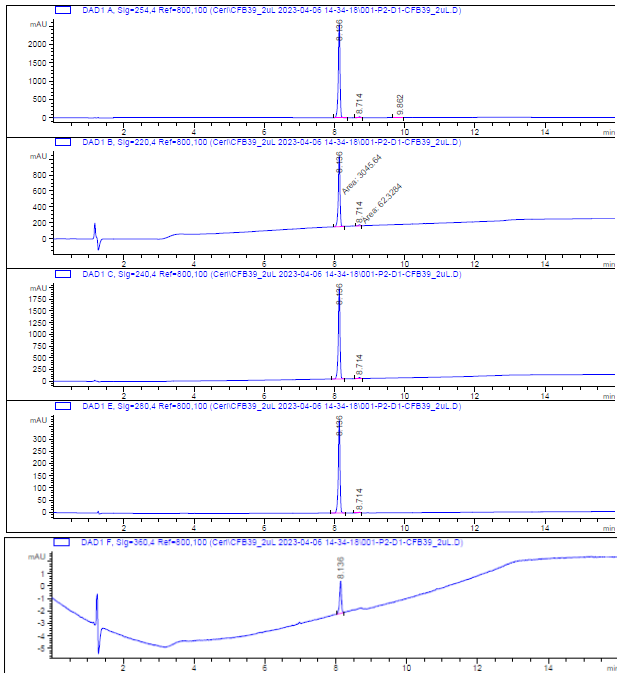

Signal 1: DAD1 A, Sig=254,4 Ref=800,100

Peak #	RetTime [min]	Type	Width [min]	Area [mAU*s]	Height [mAU]	Area %
1	8.136	BB	0.0537	8923.36523	2558.14746	99.0297
2	8.714	BB	0.0516	80.93781	23.83110	0.8982
3	9.862	BB	0.0800	6.49790	1.18536	0.0721
Totals :				9010.80095	2583.16392	

Signal 2: DAD1 B, Sig=220,4 Ref=800,100

Peak #	RetTime [min]	Type	Width [min]	Area [mAU*s]	Height [mAU]	Area %
1	8.136	MM	0.0571	3045.64063	888.86688	97.9946
2	8.714	MM	0.0727	62.32842	14.28430	2.0054
Totals :				3107.96905	903.15118	

Signal 3: DAD1 C, Sig=240,4 Ref=800,100

Peak #	RetTime [min]	Type	Width [min]	Area [mAU*s]	Height [mAU]	Area %
1	8.136	BB	0.0512	6697.77637	1943.24243	98.8094
2	8.714	BB	0.0522	80.70422	23.40786	1.1906
Totals :				6778.48059	1966.65029	

Signal 4: DAD1 E, Sig=280,4 Ref=800,100

Peak #	RetTime [min]	Type	Width [min]	Area [mAU*s]	Height [mAU]	Area %
1	8.136	BB	0.0510	1308.80823	381.43607	99.0875
2	8.714	BB	0.0553	12.05343	3.25029	0.9125
Totals :				1320.86166	384.68636	

Signal 5: DAD1 F, Sig=360,4 Ref=800,100

Peak #	RetTime [min]	Type	Width [min]	Area [mAU*s]	Height [mAU]	Area %
1	8.136	BB	0.0540	9.34927	2.59737	100.0000
Totals :				9.34927	2.59737	

A3.3 Compounds from chapter III

Tri-*tert*-butyl 2,2',2''-(10-(2-((4-nitrobenzyl)oxy)-2-oxoethyl)-1,4,7,10-tetraazacyclododecane-1,4,7-triyl)triacetate, **25** – LCMS method 1

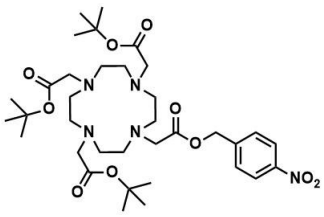

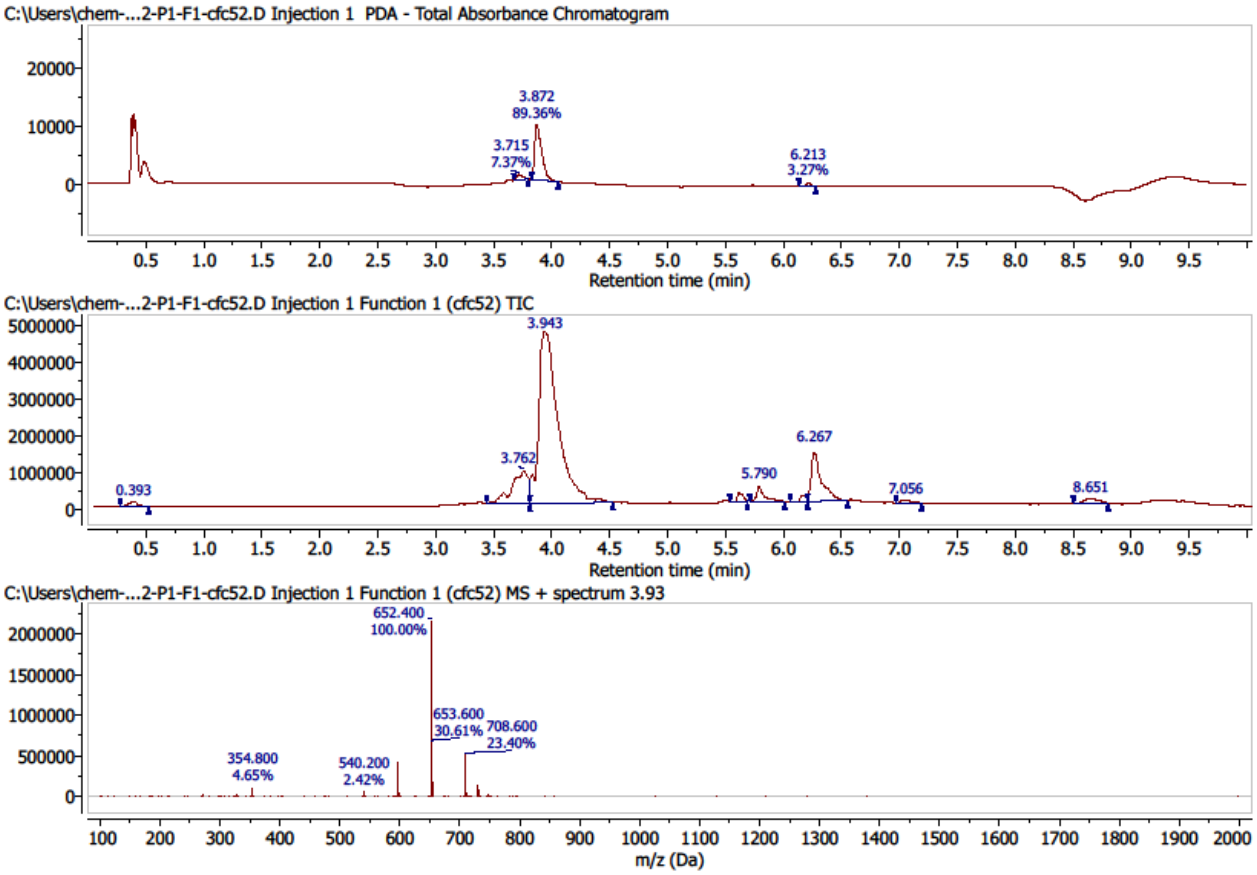

2,2',2''-(10-(2-((4-Nitrobenzyl)oxy)-2-oxoethyl)-1,4,7,10-tetraazacyclododecane-1,4,7-triyl)triacetic acid, **26** - LCMS method 1

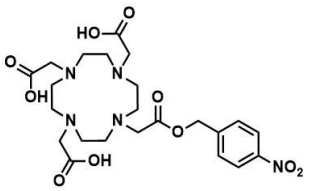

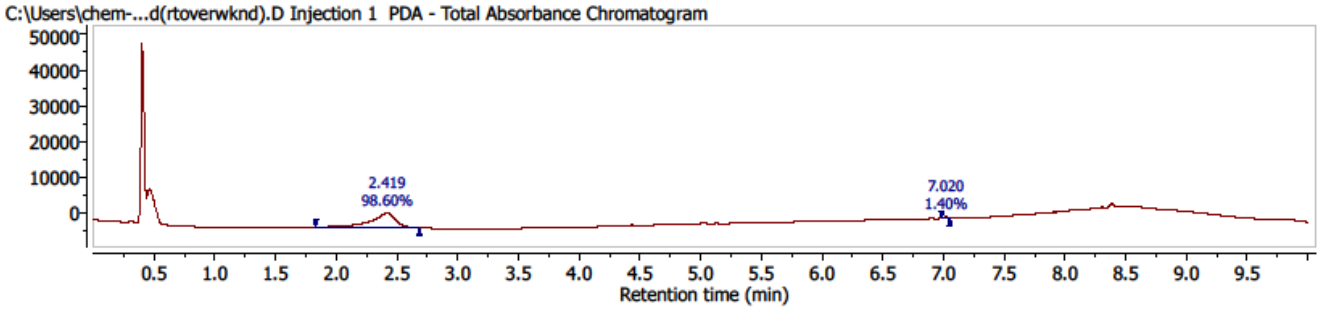

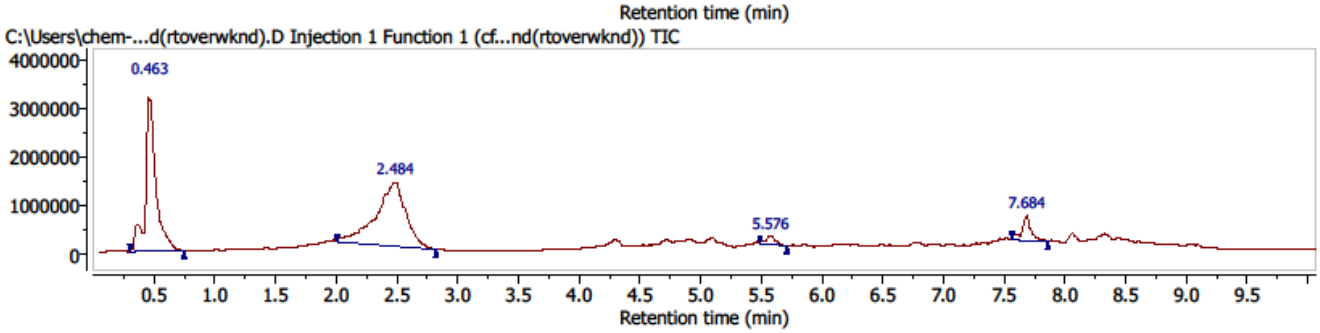

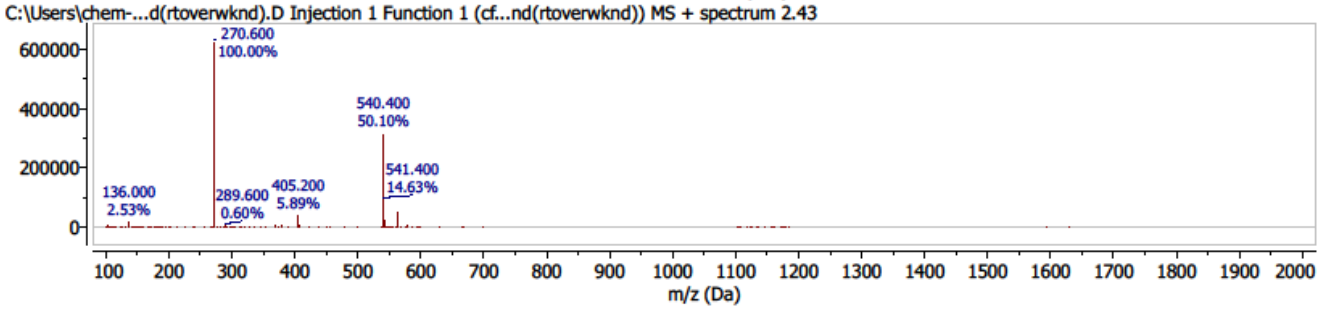

(1-Methyl-2-nitro-1*H*-imidazol-5-yl)methyl 2-bromoacetate, **30** – LCMS method 1

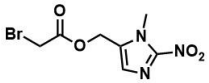

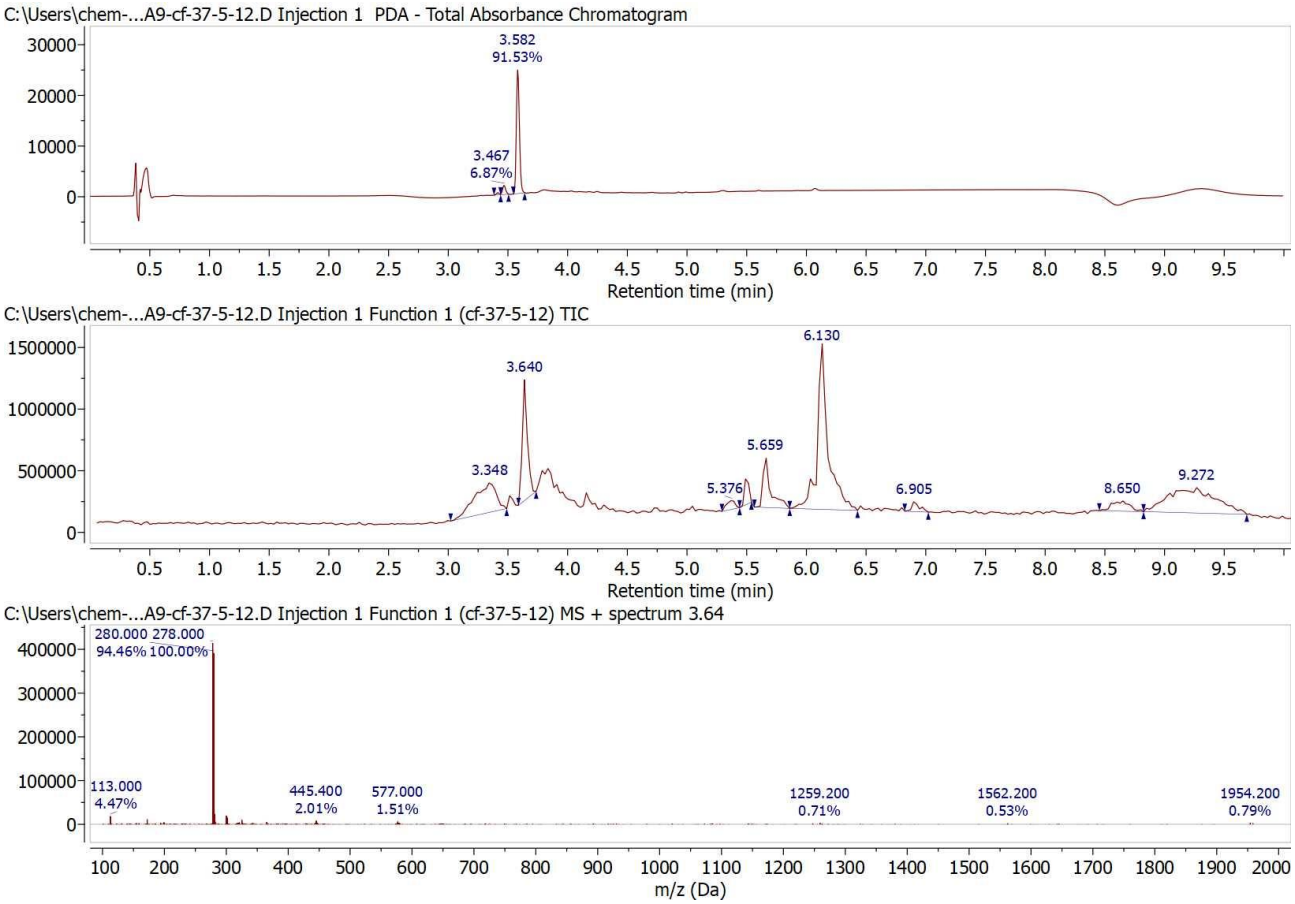

Tri-*tert*-butyl 2,2',2''-(10-(2-((1-methyl-2-nitro-1H-imidazol-5-yl)methoxy)-2-oxoethyl)-1,4,7,10-tetraazacyclododecane-1,4,7-triyl)triacetate, **31** – LCMS method 1

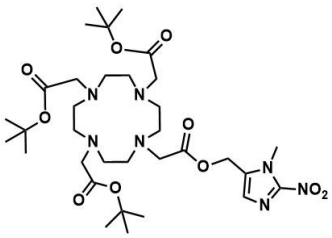

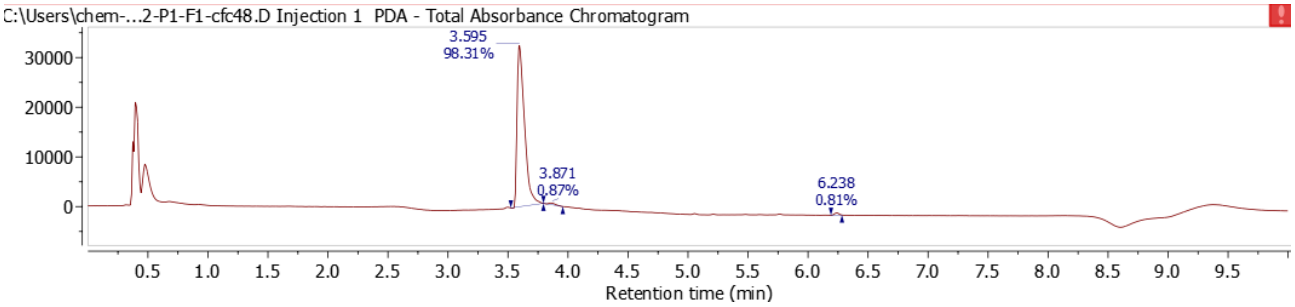

2,2',2''-(10-(2-((1-Methyl-2-nitro-1*H*-imidazol-5-yl)methoxy)-2-oxoethyl)-1,4,7,10-tetraazacyclododecane-1,4,7-triyl)triacetic acid, **32** – LCMS method 2

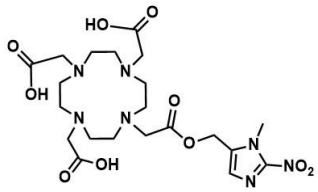

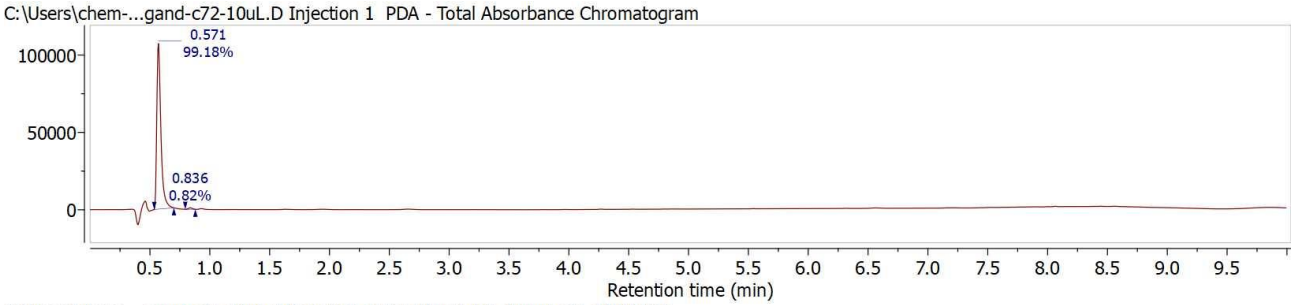

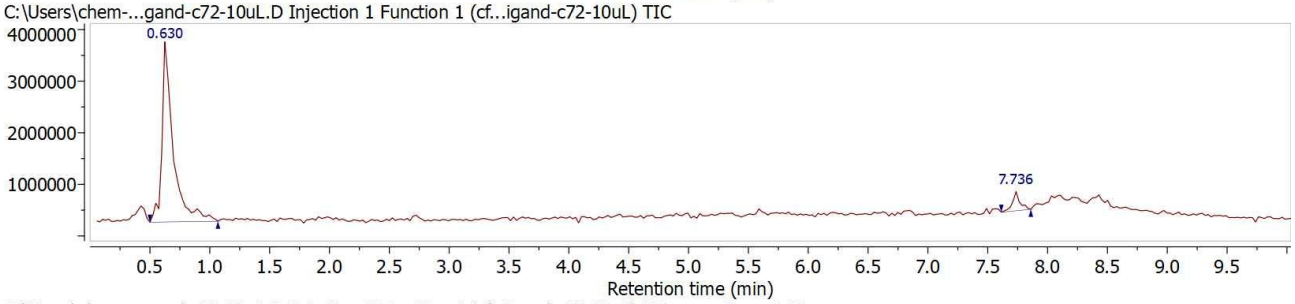

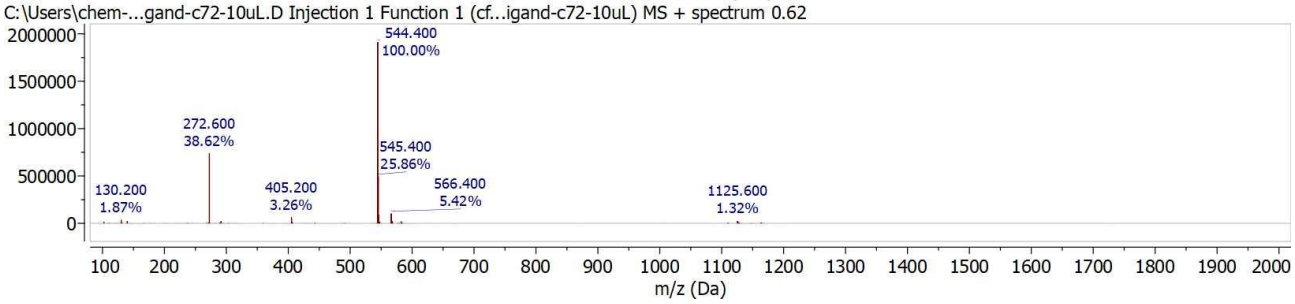

Tri-*tert*-butyl 2,2',2''-(10-(2-(benzyloxy)-2-oxoethyl)-1,4,7,10-tetraazacyclododecane-1,4,7-triyl)triacetate, **51** – Analytical HPLC method 2A

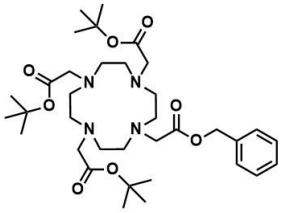

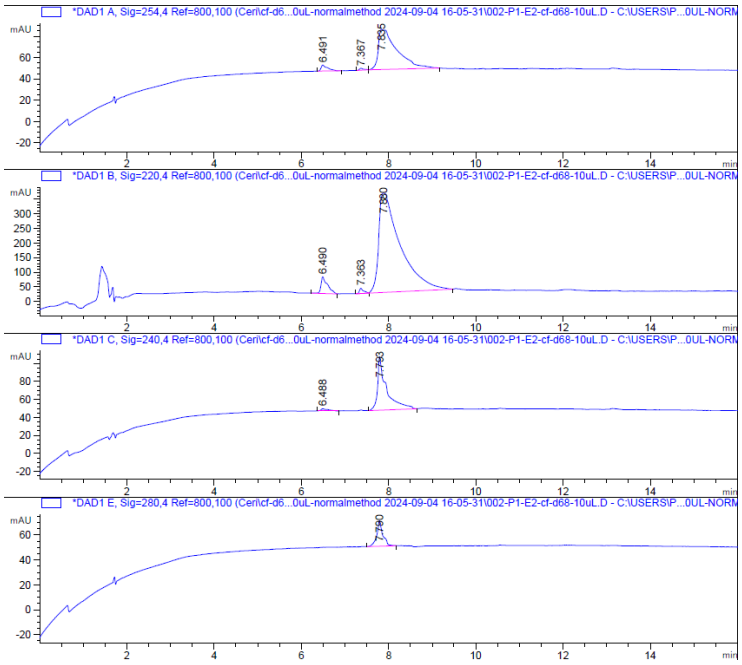

Signal 1: DAD1 A, Sig=254,4 Ref=800,100
Signal has been modified after loading from rawdata file!

Peak #	RetTime [min]	Type	Width [min]	Area [mAU*s]	Height [mAU]	Area %
1	6.491	BV R	0.1346	57.93521	5.64973	4.8358
2	7.367	BB	0.0906	11.61551	1.76897	0.9695
3	7.835	BB	0.3714	1128.50159	37.78876	94.1947
Totals :				1198.05231	45.20746	

Signal 2: DAD1 B, Sig=220,4 Ref=800,100
Signal has been modified after loading from rawdata file!

Peak #	RetTime [min]	Type	Width [min]	Area [mAU*s]	Height [mAU]	Area %
1	6.490	VB R	0.1382	591.11090	56.91418	4.7556
2	7.363	BV E	0.0899	118.21483	17.94540	0.9511
3	7.880	VV R	0.4392	1.17204e4	339.96286	94.2933
Totals :				1.24298e4	414.82244	

Signal 3: DAD1 C, Sig=240,4 Ref=800,100
Signal has been modified after loading from rawdata file!

Peak #	RetTime [min]	Type	Width [min]	Area [mAU*s]	Height [mAU]	Area %
1	6.488	BB	0.1487	28.01552	2.39183	3.1786
2	7.793	BB	0.1895	853.36548	59.42991	96.8214
Totals :				881.38100	61.82174	

Signal 4: DAD1 E, Sig=280,4 Ref=800,100
Signal has been modified after loading from rawdata file!

Peak #	RetTime [min]	Type	Width [min]	Area [mAU*s]	Height [mAU]	Area %
1	7.790	BB	0.1239	197.66843	20.60901	100.0000
Totals :				197.66843	20.60901	

2,2',2''-(10-(2-(benzyloxy)-2-oxoethyl)-1,4,7,10-tetraazacyclododecane-1,4,7-triyl)triacetic acid, **52** – Analytical HPLC method 1A

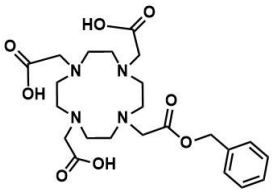

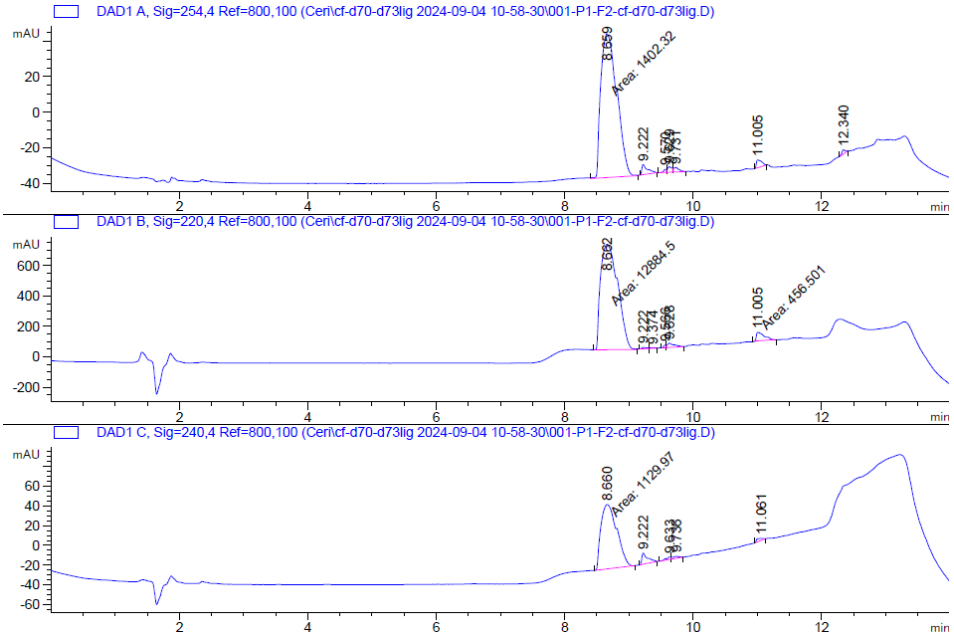

Signal 1: DAD1 A, Sig=254,4 Ref=800,100

Peak #	RetTime [min]	Type	Width [min]	Area [mAU*s]	Height [mAU]	Area %
1	8.659	MM	0.2896	1402.31934	80.69407	93.1688
2	9.222	BB	0.0832	35.23592	5.69580	2.3410
3	9.570	BV	0.0440	5.14081	1.76249	0.3416
4	9.629	VV	0.0689	15.37317	3.09774	1.0214
5	9.731	VB	0.0774	14.80011	2.52623	0.9833
6	11.005	BB	0.0712	24.01400	4.43028	1.5955
7	12.340	BB	0.0503	8.25489	2.33183	0.5484
Totals :				1505.13823	100.53844	

Signal 2: DAD1 B, Sig=220,4 Ref=800,100

Peak #	RetTime [min]	Type	Width [min]	Area [mAU*s]	Height [mAU]	Area %
1	8.662	MM	0.3098	1.28845e4	693.13135	94.3385
2	9.222	BV	0.0651	40.87700	9.15284	0.2993
3	9.374	VB	0.0744	18.32190	3.31853	0.1342
4	9.566	BV	0.0414	46.65302	17.30879	0.3416
5	9.628	VB	0.0980	210.87888	28.27490	1.5440
6	11.005	MM	0.1348	456.50125	56.45050	3.3424
Totals :				1.36577e4	807.63691	

Signal 3: DAD1 C, Sig=240,4 Ref=800,100

Peak #	RetTime [min]	Type	Width [min]	Area [mAU*s]	Height [mAU]	Area %
1	8.660	MM	0.2875	1129.97437	65.51482	90.9467
2	9.222	BB	0.0840	70.90374	11.32937	5.7067
3	9.633	BV	0.0709	12.38240	2.37123	0.9966
4	9.736	VB	0.0908	13.20370	1.90740	1.0627
5	11.061	BB	0.1025	15.99366	1.97435	1.2873
Totals :				1242.45787	83.09717	

Europium nitrobenzyl complex (EuNB) **18a** – LCMS method 2

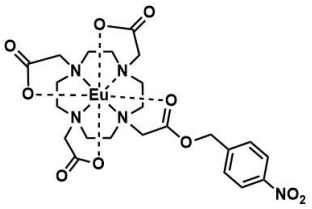

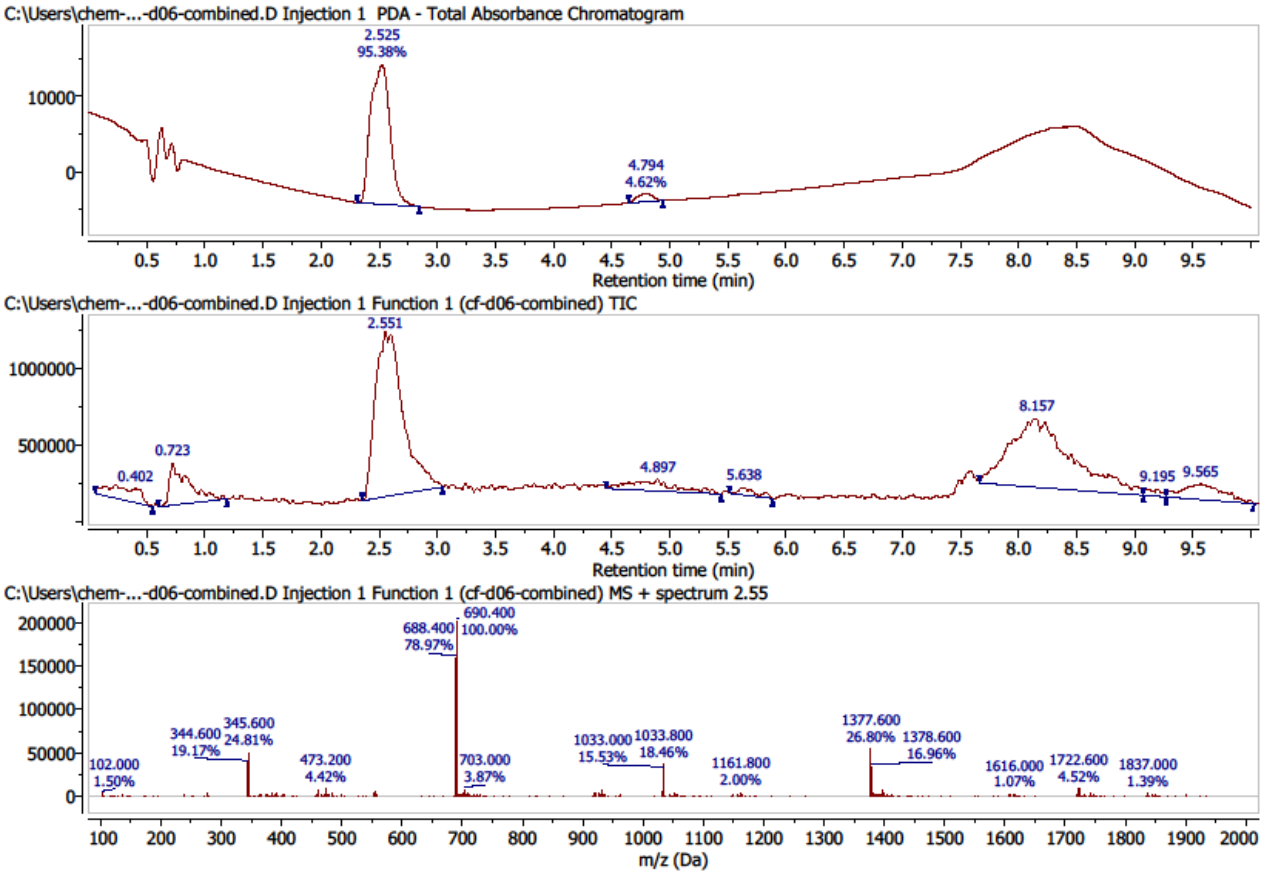

Europium nitrobenzyl complex (EuNB) **18a** – Analytical HPLC method 1A

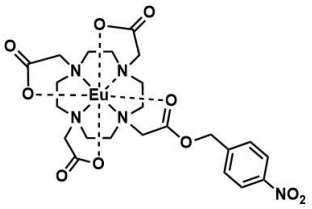

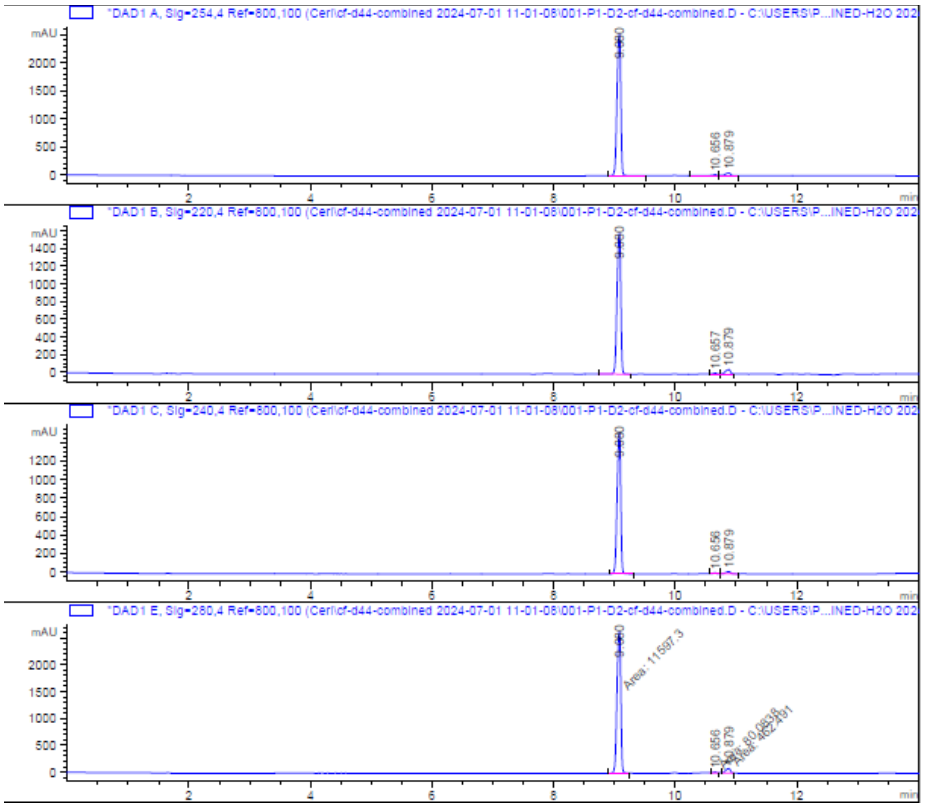

Signal 1: DAD1 A, Sig=254,4 Ref=800,100
Signal has been modified after loading from rawdata file!

Peak #	RetTime [min]	Type	Width [min]	Area [mAU*s]	Height [mAU]	Area %
1	9.080	BV R	0.0710	1.08583e4	2532.66089	96.5157
2	10.656	VV R	0.0834	114.38853	19.79097	1.0168
3	10.879	VV R	0.0953	277.60193	46.71708	2.4675
Totals :				1.12502e4	2599.16894	

Signal 2: DAD1 B, Sig=220,4 Ref=800,100
Signal has been modified after loading from rawdata file!

Peak #	RetTime [min]	Type	Width [min]	Area [mAU*s]	Height [mAU]	Area %
1	9.080	VB R	0.0699	6814.35205	1593.28894	95.5534
2	10.657	BV	0.0549	40.13428	10.43367	0.5628
3	10.879	VB	0.0904	276.97504	50.14054	3.8838
Totals :				7131.46136	1653.86315	

Signal 3: DAD1 C, Sig=240,4 Ref=800,100
Signal has been modified after loading from rawdata file!

Peak #	RetTime [min]	Type	Width [min]	Area [mAU*s]	Height [mAU]	Area %
1	9.080	BB	0.0678	6264.52979	1530.38879	97.4399
2	10.656	BV	0.0588	35.15849	9.57716	0.5469
3	10.879	VV R	0.0902	129.43283	23.15787	2.0132
Totals :				6429.12110	1563.12382	

Signal 4: DAD1 E, Sig=280,4 Ref=800,100
Signal has been modified after loading from rawdata file!

Peak #	RetTime [min]	Type	Width [min]	Area [mAU*s]	Height [mAU]	Area %
1	9.080	MM	0.0732	1.15973e4	2641.97388	95.5306
2	10.656	MM	0.0703	80.08376	18.98098	0.6597
3	10.879	MM	0.0937	462.49091	82.28905	3.8097
Totals :				1.21398e4	2743.24391	

Terbium nitrobenzyl complex (TbNB) **18b** – LCMS method 2

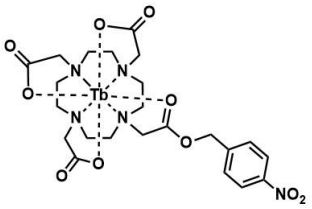

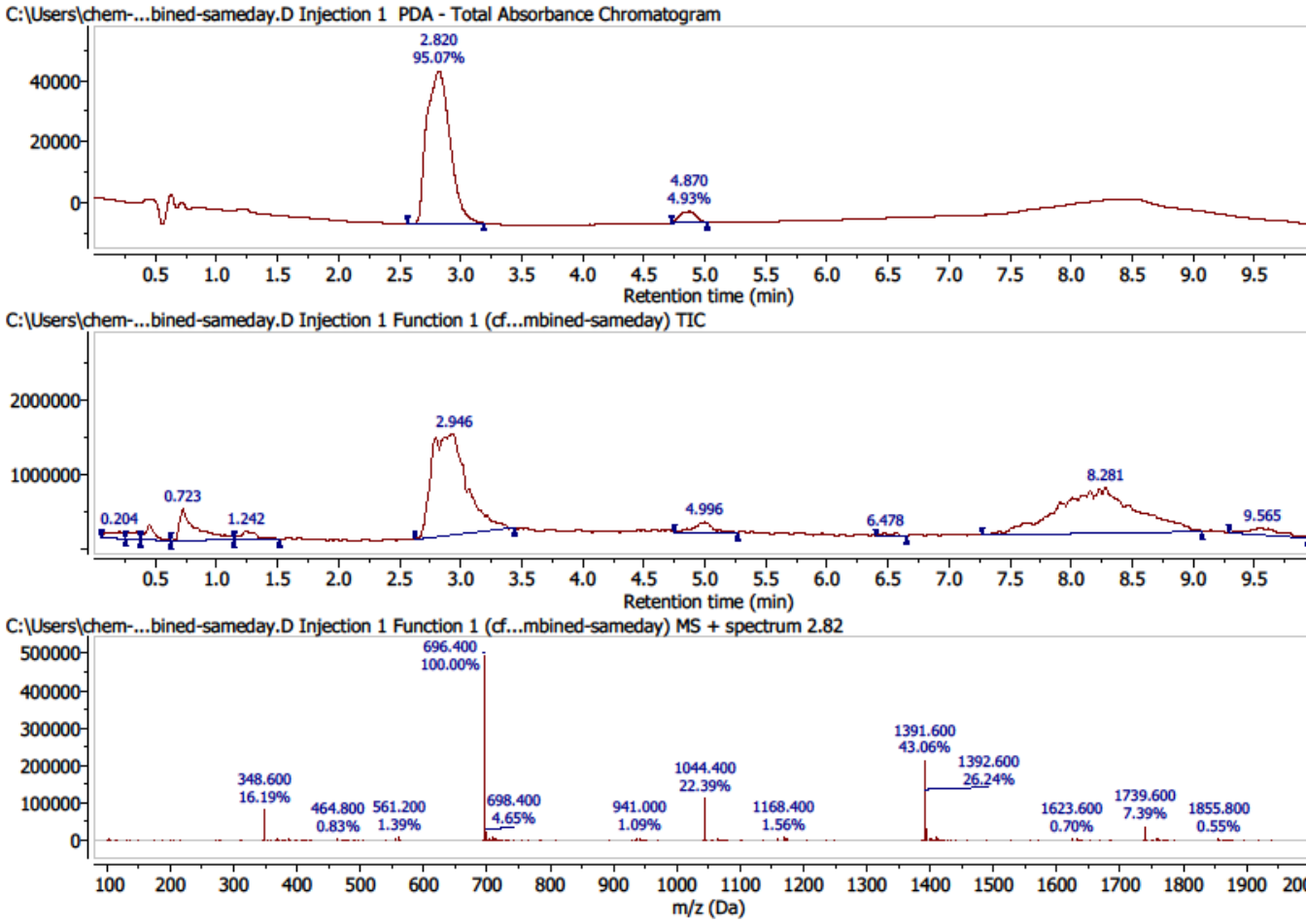

Terbium nitrobenzyl complex (TbNB) **18b** – Analytical HPLC method 1A

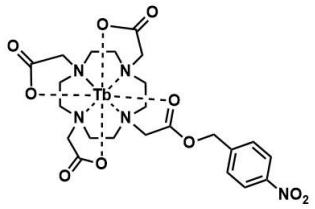

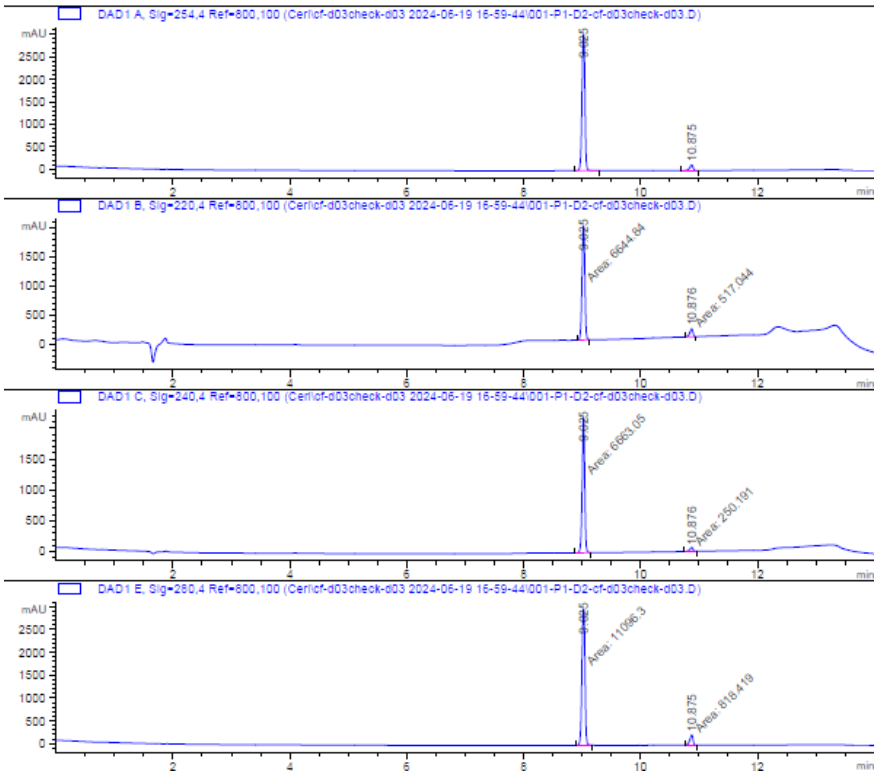

Signal 1: DAD1 A, Sig=254,4 Ref=800,100

Peak #	RetTime [min]	Type	Width [min]	Area [mAU*s]	Height [mAU]	Area %
1	9.025	BB	0.0548	1.06195e4	3035.96606	95.7272
2	10.875	BB	0.0586	474.00876	123.91591	4.2728
Totals :				1.10935e4	3159.88197	

Signal 2: DAD1 B, Sig=220,4 Ref=800,100

Peak #	RetTime [min]	Type	Width [min]	Area [mAU*s]	Height [mAU]	Area %
1	9.025	MM	0.0563	6644.84229	1965.71191	92.7806
2	10.876	MM	0.0635	517.04388	135.71552	7.2194
Totals :				7161.88617	2101.42743	

Signal 3: DAD1 C, Sig=240,4 Ref=800,100

Peak #	RetTime [min]	Type	Width [min]	Area [mAU*s]	Height [mAU]	Area %
1	9.025	MM	0.0504	6663.04590	2203.55713	96.3810
2	10.876	MM	0.0655	250.19104	63.66663	3.6190
Totals :				6913.23694	2267.22376	

Signal 4: DAD1 E, Sig=280,4 Ref=800,100

Peak #	RetTime [min]	Type	Width [min]	Area [mAU*s]	Height [mAU]	Area %
1	9.025	MM	0.0617	1.10963e4	2997.78491	93.1310
2	10.875	MM	0.0618	818.41882	220.74960	6.8690
Totals :				1.19147e4	3218.53452	

Gadolinium nitrobenzyl complex (GdNB) **18c** – LCMS method 2

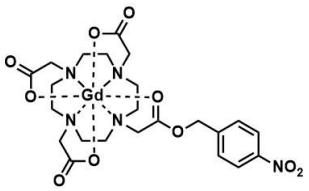

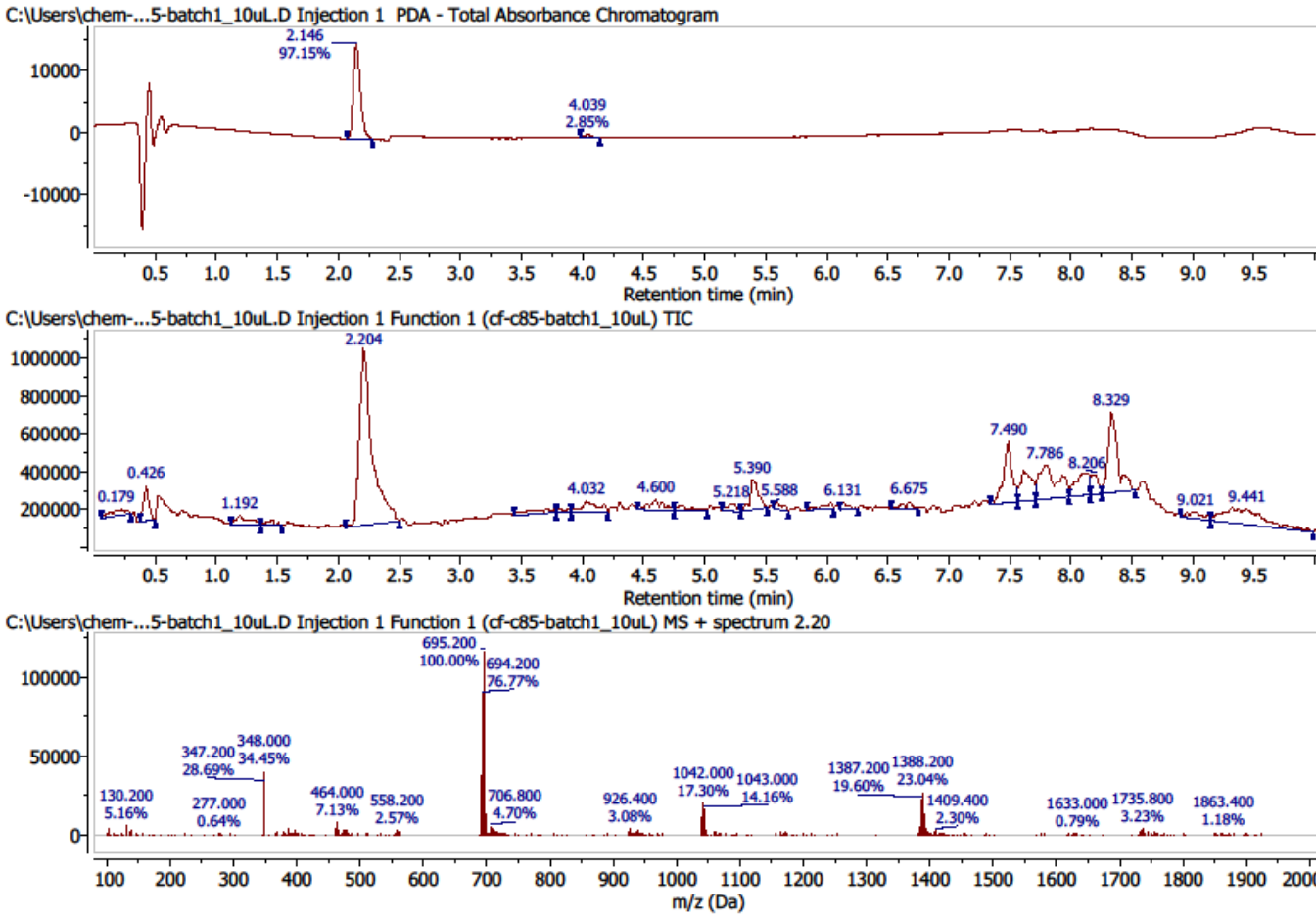

Gadolinium nitrobenzyl complex (GdNB) **18c** – Analytical HPLC method 1A

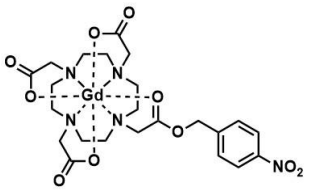

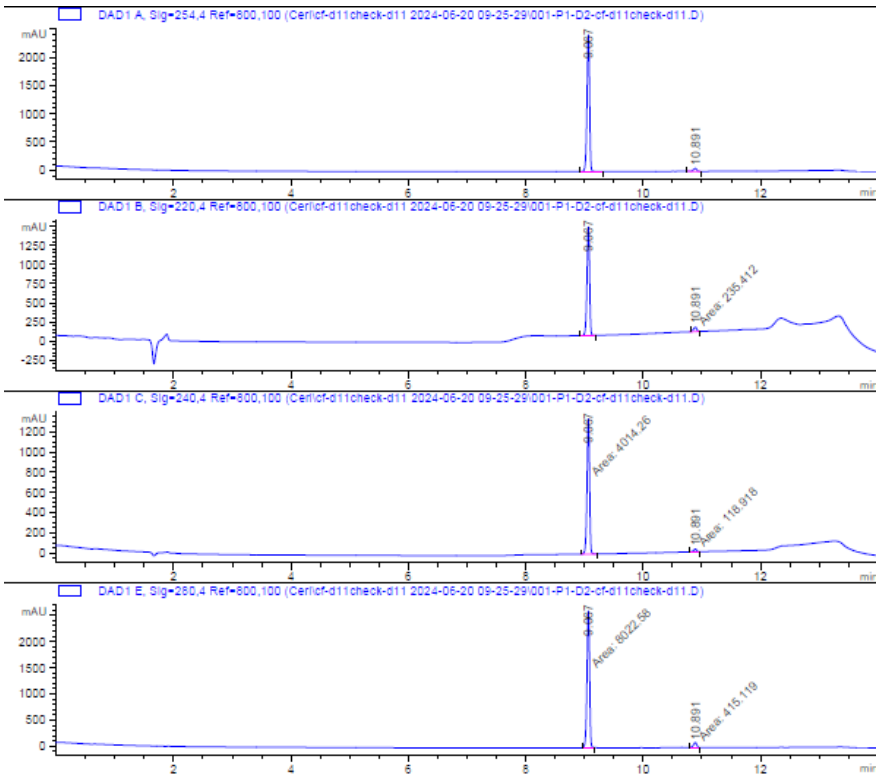

Signal 1: DAD1 A, Sig=254,4 Ref=800,100

Peak #	RetTime [min]	Type	Width [min]	Area [mAU*s]	Height [mAU]	Area %
1	9.067	BB	0.0474	7360.82080	2428.98340	97.1821
2	10.891	BB	0.0618	213.43527	53.21606	2.8179
Totals :				7574.25607	2482.19946	

Signal 2: DAD1 B, Sig=220,4 Ref=800,100

Peak #	RetTime [min]	Type	Width [min]	Area [mAU*s]	Height [mAU]	Area %
1	9.067	BB	0.0475	4317.02295	1419.23792	94.8289
2	10.891	MM	0.0669	235.41168	58.67155	5.1711
Totals :				4552.43463	1477.90946	

Signal 3: DAD1 C, Sig=240,4 Ref=800,100

Peak #	RetTime [min]	Type	Width [min]	Area [mAU*s]	Height [mAU]	Area %
1	9.067	MM	0.0497	4014.26343	1345.05127	97.1228
2	10.891	MM	0.0705	118.91805	28.12196	2.8772
Totals :				4133.18148	1373.17323	

Signal 4: DAD1 E, Sig=280,4 Ref=800,100

Peak #	RetTime [min]	Type	Width [min]	Area [mAU*s]	Height [mAU]	Area %
1	9.067	MM	0.0510	8022.57764	2623.73413	95.0802
2	10.891	MM	0.0697	415.11920	99.21050	4.9198
Totals :				8437.69684	2722.94463	

Europium nitroimidazole complex (EuNI) **19a** – LCMS method 2

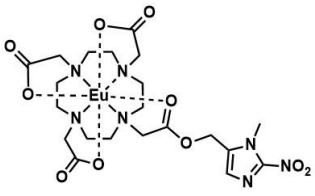

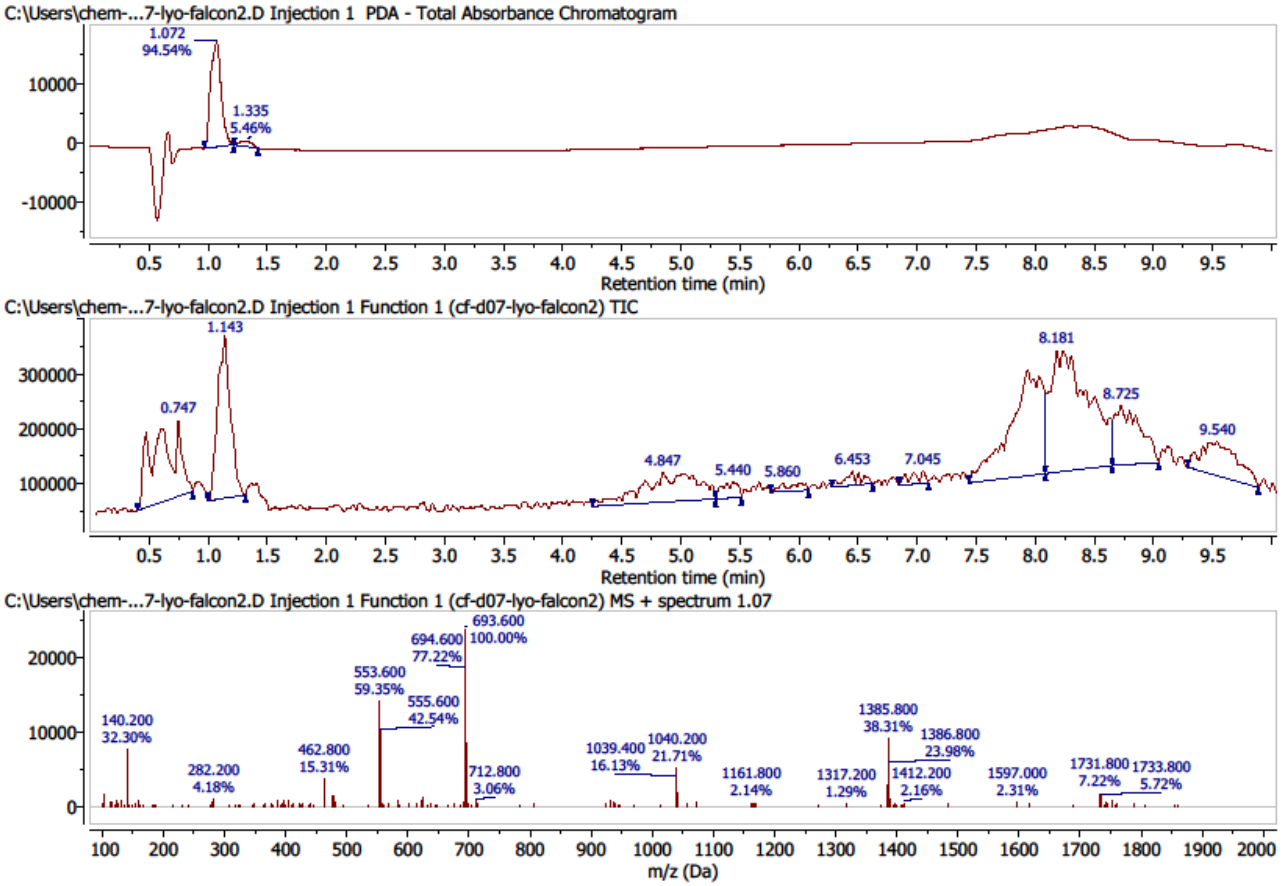

Europium nitroimidazole complex (EuNI) **19a** – Analytical HPLC method 1A

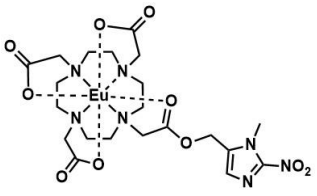

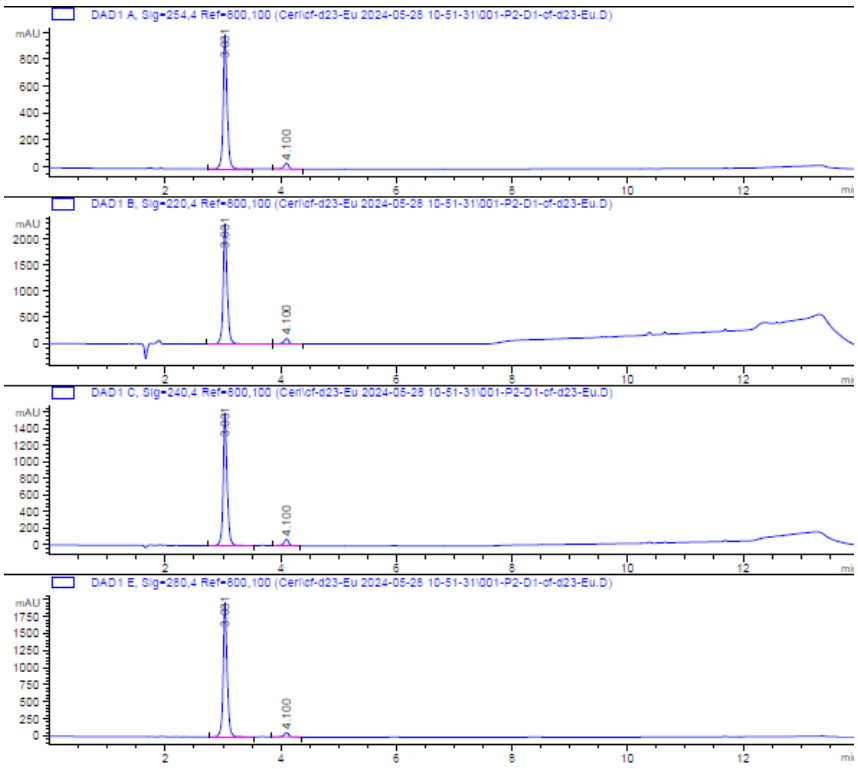

Signal 1: DAD1 A, Sig=254,4 Ref=800,100

Peak #	RetTime [min]	Type	Width [min]	Area [mAU*s]	Height [mAU]	Area %
1	3.031	BB	0.0690	4721.63525	1001.20709	94.9336
2	4.100	BB	0.0837	251.98569	44.73561	5.0664
Totals :				4973.62094	1045.94270	

Signal 2: DAD1 B, Sig=220,4 Ref=800,100

Peak #	RetTime [min]	Type	Width [min]	Area [mAU*s]	Height [mAU]	Area %
1	3.031	VV R	0.0712	1.11612e4	2308.98462	94.8664
2	4.100	BB	0.0835	603.97437	107.60862	5.1336
Totals :				1.17652e4	2416.59324	

Signal 3: DAD1 C, Sig=240,4 Ref=800,100

Peak #	RetTime [min]	Type	Width [min]	Area [mAU*s]	Height [mAU]	Area %
1	3.031	BB	0.0701	7590.58936	1606.93164	94.4154
2	4.100	BB	0.0835	448.97531	79.93547	5.5846
Totals :				8039.56467	1686.86711	

Signal 4: DAD1 E, Sig=280,4 Ref=800,100

Peak #	RetTime [min]	Type	Width [min]	Area [mAU*s]	Height [mAU]	Area %
1	3.031	BB	0.0705	9407.59473	1977.32581	96.2586
2	4.100	BB	0.0836	365.65176	65.05544	3.7414
Totals :				9773.24649	2042.38125	

Terbium nitroimidazole complex (TbNI) **19b** – LCMS method 2

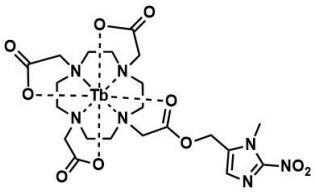

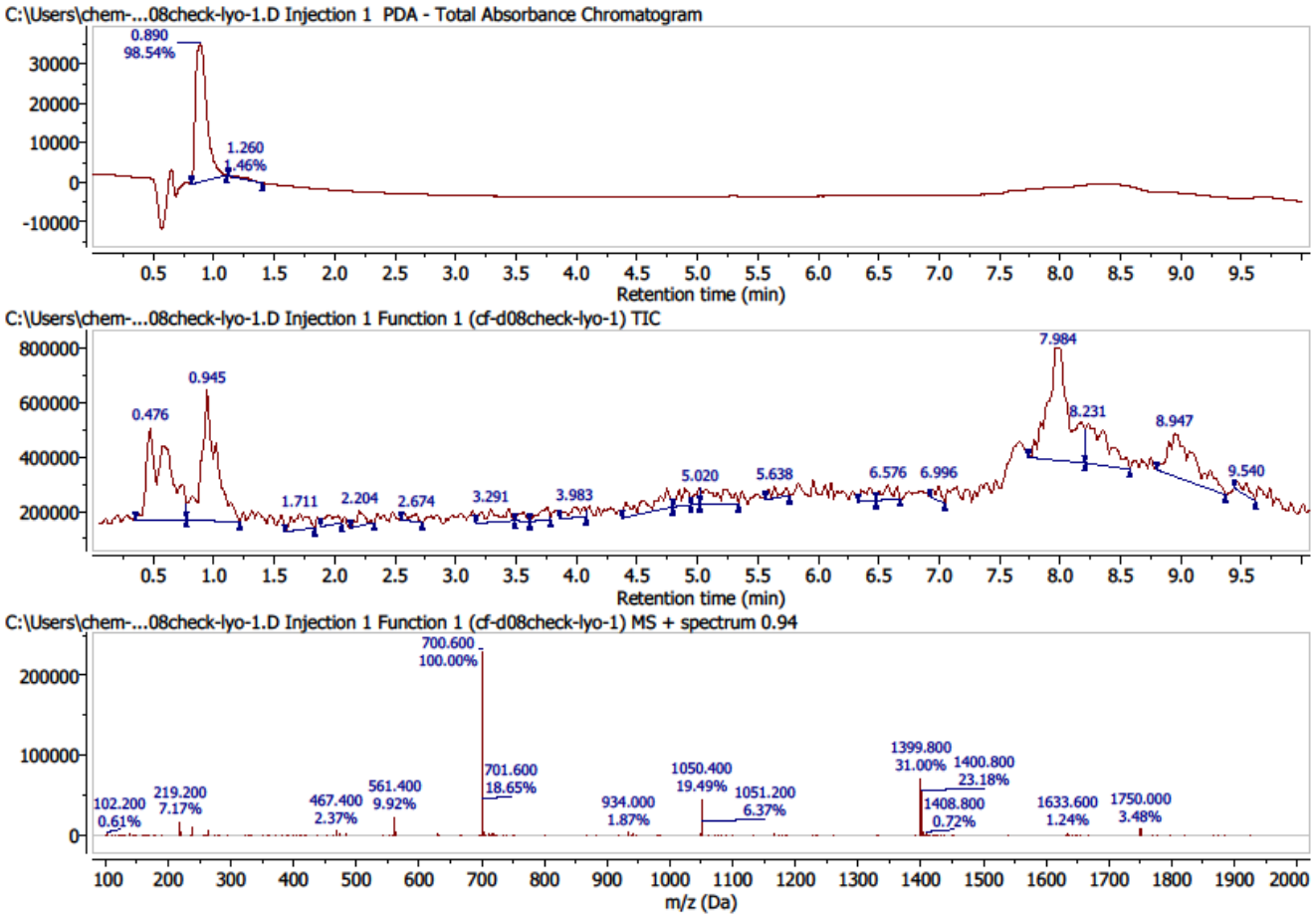

Terbium nitroimidazole complex (TbNI) **19b** – Analytical HPLC method 1A

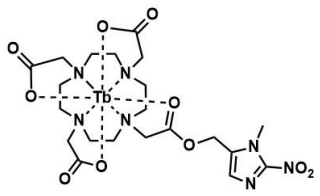

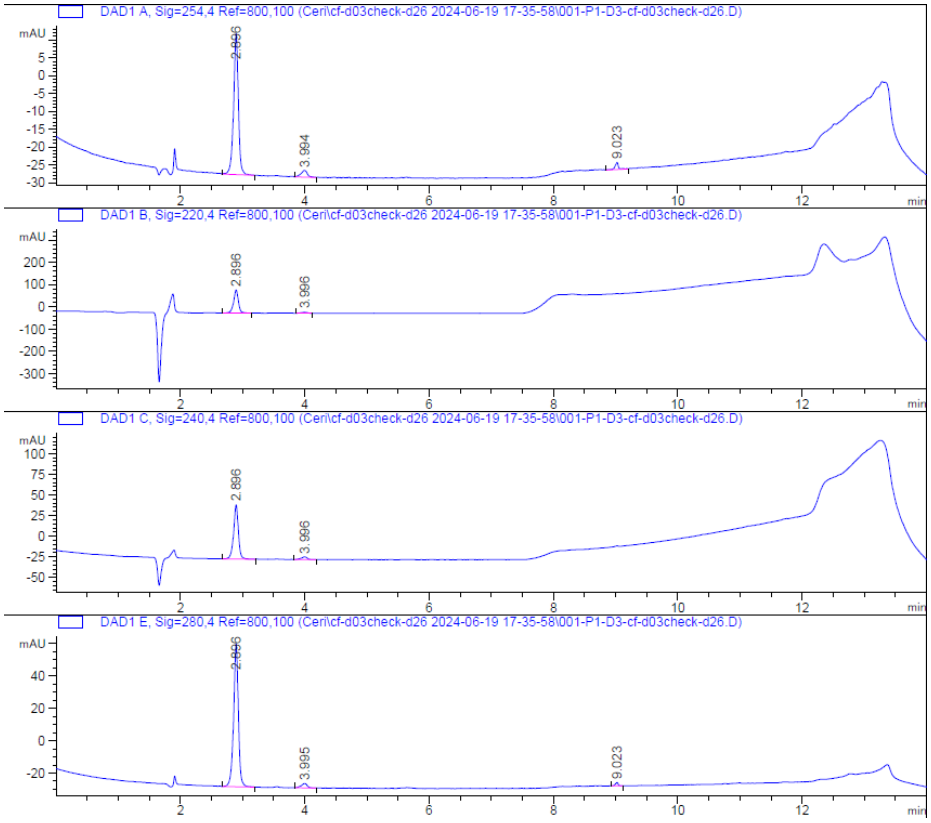

Signal 1: DAD1 A, Sig=254,4 Ref=800,100

Peak #	RetTime [min]	Type	Width [min]	Area [mAU*s]	Height [mAU]	Area %
1	2.896	BB	0.0794	211.72600	39.57319	90.7770
2	3.994	BB	0.1056	13.33914	1.86112	5.7191
3	9.023	BV R	0.0590	8.17242	1.98711	3.5039
Totals :				233.23755	43.42142	

Signal 2: DAD1 B, Sig=220,4 Ref=800,100

Peak #	RetTime [min]	Type	Width [min]	Area [mAU*s]	Height [mAU]	Area %
1	2.896	BV R	0.0790	553.90564	104.16051	95.6416
2	3.996	BB	0.0890	25.24172	4.03546	4.3584
Totals :				579.14736	108.19597	

Signal 3: DAD1 C, Sig=240,4 Ref=800,100

Peak #	RetTime [min]	Type	Width [min]	Area [mAU*s]	Height [mAU]	Area %
1	2.896	BB	0.0793	351.02808	65.72652	93.9577
2	3.996	BB	0.1041	22.57433	3.24765	6.0423
Totals :				373.60241	68.97418	

Signal 4: DAD1 E, Sig=280,4 Ref=800,100

Peak #	RetTime [min]	Type	Width [min]	Area [mAU*s]	Height [mAU]	Area %
1	2.896	BB	0.0791	470.40955	88.36967	94.9189
2	3.995	BB	0.1002	18.58730	2.67167	3.7505
3	9.023	BV R	0.0497	6.59406	2.03839	1.3305
Totals :				495.59091	93.07973	

Gadolinium nitroimidazole complex (GdNI) **19c** – LCMS method 2

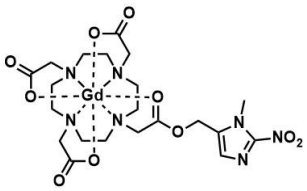

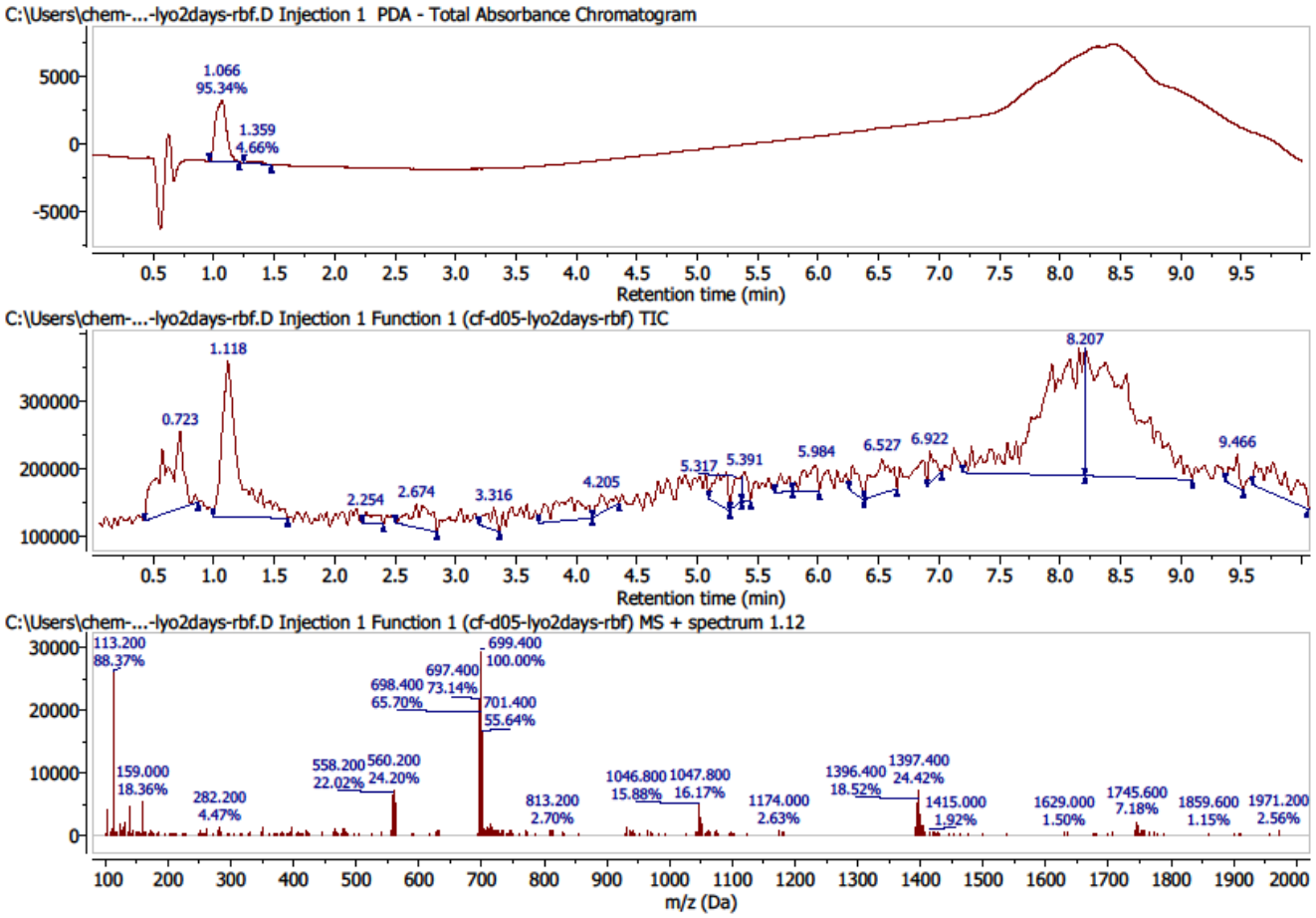

Gadolinium nitroimidazole complex (GdNI) **19c** – Analytical HPLC method 1A

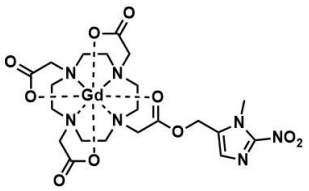

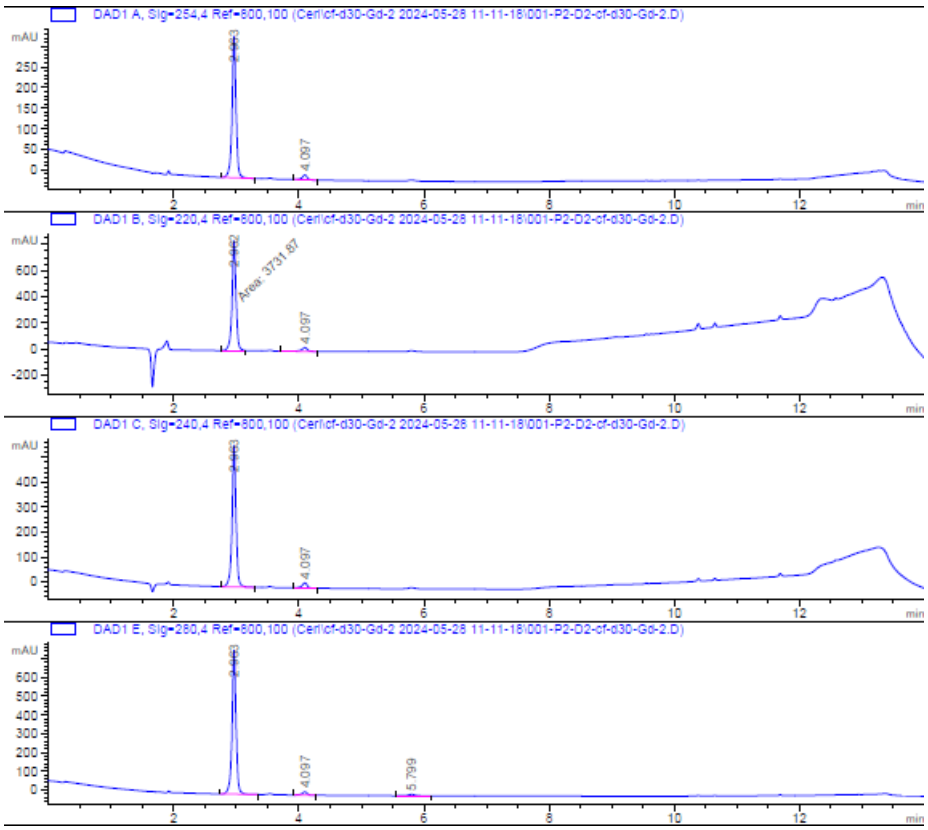

Signal 1: DAD1 A, Sig=254,4 Ref=800,100

Peak #	RetTime [min]	Type	Width [min]	Area [mAU*s]	Height [mAU]	Area %
1	2.963	BB	0.0659	1530.90210	344.14487	95.9053
2	4.097	BB	0.0817	65.36169	11.79296	4.0947
Totals :				1596.26379	355.93783	

Signal 2: DAD1 B, Sig=220,4 Ref=800,100

Peak #	RetTime [min]	Type	Width [min]	Area [mAU*s]	Height [mAU]	Area %
1	2.962	MM	0.0739	3731.86816	841.92188	95.2367
2	4.097	BB	0.0916	186.65054	29.19338	4.7633
Totals :				3918.51871	871.11526	

Signal 3: DAD1 C, Sig=240,4 Ref=800,100

Peak #	RetTime [min]	Type	Width [min]	Area [mAU*s]	Height [mAU]	Area %
1	2.963	BB	0.0659	2522.19189	566.84747	95.5290
2	4.097	BB	0.0833	118.04552	21.08798	4.4710
Totals :				2640.23741	587.93546	

Signal 4: DAD1 E, Sig=280,4 Ref=800,100

Peak #	RetTime [min]	Type	Width [min]	Area [mAU*s]	Height [mAU]	Area %
1	2.963	BB	0.0660	3416.86890	765.90320	95.6125
2	4.097	BB	0.0832	95.88809	17.14798	2.6832
3	5.799	BV R	0.1181	60.90603	7.24036	1.7043
Totals :				3573.66302	790.29154	

Europium benzyl complex (EuBn) **22a** – Analytical HPLC method 1A

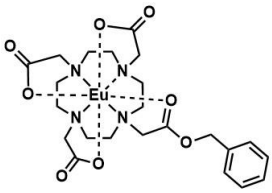

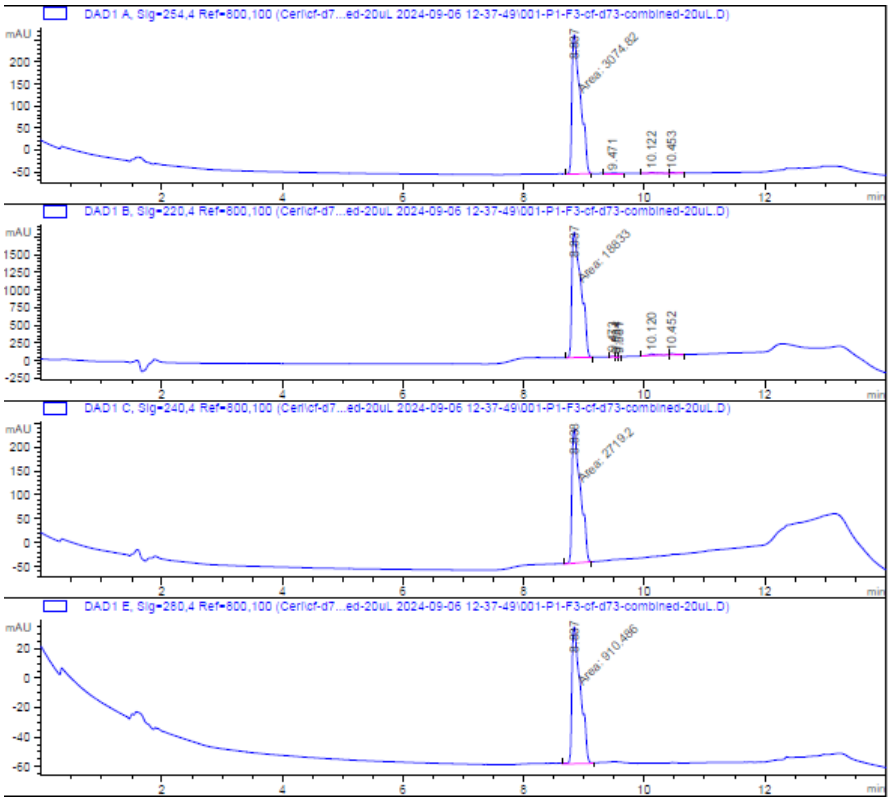

Signal 1: DAD1 A, Sig=254,4 Ref=800,100

Peak #	RetTime [min]	Type	Width [min]	Area [mAU*s]	Height [mAU]	Area %
1	8.837	MM	0.1619	3074.82300	316.51300	98.6913
2	9.471	BB	0.1046	9.25713	1.12971	0.2971
3	10.122	BV	0.1345	20.59275	2.06152	0.6610
4	10.453	VB	0.0877	10.92334	1.72970	0.3506
Totals :				3115.59621	321.43392	

Signal 2: DAD1 B, Sig=220,4 Ref=800,100

Peak #	RetTime [min]	Type	Width [min]	Area [mAU*s]	Height [mAU]	Area %
1	8.837	MM	0.1762	1.88330e4	1781.68335	98.2755
2	9.473	BV	0.0525	27.63516	7.57831	0.1442
3	9.534	VV	0.0239	5.27953	3.25249	0.0275
4	9.581	VV	0.0461	7.68636	2.23390	0.0401
5	10.120	BV R	0.1237	192.34634	21.03777	1.0037
6	10.452	BV R	0.0802	97.52488	16.69501	0.5089

Signal 3: DAD1 C, Sig=240,4 Ref=800,100

Peak #	RetTime [min]	Type	Width [min]	Area [mAU*s]	Height [mAU]	Area %
1	8.838	MM	0.1622	2719.19775	279.45468	100.0000
Totals :				2719.19775	279.45468	

Signal 4: DAD1 E, Sig=280,4 Ref=800,100

Peak #	RetTime [min]	Type	Width [min]	Area [mAU*s]	Height [mAU]	Area %
1	8.837	MM	0.1634	910.48566	92.86311	100.0000
Totals :				910.48566	92.86311	

Terbium benzyl complex (TbBn) **22b** – Analytical HPLC method 1A

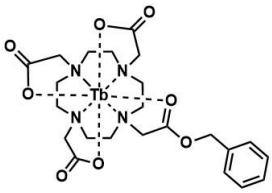

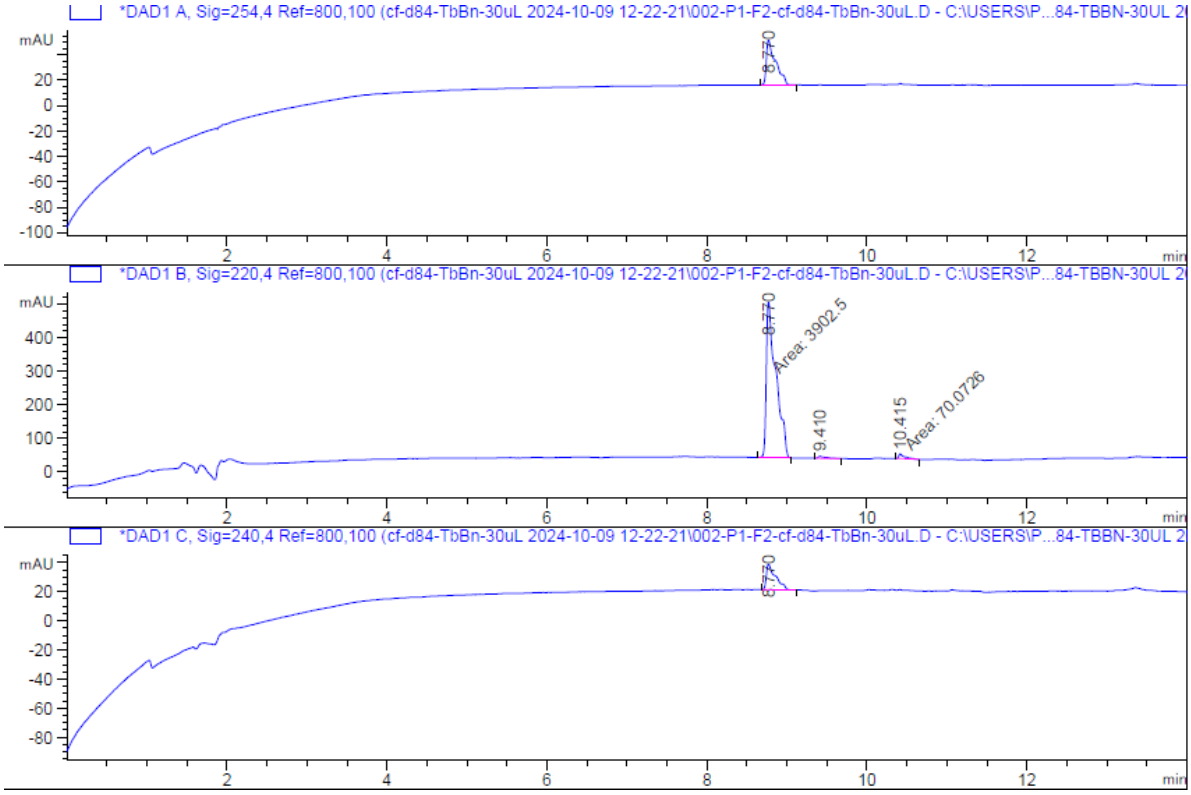

Signal 1: DAD1 A, Sig=254,4 Ref=800,100
Signal has been modified after loading from rawdata file!

Peak #	RetTime [min]	Type	Width [min]	Area [mAU*s]	Height [mAU]	Area %
1	8.770	BB	0.1085	281.87323	35.18276	100.0000
Totals :				281.87323	35.18276	

Signal 2: DAD1 B, Sig=220,4 Ref=800,100
Signal has been modified after loading from rawdata file!

Peak #	RetTime [min]	Type	Width [min]	Area [mAU*s]	Height [mAU]	Area %
1	8.770	MM	0.1398	3902.50146	465.27966	97.2110
2	9.410	BV R	0.0884	41.89270	6.31290	1.0435
3	10.415	MM	0.0865	70.07259	13.49830	1.7455
Totals :				4014.46675	485.09086	

Signal 3: DAD1 C, Sig=240,4 Ref=800,100
Signal has been modified after loading from rawdata file!

Peak #	RetTime [min]	Type	Width [min]	Area [mAU*s]	Height [mAU]	Area %
1	8.770	BB	0.1087	140.56416	17.50330	100.0000
Totals :				140.56416	17.50330	

Gadolinium benzyl complex (GdBn) **22c** – LCMS method 2

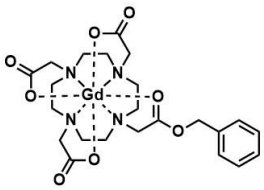

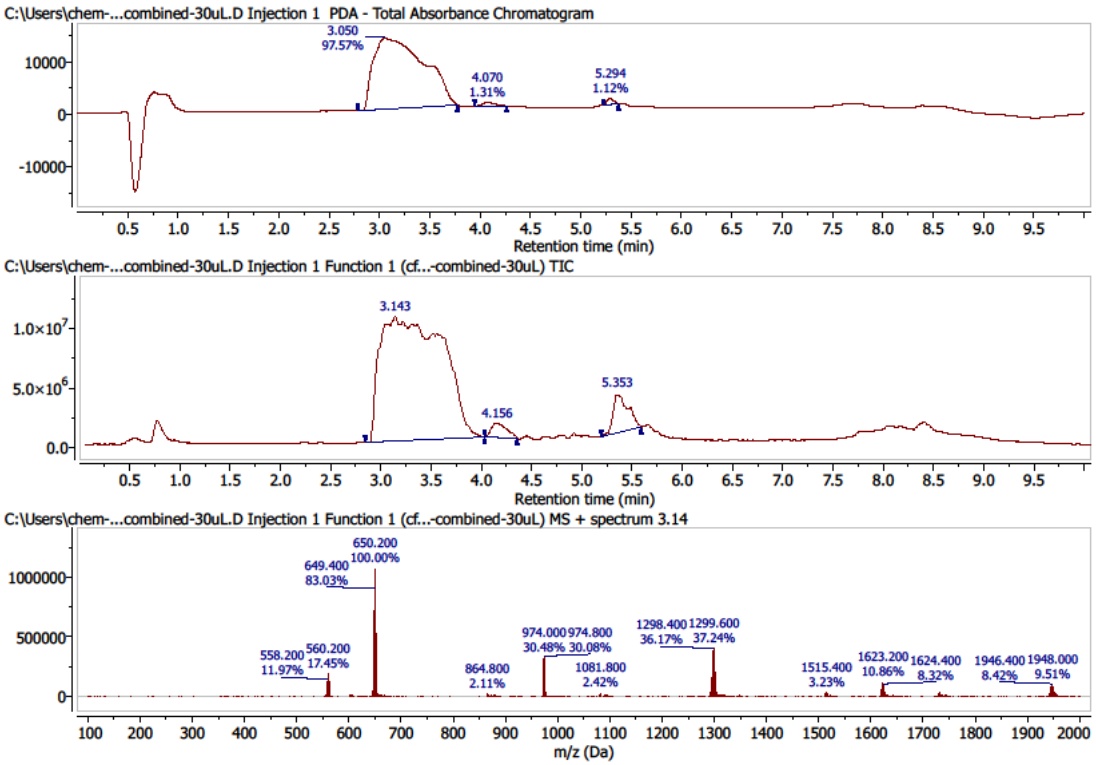

Gadolinium benzyl complex (GdBn) **22c** – Analytical HPLC method 1A

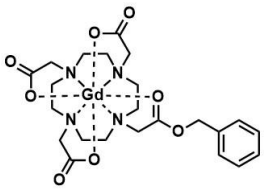

Note: peak around 8.4 min (at 240 nm and 254 nm) also appears in the water blank

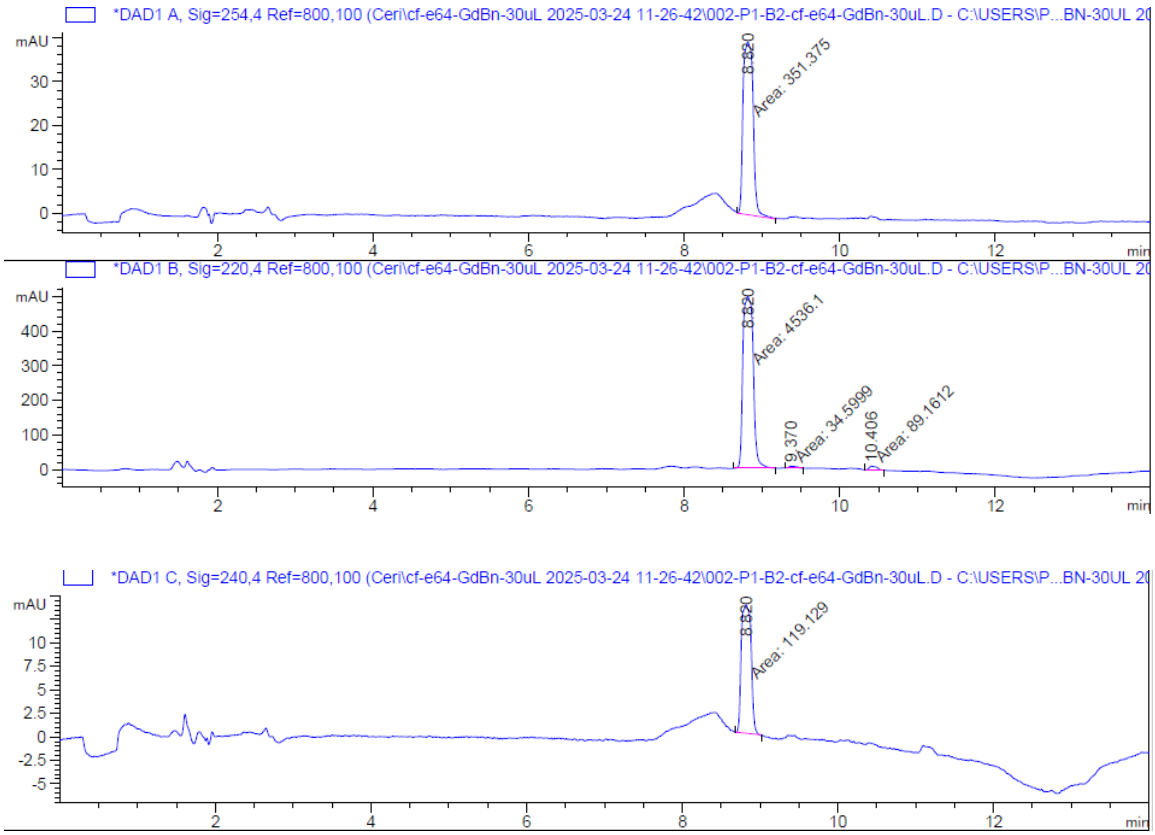

Signal 1: DAD1 A, Sig=254,4 Ref=800,100
Signal has been modified after loading from rawdata file!

Peak #	RetTime [min]	Type	Width [min]	Area [mAU*s]	Height [mAU]	Area %
1	8.820	MM	0.1489	351.37515	39.33614	100.0000
Totals :				351.37515	39.33614	

Signal 2: DAD1 B, Sig=220,4 Ref=800,100
Signal has been modified after loading from rawdata file!

Peak #	RetTime [min]	Type	Width [min]	Area [mAU*s]	Height [mAU]	Area %
1	8.820	MM	0.1526	4536.10254	495.29715	97.3441
2	9.370	MM	0.1119	34.59988	5.15204	0.7425
3	10.406	MM	0.1230	89.16119	12.08180	1.9134
Totals :				4659.86362	512.53099	

Signal 6: DAD1 C, Sig=240,4 Ref=800,100
Signal has been modified after loading from rawdata file!

Peak #	RetTime [min]	Type	Width [min]	Area [mAU*s]	Height [mAU]	Area %
1	8.820	MM	0.1450	119.12904	13.69464	100.0000
Totals :				119.12904	13.69464	

A3.4 Compounds from chapter IV

Phenol triacid, **100** – Analytical HPLC method 4

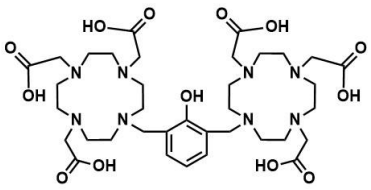

Total absorbance chromatogram:

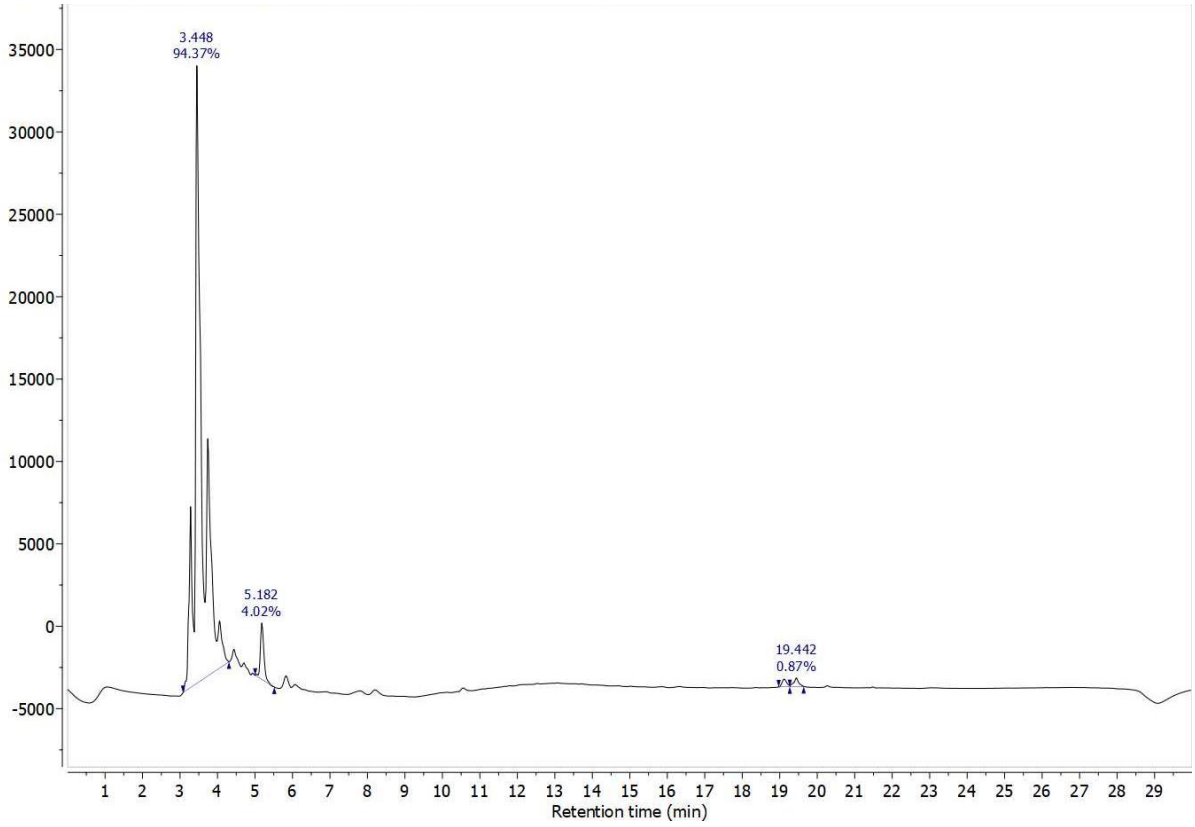

LuLuOH, **93Lu** – Analytical HPLC method 4

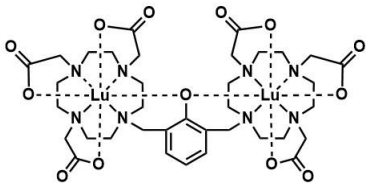

Total absorbance chromatogram:

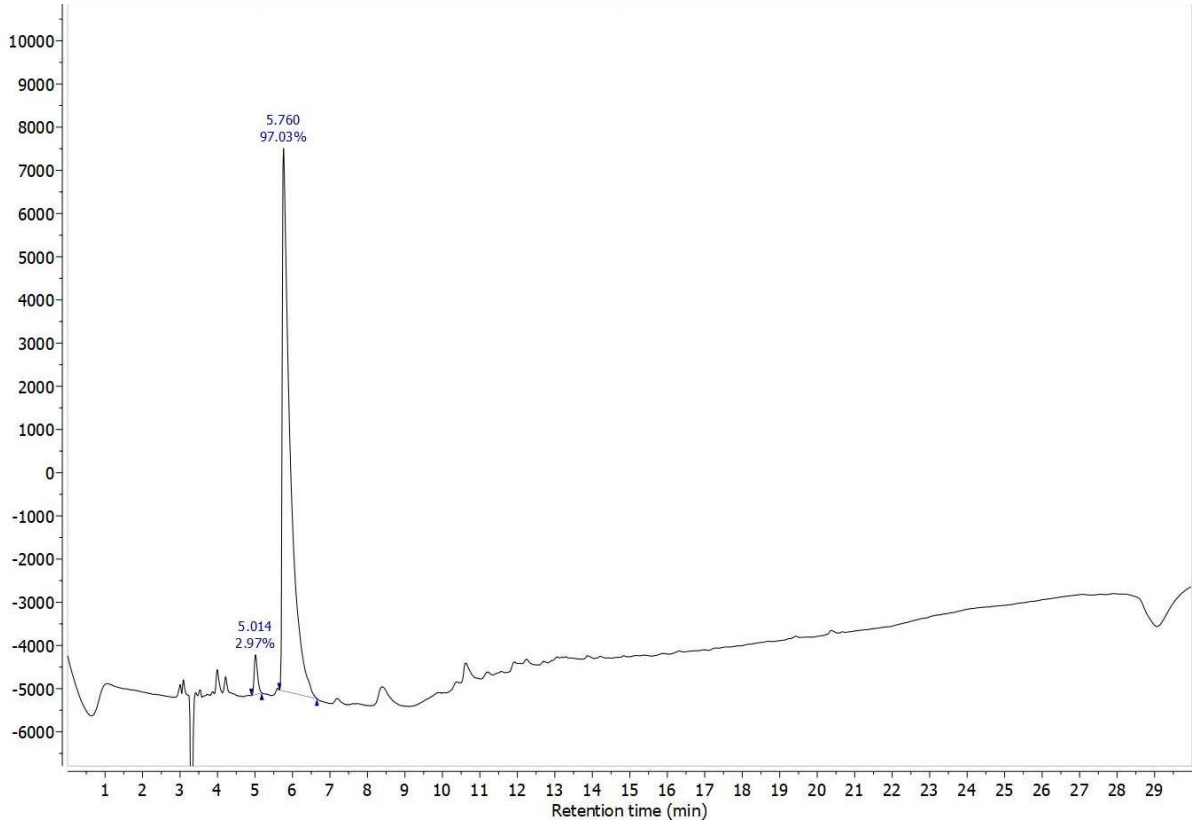

TbTbNH$_2$, **54** – Analytical HPLC method 4

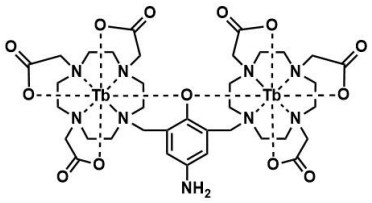

Total absorbance chromatogram:

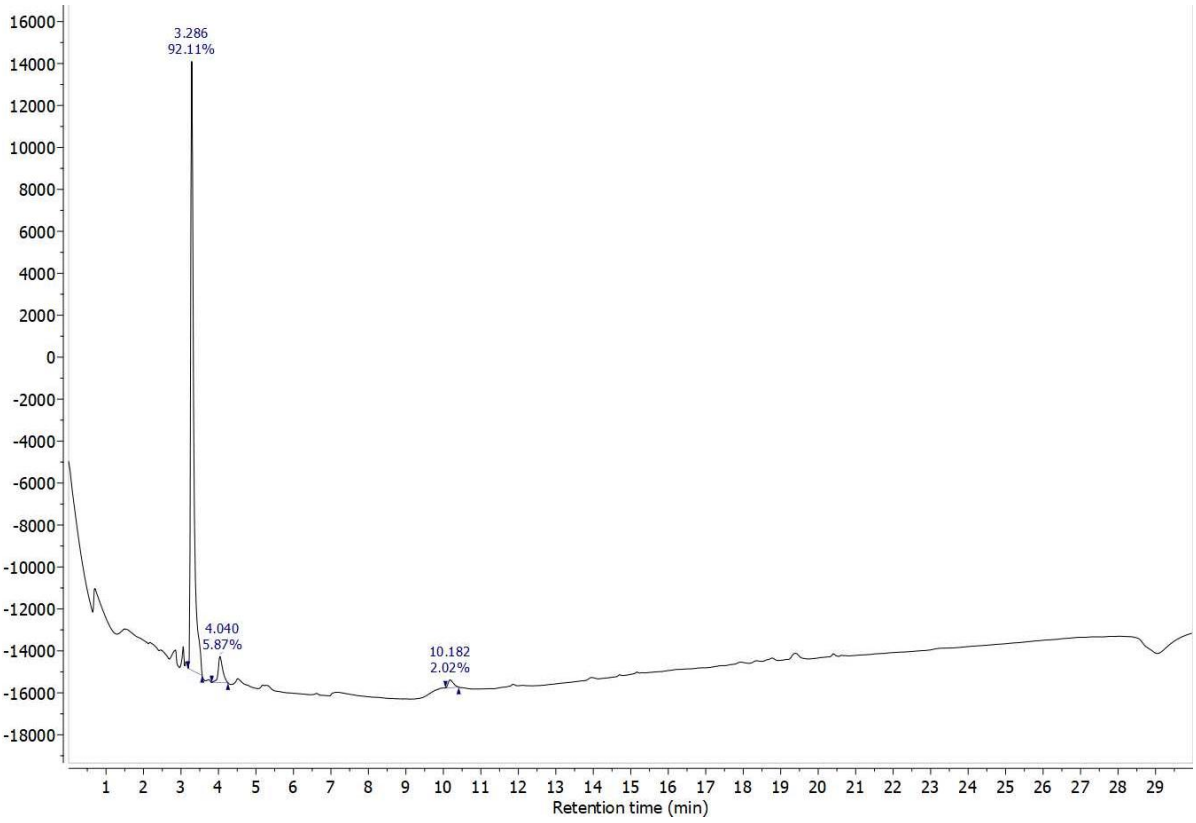

TbTbAzo, **53** – Analytical HPLC method 4

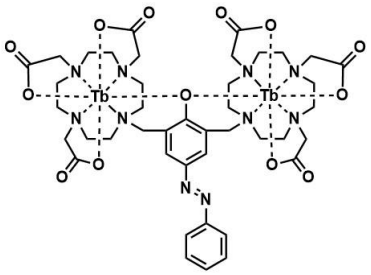

See also Figure A4.2.

Total absorbance chromatogram: